Application of fibre Bragg gratings for stress management in soft tissue biomechanics

Koulaxouzidis, Andreas

APPLICATION OF FIBRE BRAGG GRATINGS FOR STRESS MEASUREMENT IN SOFT TISSUE BIOMECHANICS

by

Andreas V Koulaxouzidis

A thesis submitted for the degree of
Doctor of Philosophy
in Biomedical Engineering

Department of Medical Engineering and Physics
Department of Electronic Engineering
King's College London
University of London

November 2000

CONTAINS PULLOUTS

to my parents

Vassilios and Maria

ABSTRACT

Interfaces of the human body with supporting surfaces are an active area of research in rehabilitation medicine. The engineering challenge is to design supporting surfaces that provide the desired mechanical properties and at the same time protect the soft tissues from necrosis and ulceration. It is believed that ulcers occur at the points were maximum vertical and shear stresses are observed. Persons with paralysis, peripheral vascular disease, diabetes, or other diseases that affect tissue viability are particularly at risk. However, whereas the role of pressure has been extensively studied, the role of shear has not, due to lack of instrumentation.

This thesis concerns the design of a shear and vertical stress transducer with application to the in-shoe measurement of stresses between the foot and the shoe insole. The transducer utilises fibre Bragg gratings written in optical fibres as the strain sensing element. The reflection spectrum of the Bragg grating is a narrow band around a central wavelength which shifts when axial strain is applied on the fibre. The Bragg gratings are then fitted into an elastically deforming structure is such a way that enables the calculation of the vertical and shear stress applied on the structure. Many similar structures can be connected in series to form a quasi-distributed in-shoe stress transducer. The measurement of the wavelength shift of the reflected light is based on multichannel spectroscopy using a CCD imaging spectrograph.

Two methods for the design of the stress sensor have been investigated. The first is based on the theory of elastic bending of beams. The sensor consists of two Bragg gratings fitted inside a metallic structure which is able to deform elastically under shear stress. This elastic deformation produces strain on the grating which results in wavelength shift. This sensor is able to resolve the magnitude and direction of shear stress. The experimental results in an enlarged version of the sensor (40mm diameter, 10mm thick) showed linear response to shear stress within ±10% in the range 0 to 250kPa. Sensitivity of the sensor response to shear direction was also observed, which was measured to be ±15%.

The second method is based on the theory of elasticity of solid polymers. Application of stress produces axial strain on the embedded fibres which can be calculated by measuring the wavelength shift of the reflected spectrum. Three fibres are embedded into each sensor, enabling the simultaneous measurement of vertical and shear components of stress acting on the top surface of the sensor. The experimental results from the measurement of three sensors (dimensions 10x10x3mm^3) showed linear response within ±15% in the range 0 to 120kPa. The average responsivity was measured to be 1.3pm/kPa for vertical stress, and 5pm/kPa and 0.5pm/kPa for shear stress parallel and perpendicular to the fibre axis respectively.

ACKNOWLEDGEMENTS

I acknowledge with gratitude my indebtedness to my supervisors: Dr Vincent Handerek for allowing me to undertake this research, and for his invaluable help and guidance throughout; Prof. Colin Roberts for his useful comments and suggestions particularly during the experimental evaluation of the transducers and during the writing up; Dr Melanie Holmes for her assistance and invaluable insight in the theoretical design, as well as for her thoroughness and speed in proof reading this manuscript. I am grateful to Dr Marilyn Lord for her guidance during the first stages of this research, and for allowing me to undertake this research.

Help and advice throughout the course of this research was forthcoming from many sources and I extend my thanks and appreciation to: Dr David Fenner and Dr Mike Clode, (Department of Mechanical Engineering) for their help and advice on the early stages of the transducer design; Mr B. Travel (Mech. Eng.), and Mr K Jennings of the Mechanical Engineering Section (ME&P) for fabricating the component parts of the experimental setup; Ms S Hails (ME&P) for helping me with the drawings of the metallic transducer.

A special thank to Dr. Raman Kashyap (BT laboratories, Martlesham Heath, Ipswich UK) for his invaluable help by kindly fabricating the fibre Bragg gratings used in this study.

I am particularly grateful to the Joint Research Committee for offering the studentship and funding this research.

I would also like to thank my friends Costas V, Andreas D, Katerina G, Giannis K, and Maria M, for taking me away from all this during this study.

CONTENTS

LIST OF TABLES

Chapter 6

LIST OF FIGURES

Chapter 2

Chapter 3

Chapter 4

Chapter 5

Chapter 6

Chapter 7

CHAPTER 1

Introduction

Mechanical forces acting on the skin produce stresses inside the soft tissue, which can be sufficient to prevent the blood supply in the contact region. Prolonged application of large forces leads to cell necrosis and ulceration (Scales, 1990). Patients with paralysis, the bedridden, wheelchair users, and patients with lower-limb prostheses are at high risk from the devolopment of pressure sores (Sanders *et al.*, 1996). Diabetic patients, who also suffer from peripheral vascular disease and peripheral neuropathy often develop plantar ulcers (Boulton ,2000). It is believed that mechanical stresses during walking play an important role in the plantar ulcer development.

The in-shoe mechanical stresses between the foot and the insole can be resolved into normal and shear components with respect to the plantar surface. Previously, research was focused on the effects of vertical pressure only, mainly due to the lack of instrumentation for shear stress measurements. Pollard *et al.* (1983) suggested that neuropathic ulcers occur in sites of maximum vertical or shear stress. He also suggested that footwear affect shearing stresses. The first in-shoe shear stress transducer was developed by Tappin *et al.* (1980). This transducer utilised magneto-resistive technology and measured shear stress in longitudinal and transverse directions. Several other transducers have been developed for the measurement of in-shoe shear stresses, utilising copolymer piezoelectric film transducers, and light intensity modulation.

In this thesis we demonstrate for the first time a fibre-optic transducer for the measurement of in-shoe shear stress. The use of optical fibres is expected to overcome the disadvantages of the existing sensors. Due to the small size of optical fibres, the size of every stress sensor can be small. Therefore, a large number of sensors can be fitted in the shoe insole, enabling quasi-distributed sensing. The absence of electrical conductivity of the fibres eliminates the danger of electric shock for both patient and operator. Optical signals travelling inside the fibres are not affected by the surrounding electromagnetic fields, the main source of noise in most sensing systems. Many fibre-optic sensors for point or quasi-distributed sensing have been developed. Fibre Bragg grating (FBG) strain sensors were eventually chosen as most suitable for this application because of their simple structure, their multiplexing capabilities, and their ability to be photo-inscribed into a single fibre.

1.1 Aims and Objectives

The overall aim of this study is to investigate the feasibility of a shear stress transducer using fibre Bragg gratings, with a primary target application the measurement of in-shoe stresses. The specific objectives of this study are:

- to design a sensor which will be able to measure the magnitude and direction of shear stress acting on its top surface, and to achieve maximum sensitivity of the sensor for the desired stress operating range.
- to implement the sensor and experimentally evaluate the principle of operation.
- to test the sensor response to static vertical and shear stress.

1.2 Outline of Thesis

This thesis is composed of seven chapters. Following the introductory Chapter 1, Chapter 2 reviews the subject areas relevant to the research described in the thesis. This includes a background review of the recent techniques for the measurement of pressure and shear stresses applied on the soft tissue in the skin-prosthesis interface, with particular reference to the methods for in-shoe pressure and shear stress measurements. The available optical fibre sensors for point and quasi-distributed sensing will be briefly reviewed, along with comments on their applicability for the implementation of an in-shoe sensor. The chapter continues with the description of the principle of operation of the fibre Bragg grating sensor and its fabrication methods. The methods for the interrogation of fibre Bragg grating array sensors will then be reviewed, and their suitability for the implementation of the in-shoe transducer will be examined.

The experimental setup, which was implemented for the laboratory testing of the sensor response to vertical and shear stress, will be described in chapter 3. The optoelectronic system for reading the fibre Bragg grating sensors will also be described. The system was calibrated and tested prior to measuring the sensor response. The calibration procedure will be explained in that chapter.

Two different methods have been developed for the implementation of the shear stress sensor, named the "*metallic sensor*", and the "*elastomer sensor*". The design, principle of operation, and the experimental evaluation of the metallic sensor will be presented in chapter 4. Issues from the theory of the elastic bending of beams which are directly related to the sensor design, will also be given.

The elastomer sensor will be presented in chapters 5 and 6. Chapter 5 describes the design of the sensor using the classic theory of elasticity in solid polymers, which is based on the assumption that the elastic behaviour of the material is independent of the presence of the embedded optical fibres. The theory of elasticity in solid polymers will be briefly described. Experimental results from a single-fibre sensor will also be given.

The theoretical model the elastomer sensor is reconsidered in chapter 6, using the theory of composite materials. The fabrication procedure, and the experimental results from measuring three elastomer sensors will be presented. Comparison of the theoretical predictions of the two models, with the experimental results from the measurement of the sensor response to shear and vertical stress will be given in this chapter.

Chapter 7 concludes this thesis with a general discussion on the performance of the shear stress sensor, and suggestions for future improvement of the sensor and the development of the in-shoe transducer.

CHAPTER 2

Background and Literature Review

Introduction

The factors which could lead to the development of pressure sores, and the role of the mechanical stresses on ulcer formation will be explained in this chapter. The methods which have recently been used for the measurement of the stresses applied on the skin will be briefly reviewed, with particular reference to the measurement of in-shoe pressure and shear stresses. The potential advantages of optical fibre sensors for point and quasi-distributed sensing, and especially those of fibre Bragg gratings, will be discussed. The principle of operation of the fibre Bragg grating as strain sensor will then be explained. Finally, the current techniques for grating fabrication, and the methods for the interrogation of multiple Bragg grating array sensors will be reviewed.

2.1 Mechanical stresses on ulcer formation

The mechanical force applied externally on the skin surface is an important factor in the development of skin damage and pressure sores. According to Bader, a pressure sore is the result of tissue necrosis caused by the occlusion of the blood supply to the skin and the underlying soft tissues following sustained compression of blood vessels. Tissue damage occurs when stress above a critical value acts for a critical period of time in the tissues between the skeleton and a surface supporting the body. Healthy subjects do not develop pressure ulcers because, due to the motions of the body, stresses are not applied for sufficient time and magnitude. (Bader, 1990, pg.15).

Several factors responsible for the development of pressure sores are (Bader, 1990, pg.31):

- reduced blood flow to the tissue under stress because of heart failure or other cardiovascular diseases
- immobility of patients lying or sitting on a hard surface for prolonged times
- reduction of tissue stiffness due to dehydration as a result of blood loss, diuretic therapy, and diabetes.

The interface stresses are transmitted through the soft tissues, producing stresses and strains inside the tissue. The mechanical properties of the soft tissue will therefore influence the

breakdown process. Areas with minimal tissue covering over bony prominences are more susceptible to breakdown than areas of thick tissue and reduced stiffness (Bader, 1990, pg.191).

Because persons with disabilities usually subject the skin and underlying soft tissue to stresses for longer duration than in normal subjects, the tissues are at higher risk of breakdown. Persons with paralysis, peripheral vascular disease, diabetes, or other diseases that affect tissue viability and quality are particularly at risk (Sanders *et al.*, 1996). Individuals who use wheelchairs or who are bedridden, including those with spinal cord injury or other functional restrictions are at particular high risk from ulcers in the sacral and ischial regions. Patients with a lower-limb prostheses subject their residual limb to repetitive pressure, which often leads to tissue breakdown. Persons with insensate feet or poor circulation in their extremities often experience foot ulcers (Sanders *et al.*, 1996).

The mechanical stress can be divided into two components, direct stress normal to the skin surface, and shear stress applied tangentially to the surface. The effect of normal stress has been examined for continuous pressure of high magnitude (Kosiak *et al.*, 1958), and for repetitive mechanical loading (Brand, 1976). Both conditions lead to ulcer formation. The combination of normal and shear stress has been found to be particularly damaging to the skin and underlying tissues. Bennett *et al.* (1979) reported that at a sufficiently high magnitude of shear stress (approx. 10kPa), the normal stress necessary to occlude blood flow was reduced by one-half if a simultaneous shear stress was applied. Later, Zhang and Roberts (1993) investigated the effect of shear forces externally applied to skin surface on the underlying tissues. Vertical stress in the range of 3.8-13kPa was applied on the dorsal aspect of thigh in four healthy subjects. Shear stress was simultaneously applied in the range 1-12.5kPa. The effect of stresses on the tissue was examined by measuring the skin blood flow using a laser Doppler flowmeter. They concluded that when shear stress equal to the vertical stress was applied, the blood flow reduced by 45% from the flow when only vertical stress was applied. The study suggests that the resultant force is the most critical parameter in assessing the effect of stress applied on the skin, and that shear stress has the same effect of vertical stress on the skin and underlying tissue.

2.2 Measurement of interface stresses

The importance of vertical and shear stress to skin damage and ulcer formation has therefore been well established. The design challenge for the rehabilitation engineer is to create a body support interface that provides stability but avoids excess loading of the skin contact region which could lead to tissue breakdown (Sanders *et al.*, 1996). Once breakdown occurs, a period of rest is required and the person is unable to use the wheelchair, prosthesis, or shoe.

This can impair mobility and be very frustrating for the patient. In several cases, the tissue does not heal and surgery to repair or remove tissue is required (Sanders and Daly, 1996).

Of potentially strong benefit in prosthetics are measurement methods to quantitatively analyse the interface stresses. They are necessary tools during the design and fitting of the artificial socket, since they allow the comparison of interface stresses for different socket designs, alignments, and materials (Sanders, 1995). They can also allow evaluation and improvement of analytical computer models intended to predict interface stresses. For example, Reynolds and Lord (1992) have used Finite Element modelling for the compression of the residual lower limb contained in a prosthetic socket. The direct pressure at the limb-socket interface for different material properties and socket alignment and rectification are inputs of the computer model. This allows the assessment of the tissue loading before the prosthesis is fabricated or fitted on the amputee patient.

The methods which already exist, their capabilities, applications and limitations, will be presented in the next sections. Many sensing methods have been developed for measuring mechanical stress on the skin. The interest of this review will mainly be focused on the shear stress sensors. Because the primary target application of the fibre-optic sensor presented in this thesis is the measurement of in-shoe shear stresses, emphasis will be given in the presentation of the available devices and methods for measuring stresses beneath the foot.

2.2.1 Measurement of stress at the residual limb-prosthetic socket interface

The sensors used for the measurement of interface stress between the residual limb and the prosthetic socket are divided in two groups, based on the method of placement of the sensor at the interface (Sanders, 1995). The first group includes sensors which are inserted between the skin and the socket. A widely used sensor is a diaphragm deflection strain gauge (Kulite[1] sensor). The sensing element is 3.2mm in diameter and 0.8mm in thickness, which is able to measure normal stress only. It is a monolithic integrated circuit Wheatstone bridge formed on the silicon diaphragm. Several problems associated with this transducer are the relatively high stiffness of the sensor compared to the tissue and the prosthesis material, which disturbs the stress distribution on the sensor diaphragm and leads to underestimation of the normal stress by 10% (Patterson and Fisher, 1979). Other limitations of the sensor are i) the presence of the cables restricts the movement of the patient during test, ii) it provides data for a single isolated point, iii) misalignment of the sensor occurs while wearing and removing the socket (Sanders, 1995). Quasi-distributed sensing has been achieved using piezoresistive sensor

[1] Kulite Semiconductor Products, Inc. 1 Willow Tree Road, Leonia, NJ 07605

arrays made by Tek-Scan[1] (Sanders *et al*, 1992). The measurements, however, are restricted to normal stresses only.

By fitting the sensors in the socket wall, the problem of tissue deformation and misalignment were eliminated. Sanders and Daly (1993) demonstrated a three-directional force transducer system. A cantilever beam deflection principle was used for the measurement of the two components of shear stress, each one measured using four strain gauges in bridge configuration attached on the sides of the cantilever. A diaphragm strain gauge measures the vertical stress. The full-scale output was measured 175kPa for vertical and 75kPa for shear stress. Resolution of 0.15kPa, 0.73% crosstalk, and a dynamic response of 117Hz were also measured. The active area of the sensor is 6mm in diameter, the overall size however restricts its practical use. Furthermore, amplification electronics must be carried by the patient. Distributed sensing in four locations in the residual limb-prosthesis interface was performed.

Williams *et al.* (1992) proposed a three-dimensional sensor of small size and shape. It is 16mm in diameter and 3.8mm thick. Shear measurement is achieved using three aluminium disks, each of the outer two containing a semiconductor field coil and the centre one containing a magnet. This is an improved version of the unidirectional shear stress sensor presented by Tappin *et al.* (1980). All disks are separated by layers of rubber which deform under shear loading, causing a position change of the magnet relative to the field coils. For normal stress measurement, a strain gauged diaphragm on an annular ring was allowed to move along four mounting pins when the diaphragm was deflected by a fixed indenter. The strain-gauged diaphragm is positioned below the shear sensing element described above. The force measuring range is 0-50N for shear and 0-100N for vertical (roughly 250kPa shear and 500kPa vertical), 5% accuracy, and dynamic response 0.1-100Hz. In-bench testing showed that crosstalk between the two perpendicular shear directions was minimal, but the hysteresis was relatively large, approximately 8% fullscale output and, 2% for vertical. Due to the viscoelastic nature of rubber, 5% creep in shear was reported.

2.2.2 Foot pressure measurement

It has already been mentioned that patients suffering from diabetes mellitus are at high risk of developing foot ulceration. Foot ulceration in diabetic patients can be caused when one or more of the following factors exist (Boulton, 2000):

- Peripheral Vascular Disease (PVD). A minor injury and subsequent infection of the foot increases the demand for blood supply. The reduced circulatory capacity of the patient suffering from PVD can possibly lead to ulceration.

[1] Tek-Scan Inc., 307 West First Street, South Boston, Ma, USA.

- Diabetic Neuropathy. This condition results in sensory loss of pain and reduction of sweating. The insensate and dry foot is at great risk of painless injury and subsequent ulceration.
- Deformity. Any deformity occurring in the diabetic foot, for example prominence of metatarsal heads, increases ulcer risk because of unusual load distribution.

When many of the above factors simultaneously exist, the risk of foot ulceration at the points of maximum vertical or shear stress is increased. Several researchers have been working on the measurement of the stresses developed on the plantar surface during walking, and many instrumentation methods have been developed. The measuring techniques can be classified into two categories:

1. Techniques for barefoot measurement
2. Techniques for in-shoe measurement.

All devices developed for measuring barefoot plantar stresses are floor-mounted rectangular surfaces and measure less than three quarters of a metre square. As a result, only one step can be analysed at a time from a walk consisting of several. A second disadvantage is that the walk is usually altered in order to step on the device, which can lead to false measurements.

Early devices for measuring pressure between the barefoot and the ground during walking, as well as devices for in-shoe measurements have been extensively reviewed elsewhere (Lord *et al.*, 1986; Alexander *et al.*, 1990; Cobb and Claremont, 1995; Hosein, 1996; Pitei, 1998). A brief review of the latest devices will be given here.

2.2.2.1. Barefoot measurement

A popular method for dynamic measurement of the stress distribution on the plantar surface is the dynamic pedobarograph described by Franks *et al.* (1986). In this system, a photographic paper foil is placed on top of a glass plate. The upper surface of the foil is covered with light-proof material to eliminate background illumination. When the glass plate is illuminated at the edges, it acts as a light guide and total internal reflection occurs at the glass-air boundaries. Application of pressure on the foil brings it in contact with the glass, and no total internal reflection occurs. Light rays illuminate the lower side of the foil. The intensity of the scattered light is proportional to the pressure applied. The scattered light from the foil is reflected from a mirror and filmed on the side with 25 frames/s. This system provides higher spatial resolution than any other method based on discrete transducers (Franks, 1997). The system is capable of measuring vertical stress up to 2000kPa. Disadvantages of the system are the relatively low dynamic response, the large size, and the complex calibration procedure.

Hughes *et al.* (2000) have recently demonstrated a high resolution pressure sensor for barefoot measurements. The device uses an interferometry technique that involves the use of a He-Ne laser. The laser beam is expended and directed through a plate made of a transparent material (Perspex). Part of the beam is reflected at the bottom of the plate, while the rest continues through the plate until being reflected off the top surface of the plate. The two beams then combine and interfere at a certain point, where an interference pattern is produced. This pattern is then captured by a CCD camera and transferred to a computer for signal processing of the interference pattern. The system was demonstrated using a 500x700 pixels CCD camera, capable of capturing 25frames/s. The dimensions of the sensing area (equal to the dimensions of the transparent plate) were 6cm x 9cm, giving a spatial resolution equal to 70pixels/cm^2. The dynamic range of the system was measured to be 1-1000kPa. Drawbacks of the system are the large thickness of the sensing plate and the supporting metallic frame (overall dimensions are not reported), and the relatively low stress resolution of the system (50kPa) limited by the viscoelastic nature of the transparent material.

Thinner, lighter, and therefore more compact devices are the pressure-mat devices. The spatial resolution depends on the number of discrete sensors per unit area, and, to date, it is lower than the resolution of the optical pedobarograph. These systems utilise capacitive transducers, force-sensitive resistors, or piezoelectric material for the implementation of the discrete sensing elements. Table 2.1 gives details of currently available pressure-mat systems.

Source/Device	Mat dimensions	Number of transducers /type
Novel[1] Gmbh EMED System	310mm x 480mm	2 to 9 per cm^2 / capacitive
Cavanagh and Hennig (1982)	150mm x 375mm	512 / piezoelectric
TekScan[2] Inc.	500mm x 500mm x2mm	2064 / force-sensitive resistors

Table 2.1: Available pressure-mat systems.

The main disadvantage of all the previous devices is that they can only measure vertical stress. Discrete-transducer pressure-mat systems for measuring shear stress have not been reported. Shear forces can be measured using force-platforms. They utilise strain gauges (AMTI[3]), or piezoelectric transducers (Kistler[1]) to measure the vertical and horizontal components of the total force applied on the platform during walking. A major disadvantage

[1] Novel$_{Gmbh}$ Beichstrasse 8, 8000 Munchen 40, Germany
[2] TekScan Inc., 451 D Street, Boston, MA, 02210, USA
[3] Advanced Mechanical Technologies Inc., Newton, MA

is the inability to provide information of the stress distribution on the plantar surface. Furthermore, it is possible that more than one foot is in contact with the measuring surface. In that case, the device output will contain information from both feet. It is apparent that this is a problem when the device is used for measuring the magnitude and timing of peak forces. Recently, however, Begg and Rahman (2000) proposed a method for reconstruction of foot-ground reaction forces from force-platform readings of two consecutive footfalls. The force-time curve can be estimated within 3% accuracy, provided that the sampling rate is high (200Hz), and an undisturbed, previously recorded, force-time curve is available.

2.2.2.2. In-shoe measurement

In-shoe stress measurements have two advantages compared to barefoot measurements. Firstly, the effect of footwear on the plantar stress distribution, and the subsequent ulceration can be investigated. Secondly, in-shoe systems can measure stress during several consecutive steps. The main disadvantage of these systems is the relatively low resolution compared to barefoot measurements, which is limited by the size of the sensing elements. Problems related to the thickness and rigidity of the sensors have also been mentioned (Hosein, 1996, pg.71). A stiff transducer could also act as a local hard spot causing pain to the subject with the result that the gait is altered in order to avoid pain.

In this section, the most important in-shoe transducers for vertical and shear stress measurement will be described. The transducers are classified in two categories: vertical pressure measurement only, and shear (or shear and vertical) stress measurement.

- **vertical stress measurement**

Vertical pressure measurement has been achieved using capacitive transducers. A capacitive transducer consists of two conducting plates separated by a dielectric layer. Application of stress normal to the plates causes elastic compression of the dielectric layer, which thus increasing the capacitance. An electronic system is then used to interface the transducer to a computer for signal processing and storage. One commercially available system is the Computer Dyno Graph System (CDG System) by Infotronic[2], which provides insole layers incorporating 8 prepositioned 30x30x1.5 (mm) transducers. The readout system is carried by the patient, and is capable of storing data for 20s at a sampling rate of 50scans/s per transducer. The data are then downloaded to the computer for further analysis. The accuracy of this system is 10% full scale. A second system which utilises capacitive sensors is the EMED System by Novel$_{Gmbh}$[3]. The insole layer accommodates 72 transducers, 1 per cm^2.

---

[1] Kistler Instruments Ltd, Alresford House, Mill Lane, Alton, Hampshire GU34 2QJ, UK
[2] Infotronic Medical Engineering, PO Box 73, 7650 AA Tubbergen, Netherlands.
[3] Novel$_{Gmbh}$' Beichstrasse 8, 8000 Munchen 40, Germany.

The dynamic range is 20-1.5MPa, and the highest sampling rate is 200scans/s. Both spatial resolution and sampling frequency are significantly higher than the CDG System.

A number of commercial systems have been developed using force-sensitive resistive (FSR) technology. The sensors are implemented by printing conductive electrodes onto a lower plastic sheet, and fixing a conductive polymer or elastomeric sheet on the top. Application of vertical pressure brings the material in contact with the electrodes, and a resistor is created. Electrical resistance decreases as the vertical load increases. The Langer Biomechanics Group[1] has developed the Electrodynamograph System (EDG System). Each foot insole has 7 sensors with dimensions 16x12.7x0.4 (mm) with a pressure sensitive area 11x5.5 (mm). The measurement range is 0-1.5MPa with sensitivity of ±30kPa. The sensors exhibit nonlinearity of 5-10%, a high hysteresis error of 15-20% and drift of 8% after 1min (Cobb and Claremont, 1995). Data acquisition and storage is done by a waist-mounted unit, which is able to read at 200samples/s for 5s. FSR technology is used by TekScan[2] F-Scan Gait Analysis System. This system uses conductive and resistive inks on a flexible mylar substrate to form a matrix of 960 sensors on a disposable, 0.1mm thick, insole. Each square 5mm^2 sensing element is formed by depositing a layer of resistive ink between two orthogonal conductors. Aluminium tracks deposited on the external surfaces provide connection to a small instrumentation unit worn on the ankle. The matrix is scanned at 165Hz per sensor with a resolution of 8 bits, giving a sensitivity of ±4kPa. Data are transmitted over a lightweight cable to a computer. The advantage of this device is that the insoles can be cut to size. Rose *et al.* (1992) have used this device for static and dynamic measurements in normal subjects. Calibration between the sensors was found to be poor, and the sensors showed significant wear with use.

Nevill *et al.* (1995) have used copolymer (PVdF-TrFE) piezoelectric film to develop a 10 x 10 x 2.8 mm direct pressure sensor. The sensor was cut from a laminate formed by bonding 500μm copolymer film between an upper brass sheet and a lower double-sided copper-clad board. The laminate provided sufficient stiffness to prevent significant errors caused by lateral stretching and bending of the film. Eight sensors were placed in a 3mm thick insole. An instrumentation unit containing 8 charge amplifiers is strapped to each ankle. A further waist-mounted unit provides power to the two ankle units and an interface to connect the system with a computer. Over the measurement range 0-1MPa, linearity was found to be <1.5%, hysteresis error <1.5% and resolution ±1kPa. The frequency response

[1] The Langer Biomechanics Group UK, Unit 7, The Green, Cheadle, Stock-On-Trent, UK.
[2] TekScan Inc., 451 D Street, Boston, MA, 02210, USA

extends from 0.008Hz to 250Hz. The sensors are sensitive to the variation of temperature and humidity and compensation is applied to the data.

A new system for vertical stress measurement has recently been developed by Pataky *et al.* (2000). The system utilises FSR sensors, 1mm thick, which are attached at the area of interest by an adhesive tape. The advantage of the sensors is their long life. The performance of the sensors is claimed to be decreased by 5% after 10 million cycles. The readout system weights 280g and is carried by the patient. It is able to scan 2 sensors at 96Hz, and the storage capacity is 8 days or 60,000 steps. The device is mainly intended to be used as a compensatory mechanism for the loss of pain sensation, by continuously measuring the pressure at the points of interest. A sound alarm signal informs the user for pressure above a threshold set by the operator. The main disadvantage of the device is the small number of sensors which can be read. The size of the sensors was not reported.

- **shear stress measurement**

To investigate the effect of shear forces in ulcer development, a discrete shear transducer utilising magneto-resistors was developed by Tappin and Pollard (1980). The magneto-resistive principle relies on the change of the resistance of a semiconductor magneto-resistor by changing the surrounding magnetic field. Two non-magnetic stainless steel disks, 16mm in diameter were bonded together with a layer of silicone rubber to produce a device 2.8mm thick. The magneto-resistor was fixed on one of the disks. A permanent magnet was fixed on the other disk, opposite to the magneto-resistive element. One of the disks had a ridge which matches the groove made on the other disk. This arrangement restricts the relative motion of the upper disk under shear stress to one direction only, parallel to the groove axis. Movement of the permanent magnet with respect to the magneto-resistive element results in change in the resistance proportional to the applied force. The elasticity of the silicone rubber provides the restoring force to return the magnet to its equilibrium position. Deflection of the magnet by 0.6mm corresponds to shear stress equal to 250kPa. By aligning the groove in either the longitudinal or the transverse direction, relative to the foot, the related shear component could be measured. A bridge circuit provides temperature compensated output voltage. The frequency response exceeds 500Hz.

Laing *et al.* (1992) used similar sensors for in-shoe measurements. The sensors were 10mm in diameter and 1mm thick. The data acquisition and storage was done by a portable unit carried by the patient. The data from 8 transducers could be acquired and stored in the unit for 8s at 125Hz per transducer. The data are then downloaded to a computer.

Lord and Hosein (Lord and Hosein, 2000; Hosein and Lord, 2000) have recently presented clinical results from measuring in-shoe vertical and shear stress in diabetic patients and normals using a biaxial magneto-resistive shear stress transducer. The transducer is a

biaxial version of the transducer developed by Williams *et al.* (1992) which was described in section 2.2.1. The in-shoe transducer accommodates 3 sensors and is shown in Fig.2.1.

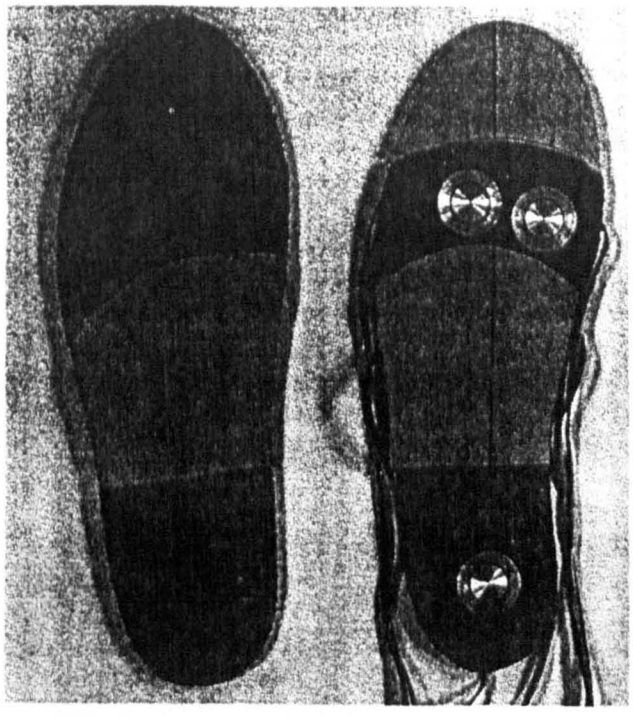

Fig.2.1: The magneto-resistive in-shoe shear stress transducer developed by Hosein and Lord (2000).

A uni-axial shear stress sensor was developed by Lebar *et al.* (1996). The transducer consists of an upper and lower bronze component, each measuring 15mm in diameter and 3.8mm in thickness. The lower component accommodates the electro-optical circuitry, which is a LED and a photodiode. A central groove limits the movement of the upper component to that of unilateral translation. The upper component has a wedge-shaped protrusion in the centre. Two compartments on the lower component contain 2 spring plates, which provide the restoring force as shear stress is applied. When subjected to shear stress, the wedge either increased or decreased the amount of light passing from the LED to the photodiode. Static calibration of the sensor to a shear force of 22.3N applied along the groove in both directions, gave mean non-linearity and hysteresis of 6.6% and 11.1% respectively. Crosstalk to shear perpendicular to the groove was measured as 1% of full-scale. Clinical results from measurement of in-shoe shear stresses at four locations were also reported. A major disadvantage of the sensor is that the shoe has to be removed and the sensor rotated by 90° in order to measure longitudinal and transverse shear stress. Furthermore, the responsivity of the sensor to shear depends strongly on the direction of shear stress (-21mV/N at reverse shear, and 14mV/N for forward shear).

A biaxial in-shoe shear force transducer has also been developed by Akhlaghi and Pepper (1996). Four 10x10x3.6 mm piezoelectric shear stress sensors are fitted per shoe insole,

enabling the measurement of the two components of shear stress to be recorded in both feet simultaneously, Fig.2.2. The connection of the sensors to the ankle-mounted charge amplifier unit was done by two 1mm diameter coaxial cables per sensor. Static calibration of the sensors was done for shear force 0N to 200N. The linearity and resolution of the system was measured to be 2% and 1N respectively.

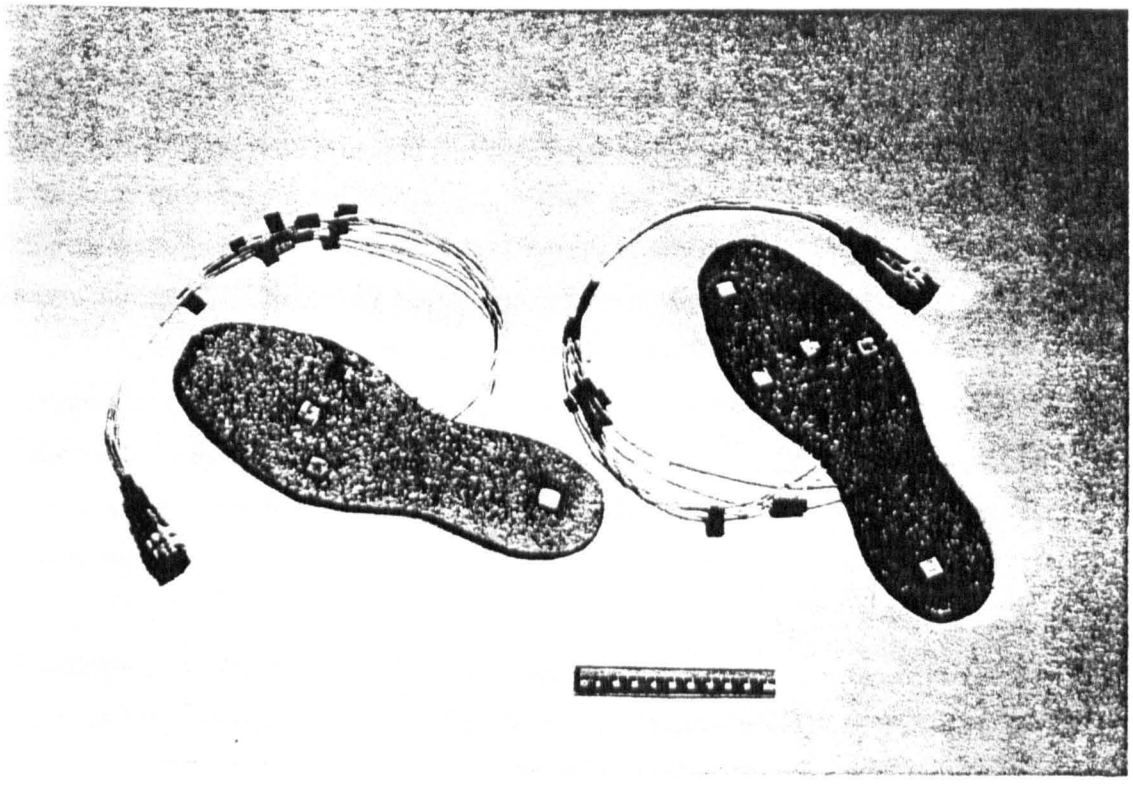

Fig.2.2: Biaxial in-shoe shear stress transducer developed by Akhlaghi and Pepper (1996).

2.3 Transducer specifications

The transducer specifications, which are presented in this section, are based on the results from previous studies of in-shoe shear and vertical stress measurements, using the devices mentioned in section 2.2.2.2.

Spatial resolution

Spatial resolution of a discrete-sensor transducer is determined by the sensor dimensions and the distance between adjacent sensors. High spatial resolution requires small sized sensors. Furthermore, a large sensor area underestimates the local peak stresses, due to averaging of the stress applied on the sensor (Hosein, 1996, pg.64). A small sensor size is therefore required. Lord (1993) concluded that, maximum peak pressures could be measured accurately if the sensing element had an area of 0.1mm x 0.1mm. At present there is no system with such a high resolution.

In this thesis, the principle of operation of a new sensor will be evaluated by considering a 10mm diameter metallic sensor (chapter 4), and a 10mmx10mm square elastomer sensor (chapters 5,6). This size is similar to the recent in-shoe transducer dimensions, for example the 10mm-diameter sensor by Laing *et al.* (1992), and the 10mm square sensor by Akhlaghi and Pepper (1996). The sensor thickness was chosen to be 3mm, which allows its fitting in a 4-mm insole (Hosein, 1996, pg.139).

Dynamic range

The different sensor sizes, as well as the clinical trials in a wide variety of subjects, show significant variation of the maximum in-shoe vertical and shear stresses measured by different researchers. Based on the recent results of Hosein and Lord (2000), and Lord and Hosein (2000), for studies on normal subjects and diabetic patients using the magneto-resistive biaxial shear stress transducer developed by Williams *et al.* (1992), the overall maximum shear stress is expected to be 130kPa. The maximum vertical stress was measured using the F-Scan system (section 2.2.2.2), and was found to be 370kPa. For safety, our sensors will be designed to withstand and measure shear stress up to 250kPa, and up to 500kPa vertical stress respectively.

Resolution

The device should be able to distinguish increments of 5kPa or less in both vertical and shear stress modes (Hosein, 1996,pg.64).

Frequency response

The highest frequency component during walking is expected to be approximately 75Hz (Simon *et al.* 1981). In accordance to the Nyquist sampling theory, the sampling rate of the readout system should be at least twice, ie. 150Hz. In practice the sampling rate required usually is three to ten times higher than the maximum frequency under investigation. The required scanning speed of the FBG readout system in our system was chosen to be 300Hz.

Number of sensors

The largest number of sensors is found in the in-shoe transducers developed by Laing *et al.* (1992), and Aghlaghi and Pepper (1996), where both systems are able to acquire data from 4 sensors per shoe. Previous studies (Hosein, 1996, Lord and Hosein, 2000), shows that maximum stresses occur below the heel, the 5 metatarsal heads, and the hallux. The sensor dimensions, and the FBG readout system, which will be designed and proposed in this thesis (section 7.4), will enable the placement and acquisition of 18 sensors (9 per shoe insole), and the simultaneous measurement of shear and vertical stress.

Other features

- Non-toxic, hypo-allergenic sensor materials and insole layer
- Easy and quick setup and calibration procedures
- Reasonable cost. Table 2.2 gives approximate prices of some commercially available systems, valid on the date of publication.

Company name	Product	Cost
TekScan	'F-Scan' in-shoe pressure system	£15000
Kistler Instruments (UK) Ltd.	Force platforms 'Parotec' in-shoe pressure system	£9200-23000 £9700-11100
Preston Communications Ltd[1].	'Mustgrave footprint', single / double force platform, utilising FSR technology	£15000 / £22000
Novel$_{Gmbh}$	EMED in-shoe system and pressure platforms	£7000-£20000

Table 2.2: Comparable costs of commercial systems for measuring force and pressure beneath the foot (Booth *et al.*, 1998).

2.4 Problems encountered in the existing systems

The hypothesis that shear stresses applied on the soft tissue as a result of wearing prosthetics and shoes are significant in the development of tissue ulcers, has been established for more than 20 years ago (Bennett *et al.*, 1979). Since then, many researchers have being working on the development of reliable devices for measuring those stresses and to provide clinical evidence to support this hypothesis (Cobb and Claremont, 1995). Clinical evaluation of those devices which were briefly presented in the previous sections, showed practical problems and limitations. Common drawback of the previous methods is the necessity of electronic devices to be carried by the patient during testing for filtering, amplification, and storage of the signals received by the sensors in order to improve the signal-to-noise ratio. For the case of in-shoe measurements, which is the main application of interest in this study, those circuits have to be placed as close to the in-shoe layer as possible in order to reduce the electrical resistance and noise-collecting ability of the wires that connect the sensors with the readout system. Ankle-mounted or waist-belted are the two configurations used for the attachment of the devices to the subject, which, combined with the relatively thick cables, are likely to cause discomfort and obstruct the normal gait of the subject.

[1] Preston Communications Ltd., New Cross, Dinbren Road, Llangollen, Clwyd LL20 9TF, UK.

Both the complexity of the readout system, and also the size of the body-mounted devices and cables increase when a large number of sensors have to be used for distributed sensing of in-shoe stresses. Up to date, the piezoelectic device for biaxial shear stress measurement developed by Akhlaghi and Pepper, utilises the largest number of sensors (8 sensors, 4 per foot) (Akhlaghi and Pepper, 1996). The size of the sensors is sufficiently small to allow a larger number of sensors per foot insole. Such application has been reported by Nevill *et al.*, who fitted 8 sensors per foot (Nevill *et al.*, 1995). In that case, however, vertical only stress was measured, which reduces the required number of charge amplifiers to one per sensor, instead of two for biaxial stress sensing.

Distributed in-shoe shear stress sensing can therefore be achieved only if the size of the sensing elements is small, and the readout system is capable of interrogating many sensors without disturbing the measurement with its size or weight. The relatively large diameter (16mm) of the triaxial transducer developed by Williams *et al.* does not allow the simultaneous shear stress measurement of the five metatarsal heads (Williams *et al.*, 1992) since there is not enough space between adjacent sensors to accommodate the insole mounting shown in Fig.2.1 (Hosein, 1996, pg.143). The same restriction applies to the optoelectric sensor developed by Lebar *et al.* (1996). The magneto-resistive sensor by Laing *et al.*, is only 10mm in diameter, however uni-directional shear stress measurement was only reported (Laing *et al.*, 1992).

A source of error, which was measured to be particularly important in the piezoelectric-based transducers, is the susceptibility to electromagnetic interference (Cobb and Claremont, 1995).

In order to overcome these various difficulties and to achieve the demands of high sensitivity and small size, a new approach of transduction using fibre Bragg grating sensors is proposed in this thesis. The use of fibre Bragg gratings has a number of potential advantages, which will be presented after reviewing the recent methods for point sensing using optical fibres.

2.5 Selection of the optical fibre sensor for the in-shoe transducer

A brief review of the existing optical fibre sensors for axial strain measurement will be given in this section. The sensors are mainly examined in terms of their applicability for the implementation of the shear stress transducer, rather than comparing their specifications as strain sensors. Specifications regarding the strain and temperature sensitivity and dynamic range can be found in the relevant references.

The wide variety of optical fibre techniques, the sensor types, and their applications, have been extensively reviewed in the textbooks of Culshaw and Dakin (1989), Grattan and Meggitt (1995), and Grattan and Meggitt (1998), and recently in the review paper by Grattan

and Sun (2000). Generally, optical fibre sensors are divided in two categories: *extrinsic* and *intrinsic* fibre sensors. Extrinsic sensors are defined as those in which the light is guided by the fibre, but the interaction of the light with the quantity in the measurement takes place outside the fibre. Intrinsic optical sensors are those where the sensor action takes place inside the fibre itself (Grattan and Ning, 1998). Intrinsic fibre sensors can be further subdivided using a basis of whether the sensor is doing *single-point* measurements, i.e. a specific point at a particular location, or it offers *distributed* sensing, which can be achieved using optical time domain reflectometry (OTDR) techniques. A number of sensor techniques have been developed for distributing sensing, where a quantity (usually stress or strain) can be measured at any point along the length of the fibre. This involves accurate measurement of the time-of-flight of short light pulses in the fibre, which are generated by nanosecond pulsed lasers. An intermediate category is the *quasi-distributed* sensor, where a series of point-sensors are linked together to give measurements at several discrete locations in space (Grattan and Ning, 1998, pg.5).

For this particular application, the stress sensitivity must be confined to inside the body of the sensors which will be installed in a shoe insole. It is therefore desired that the fibre is insensitive to stress everywhere except in the part of the fibre which is attached to the sensor body. Extrinsic sensors are not particularly useful because accurate alignment of external optics is required. This is because when the light emerges from the fibre and is then launched again into the same or another fibre, optical power loss is significant. This limits the number of sensors that could be simultaneously used for a given source, and a given detection system sensitivity. The main applications of extrinsic sensors are in measuring displacement and angular position, vibration, acceleration, and pressure. The measuring techniques and sensor descriptions are given in the textbook by Udd (1991).

Fully distributed sensing, on the other hand, is not required. The spatial resolution limitation of the distributed sensors, as well as the relatively high cost of the short-pulse source and the readout system, prevents their use for this particular application.

It is apparent that, for in-shoe stress measurement, intrinsic fibre sensors must be used, and the situation falls into the category of quasi-distributed sensing. Fig.2.3 gives some examples of intrinsic sensors which can be used to detect axial strain at a particular length of the fibre. The strain is transferred to the fibre directly by either some form of adhesive, or embedded in the structure under test (Turner *et al.*, 1990).

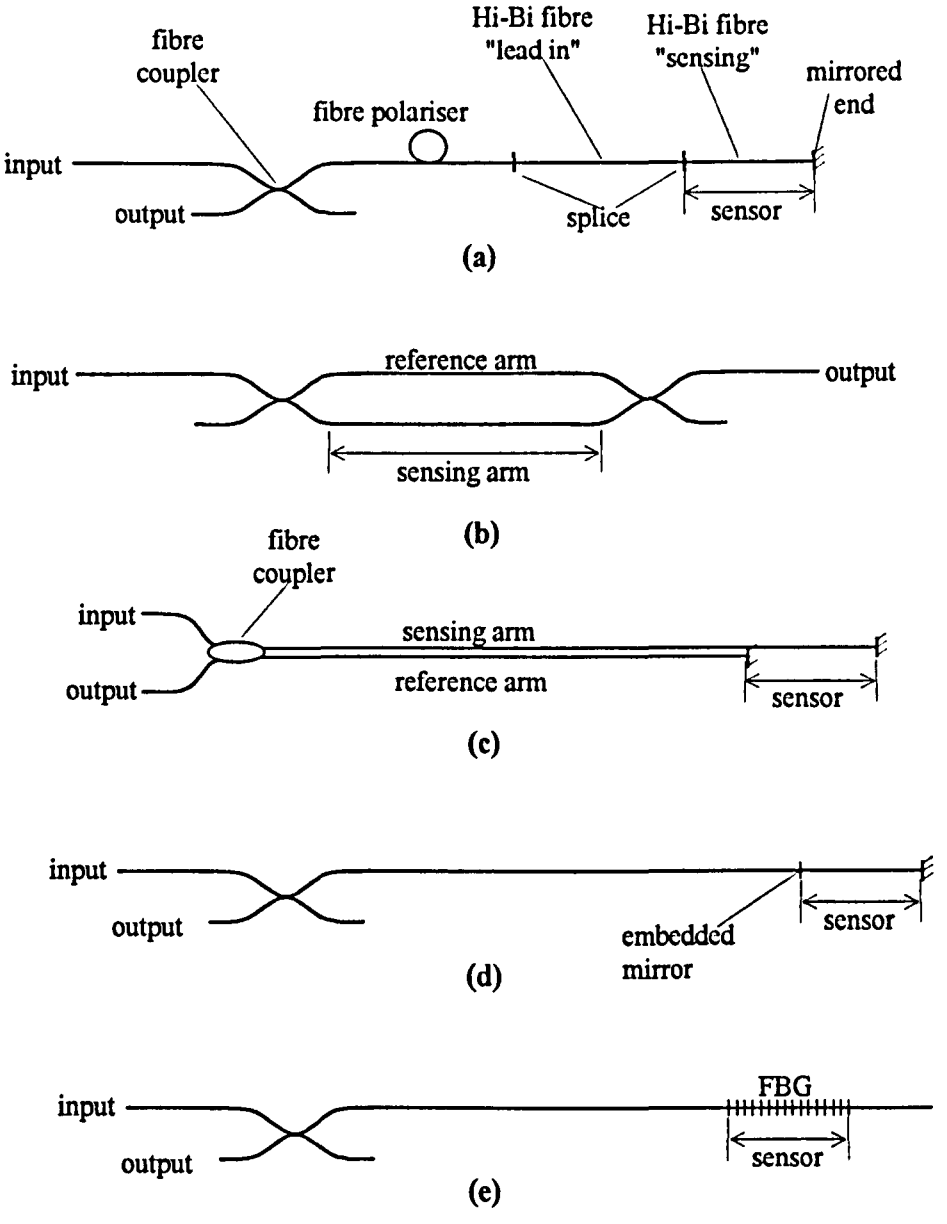

Fig.2.3: Schematic diagrams of four major intrinsic fibre optic strain sensor types. (a) polarimetric sensor, (b) Mach-Zehnder interferometric sensor, (c) localised Michelson interferometric sensor, (d) Fabry-Perot interferometric sensor, and (e) fibre Bragg grating sensor. The input is typically a laser diode or LED, and the output a photodiode or spectrometer (Turner *et al.*, 1990).

In the polarimetric sensor, Fig.2.3(a), linearly polarised light is launched into one of the polarisation axes of the "lead-in" Hi-Bi (high birefringence) fibre, and then spliced at the "sensing" length of the fibre with a relative 45° rotation of the polarisation eigenaxes (Wojtek *et al.*, 1993). Application of axial strain changes the physical length and the refractive index of the sensing length, which produces a change of the polarisation state of the reflected light, which results in change of the light intensity arriving at the detector. Disadvantages of the sensor are the requirement for specialised fibre and expensive fibre components (fibre polariser), and the relatively low sensitivity to strain compared to the interferometric and grating sensors (Turner *et al.*, 1990). Precision fibre splicing at 45°

between the lead-in and the sensing fibre is also required, which complicates the sensor preparation.

The localised Mach-Zehnder and Michelson interferometers are shown in Fig.2.3(b) and Fig.2.3(c) respectively. Axial stress applied on the sensing arm modulates the optical path length of the sensing arm, and hence the optical path difference of the interferometer. This results in sinusoidal modulation of the intensity of light in the output (Jones and McBride, 1998). The stress is calculated by measuring the intensity change, or the number of fringes (complete circles of the intensity). Disadvantages of those two configurations are i) the need for two fibres per sensor, ii) the difficulty to localise sensing. Localisation in case of the Mach-Zehnder interferometer requires the reference arm to be isolated from strain. In case of the Michelson interferometer the two arms must be carefully adhered to each other to avoid noise due to non-common path lengths of the lead fibres (Turner *et al.*, 1990).

The interferometric sensors described above are mainly rejected due to the need of two fibres per sensor. This would significantly increase the complexity of the sensor fabrication. In particular, the implementation of the in-shoe transducer seems to be impossible with the Mach-Zehnder configuration. It is quite difficult, or even impossible, to isolate the reference arm from vibrations during walking. The same applies to the localised Michelson sensor. Even though the pair of "lead-in" fibres are adhered to each other for close matching of the lead lengths, it could still result in significant noise due to non-common path length in the leads (Turner *et al.*, 1990).

Another interferometric sensor is the in-fibre Fabry-Perot (etalon) sensor shown in Fig.2.3(d). The intensity of light arriving at the detector, as the result of multiple reflections inside the cavity, is related with the cavity length (the distance between the two mirrors). Application of axial stress changes the cavity length, which can be calculated by measuring the change in the intensity of the reflected light. The Fabry-Perot resonator is described in the textbook by Silfvast (Silfvast, 1996, pp.300-308). Advantages of this sensor are the small physical length, and the single-fibre connection to the readout system. The embedded mirror required for the construction of the in-fibre etalon is made by chemical deposition of reflective material (TiO_2) on the cleaved ends of the fibre prior to fusion splicing (Lee and Taylor, 1988). This technique provides ease of fabrication, but reduces the mechanical strength of the fibre. Sirkis *et al.* (1995) have demonstrated the fabrication of in-fibre etalon by splicing a short segment of silica hollow-core fibre between two sections of single-mode fibre to form a mechanically robust strain sensor. The fabrication procedure, however, requires high precision cleaving and splicing equipment, and careful control of the splicing procedure.

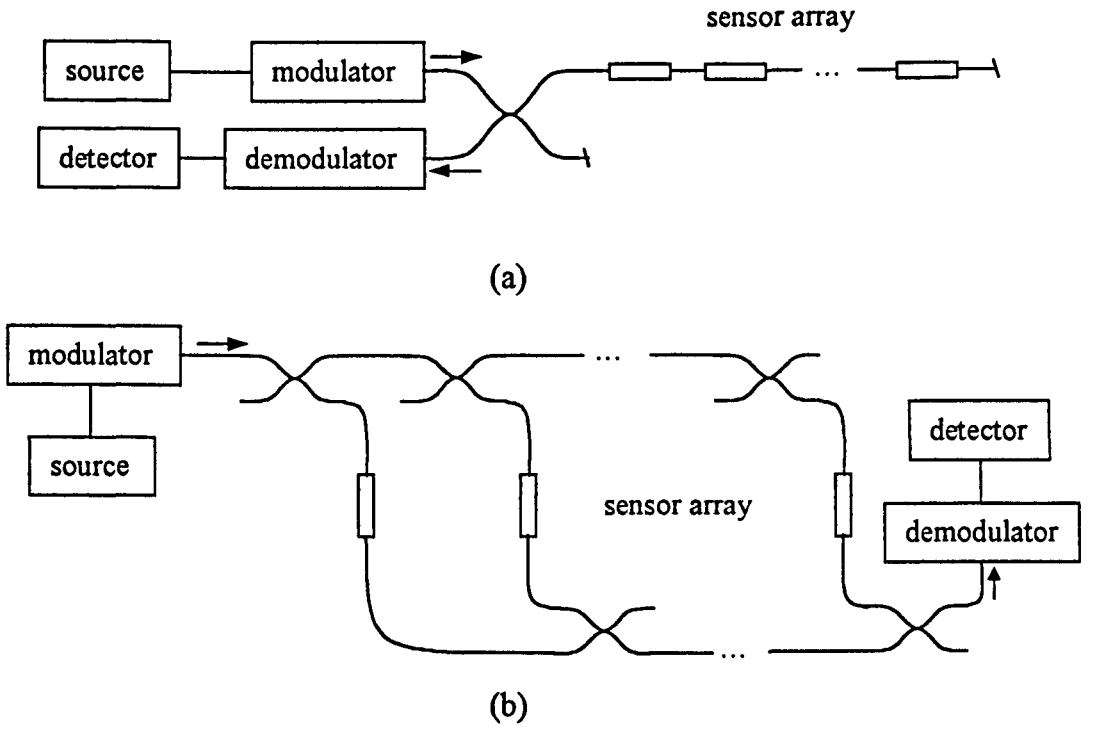

Fig.2.4: Multiplexing of interferometric fibre sensors. (a) Serially multiplexed in reflective configuration. (b) Transmissive ladder configuration. (Jones and McBride, 1998, pp.136-137)

Fig.2.4 shows two frequently used configurations for quasi-distributed sensing using interferometric fibre sensors. Reflective sensors can be connected in series as shown in Fig.2.4(a). The stress information from each sensor can be obtained using Optical Time Domain Reflectometry (OTDR) (Zimmermann *et al.*, 1989). In this method, short laser pulses (on the order of 100ps or less) are launched in the sensor array, and each sensor is identified by the time taken for light to travel from the source to the sensor, and back to the detector. The spatial resolution is limited by the pulse duration, which is often of the order metres (Jones and McBride, 1998, pg.141). This means that, the in-fibre strain elements fitted in the insole would have to be separated by metres of fibre which would also have to be installed inside the insole. This would increase the overall length of the fibre, increasing the optical power losses and the complexity of implementing the insole. Assuming that the strain elements in series are in-fibre Fabry-Perot etalon, then partial reflection of the light passing the mirrors will result in attenuation of the power arriving at the detector, and in different signal-to-noise ratio between the sensors, depending on the distance of a particular sensor from the coupler. In that case, the available power and the noise characteristics of the laser and the detector would limit the number of sensors in a series configuration (Sakai, 1986).

As mentioned earlier, the information of each sensor is allocated to a certain time slot. Because of multiple reflections, however, pulses reflected at mirrors other than the two mirrors constituting the sensor subject to measurement, might arrive simultaneously at the

detector within this particular slot (Wosinski *et al.*, 1992). This kind of crosstalk is a limiting factor of the spatial resolution which can be achieved with interferometric sensors in series configuration.

Fig.2.4(b) is an example of ladder configuration of transmissive sensors. Because the light passes through the same number of couplers, this configuration gives the advantage of providing equal power to every sensor (Jones and McBride, 1998, pg.137). A readout system for interferometric sensors based on Frequency Division Multiplexing (FDM) using a frequency-modulated laser source was used by Sakai (1986) in order to compare the series and parallel configurations for different number of sensors, in terms of crosstalk and signal-to-noise ratio. He concluded that parallel configuration should be chosen when 10 sensors or more have to be interrogated using the FDM technique. It is apparent, however, that in this particular application a large number of couplers would be required (108 couplers for 9 sensors per shoe, 3 fibre strain sensors per stress sensor), and equal number of fibres coming out of the shoes. The cost and the complexity of the transducer would therefore be significant.

The fibre Bragg grating strain sensor is shown in Fig.2.3(e). Axial strain produces shift of the reflected Bragg wavelength. This sensor was selected as the most appropriate strain sensing element for the implementation of the shear stress transducer. The potential advantages of the Bragg gratings will be presented in the next section. The principle of operation of the fibre Bragg grating strain sensor and a brief review of the fabrication techniques will be discussed in section 2.7.

2.6 Potential advantages of fibre Bragg gratings for in-shoe measurements

In the particular application presented in this thesis, the use of discrete fibre Bragg gratings (FBG) appear to offer considerable potential. The system has a number of potential advantages, which are listed below.

- Easy interrogation of multiple sensors. A large number of Fibre Bragg Gratings (FBG), which are the strain sensing elements used in a way similar to electric strain gauges, can be interrogated from the same optoelectronic readout system using multiplexing techniques like Time Division Multiplexing (TDM), and/or Wavelength Division Multiplexing (WDM). Generally, the same readout system is required for reading one or more FBG sensors. The modifications required of the readout system for multiple FBG reading concern issues of source and detector bandwidth, source optical power, and the required strain resolution and acquisition speed (number of samples per second per

FBG). These issues will be considered for different readout system methods in section 2.8.

- Small size of the stress sensor. The small size of the FBG strain sensor, which has a diameter equal to the fibre diameter (80μm to 125μm), and a length as small as 1mm, promises small overall dimensions of an in-shoe stress sensor.
- Thin, flexible, and lightweight connection cables. The FBGs can be photo-inscribed at different locations along the fibre length, in a single optical fibre. This property gives the potential advantage of using only one fibre per shoe insole, which connects the FBGs fitted inside the sensor structure in series. This fibre is used to carry the light from the source to the in-shoe sensors, and the reflected light from the FBGs back to the readout system. A single, 1mm thick optical fibre cable, can be the only link between the insole and the readout system.
- Minimal weight carried by the patient. The readout system can be used to remotely acquire the data via an optical cable link. No other devices except of the in-shoe transducer need to be carried by the patient.
- Simultaneous measurement of shear and vertical stress can be measured by proper fitting and orientation of a number of FBGs in an elastically deforming structure. The elastomer sensor which will be presented in chapters 5 and 6, is a triaxial stress sensor.
- Insensitivity to electromagnetic noise. Fibre-optic strain sensors are insensitive to electromagnetic interference (Turner *et al.*, 1990).
- No electrical conductivity. An all-optical in-shoe transducer eliminates electric shock hazard to the subject.
- A potentially long life of the in-shoe sensor is expected. Because the degradation of the FBG in time is very slow, the life of the sensor is expected to be mainly determined by the lifetime of the sensor structure, rather than the grating lifetime. The predicted reduction of the reflectivity of a Bragg grating written in a Ge-doped fibre operated at 80°C for 25 years is only 8% with respect to its initial value (Othonos and Kali, 1999).
- Low fabrication cost. The fabrication of FBGs requires expensive UV laser equipment. However, the extensive use of FBGs in telecommunications has drastically reduced the price of the FBGs, which can be customised to the required specifications. This only applies to large volume orders.

2.7 Fibre Bragg Grating (FBG)

The formation of FBGs in photosensitive fibres will be presented in section 2.7.1. The reflection properties of a uniform FBG will be presented in section 2.7.2. The most

frequently used fabrication techniques will be presented in section 2.7.3. The response of the FBG to strain and temperature variation will be explained in section 2.7.4.

2.7.1 Photosensitivity and grating formation

The development of the fibre Bragg grating came after the discovery of photosensitivity in optical fibres. Photosensitivity refers to a permanent change in the refractive index of the core of a fibre when exposed to light with a particular wavelength and intensity (Othonos and Kalli, 1999, pg.9). Initially, photosensitivity was thought to occur only in germanium-doped fibres, due to the presence of oxygen-deficient germania defects (Kashyap, 1994). However, with the demonstration of photosensitivity in most types of fibre, it is apparent that photosensitivity is the result of a various mechanisms: photochemical, photomechanical, and thermochemical (Othonos and Kalli, 1999, pg.10). Photosensitivity was first demonstrated in 1978 by Hill *et al.* They showed that an intensity-dependent refractive index change occurred in the core of the optical fibre by two counter-propagating visible laser beams (Hill *et al.*, 1978). This was the first method for writing Bragg gratings in fibres and is called the "internal method". It was later shown that even stronger effects occurred if the core was exposed to ultraviolet radiation (Meltz *et al.*, 1989) close to the absorption peak of germania-related defect (Bures *et al.*, 1982; Hand and Russell, 1990;) at a wavelength of 242nm (Yuen, 1982). High absorption prevented the use of counter-propagating waves in the ultraviolet band. Therefore, the production of gratings in the UV region was only possible by externally interfering two UV beams at the fibre (Meltz *et al.*, 1989), as shown in Fig.2.5. The regions of high intensity cause an increase in the local refractive index of the photosensitive core, while the dark regions remain unaffected. At each interface between two regions of differing index, a small reflection occurs. The amplitude of the resultant reflected wave can be large, and is determined by the superposition of all the individual weak reflections (Handerek, 1998, pg.338). The resultant wave has a maximum amplitude when all of these components are in phase. In this condition, the separation Λ between each adjacent pair of reflectors, which is equal to the period of the interference pattern must be equal to half an optical wavelength. Hence, the strongest reflection occurs at the Bragg wavelength λ_B given by (Hill and Meltz, 1997):

$$\lambda_B = 2n_{eff}\Lambda \tag{2.1}$$

where n_{eff} is the effective refractive index of the fibre at that wavelength.

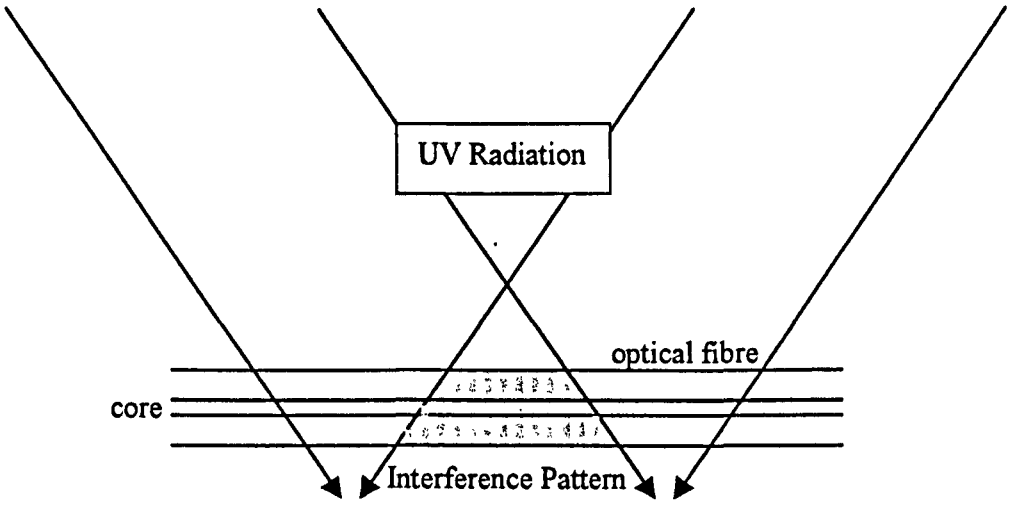

Fig.2.5: Photoinduced Bragg grating formation in the core of a germania-doped silica optical fibre.

The required UV light for the fabrication of FBGs can be produced by various sources including KrF excimer lasers (Zhang *et al.*, 1994), dye lasers (Meltz *et al.*, 1989), and frequency doubled argon-ion lasers (Kashyap *et al.*, 1993). Index changes are generally on the order of 10^{-3} or less, although in fibres with enhanced photosensitive response (hydrogen-loaded fibre), index shifts greater than 10^{-2} have been reported (Lemaire *et al.*, 1993).

2.7.2 Reflection properties of uniform Bragg gratings

The simplest form of a fibre Bragg grating consists of a periodic perturbation of the refractive index in the core with a constant amplitude and period, named uniform Bragg grating (Othonos and Kalli, 1999, pg.96). The reflectivity is given by (Othonos and Kalli, 1999, pg.97):

$$R(\ell,\lambda) = \tanh^2(\Omega\ell) \tag{2.2}$$

where ℓ is the grating length, and λ is the wavelength. The coefficient Ω is given by:

$$\Omega = \frac{\pi\Delta n}{\lambda}\left(1 - V^2\right) \tag{2.3}$$

where Δn is the amplitude of the induced refractive index perturbation (typical values 10^{-5} to 10^{-3}), and V is the normalised frequency of the fibre, given by (Othonos and Kalli, 1999, pg.96):

$$V = \left(\frac{2\pi}{\lambda}\right)\alpha\left(n_{co}^2 - n_{cl}^2\right)^{1/2} \tag{2.4}$$

where α is the core radius and n_{co}, n_{cl} are the refractive index of the core and cladding respectively. Eq.(2.2) shows that the reflectivity increases as the induced index modulation increases, and as the length of the grating increases.

An approximate value of the full-width half-maximum (FWHM) bandwidth of the grating is given by (Othonos and Kalli, 1999, pg.97):

$$\Delta\lambda = \lambda_B s\sqrt{\left(\frac{\Delta n}{2n_0}\right)^2 + \left(\frac{1}{N}\right)^2} \tag{2.5}$$

where n_0 is the average refractive index of the grating, and N is the number of the grating planes[1]. The parameter s is equal to ~1 for strong gratings (reflectivity ~100%), whereas s is equal to ~0.5 for weak gratings. The grating bandwidth is typically equal to ~0.05 to 0.3nm in most sensor applications (Kersey *et al.*, 1997).

2.7.3 Fabrication of Bragg gratings

The most common methods for fabricating FBGs are briefly discussed in this section. Advantages and disadvantages of each method are also given.

Traditional interferometer

The interferometer of the type used by Meltz *et al.* in their external writing technique is shown in Fig.2.6 (Meltz *et al.*, 1989). A beam splitter is used to produce two beams which can be interfered at the fibre by the use of two beam steering mirrors. This arrangement allows the angle of the beams to be varied so that the period of the interference pattern at the fibre can be altered. Cylindrical lenses are used to produce a stripe focus at the fibre.

[1] each interface between regions of different refractive index is named grating plane (Othonos and Kalli, 1999, pg.95).

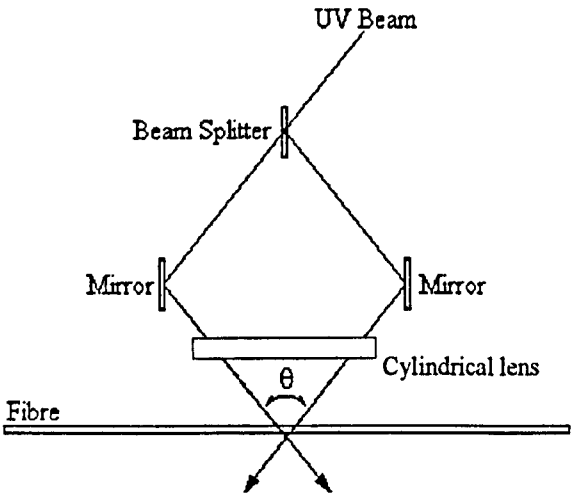

Fig.2.6: Traditional mirror interferometer used for external writing of gratings (Meltz *et al.*, 1989).

The advantage of this method is the ability to change the Bragg wavelength by altering the mutual angle θ which changes the grating period, given by the following equation (Kashyap, 1994):

$$\Lambda = n_{uv}\lambda_{uv}\sin(\theta/2) \tag{2.6}$$

where λ_{uv} is the wavelength of the UV writing beam, and n_{uv} is the refractive index of the core for the UV wavelength.

The optical devices required for this technique (beam splitter, mirrors, lenses) are relatively cheap and this makes the method attractive. However, this method cannot be used where writing times are to be long. Since there are several mirrors which can transmit vibration, differential path length changes can smear out the grating over the grating writing period. Interferometric method is still used for writing gratings using a single UV pulse (Askins *et al.*, 1992; Archambault *et al.*, 1993).

Right-angle prism

An alternative to the interferometric method is shown in Fig.2.7 (Kashyap *et al.*, 1990).

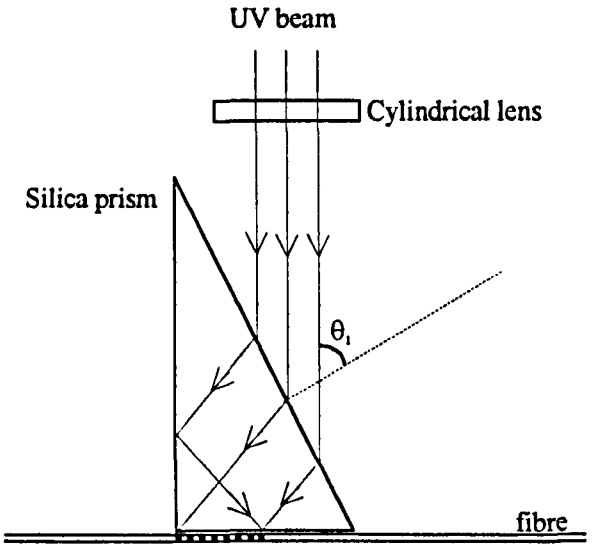

Fig.2.7: Prism Interferometer for writing gratings in optical fibres (Kashyap *et al.*, 1990).

The ultraviolet beam is directed through the hypotenuse face of a right-angle prism toward the apex in such a way that only half the beam is incident at the back face. The other half undergoes a reflection from the side face. The reflected half of the beam is directed toward the back face of the prism where it can interfere with the rest of the beam. The fibre is placed at the back face. A single cylindrical lens is used to bring the beam to a line focus at the fibre.

The interferometer is intrinsically stable since the path difference is generated within the prism and remains unaffected by vibrations. Careful angular alignment of the interferometer, however, is required for the selection of reflection wavelength.

The phase mask technique

The two techniques described above are not ideally suited to writing gratings for a precise wavelength, since the angles of the interfering beams are difficult to set up. A simpler technique shown in Fig.2.8 is based on the replication of a relief grating formed as a phase mask in UV transmitting silica (Kashyap *et al.*, 1993). A phase grating is fabricated by exposing the silica mask plate to e-beams, followed by dry plasma etching. A UV beam is diffracted by the mask into -1, 0, and +1 orders. It is not essential to block the 0-order beam while writing, since the intensity in the 0 order is usually very low (<5%). The -1 and +1 orders interfere at the fibre core.

The grating wavelength is given by (Hill *et al.*, 1993):

$$\lambda_B = n_{eff} \Lambda_m \tag{2.7}$$

where Λ_m is the mask period.

This interferometer is highly stable, is insensitive to beam translation, and is extremely compact. It has simplified grating production by relaxing both the temporal and spatial coherence requirements of the laser source. High reflectivity Bragg gratings can be produced by long time exposure of the fibre.

The main disadvantage of the phase mask is that it can only produce gratings of a specific wavelength. Fabrication of different wavelengths requires different masks. Limited tuning of the Bragg wavelength has been demonstrated by pre-straining the fibre before the exposure (Zhang *et al.*, 1994), by magnifying the phase mask periodicity (Prohaska *et al.*, 1993), or by tilting the fibre with respect to the phase mask (Othonos and Lee, 1995).

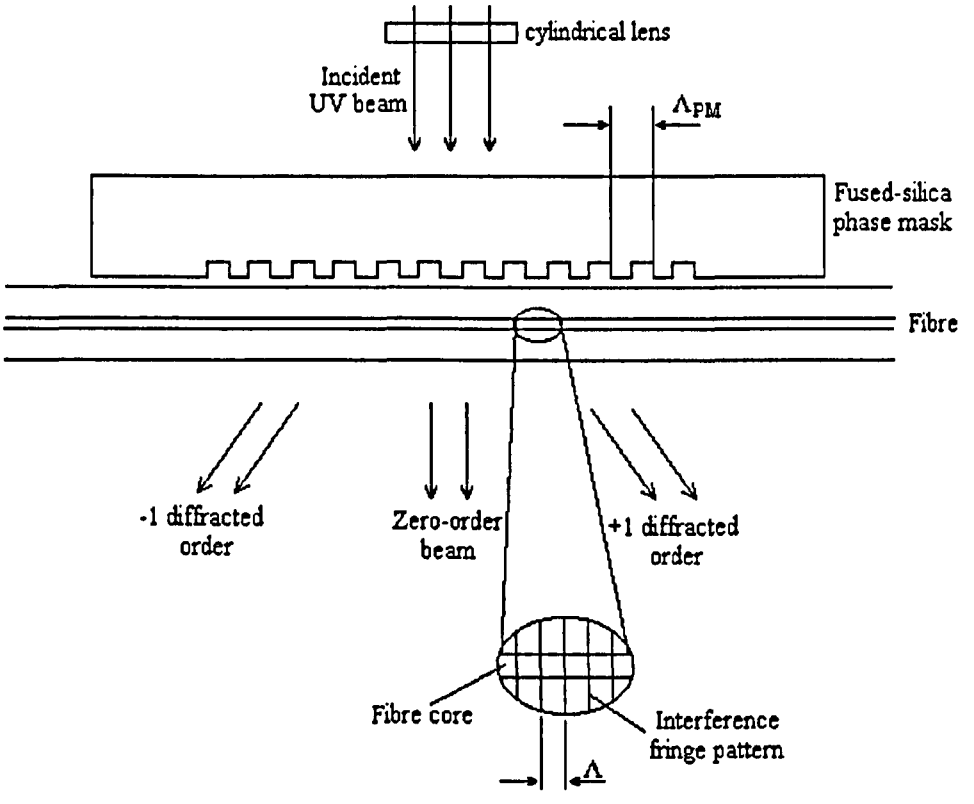

Fig.2.8: Fibre Bragg grating fabrication based on the phase mask exposure (Kashyap *et al.*, 1993).

The phase mask interferometer

A tunable phase mask interferometer is shown in Fig.2.9. A phase mask is placed normally to the path of a UV beam to act as a beam splitter, and the ±1 orders are reflected by two mirrors to intercept at the fibre. The mirrors are rotatable so that the angle θ can be changed. This system provides tunability of the Bragg wavelength by 250nm. Repeatability of 1nm has been demonstrated by simple adjustment of the mirror angle (Kashyap, 1998).

The FBGs which were used throughout this study were fabricated at BT Labs using the phase-mask interferometer[1]. The UV source was an intracavity frequency-doubled, argon-ion laser. 488nm wavelength radiation was doubled to generate 244nm UV emission (Kashyap, 1999, pg.105). The gratings were written in a single-mode, 125μm diameter, Ge-doped fibre, after removing the acrylic coating. The fibres were exposed to the ~5mm long interference pattern, for a time period between 4 and 10min. The UV power was ~110mW (CW). The properties of the gratings will be discussed in section 3.5.3.

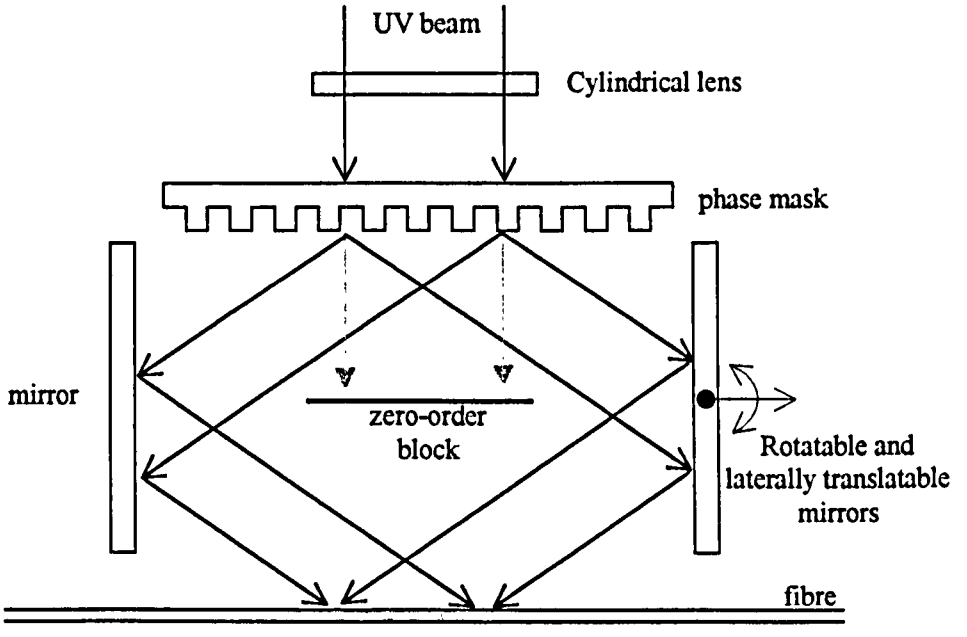

Fig.2.9: The phase-mask used as a beam splitter in an interferometer for inscription of fibre gratings (Kashyap, 1999, pg.63).

2.7.4 Fibre Bragg grating strain sensor

The basic principle of operation commonly used in a FBG-based sensor system is to monitor the shift in wavelength of the reflected "Bragg" signal with the changes in the measurand (e.g. strain, temperature). The Bragg condition is given by eq.(2.1).

Application of axial strain on the fibre, and/or temperature change, will result in wavelength shift of the Bragg wavelength. The fractional change in the Bragg wavelength when the temperature of the grating is raised by ΔT and when it also experiences an axial strain ε is given by (Kanellopoulos *et al.*, 1995):

[1] The FBGs were kindly fabricated by Dr. Raman Kashyap at BT laboratories, Martlesham Heath, Ipswich, IP5 3RE, UK.

$$\frac{\Delta\lambda_B}{\lambda_B}=\left(\frac{1}{n}\frac{\partial n}{\partial T}+\frac{1}{\Lambda_B}\frac{\partial \Lambda_B}{\partial T}\right)\Delta T+\left(\frac{1}{n}\frac{\partial n}{\partial \varepsilon}+\frac{1}{\Lambda_B}\frac{\partial \Lambda_B}{\partial \varepsilon}\right)\varepsilon \quad (2.8)$$

where n is the effective refractive index of the fibre core for the particular wavelength λ_B. The second term in eq.(2.8) represents the strain effect on an optical fibre. This corresponds to a change in the grating period and the strain-optic induced change in the refractive index. The coefficients for ΔT and ε above have been measured experimentally for a Bragg wavelength of 837.3nm (Kanellopoulos *et al.*, 1995):

$$\frac{\Delta\lambda_B}{\lambda_B}=8.8\times10^{-6}\Delta T+0.8\times10^{-6}\varepsilon \quad (2.9)$$

where ΔT is measured in degrees Celsius and ε in microstrain. If for example we consider a wavelength shift of 1nm, this will correspond to ε=1500$\mu\varepsilon$, or ΔT=135°C. Eq.(2.9) describes a linear shift of Bragg wavelength with strain or temperature variation.

A significant limitation of FBG sensors is their dual sensitivity to strain and temperature. This creates a problem for sensor systems designed to monitor strain, as temperature variations along the fibre path can lead to false strain readings. For example, the wavelength shift caused by a change in temperature by 1°C for a grating with λ_B=800nm will produce an error in the estimated strain of ~10$\mu\varepsilon$. Temperature compensation is usually necessary to keep the accuracy into the acceptable limits.

In case of the in-shoe transducer, a possible solution could be the use of reference gratings embedded into the shoe insole, isolated from strain. Wavelength shift in that case would be caused by temperature variation only.

Error due to temperature is expected to be small in the case of in-shoe measurements, due to the relatively short measuring time. An initial calibration of the transducer a few minutes after wearing the shoes will probably be enough to take accurate measurements without the need for temperature compensation. Because only the individual stress sensing elements have been developed during this study, instead of the complete in-shoe transducer, the necessity of temperature compensation was not evaluated.

2.8 Interrogation systems for FBG arrays

A review on recent interrogation techniques for quasi-distributed sensing using FBGs will be presented in this section. The aim of this section is to present those techniques with particular reference to their applicability for the implementation of the in-shoe stress transducer. It is therefore important to present the required specifications of the readout system for this particular application before commenting on the applicability of each method. The specifications of the readout system are related to the desired specifications of the in-shoe transducer (section 2.3), and they will be presented in section 2.8.1. The review

concerns interrogation systems using tunable bandpass filters (section 2.8.2), tunable laser sources (section 2.8.3), as well as interferometric techniques (section 2.8.4).

2.8.1 Readout system requirements

The readout system is responsible for the collection of the reflected signal from the Bragg gratings fitted in the shoe insole. Assuming 18 triaxial stress sensors (9 sensors per shoe), each one requiring 3 FBGs, the system must be able to read 54 FBGs simultaneously. The scanning speed for each grating must be at least equal to 300Hz. The desired dynamic range is 0kPa to 500kPa for vertical stress, –250kPa to +250kPa at any direction of shear stress, with a resolution equal to 5kPa. The required dynamic range / resolution ratio is therefore 100:1. Very important factors in choosing the interrogation system will also be the cost and the complexity. The use of expensive optoelectronic components and devices should also be avoided in order to keep the overall cost of the transducer as close as possible to the cost of other commercial devices (Table 2.2). It is important that the connection of the FBGs with the readout system will occupy a minimum number of fibres (one fibre per shoe insole ideally) and a minimum fibre length. Complicated interconnection schemes will make the insole fabrication difficult or even impossible.

After determining the total number of FBGs, it is possible to examine the topology of the FBGs in the array, which depends on the interrogation method. A frequently used method is Wavelength Division Multiplexing (WDM) of FBGs corresponding to different Bragg wavelengths. Theoretically, in a WDM system, a single fibre could accommodate all the FBGs, provided that no overlapping of the reflected spectra occurs. This requires that the FBGs are sufficiently separated in wavelength. The minimum wavelength separation can be estimated by considering the operating bandwidth of each FBG. The average wavelength shift at the 800nm band, for a dynamic range equal to $\pm 2500\mu\varepsilon$ is approximately ±1.5nm. Allowing 1nm gap between adjacent gratings in order to avoid overlapping, then a bandwidth of 4nm per FBG is required. The total bandwidth of the uni-dimensional FBG array will be:

<total number of FBGs> x <bandwidth per FBG> = 54x4 = 216nm

The majority of sources (ie. LEDs, tunable lasers), as well as the demultiplexing systems (ie. tunable filters, spectrometers) have generally smaller operating bandwidths, as will be seen in the next section. It is therefore necessary to divide the FBGs into more than one fibres, where the FBGs on different fibres share the same bandwidth. In that case, combination of WDM and Time Division Multiplexing (TDM) have to be used for demultiplexing the signals from individual FBGs. Examples of such systems will be given in sections 2.8.2 to 2.8.5.

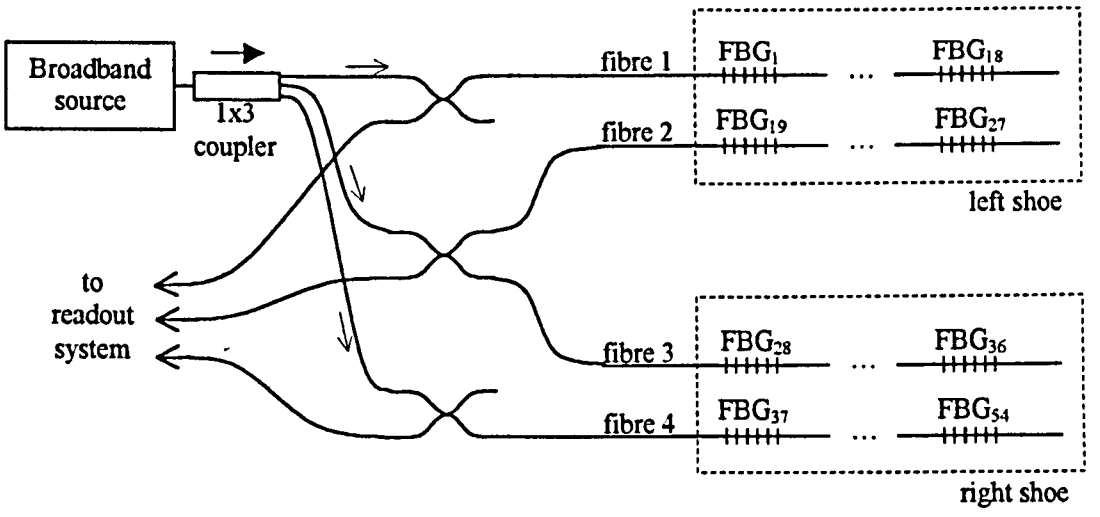

Fig.2.10: Possible arrangement of the FBGs inside the shoe insoles. Three groups of FBGs are shearing the source bandwidth: FBG_{1-18} (fibre1), FBG_{19-36} (fibres 2 and 3), and FBG_{37-54} (fibre 4).

A possible configuration, which does not significantly increase the complexity or the cost of the system, is shown in Fig.2.10. The FBGs are written in 4 fibres. In this configuration, we assume that the FBGs are divided in 3 groups of 18 FBGs, each group receiving the same bandwidth from a broadband source. Since each insole contains only 27 FBGs, fibres 2 and 3 contain only 9 FBGs each. In order to make maximum use of the available bandwidth, the FBGs on those two fibres can be written at different wavelengths with respect to each other. Therefore, even though the FBG array consists of 4 fibres, the source bandwidth is only used 3 times instead of four, keeping the interrogation system as simple as possible.

The required source bandwidth for the arrangement shown in Fig.2.10 is: 18x4 = 72nm. An example of a source, which can deliver this bandwidth, is the Superluminescent Light emitting Diode (SLD). Semenov *et al.* (1993) have developed an SLD operating at the 800nm band with a bandwidth equal to 68nm. Commercial SLDs are now available with bandwidth up to 80nm (SUPERLUM[1] SLD-371).

2.8.2 Interrogation using tunable bandpass filters

A commonly used WDM technique for interrogating FBG sensors is based on the use of tunable Fabry-Perot filters. A system based on tunable FP filter is shown in Fig.2.11 (Davis *et al.*, 1995). Light reflected from an array of FBGs in a series configuration is passed through a FP filter which passes one narrowband wavelength component, depending on the spacing between the mirrors in the device. The distance between the mirrors, and hence the

[1] SUPERLUM Ltd., P.O. Box 73, E-538, 111538 Moscow, Russia.

bandpass wavelength of the filter, can be tuned by controlling the piezoelectric stacks on which the mirrors are mounted. In operation, the light reflected from the grating sensors is returned to the FP filter via the coupler. As the filter is tuned, the bandpass scans over the return signals from the gratings, and the Bragg wavelengths can be calculated and recorded by measuring the filter driving voltage as the return signals are detected. Typical characteristics of the filter are a free spectral range of 50nm, and a bandpass bandwidth of 0.3nm (Davis *et al.*, 1995). The system is capable of scanning each FBG at 300Hz. Faster FP filters are also available with scan rates up to ~1kHz (Kersey *et al.*, 1997). The minimum resolvable wavelength shift is approximately 1pm, equivalent to a strain resolution of 1με. The system has been demonstrated for demultiplexing 16 FBGs on a single fibre, achieving a dynamic range equal to 2000με per sensor.

The maximum number of FBGs in the above configuration is limited by the wavelength separation of the FBGs, and the scanning range of the FP filter. If the FBGs are separated by 4nm, then a maximum of only 12 FBGs can be interrogated.

Davis *et al.* (1996) have modified their system in order to measure strain in larger FBG arrays. The system is schematically illustrated in Fig.2.12. Optical fibre switches are used to allow the measurement of strain along five strings of 12 FBGs each. The strings are illuminated by an ELED source with central wavelength 1.3μm. The system is capable of scanning each FBG at 2.5s intervals with 50 averages/FBG, achieving a resolution of 1με.

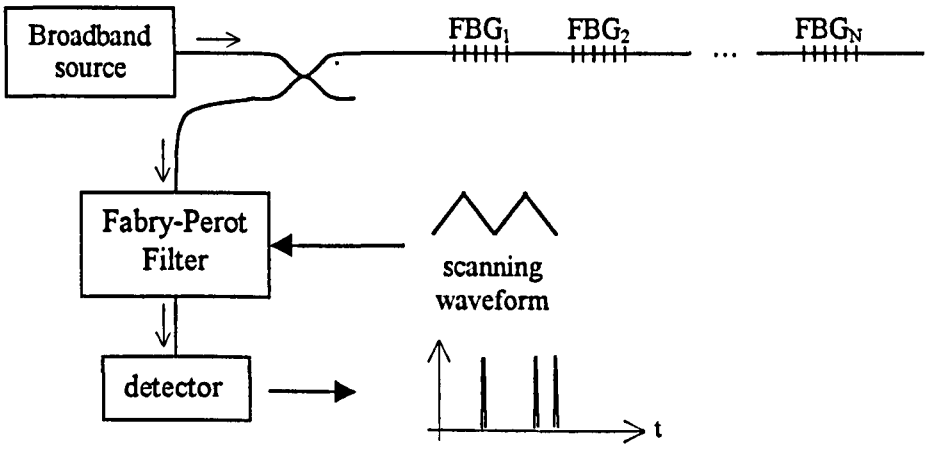

Fig.2.11: Scanning readout system using Fabry-Perot filter (Davis *et al.*, 1995).

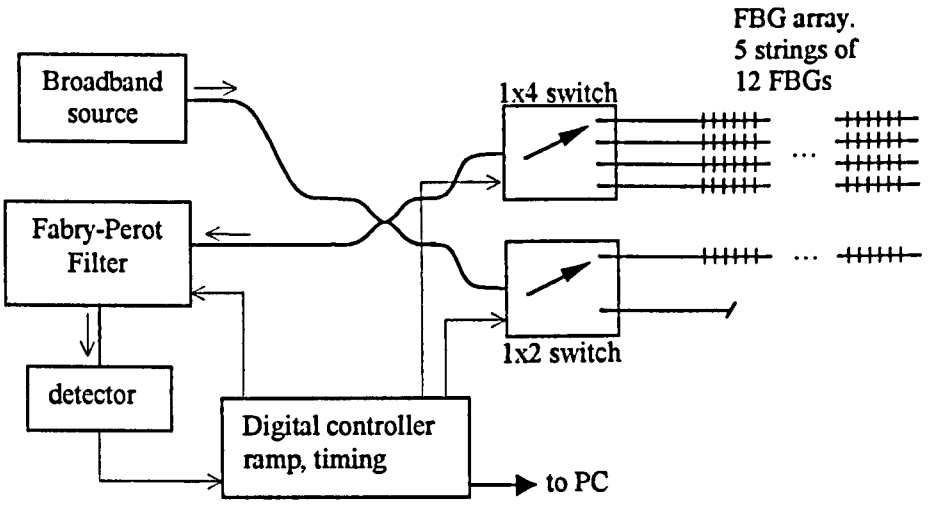

Fig.2.12: Combined WDM/TDM interrogation system using Fabry-Perot filter (Davis *et al.*, 1996).

The application of the interrogation system shown in Fig.2.12 for the in-shoe transducer requires a 1x3 optical switch. The FBG array shown in Fig.2.10 is directly connected to the 3 output ports of the switch. The system satisfies the requirements for the number of sensors and the dynamic range/resolution ratio, however it is too slow for dynamic measurements. The desired dynamic response (300 scans/FBG) could be achieved by increasing the scanning speed of the FP filter to 900Hz. After each scanning cycle, which lasts for 1/900=1.11ms, another string has to be connected before the next scan begins. Because the 3 strings must be scanned at 300Hz, 900 switches/s will be required. The switching time should also be minimised to allow sufficient time for the FP filter to scan the entire bandwidth. Switching speed of the order of 10μs would be required. This speed is still beyond the capabilities of most commercial optical switches.

Another type of tunable bandpass filter used in WDM systems is the Acousto-Optic Tunable Filter (AOTF). The operation of an AOTF is based on the diffraction of light produced by an acoustic wave travelling through a transparent medium. The acoustic wave, which is generated by a piezoelectric element, produces a periodic variation of strain along its path, which, in turn, produces periodic variation of the refractive index within the medium due to the photoelastic effect. As the light beam passes through the medium and crosses the acoustic wave, it is diffracted (Senior, 1992, pg.545). The output of the AOTF is a narrow-band spectrum (typically 1nm, Xu *et al.*, 1996). The central wavelength of the filter is determined by the RF frequency which drives the piezoelectric element, which in turn determines the period of the induced grating in the transparent medium.

The use of Acousto-Optic Tuneable Filter (AOTF) for the interrogation of Bragg grating sensors was initially presented by Xu *et al.* (1993). Experimental results were given using only 1 FBG as a strain and temperature sensor. The transmission spectrum of the high-reflectivity (99%) FBG was passed through the filter. Frequency Shift Keying (FSK) of the

RF drive to the AOTF was applied to track the wavelength shifts of the FBG written at 1300nm. The filter had a tuning range of 1.2-2.5μm and a bandwidth of 4nm. The strain resolution of the system was not reported. Xu *et al.*, (1996) used a similar filter (operating range 1.2-1.4μm, bandwidth 3.3nm) to measure the wavelength shift from the reflection spectrum of a 55% reflectivity FBG written at 1300nm. A resolution of 0.4με for dynamic measurements up to 10Hz (100ms measuring period) was measured.

Varasi *et al.* (1996) presented an integrated optical spectrometer using AOTF for the interrogation of multiple Bragg gratings on a single fibre, embedded in composite material. The system was used in scanning mode, in a way similar to the FP scanning filter shown in Fig.2.11. The ramp voltage in this case was driving a Voltage Controlled Oscillator (VCO), which produces the RF acoustic wave for the tuning of the AOTF (operating range 800-1400nm, resolution 0.4nm). Drawback of this configuration is the low strain resolution, which was measured to be 400με.

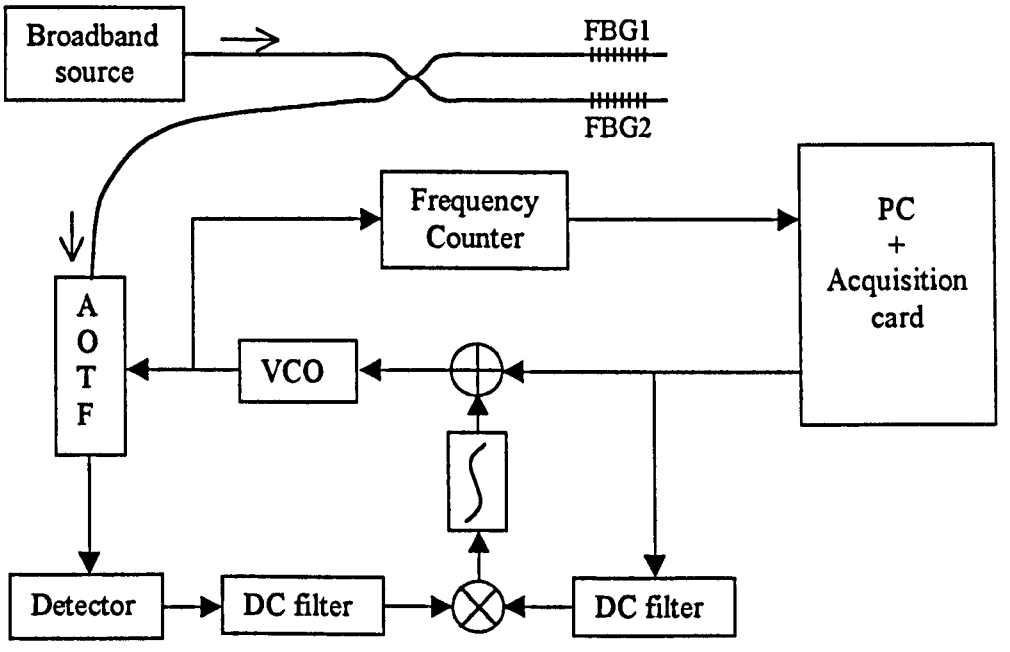

Fig.2.13: Block diagram of an FBG interrogation system using AOTF and wavelength tracking electronics (Geiger *et al.*, 1995).

Geiger *et al.* (1995) demonstrated an electronic lock-in system using AOTF (operating range 1.2-1.4μm, bandwidth 3.3nm) to track the wavelength of two FBGs (1297nm and 1311nm), as shown in Fig.2.13. Tracking the optical wavelength of an input signal is obtained by applying a frequency-shift-keyed (FSK) signal to the AOTF. This results in a square wave amplitude modulation of the transmitted light, where the peak-to-peak modulation is a function of the difference between the grating wavelength and the centre wavelength of the AOTF, and its polarity depends on which direction the AOTF and the grating are offset in wavelength. The square wave output from the optical receiver is

multiplexed by the modulating signal, thereby controlling the central AOTF wavelength to track the central wavelength. Once the central wavelength of the AOTF coincides with the Bragg wavelength of the grating, the amplitude modulation of the light at the dither frequency will be zero. Because the mean frequency drive to the AOTF determines the central AOTF wavelength, measuring this frequency can monitor the grating wavelength. The strain resolution of this system is 1με. The same tracking system was used by Varasi *et al.* (1996), where the tunable filter in that case was the AOTF-based integrated optical spectrometer. Static strain resolution equal to 0.1με was reported.

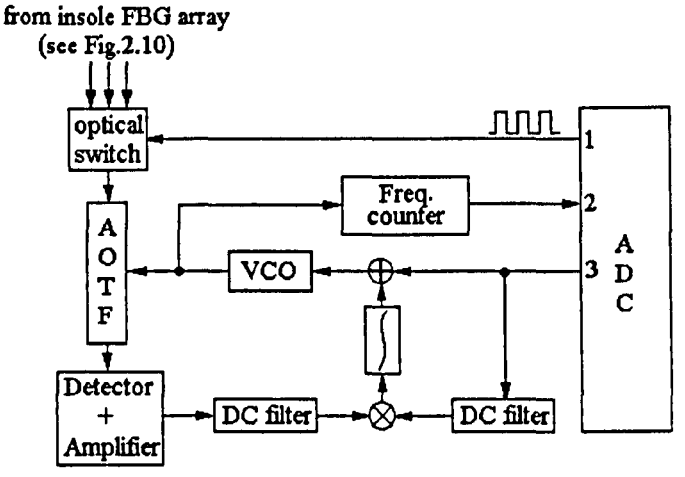

Fig.2.14: General diagram of the AOTF tracking system for the in-shoe stress transducer. Port 1 of the ADC controls the optical switch, port 2 measures the mean frequency of the filter, and port 3 applies the bias and dither voltage.

A possible configuration for the implementation of the readout system for the in-shoe transducer, using AOTF in tracking mode, is given in Fig.2.14. The optical switching requirements are the same as previously explained for the FP filter configuration. Furthermore, the tracking procedure introduces limitations on the minimum tuning speed of the AOTF which can be derived from the bias and dither frequencies. The bias voltage is the DC term of the voltage waveform generated by the computer, which is responsible for selecting a particular FBG from the string. A superimposed square wave ripple is the dithering voltage, which is used for the fine tuning of the filter. For 300Hz sampling rate, the bias voltage changes at intervals $T_B=1/f_B$, where f_B is the bias frequency given by:

$$f_B = \text{sampling rate X number of sensors} = 300x54=16.2kHz$$

Assuming 10 periods of the dither voltage in order to detect the Bragg wavelength, the dither frequency in our system must operate at:

$$f_D = \text{bias voltage frequency X 10 periods per sensor} = 162kHz$$

Hence, $T_B=1/f_B=60\mu s$, and $T_D=1/f_D=6\mu s$. It is apparent that the tracking system will operate properly if only the tuning speed of the AOTF is sufficiently smaller than 6μs, in order for the dither signal to be detected. A narrow-bandwidth (0.2nm) AOTF operated at 1550nm,

having a tuning speed equal to 10μs has been reported (Paek *et al.*, 1998). The wavelength resolution of the filter has been enhanced by utilising a diffraction grating in the output of the transparent medium. A device operating in the 800nm band, 1.5nm wavelength resolution, and 15μs tuning speed, is commercially available[1] at the price of £15000. Adding the cost of the 1x3 optical switch, and the rest of the optoelectronic equipment, it is expected that the total cost of the transducer will exceed the cost of other commercial devices (Table 2.2).

2.8.3 Interrogation using tunable laser sources

In the previous techniques, the FBG array was illuminated by a broadband source (ELED or SLD), and the absolute Bragg wavelength was measured by scanning the wavelength band with a narrow-band bandpass filter. A single detector connected at the filter output determines the peak intensity corresponding to the Bragg wavelength, which is equal to the central wavelength of the filter. The tunable filter methods offer high resolution at static strain measurements, or at low frequencies. The wavelength resolution, however, is sensitive to the signal-to-noise ratio of the optical power arriving at the detector. The signal-to-noise ratio is often low, due to the relatively low power density characteristics of the broadband sources, and the narrow band reflection of the gratings (Ball *et al.*, 1994). For high frequency dynamical measurements the scanning frequency has to be increased. This results in reduction of the amount of optical energy arriving at the detector per sampling period, therefore in further reduction of the signal-to-noise ratio, which in turn reduces the wavelength resolution of the detection system (Kersey *et al.*, 1997).

The optical throughput power penalty of a scanned filter can be avoided using a narrow-linewidth, wavelength tunable laser source. Ball *et al.* (1994) demonstrated the use of a wavelength-tunable erbium fibre laser for the interrogation of multiple FBG temperature sensors written on a single fibre. The laser utilises two FBGs written on an erbium-doped fibre to form a 2cm laser cavity. The fibre laser was mounted on a piezo-translator. The wavelength tuning is achieved by driving the piezo-translator with a saw tooth waveform. This fibre laser delivers 2mW, and the tunable wavelength range is 1552.2nm to 1554.5nm. Three FBG sensors were used for the demonstration of the system. High wavelength resolution, equal to 2.3pm was measured. The limited tuning range of the laser, however, prevents the use of the laser with large FBG arrays.

Yun *et al.* (1998) developed a WDM-based FBG array interrogation system using a wavelength swept fibre laser (WSFL), Fig.2.15. The WSFL has a scanning Fabry-Perot filter in the cavity to sweep the laser output wavelength continuously and repeatedly over a range

[1] Model N48046-2-0.80-FOPM, N64020-200-1ASDFS synthesiser driver, N77015 PC card and software, supplied by ELLIOT SCIENTIFIC Ltd., Gladstone Place, 36-38 Upper Marlborough Rd, St.

of 28nm (1538nm to 1566nm). The average output power was 3.3mW, and the linewidth <0.1nm. The wavelength of each sensing grating is calculated by measuring the time interval between the detection of the reflection peak from the reference grating and that of a sensing grating. Static and dynamic strain measurements with a resolution of 0.47με (rms) at a sampling rate of 250Hz were demonstrated.

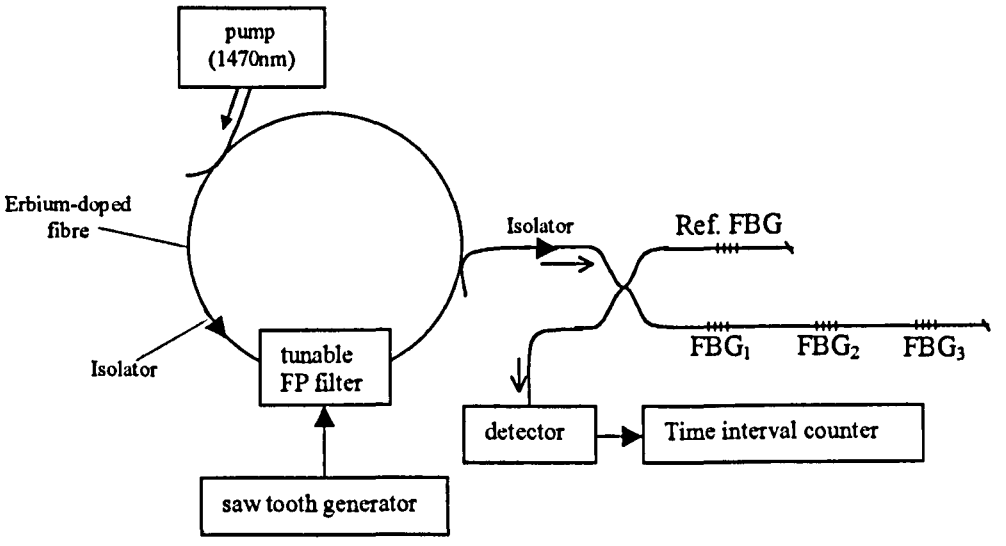

Fig.2.15: FBG array interrogation system using a wavelength-swept fibre laser (Yun *et al.*, 1998).

The main disadvantage of the tunable laser interrogation techniques mentioned above is the relatively low tuning bandwidth, which limits the length of the FBG array. The required wavelength separation of the FBGs at the 1500nm band, which is the operating wavelength band of the WSFL, is ~7nm. This is obtained by eq.(2.5) for $\Delta\varepsilon=\pm 2500\mu\varepsilon$, plus 1nm to avoid overlapping. Hence, up to 4 FBGs only can be interrogated. The complexity and cost of fabricating the fibre laser is another disadvantage.

Koo *et al.* (1999) have proposed a dense wavelength division multiplexing (DWDM) scheme using Code Division Multiplexing (CDM), capable of potentially multiplexing over 100 FBGs in a single serial sensor array using a 40nm-bandwidth source. The CDM technique allows a large reduction of the wavelength separation between Bragg grating sensors down to the FBG bandwidth (0.3nm). The operation of the system was demonstrated for two FBGs (0.3nm bandwidth, 60% reflectivity), written at close wavelengths (1535.2nm and 1535.5nm), which were connected in series with a 100m delay fibre length between them. A tunable laser was intensity modulated in an on-off fashion by an electro-optic switch driven by an electronic pseudorandom bit sequence (PRBS) generator. The reflected signals from the FBGs were multiplied by a time-shifted PRBS. By choosing a proper time delay in the reference channel, taking the difference of the mixer output, and extracting the envelope

information from the pulse code modulated signal, the output from a particular FBG is selected. The strain information is derived by the wavelength scanning of the tunable laser source. Dynamic range 0 to 500με, with the resolution to be in the microstrain range was reported.

The dynamic range / resolution, and the proposed size of the FBG array, are both acceptable for the implementation of the in-shoe transducer. No information, however, is given on the capability of the system for dynamical measurements. Furthermore, the requirement for a length of delay fibre between the FBGs would make it very difficult to fit such a system inside the insole.

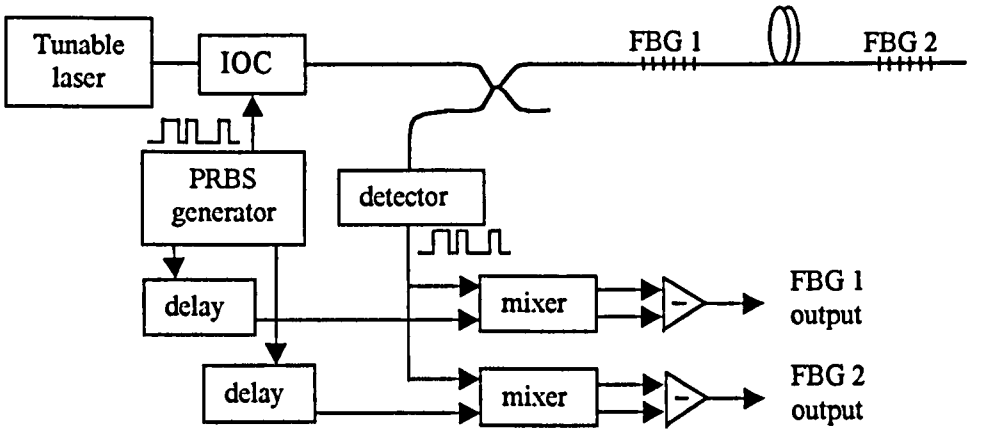

Fig.2.16: FBG Interrogation system using WDM and CDM (Koo *et al.*, 1999).

Ferreira *et al.* (1998) demonstrated an FBG interrogation system using a frequency-modulated multimode laser diode, which illuminates a FBG. The reflected light from the grating generates a carrier signal as the result of the overlapping between the FBG reflection spectrum, and one of the frequency-modulated laser modes. The change in Bragg wavelength is measured by tracking the phase of the carrier at the detector output. Dynamical strain measurement at 200Hz was performed. Strain resolution of $2p\varepsilon/\sqrt{Hz}$, and dynamic range up to 60dB was obtained. The multiplexing capability of this technique was demonstrated for two FBGs illuminated by two multimode diodes modulated at different frequencies. Provided that there is no overlap between the diode wavelengths and the gratings, two different carriers are detected. Advantages of the system are the high dynamic range and the low cost of the laser diode, compared to the tunable fibre lasers. Demultiplexing scheme for a large FBG array has not been demonstrated.

An intensity based scheme for interrogation of FBG sensors using a pulsed laser diode as the system optical source was demonstrated by Wilson *et al.* (1997). Two modes of a single laser diode are used as a dual-wavelength source for grating illumination. The FBG is written such that the Bragg wavelength lies between the two illuminating wavelengths. Strain applied on the FBG results in modulation of the intensity of the reflected dual-wavelength components. The algorithm provides a self-referencing mechanism to

compensate for intensity perturbations. Interrogation of multiple FBGs is achieved by pulsing the laser output and applying TDM. The system requires that the FBGs are all written at the same wavelength and connected in parallel configuration. Different delay fibre length for each FBG is also required. Quasi-static measurements from three FBGs were performed. Dynamic range equal to 350με and resolution ~5με were reported. The low dynamic range / resolution ratio, the parallel configuration which requires a different fibre for each FBG, the delay fibre lengths, and the large number of couplers, prevent the use of the method for the development of the in-shoe transducer.

2.8.4 Interferometric techniques

A technique for dynamic strain measurement of multiple FBGs written on a single fibre using combined WDM/TDM with interferometric detection was proposed by Kersey *et al.* (1992), Fig.2.17. Pulsed light from a broadband source is coupled into an FBG string. The gratings are sufficiently separated such that the reflected pulse from each FBG arrives at the detection system at different time intervals. The pulses are fed into a Mach-Zehnder interferometer. The output of the interferometer is gated to derive the interferometric signal from a particular FBG. The wavelength shift of each FBG is linearly transposed into the phase shift of separate low-frequency electrical carrier signals. The system was demonstrated with a single FBG written at 1550nm. Dynamic strain resolution equal to $0.6n\varepsilon/\sqrt{Hz}$ at frequencies >100Hz was measured.

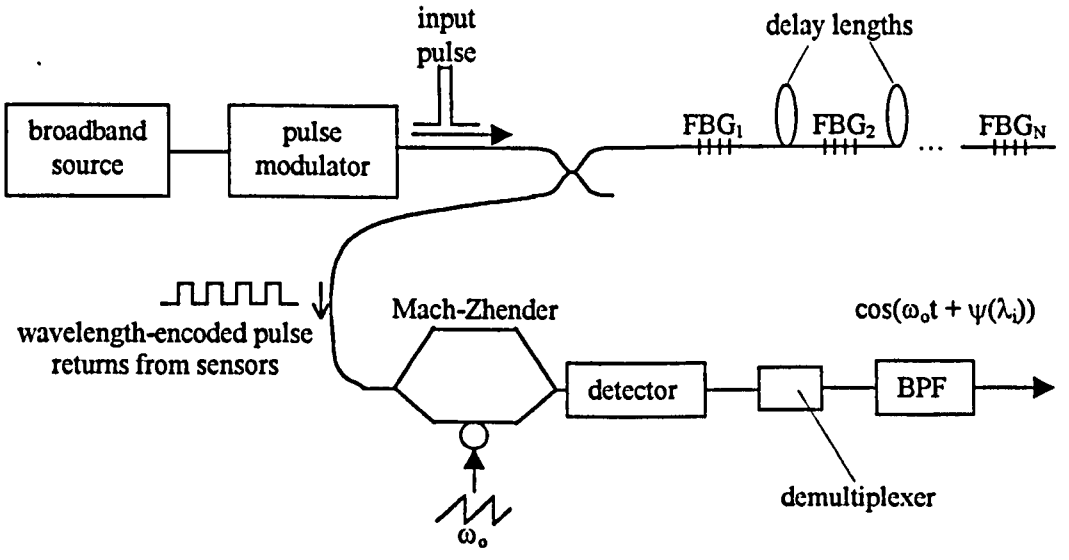

Fig.2.17: FBG sensor array interrogation using phase-sensitive detection (Kersey *et al.*, 1992).

The need for delay fibre length between the FBGs precludes the application of this method for the development of the in-shoe transducer. A fully WDM modification of the above system, which eliminates the use of delay fibres, was described by Berkoff and Kersey (1996). The pulsed modulated source is substituted by a continuous, broadband diode-

pumped Er-doped fiber superfluorescent source (power=1mW, operation band = 1525nm-2565nm) was used to illuminate four FBGs written at different wavelengths. The output port of the interferometer was coupled to the input of a four-channel bandpass wavelength division multiplexer (BWDM), which separates the composite interferometer phase signal into four output channels that correspond to a wavelength band about each of the FBG wavelengths. Each output contains the phase-modulated interferometric signal corresponding to a particular FBG. Dynamic strain measurement is achieved by measuring the phase change of the signal. The drawback of the method is the need of highly selective, closely spaced in wavelength bandpass filters, as many as the number of FBGs in the array. For large sensor arrays, those filters are not yet commercially available.

The measurement of the Bragg wavelength from a multiplexed FBG array can be achieved by passing the light through a scanning Michelson interferometer and processing the resulting interferogram to determine the peak wavelengths. Flavin *et al.* (1997) reported the interrogation of two FBGs with Bragg wavelengths 1.3 and 1.56μm. High wavelength resolution (0.005nm) was achieved by applying Hilbert transform processing on a short-scan interferogram (scanned optical path difference: OPD= 1.2mm). The Hilbert transform method was also applied by Rochford and Dyer (1999), to accurately measure the Bragg wavelength of much closer FBGs. The demodulation of three FBGs (1555, 1558, and 1560nm) was demonstrated by processing the interferogram obtained by OPD scanning equal to 20.2mm. The wavelength resolution was measured to be 19pm. The above method, even though it provides accurate calculation of the Bragg wavelength, it is not applicable for dynamic strain monitoring due to the relatively slow scanning process. Static strain measurements have only been reported.

2.8.5 Miscellaneous techniques

A low cost technique for the interrogation of FBGs written on the same fibre is based on the use of a matched filter grating array operated in the transmitted mode, as shown in Fig.2.18 (Davis and Kersey, 1995). Each FBG of the filter is matched with one of the sensing FBGs, and mounted on a separate piezoelectric stretcher. Independent stretching of the filter gratings is allowed by applying voltage to the piezoelectric stretchers. To track the corresponding sensing FBG, the stretchers are driven by a small dither signal, and a feedback loop is used to accurately detect the central frequency of the sensing FBG. The system was tested with two sensing FBGs. The dynamic range was measured to be 0-500με. The dynamic response of the system was measured for frequency 27Hz, giving minimum detectable signal equal to 0.001με/√Hz for frequencies >3Hz.

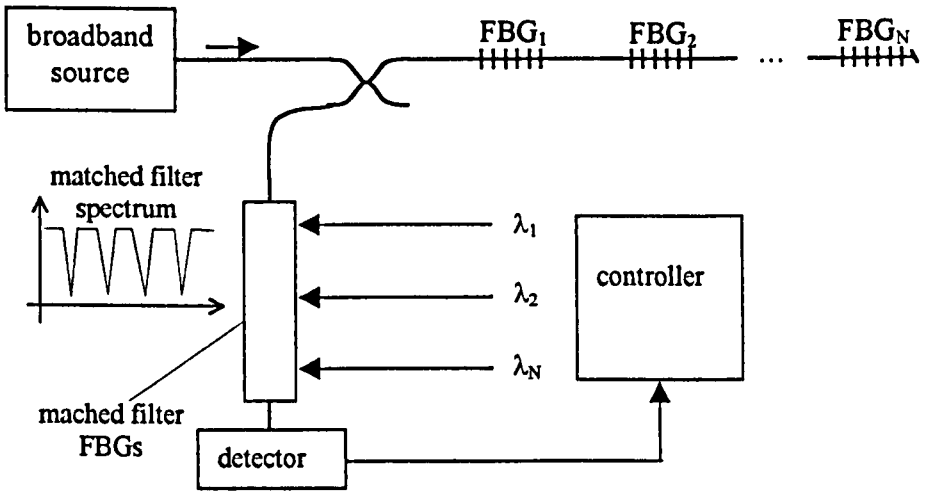

Fig.2.18: FBG interrogation using matched filter gratings (Davis and Kersey, 1995).

The disadvantage of this method is the need for identical filter FBGs with the corresponding sensor gratings. This is particularly difficult to be achieved in practice because each FBG has to be written at different wavelength to allow WDM interrogation. For that purpose, the FBGs are written using one of the interferometric techniques, which allow tuning of the grating wavelength, but also suffer from relatively low repeatability (section 2.7.3).

Hu *et al.* (1997) have proposed an FBG interrogation technique based on digital spatial and wavelength division multiplexing (DSWDM), using an imaging spectrograph with a two-dimensional CCD camera, as shown in Fig.2.19. Light from a broadband LED source is coupled into several single-mode optical fibres. Each fibre has a number of FBGs with predetermined, different FBGs. The reflected light from the FBGs in each fibre channel is coupled into a separate lead fibre, and all lead fibres are connected to the input slit of an imaging spectrograph with a two-dimensional CCD camera installed in the output port. The imaging spectrograph separates light beams from different fibres along pixel columns of the CCD. The bulk grating of the spectrograph diffracts different wavelengths in different directions along the x-axis, and forms spots along different pixel rows of the CCD. The precise Bragg wavelength is obtained by the location of the spot along the x-axis. The system was demonstrated with a spectrometer having a 600lines/mm bulk grating, and 512x512 pixel CCD camera, and two fibre channels, the first one having 3 FBGs (824, 830, and 853nm) and the second one having 2 FBGs (830 and 853nm). For this particular CCD/spectrometer configuration, resolution of 0.1nm was achieved. The system is potentially capable of interrogating a total of 175 FBGs with each sampled at 30Hz.

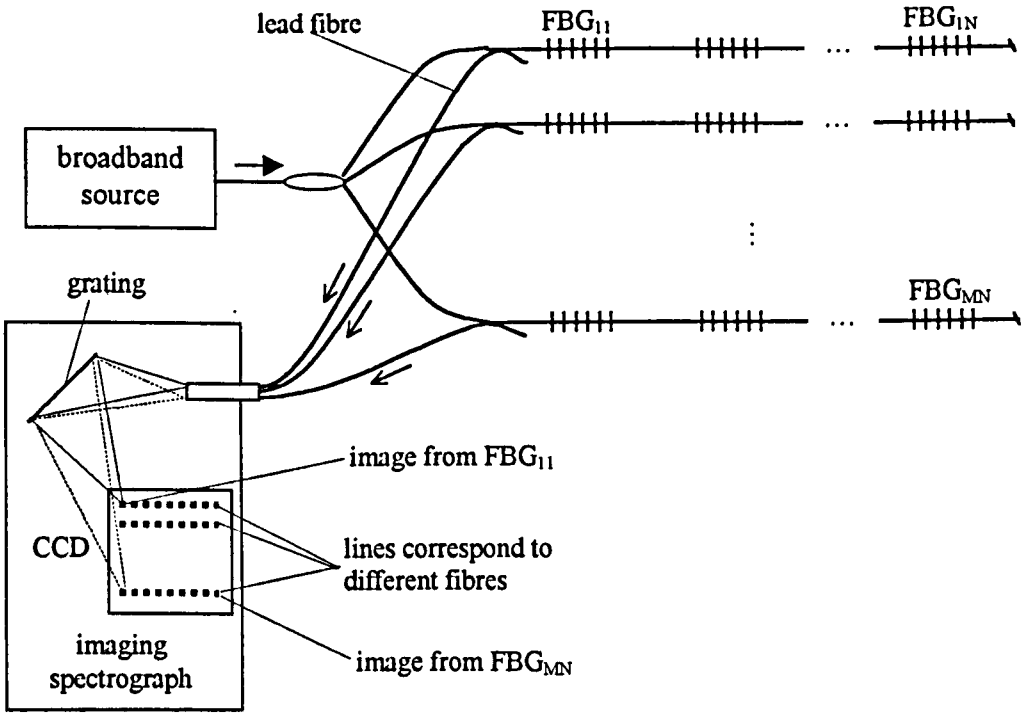

Fig.2.19: FBG interrogation system using DSWDM technique (Hu *et al.*, 1997).

A similar system was used as the FBG interrogation system during this study. The description of the system, as well as the peak detection algorithm used to increase the wavelength resolution of the system to ~1pm were presented by Ezbiri *et al.* (1998). The system will be described in detail in chapter 3. A suggestion for improving the sensitivity and acquisition speed of the system, with all the required modifications in order to operate as the readout system for the in-shoe transducer will be given in chapter 7.

2.9 Summary

Mechanical forces acting on the skin produce stresses inside the soft tissue which can be sufficient to occlude the blood supply in the contact region. Prolonged application of large forces leads to cell necrosis and ulceration. It is believed that mechanical stress plays an important role in plantar ulcer development in individuals with diabetes mellitus. Recently, several transducers have been developed for measuring in-shoe shear stress using magneto-resistive technology, light intensity modulation, and piezoelectric materials. Common drawbacks in the existing methods are the relatively large size of the sensors, and the difficulty in interrogating many sensors simultaneously in order to achieve distributed sensing. Optical fibre sensors, particularly the fibre Bragg gratings, offer significant advantages for this application in terms of size, speed, multiplexing capability, and readout system simplicity. The fabrication techniques and the principle of operation of the FBG strain sensor were briefly described. A review of the recent methods for the interrogation of

FBG arrays was presented, with particular reference to the applicability of each of those systems to the development of the in-shoe stress transducer readout system.

CHAPTER 3

Experimental setup

Introduction

In this chapter the experimental setup for testing the sensor is explained in detail. The entire arrangement was installed on an optical table, and all the experiments were carried out at the optics laboratories of the Department of Electronic Engineering.

The aim of developing the experimental setup was to provide us the experimental data in order to prove the principle of operation of the two sensor methods which have been theoretically designed and will be extensively described in chapters 4-6. It would also provide enough information regarding i) weak points of the sensor design, which are generally difficult to be theoretically predicted, ii) advantages and disadvantages of both metallic and elastomer sensors, and iii) future improvements of the sensor performance. At the preliminary stage of the sensor design which is presented in this thesis, we were mainly interested to test fundamental features concerning the sensors. More specifically, we were interested to measure the linearity, sensitivity, and dynamic range with respect to shear stress, as well as the cross-sensitivity to vertical stress of the sensors, with particular emphasis to satisfy the specifications for the development of the in-shoe shear stress transducer, which were presented in section 2.3. Dynamic measurements of the sensor behaviour for frequencies above 3Hz require significant modifications of the setup and investment in faster readout equipment and were not feasible during this study.

Regarding the metallic sensor approach, the experimental arrangement was initially used to measure the sensor structure's response to shear and vertical stress, and the structure behaviour under different directions of shear, for an enlarged version of the sensor. It was also used to measure the wavelength shift of a fibre Bragg grating installed in the sensor structure. The setup was then modified to measure the elastic properties of the materials examined for the implementation of the elastomer sensor, i.e. the Young's modulus and the shear modulus of elasticity. It was also used to test the response of the elastomer sensor to shear and vertical stress.

The mechanical apparatus for measuring the sensor response to shear and vertical stress will be described in section 3.1. The calibration procedure of the stress measuring system

will be explained in section 3.2. The capability of the system for dynamic measurements is tested in section 3.4. The description of the optoelectronic readout system and its calibration are explained in sections 3.5 and 3.6.

3.1 Mechanical apparatus

The mechanical apparatus used to apply shear and vertical stress on the sensor will be explained in detail in section 3.1.1 where the system used for the measurement of the metallic sensor will be described. Section 3.1.2 describes the modifications on the system in order to measure the response of the elastomer sensor to shear and vertical stress. The experimental setup for the measurement of the elastic properties of the materials, which are required for the theoretical design of the elastomer sensor is also described. The measurement of the shear modulus of elasticity is discussed in section 3.1.3, and the measurement of the Young's modulus of elasticity in section 3.1.4.

3.1.1 Apparatus for measuring the metallic sensor

The design and principle of operation of the metallic sensor will be discussed in detail in chapter 4. In order to describe the experimental setup, we only need to consider the sensor as a metallic structure consisting of two parallel disks separated by a number of metallic pins. The upper disk is able to deflect parallel to the lower one under the application of shear stress on its top surface, as a result of the bending of the pins. The displacement of the upper disk produces strain on the FBG installed between the disks, which is proportional to the applied shear stress.

In this section we describe the apparatus for the application and measurement of shear and vertical stress on the sensor structure, and the measurement of the relative displacement of the upper disk with respect to the lower one. This is given schematically in Fig.3.1. The sensor structure is placed between a fixed aluminium base and a moving plate (top plate), which is able to move in the x and y directions, but not in the z direction. This is achieved by using two uni-directional translation stages, stage 1 and stage 2, assembled together as shown in the figure. High precision translation stages[1] were used in this crucial part of the setup for three reasons. First, any motion of the top plate in the z-direction must be blocked. This ensures that the shear force applied by the electromagnetic vibrator will produce deflection of the top plate at the x-direction only, and hence uni-directional displacement of

[1] Stage 1: Photon Control, stage 2: Physik Instrumente

the upper disk of the sensor. Second, any tilt angle[1] around y-axis must be minimised. Tilting of the top plate will produce asymmetric vertical loading of the pins, leading to unpredictable response of the structure to shear stress. Finally, the friction between the moving plates of the stages should be minimised. This is particularly important for stage 1. The friction in this case results in uncertainty of measuring the actual shear force which is transferred from the vibrator to the upper disk. More specifically, the force sensor measures larger shear force, which is the sum of the actual shear force applied on the sensor and the friction. For that purpose, the stages were disassembled, and the bearings cleaned and lubricated in order to further reduce friction.

A picture of the apparatus shown schematically in Fig.3.1, is given in appendix II (picture 2).

[1] The tilt angle in this case is defined as the angle between the perpendicular to the top surface of the top plate and the y-axis. It can be caused by eccentric loading of the top disk. More information on translation stage properties can be found in LINOS Photonics, (1999).

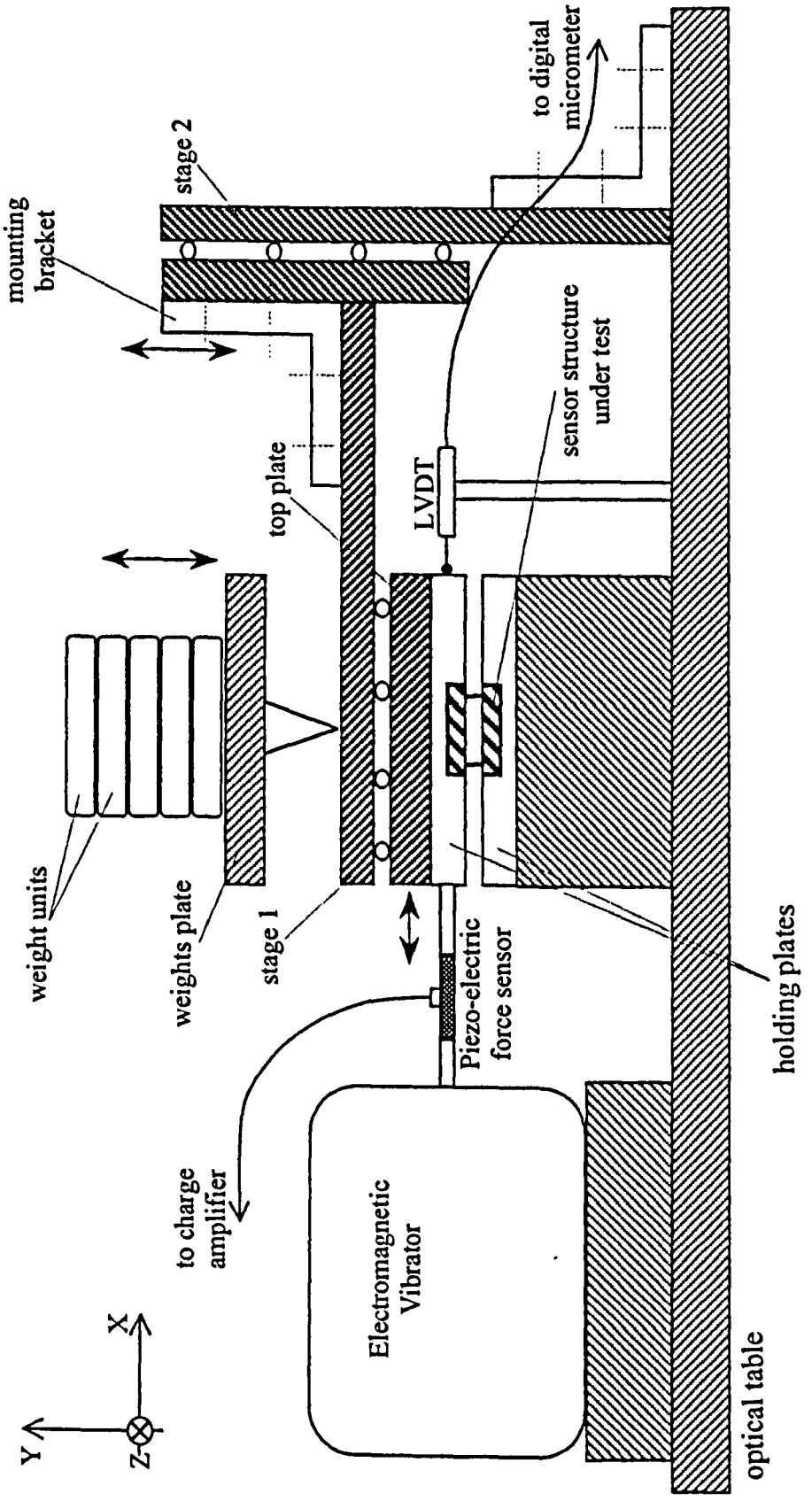

Fig.3.1: The mechanical apparatus for measuring the metallic sensor, which shows the placement of the sensor between the fixed base and the moving top plate.

The vertical stress is applied by a third stage (not shown), identical to stage 2, which enables the movement of the weights in the vertical direction only. To avoid eccentric loading and prevent tilting of the top disk, the vertical load is applied above the centre of the sensor disk. The vertical stress can be discretely varied by changing the number of known weight units placed on the weights plate.

The sensor structure is held by two auxiliary aluminium plates (holding plates). One of them is screwed to the base and the other one to the bottom surface of the top plate. These plates are carefully drilled at a radius equal to the disk diameter in order to minimise the gap between the sensor disks and the holding plates. These plates are necessary in order to prevent slippage of the sensor, or of the top plate, due to shear. Furthermore, the sensor can be rotated inside the holding plates with respect to the vertical axis passing through the centre of the disks. This simplifies the task of measuring the response of the structure to shear stress in different directions. The sensor is simply rotated to the desired angle, while the rest of arrangement remains the same. Another reason for using the holding plates is the ability to measure sensor structures having different disk diameters by simply replacing the holding plates without altering the rest of the setup.

It can be noticed that the horizontal force acting on the sensor is not the result of shear stress applied on the top surface of the upper disk, which will be the case of the real sensor as a result of the friction between the plantar skin and the surface. The horizontal force acting on the sensor in the setup shown in Fig.3.1 is applied on the side surface of the disks. If, for example, the E/M vibrator pushes the top plate, the top disk will deflect towards the right (positive x-axis) as a result of the force acting on the side of the upper disk, specifically in the interface region between the disk and the holding plate. This force produces exactly the same pin deformation as the one caused by an equal shear force acting on the upper surface of the sensor. Since the purpose of the following experiments is the investigation of the pin deformation caused by a horizontal force, the way which this force is applied is not important, as long as it is always applied on the upper end of every pin. In the following sections, as well as in section 4.3 where the experimental results for the metallic sensor are presented, the term "shear force" is still used, but it actually refers to the horizontal side forces explained above.

The reaction to the horizontal force acting on the side of the upper disk will be an opposite force acting on the side surface of the lower disk. These two forces tend to rotate the sensor with respect to the z-axis, which can be prevented by minimising the gap between the disks and the tracks on the holding disks, and by keeping the sensor disks as deep as possible into the holding plates.

A piezo-electric force sensor[1] (Kistler, type 9301A) measures the shear force applied on the top plate. The horizontal displacement of the top plate is measured using an LVDT displacement sensor (Tesatronic[2], type 32.10801). Fig. 3.2 shows the block diagram of the equipment and the required connections. The E/M vibrator (Goodmans Industries Ltd, type:390A) is driven by a mechanical impedance power amplifier (Bruel & Kjaer, type 2712). The frequency and amplitude of the shear force is controlled by a signal generator (Thandar Electronics Ltd, type TG501). The linear variable differential transformer (LVDT) sensor is read out by a digital micrometer (Tesatronic, model TTD 20). A charge amplifier (Kistler[1], type 5007) is used to read out the force sensor. The output of the charge amplifier, as well as the analogue output of the micrometer, are connected to the input channels of a digital storage oscilloscope[3] (LeCroy 9314) for the simultaneous monitoring of the shear force and the horizontal displacement.

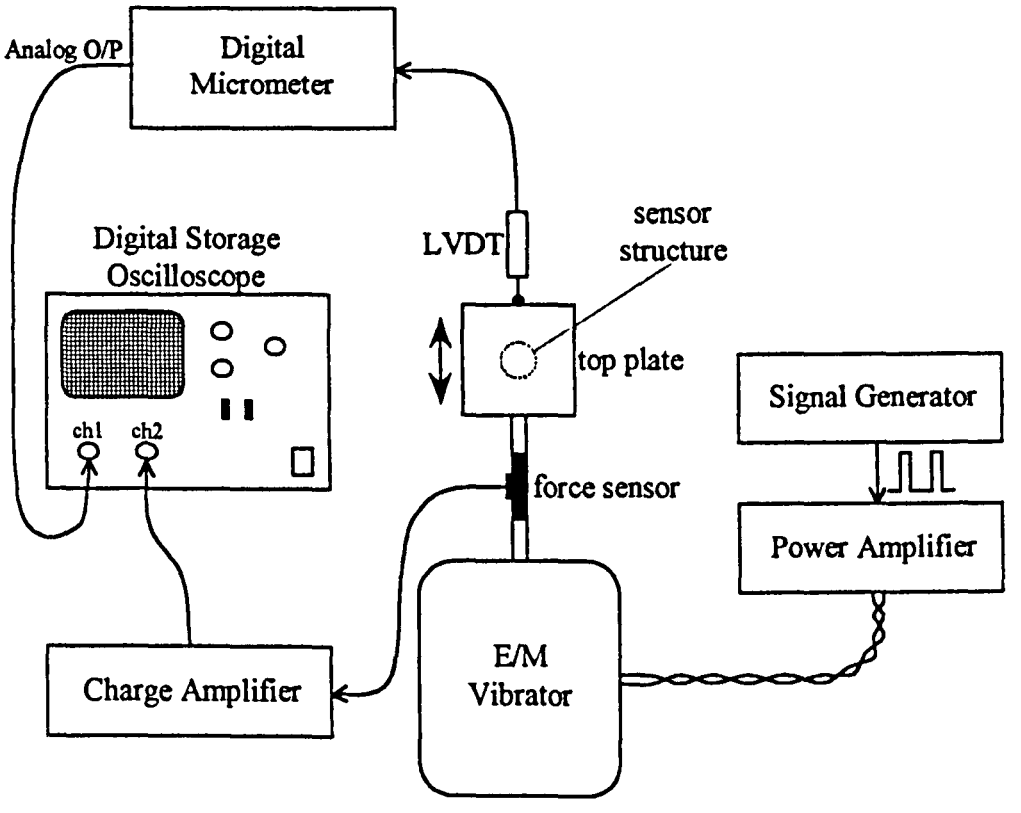

Fig. 3.2: Experimental arrangement for the application of shear force on the top plate and the measurement of shear force and upper disk displacement.

The E/M vibrator, the base, the top plate assembly, the LVDT sensor, and the vertical load assembly are all firmly mounted on an optical table in order to minimise external vibrations during the measurements.

---

[1] Kistler Instrumente AG, CH-8408 Winterthur, Schweiz, tel: (052) 831111.

[2] Brown&Sharpe TESA SA, Bugnon 38, CH-1020, Suisse, tel: +41 21 6341551.

[3] LeCroy Ltd., 27 Blacklands Way, Abingdon Business Park, Abingdon, Oxon, OX14 1DY.

Before proceeding to the testing of the structure, it is necessary to transform the vertical weight and the output voltage of the charge amplifier in terms of stress on the sensor. The output voltage of the micrometer, which corresponds to horizontal displacement, should also be expressed in length units.

Assuming uniform distribution of the vertical stress σ_y over the upper disk, we obtain:

$$\sigma_y = \frac{F_v}{A} = \frac{m_v g}{\pi r^2} \tag{3.1}$$

where F_v is the vertical force acting on the upper disk, A is the area of the top surface, r the disk radius, and g is the acceleration of gravity. The total mass m_v, which is placed on the sensor, will be the summing of the mass of the top plate assembly (masses of the upper moving plate, stage 1,mounting bracket, and moving plate of stage 2), plus the moving parts of the weights plate (including the mass of the weight units). For r=5mm, eq.(3.1) gives:

$$\sigma_y = 125 m_v \ (\text{kPa}) \tag{3.2}$$

The digital oscilloscope displays and measures the voltage of the output of the charge amplifier (channel 1), as well as the analogue voltage output of the micrometer (channel 2). The voltage readings from channel 1 must be transformed in order to express shear stress. The charge amplifier was configured (according to the operation instructions) to provide responsivity R_1 equal to 0.2V/N. The output voltage of the charge amplifier V_1 is given by:

$$V_1 = F_{sh} R_1 \tag{3.3}$$

Eq.(3.3) can be used to calculate the shear force F_{sh} applied by the vibrator, which can be used to calculate the shear stress on the sensor:

$$\tau_{yx} = \frac{F_{sh}}{A} = \frac{V_1}{R_1 A} \tag{3.4}$$

For a sensor radius r=5mm, eq.(3.4) gives:

$$\tau_{yx} = 63.7 V_1 \ (\text{kPa}) \tag{3.5}$$

Eq.(3.5) was derived by using R_1=0.2V/N, as this is given in the data sheet of the charge amplifier. However, the shear stress readout system was calibrated prior to the experiments in the expected operating range. The calibration procedure and the derived transformation of charge amplifier output voltage to shear stress, will be given in section 3.2.3.

The voltage readings from channel 2 can be transformed to μm using the responsivity R_2 of the micrometer:

$$R_2 = 10 \text{mV}/\mu\text{m} \tag{3.6}$$

Hence:

$$\delta = 100 V_2 \ (\mu\text{m}) \tag{3.7}$$

Eq.(3.7) is used to calculate the upper disk displacement by measuring the micrometer output voltage V_2, where V_2 in the above equation is in (V).

3.1.2 Apparatus for testing the elastomer sensor

The elastomer sensor consists of a solid block of material in which FBGs are embedded, as will be explained chapter 5. Contrary to the metallic sensor where the deflection of the pins determines the performance of the sensor, in this case the deformation of the entire block of the material contributes to the response of the sensor. It was mentioned in the previous paragraph that, instead of shear stress applied on the top surface of the metallic sensor, similar results could be obtained by applying horizontal force on the side of the upper disk via the holding plates shown in Fig.3.1.

The use of similar holding plates for the testing of the elastomer sensor is expected to significantly affect its response to shear stress. The reason for this is shown in Fig.3.3. The outer shape of the material, as well as the internal stress distribution when the forces are applied on the interface region between the side surfaces of the holding plates and the sensor (Fig.3.3a), will be different from the deformation of the material when no holding plates are used and shear stress is applied on the top surface as the result of friction between the material and the top plate (Fig.3.3b). Since in-shoe shear stresses are developed due to friction between the foot plantar surface and the sensor, the sensor should be measured without using holding plates. The drawback of removing the holding plates is that measurements can be taken for shear stress up to a maximum value which is proportional to the vertical stress and the constant of static friction. Larger values of shear stress will result in slippage of the top plate.

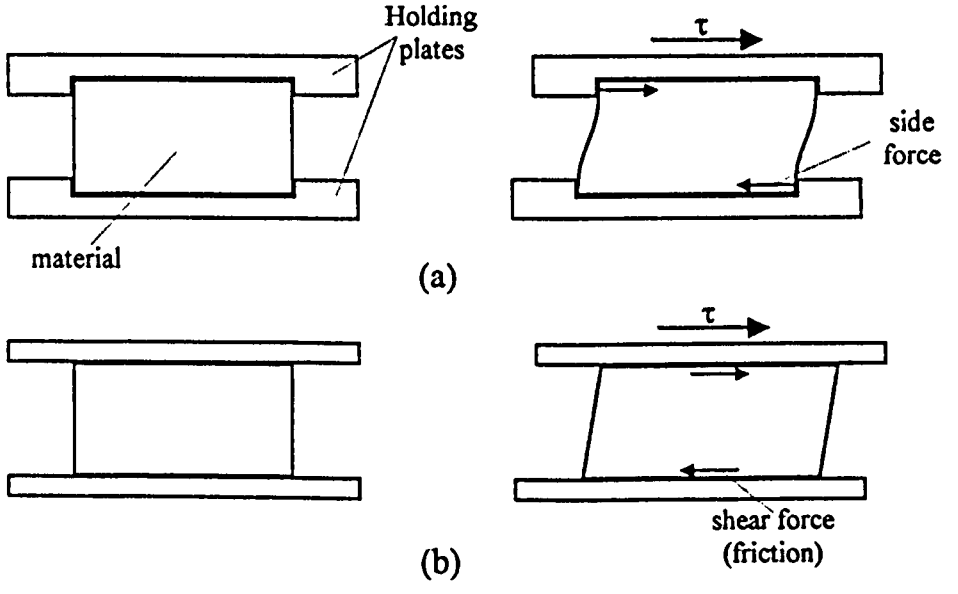

Fig.3.3: (a) deformation of the elastomer material due to the side forces applied by the holding plates. (b) deformation and shear force development due to friction.

The mechanical apparatus shown in Fig.3.1 can therefore be used for testing the elastomer sensor after removing the holding plates. To prevent damage of the LVDT micrometer head due to slippage of the top plate, the LVDT was placed on the left-hand side with respect to the plate (referring to Fig.3.1) so that it measures the distance which it travels away.

The charge amplifier output voltage is used to calculate the applied shear stress. It will be given by eq.(3.4), where A in this case is the area of the top surface of the elastomer sensor. For a 10x10 mm square top surface and R_1=0.2V/N, we obtain:

$$\tau_{yx} = 50V_1 \text{ (kPa)} \tag{3.8}$$

The arrangement shown in Fig.3.1 and Fig. 3.2 can be used to measure the response of the elastomer sensor under variable shear stress by varying the driving current of the E/M vibrator. The vertical load can also be varied discretely, as described in the previous section.

3.1.3 Measurement of the shear modulus of elasticity

We define the shear modulus of elasticity G using the theory and notation used for describing the behaviour of elastic solids, as is extensively presented in the textbook by Timoshenko and Gere (1973).

Let us consider the solid block of elastomer shown in Fig.3.4. The shear stress τ_{yx} is applied on the top surface parallel to the x-axis, causing elastic deformation of the material.

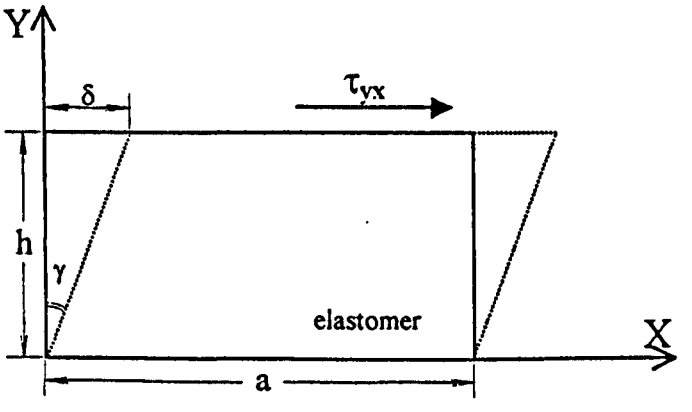

Fig.3.4: Deformation of a solid block of material under shear stress.

The shear modulus of elasticity (or modulus of rigidity) G is defined by the ratio:

$$G = \frac{\tau_{yx}}{\gamma} \tag{3.9}$$

where the angle γ is the shear strain on the material. It is given by:

$$\gamma = \arctan\frac{\delta}{h} \tag{3.10}$$

where δ is the relative displacement of the top surface with respect to its initial position, and h is the height of the block. The shear stress is given by:

$$\tau_{yx} = \frac{F_{sh}}{A} \tag{3.11}$$

where F_{sh} is the shear force measured by the force transducer, and A the top surface area. For a square top surface of side a, eq.(3.11), using eq.(3.4), gives:

$$\tau_{yx} = \frac{V_l}{R_l a^2} \tag{3.12}$$

As shown by eq.(3.9), G can be measured by plotting τ_{yx} and γ, as given by eq.(3.12) and eq.(3.10) respectively, and calculating the slope of the curve. The relative displacement δ is measured by eq.(3.7).

3.1.4 Measurement of the Young's Modulus of elasticity

Another important parameter of the material which is necessary for the elastomer sensor design, is the Young's modulus of elasticity E. Let us consider again the solid block of material which is now subjected to vertical compression, Fig.3.5. By definition, E is given by (Timoshenko and Gere, 1973):

$$E = \frac{\sigma_y}{\varepsilon_y} \tag{3.13}$$

where σ_y is the vertical stress and ε_y is the strain of the material on y-direction. According to eq.(3.13), E can be measured by plotting σ_y as a function of ε_y and calculating the slope of the curve.

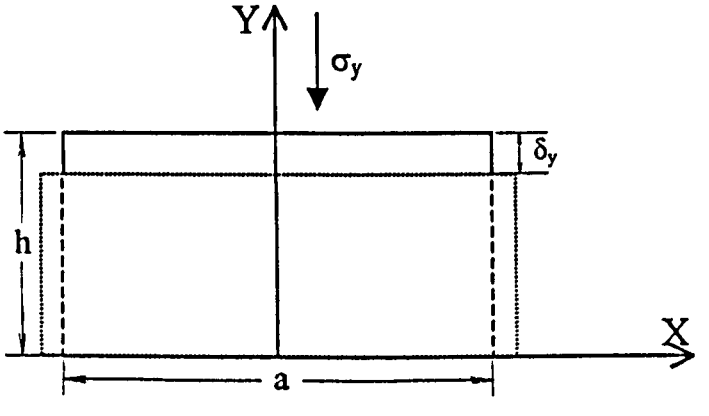

Fig.3.5: Vertical compression of a solid block of material.

It is already mentioned (section 3.1.1) that vertical stress can be measured by adding all the weights placed above the sensor, which in this case is a solid block of the material under test, and then apply eq.(3.1), which can be re-written as follows:

$$\sigma_y = \frac{m_v g}{a^2} \tag{3.14}$$

A drawback of this indirect method of measuring vertical stress is the error introduced by the fact that all the weight units are not identical, as will be seen in section 3.2.3, therefore the total mass cannot be known precisely.

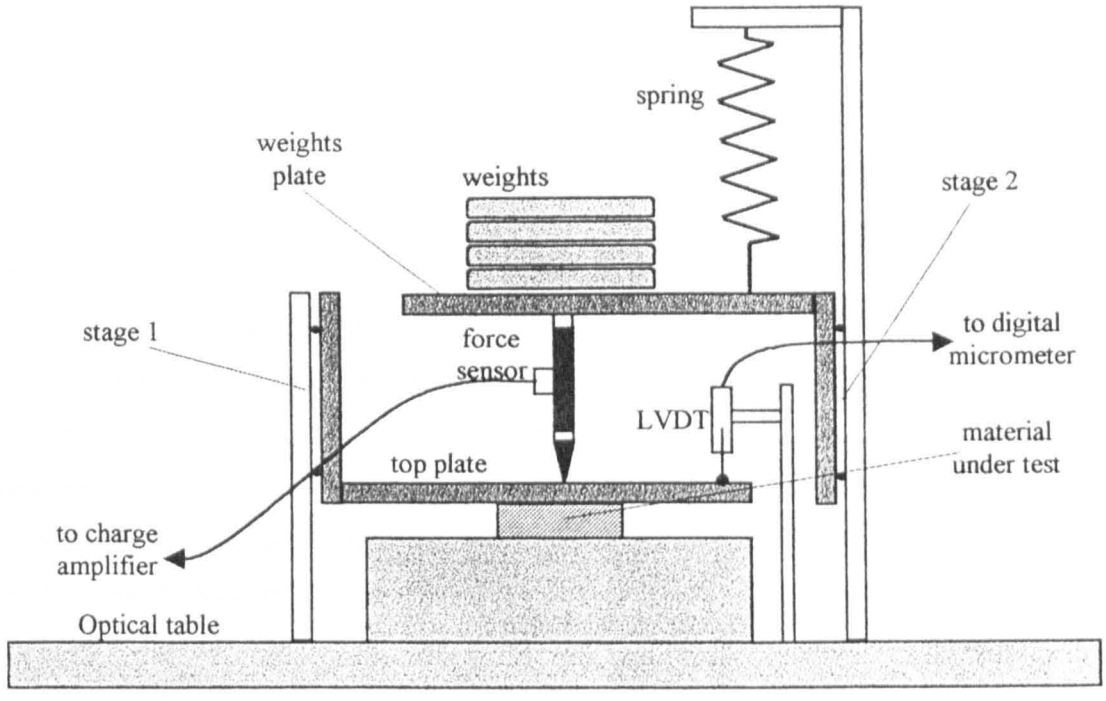

Fig.3.6: Experimental arrangement for measuring the Young's modulus of elasticity.

It is possible to measure vertical stress directly using the force transducer. For that purpose, the experimental apparatus was modified as shown in Fig.3.6. In this figure, the force transducer measures the vertical load applied on the top plate. It must be mentioned that, since we are only interested in measuring vertical compression during this experiment, the horizontal translation stage (stage 1, Fig.3.1) was removed. A picture of the experimental setup for the measurement of the E-modulus is given in appendix II (picture 1).

The weight of the top plate is always applied on the sample under test throughout the experiment. Therefore, the minimum value of vertical stress occurs when the weights plate is lifted so that it does not touch the top plate, and corresponds to the weight of the top plate. The overall weight of the top plate (moving part of stage 1 plus mounting bracket) was measured to be 0.38kg, as will be discussed in section 3.2.3. Eq.(3.14). For a=10mm, this gives 38kPa, which is the equivalent stress on the material.

The vertical compression is measured using the LVDT, which is now positioned to measure the vertical displacement of the top plate. In order to compensate the weight of the weights plate (0.38kg, equal to the weight of the top plate), a spring was prestrained so that the weight plate just touches the top plate when no weight units are placed on it. Omitting this spring would limit the measurements for stresses above 76kPa (38kPa from top plate plus 38kPa from weights plate).

A second spring, identical to the previous one, could be used to compensate the weight of the top plate. However, it was noticed in practice that some initial vertical load was necessary in order to make sure that the top plate is in contact with the entire top surface of the sample. This was due to the fact that the upper and lower surfaces of the samples could not be manufactured precisely smooth and parallel to each other. The initial vertical stress compresses the material and eliminates gaps between the material and the metallic surfaces. Examining the interface region with a magnification lens, it was observed that the stress applied by the top plate (38kPa) was sufficient to prevent non-uniform loading of the sample. The compression of the material for shear stresses smaller than 38kPa can be estimated by extrapolating the experimental data.

The experimental setup explained in this paragraph will also be used for the testing of the elastomer sensor response to vertical stress. The LVDT in that case is not necessary, since the vertical stress and the Bragg wavelength shift of the embedded grating must only be measured. The experimental setup for the measurement of the Bragg wavelength shift will be discussed in sections 3.5 and 3.6.

3.2 Experimental testing and calibration of the stress measuring system

The stress measuring system is described in section 3.2.1. The stress resolution of the system, and the calibration procedure will be discussed in sections 3.2.2 and 3.2.3 respectively.

3.2.1 System description

The stress measuring system consists of the piezoelectric force sensor, the charge amplifier, and the digital oscilloscope, as shown in Fig. 3.2. When axial force is applied on the piezoelectric element, electrostatic charge signal is generated. The phenomenon is called piezoelectricity, and it has been utilised in the design of several types of force and pressure transducers (Rangan *et al.*, 1994, pp.143-145). This signal is in turn converted by the charge amplifier into an electric voltage which is recorded by the oscilloscope.

Table 3.1 gives a list of the most important specifications of the force sensor. More information and the complete data sheets are given in the operation manual[1].

A typical response of the stress measuring system is given in Fig.3.7. The plot is taken by downloading the data points from the oscilloscope. At time t_1=3sec, constant axial force is applied on the force sensor. We notice that from t_1 to t_2, where the stress is kept constant, the output voltage of the charge amplifier exponentially decreases and tends to return to zero.

[1] Kistler Piezo-instrumentation "Operating Instructions – Quartz force links", B6.013e Ed.8.68 p.3

At t_2=8.5sec, the stress is removed, causing a fast reduction of the output voltage which reaches a negative value. After t_2 the voltage exponentially increases to zero.

Dynamic range	±2500N
Responsivity[1] (R_1)	0.2V/N
Resolution	0.01N
Linearity	≤1%
Error due to eccentric loading	2%
Frequency response[2]	180kHz

Table 3.1: Specifications of Kistler force sensor[1].

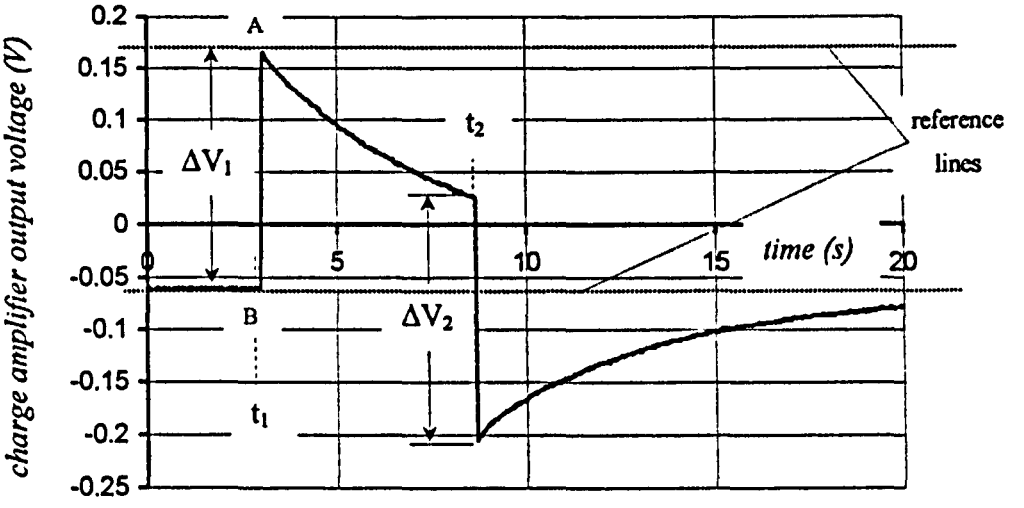

Fig.3.7: Typical time response of the force readout system.

For the low frequency measurements carried out in this study (stress is varied up to 3Hz when testing the sensor), the measurement of the mean output voltage between t_1 and t_2 will introduce error in calculating the stress, since this is dependent on the duration t_2-t_1, and hence on the period of the stress pulses. The magnitude of shear stress is calculated by measuring the transient voltage during the application of stress, ΔV_1, or during the removal of stress, ΔV_2, provided that the transient times Δt_1 and Δt_2 are much smaller than the time constant of the exponential drift. When the transient times are equal, then ΔV_1=ΔV_2.

[1] Depends on charge amplifier gain, which was set to 5 mechanical units / V.

[2] Kistler Piezo-instrumentation "Charge amplifier", B11.5007e Ed.7.81 p.4

3.2.2 Measurement of the stress resolution

The transient voltage is measured by holding the trace on the oscilloscope screen and manually placing two reference lines at points A and B, as shown in Fig.3.7. The oscilloscope measures the voltage difference between those two lines. This procedure introduces the following sources of error:

1. Quantisation error caused by the analogue to digital (A/D) conversion of the sampled charge amplifier output voltage. It is determined by the dynamic range of the instrument and the byte length of the A/D converter. Table 3.2 shows the quantisation error of the LeCroy oscilloscope, as this is measured for different voltage scale levels.

scale (mV/div)	Quantisation error (mV)	scale (mV/div)	Quantisation error (mV)
50	0.8	500	8
100	2	1000	20
200	3	2000	30

Table 3.2: Quantisation error on the oscilloscope at different scales.

2. Uncertainty of the precise location of points A and B Fig.3.7, due to noise on the output of the charge amplifier. This can be clearly seen in Fig.3.8, which shows the output voltage when no force is applied on the sensor. The maximum peak-to-peak variation does not exceed 2mV. The noise could be eliminated using a low-pass filter. However, comparing the noise with the quantisation error given in Table 3.2, we realise that no significant improvement on the resolution of the system would be achieved by using such a filter. Except by the 50mV/div scale, which was not used during the experiments, the noise is less or equal to the quantisation error at any other scale.

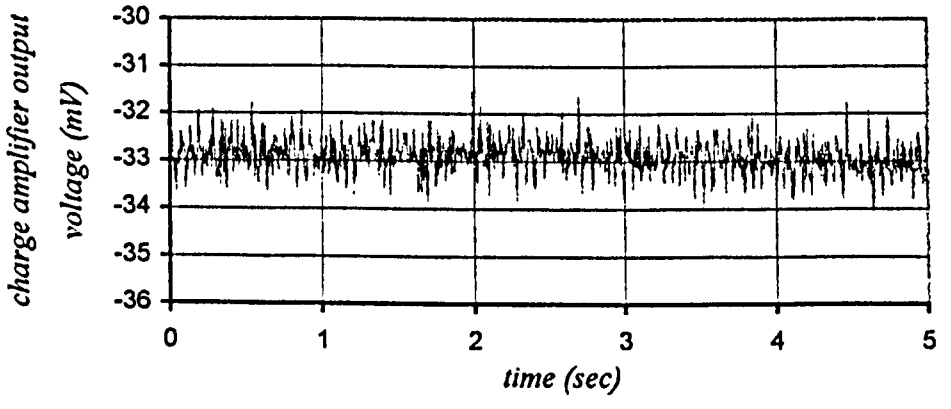

Fig.3.8: Noise of the stress measuring system.

The error in measuring the charge amplifier output voltage sets the actual resolution of the stress readout system. At a voltage scale 50mV/div, the resolution is limited by the 2mV noise. Only voltage differences above 2mV can be measured, which can be converted to force resolution using eq.(3.3). The stress resolution of the system can be calculated using eq.(3.5) and eq.(3.8) for the measurement of the metallic and the elastomer sensor respectively. Averaging of the signal can improve the resolution, but it will significantly reduce the speed of the readout system. For any other voltage scale, the quantisation error dominates, reducing the resolution of the system as the scale increases. Table 3.3 shows the voltage error, the force resolution, and the stress resolution for the metallic and the elastomer sensor, for different voltage scales.

voltage scale (mV/div)	error in measuring voltage (mV)	force resolution (N)	resolution for metallic sensor (kPa)	resolution for elastomer sensor (kPa)
50	2	0.01	0.13	0.1
100	2	0.01	0.13	0.1
200	3	0.015	0.2	0.15
500	8	0.04	0.51	0.4
1000	20	0.1	1.27	1
2000	30	0.15	1.91	1.5

Table 3.3: Actual (measured) resolution of the stress readout system

3.2.3 Calibration

Before using the stress readout system, it is important to measure the system response over the entire operating range (0-500kPa, section 2.3). The linearity and responsivity of the piezoelectric force sensor and charge amplifier, as those are given by the manufacturer and quoted in Table 3.1, cannot be assumed for the entire testing system. We have already seen in the previous section that the resolution of the stress measuring system is up to 15 times lower than the resolution of the piezoelectric transducer, due to the use of the oscilloscope (comparing the value from Table 3.1 and Table 3.3, column 3).

Another parameter that deteriorates the accuracy of our measuring system is the friction between the moving parts of the translation stages. Cleaning and lubrication (section 3.1.1) reduces friction but does not eliminate it. As a result, the shear stress transferred from the vibrator to the sensor (Fig.3.1) will be less than the measured by an amount equal to the friction, which depends on the friction constant and the vertical stress. The friction cannot be accurately measured, therefore error will be introduced.

As the shear and vertical stresses increase, bending moments can be developed in the testing apparatus due to possible buckling of the connecting rods (Fig.3.1), which could produce asymmetrical loading of the force transducer, and hence error in measuring stress. The manual loading of the weights on the weight plate could also produce asymmetrical loading of the force sensor due to bending moments. This applies in the setup for the measurement of the Young's modulus and the measurement of the sensor response to vertical stress, Fig.3.6.

For all those reasons mentioned above we decided to calibrate the system and test its linearity in the required operating range prior to use it for testing the sensors. Initially, we measured the response of the force transducer by placing a number of weights directly on the sensor, as shown in Fig.3.9. The sensor was screwed on the optical table. A 1-inch diameter aluminium disk was then screwed on the top end of the sensor. This disk serves as the plate where the weight units can be placed. Ten steel disks with diameter equal to the aluminium disk, and weight approximately 50g each, were used as the known weights. The equal disk diameter between the aluminium disk and the weight disks helps to align the centre of gravity of the weights with the axis of the transducer, in order to avoid eccentric loading. Each steel disk was numbered and measured using a precision scale (OHAUS Precision Standard[1]). The precise weight of each disk is given in Table 3.4.

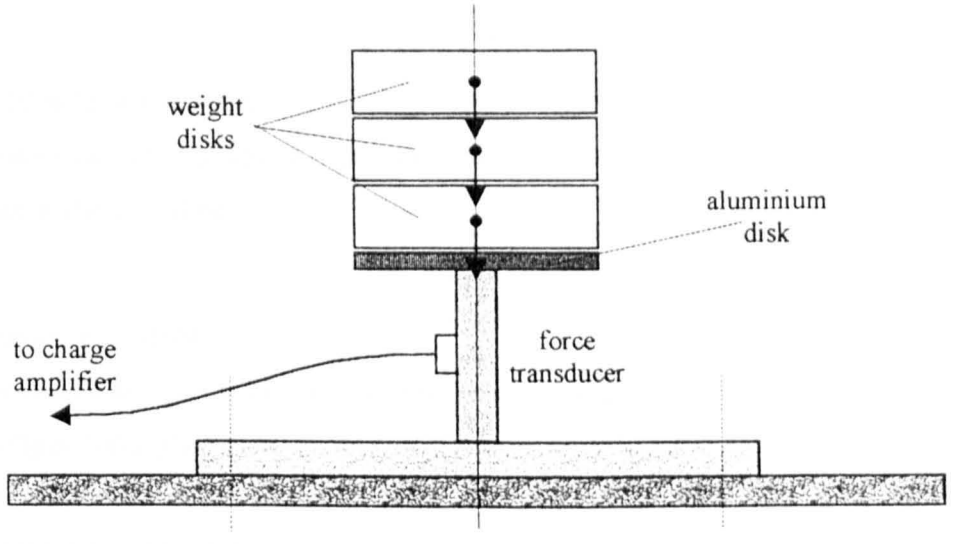

Fig.3.9: Testing of the force transducer in the range 0-5N

The weights were placed and aligned vertically on the transducer, starting from disk 1 and adding one disk at a time. The transducer response to axial stress was measured by recording the charge amplifier output voltage difference ΔV_2 (see also Fig.3.7) during the

[1] Ohaus, P.O. Box 900, 29 Hanover Road, Florham Park, NJ 07932,USA.Tel:(973)377-9000

removal of the weights. The voltage difference ΔV_1 could not be used in this experiment since a few seconds were necessary to vertically align the weights with the aluminium disk. The weights were then removed by manually lifting the weights. Practice was necessary in order to remove the weights as quickly as possible, without accidentally applying vertical compression on the transducer while lifting the weights.

It is important to mention that the setup described in this section will enable the calibration of the force transducer for measuring compressive forces only. Calibration of the sensor for extension forces is not necessary, since all the experiments carried out during this study produce compression of the transducer. This is clear in Fig.3.6 where the force transducer is compressed between the top plate and the weight plate while measuring the sensor response to vertical load. Compression also occurs during shear stress measurements, Fig.3.1, since the vibrator rod is in simple contact with the force transducer, therefore it can only push the top plate, and hence compress the force transducer. Since each transducer must be measured for shear stress in the range –250 to 250kPa, and for vertical stress 0 to 500kPa, we conclude that the maximum compressive stress which will be applied to the force transducer during the sensor tests will be 500kPa.

The transducer must therefore be calibrated in the range 0 to 500kPa. Since the actual variable measured is force, the stress range must be converted to force range. In case of the metallic sensor, stress is applied at the area of the upper disk, hence the maximum force will be given by eq.(3.1):

$$F_{max} = \sigma_y A = \sigma_y \pi r^2 \tag{3.15}$$

For σ_y=500kPa and r=5mm, eq.(3.15) gives $F_{max} \cong 40N$. Similarly, The maximum force, which corresponds to 500kPa in case of the elastomer sensor, where stress is applied on its top square surface, will be:

$$F_{max} = \sigma_y a^2 \tag{3.16}$$

For a=10mm, F_{max}=50N.

The results are shown in Fig.3.10. The location of each data point indicates the number of the weight disks placed on the sensor. The corresponding force (x-axis) is calculated by summing the masses of the weights, as they are given in Table 3.4. The voltage scale on the oscilloscope was set to 200mV/div, giving a maximum error of 3mV.

disk number	weight (g)	disk number	weight (g)
1	50.31	6	50.35
2	50.30	7	50.27
3	50.28	8	50.26
4	50.36	9	50.37
5	50.32	10	50.32

Table 3.4: Measured weight of the steel disks

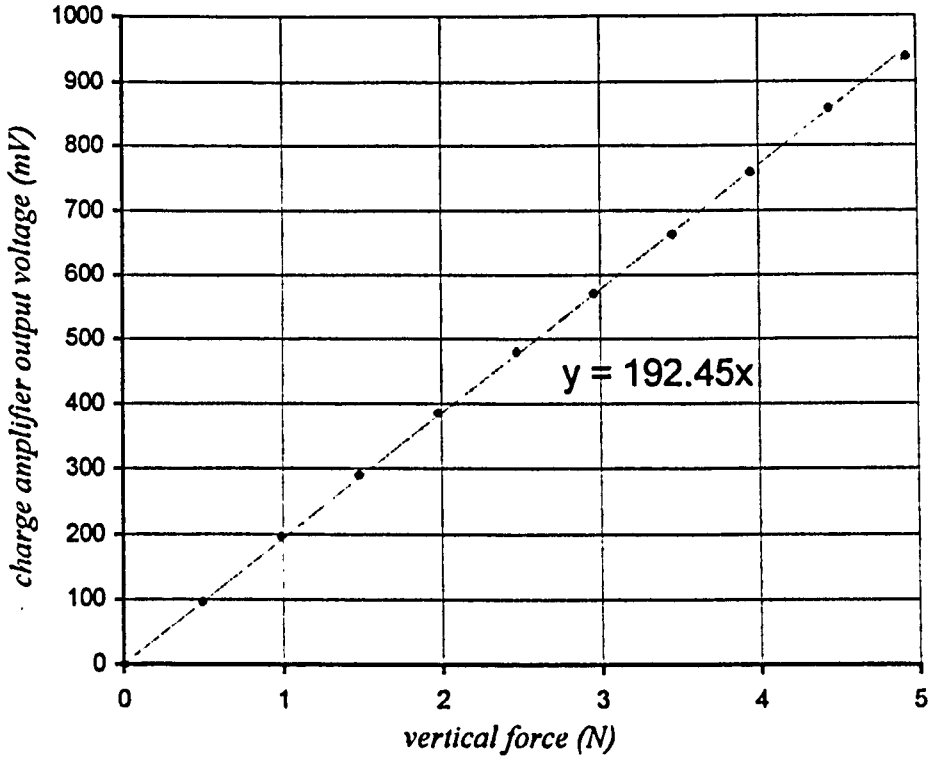

Fig.3.10: Force transducer calibration in the range 0-5N

The expected linear response of the transducer is clearly observed. The trendline equation gives the experimental value of the responsivity of the system, which is 0.19245V/N. We can see that the experimental value is very close to the one given by the data sheet (R_1, Table 3.1).

The main reason for calibrating the force transducer apart from the experimental apparatus as shown in Fig.3.9, is to measure the weight of the weights plate assembly. The precision scale could not be used because the weight was out of the measuring range of the instrument. The weight could be measured by disassembling the stage and measure each part (holding bracket, mounting bolts and nuts, moving part of stage) separately, using a different scale. However, the measurement of the weights plate assembly without disassembling it gives the advantage of measuring the repeatability of the application of the vertical stress, as well as identifying any problems related to friction. Finally, the experiment shown in Fig.3.9 gives one method for calibrating the sensor for forces lower than the weight of the weights plate,

which is the minimum vertical load that can be applied on the sensor and simultaneously measured by the force transducer.

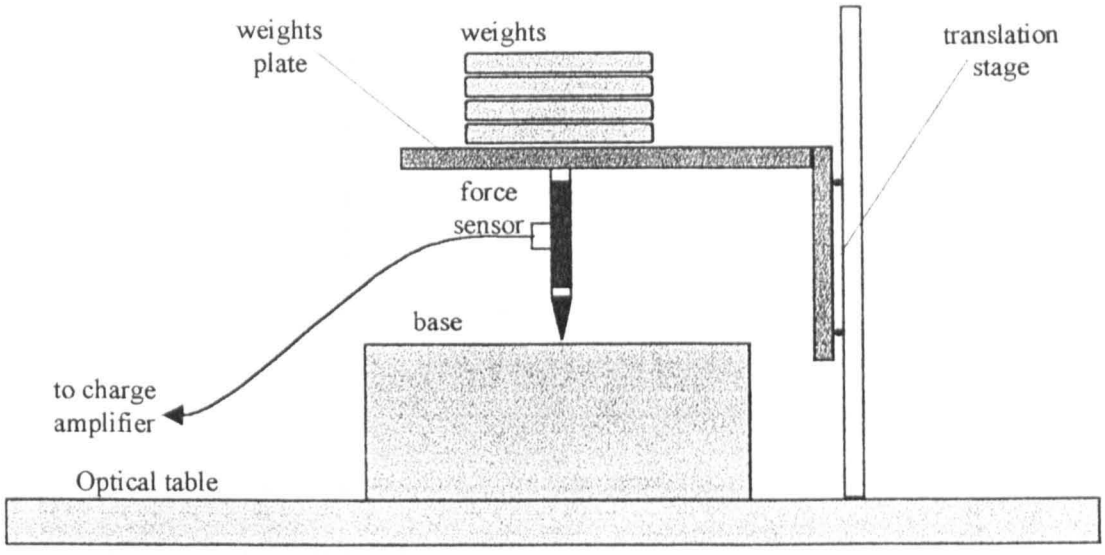

Fig.3.11: Calibration of the force sensor in the range 5 to 50N.

Fig.3.11 shows the experimental setup which was used for the measurement of the weights plate mass (when no weight units are placed on the plate), as well as for the calibration of the force sensor for forces larger than 5N. The translation stage is manually lifted and the voltage difference is measured during the removal of the weights (ΔV_2, Fig.3.7). In this case, the reason for measuring ΔV_2 instead of ΔV_1 is to avoid the peaks that appear due to the impact forces developed instantly when the transducer contacts with the metallic base. Typical time response of the charge amplifier output during manual application of vertical force equal to ~18N, is shown in Fig.3.12. The graph corresponds to one full screenshot taken with the time base set to 1s/div. Approximately 4 to 5 periods were recorder in the 10s interval, and then the trace was held in order to measure ΔV_2. From all the displayed pulses, the fastest transient was selected to measure ΔV_2. In this particular example, the off-transients of the first or second pulse could be used.

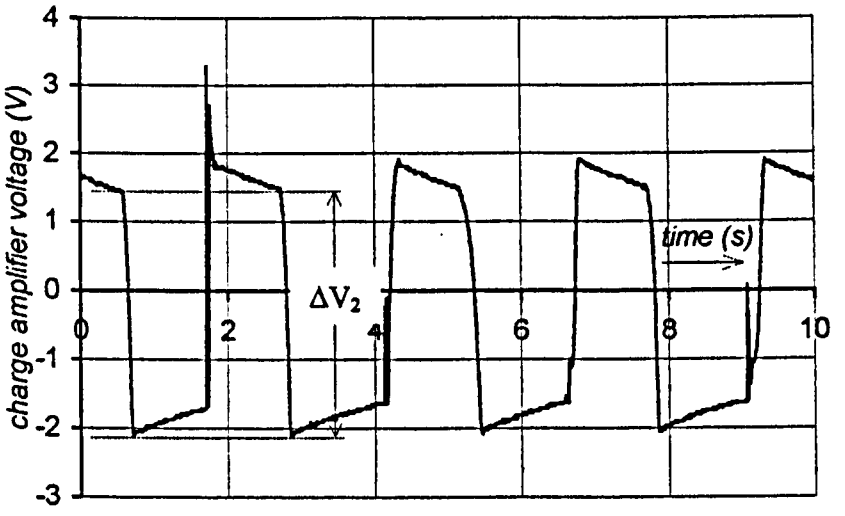

Fig.3.12: Time response of the force sensor after manual application vertical force equal to ~18N.

In order to check the repeatability in measuring the vertical stress, the weights plate was repetitively applied on the force transducer. Each value was measured by following the procedure described previously. Table 3.5 gives the measured charge amplifier output voltages when only the weights plate is applied on the force transducer. The average voltage gives 726mV, which corresponds to 3.8N (0.384kgr), as given by eq.(3.3). The maximum error is approximately ±12mV, which is caused by the limited resolution of the readout system as explained in section 3.2.2, which in this case is 3mV (scale 200mV/div), as well as by the friction in the translation stage.

725	728	725	731	725
725	713	725	725	728
725	725	731	731	731
741	725	722	713	725

Table 3.5: Voltage ΔV_2 (mV) by repetitively measuring the weighs plate.

In order to calibrate the force transducer for force up to 50N, a number of known weight units has to be placed on the weights plate. Two types of weight units were used. Both units are commercially available optical mounting plates which were available in the laboratory. The mass of each unit will be denoted by the symbol m_{Ai} and m_{Bj} for units A and B respectively, where the indexes i,j are used to identify each unit. They are rectangular steel plates ($77x51x10mm^3$). They can be placed one over the other on the weights plate to form the desired vertical load. Each plate was indexed, and measured using a precision scale (OERTLING TP40 Precision scale). Table 3.6 gives the mass of each unit.

index i	m_{Ai}(g)	m_{Bi}(g)	index	m_{Ai}(g)	m_{Bi}(g)
1	248.51	223.34	6	249.95	223.01
2	249.63	222.75	7	251.81	221.31
3	248.55	224.12	8	249.32	222.90
4	248.81	221.71	9	248.76	223.12
5	248.88	223.20	10	249.07	224.05

Table 3.6: Measured weights of unit types A and B.

The total force on the sensor can be calculated by the following equation:

$$F = \left(m_{wp} + \sum_{i=1}^{N} m_{Ai} + \sum_{i=1}^{M} m_{Bi} \right) g \tag{3.17}$$

where m_{wp} is the mass of the weights plate, 0.384kg, and N,M the number of units A and B respectively.

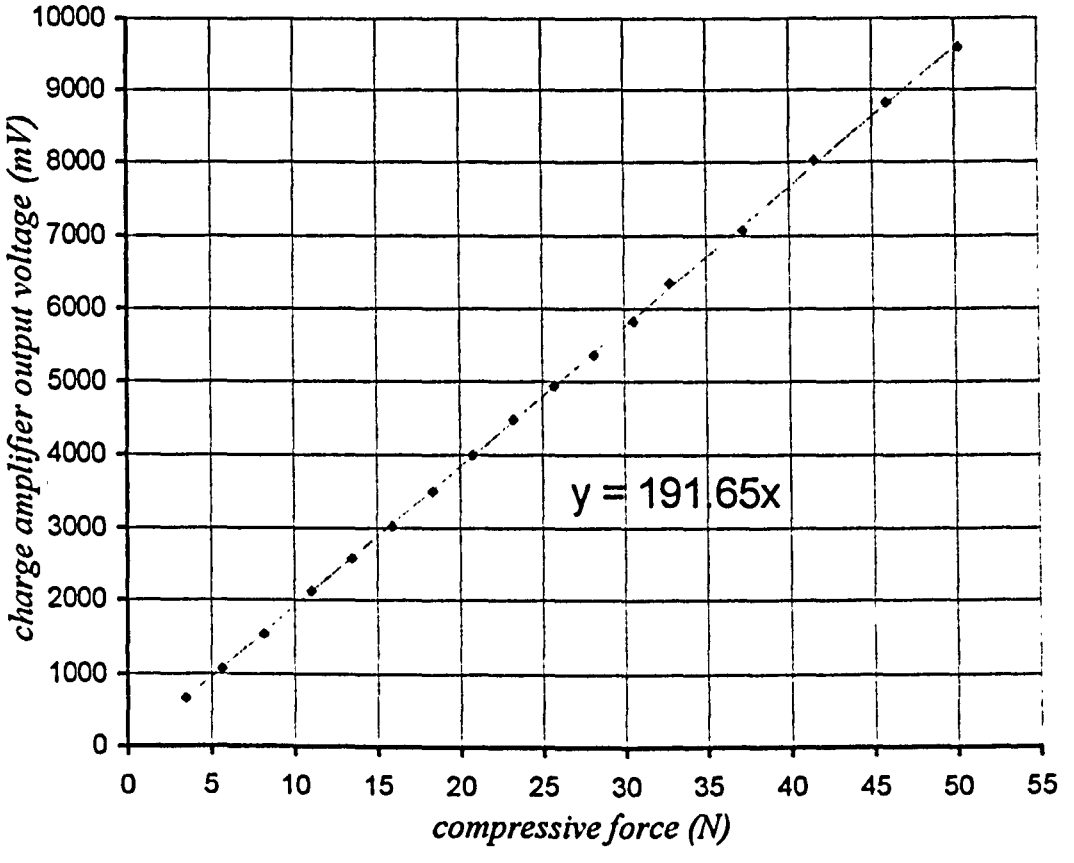

Fig.3.13: Force transducer calibration in the range 3.78-50N

Fig.3.13 shows the transducer response for vertical force in the range 3.78N (weights plate only) to 50N. The predicted error in measuring the voltage is ±12mV, as explained earlier in this section. The responsivity of the stress readout system in the 3.78-50N range is measured 0.192V/N, as shown by the trendline. The value is very close to the experimental value derived from the calibration of the transducer in the 0-5N range, and close to the

manufacturer specifications. In all the experiments carried out for both the metallic and elastomer sensor, we are using R_1=0.192V/N, as measured experimentally.

The calibrated force readout system was then used to measure the weight of the top plate assembly and the repeatability with respect to the vertical stress. For that purpose we followed exactly the same procedure as done earlier for the measurement of the weights plate. In this case, the top plate assembly (shown in Fig.3.1) was placed over the sensor. The oscilloscope scale set to 500mV/div (resolution 8mV). The measurement repeated several times and the measured output voltage for all the measurements is given in Table 3.7. The average voltage is 1443mV, which corresponds to 0.768kg (7.51N, eq.3.3). The maximum error is ±10mV.

1438	1453	1445	1438	1445
1438	1438	1445	1445	1445
1453	1445	1438	1438	1453
1438	1438	1453	1438	1445

Table 3.7: Voltage ΔV_2 (mV) by repetitively measuring the top plate.

During the testing of the shear response of the sensors using the arrangement shown in Fig.3.1, the top plate and the weights plate will be applied simultaneously above the sensor. The error in the estimation of the overall vertical load in that case will be caused by the uncertainty on the actual vertical load applied by the two plates. In terms of charge amplifier output voltage, the uncertainty will be the summing of the maximum errors measured previously, i.e. ±12mV due to the weights plate, and ±10mV due to the top plate, giving an overall maximum error of ±22mV. When only the top plate is applied, the output voltage is 726 ±12 mV, which gives error ±1.6%. Similarly, when both plates are applied, the output voltage is (726+1443) ±22mV, which gives error ±1.0%. Since the mass of all the weight units used in the experiments is precisely measured, the maximum error in calculating the vertical stress for any other vertical load will be less than 1%.

3.3 Displacement measuring system

It is already mentioned that the displacement of the top plate under shear or vertical stress is measured using a commercially available linear variable differential transformer (LVDT) transducer system (section 3.1.1). The operation is based on the variation of the mutual inductances between a primary and two secondary coils, which produces linear variation of the voltage generated on the secondary coils (Rangan *et al.*, 1994, pp.38-41).

Table 3.8 gives a list of the transducer specifications, as given in the data sheet. The maximum displacement, which was measured during the experimental investigation of the sensor and during the material testing, never exceeded 40μm, which lies inside the linear range of the transducer. The analogue output of the micrometer driving device has a fixed responsivity of 10mV/μm. Hence, the maximum voltage which had to be measured by the oscilloscope was 400mV. Table 3.9 shows the voltage scales which were used for measuring the micrometer output voltage, and the corresponding quantisation errors (see also section 3.2.2). The voltage is manually measured using the two reference lines in a similar way to the charge amplifier voltage measurement, as explained in section 3.2.2.The displacement is calculated by measuring the voltage of the micrometer output and then applying eq.(3.7).

Total measuring range	±3mm
Resolution	0.1μm
Linearity (L in mm from centre)	$0.2+2L^2$ μm
Frequency response	40Hz

Table 3.8: Specifications of Tesa displacement transducer[1].

A typical response of the micrometer output voltage under no displacement is shown in Fig.3.14. The output voltage fluctuates by approximately 2mV (±1mV from 0V). Some peaks of maximum ±5mV randomly appear on the signal, which can be neglected during the manual measurement of the micrometer output voltage.

scale (mV/div)	Quantisation error (mV)	scale (mV/div)	Quantisation error (mV)
5	0.08	50	0.8
10	0.2	100	2
20	0.3		

Table 3.9: Quantisation error on the oscilloscope at different scales

Examining the quantisation error values as given in Table 3.9, and the noise (2mV), we can estimate the resolution of the micrometer readout system. The noise of the micrometer output is the dominating source of error, which corresponds to 0.2μm actual resolution of the system. Averaging the output voltage decreases the resolution down to 0.1μm, which is the best resolution that could be achieved with the specific LVDT micrometer system, Table 3.8.

[1] "Electronic probes", Tesa B&S SA, http://www.tesabs.ch/pdf/palpe.pdf

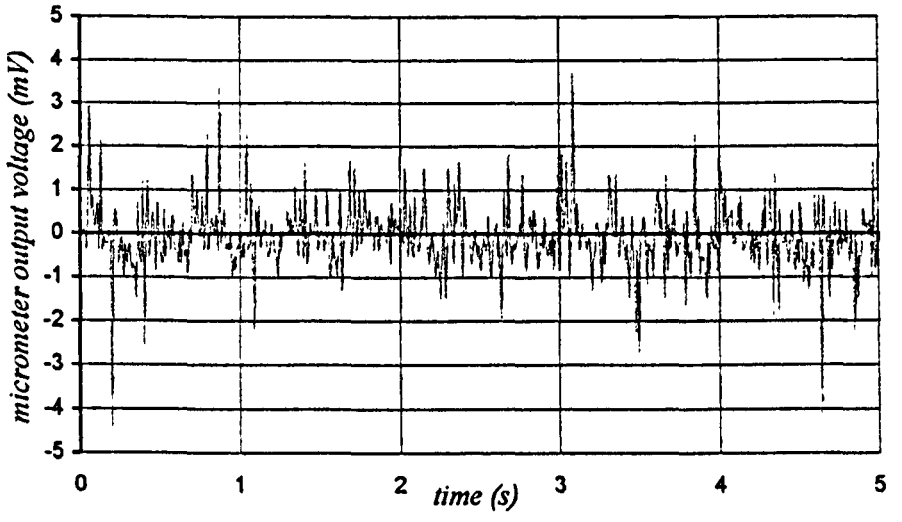

Fig.3.14: Noise on micrometer output voltage.

The micrometer readout system was not calibrated experimentally. One reason was that no other displacement system having a resolution of 0.1μm, and accurately calibrated in order to use it as reference, was available. Another reason is that, contrary to the force transducer which is part of the mechanical apparatus for the application of shear (or vertical) stress, the displacement sensor does not participate in or disturb the mechanical apparatus in any way. It is mounted on a separate rod, which is firmly fixed on the optical table. After the LVDT probe is aligned parallel to the shear stress direction (force sensor axis), and the initial displacement has been adjusted in order to get zero output voltage for best linearity, then we have no reason to doubt the calibration done by the manufacturer.

3.4 Capability of the mechanical testing system for dynamical measurements

It has already been mentioned in the introduction of this chapter that the primary task of the experiments was to evaluate the response and linearity of the metallic and elastomer sensors at low frequencies of shear stress. The main reason which prevented dynamical measurements on the sensors was the speed of the optoelectronic readout system used for the measurement of the Bragg wavelength shift, which will be presented in section 3.6. It will be shown that variations of the Bragg wavelength of up to approximately 3Hz could be measured by that system.

In this section, the results from the measurement of the mechanical system response to frequencies of shear stress up to approximately 200Hz will be presented. The aims of this experiment were:

1. To examine the system response to shear stress up to 3Hz, which is the range of interest for the experimental evaluation of the sensors.

2. To examine the capability of the mechanical apparatus, as well as of the stress and displacement readout systems to operate at higher frequencies. That would enable dynamical measurements of the sensors in the future, provided that the Bragg wavelength readout system is upgraded to a faster one (see section 7.4).

The setup which was tested is the mechanical apparatus shown in Fig.3.1. The metallic sensor structure, which will be presented in chapter 4, was placed between the holding plates. A sinusoidal voltage drives the vibrator which produces sinusoidal shear stress variation on the top plate. The purpose of the metallic sensor structure in this experiment is to provide the returning force on the top plate. In other words, the metallic structure and the top plate act as a spring-mass system.

The magnitude of the shear force was varied between 0 to 1.12N (eq.3.3 for V_1=0.215V), which in case of the metallic sensor, corresponds to 0 to 15kPa shear stress. The relatively low magnitude of shear stress, as well as the use of sinusoidal driving voltage instead of square pulses, were chosen in order to avoid strong impact forces that occur during the rise of each pulse. Those forces could damage the sensor, and would deteriorate the accuracy of the mechanical setup. Our system is vulnerable to impact forces because the vibrator shaft is in simple contact with the force sensor. Whenever the vibrator is driven in a way which causes temporary lack of contact between the vibrator axis and the force sensor, strong impact forces will be developed as a result of the acceleration of the vibrator shaft while not in contact. These impact forces are expected to be larger in case of square pulses compared to sinusoidal stress due to the higher forces applied on the shaft during the on-cycle of each pulse. It was therefore necessary to apply a DC biasing voltage to the vibrator in order to make sure that the contact between the force sensor and the vibrator shaft is never lost. It is reminded that the minimum force applied on the top disk is 0N. The force cannot change sign as a result of the simple contact between the vibrator and the force sensor, therefore the top plate can only be pushed.

The graphs shown in Fig.3.15 to Fig.3.18 are time responses of both stress and displacement readout systems, as they were simultaneously recorded by the oscilloscope. The primary y-axis gives the charge amplifier output voltage. The secondary y-axis (right) gives the micrometer output voltage. Examining those graphs we can notice the following:

1. The amplitude of the displacement oscillations of the top plate is constant for frequencies up to 10Hz, under constant amplitude of shear stress. This is clearly shown in Fig.3.15 and Fig.3.16, which give the responses at 1Hz and 10Hz respectively. The amplitude oscillates between 0 and 4.6μm ($\Delta V_2 \cong 46$mV). A gradual reduction of the amplitude is observed as the frequency increases above 10Hz. At 25Hz for example, Fig.3.17, the amplitude of the oscillations has been reduced to 3.5μm (approx. 25% reduction). The amplitude of the micrometer output voltage reduces by 3dB at 37Hz, as shown in Fig.3.18. Two factors are responsible for the observed reduction in the

amplitude of the displacement oscillation. The first one is the relatively low frequency response of the displacement sensor (Table 3.8), which has a –3dB response at 40Hz. The second factor is the relatively large mass of the moving top plate, which causes reduction of the amplitude of the oscillations of the spring-mass system (metallic structure – top plate).

2. Phase delay of the measured displacement with respect to the applied shear stress is observed, which is a function of the frequency. An estimation of the phase delay $\Delta\phi$ can be calculated using the following equation:

$$\Delta\phi = \omega\Delta t = 2\pi f\Delta t \tag{3.18}$$

where f is the driving frequency of the vibrator and ΔT is the time delay which can be measured from the graphs, as shown in Fig.3.16. Table 3.10 gives the phase delay for several frequencies. The inertia of the top plate is responsible for the observed phase delay.

3. For frequencies above 37Hz the measured displacement further decreases. No displacement oscillations are observed for frequencies above 60Hz.

Based on the previous observations, we conclude that the mechanical apparatus, as well as the equipment for measuring shear stress and displacement, can be used for frequencies up to approximately 10Hz, which is well above the maximum frequency of our experiments. However, no conclusions could be derived regarding possible time delay between the stress input and the sensor response, because this is affected by the inertia of the top plate. Since the micrometer response significantly decays above 10Hz, the system could not be used for dynamic measurements on the sensors above that frequency. The system is also not appropriate for dynamical measurements of Young's modulus and shear modulus of elasticity, because accurate measurement of the magnitude and phase of the applied stress and the observed strain on the materials is required[1].

The shear stress frequency was further increased in order to examine the response of the force transducer. The amplitude and the shape of the measured force remained unaltered for frequencies up to approximately 140Hz. Distortion of the sinusoidal shape was observed for frequencies 95-105Hz as shown in Fig.3.19 for 100Hz. For frequencies above 140Hz the magnitude of the measured stress decreases. The shape of the force transducer output voltage appears significantly distorted for frequencies between 180-200Hz, revealing strong resonance on the apparatus. The shape of the output voltage appears strongly dependent on the applied frequency. Fig.3.20 shows the trace obtained for 190Hz. The maximum

frequency applied on the system was 200Hz, where the output voltage dropped by 3dB. The observed distortion is possible to be caused by resonance of the bearings inside the top plate. Another reason is that the vibrator shaft is in simple contact with the force sensor, which is firmly attached on the top plate. Temporal loss of contact of the vibrator shaft with the force sensor could lead to unpredicted variation of the stress applied on the top plate.

It was clearly observed that the mechanical apparatus could be applied to stress measurements up to 95Hz, where the problem of distortion starts to appear for the first time. The measured shear stress shows no amplitude reduction or noticeable distortion.

The use of the system for frequencies above 95Hz should therefore be avoided. Furthermore, the amplitude of the measured stress is reduced. Since the frequency response of the force readout system (180kHz, Table 3.1) is three orders of magnitude above the maximum frequency used in the previous experiment (200Hz), we can accept that the observed reduction of the amplitude is real, and it is not caused by false reading of the force readout system.

The electromagnetic vibrator seems to be responsible for the reduction in shear stress applied on the top plate, for frequencies above 140Hz. The frequency response of the vibrator is given in the specification data equal to 350Hz (-3dB). However, the presence of the mass of the top plate (measured 0.25kg), which is actually larger than the mass of the vibrator moving shaft (approximately 0.1kg), is possible to reduce the frequency response of the overall system down to the measured value of approximately 200Hz.

frequency f (Hz)	Time delay Δt (msec)	phase delay $\Delta\phi$ (rad)
1	31.5	0.20
10	12.6	0.79
25	11.0	1.73
37	10.5	2.44

Table 3.10: Measured phase delay of the displacement with respect to shear stress

[1] The viscoelastic behaviour of the material during dynamic measurements can be explained by considering the complex modulus of elasticity, which is measured by knowing the amplitude and phase of the applied stress and the measured strain (Ward, 1983, pp.95-97).

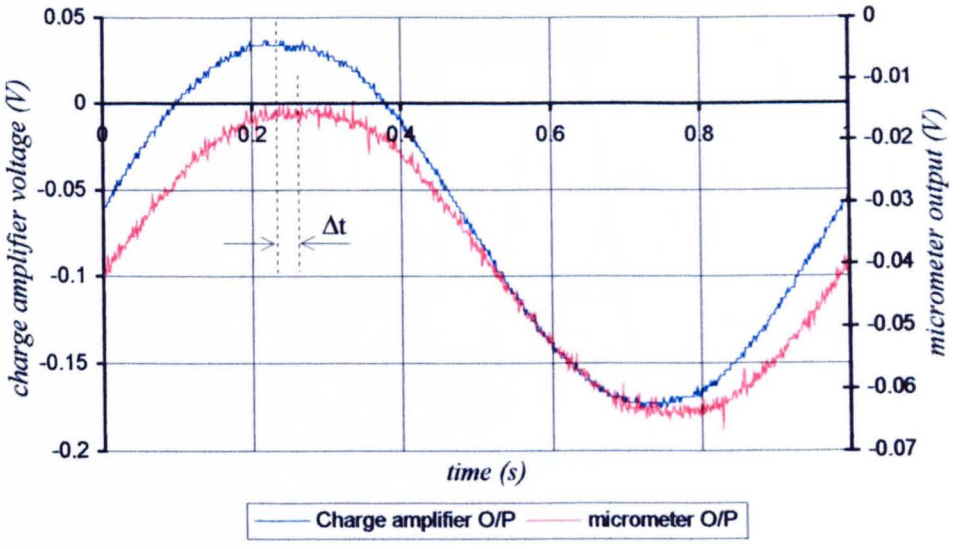

Fig.3.15: System response to 1Hz sinusoidal shear stress.

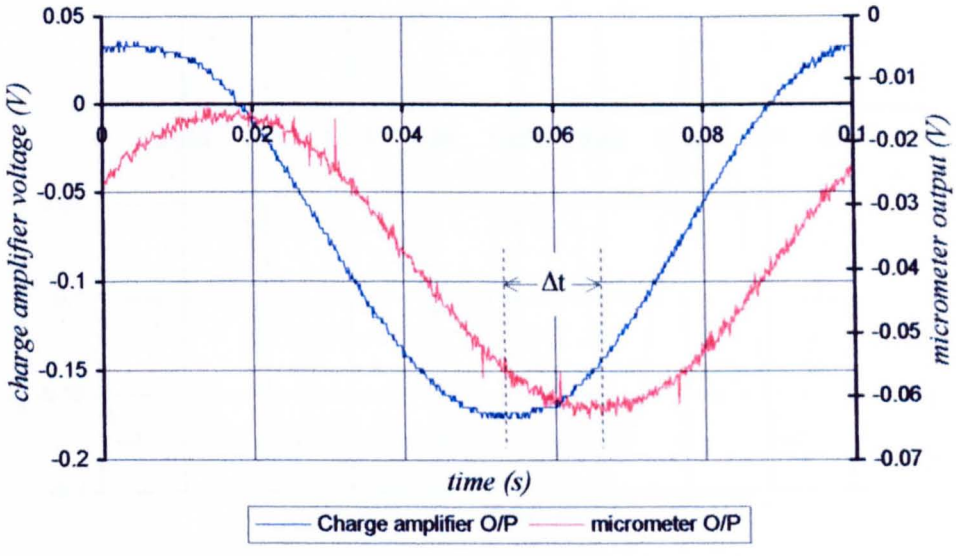

Fig.3.16: System response to 10Hz sinusoidal shear stress.

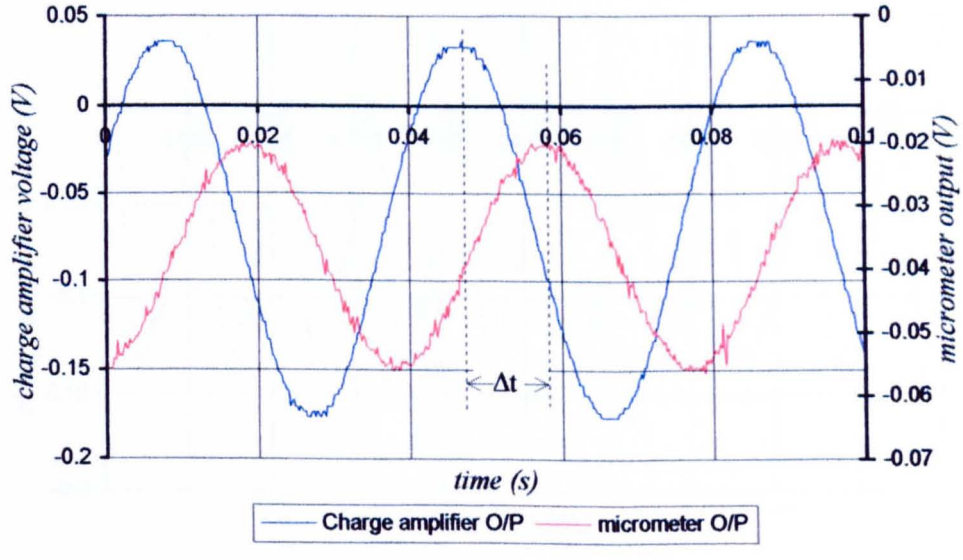

Fig.3.17: System response to 25Hz sinusoidal shear stress.

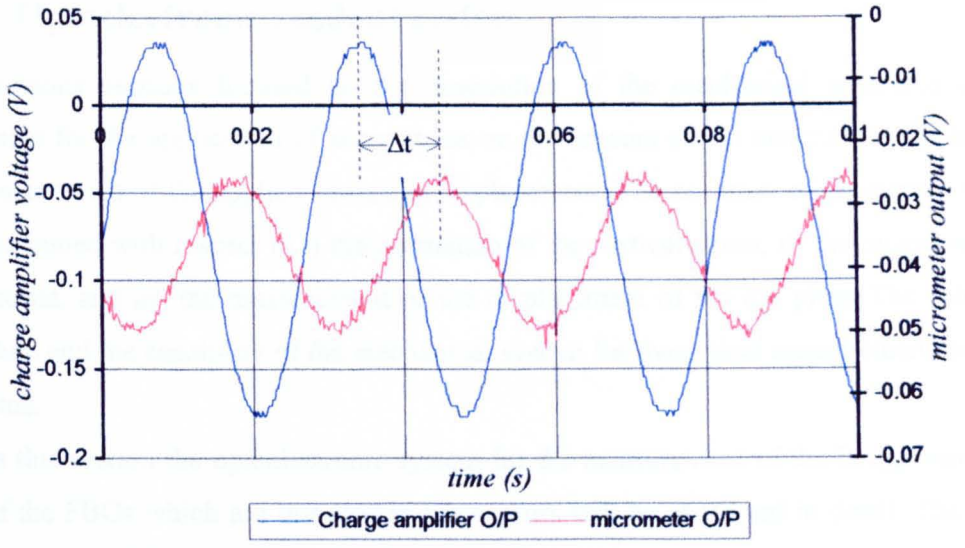

Fig.3.18: System response to 37Hz sinusoidal shear stress.

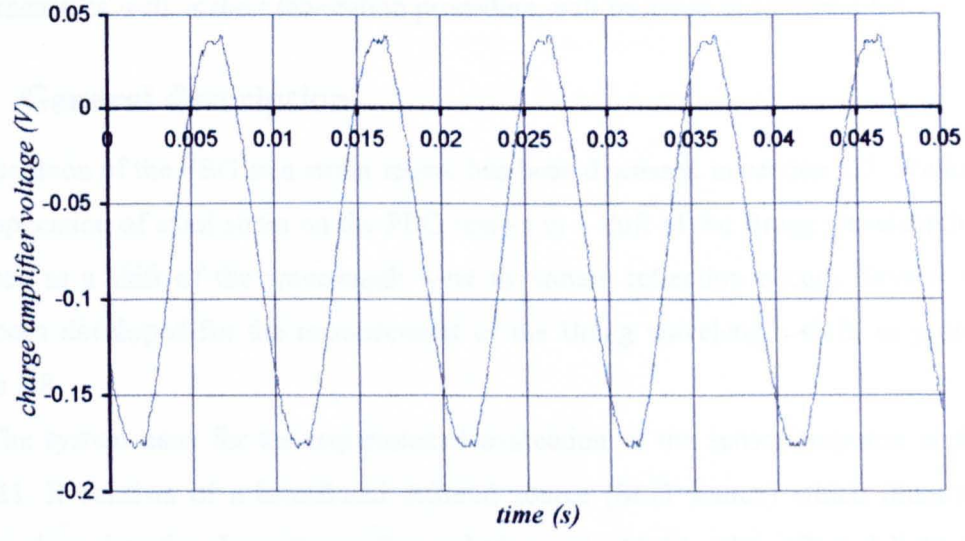

Fig.3.19: Stress transducer response at 100Hz sinusoidal shear stress.

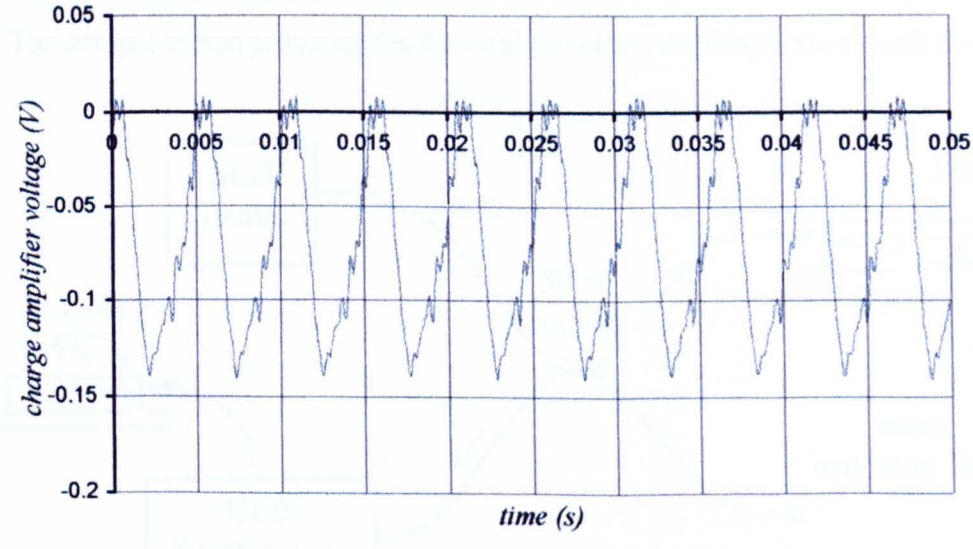

Fig.3.20: Stress transducer response at 190Hz sinusoidal shear stress.

3.5 Optoelectronic readout system

The previous sections focused on the description of the mechanical apparatus and the equipment for the application of shear stress on the sensors or the materials under test, and the measurement of the applied stress and displacement. The accuracy of the system has also been examined with respect to i) the estimation of the vertical stress, ii) the measurement of shear stress, and iii) the measurement of the displacement of the top plate. The calibration procedure and the capability of the mechanical system for dynamical measurements was also presented.

In this section the optoelectronic system for the measurement of the Bragg wavelength shift of the FBGs which are installed in the sensors will be explained in detail. The general characteristics of the optoelectronic devices and components will be presented in sections 3.5.1 and 3.5.2. The characteristics of the FBGs which were used throughout the experiments, as well as their fabrication procedure, will be given in section 3.5.3.

3.5.1 General description

The operation of the FBG as a strain sensor has been discussed in section 2.7. We have seen that application of axial strain on the FBG results in a shift of the Bragg wavelength. This is observed as a shift of the wavelength were maximum reflection occurs. Several methods have been developed for the measurement of the Bragg wavelength shift, as presented in section 2.8.

The system used for the experimental evaluation of the sensor response is shown in Fig.3.21. It consists of a broadband infrared source (SLD source) which illuminates the grating via a directional coupler with a splitting ratio 50:50. The reflected light from the grating is fed into the spectrometer after passing through the coupler. The reflected spectrum is read by the CCD detector, and transferred into the computer via an analogue to digital board. The computer then processes the data and calculates the Bragg wavelength shift.

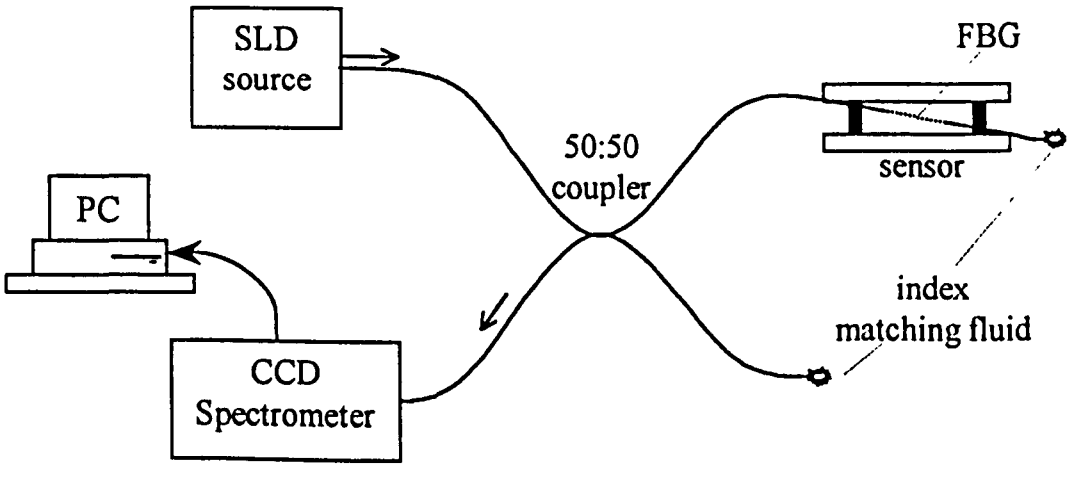

Fig.3.21: General diagram of the Bragg wavelength shift readout system.

The unused end of the coupler is immersed into index matching fluid to prevent back reflections and make sure that only the light reflected by the FBG arrives at the spectrometer. The system shown in Fig.3.21 can be used for both the metallic and the elastomer sensor, by simply removing the sensor and connecting the grating from another sensor on the same output of the coupler.

3.5.2 Devices and components

The specifications and the purpose of each component are presented in this section.

SLD source

It has already been mentioned (section 2.8.1) that a high power, continuous, and broadband source (80nm) is required in order to enable WDM of the FBGs in the final version of the in-shoe transducer where many gratings will be used. However, during the initial experiments on the characterisation of the sensors only a small number of FBGs is used, which enables the use of a lower bandwidth and power, but much cheaper continuous light source.

A superluminescent light emitting diode (InGaAsP/InP SLD) was selected (Hamamatsu SLD840), driven by a laser diode driver (Melles Griot 06DLD201). Advantages of this source are i) fibre-pigtailed using a single-mode fibre, equal diameter as the coupler fibre (125μm) ii) higher output power compared to conventional light emitting diodes (LED). The fibre output power was measured[1] as 0.31mW at a driving current 82mA[2]. iii) Sufficient bandwidth for our experiments. This is approximately 20nm, as shown in Fig.3.22, which gives the spectrum at 82mA as this is measured by an optical spectrum analyser (OSA) (Anritsu MS9001A). iv) The entire spectrum is inside the operating bandwidth of the spectrometer, which will be described next, and covers the operating range of the FBGs.

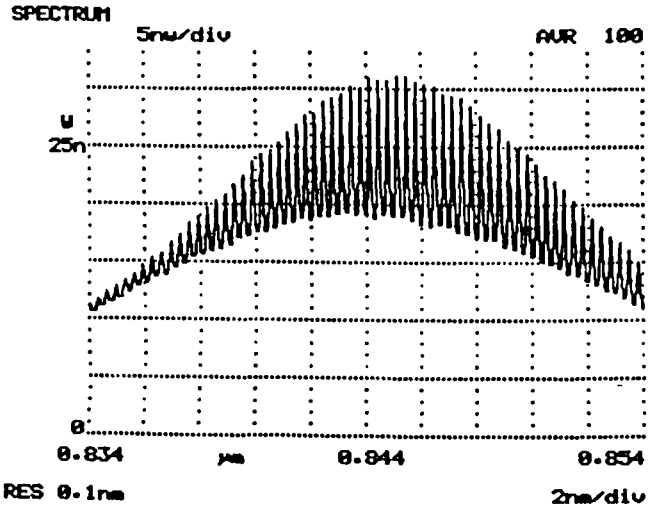

Fig.3.22: SLD spectrum at 82mA driving current. Screenshot from OSA.

[1] using the Advantest Optical Power Meter, TQ8210, detector TQ82018.
[2] The maximum current of the source was 87mA. For safety, the maximum current was set to 82mA.

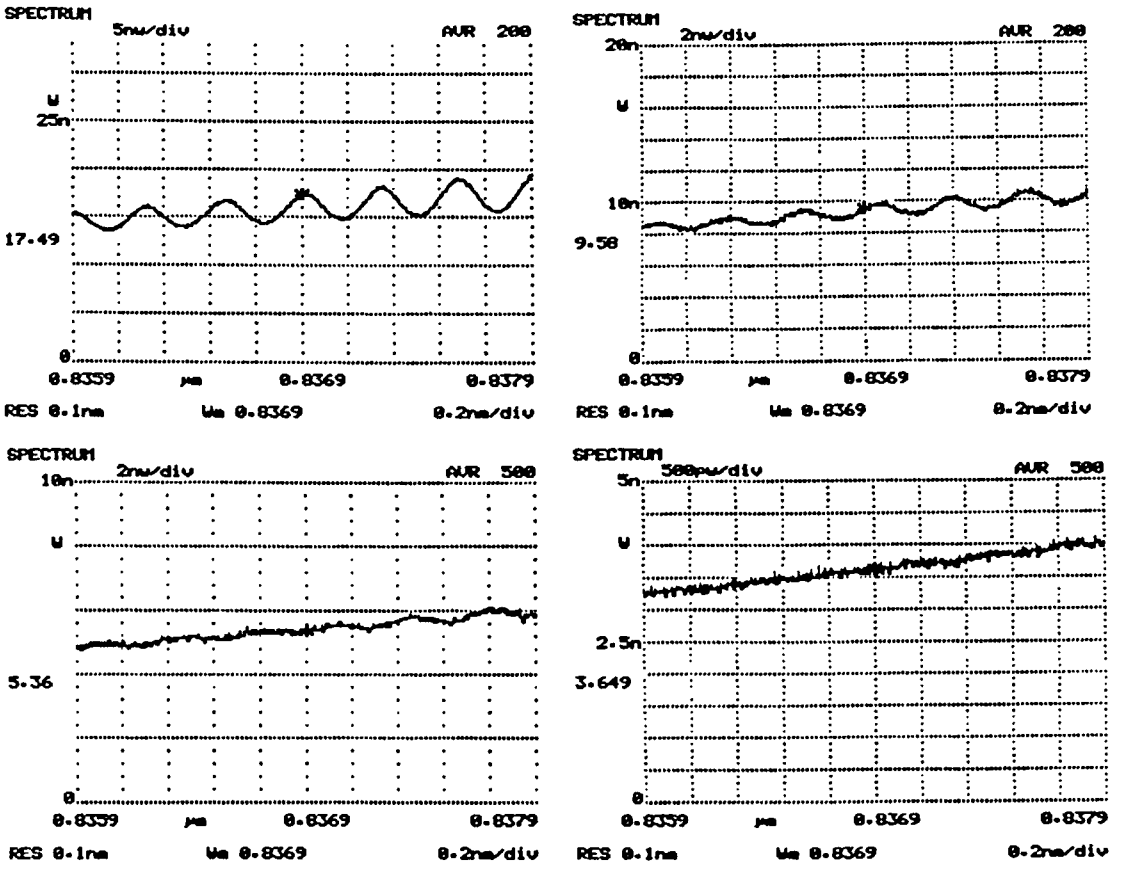

Fig.3.23: SLD spectrum, centred at 837nm at 82mA (top left), 75mA (top right), 68mA (bottom left) 62mA (bottom right). Screenshots from OSA.

The fibre output of the source was fusion spliced to the input fibre of the coupler. Fusion splicing was used for all the optical fibre connections in order to minimise splicing losses. Typical losses are ≤0.1dB for fusion splicing, and around 0.25dB for commercial mechanical splices (Senior, 1992, pp.228, 232). In practice however, we experienced splicing losses up to 1dB.

The structure of an SLD is similar to that of laser diodes, with antireflection coating on the output facet. The operation of the SLD and further reading, is given by Senior (1992, pp.393-395). As it is not possible to achieve a perfect antireflection coating, the residual reflection from the output facet introduces Fabry-Perot modes superimposed on the output spectrum, as clearly shown in Fig.3.22. Kashima *et al.* (1988) presented a InGaAsP/InP SLD operating at 1300nm, which utilises a light diffusion surface placed diagonally on the active layer within the device to suppress the Fabry-Perot modes. Similar emission spectra (after suppression) to the one shown in Fig.3.22 have been reported. Fig.3.23 shows the spectrum of the fibre output for several driving currents, around the operating wavelength region of the FBGs (837nm). The Fabry-Perot resonance clearly appears for driving currents >62mA.

Fibre Coupler

The fibre coupler (Gould[1]) is used to drive the reflected spectrum from the grating into the spectrometer. The characteristics are given in Table 3.11. One of the outputs is spliced to the sensor fibre, the other one is not used and is index matched.

split ratio (%)	50:50
insertion loss (dB per output)	3.4
operating range (nm)	780-850
fibre	single mode at 780nm, cladding diameter 125μm

Table 3.11: Optical specifications of the coupler

CCD spectrometer

We used the Ocean-Optics[2] SD-1000 spectrometer which was available in the laboratory. It is an integrated spectrometer with a linescan CCD detector. The intensity of each pixel, which corresponds to a different wavelength inside the operating rage of the instrument, is acquired by an A/D card[3]. The specifications of the spectrometer/acquisition board system are given in Table 3.12.

grating (lines/mm)	1800
input slit (μm)	10
difraction efficiency (%)	30
operating range (nm)	790-860
resolution (nm)	0.1
CCD detector	1024 pixel linear CCD array
A/D conversion	12bits
maximum acquisition speed (scans/sec)	12

Table 3.12: Spectrometer specifications as given in the instruction manual.

The returned light from the FBG is launched into the spectrometer, which images the spectrum on the 1024 element CCD array. The principle of operation of the CCD detector is

[1] Gould Electronics Inc., Fiber Optics Division, 1121 Benfield Boulevard, Millersville, MD 21108 USA, tel:(410)987-5600

[2] Ocean Optics Inc., 1237 Lady Marion Lane, Dunedin, FL 34698-5314, tel(813)733-2447

[3] National Instruments Lab-PC+ board.

described in DALSA Inc. (1995) databook. The CCD pixels integrate the amount of light incident during each integration period, which is determined by the acquisition speed. The camera settings and the acquisition of the pixel intensity is done by software written in LabVIEW®.

The maximum acquisition speed defines the number of the full scans (1024 samples each, one sample per pixel) that can be taken using the specific data acquisition board. Replacing the board could increase the acquisition speed. However, even at 12samples/sec which can be obtained with the specific A/D board, the signal to noise ratio of the measured spectrum is significantly reduced compared to slower acquisition speeds, resulting in lower accuracy of detecting the Bragg wavelength. Most of the experiments were taken by setting the acquisition speed equal to 6scans/sec. The performance of the FBG readout system will be described in detail in section 3.6.1.

3.5.3 Fibre Bragg gratings

The fibre Bragg gratings used in this study were fabricated at the BT laboratories[1]. The gratings were written on a Ge-doped, single mode fibre at 800nm, cladding diameter 125μm, made at BT. The method used was the tunable phase-mask interferometer method, presented in section 2.7.2. An intracavity frequency-doubled, argon-ion laser was used to produce the UV beam, which gave approximately 110mW continuous power at 244nm. The operation of this laser is described by Kashyap (1999, pp.104-105). The protective polymer coating of the fibre was stripped[2] and aligned in front of the interferometer, which was tuned to the desired Bragg wavelength. The exposure time varied between 3min and 10min at a constant power of 110mW.

Several gratings were written with this system. Table 3.13 shows the typical specifications of the gratings. The transmission loss, bandwidth, and Bragg wavelength were measured using the OSA. The length of the grating is determined by the length of the UV interference pattern. The given value is approximate, and is obtained by considering the diameter of the two UV interfering beams, which was 5mm.

Transmission loss (dB)	1.5-8
Bragg wavelength (nm)	836.45-836.8
Bandwidth (nm)	0.3
Length (mm)	5

Table 3.13: Specifications of the FBGs.

[1] BT Advanced Communications Technology Centre, Martlesham Heath, Ipswich IP5 3RE, UK.

[2] Liquid stripper was used instead of the mechanical one, in order to avoid damage of the cladding surface. In this case we applied 'OF Stripper-10' for 2min, and then cleaned with a lens cleaning tissue and methanol.

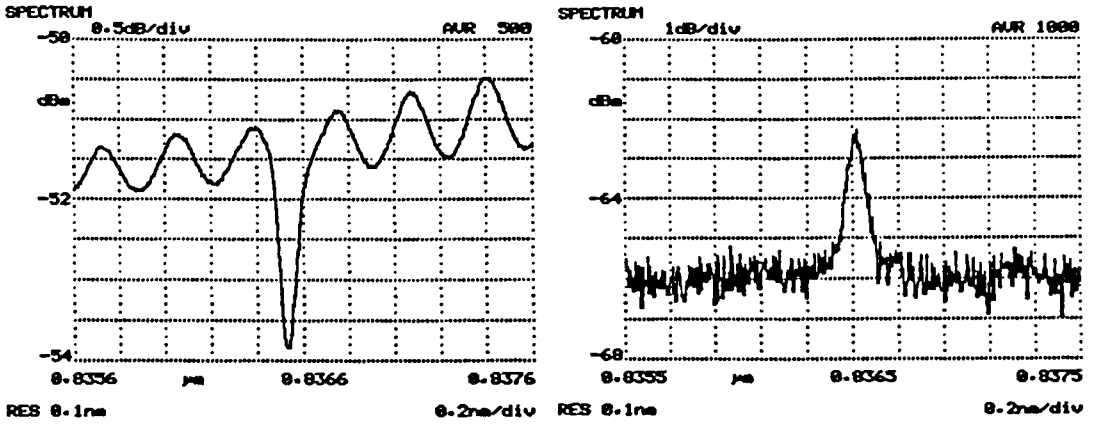

Fig.3.24: Measured transmission (left) and reflection (right) spectra of a FBG.

3.6 Bragg wavelength readout system

The system used for the calculation of the Bragg wavelength, which composes of the CCD spectrometer and the PC with the appropriate hardware and software is described in detail in this section. Essential features of the system are:

1. High accuracy in measuring Bragg wavelength shift. This requires that the CCD spectrometer is properly calibrated and the wavelength which corresponds to every pixel is accurately known. A calibrated readout system is necessary in order to derive the actual response of the sensor under test. This particular CCD spectrometer was calibrated by the manufacturer, but we also measured its response as a part of the entire optoelectronic system shown in Fig.3.21, and using one of our gratings.
2. The wavelength resolution of the system should comply with the shear and vertical stress resolution expected from the stress transducer (5kPa, section 2.3).
3. The system should be fast enough to enable real-time measurements. Ideally the system should have an acquisition speed ≥300Hz for dynamical measurements, which is far above the capability of this particular system. However, for low frequency measurements presented in this study, a slower and more cost effective system could be used.
4. Robust and reliable system. The readout system was used for more than two years, and the reliable performance should be assured. The small size and weight, as well as the integration of the CCD detector and spectrometer into a compact device were advantages of the particular system.

The Bragg wavelength detection and the resolution enhancement are described in section 3.6.1. The experimental testing of the wavelength resolution is given in section 3.6.2. The

calibration procedure and the experimental derivation of the Bragg wavelength shift due to axial strain of the grating will be presented in section 3.6.3.

3.6.1 Bragg wavelength peak detection.

The Bragg wavelength is calculated by processing the data received by the CCD detector using Labview® software. Two programs have been developed and used throughout the experiments. The first one displays in real time the reflection spectrum of the FBG, and calculates the Bragg wavelength. The acquired spectra can be stored for further processing. A typical screenshot of the program is given in appendix III, picture 1. The second program calculates and displays the Bragg wavelength shift with respect to a reference wavelength. The reference wavelength was measured before each experiment by measuring the Bragg wavelength of the sensor grating under test when no stress was applied on the sensor, for a period of a few seconds (10s). The average value was then inserted as the reference wavelength in the program. A typical screenshot of the program is given in appendix III, picture 2.

The data are collected in 1024-element vectors, where the index of each element represents the pixel location. The value of the element gives the intensity of the incident light of the pixel. The value varies in the range –2000 to +2096, limited by the 12-bit byte length of the A/D conversion. The precise wavelength which corresponds to each pixel is given by[1]:

$$\lambda = -3.4562 \cdot 10^{-5} i^2 + 0.1051 i + 788.7618 \qquad (3.19)$$

where i is the index of the vector element (location of pixel), and λ the optical wavelength.

The accuracy of measuring the Bragg wavelength using a CCD spectrometer system is limited by the resolution of the bulk optic diffraction grating, and the number of pixels of the CCD array. If for example, we calculate the Bragg wavelength by finding the pixel location where maximum intensity is observed, and then applying eq.(3.19), resolution equal to 0.1nm could be achieved. For this particular spectrometer, the resolution is limited by the diffraction grating (0.1nm), not from the number of pixels. This can be understood by considering the wavelength spread on the CCD active area (790 to 860nm) and the number of pixels (1024). This gives the wavelength separation between adjacent pixels: 70nm/(1024-1) ≅0.07nm, which is an order of magnitude smaller than the diffraction grating resolution. This is an approximate value of the wavelength separation where linear wavelength distribution was assumed, not the actual given by eq.(3.19).

The resolution can be improved by using a deconvolution of the FBG spectrum and the pixel resolution of the spectrometer by processing a number of pixels around the expected peak wavelength. Ezbiri *et al.* (1998) have demonstrated the theoretical and experimental

[1] The calibration was done by the Ocean Optics Inc., and the coefficients are as given in the data sheet.

results of resolution enhancement by comparing the Centroid Detection Algorithm (CDA), and the polynomial fit using the Least Squares Method (LSQ) for several signal to noise ratios (SNR) and number of pixels utilised. Wavelength resolution of ~1pm was obtained by using LSQ for 5 pixels around the peak (LSQ_5). The method fits a quadratic polynomial to sequential pixels of the peak region, which approximates the FBG reflection spectrum.

3.6.2 Measurement of the wavelength resolution

LSQ_5 was selected for the Bragg wavelength detection. However, lower resolution was observed during our experiments compared to the expected (1pm), due to the insufficient SNR of the acquired data. This is mainly caused by the low integration time[1], and by the absence of averaging, which were both set to the minimum values in order to increase the readout speed. Setting the integration time to minimum (40ms) and no averaging was the only way of increasing the acquisition speed above 2scans/sec.

For the experimental evaluation of the wavelength resolution, one FBG was connected to the readout system. The transmission loss of this particular grating was ~4dB. No axial strain or temperature variation was applied on the grating during the measurements. The driving current of the SLD source was 82mA. Setting the integration time to 40ms and the acquisition speed to 4scans/s, we measure the reflected spectrum, which is shown in Fig.3.25. The intensity fluctuation of the pixel with the maximum intensity due to noise is also shown on the same figure. This fluctuation results in random variation of the polynomial which is fitted using the LSQ algorithm, which in turn results in fluctuation of the detected Bragg wavelength shift, Fig.3.26. The SNR is defined by:

$$\mathrm{SNR} = \frac{\text{peak intensity}}{\text{noise intensity}} \tag{3.20}$$

which gives SNR≅6. The maximum error in measuring the Bragg wavelength is approximately ±10pm. Hence, the minimum wavelength difference that can be measured is 20pm. This value defines the actual resolution of the readout system.

Fig.3.27 to Fig.3.32 show the measured spectrum, intensity fluctuation, and Bragg wavelength fluctuation for different acquisition speeds and source currents. Following the same procedure as described above, the actual wavelength resolution of the system can be calculated. Table 3.14 summarises the measured resolution for the four different combinations of source current and scanning speed which were examined.

---

[1] the time interval that the photoelements (pixels) are allowed to collect the electric charge generated by the incident light. (DALSA Inc.,1995, p.16).

It must be mentioned that the driving current was always set to maximum current throughout the experiments in order to get the highest possible SNR and hence the best resolution. In this experiment it was reduced to 62mA[1] in order to simulate optical losses of the reflected light due to unequal reflectivity and/or spicing losses when different FBGs are spliced and measured.

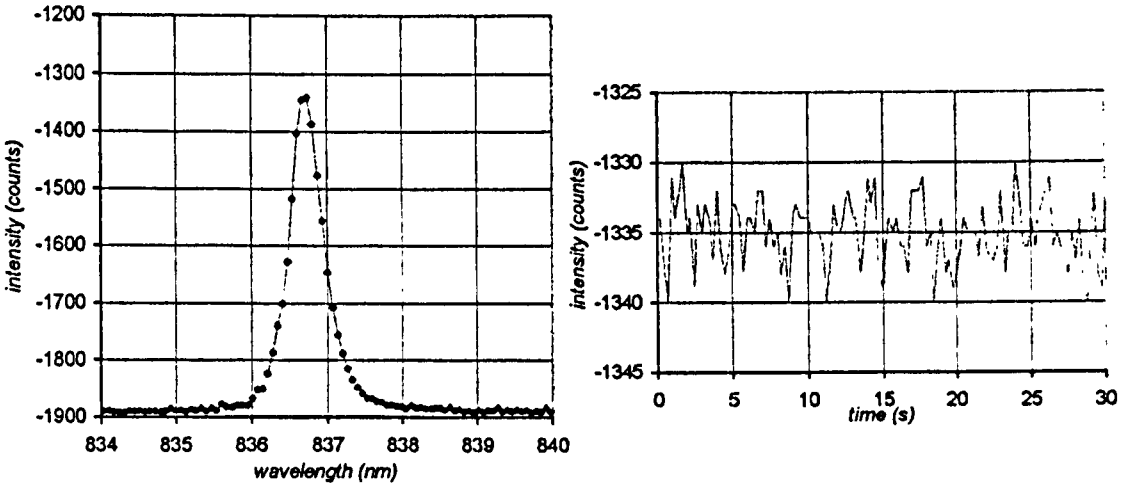

Fig.3.25: Reflection spectrum (left) and peak intensity fluctuation (right), at 4scans/s, source current 82mA.

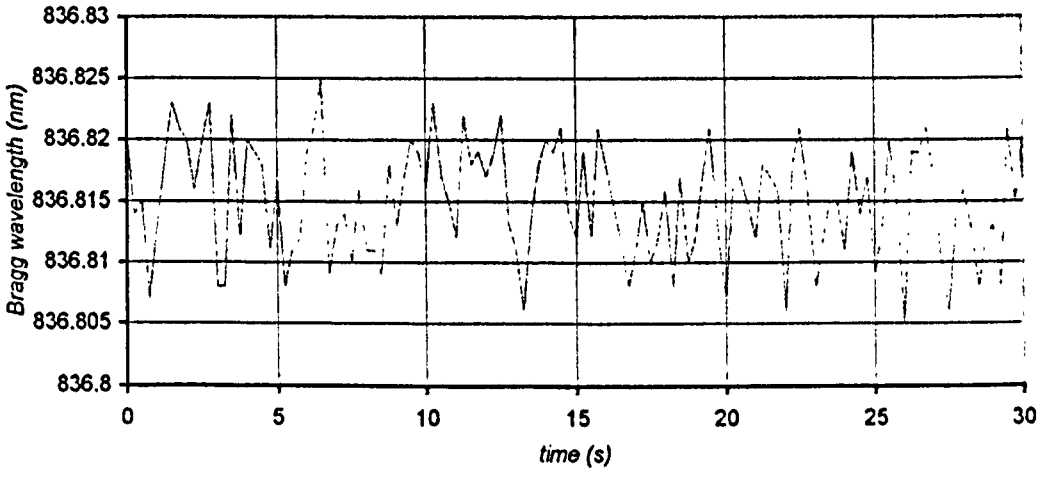

Fig.3.26: Bragg wavelength fluctuation at 4scans/s, source current 82mA.

[1] The source spectrum in this case is shown in Fig.3.23.

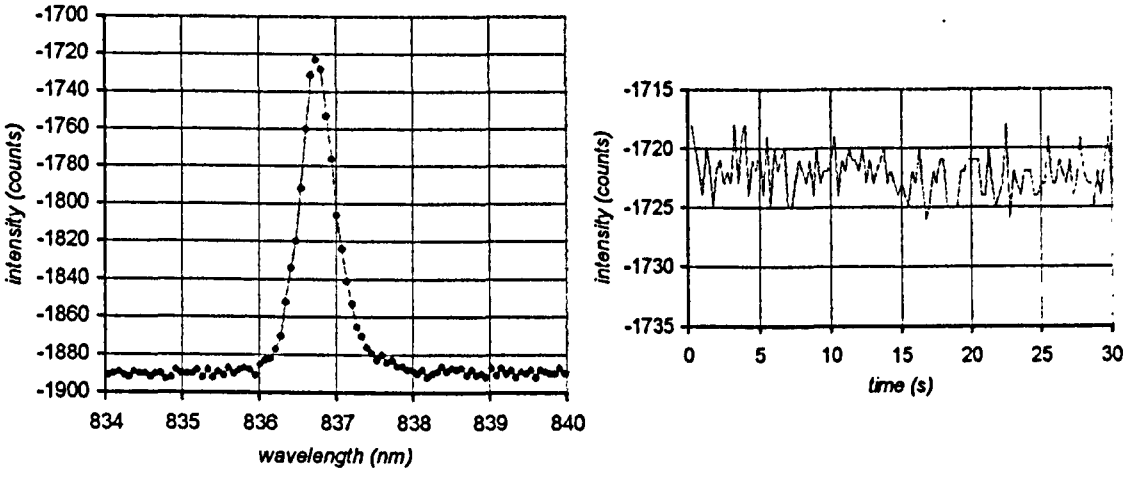

Fig.3.27: Reflection spectrum (left) and peak intensity fluctuation (right), at 4scans/s, source at 62mA.

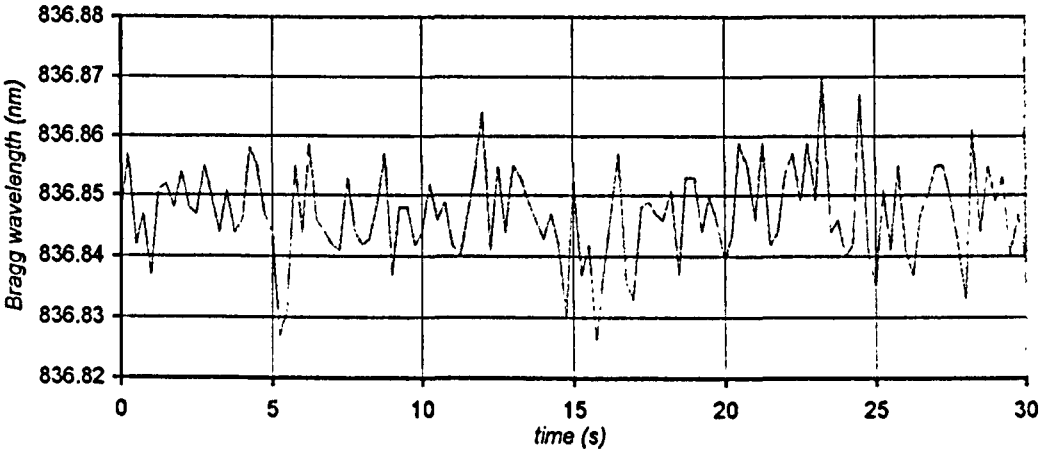

Fig.3.28: Bragg wavelength fluctuation at 4scans/s, source current 62mA.

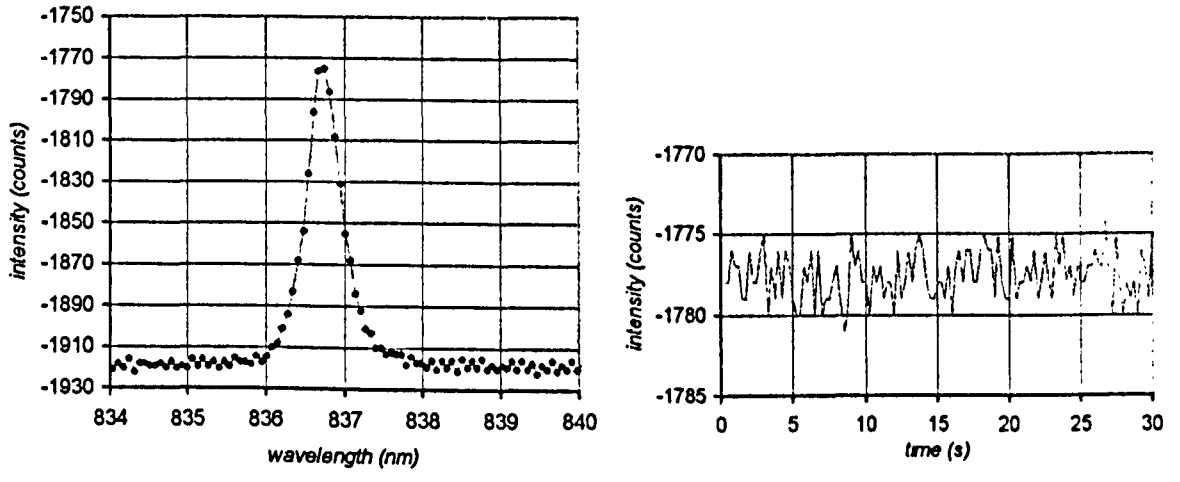

Fig.3.29: Reflection spectrum (left) and peak intensity fluctuation (right), at 12scans/s, source current 82mA.

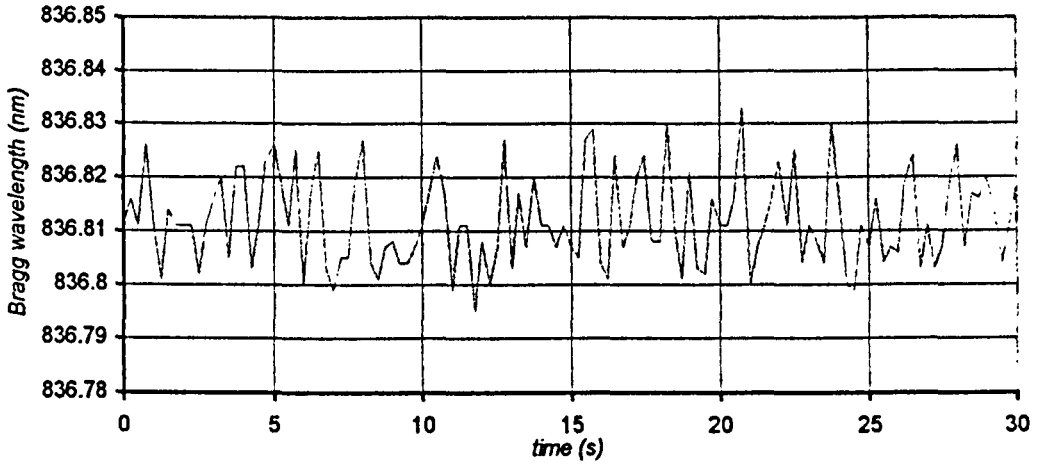

Fig.3.30: Bragg wavelength fluctuation at 12scans/s, source current 82mA.

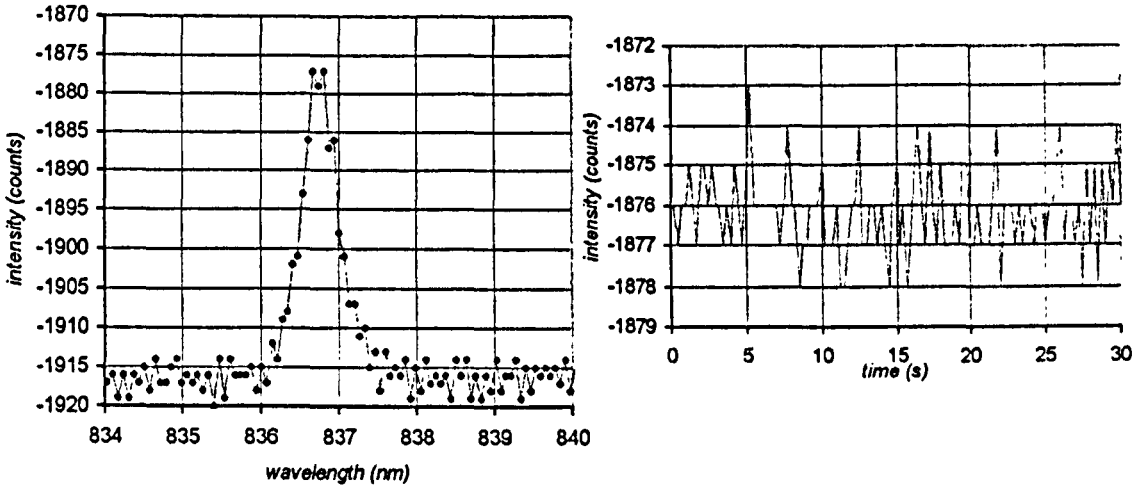

Fig.3.31: Reflection spectrum (left) and peak intensity fluctuation (right), at 12scans/s, source 62mA.

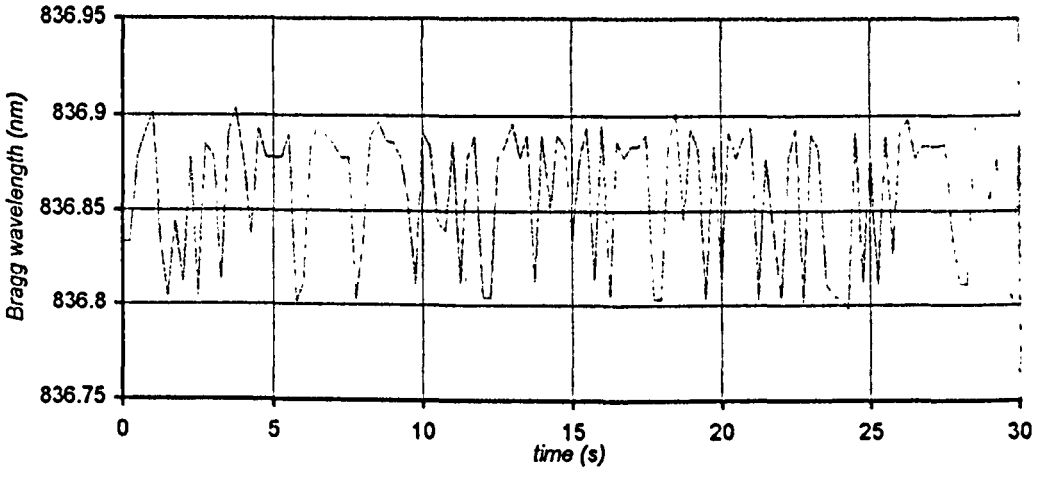

Fig.3.32: Bragg wavelength fluctuation at 12scans/s, source current 62mA.

Settings	SNR	max intensity fluctuation (counts)	max peak detection error (nm)	measured resolution (nm)
4scans/s 82mA	6	10	±0.010	0.02
4scans/s 62mA	2.6	7	±0.045	0.09
12scans/sec 82mA	2.8	7	±0.040	0.08
12scans/sec 62mA	1.5	5	±0.050	0.1

Table 3.14: Measurement of wavelength resolution for different acquisition speeds and source currents.

3.6.3 Experimental testing of the Bragg wavelength shift due to axial strain on the FBG

It has been mentioned (section 2.7.3) that the application of axial strain on the FBG produces Bragg wavelength shift which is proportional to the applied stain. The rate of change of the wavelength shift due to strain depends on the Bragg wavelength of the grating (eq.2.5). It is therefore expected that, if the FBG is subjected to axial strain, the wavelength shift measured by the CCD spectrometer and the peak detection algorithm should provide a linear relationship with the axial strain. Deviation from the expected linear response can be observed due to several factors, which reveal the need for experimental calibration of the Bragg grating strain sensor and the readout system before using it for measuring the sensor performance. Those factors, together with other reasons for testing the readout system are listed below.

1. Temperature fluctuations during the measurements introduce shift in the Bragg wavelength (eq.2.5). Since no temperature compensation can be done by the readout system, errors in measuring the grating response to strain will be introduced. The experiment was done on the same optical table were the sensor measuring apparatus is installed, and the temperature was monitored throughout the calibration procedure.
2. The intensity of light which illuminates the gratings varies with wavelength due to the Fabry-Perot resonance in the SLD source, as explained in section 3.5.2. Since the bandwidth of the grating (~0.3nm FWHM) is comparable to the period of the fluctuations (~0.3nm, Fig.3.23), not only the intensity of the reflected spectrum but also its shape is expected to vary as the Bragg wavelength shifts. The distortion of the reflected spectrum will cause error in the polynomial fit and peak detect algorithm. The

effect of this error and its importance will be experimentally measured by examining possible periodicity (at ~0.3nm) of the nonlinearity on the Bragg shift – axial strain curve.

3. If the expected linear response is observed, then an expression between the wavelength shift and the applied strain on the fibre can be derived from the experimental data. This expression will then be used throughout the experimental evaluation of the sensors.
4. The FBG reflected spectrum under different values of axial strain will be recorded. Comparing those spectra with the ones measured from the embedded FBGs into the elastomer sensor, conclusions can be obtained regarding the effect of fibre embedding to the reflected spectrum, and hence for the stress distribution along the grating. This will be discussed in chapters 5 and 6.
5. The axial strain on the fibre will be extended up to the maximum value of 2500με, therefore the mechanical strength of the fibre will be experimentally tested. Even though the fibre is certified for strain up to 2500με, the coating removal in the grating region reduces the strength of the fibre due to flaws on the silica surface (Olshansky and Maurer, 1976). UV exposure also reduces the mechanical strength of the fibre. Faced *et al.* (1997) conclude that the mean breaking stress of the fibre depends on the UV wavelength, by measuring the breaking stress after exposure to pulsed UV at 193nm and 248nm, the latter wavelength causing greater damage. However, the CW irradiation used for the grating fabrication causes only a small reduction of the breaking stress compared with a pristine fibre. The mechanical resistance of fibres exposed to pulsed or CW UV radiation is discussed by Varelas *et al.* (1997) where pulsed irradiation significantly reduces the mechanical strength compared to the CW exposure.

Fig.3.33 shows the apparatus used to obtain the wavelength shift – axial strain of the FBG. The transmission loss of the FBG was measured to be ~4dB and the Bragg wavelength 836.6nm. The fibre was attached to two rods. One of them was mounted on an x-translation stage. The fibre length $\Delta\ell$ was increased by rotating the positioning control of the stage. $\Delta\ell$ was measured by reading the value on the control having a resolution 10μm. The fibre was slightly prestrained to 50με to make sure that the fibre was straight. The air temperature close to the grating was measured by a thermocouple connected to a digital thermometer. The temperature resolution was 0.1°C. The fibre spliced to the readout system which was set to 4scans/s. The SLD current was 82mA, giving 0.03nm wavelength resolution (section 3.6.2).

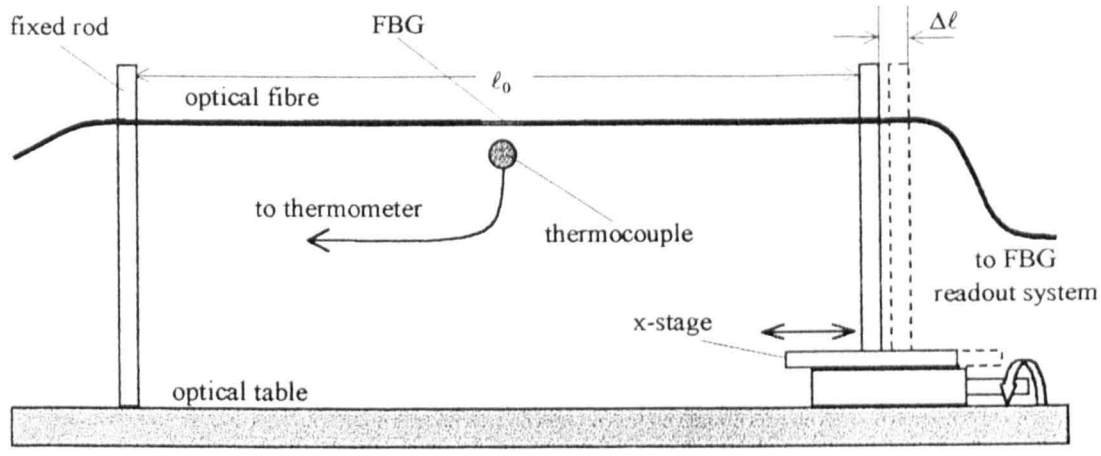

Fig.3.33: Experimental arrangement for the calibration of the Bragg wavelength readout system.

The axial strain ε is given by $\Delta\ell/\ell_0$, where ℓ_0=1m is the unstrained length of the fibre. Fig.3.34 shows the Bragg wavelength shift as a function of axial strain. Each data point is obtained by increasing $\Delta\ell$ so that wavelength shift approximately equal to 0.05nm is measured. The y-error bars show the 0.03nm error due to the wavelength resolution. The 10μm accuracy in measuring $\Delta\ell$ corresponds to 10με strain accuracy. Linear response of the wavelength shift – axial strain is clearly observed. The linear trendline gives the Bragg shift – strain equation:

$$\Delta\lambda_B = 515.6 \cdot 10^{-6} \varepsilon \tag{3.21}$$

where ε in με.

The duration of the experiment was approximately 30mins. The ambient laboratory temperature during that time decreased from 24.1°C to 23.8°C. The corresponding Bragg wavelength shift is approximately –0.002nm (eq.2.5). This shift was not possible to be measured since it is an order of magnitude smaller than the wavelength resolution of the readout system.

Comparing eq.(3.21) with eq.(2.9) for λ_B=837nm, we conclude that the strain sensitivity of the FBG is approximately 25% lower than that measured by Kanellopoulos *et al.* The measured difference in strain sensitivity can be partly explained by a possible difference of the refractive index of the core between the two fibres. This can lead to a variation of the strain coefficient by a maximum of 20%. A second reason which could explain the unexpectedly low response of the FBG in this experiment is the deformation of the fibre coating. The fibre is attached on the two rods without removing the fibre coating, and hence the stress is transferred on the fibre via the coating. Deformation of the coating would therefore result in lower actual elongation of the fibre compared to the measured displacement of the rods, resulting in lower Bragg wavelength shift.

The axial strain in this experiment increased up to 2800με without braking the fibre, which ensures that the fibre will withstand the theoretically predicted maximum strain during

the sensor operation. However, the fibre should be re-coated around the grating to avoid reduction of the mechanical strength due to flaws on the silica surface (Olshansky and Maurer, 1976).

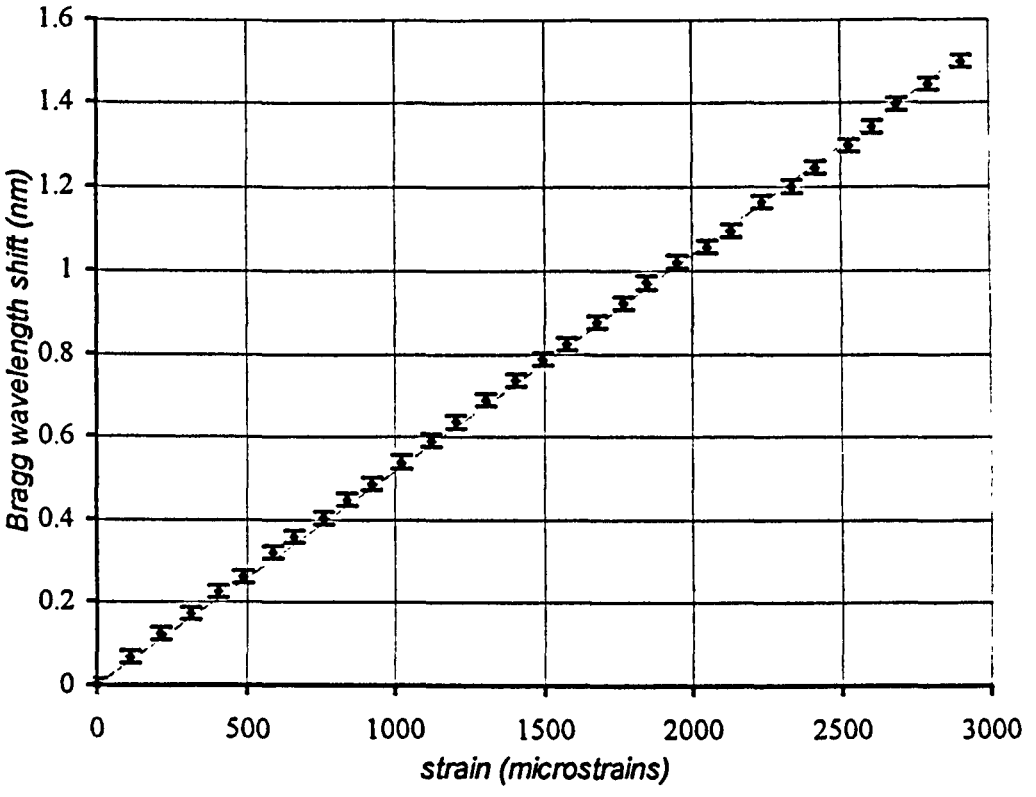

Fig.3.34: Bragg wavelength shift as a function of axial strain.

The reflection spectra as measured for every data point are plotted on the same graph, as shown in Fig.3.35. Periodic peak intensity fluctuation is clearly observed. Comparing this graph with the spectrum of the SLD source given in Fig.3.23 (top left), and measuring the period of the fluctuations which in both cases is approximately 0.3nm, we infer that the fluctuation of the FBG reflection spectrum intensity is the result of the source Fabry-Perot resonance. However, no distortion of the reflected spectrum can be observed. This can also be verified by examining the wavelength shift – axial strain experimental data, Fig.3.34. The data points do not present periodic shift with respect to the linear trendline, or it is lower than the wavelength resolution of the readout system.

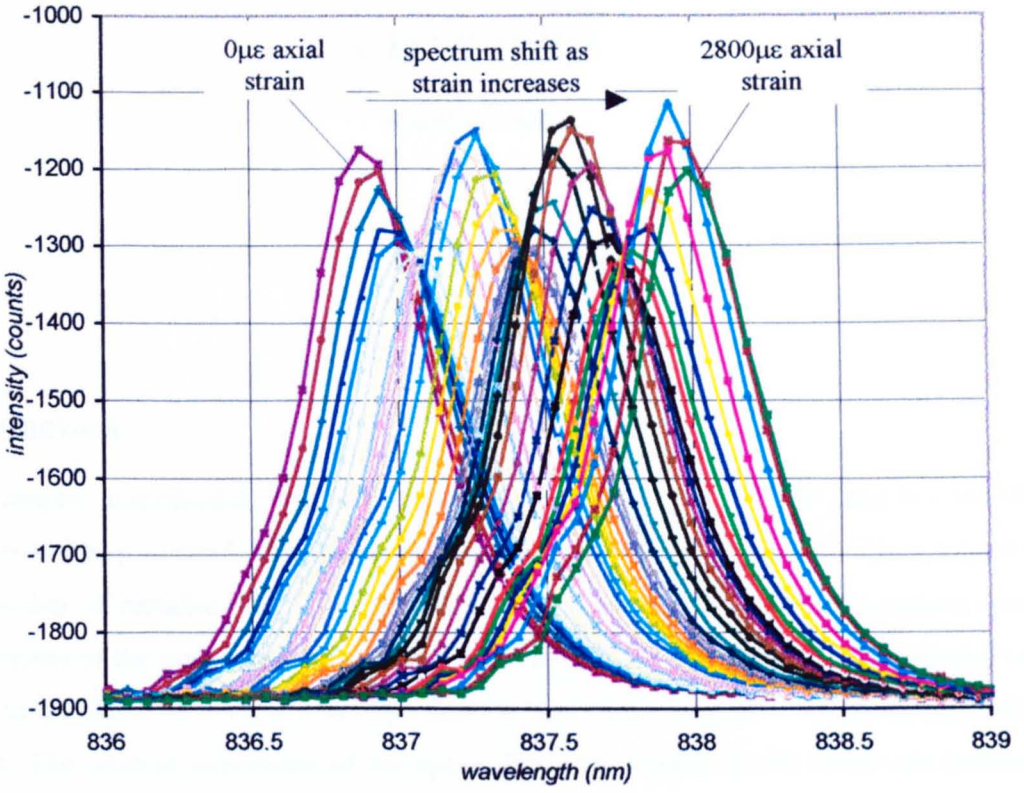

Fig.3.35: Reflection spectra at different strains, as measured on a FBG subjected to axial strain.

3.7 Conclusion

The experimental setup for the experimental evaluation of the sensor response to vertical and shear stress was presented in this chapter. The optoelectronic system for the measurement of the Bragg wavelength shift of the FBGs was also presented. The calibration procedure of the stress measuring system showed linear response in the entire range of interest (0-50N). The responsivity was measured to be 0.192V/N, and the resolution 0.01N to 0.15N, depending on the scale setting of the oscilloscope. This corresponds to stress resolution in the range 0.1kPa to 2kPa, which is better than the required sensor resolution (5kPa). The accuracy in measuring displacement is limited by the micrometer resolution, which is equal to 0.1μm. The FBG readout system was also tested. Linear response was measured for axial strain up to 2800με. The responsivity was found to be ~0.5pm/με, and the wavelength resolution in the range 0.02nm to 0.1nm, depending on the source optical power and the acquisition speed.

The suitability of the experimental setup for dynamic measurements was also tested. It was found that the system could be used for dynamic measurements up to 3Hz, limited by the acquisition speed of CCD spectrometer. Testing of the mechanical apparatus showed that it could be used for frequencies up to 10Hz.

CHAPTER 4

Metallic sensor

Introduction

In this chapter, a method for measuring biaxial shear stress using FBGs fitted in a metallic structure will be presented. The sensor body consists of two parallel metallic discs, separated by a number of metallic pins. Application of shear stress on the top surface causes lateral displacement of the upper disk with respect to the lower one. The pins are deflected in a way similar to the elastic deflection of a beam fixed at both ends when shear forces are applied on its ends. The relative movement of the upper disk with respect to the lower one produces elongation or contraction of the prestrained FBGs which are firmly attached between the two disks. Measuring the Bragg wavelength shift from the two FBGs, the magnitude and direction of the shear stress can be calculated by solving a system of two equations.

The theoretical design of the sensor is based on the theory of elastic bending of beams. The aim of the design was to estimate the dimensions and the Young's modulus of elasticity for the metallic pins in order to achieve maximum sensitivity of the sensor in the required operating range, and to prevent breakage of the fibres due to overstraining.

The chapter begins with a brief presentation of the theory of the elastic bending of beams, section 4.1. Each metallic pin of the sensor will be considered as an elastic column fixed at both ends, and the deflection of the upper end due to vertical and shear stress will be examined using the theory of elasticity. The theoretical design of the sensor will be described in section 4.2. The experimental evaluation will be presented in section 4.3. Two enlarged versions of the sensor (40mm diameter and 10mm thick) where tested by applying low-frequency shear stress pulses and measuring the pin deflection for different directions of shear. One FBG was then installed in the enlarged structure and the FBG response was measured. Finally, the results from measuring the elastic behaviour of an actual-size sensor (10mm diameter and 3.5mm thick) will be presented.

4.1 Background theory

In this section we present some basic issues of the elastic bending of beams theory. Only those that are directly relevant to the sensor design will be described in detail. Many

textbooks have been written on the mechanics and strength of materials, where the reader can find more detailed information on beam bending under several loading conditions. In this analysis we follow the same notation as used by Timoshenko and Gere (1973, pp.190-210), in order to derive an expression for the deflection of the free end of a beam under shear load. The effect of axial load on the beam deflection, as well as the deformation of the beam due to buckling will also be described.

4.1.1 Deflection of a cantilever beam

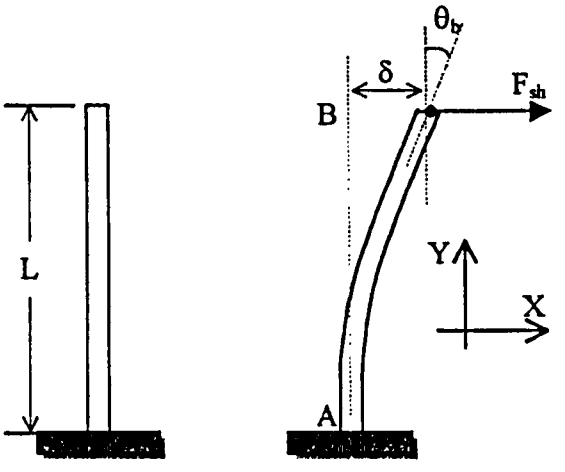

Fig.4.1: Deflection of a cantilever beam under shear load

A linearly elastic cantilever beam fixed at the lower end is shown in Fig.4.1. The deflection δ of the point B under shear force F_{sh} which is applied horizontally, is given by (Timoshenko and Gere, 1973, pg.203):

$$\delta = \frac{F_{sh} L^3}{3EI} \tag{4.1}$$

where L is the length, E is the Young's modulus, and I is the moment of inertia of the cross-sectional area with respect to the neutral axis of the beam[1]. The equation above is accurate for small deflections, where the shear force can be considered tangential to the end B of the beam. For larger deflections, the horizontal force must be analysed to a tangential and a normal component to the cross-section area of the beam at point B, and the a xial extension must also be taken into account, as will be explained in section 4.1.3.2.

For a beam having a solid, circular cross-section of diameter d, the moment of inertia of the cross-section area is given by:

$$I = \frac{\pi d^4}{64} \tag{4.2}$$

[1] The moment of inertia of the cross-section area around a neutral axis is also called second moment of area (Timoshenko and Gere 1973, pg.544). Referring to Fig.4.1, for a circular cross-section of the beam, the neutral axis is parallel to the z-axis and passes through the centre of the cross-section.

The second moment of area given by eq.(4.2) should not be confused by the polar moment of inertia of a mass, which is sometimes given the same symbol I.

The angle of rotation θ_b at the free end B is given by:

$$\theta_b = \frac{F_{sh}L^2}{2EI} \tag{4.3}$$

4.1.2 Deflection of a beam fixed at both ends

The calculation of the deflection of a long, linearly elastic beam, when both ends are fixed and a shear force is applied to one of its ends, is more complex than the case of the cantilever beam described previously. In this section, we assume that the beam is firmly supported between 2 surfaces, as shown in Fig.4.2. The top surface is able to move laterally with respect to the lower one under shear force, in a way that the two surfaces always stay parallel to each other. The forces and moments acting on the contact region between the beam and the surfaces are responsible for the elastic deformation of the beam.

In the following analysis we assume that shear force F_{sh} is the only external force applied on the top surface. The effect of vertical load will be examined in section 4.1.3. We also assume that the displacement δ of the top surface is very small compared to the length L of the beam. Therefore, the distance between the two surfaces can be considered constant and equal to the length of the beam.

Due to the static equilibrium of the beam, the summing of all the forces on the X-axis must be zero, therefore:

$$F_{sh} - R_a = 0 \tag{4.4}$$

where R_a is the reaction at point A. Furthermore, the summing of the bending moments about an axis through the cross section at point B must also be zero:

$$R_a L - M_b - M_a = 0 \tag{4.5}$$

where M_a and M_b are the bending moments at the fixed points A and B respectively. Similarly, at any distance y from point A, the bending moment will be given by:

$$-M + R_a y - M_a = 0 \tag{4.6}$$

where M is the bending moment at y. Eq.(4.5) and eq.(4.6) give:

$$M = R_a y - R_a L + M_b \tag{4.7}$$

The deflection υ is calculated by integrating the differential equation for the deflection curve of the beam, given by (Timoshenko and Gere, 1973, pg.192):

$$\frac{d^2\upsilon}{dy^2} = -\frac{M}{EI} \tag{4.8}$$

Eq.(4.8) is used with the following sign convention: (1) the X and Y axis have the positive directions shown in Fig.4.2, (2) the deflection υ is positive when in the positive X direction,

and (3) the bending moment M is positive when it produces compression on the left-hand side of the beam. Substitution of eq.(4.7) to eq.(4.8) gives:

$$\frac{d^2\upsilon}{dy^2} = -\frac{R_a}{EI}y + \frac{R_aL}{EI} - \frac{M_b}{EI} \tag{4.9}$$

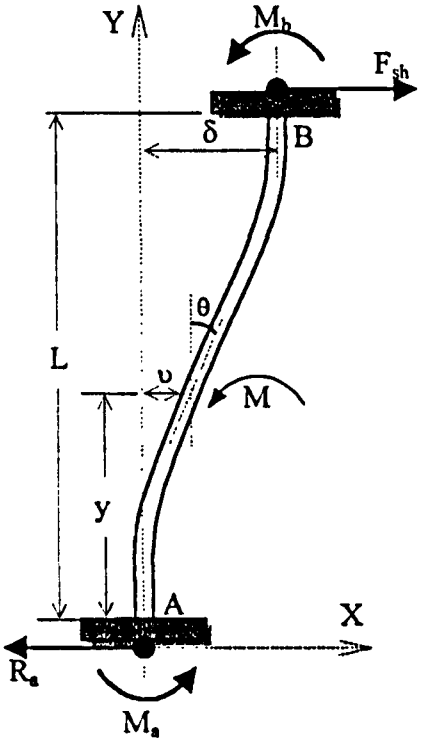

Fig.4.2: Deflection of a beam fixed at both ends under shear load.

Integration gives:

$$\frac{d\upsilon}{dy} = -\frac{R_a}{2EI}y^2 + \frac{R_aL - M_b}{EI}y + C_1 \tag{4.10}$$

It can be seen from Fig.4.2 that, for small deflections, dυ/dy is equal to the angle θ between the tangent to the beam at y and the Y axis. A second integration gives:

$$\upsilon(y) = -\frac{R_a}{6EI}y^3 + \frac{R_aL - M_b}{2EI}y^2 + C_1y + C_2 \tag{4.11}$$

The reaction R_a is equal to the applied shear force F_{sh} (eq.4.4). Therefore, there are three unknowns in equations (4.10) and (4.11), the bending moment M_b and the constants C_1 and C_2, and three boundary conditions:

$$\begin{aligned} &\text{i)} \quad \upsilon(0) = 0 \\ &\text{ii)} \quad \theta(0) = 0 \\ &\text{iii)} \quad \theta(L) = 0 \end{aligned} \tag{4.12}$$

Application of these conditions to the preceding equations gives:

$$C_1 = 0$$
$$C_2 = 0 \qquad (4.13)$$
$$M_b = \frac{F_{sh}L}{2}$$

The displacement δ of the top end of the beam (point B) is given by substitution of eq.(4.13) to eq.(4.11) for y=L:

$$\delta = \frac{F_{sh}L^3}{12EI} \qquad (4.14)$$

Comparing eq.(4.14) with eq.(4.1), we notice that the deflection of the free end of a cantilever beam is 4 times larger than the deflection of the top end of the same beam under the same shear force when both ends are fixed.

4.1.3 Effects of vertical load on beam deflection

In the preceding sections we assumed that the shear force was the only force acting on the top end of the beam. Application of vertical load on the top end will produce axial compression of the beam due to elasticity, as will be discussed in section 4.1.3.1. When the vertical force is applied together with shear, additional deflection of the beam due to the vertical force will occur. This effect is described in section 4.1.3.2. For large values of vertical load, the beam bends and deflects laterally due to the buckling effect, which is explained in section 4.1.3.3.

4.1.3.1. Vertical compression of beam

A vertical force F_v is applied to a linearly elastic cantilever beam as shown in Fig.4.3. The reaction at the fixed end is the vertical force R_v. The compressive axial strain ε_y on the beam can be found by the equation which defines the Young's modulus of elasticity:

$$E = \frac{\sigma_y}{\varepsilon_y} \qquad (4.15)$$

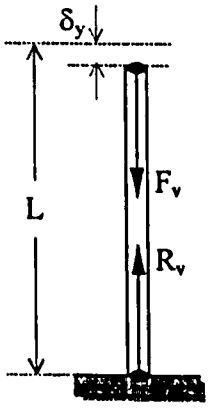

Fig.4.3: Beam compression due to axial load

where σ_y is the vertical stress. Assuming uniform distribution of stress on the cross section area A of the beam, we obtain:

$$\sigma_y = \frac{F_v}{A} \tag{4.16}$$

For a circular cross section with diameter d, eq.(4.16) gives:

$$\sigma_y = \frac{4F_v}{\pi d^2} \tag{4.17}$$

Substitution to eq.(4.15) gives:

$$\varepsilon_y = \frac{4F_v}{\pi E d^2} \tag{4.18}$$

The vertical compression δ_y is given by:

$$\delta_y = \varepsilon_y L = \frac{4F_v L}{\pi E d^2} \tag{4.19}$$

By convention, an axial force is considered positive when it produces extension of the beam. In this particular case, F_v produces compression of the beam, so it is negative. It can be seen from eq.(4.18) and eq.(4.19) that the axial strain and axial deflection of the beam are also negative.

4.1.3.2. Simultaneous vertical and shear load

We will now assume that the linearly elastic cantilever beam is subjected to the vertical and shear force simultaneously, as shown in Fig.4.4. For small deflection δ we can assume that the shear force F_{sh} is responsible for the lateral deflection of the beam, as given by eq.(4.1), and the vertical force F_v is responsible for the axial compression of the beam, as given by eq.(4.19). However, more accurate estimation of the deflection of the beam can be found by considering the angle of rotation θ_b and analysing the shear and vertical forces to axial and tangential components. In this case, the contribution of both shear and vertical force in the axial and lateral deflection of the beam is taken into consideration.

For the shear force, the axial and tangential components respectively are:

$$F_{sh,a} = F_{sh} \sin\theta_b \tag{4.20}$$

$$F_{sh,t} = F_{sh} \cos\theta_b \tag{4.21}$$

Similarly, the axial and tangential components for F_v are:

$$F_{v,a} = F_v \cos\theta_b \tag{4.22}$$

$$F_{v,t} = F_v \sin\theta_b \tag{4.23}$$

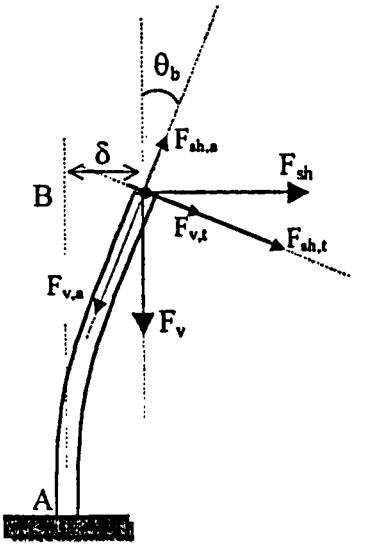

Fig.4.4: Deflection of a cantilever beam under shear and vertical load

The summing of the axial components will produce compression or extension of the beam (as given by eq.4.19), depending of the sign of the total axial force ΣF_a:

$$\Sigma F_a = F_{sh,a} + F_{v,a} \tag{4.24}$$

The lateral deflection of the beam can be calculated using eq.(4.1), where F_{sh} in this case is the total shear force ΣF_t:

$$\Sigma F_t = F_{sh.t} + F_{v,t} \tag{4.25}$$

In the special case were F_v is always negative, i.e. produces axial compression of the beam, as shown in Fig.4.4, $F_{sh,t}$, and $F_{v,t}$ have always the same sign. Therefore, the lateral deflection given by eq.(4.1) will be increased as a result of the vertical load.

The preceding analysis gives a better approximation for the deflection of a cantilever beam under simultaneous shear and axial load, compared to the simple superposition of the deflection due to shear (section 4.1.1) and vertical force (section 4.1.3.1). In many practical designs, especially when the expected deflection is small compared to the length of the beam the error can be tolerated. However, if the deflection of the free end of the beam must be calculated precisely, or an analytical expression for the deflection curve is required, then it is necessary to follow the analysis given in section 4.1.2.

4.1.3.3. Buckling of beams

When a beam is subjected to axial compressive load, it may bend and deform laterally. This effect, which is known as buckling of beams, can be observed in a long beam compared to its diameter when the axial load is greater than a critical value. Buckling is a very important

issue when designing structures with beams or columns, since it can lead to permanent beam failure. The deformation introduced by buckling can be elastic or inelastic, depending upon the slenderness of the beam. More information on buckling of beams can be found in textbooks related to beam and column structures design (Timoshenko and Gere, 1973, pp.368-396, Timoshenko, 1969) where many examples for different beam shapes, end supports, and axial loads have been examined.

Let us now consider a long, elastic beam fixed at both ends (see also section 4.1.2), which is compressed by a centrally applied force (a load acting through the centre of the cross section), as shown in Fig.4.5.

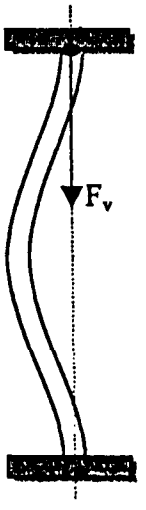

Fig.4.5: Buckling of beam with fixed ends

The critical load P_{cr} for this beam is given by (Timoshenko and Gere, 1973, pg.378):

$$P_{cr} = \frac{4\pi^2 EI}{L^2} \tag{4.26}$$

If the vertical force on the beam is less than the critical load, the beam remains constant and undergoes only axial compression (see section 4.1.3.1). In this case, if a shear force is applied and a small deflection is occurred, the beam will return to its straight form when the shear force is removed. If, however, the vertical force is equal or larger than the critical value, then the beam will have a small deflection similar to the one shown in Fig.4.5. A small shear load will produce further deflection which does not disappear when the shear load is removed. In that case, it is possible that the beam will collapse.

If the axial load is extremely small in comparison with the critical load (less than 2%, Timoshenko and Gere, 1973, pg.371), then the effect of buckling can be neglected and the usual beam deflection equations described in the previous sections may be used.

4.2 Sensor Design

In the following sections, the method for measuring shear stress by proper arrangement of FBGs in an elastic structure, as well as the theoretical design of the sensor will be presented in detail. The main objectives of the theoretical analysis are:

1. To examine the applicability of the method for the implementation of a sensor which would be able to satisfy the specifications set in section 2.3.
2. To calculate all the mechanical parameters of the sensor
3. To derive a mathematical model for the calculation of the stress under measurement via the Bragg wavelength shift, in other words to determine the sensor transfer function.
4. To predict any significant drawbacks of the method that could lead to rejection of the method before proceeding to the laboratory testing.

The main objective of the following analysis was to estimate the mechanical parameters of the sensor (material properties, arrangement of fibres, and structure dimensions), in order to fabricate the sensor and proceed to the experimental evaluation of the method. Since the precise determination of the behaviour of the sensor structure was not our first priority at this stage, the theory of elasticity, as it was presented in section 4.1, could be applied by considering a simplified model of the sensor. Any assumptions and simplifications made during the sensor design will be identified in the next sections.

The principle of operation and the general description of the sensor will be presented in section 4.2.1. The design continues with the calculation of the mechanical parameters of the sensor structure for optimum performance, section 4.2.2. Other issues discussed in section 4.2.2 are i) the theoretical prediction of sensor response to unidirectional shear stress using only one FBG, and ii) the effect of vertical stress on shear response. The design continues with the mathematical analysis of a sensor having 2 FBGs fitted in the sensor body, in order to derive the system of equations for the determination of the magnitude and direction of the applied shear stress. This is discussed in section 4.2.3.

4.2.1 Principle of operation and general description

The strain sensing elements used in this method are fibre Bragg gratings. Since Bragg wavelength shift is caused by axial strain on the fibre, it is apparent that, in order to measure shear stress applied on the sensor active surface, strain must be transferred from the surface to the FBG. The sensor body must therefore be able to deform elastically, causing elongation or contraction of the FBG, which is firmly fixed inside the sensor.

An essential requirement is that the sensor will be able to measure shear at any direction parallel to the active surface, in other words the magnitude and direction of shear stress must

be resolved from the measured Bragg wavelength shift. Therefore, more than one FBG will be necessary in order to calculate both magnitude and direction.

In order to achieve equal sensitivity of the sensor at any direction of shear, it is necessary to ensure that the sensor structure undergoes the same deformation at any direction of shear, for constant magnitude of shear stress. This behaviour could be expected by a structure made of an isotropic[1] material, which has an axis of symmetry perpendicular to the active surface of the sensor.

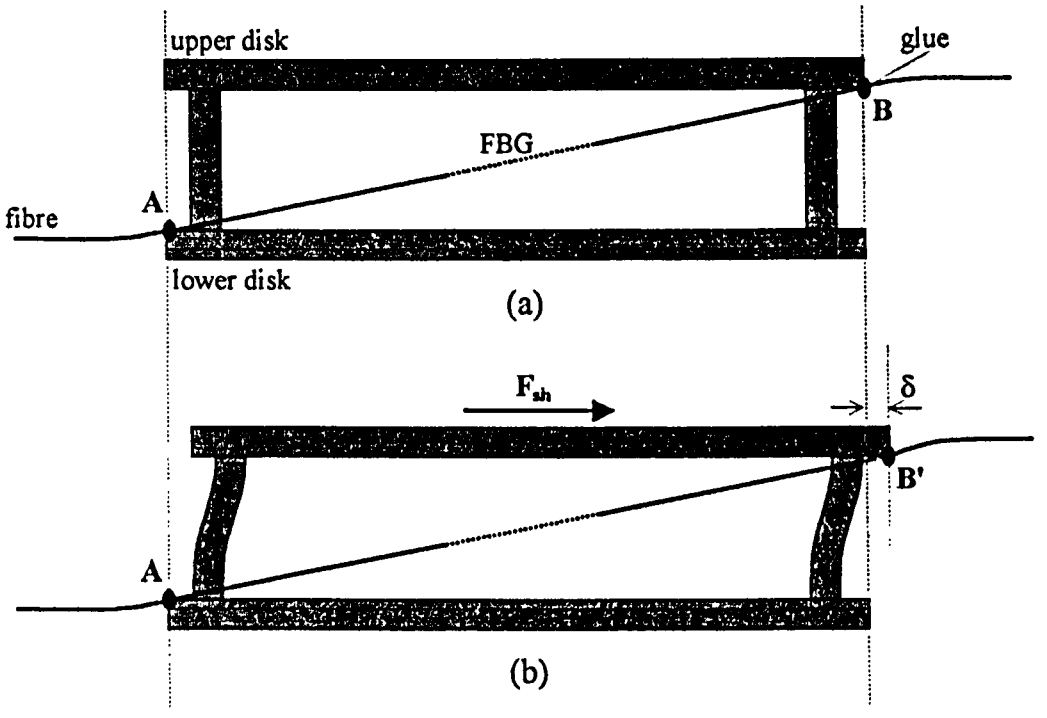

Fig.4.6:General diagram of the sensor. (a) at zero state, (b) under shear stress.

Fig.4.6(a) shows a side view of a sensor structure that complies with the above requirements. The fibre placement is also shown. The sensor body consists of two parallel disks held together by cylindrical pins. The fibre is firmly fixed on the lower disk at point A, and on the upper disk at point B. Application of shear stress on the top surface causes lateral displacement of the upper disk with respect to the lower one, Fig.4.6(b). The pins are deflected in a way similar to the deflection of a beam fixed at both ends and shear force is applied to one of its ends (section 4.1.2). Assuming elastic deformation of the pins, the upper disk will return to its initial position when shear is removed.

The deflection of the upper disk causes point B to move laterally. If the lower disk is fixed, then point A is stationary. Therefore, the length of the fibre between the two disks, which is equal to the distance between points A and B, will vary according to the applied shear stress. The induced strain on the fibre can be calculated by measuring the Bragg wavelength shift of the FBG, which is located between points A and B.

[1] a material which has the same elastic properties in all directions (Hull and Clyne, 1996, pg.82).

Referring to Fig.4.6, application of shear towards the right-hand side causes extension of the FBG. When shear is applied towards the left-hand side, the length AB is decreased. It is clear that, in the later case, strain can be measured if only the fibre is pre-strained at zero state (under no shear load).

4.2.2 Mechanical design

The main objectives of the design are:

1. The choice of the material for the two disks and the pins.
2. The determination of the maximum permitted horizontal displacement of the top disk so that the strain on the fibre will always be below the safety limit (+2500με, section 3.6.3).
3. The calculation of the pin diameter.
4. The determination of the dimensions for every part of the structure.
5. The elimination of the effect of vertical stress on the sensor performance.

The above issues are described in the next subsections.

4.2.2.1. Choice of materials

Regarding the construction of the disks, it is important to select a hard material (high Young's modulus) so that they will not deform elastically or plastically under the application of vertical or shear load. Any deformation of the disks will affect the deflection of the pins, since unpredictable bending moments will appear on the joints between the pins and the disks.

Fig.4.7 gives some examples of possible modes of sensor failure due to disk deformation. It is assumed that the pins are firmly fixed on the lower disk, which is made of an ideally incompressible material. Case (a) can be observed when the top disk is made of a relatively soft material, or when the disk thickness is very small. The disk will then be deformed under vertical stress in a way similar to a diaphragm. Bending moments will be introduced on the pins as the result of the disk bending, therefore neither of the models of the cantilever beam (section 4.1.1) or of the beam fixed at both ends (section 4.1.2) could be applied. The former model requires free upper end (no bending moments), and the later requires firmly supported ends (no rotation of upper end). In case (b), application of vertical load causes vertical compression of the disk in the contact region. This can happen when the disk material has a low E modulus. The distance between the two disks h' will be a function of the applied vertical stress. This will introduce error when using the sensor for shear stress measurements.

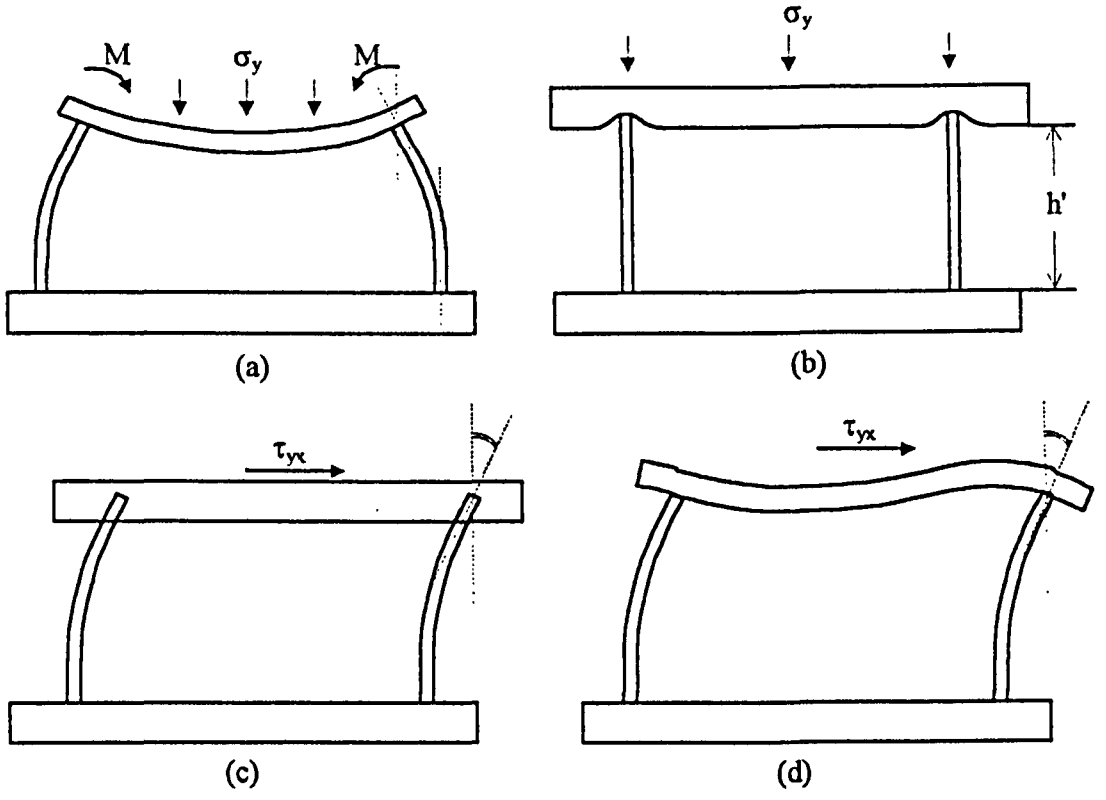

Fig.4.7: Some examples of sensor failure due to incorrect choice of disk material.

The effect of shear stress on the disk deformation is given Fig.4.7 (c) and (d). In case (c) the disk is deformed in the contact region with the pin, causing rotation of the pin axis with respect to the perpendicular to the disk surface. This effect can be observed when the material used for the disk is softer compared to the one used for the pins. The estimation of the pin deflection in this case is complex, since the reactions on the pins cannot be calculated without knowledge of the stress distribution at the interface region, which is not always known. In case (d) the deflection of the pins will be affected by the deformation of the top disk due to shear stress. This situation may occur when the disk thickness is small compared to its diameter.

In practice, more than one of the problems mentioned above could exist simultaneously, reducing the accuracy of the sensor in measuring the shear stress. Furthermore, the stress distribution on the top disk, which is considered uniform throughout this study, is generally not known.

Choosing a highly stiff material can reduce the effect of the problems stated previously. However, stiff materials have the drawback of difficult processing, therefore the hardness has to be compromised. The fabrication of the sensor requires accurate drilling in order to fix the pins on the disks. It is therefore necessary to select a material which is easy to be processed in an ordinary mechanical workshop. The stiffness of some typical engineering materials in terms of Young's modulus is given in Table 4.1.

Another important factor on selecting the material is its compatibility with at least one of the commercially available adhesives, since the optical fibre will be glued to the surface of the disk.

Based on the required properties mentioned above, stainless steel was finally chosen, since it offers the properties mentioned above, it is relatively cheap, and easily available.

Material	SiC	Steel	Ti	SiO_2	Al alloy	PVC	Hard Epoxy	High Density Polyethylene
E (GPa)	450	190-220	110	72	70-80	4.1	2-4	1.2

Table 4.1: Modulus of elasticity for some popular engineering materials (Charles *et al.*,1997; Budinsky, 1999).

The choice of the material for the fabrication of the pins is also very important, since their performance under shear will determine the specifications of the sensor. Linear elasticity and isotropy are essential properties to assure elastic bending under shear. The material should enable the easy fabrication of the relatively small diameter pins. A material that is commercially available directly in the form of rod or wire at the desired diameter would be ideal. It should also enable easy and robust joint with the material of the disks.

Again, metals have significant advantages with respect to the above characteristics, compared to polymers. Stainless steel (E=200GPa) was finally chosen because it is not affected by corrosion, and can be purchased in rod or wire form at the desired cross section diameter.

4.2.2.2. Calculation of the maximum allowable deflection of the top disk

Let us now consider a vertical section of the sensor which passes through the centre of the disks, as shown in Fig.4.8. The diagram is simplified for the purpose of the following theoretical analysis. We assume that the pins are made of a linearly elastic and isotropic material with Young's modulus E, and that they are firmly fixed on the disks. A FBG is pre-strained and firmly fixed on the disks, in a way that no relative movement of the fibre with respect to the lower and upper disk is possible at the contact points A and B respectively.

In the following analysis we will also assume that (1) only one FBG is fitted in the sensor, and (2) the vector of shear stress τ_{yx} lays on the same vertical plane as the fibre (plane ABC, Fig.4.8). This is the case where shear stress produces the maximum strain on the fibre due to the displacement of the top disk, as it will be shown in section 4.2.3 (eq.(4.96) for ω=0).

Due to the cylindrical cross section of the pins, the deflection of the top disk is expected to be insensitive to the direction of the applied shear stress. Therefore, the equations derived

in this section could also be applied for an FBG which lays on any vertical plane which passes through the centre of the disks.

As mentioned previously (section 4.2.1), the fibre is pre-strained in order to enable the measurement of shear stress at both directions. We also know that, for safe operation of the FBG strain sensor, the axial strain on the fibre must not exceed 2500με. Therefore, there is a maximum allowable displacement δ_{max} of the top disk. Larger displacements than δ_{max} will increase the risk of fibre breakage. Since the disk movement is caused by the shear stress applied on the top surface, there is a maximum allowable value for the shear stress, $\tau_{yx_{max}}$ that could be measured by this sensor. The main objective of the following analysis will be to find an expression for δ_{max} as a function of the sensor geometry.

When the applied shear stress causes reduction of the fibre length, the strain on the fibre will be reduced. That will happen when τ_{yx} has opposite sign compared to the one shown in Fig.4.8. The maximum value of shear stress that can be measured corresponds to zero strain in the fibre. Larger shear stresses than the above limit cannot produce compression of the fibre, since it is free to bend due to gravity, hence no strain will be introduced on the FBG, and the shear stress will not be detected. The operating range of this sensor is therefore limited to stress values which produce fibre axial strain in the range 0 to +2500με.

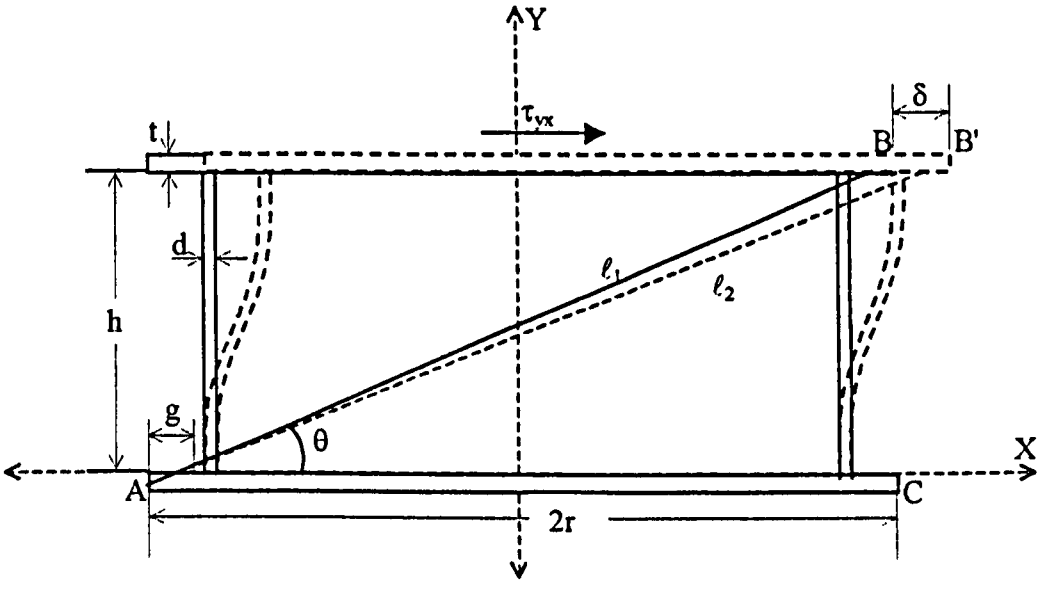

Fig.4.8: Theoretical model of the sensor for the calculation of maximum allowable displacement, based on bending of beams fixed at both ends.

For equal dynamic range in both ways of shear, the fibre must be pre-strained to half the value of the safety factor, prior to fixing the fibre. Therefore, under no shear stress on the top disk, the strain on the fibre must be ε_i=1250με.

Let ℓ_1 be the length of fibre between A and B. From the right angle ACB we obtain:

$$\ell_1 = \sqrt{4(r-g)^2 + h^2} \tag{4.27}$$

where r is the disk radius, and g is the vertical projection of the bonded length of the fibre. By definition, the strain ε_1 will be given by:

$$\varepsilon_1 = \frac{\ell_1 - \ell_0}{\ell_0} \tag{4.28}$$

where ℓ_0 corresponds to the unstrained length of the fibre. Application of shear stress τ_{yx} causes horizontal deflection of the top disk by δ. The new length of the fibre ℓ_2 will be:

$$\ell_2 = AB' = \sqrt{[2(r-g)+\delta]^2 + h^2} \tag{4.29}$$

Let ε_2 be the fibre strain at the new location. It will be given by:

$$\varepsilon_2 = \frac{\ell_2 - \ell_0}{\ell_0} \tag{4.30}$$

The fibre strain has been changed by:

$$\Delta\varepsilon = \varepsilon_2 - \varepsilon_1 = \frac{\ell_2 - \ell_1}{\ell_0} \tag{4.31}$$

Since ε_2 gets values in the range 0 to +2500$\mu\varepsilon$, the strain change $\Delta\varepsilon$ varies between −1250 to +1250$\mu\varepsilon$. Eq.(4.31) gives:

$$\ell_2 = \ell_1 + \ell_0 \Delta\varepsilon \tag{4.32}$$

Solving eq.(4.28) for ℓ_0 and substitution to eq.(4.32) gives:

$$\ell_2 = \ell_1 \left(1 + \frac{\Delta\varepsilon}{1+\varepsilon_1}\right) \tag{4.33}$$

Eq.(4.27), eq.(4.29), and eq.(4.33) give:

$$\delta = \sqrt{\left[4(r-g)^2 + h^2\right]\left(1 + \frac{\Delta\varepsilon}{1+\varepsilon_1}\right)^2 - h^2} - 2(r-g) \tag{4.34}$$

We already know (eq.2.9 for $\Delta T=0$) that the axial strain change on the fibre is related to the Bragg wavelength shift by the following equation:

$$\frac{\Delta\lambda_B}{\lambda_B} = 0.8\Delta\varepsilon \tag{4.35}$$

Substitution into eq.(4.34) gives an expression for the displacement δ with respect to the Bragg wavelength shift $\Delta\lambda_B$:

$$\delta = \sqrt{\left[4(r-g)^2 + h^2\right]\left(1 + \frac{\Delta\lambda_B}{0.8\lambda_B(1+\varepsilon_1)}\right)^2 - h^2} - 2(r-g) \tag{4.36}$$

The maximum allowable displacement δ_{max} can be calculated by eq.(4.34) for $\Delta\varepsilon=\Delta\varepsilon_{max}=1250\mu\varepsilon$, and it is determined by the dimensions of the sensor:

$$\delta_{max} = \sqrt{\left[4(r-g)^2 + h^2\left(1+\frac{\Delta\varepsilon_{max}}{1+\varepsilon_1}\right)^2 - h^2\right]} - 2(r-g) \tag{4.37}$$

Solving eq.(4.34) for $\Delta\varepsilon$ we obtain an expression of $\Delta\varepsilon$ as a function of the displacement δ:

$$\Delta\varepsilon = \left(\sqrt{\frac{[2(r-g)+\delta]^2 + h^2}{4(r-g)^2 + h^2}} - 1\right)(1+\varepsilon_1) \tag{4.38}$$

4.2.2.3. Estimation of pin diameter

The value of δ_{max} which is given by eq.(4.37) will be used for the determination of the pin diameter. We have already mentioned (section 4.2.2.2) that the pins are made of a linearly elastic and isotropic material and they are firmly fixed to the disks. Shear load applied to the top disk will produce lateral deflection of the pins in a way similar to the deflection of a beam fixed at both ends, as described in section 4.1.2. The objective in this section is to calculate the pin diameter for a given length and pin material in order to obtain the required pin stiffness.

The analysis presented in section 4.1.2 is valid for long beams, where the length of the beam is much greater than its diameter. However, this is not true in this case, since the length of the pins cannot be longer than a few millimetres, as limited by the desired sensor dimensions. Deviation between the theoretically calculated pin deflection compared to the experimental results, for a given pin diameter, is therefore expected. Since the main purpose of this study was to evaluate qualitatively the concept of measuring shear stress with the proposed sensor structure, we can tolerate the error introduced due to this unsatisfied assumption, and obtain an estimation for the required pin diameter.

By the definition of shear stress, the shear force F_{sh} acting on the top disk will be given by:

$$F_{sh} = \tau_{yx} A \tag{4.39}$$

where A is the disk area:

$$A = \pi r^2 \tag{4.40}$$

The shear force per pin F'_{sh} is given by:

$$F'_{sh} = \frac{F_{sh}}{N} \tag{4.41}$$

where N is the number of pins. The top end of each pin will be deflected by (eq.4.14):

$$\delta = \frac{F'_{sh} h^3}{12EI} \tag{4.42}$$

where h is the distance between the disks (pin length), and E and I the Young's modulus and moment of inertia of the pins respectively. Substitution of eq.(4.2), eq.(4.39), eq.(4.40), and eq.(4.41) into eq.(4.42) gives:

$$\delta = \frac{16r^2h^3\tau_{yx}}{3NEd^4} \tag{4.43}$$

The maximum deflection will given by eq.(4.43) for $\tau_{yx} = \tau_{yx_{max}}$ (=250kPa):

$$\delta_{max} = \frac{16r^2h^3\tau_{yx_{max}}}{3NEd^4} \tag{4.44}$$

The condition for fibre safety requires that the maximum deflection given by eq.(4.44) must always be smaller or equal to the value given by eq.(4.37). Hence:

$$\frac{16r^2h^3\tau_{yx_{max}}}{3NEd^4} \le \sqrt{\left[4(r-g)^2 + h^2\left(1+\frac{\Delta\varepsilon_{max}}{1+\varepsilon_1}\right)^2 - h^2\right]} - 2(r-g) \tag{4.45}$$

Solving eq.(4.45) for d we obtain:

$$d \ge \sqrt[4]{\frac{16r^2h^3\tau_{yx_{max}}}{3NE\left(\sqrt{\left[4(r-g)^2 + h^2\left(1+\frac{\Delta\varepsilon_{max}}{1+\varepsilon_1}\right)^2 - h^2\right]} - 2(r-g)\right)}} \tag{4.46}$$

If the diameter of every pin is greater than the one given by eq.(4.46), then the strain on the fibre will always be kept within the safety limit ($\varepsilon_2 \le 2500\mu\varepsilon$), provided that the shear stress under measure does not exceed the maximum allowable value $\tau_{yx_{max}}$. In the special case where the pin diameter is equal to the one given by eq.(4.46), the entire operating range of the FBG strain sensor is used, which corresponds to the highest sensitivity of the sensor to shear stress. Hence, the equal sign in eq.(4.46) gives the pin diameter for optimum sensor performance.

4.2.2.4. Numerical application on sensor design

The equations derived in sections 4.2.2.2 and 4.2.2.3 will be used to determine the dimensions of every part of the sensor. The outer dimensions of the sensor are restricted by the specifications explained in section 2.3. According to those specifications, we set r=5mm. The total height of sensor is set to 3mm, which is equal to the summing of the pin length and the disk thickness (Fig.4.8):

$$h + 2t = 3mm \tag{4.47}$$

Both disks must have enough thickness to eliminate the problems shown in Fig.4.7(a) and (d). However, increasing the thickness t, the length of the pins h must be reduced according to eq.(4.47), which in turn increases the error introduced by the application of beam bending theory for the estimation of the required pin diameter, as explained in section 4.2.2.3. Choosing t=0.5mm, the pin length will be h=2mm.

The maximum deflection will be given by eq.(4.34) for $\Delta\varepsilon$=1250$\mu\varepsilon$. Substitution gives:

$$\delta_{max} \cong 13\mu\varepsilon \tag{4.48}$$

As mentioned previously, maximum displacement will be observed for the maximum applied shear stress, $\tau_{yx_{max}} = 250\text{kPa}$. Fig.4.9 shows the variation of the optimum pin diameter with respect to the number of pins, as this is given by eq.(4.46), for different pin materials.

For a sensor structure made of 4 steel pins (E=200GPa), the required pin diameter will be:

$$d = 0.4\text{mm} \tag{4.49}$$

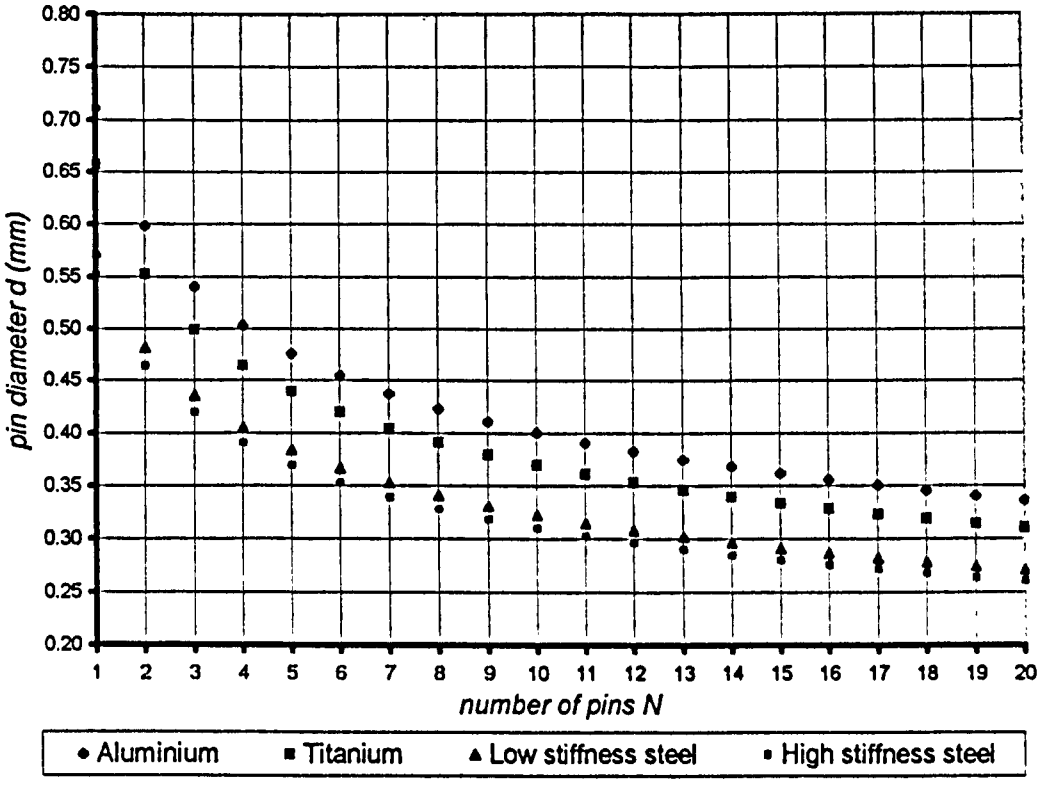

Fig.4.9: Pin diameter as a function of the number of pins N and E modulus for 4 materials having different E modulus.

4.2.2.5. Grating response to shear stress

In section 4.2.2.3 we have examined the relation between the maximum applied shear stress on the top disk of the sensor and the produced lateral deflection of the pins, which is given by eq.(4.43). Without considering the maximum values and solving the equation with respect to the applied shear stress, we obtain:

$$\tau_{yx} = \frac{3NEd^4\delta}{16r^2h^3} \tag{4.50}$$

It is reminded that eq.(4.50) is only valid for shear stress applied parallel to the vertical plane defined by the fibre axis. The lateral deflection in turn is related with the induced strain change on the fibre by eq.(4.34). Substitution into eq.(4.50) gives:

$$\tau_{yx} = \frac{3NEd^4}{16r^2h^3}\left(\sqrt{\left[4(r-g)^2 + h^2\left(1+\frac{\Delta\varepsilon}{1+\varepsilon_1}\right)^2 - h^2\right]} - 2(r-g)\right) \quad (4.51)$$

Substituting $\Delta\varepsilon$ from eq.(4.35) we derive the equation which relates the measured Bragg wavelength shift $\Delta\lambda_B$ with the applied shear stress:

$$\tau_{yx} = \frac{3NEd^4}{16r^2h^3}\left(\sqrt{\left[4(r-g)^2 + h^2\left(1+\frac{\Delta\lambda_B}{0.8(1+\varepsilon_1)\lambda_B}\right)^2 - h^2\right]} - 2(r-g)\right) \quad (4.52)$$

Eq.(4.51) and eq.(4.52) show linear variation of the fibre strain change and Bragg wavelength shift, respectively, with the applied shear stress. This can be clearly shown by graphically presenting the above equations, Fig.4.10. Table 4.2 summarises the values of all the constants appeared in the above equations and used for drawing the graph, as they were calculated in section 4.2.2.4.

description	symbol	value	unit
Young's Modulus of elasticity of pin material (st. steel)	E	200×10^9	Pa (N/m^2)
pin length	h	2×10^{-3}	m
pin diameter	d	0.4×10^{-3}	m
number of pins	N	4	-
disk radius	r	5×10^{-3}	m
disk thickness	t	0.5×10^{-3}	m
bonded length of fibre	g	1×10^{-3}	m
fibre strain at zero shear stress	ε_1	1250×10^{-6}	strain
Bragg wavelength	λ_B	836.5	nm

Table 4.2: Summary of the sensor parameters.

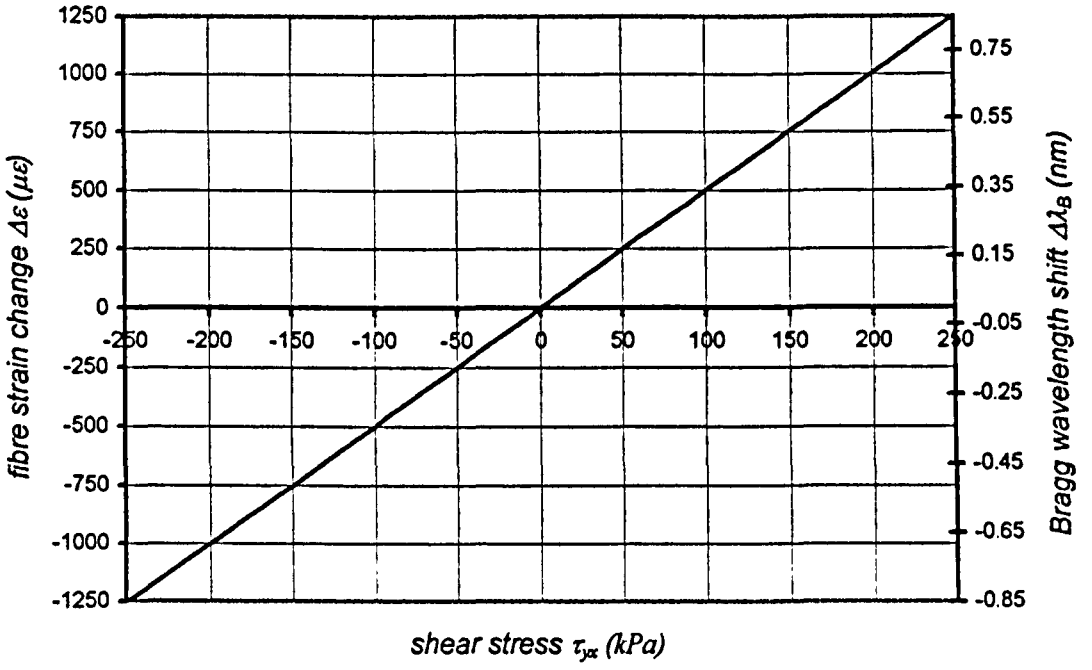

Fig.4.10: Sensor response to shear stress. The primary y-axis (left) shows the theoretical variation of the fibre strain $\Delta\varepsilon$ with respect to shear stress, as given by eq.(4.51). The secondary y-axis (right) shows the Bragg wavelength shift $\Delta\lambda_B$ with respect to shear stress, as given by eq.(4.52).

4.2.2.6. Effect of vertical stress on sensor performance

All the necessary dimensions for the sensor construction are now known. However, before proceeding to the fabrication stage, it is important to examine theoretically the strength of the structure. In the previous analysis we considered τ_{yx} as the only stress applied on the sensor. We already know that vertical stress will also be applied during in-shoe shear stress measurements. Since the sensor presented in this chapter is capable of measuring shear stress only, the sensor must be insensitive to vertical stress. More specifically, the sensor structure must be designed in a way that (1) it withstands the maximum vertical stress on the top disk without any plastic deformation or, in the worst case, permanent damage of the structure or fibre breakage, and (2) it minimises the error due to the crosstalk with the vertical stress.

The deformation of the sensor structure under vertical stress can be easily examined by approximating the pins with the model of the cantilever beam (section 4.1.1), instead of the more accurate, but also more complex model of the beam fixed at both ends which was used to describe the sensor response to shear (sections 4.2.2.2, 4.2.2.3). This model is given in Fig.4.11. Comparing eq.(4.1) and eq.(4.14), we conclude that the model shown in Fig.4.11 overestimates the horizontal deflection. In other words, it describes a structure which exhibits lower shear stiffness than the model of the beam fixed at both ends (Fig.4.8), and represents a worse case than the reality. Therefore, if we conclude that the model shown in Fig.4.11 withstands the vertical stress without permanent deformation, then we ensure that the actual sensor will also perform well.

Fig.4.11(b) shows the deformation of the sensor when vertical stress σ_y and shear stress τ_{yx} are applied on the top disk simultaneously. The top end of the fibre (point B on the top disk) will be displaced horizontally by δ and vertically by δ_y. The vertical displacement is the result of the axial forces acting on the pins. The tangential forces acting at the free end of each pin cause the horizontal deflection of that pin. The shear and vertical forces on every pin can be analysed to axial and tangential components as described in section 4.1.3.2, and shown in Fig.4.4. The dashed symbols are used to distinguish the forces acting on each pin from the total forces acting on the top disk. Hence, referring to Fig.4.4, the angle of rotation θ_b will be given by eq.(4.3), which in this case can be written as:

$$\theta_b = \frac{32F'_{sh}h^2}{\pi Ed^4} \tag{4.53}$$

where F_{sh}' is the shear force on each pin, given by:

$$F'_{sh} = \frac{\tau_{yx}A}{N} = \frac{\tau_{yx}\pi r^2}{N} \tag{4.54}$$

The vertical force on each pin is given by:

$$F'_v = \frac{\sigma_y A}{N} = \frac{\sigma_y \pi r^2}{N} \tag{4.55}$$

The total tangential force on each pin, given by (eq.4.25):

$$\Sigma F'_t = F'_{sh,t} + F'_{v,t} \tag{4.56}$$

Substitution using eq.(4.21) and eq.(4.23) gives:

$$\Sigma F'_t = F'_{sh}\cos\theta_b + F'_v \sin\theta_b \tag{4.57}$$

Similarly, the total axial force on each pin $\Sigma F_a'$ can be found by combining eq.(4.24), eq.(4.20), and eq.(4.22):

$$\Sigma F'_a = F'_{sh}\sin\theta_b + F'_v \cos\theta_b \tag{4.58}$$

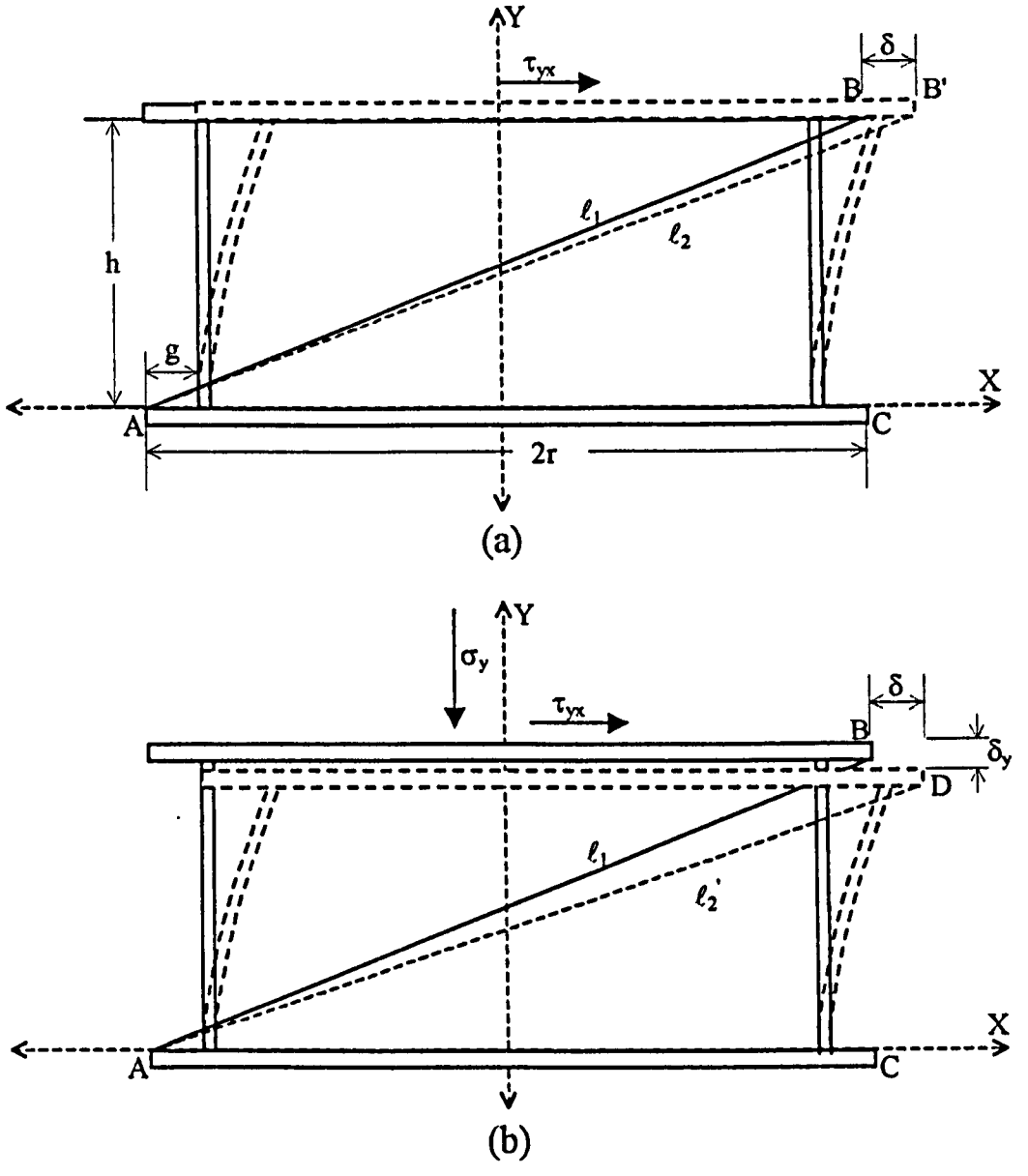

Fig.4.11: Top disk deflection of (a) the ideal (incompressible) sensor, and (b) actual (compressible) sensor, under shear and vertical load. The pins are considered as cantilever beams.

The maximum angle of rotation $\theta_{b,max}$ can be calculated by eq.(4.53) using eq.(4.54), for $\tau_{yx}=\tau_{yx,max}=250$kPa. Substitution gives $\theta_{b,max}=0.039$rad (=2.2°). Since the angle of rotation θ_b is small, we can write:

$$\cos\theta_b \approx 1 \tag{4.59}$$

$$\sin\theta_b \approx 0 \tag{4.60}$$

Hence, the total tangential force per pin can be approximated by (eq.4.57):

$$\Sigma F_t' \approx F_{sh}' \tag{4.61}$$

Eq.(4.61) shows that the lateral displacement δ is caused solely by the shear force acting on the top disk. The vertical compression δ_y on the other hand can be assumed to be caused by the vertical force only, since eq.(4.58) gives:

$$\Sigma F_a' \approx F_v' \tag{4.62}$$

It was mentioned in section 4.1.3.3 that a beam can be collapsed due to buckling, when the axial load exceeds a critical value. It is therefore important to ensure that the critical load of every pin in the sensor structure will be well above the maximum expected vertical force in order to avoid permanent damage of the sensor. The critical load P_{cr} of each pin is given by eq.(4.26), which can be written as:

$$P_{cr} = \frac{\pi^3 d^4 E}{16h^2} \tag{4.63}$$

Substitution gives P_{cr}=2480N. The maximum axial force on every pin can be calculated by eq.(4.62) using eq.(4.55) for $\sigma_y=\sigma_{y,max}$=500kPa, which gives $\Sigma F'_{a,max}$=9.8N. This value is less than 0.4% of the critical value, therefore the structure will not collapse and the effect of buckling can be neglected (see also section 4.1.3.3).

It is reminded that eq.(4.26) is valid for long beams, where the beam diameter is much smaller than its length. This condition is not satisfied, since the pin length is only four times larger than the pin diameter. The critical value calculated above is a rough estimation, which is accepted only because it shows a much greater value than the maximum expected vertical load. It is therefore reasonable to assume that, even if the actual P_{cr} is significantly lower (for example one order of magnitude lower) than the estimated by eq.(4.26), it will still be larger than F'_v and the sensor structure will be safe.

After examining the strength of the sensor structure to vertical stress, the next step is to predict theoretically the effect of vertical compression on the measured shear stress. As it can be seen from Fig.4.11(b), application of both vertical and shear stress to the top disk will result in a different fibre length ℓ'_2, compared to the fibre length ℓ_2 in the ideal case of a vertically incompressible sensor, Fig.4.11(a). Therefore, the measured strain on the FBG varies with the applied vertical load, which introduces error in measuring shear stress. The estimation of this error will be discussed next. In the following analysis we can return to the model of the beam fixed at both ends in order to obtain more accurate results, since the bending shape of the beam is not taken into consideration. The reference diagram, however, will still be the one shown in Fig.4.11.

First, we will consider the ideal case of the incompressible sensor, Fig.4.11(a). Application of shear stress will produce axial strain on the fibre, which will be given by eq.(4.38). Application of vertical stress does not alter the strain on the fibre, hence the measured shear stress τ_{yx}, as this is calculated by eq.(4.51), will not be affected by the vertical stress.

Let us now consider the actual case of a vertically compressible sensor, Fig.4.11(b). The new length of the fibre ℓ'_2 is equal to the length AD, and it is given by:

$$\ell'_2 = \sqrt{(h-\delta_y)^2 + [2(r-g)+\delta]^2} \tag{4.64}$$

The new strain of the fibre ε' will be given by:

$$\varepsilon_2' = \frac{\ell_2' - \ell_0}{\ell_0} \tag{4.65}$$

The new fibre strain change $\Delta\varepsilon'$ is given by:

$$\Delta\varepsilon' = \varepsilon_2' - \varepsilon_1 = \frac{\ell_2' - \ell_1}{\ell_0} \tag{4.66}$$

Substituting ℓ_0 from eq.(4.28), ℓ_1 from eq.(4.27), and ℓ_2' from eq.(4.64), we obtain:

$$\Delta\varepsilon' = \left(\sqrt{\frac{(h-\delta_y)^2 + [2(r-g)+\delta]^2}{h^2 + 4(r-g)^2}} - 1 \right)(1+\varepsilon_1) \tag{4.67}$$

The vertical compression δ_y is given by eq.(4.19) where the vertical force causing the compression is $\Sigma F_a'$:

$$\delta_y = \frac{4\Sigma F_a' h}{\pi E d^2} \tag{4.68}$$

Using eq.(4.62) and eq.(4.55) we obtain:

$$\delta_y = \frac{4r^2 h \sigma_y}{NEd^2} \tag{4.69}$$

Eq.(4.67) gives the actual strain change on the FBG, which is caused by the presence of both shear and vertical load. This is the strain change, which is measured via the Bragg wavelength shift. Since the sensor was assumed incompressible while deriving the equation which relates the measured fibre strain change with the applied shear stress τ_{yx} (section 4.2.2.5), the calculated shear stress τ_{yx}' will differ from the actual one, and will be given by eq.(4.51) for $\Delta\varepsilon=\Delta\varepsilon'$:

$$\tau_{yx}' = \frac{3NEd^4}{16r^2h^3}\left(\sqrt{\left[4(r-g)^2 + h^2\left(1+\frac{\Delta\varepsilon'}{1+\varepsilon_1}\right)^2 - h^2\right]} - 2(r-g) \right) \tag{4.70}$$

Hence, the application of simultaneous shear and vertical load introduces error in measuring the shear stress, which is equal to the difference between τ_{yx}', given by eq.(4.70) and τ_{yx} given by eq.(4.51). The absolute percentage error will be given by:

$$\text{error} = \frac{\left\| \tau_{yx} \right| - \left| \tau_{yx}' \right\|}{\left| \tau_{yx} \right|} \times 100\% \tag{4.71}$$

Eq.(4.71) is graphically presented in Fig.4.12 as a function of the applied shear stress. The three plots correspond to three different values of vertical stress, i.e. $\sigma_{y,max}$, $\sigma_{y,max}/2$ and $\sigma_{y,max}/4$. The graph shows that the estimated error is less than 5% for any value of vertical stress as long as the magnitude of shear stress is larger than 60kPa. For smaller magnitude of

shear stress, the error is significantly increased as the magnitude of the vertical stress increases.

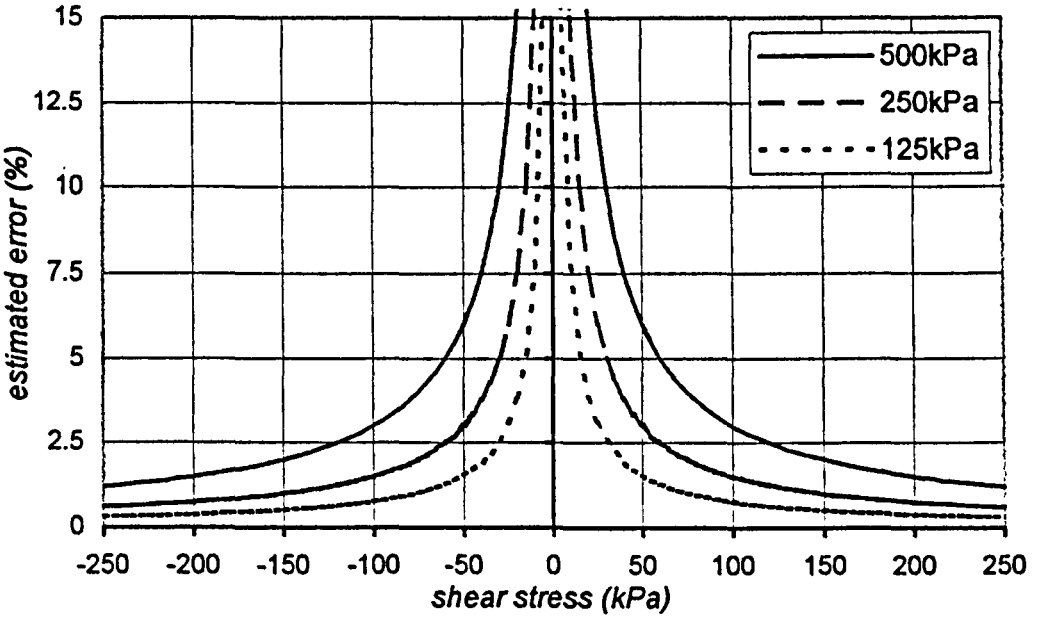

Fig.4.12: Theoretically estimated error in shear stress measurement due to the application of vertical stress, for 3 different values of vertical stress.

The poor performance of the sensor in terms of measuring precision at small shear stresses can be improved by careful selection of the structure parameters. Due to the already small pin length h, we keep this parameter fixed to h=2mm. Reduction of the disk radius r would increase the risk of fibre breakage due to excess fibre bending at the points where the fibre enters and leaves the sensor. It is also important to keep the sensor radius small in order to achieve high spatial resolution in measuring in-shoe shear stress. For those reasons we keep the disk radius fixed to r=5mm. The remaining parameters are 1) the number of pins N, 2) the pin diameter d, and 3) the E modulus of the pin material. The choice of those 3 parameters will now be reconsidered in order to achieve both goals of fibre safety and sensor insensitivity to vertical stress. For that purpose, we will examine the maximum absolute error in measuring shear stress due to vertical compression of the pins, as this is defined by eq.(4.71). Based on the results shown in Fig.4.12, maximum error will occur when maximum vertical and minimum shear stresses are applied simultaneously. Those values are $\sigma_y=\sigma_{y,max}$ (=500kPa), and τ_{yx}=5kPa. The minimum shear stress is set by the desired shear stress resolution (section 2.3).

Fig.4.13 shows the contour plot of the theoretically predicted absolute error in shear stress measurement. The plot is drawn by varying the pin diameter discretely from 1 to 20, and the E modulus from 80GPa to 220GPa with a step of 10GPa. For every pair of N and E values, the maximum absolute error was calculated by following the next steps:

1. Calculation of the optimum pin diameter using eq.(4.46), (section 4.2.2.3).

2. Calculation of the horizontal deflection δ, as given by solving eq.(4.50) for δ, using the pin diameter found in step 1.
3. Calculation of the vertical compression δ_y as given by eq.(4.69), again for the optimum pin diameter found in step 1.
4. Calculation of $\Delta\varepsilon$ and $\Delta\varepsilon'$ using eq.(4.38) and eq.(4.67), respectively.
5. Calculation of τ_{yx}, τ_{yx}' from eq.(4.51) and eq.(4.70), respectively.
6. Calculation of the maximum absolute error using eq.(4.71).

As it can be seen in Fig.4.13, the error can be reduced by selecting a high E modulus and by increasing the number of pins. For a sensor made of 4 steel pins (E=200GPa), having the optimum diameter of 0.4mm (eq.4.49), the expected maximum error is 60%.

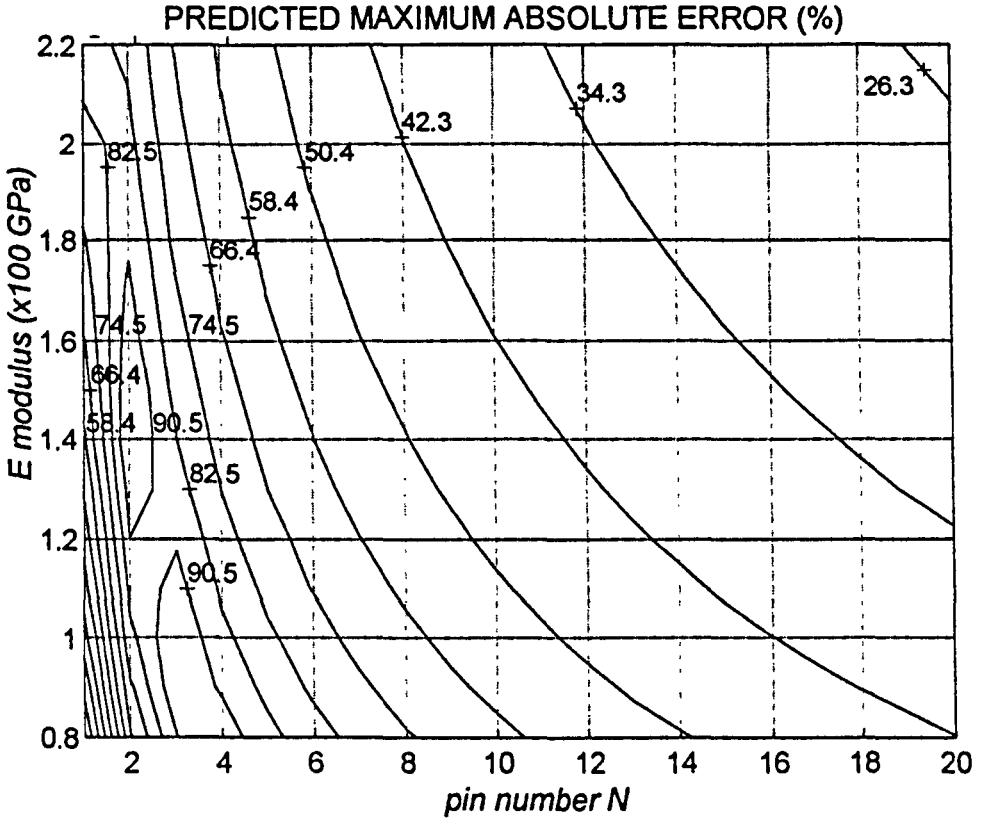

Fig.4.13: Maximum absolute error in measuring shear stress due to vertical stress, for different N and E values. The shear stress is assumed constant and equal to 5kPa.

It is important to note that, any alteration in the sensor parameters shown in Table 4.2, requires the pin diameter to be recalculated in order to ensure that the FBG will not be overstrained under any shear stress between –250 to 250kPa, a condition which was discussed in section 4.2.2.3. This is executed in step 1 of the procedure above.

4.2.2.7. Effect of the fibre on sensor performance

In the preceding theoretical analysis the presence of the prestrained fibre fixed to the disks was neglected. In this section, we will examine the effect of the prestrained fibre. We will assume that one fibre is fixed into the sensor, and that a shear stress τ_{yx} is applied parallel to the fibre, as shown in Fig.4.14. The pins will be deflected in the direction of increasing x, due to the shear force F_{sh}. From the static equilibrium of the top disk at the x-direction, the deflection δ' will be such that the overall forces acting on the top disk will be zero:

$$\Sigma\vec{F} = 0 \therefore F_{sh} - 4F_p - T_x = 0 \tag{4.72}$$

where F_p is the force applied by each of the four pins, and T_x is the projection of the fibre tension T. In this section the displacement δ' will be calculated, and then compared with the displacement of the metallic structure without fibre attached on it, which was found in section 4.2.2.2.

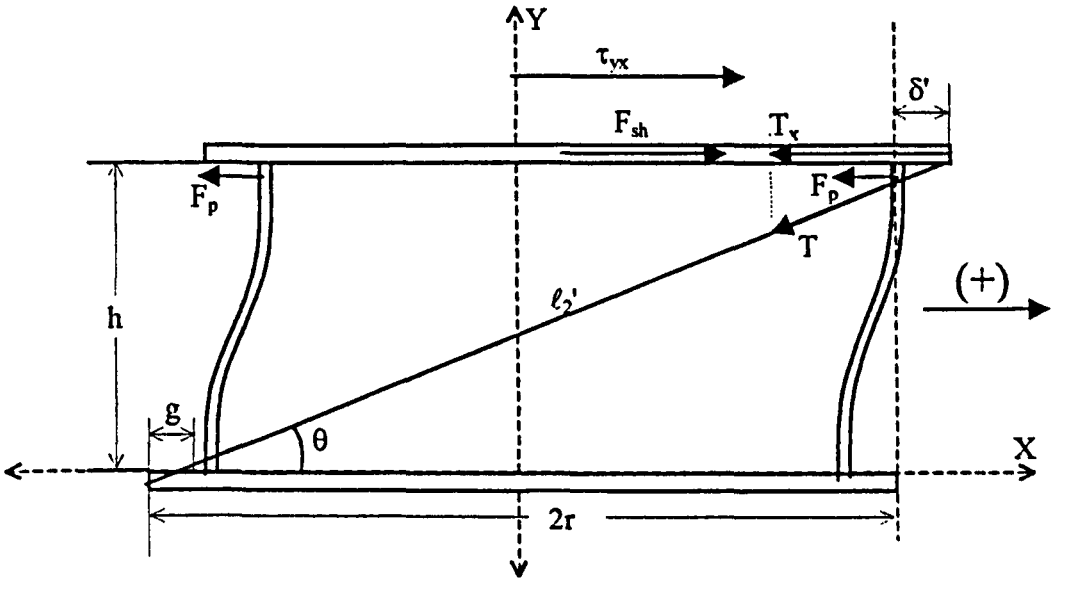

Fig.4.14: The prestrained fibre applies the force T on the disk, which, in this case, opposes the applied force F_{sh}.

Firstly, the horizontal component of the fibre tension T_x will be calculated. The length ℓ_2' of the fibre when the displacement is equal to δ' is given by:

$$\ell_2' = \sqrt{[2(r-g)+\delta']^2 + h^2} \tag{4.73}$$

The axial strain on the fibre ε_2' will be given by:

$$\varepsilon_2' = \frac{\ell_2' - \ell_0}{\ell_0} \tag{4.74}$$

where ℓ_0 is the unstrained length of the fibre. ℓ_0 can be calculated since the length of the fibre ℓ_1 and the axial strain on the fibre ε_1 for the unstressed sensor are known. As mentioned previously in section 4.2.2.2, ε_1=1250με and the length ℓ_1 is given by (eq.4.27):

$$\ell_1 = \sqrt{4(r-g)^2 + h^2} \tag{4.75}$$

The length ℓ_0 is calculated from the equation:

$$\varepsilon_1 = \frac{\ell_1 - \ell_0}{\ell_0} \therefore \ell_0 = \frac{\ell_1}{1+\varepsilon_1} \tag{4.76}$$

The axial strain on the fibre ε_2' is also given by:

$$\varepsilon_2' = \frac{\sigma_f}{E_f} \tag{4.77}$$

where σ_f is the axial stress at the cross-section area of the fibre, and E_f the modulus of the fibre. By definition, σ_f is given by:

$$\sigma_f = \frac{T}{A_f} \tag{4.78}$$

where $A_f = \pi r_f^2$ is the fibre cross-section area. Solving eq.(4.78) for T, and substitution gives:

$$T = \sigma_f A_f = \sigma_f \pi r_f^2 = \varepsilon_2' E_f \pi r_f^2 \tag{4.79}$$

The horizontal component T_x will be:

$$T_x = T\cos\theta = \varepsilon_2' E_f \pi r_f^2 \cos\theta \tag{4.80}$$

Substitution of ℓ_2' (eq.4.73) to eq.(4.74), and then ε_2' to eq.(4.80), gives:

$$T_x = E_f \pi r_f^2 \frac{\sqrt{[2(r-g)+\delta']^2 + h^2} - \ell_0}{\ell_0} \cos\theta \tag{4.81}$$

The magnitude of the horizontal force applied by each pin F_p, which opposes the external force F_{sh}, is given by (eq.4.14):

$$F_p = \frac{12EI\delta'}{h^3} \tag{4.82}$$

where I is the moment of inertia, given by eq.(4.2). The external shear stress F_{sh} is given by (eq.4.39 and eq.4.40):

$$F_{sh} = \tau_{yx} \pi r^2 \tag{4.83}$$

where r is the disk radius. Substitution of eq.(4.81), eq.(4.82), and eq.(4.83) to eq.(4.72) gives:

$$\frac{48EI\delta'}{h^3} + \frac{E_f \pi r_f^2 \cos\theta}{\ell_0} \sqrt{[2(r-g)+\delta']^2 + h^2} - \tau_{yx} \pi r^2 - E_f \pi r_f^2 \cos\theta = 0 \tag{4.84}$$

The above equation can be simplified using the following constants:

$$\alpha = \frac{48EI}{h^3} \tag{4.85}$$

$$\beta = \frac{E_f \pi r_f^2 \cos\theta}{\ell_0} \tag{4.86}$$

$$\gamma = 2(r - g) \tag{4.87}$$

$$\zeta = \tau_{yx} \pi r^2 + E_f \pi r_f^2 \cos\theta \tag{4.88}$$

Substitution to eq.(4.84) and taking the square gives:

$$(\beta^2 - \alpha^2)\delta'^2 + 2(\gamma\beta^2 + \alpha\zeta)\delta' + [\beta^2(\gamma^2 + h^2) - \zeta^2] = 0 \tag{4.89}$$

Eq.(4.89) is a quadratic equation with respect to the unknown δ'. Only the solution which gives $-13\mu m \le \delta' \le 13\mu m$, where $13\mu m$ is the maximum displacement calculated by considering the sensor structure only, section 4.2.2.4, is accepted. This solution is drawn in Fig.4.15 for $-250kPa \le \tau_{yx} \le 250kPa$. The other parameters are: E_f=72GPa, r_f=62.5μm, E=200GPa, d=0.4mm, r=5mm, g=1mm, ε_1=1250με, h=2mm. The angle θ is given by:

$$\theta = \arctan\left(\frac{h}{2r}\right) \cong 11^\circ \tag{4.90}$$

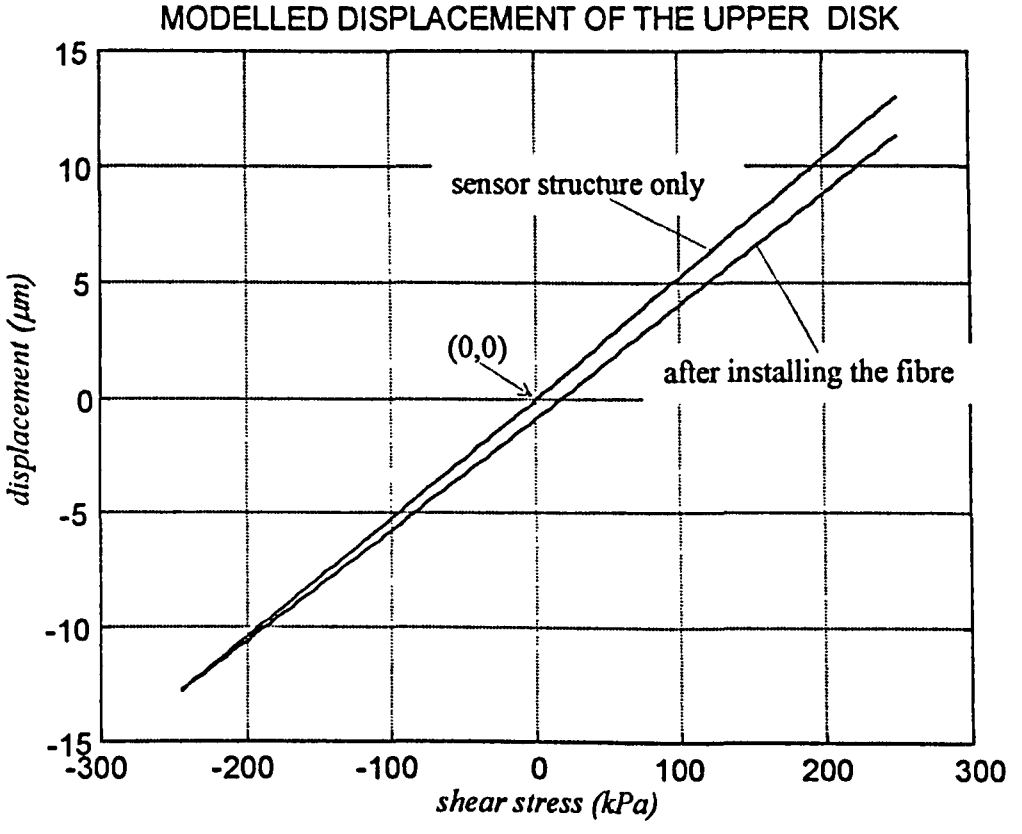

Fig.4.15: Displacement of the upper disk as a function of shear stress applied parallel to the fibre for the sensor body with, and without the optical fibre attached.

The displacement of the structure without the optical fibre when no fibre is installed, as given by eq.(4.43), is also plotted on the same graph. For τ_{yx}= –250kPa, the tension T is zero (because $\varepsilon_2'=0$ since $\ell_2'=\ell_0$) therefore the fibre has no effect on the upper disk displacement. As shear stress increases, the opposing T also increases, which reduces the displacement of the metallic structure. For zero shear stress, the displacement is approximately –1μm due to the tension of the prestrained fibre $T_x\cong$–1N (eq.4.80 for $\varepsilon_2'=\varepsilon_1=1250\mu\varepsilon$). This corresponds to shear stress equal to –19kPa (eq.4.43), or to Bragg wavelength shift approximately equal to –0.065nm (eq.4.52). The maximum error in calculating the displacement due to the fibre tension occurs for τ_{yx}= +250kPa, which is equal to ~11.5%.

It is therefore expected that the attachment of the fibre on the sensor structure will introduce asymmetric response of the structure to different directions of shear stress. This unwanted effect cannot be avoided. It could be reduced however using a fibre with a smaller diameter than 125μm, which will reduce the magnitude of the fibre tension (eq.4.81).

4.2.3 Determination of the magnitude and direction of shear stress using 2 fibre Bragg gratings

In the theoretical analysis presented so far, we have described the operation of a sensor which is able to measure the magnitude of shear stress when the stress vector lays on the vertical plane defined by the fibre, i.e. plane ABC in Fig.4.8. The magnitude is calculated via the Bragg wavelength shift of the FBG, as discussed in section 4.2.2.5. In that case, the sensor utilises only one FBG and is able to measure unidirectional stress. In practice, the shear stress can be applied at any direction on the upper surface of the top disk. In that case, not only the magnitude, but also the direction of shear must be determined. Expressing the stress vector in polar coordinates, the vector can be fully determined by measuring its magnitude and the angle between the vector and a reference direction. Since two unknown quantities are presented, more than one FBG must be fitted into the sensor structure in order to derive a system of equations.

The aims of the analysis presented in this section are:

- To determine the number of FBGs needed to identify the stress vector
- To derive the system of equations

Let us assume that one FBG (FBG1) is pre-strained and attached on the lower and upper disk at the points A and B respectively, as shown in Fig.4.16. The drawing of pins is omitted to keep the diagram simple. The vertical plane AB, which is defined by the fibre and passes through the centre of the disks, will be used as a reference for the determination of the shear

stress direction. Similarly, a second FBG (FBG2) is also pre-strained and attached at the points C and D. The vertical plane CD defined by the FBG2, which also passes through the centre of the disks, defines an angle ϕ with respect to the reference plane AB.

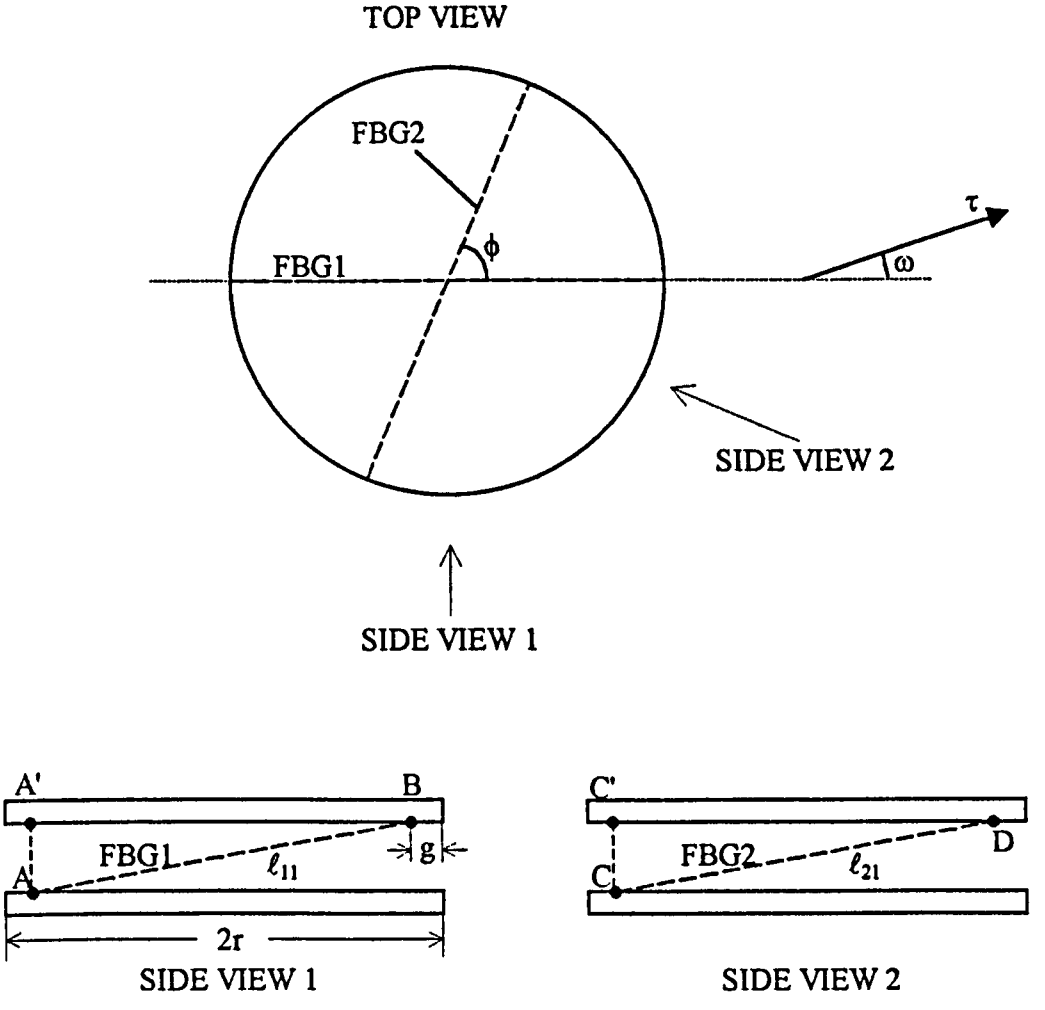

Fig.4.16: FBG arrangement for the determination of shear direction.

Let us now consider that the shear stress τ is applied on the top disk at an angle ω with respect to the reference plane. The shear stress will produce horizontal displacement δ of the upper disk with respect to the lower one at the direction of shear. It is assumed that the horizontal displacement of the upper disk is independent of the direction of shear stress. In other words, the pin deflection depends only on the magnitude of the applied shear, and it is the same for any direction of shear. It is also assumed that the two disks are not deformed under shear stress, hence the displacement occurs exclusively due to the lateral deflection of the pins. This assumption also implies that the horizontal displacement of the upper end is the same for every pin. Because the lower disk is firmly fixed, points A and C on the lower disk will remain in position under shear stress. On the other hand, points B and D on the upper disk will move to new locations, displaced horizontally by δ and at an angle ω with respect to the reference plane. Therefore, the length of both FBG1 and FBG2 will be altered, which can be calculated by measuring the strain change on the fibre via the Bragg

wavelength shift, as we have already examined for the case of a single FBG, section 4.2.2.2. We will now derive the displacement-strain equation for both FBGs by incorporating the direction of shear, i.e. the angle ω.

Let ℓ_{11} be the initial (pre-strained) length of FBG1. From the geometry of the structure, Fig.4.16 - side view 1, we obtain:

$$\ell_{11} = \sqrt{4(r-g)^2 + h^2} \tag{4.91}$$

Let A' be the vertical projection of the immovable point A on the upper disk. Let also B' be the new location of point B after the application of shear stress, Fig.4.17(a). It is noted that points A', B, B' and the auxiliary H are all laid on the upper disk plane. The length A'B' will be:

$$A'B' = \sqrt{(A'B + BH)^2 + HB'^2} \tag{4.92}$$

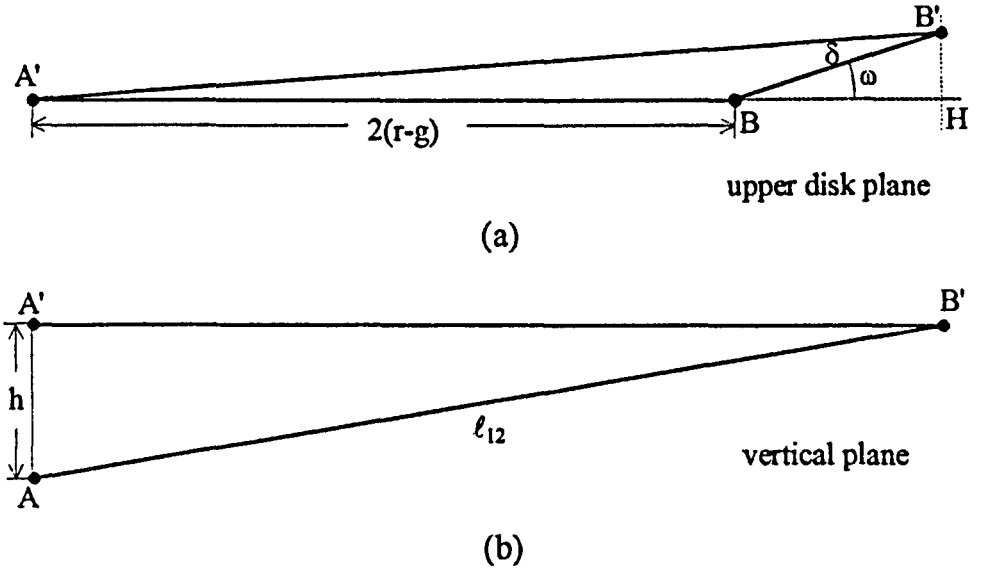

Fig.4.17: (a) Calculation of length A'B' on the upper disk plane, and (b) calculation of new fibre length ℓ_{12} of FBG1. The shear stress is applied in the direction BB'.

Substitution of the lengths A'B, BH, and HB' gives:

$$A'B' = \sqrt{[2(r-g) + \delta\cos\omega]^2 + \delta^2 \sin^2 \omega} \tag{4.93}$$

or:

$$A'B' = \sqrt{4(r-g)^2 + 4(r-g)\delta\cos\omega + \delta^2} \tag{4.94}$$

The new length of the fibre ℓ_{12} will be:

$$\ell_{12} = AB' = \sqrt{(A'B')^2 + h^2} \tag{4.95}$$

Substitution of A'B' from eq.(4.94) gives:

$$\ell_{12} = \sqrt{4(r-g)^2 + 4(r-g)\delta\cos\omega + \delta^2 + h^2} \tag{4.96}$$

Eq.(4.96) shows that, for a given shear stress τ causing the displacement δ, maximum fibre strain will occur when $\cos\omega=\pm1$. This is the case when the shear stress vector is parallel to the vertical plane defined by FBG1, producing maximum elongation (for $\omega=0$) or relaxation (for $\omega=\pi$) of the fibre, depending upon the direction of shear.

The length of the fibre ℓ_{12} can also be expressed as a function of the strain change $\Delta\varepsilon_1$ on the FBG1. Following exactly the same procedure as described in section 4.2.2.2, eq.(4.30) to eq.(4.33), we obtain:

$$\ell_{12} = \ell_{11}\left(1+\frac{\Delta\varepsilon_1}{1+\varepsilon_1}\right) \tag{4.97}$$

where ε_1 is the strain on the fibre under zero shear stress, which is set to 1250$\mu\varepsilon$ as explained in section 4.2.2.2. The strain change $\Delta\varepsilon_1$ is related to the measured Bragg wavelength shift by (eq.4.35):

$$\Delta\varepsilon_1 = \frac{\Delta\lambda_{B,1}}{0.8\lambda_{B,1}} \tag{4.98}$$

where $\lambda_{B,1}$ is the Bragg wavelength of the FBG1. Eq.(4.96), and eq.(4.97) give:

$$\ell_{11}^2\left(1+\frac{\Delta\lambda_{B,1}}{0.8(1+\varepsilon_1)\lambda_{B,1}}\right)^2 = 4(r-g)^2 + 4(r-g)\delta\cos\omega + \delta^2 + h^2 \tag{4.99}$$

Eq.(4.99) can be rewritten in the form of a second order equation with respect to the displacement δ:

$$\delta^2 + [4(r-g)\cos\omega]\delta + \left[4(r-g)^2 - \ell_{11}^2\left(1+\frac{\Delta\lambda_{B,1}}{0.8(1+\varepsilon_1)\lambda_{B,1}}\right)^2 + h^2\right] = 0 \tag{4.100}$$

Eq.(4.100) relates the unknown variables δ and ω with the measured Bragg wavelength shift $\Delta\lambda_{B,1}$.

An equation similar to eq.(4.100) can be obtained from FBG2 following the same procedure used for FBG1. The initial (pre-strained) length ℓ_{21} of the FBG2 will be:

$$\ell_{21} = \ell_{11} = \sqrt{4(r-g)^2 + h^2} \tag{4.101}$$

Referring to Fig.4.18, C' is the vertical projection of the immovable point C on the upper disk plane, and D' is the new position of point D after the application of shear stress. The length C'D' will be given by:

$$C'D' = \sqrt{(C'D + DK)^2 + KD'^2} \tag{4.102}$$

Eq.(4.102) finally gives:

$$C'D' = \sqrt{4(r-g)^2 + 4(r-g)\delta\cos(\phi-\omega) + \delta^2} \tag{4.103}$$

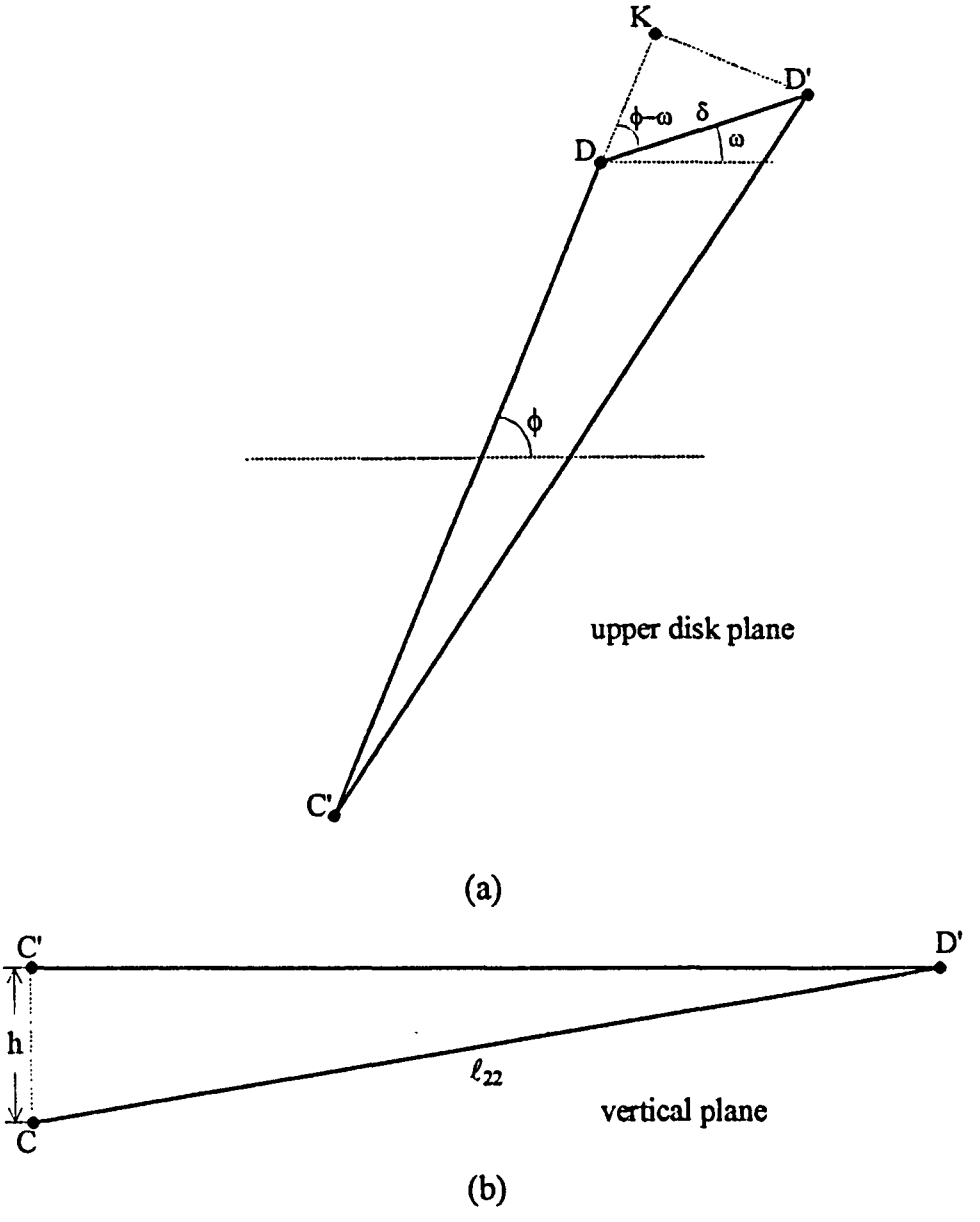

Fig.4.18: (a) Calculation of length C'D' on the upper disk plane, and (b) calculation of new fibre length ℓ_{22} of FBG2. The shear stress is applied at the direction DD'.

The new length ℓ_{22} of FBG2 is given by:

$$\ell_{22} = \sqrt{4(r-g)^2 + 4(r-g)\delta\cos(\phi-\omega) + \delta^2 + h^2} \tag{4.104}$$

It can also be expressed as a function of the strain change $\Delta\varepsilon_2$ on FBG2: If FBG2 is initially pre-strained by the same amount ε_1 as FBG1, then we can write:

$$\ell_{22} = \ell_{21}\left(1 + \frac{\Delta\varepsilon_2}{1+\varepsilon_1}\right) \tag{4.105}$$

The strain change $\Delta\varepsilon_2$ is given by:

$$\Delta\varepsilon_2 = \frac{\Delta\lambda_{B,2}}{0.8\lambda_{B,2}} \tag{4.106}$$

where $\lambda_{B,2}$ is the Bragg wavelength of the FBG2. Using eq.(4.104), eq.(4.105), and substituting $\Delta\varepsilon_2$ from eq.(4.106), we obtain a second order equation which relates δ and ω with the Bragg wavelength shift $\Delta\lambda_{B,2}$:

$$\delta^2+[4(r-g)\cos(\phi-\omega)]\delta+\left[4(r-g)^2-\ell_{21}^2\left(1+\frac{\Delta\lambda_{B,2}}{0.8(1+\varepsilon_1)\lambda_{B,2}}\right)^2+h^2\right]=0 \qquad (4.107)$$

Eq.(4.100) and eq.(4.107) can be used to calculate the upper disk displacement δ and the angle ω. Then, the magnitude of the applied shear stress can be calculated using eq.(4.50). The stress direction is given directly by the angle ω. The angle ω takes values in the range 0 to 2π, and the wavelength shift $\Delta\lambda_B$ in the range –0.82nm to +0.82nm, which corresponds to $\Delta\varepsilon$ in the range –1250 and +1250$\mu\varepsilon$ for a Bragg wavelength of 820nm, as calculated by eq.(4.35).

4.3 Experimental evaluation

It is already mentioned that the aim of this study was to design a shear stress sensor based on the reflected properties of fibre Bragg gratings, and to examine the feasibility of the adopted method. In the previous sections, the theoretical analysis of the sensor response to shear was presented, where we noticed that the measured Bragg wavelength shift is expected to vary linearly with the magnitude of the applied shear stress (section 4.2.2.5). We also examined theoretically the error introduced in shear stress measurement due to the simultaneous application of vertical stress, section 4.2.2.6. The theoretical analysis showed that it is possible to implement a shear sensor for in-shoe measurements, according to the specifications presented in section 2.3, based on the concept of the elastic deflection of a metallic structure. We also derived the two equations, eq.(4.86) and eq.(4.93), which relate the Bragg wavelength shift of two FBGs fitted into the sensor structure to the magnitude and direction of shear stress applied on the upper disk.

The next step in the sensor development was to examine experimentally the applicability of the proposed method, and the accuracy of the theoretical predictions. For that purpose, a sensor prototype had to be implemented according to the design specifications shown in Table 4.2, and the grating response to shear stress to be measured. The laboratory experiments where primarily focussed on the static response of the sensor to shear stress.

The main objectives of the laboratory experiments were:

1. The measurement of the maximum lateral displacement δ_{max} of the upper disk under maximum shear stress prior to fibre fitting. This measurement is necessary in order to avoid breakage of the FBG. Furthermore, measuring δ_{max} and comparing it with the theoretically

predicted value given by eq.(4.44), will provide a quantitative estimation of the deviation between the theoretical and the experimental results.

2. The experimental evaluation of the linear elastic deflection of the pins under shear load. It has been shown that the upper disk displacement varies linearly with the applied shear stress, eq.(4.43).
3. The examination of the plastic deformation of the structure under shear stress. In the theoretical design we had assumed that the pin deflection is purely elastic. Plastic deformation of the pins means that the upper disk will not return to its initial position after removing the shear stress, and the fibre will not restore its initial strain ε_i. Therefore, the sensor will give a non-zero reading even when no shear stress is applied. In addition to this zero state error, plastic deformation can deteriorate the sensor performance in terms of accuracy and repeatability, since it alters the structure behaviour to shear. The displacement of the upper disk, and hence the measured fibre strain, will not only depend on the current value of the applied shear, but also from the structure stiffness to shear, which in turn depends on the previous stress condition of the sensor. It is therefore important to measure the plastic deformation of the sensor, and make any necessary improvements to the sensor design in order to eliminate it.
4. The examination of the effect of vertical stress on the sensor response to shear. This was theoretically examined in section 4.2.2.6.
5. The experimental investigation of the insensitivity of the sensor structure to the direction of the applied shear stress. It is reminded that eq.(4.50), eq.(4.100), and (4.107) can be used to calculate the magnitude and direction of shear stress if only the pin deflection is independent of the direction of shear.
6. The examination of the FBG response to shear by measuring the Bragg wavelength shift with respect to shear stress. The theoretically predicted grating response to shear, at the direction parallel to the grating vertical plane is given in Fig.4.10.

The experimental setup has been presented in section 3.1.1. In the following sections we will concentrate on the results from the measurements. The experiments were divided into three parts. The first one describes the measurement of an enlarged structure made of steel pins and aluminium disks, presented in section 4.3.1. Then a same dimension sensor structure made by steel only was tested, and is presented in section 4.3.2. The results from the wavelength shift due to shear on the top disk from one FBG fitted into the structure will also be presented in that section. Finally, the results from measuring an actual dimension steel structure will be discussed in section 4.3.3.

4.3.1 Laboratory testing of metallic structure. Experiment 1: Enlarged structure with aluminium disks

It is clear from the analysis so far that the performance of the pins under shear and vertical load dominates the overall behaviour of the sensor structure, provided that the pins are firmly fixed on both disks. It is therefore important to test the pin deflection under several vertical and shear loading conditions. For that purpose, a sensor structure had to be made, following the design parameters presented in Table 4.2.

The first attempt on making the sensor in the departmental mechanical workshop was unsuccessful. The reason was that the equipment and tools were not appropriate for the construction of the small sensor structure. The main difficulty was the fitting of the pins on the 0.5mm thick disks. The pins were finally silver soldered to the disks, and the disks polished afterwards to remove the residue solder. It was also not possible to install the pins precisely parallel to each other and vertical to the disks. The result was that the sensor collapsed during the first trials. The reason for collapsing was that the pins were detached from the disks. The use of solder seemed to be inappropriate for pin fitting.

In order to solve the main fabrication problem faced on the small structure, i.e. the pin fitting, the fabrication procedure was simplified by increasing the disk diameter and thickness, leaving all the other sensor parameters unchanged and as given in Table 4.2. Because the disks are thicker, the pins can be inserted deeply into the disks and press-fitting techniques can be applied to firmly support the pins. Since the number of pins N, the pin material and diameter d, and the length h remain the same as required for the actual sensor[1], the pin deflection of this enlarged sensor will be equal to the pin deflection of the actual sensor, as predicted by eq.(4.43) for equal shear stress. The fact that the disk radius has been increased, does not affect the applied horizontal force, since, as we have already discussed in section 3.1.1, that force is not shear force due to friction on the top surface of the sensor, but acts on the side of the top disk.

The enlarged sensor was manufactured by a clock company, where more precise equipment could be used compared to our departmental workshop. The disk radius r and thickness t were 20mm and 5mm respectively. Both disks were made of aluminium, because it can be more easily processed compared to steel. The disks were drilled to approximately half the disk thickness, using a drill diameter equal to the pin diameter. The pins were then press-fitted into the holes, Fig.4.19. Stainless steel wire, 0.5mm diameter, was used for pins. Although the pin diameter is slightly larger compared to the theoretically estimated (0.4mm,

[1] The term "actual sensor" will be used next to describe the sensor structure with dimensions given by Table 4.2.

section 4.2.2.4), it was chosen because it was immediately available (standard size), and easier to process compared to thinner wires. The enlarged aluminium sensor structure is shown in pictures 7 and 8, appendix II.

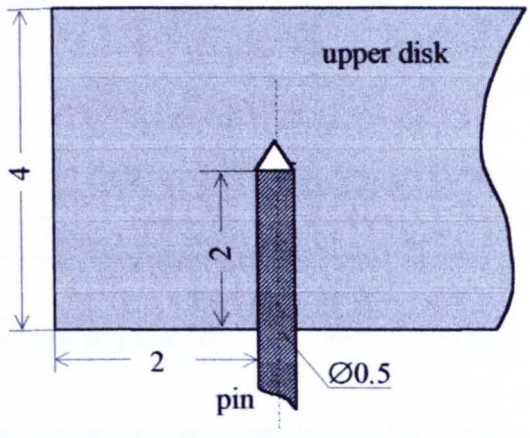

Fig.4.19: Pin installation in the enlarged aluminium structure.

4.3.1.1. Time response

The sensor structure was tested using the setup described in section 3.1.1. The E/M vibrator was driven by square pulses. The pulse amplitude was varied in order to achieve the desired shear stress.

Typical time response of the system for a pulse frequency of approximately 0.5Hz is given in Fig.4.20. The time response for input force frequency of approximately 1Hz is shown in Fig.4.21. Only the top plate assembly was placed over the sensor, which corresponds to 90kPa vertical stress on the actual sensor, as given by eq.(3.2) for m_v=0.768kg.

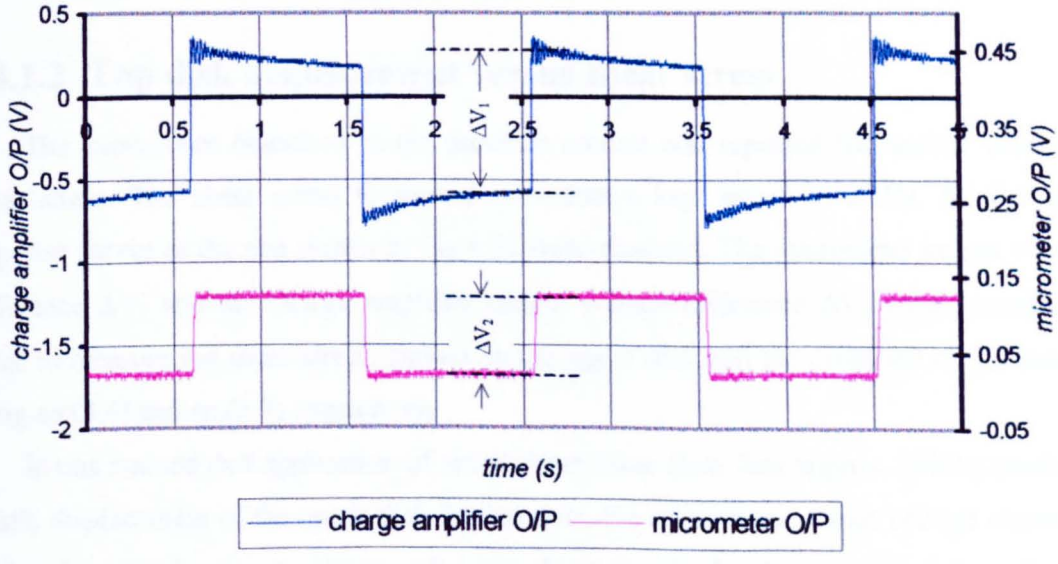

Fig.4.20: Time response of the system for input force pulses at ~0.5Hz.

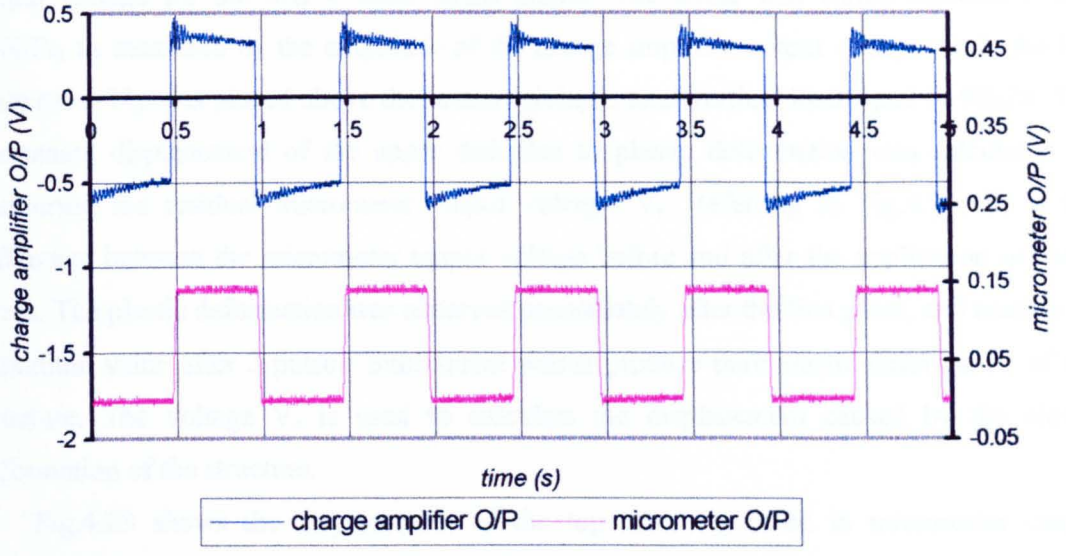

Fig.4.21: Time response of the system for input force pulses at ~1Hz.

It can be noticed that the shape of the charge amplifier output voltage is not square, as would be expected. The reason for this is the tendency of the charge amplifier output to return to zero when constant load is applied on the piezo-electric sensor. Examining the same curve, we notice that small amplitude vibrations appear immediately after each transient, which are more obvious after the raising phase. The vibrations disappear after approximately 0.2sec, when their amplitude falls below the noise level of the force readout system.

The charge amplifier voltage changes by ~850mV every loading and unloading of shear stress, which corresponds to change of shear stress from 0 to ~55kPa (eq.3.4). The measured upper disk displacement is ~9 microns, as given by eq.(3.7) for micrometer output voltage change of ~90mV. The existence of vibrations on the top disk arrangement due to shear stress transients cannot be verified with the micrometer, since their frequencies are above the dynamic range of the micrometer readout system (section 3.4).

4.3.1.2. Top disk displacement versus shear stress

The experiment described in the previous section was repeated for several values of shear stress. The shear stress frequency was always kept equal to 0.5Hz. Similar time response curves as the one shown in Fig.4.20 were obtained. The micrometer output voltage difference ΔV_1 and the charge amplifier output voltage difference ΔV_2 were recorded in order to measure the shear stress applied on the upper disk and the produced displacement, using eq.(3.4) and eq.(3.7) respectively.

It was noticed that application of small shear stress (less than approx. 20kPa) produces elastic displacement of the upper disk. In that case, the micrometer output voltage returns to its initial value (the output voltage under zero shear stress) after the removal of shear. Larger stresses on the other hand produce plastic deformation of the structure. The upper disk does not return to its initial position after the removal of shear. Fig.4.22 shows the micrometer

output voltage for the first 4 shear stress pulses. The stress was varied between 0 and 100kPa, as measured by the amplitude of the charge amplifier output voltage. Only the top plate assembly was placed above the sensor, giving a total vertical load equal to 90kPa. The permanent displacement of the upper disk due to plastic deformation was calculated by measuring the residual micrometer output voltage, V_r. Referring to Fig.4.22, V_r is the difference between the micrometer output voltage before and after the application of shear stress. The plastic deformation was observed immediately after the first pulse, and reaches its maximum value after 3 pulses. Subsequent pulses produce pure elastic deformation of the structure. The voltage V_e is used to calculate the displacement caused by the elastic deformation of the structure.

Fig.4.23 shows the displacement of the top disc, expressed in micrometer output voltage, for variable shear stress. The vertical stress was constant and equal to 90kPa. The shear stress was gradually increased on each pulse from 25kPa to 112kPa, as given by eq.(3.4) for ΔV_1=0.4V and ΔV_1=1.75V respectively. The residual displacement increases from 0 to 4.2μm (for V_r=42mV).

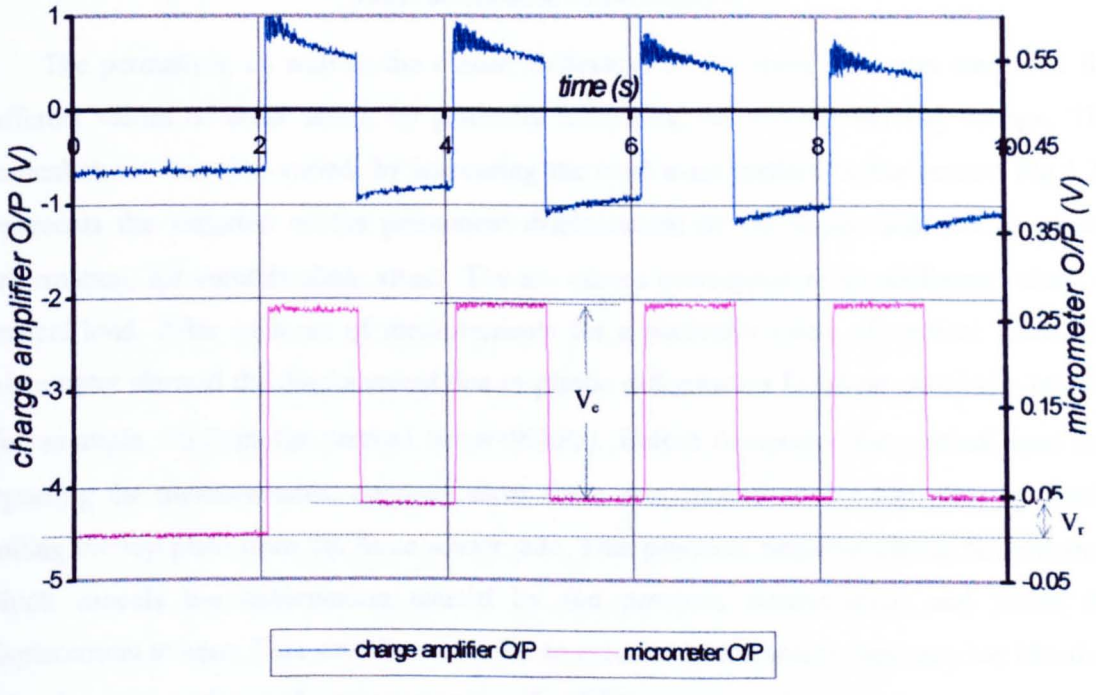

Fig.4.22: Time response of the enlarged aluminium structure under constant shear stress (100kPa), showing the residual displacement after the first and the subsequent shear stress pulses.

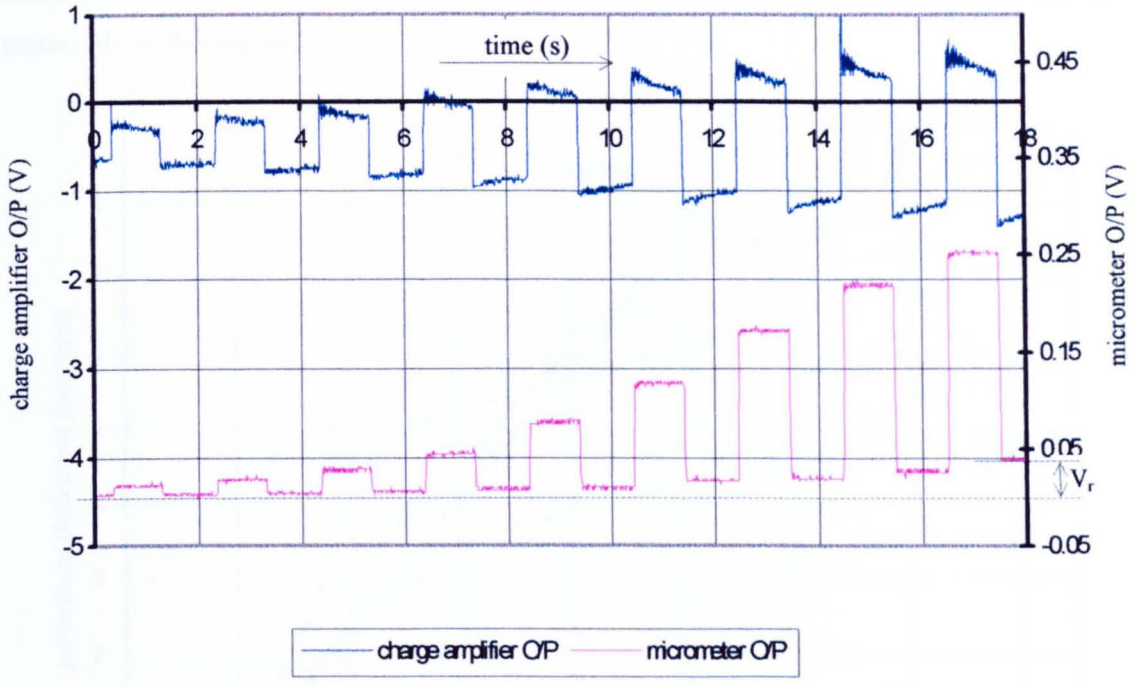

Fig.4.23: Time response of the enlarged aluminium structure under gradually increasing shear stress. The residual displacement after removing shear, which corresponds to the voltage V_r, reveals the plastic deformation of the structure.

The permanent, as well as the elastic, deflection of the upper disk was measured for different values of shear stress, by gradually increasing the vibrator driving voltage. The vertical stress was also varied, by increasing the total mass applied to the sensor. Fig.4.24 represents the variation of the permanent displacement of the upper disk due to plastic deformation, for variable shear stress. The six curves correspond to six different values of vertical load. After each set of measurements for a particular value of vertical stress, the micrometer showed the displacement due to plastic deformation for shear equal to ~160kPa (for example, +5.3μm for vertical stress=90kPa). Before increasing the vertical load and repeating the measurements, opposite shear force was applied on the top plate by gently pulling the top plate from the force sensor side. This produces negative plastic deformation, which cancels the deformation caused by the previous measurement and resets the displacement to zero. This was done in order to ensure that the sensor structure has identical shape between each set of measurements under different vertical load. To prevent accidental damage of the sensor, the maximum value of shear stress was limited to approximately 160kPa and the vertical stress to 253kPa. The performance of the aluminium sensor structure was therefore tested for half the operating range of the vertical stress, and more than half the range of shear stress.

The graph shows that plastic deformation is significantly affected not only by the shear, but also by the vertical stress. For shear stress between 20 and 80kPa the deformation rapidly increases with average slope 0.08μm/kPa (slope 1). No conclusion can be derived for the

effect of vertical load for this range of shear stress, since the measurements are not repeatable in this region.

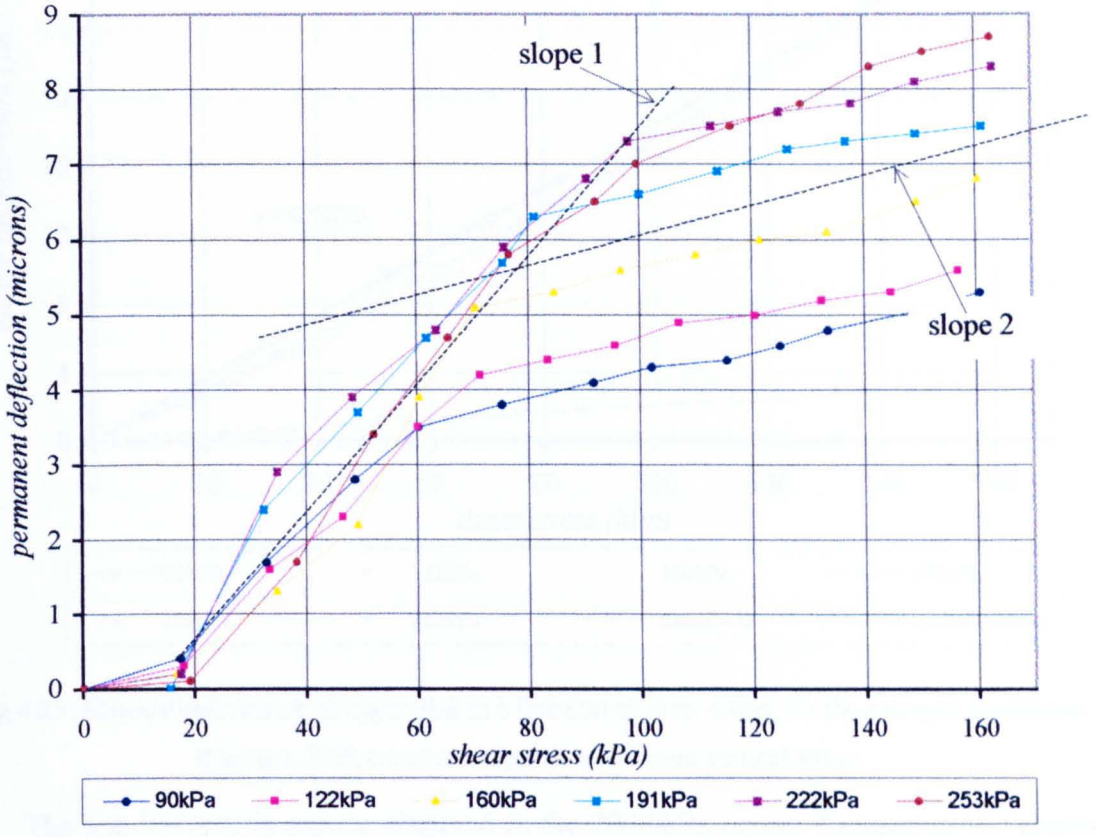

Fig.4.24: Permanent deflection of upper disk after removal of shear, as a function of shear stress. Each curve corresponds to a different vertical stress.

For larger values of shear (above 80kPa), the plastic deformation increases as the vertical stress increases. The average slope in this region is 0.01μm/kPa (slope 2).

Using the measured elastic displacement of the upper disk, which corresponds to the voltage V_e, we can draw the graph of the variation of the elastic displacement with respect to the magnitude of the applied shear stress, Fig.4.25. The deviation of the response curves from the linear trendline is noticeable. The trendline is based on the 160kPa vertical stress curve, which better approximates the average response with respect to vertical stress. The non-linear response, as well as the presence of vertical stress, will result in error in calculating the applied shear stress, for a given displacement. Using the experimental data, the maximum error in calculating shear stress, assuming linear displacement, occurs for a displacement of 5μm and is equal to approximately 30%. This error is significantly reduced as the shear stress is increased. The variation of the vertical stress from 90 to 160kPa also produces average change of the measured displacement by approximately 10%.

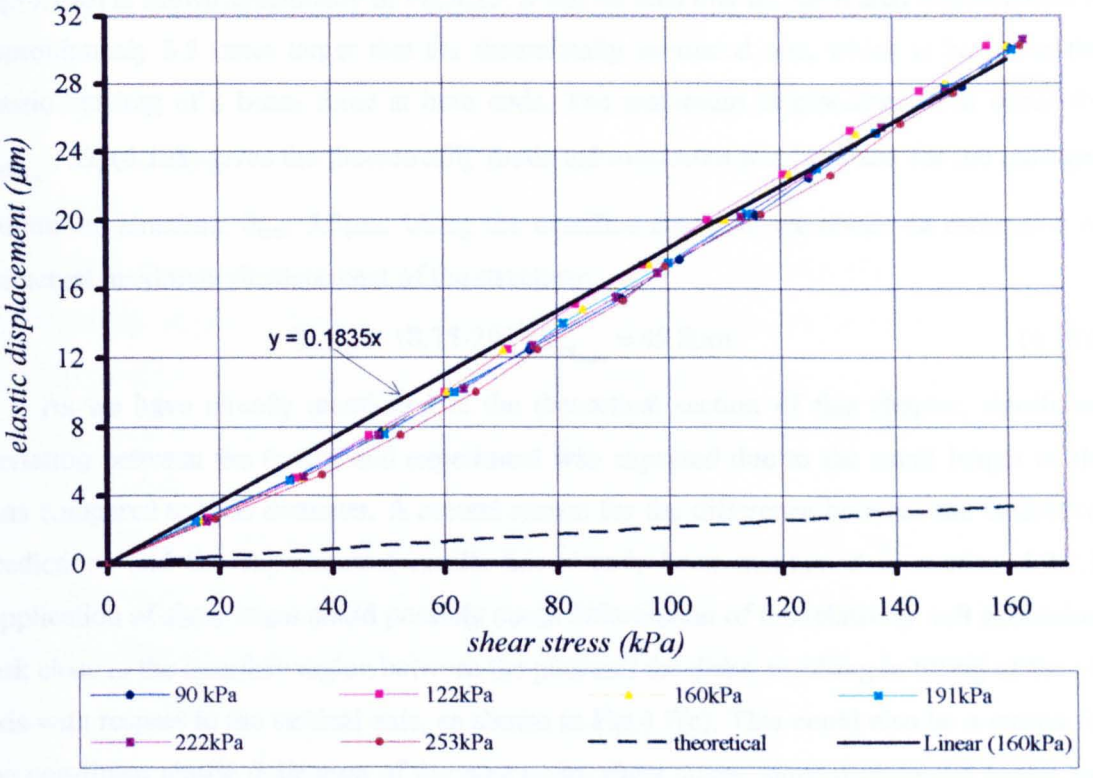

Fig.4.25: Elastic displacement of upper disk as a function of shear stress, for the enlarged aluminium structure. Each curve corresponds to different vertical stress.

The non-linearity is mainly observed in the 20-80kPa region. Comparing the graphs shown in Fig.4.24 and Fig.4.25, it is clear that the non-linearity is stronger in the shear stress region where the plastic deformation is rapidly increasing.

It has already been mentioned that one of the main objectives of the experiments was to measure the maximum displacement of the upper disk, for the maximum expected magnitude of shear stress. Assuming that the pins are firmly supported in the aluminium disks at both ends, the pin deflection will be given by eq.(4.43). Substitution of E, N, h, and r from the values given in Table 4.2, as well as the pin diameter d=0.5mm, gives the theoretical prediction of the upper disk displacement:

$$\delta = 2.13 \cdot 10^{-11} \tau_{yx} \qquad (4.108)$$

Eq.(4.108) is shown graphically in Fig.4.25. It can be seen that the measured displacement is approximately 8.5 times larger that the theoretically estimated one, which is based on the elastic bending of a beam fixed at both ends. The maximum displacement will occur for $\tau_{yx_{max}}$. Eq.(4.108) gives the theoretically predicted maximum displacement for the enlarged aluminium structure, δ_{max}=5.3μm. Using the trendline equation, we obtain an estimation of the actual maximum displacement of the structure:

$$\delta_{max,a} = 18.35 \cdot 10^{-11} \tau_{yx_{max}} = 45.8\mu m \qquad (4.109)$$

As we have already mentioned in the theoretical section of this chapter, significant deviation between the theory and experiment was expected due to the small length of the pins compared to their diameter. A second reason for the difference between the theoretical predictions and the experimental results has already been mentioned in section 4.2.2.1. Application of shear stress could possibly cause deformation of the relatively soft aluminium disk close to the interface region between the pins and the disks, resulting in tilting of the pin axis with respect to the vertical axis, as shown in Fig.4.7(c). This could also be a reason for the non-linear elastic deflection of the pins under shear stress, since it alters the forces and moments acting on the ends of each pin, and hence the pin deflection.

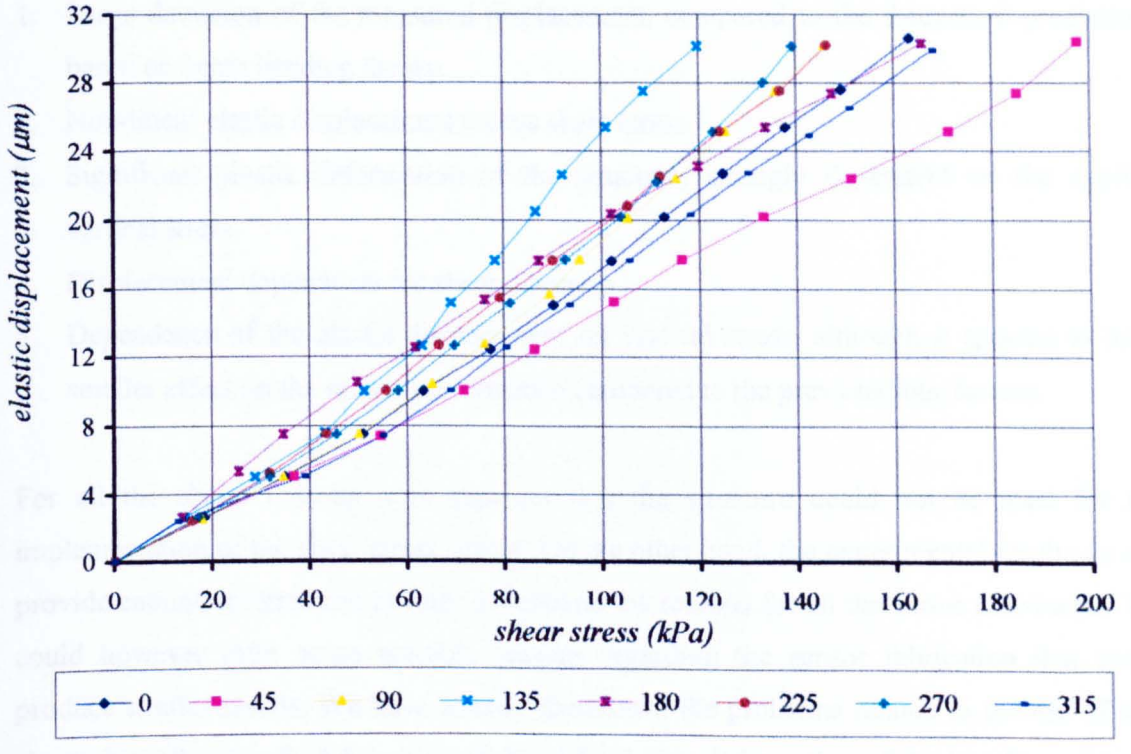

Fig.4.26: Elastic displacement of upper disk as a function of shear stress, for the enlarged aluminium sensor. Each curve corresponds to different direction of shear.

The experiments described so far show the performance of the sensor structure for unidirectional stress. Since the sensor will be used for two-dimensional sensing, it is

necessary to test the pin deflection for different directions of shear. The measurements can be done using the same setup (section 3.1.1). Measurements under different directions can be taken by rotating the sensor to the desired direction. Fig.4.26 shows the variation of the elastic deformation of the structure with respect to shear stress, for different directions of shear. Every curve is obtained by sequentially rotating the sensor by 45°. The direction 0° is assigned to the orientation of the sensor during the previous experiments regarding the unidirectional response. The vertical stress was 90kPa throughout the experiment. In order to prevent damage of the sensor structure, and based on the experience gained from the previous tests, the shear stress was increased up to the point were the elastic displacement does not exceed ~30μm.

The graph shows great dependence of the displacement with shear direction. The average gradient of the curves varies from 0.23μm/kPa at 135°, to 0.15μm/kPa at 45°. A closer examination of the curves shows significant variation of the shape compared to each other.

The results of the experiments regarding the enlarged aluminium sensor clearly shows the drawbacks of this sensor design, which are summarised below:

1. Large deviation of the measured displacement, compared to the theoretical predictions based on beam bending theory.
2. Non-linear elastic displacement versus shear stress.
3. Significant plastic deformation of the structure, strongly dependent on the applied vertical stress.
4. Displacement depends on the shear direction.
5. Dependence of the elastic displacement on vertical stress, although it appears to have smaller effect on the sensor performance compared to the previous four factors.

For all the above reasons it is apparent that the structure could not be used for the implementation of the shear stress sensor. On the other hand, the experimental results do not provide enough information to fully understand the reasons for all the above drawbacks. We could however infer some possible reasons regarding the sensor fabrication that could produce similar results. We have already mentioned the problems related to the use of soft aluminium alloy for the fabrication of the disks. Large deformation of the interface with the pins region could result in large upper disk displacement and perhaps lead to plastic deformation. Wrong theoretical estimation of the pin diameter, on the other hand, could lead to similar results, where in that case the plastic deformation and the large displacement could be due to the pin deformation only.

Imperfections of the structure fabrication is another possible source of problems. Inaccuracy of the hole diameter as well as the variation of the pin depth inside the disks

(Fig.4.19) could affect the strength of the pin-disk joint. It is also important that the four pins of the structure are accurately aligned to be parallel to each other, with their axis perpendicular to the disk surfaces. Any misalignment of a hole on the lower disk with respect to the opposite hole on the upper disk will result in tilting of the pin axis with respect to the vertical axis. Residual bending moments could also appear on the pin after the press fitting procedure, due to this misalignment. It is also important that the upper disk is positioned precisely horizontally. This assures that the vertical stress is equally transferred on the pins, as assumed during the theoretical design.

All those problems related to fabrication imperfections could affect the sensor response to shear in both cases of unidirectional and multidirectional shear stress. In order to clearly identify the source of the plastic deformation, non-linearity, and dependence to shear direction, a second sensor structure was made and tested. The alterations on its design and fabrication, as well as the experimental results are discussed in the following section.

4.3.2 Laboratory testing of metallic structure. Experiment 2: Enlarged structure with steel disks

The main considerations when designing the new sensor structure were i) to increase the strength and stiffness of the pin-disk joint, and ii) to improve the alignment of the pins and disks. The pin material, as well as all the dimensions of the structure, remained identical to those of the enlarged aluminium sensor (40mm diameter, 10mm thick). The results obtained from the new sensor could then be directly compared with the results of the aluminium structure.

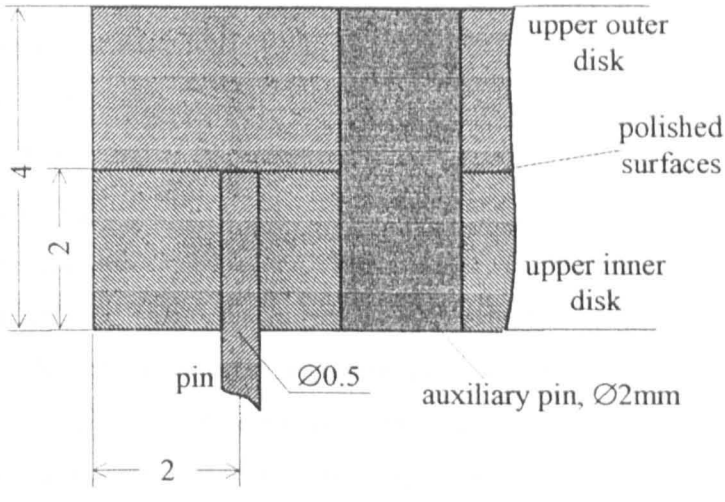

Fig.4.27: Pin installation in the enlarged steel structure.

The stiffness of the joints could be increased by fabricating the disks from steel instead of the softer aluminium. The pins were press-fitted into the disks as shown in Fig.4.27. Each of the two 4mm thick sensor disks consists of two separate steel disks of equal thickness.

The two inner disks were drilled right through, and the pins were press-fitted. The two disks (outer and inner disks) were then held together by auxiliary steel pins (4 pins per disk), which were also press-fitted. The enlarged steel sensor structure is shown in pictures 7 and 8, appendix II.

The main advantage of this pin installation procedure is that both inner disks can be manipulated as a single disk and drilled accurately. This assures that the pin holes are precisely aligned and hence no tilting or bending of the pins are expected to occur during pin fitting. It is also apparent that the pin penetration is the same for all joints, and equal to the thickness of the inner disk.

The sensor was measured using the same experimental setup which was used to test the aluminium structure, section 3.1.1.

4.3.2.1. Experimental testing of steel structure

Fig.4.28 shows the elastic displacement as a function of shear stress, for different values of vertical stress. Comparing the response of the steel sensor with the response of the enlarged aluminium sensor shown in Fig.4.25, we can see that the stiffness of the structure to shear stress has been increased by a factor of 2. The measured maximum elastic displacement, for shear stress equal to 250kPa, is approximately 24μm compared to 45.8μm for the aluminium structure (eq.4.109). It is noticed that the shear stress was increased up to $\tau_{yx_{max}}$ without the risk of over-deflecting the pins and damage the structure.

The vertical stress seems to have a similar effect on the shear response for the steel sensor, compared to the aluminium one. The average error in estimating shear stress due to vertical stress variation, is less than 10% for any value of disk displacement.

The displacement versus shear stress curves are closer to linear compared to the aluminium sensor. However, non-linearity still exists, giving a maximum error of approximately ±10% from the average linear approximation.

The theoretical response, eq.(4.108), is also plotted on Fig.4.28. The average measured displacement of the upper disk is still larger than the theoretical prediction by a factor of 4. If we assume that the pin-disk joints are perfect, which means that the two ends of each pin are firmly fixed, then the relatively large deviation from the theoretical prediction should be caused by the inaccuracy of the theoretical model based on the beam bending theory. This assumption is strongly supported by the experimental measurement of the plastic deformation of the structure, which was measured as less than 1μm for the maximum shear and vertical loading condition. For shear stress up to 160kPa (equal to the maximum shear stress applied on the aluminium sensor, Fig.4.24), the residual displacement due to plastic deformation was measured to be less than the resolution of the micrometer (0.1μm).

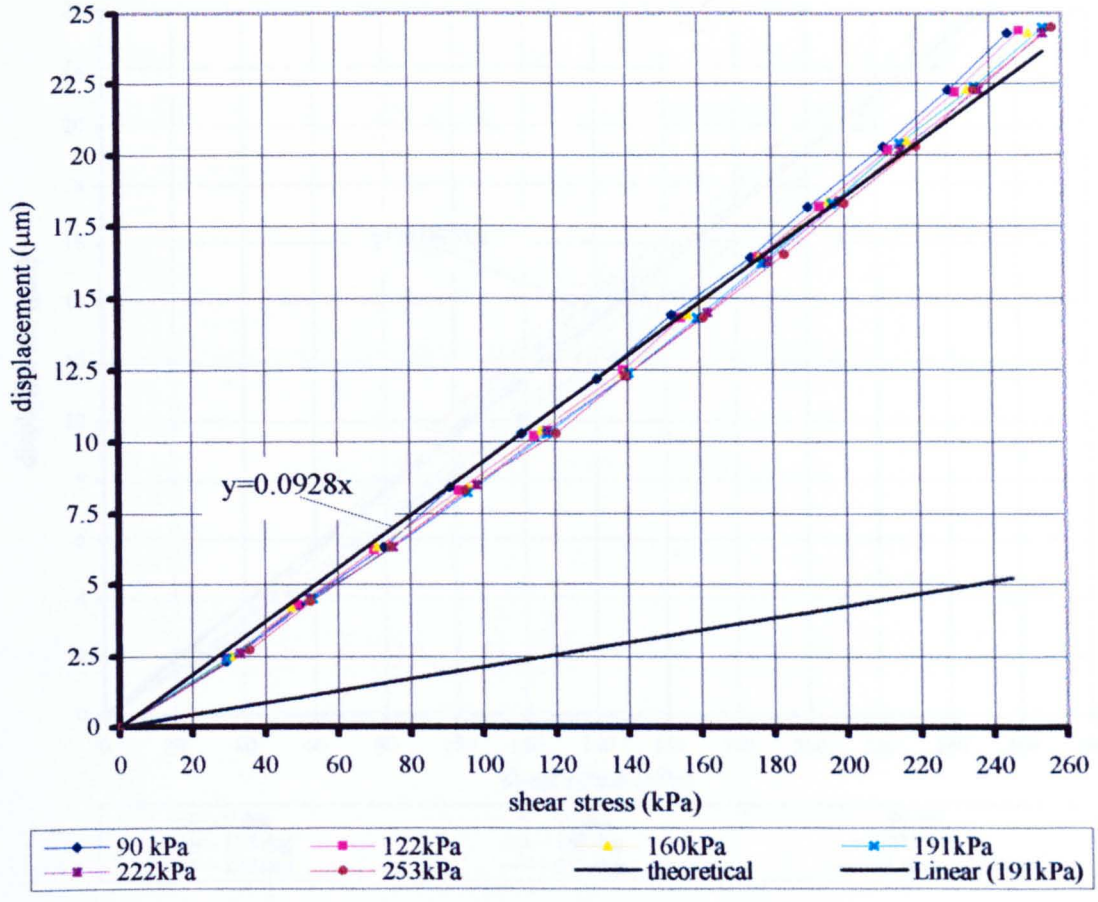

Fig.4.28: Elastic displacement of upper disk as a function of shear stress, for the enlarged steel structure. Each curve corresponds to different vertical stress.

Fig.4.29 shows the response of the steel structure to shear stress, for different directions of shear. The reference direction corresponds to the one that gave the results shown in Fig.4.28. Comparing this graph with the graph shown in Fig.4.26, it is clear that the steel structure is improved compared to the aluminium one, in terms of structural symmetry to the direction of shear. However, the response is still highly sensitive to shear direction. The average error in measuring shear stress due to the change of shear direction is approximately ±15% with respect to the average linear approximation.

Summarising the results from the experiments for measuring the disk displacement on the enlarged sensor structures, we can say that the upper disk displacement is highly dependent on the pin alignment and fitting. Non-linear response is presented in both structures. One reason that increases non-linearity is the fact that the displacement observed in both structures was several times larger than that required for the operation of a FBG in its entire strain range given by (eq.4.48). It is reminded that, the deflection of the free end of a beam due to bending, is a linear function of the applied shear force for small deflections only (Timoshenko and Gere, 1973, pg.203).

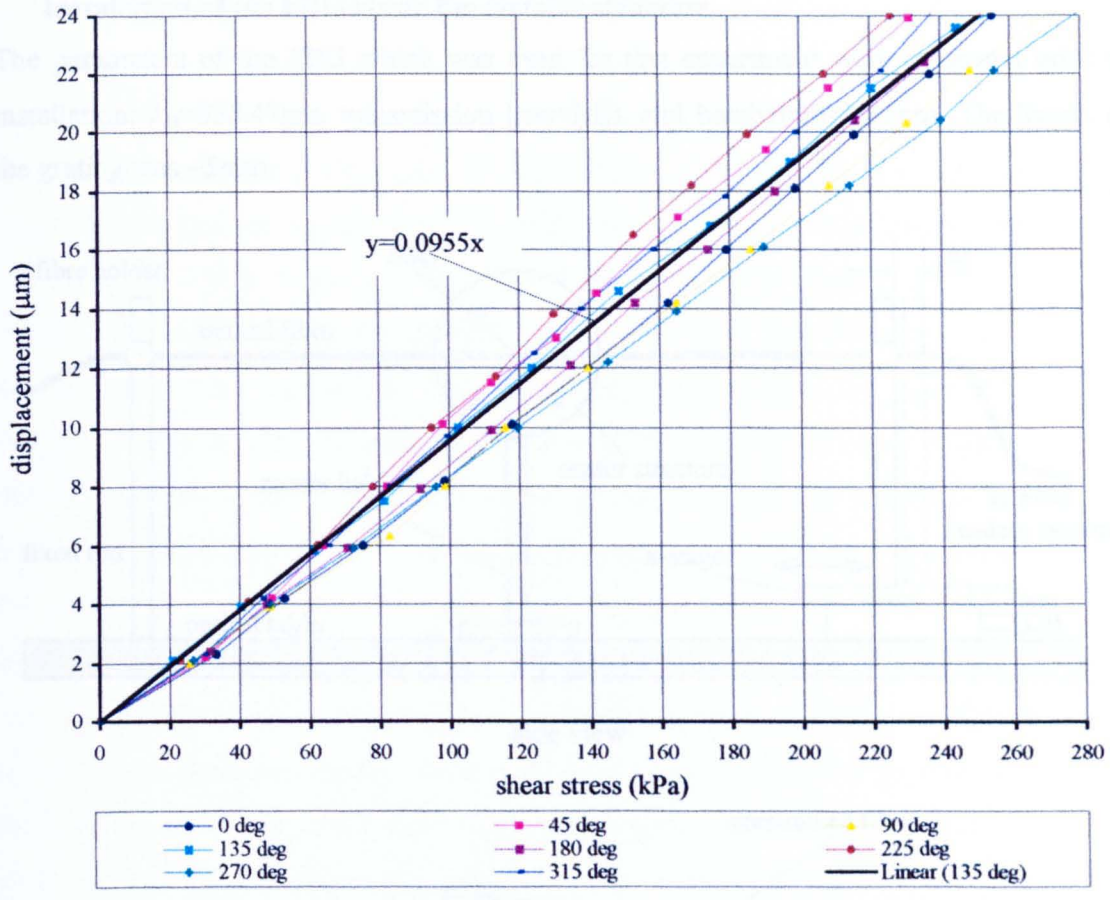

Fig.4.29: Elastic displacement of upper disk as a function of shear stress, for the enlarged steel sensor. Each curve corresponds to different direction of shear.

It is remarkable that, even though the pin installation of the steel structure was promising, the structure exhibits sensitivity to shear direction. Reasons for that can be the limited precision of the workshop equipment for drilling, pin alignment, and fitting, as well as anisotropy of the pin and disk materials.

4.3.2.2. Bragg grating response to unidirectional shear

The steel structure measured previously was used to fabricate the first enlarged version of the metallic sensor. Even though the structure is sensitive to shear direction, we could still use this structure to get the first experimental testing of the sensor performance. For this purpose, the installation of only one FBG would be sufficient to observe the Bragg wavelength shift due to disk displacement.

The aims of this experiment are:

1. The experimental evaluation of the linear relation between the upper disk displacement δ and the Bragg wavelength shift $\Delta\lambda_B$, as predicted theoretically in section 4.2.2.5.
2. The testing of the effectiveness of the glue bond between the fibre and the disks.

Installation of the FBG inside the metallic structure

The parameters of the FBG which was used for this experiment were measured prior to installation: λ_B=836.47nm, transmission loss=3dB, and bandwidth=0.45nm. The length of the grating was ~5mm.

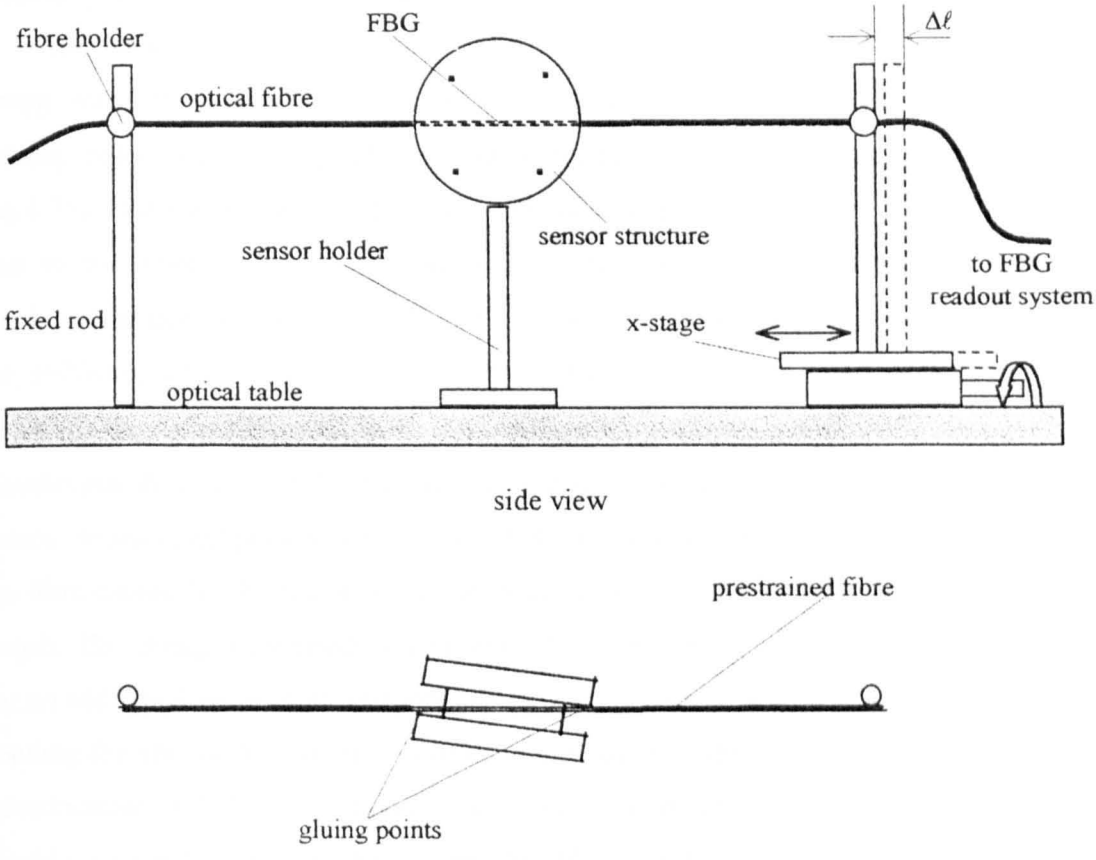

Fig.4.30: Prestraining and attachment of the FBG in the sensor structure (dimensions out of scale).

Fig.4.30 shows the apparatus used to prestrain the fibre up to the desired strain (+1250με) before gluing it on the metallic sensor body. The plastic coating of the fibre was removed at a distance approximately ±20mm[1] from the centre of the grating (equal to the diameter of the sensor), and cleaned with methanol. The fibre was passed through the sensor body without touching it, so that the FBG is located in the middle of the sensor body, and then mounted on two rods. The left one was permanently fixed on the optical table, and the right on an x-stage, which allows the fibre to be prestrained. The mounting of the fibre on the rods was done using plastic screws, which prevent fibre breakage. The fibre was connected to the FBG readout system to monitor the Bragg wavelength, and hence the strain on the fibre. The fibre was strained until the Bragg wavelength increased by ~0.85nm, which corresponds to

[1] Due to flow of the liquid fibre stripper (OF-Stripper 10), the fibre was finally stripped at approximately ±21mm.

+1250με. The height of the sensor holder was adjusted until the strained fibre reaches the sensor diameter. The sensor holder was then carefully rotated so that the fibre just touches the two disks, as shown in Fig.4.30, top view. Observation of the sensor alignment with a stereoscope is essential at this stage. The fibre was glued on the two disks by dropping the cyanoacrylate glue[1] on a needle and then gently touching the fibre at the contact points.

The sensor was cured for 16h to ensure that the glue was hardened completely. The Bragg wavelength reduced by ~0.06nm immediately after releasing the fibre from the holding poles. This corresponds to strain reduction on the fibre by approximately 90με (eq.4.35). One reason for the reduction of the axial strain is the deflection of the upper disk due to the fibre tension, as discussed in section 4.2.2.7. The theoretically predicted displacement due to tension T=1.1N (for ε_l=1250με), can be calculated by solving eq.(4.89) for r=20mm, g=3mm, and d=0.5mm. The other parameters are as in section 4.2.2.7. Eq.(4.89) then gives δ'= –0.25μm. This corresponds to $\Delta\varepsilon$= –8με (eq.4.37), and to Bragg wavelength shift $\Delta\lambda_B$= –0.006nm, which is much less than the observed shift. A second reason, which could possibly explain the additional wavelength shift is the strain reduction in the fibre caused by the elastic deformation of the glue, which causes reduction of the fibre length. The Bragg wavelength was monitored for several minutes after releasing the fibre, but no additional wavelength shift was measured. The acrylic glue is therefore acceptable for bonding the fibre to the metallic structure. The Young's modulus of the glue, according to the manufacturer, is 2-4GPa. The use of a higher E modulus material for bonding the fibre would reduce the strain relaxation of the fibre. However, because the cyano-acrylate glue can be easily removed using de-bonding agents[2], hence releasing the FBG which can then be re-used, the experiments were continued using the same glue.

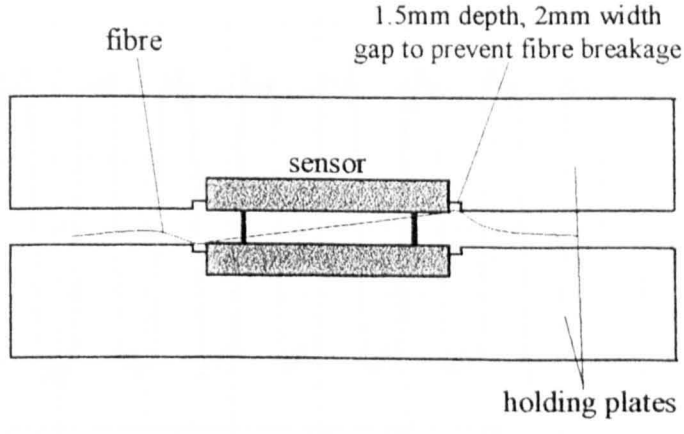

Fig.4.31: Placement of the metallic sensor into the testing apparatus, after modifying the aluminium holding plates to form a gap around the sensor to prevent fibre breakage.

[1] LOCTITE super glue

[2] RS 159-4039 cyanoacrylate debonder

Experimental evaluation of the grating response to shear stress

The sensor was tested using the setup explained in section 3.1.1. The only modification was the milling of a groove on each holding plate, each 44mm in diameter and 1.5mm deep, as shown in Fig.4.31. The groove was necessary to prevent excessive bending of the fibre at the point where it exits the sensor as a result of the presence of the top plate. The fibre is more likely to brake accidentally in the region close to the glue, because there is no coating on the fibre, and any bending moments on the fibre are maximised. This can be shown by considering the fibre as a cantilever beam and applying eq.(4.6) for y=0. Generally, the sensor requires very careful handling after the installation of the grating.

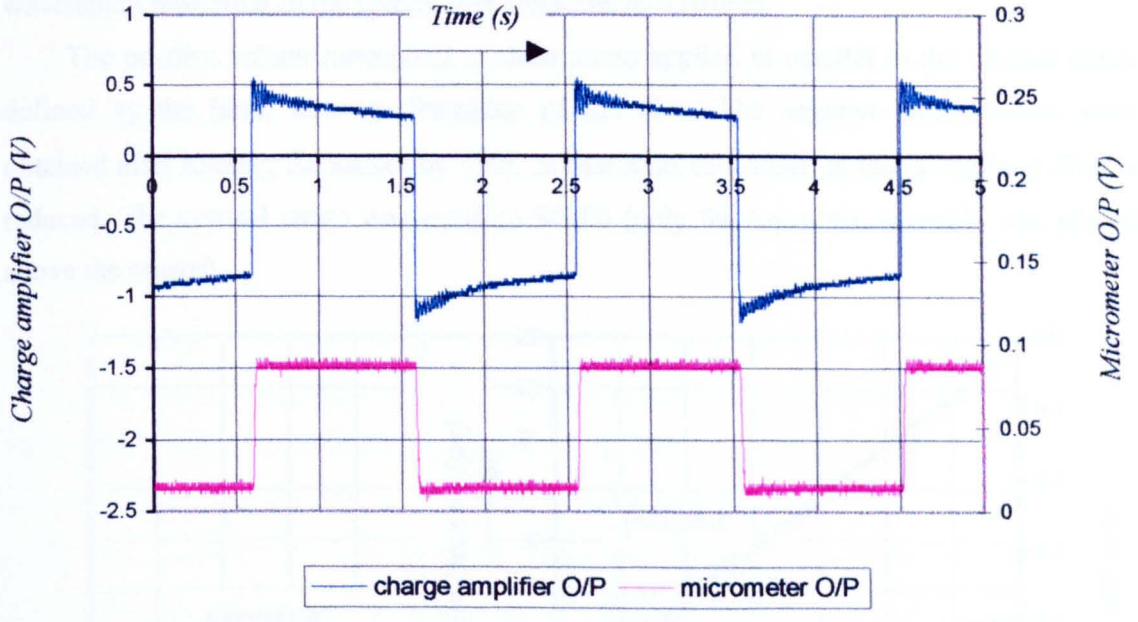

Fig.4.32: Typical time response of the enlarged metallic sensor, for ~0.5Hz, 80kPa shear stress pulses, as measured by the oscilloscope.

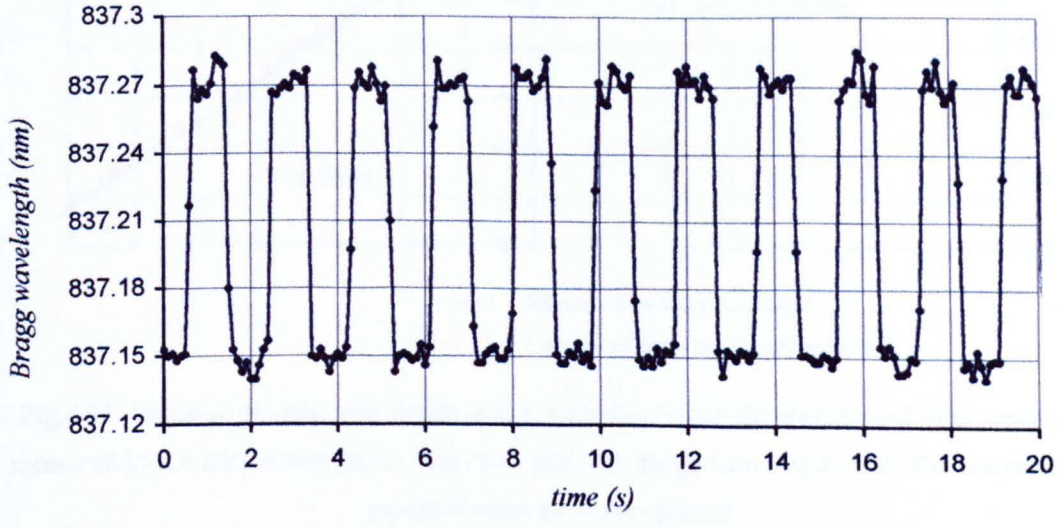

Fig.4.33: Time response of the FBG in the enlarged metallic sensor, for ~0.5Hz, 80kPa shear stress pulses, acquired at 12scans/sec.

The graph in Fig.4.32 shows the micrometer and charge amplifier output voltage, as these were simultaneously measured by the oscilloscope. Fig.4.33 shows the corresponding wavelength shift, as this is measured by the FBG readout system. The oscilloscope and the computer were not synchronised, therefore the time reference and scale are not comparable.

The amplitude of shear stress pulses was increased which in turn increased the displasement of the upper disk. For every 1μm increase in displacement, the readings of the micrometer, the force transducer, and the wavelength shift were recorded, giving the data points that are graphically presented in Fig.4.34. The micrometer voltage is transformed to microns using eq.(3.7), and the wavelength shift to displacement using eq.(4.36). The wavelength resolution of the system was measured as 0.016nm.

The positive values correspond to shear stress applied in parallel to the vertical plane defined by the fibre, causing elongation of the fibre. The negative stress values were obtained after rotating the sensor by 180°. In that case, the stress on the prestrained fibre is reduced. The vertical stress was equal to 90kPa (only the top plate assembly was placed above the sensor).

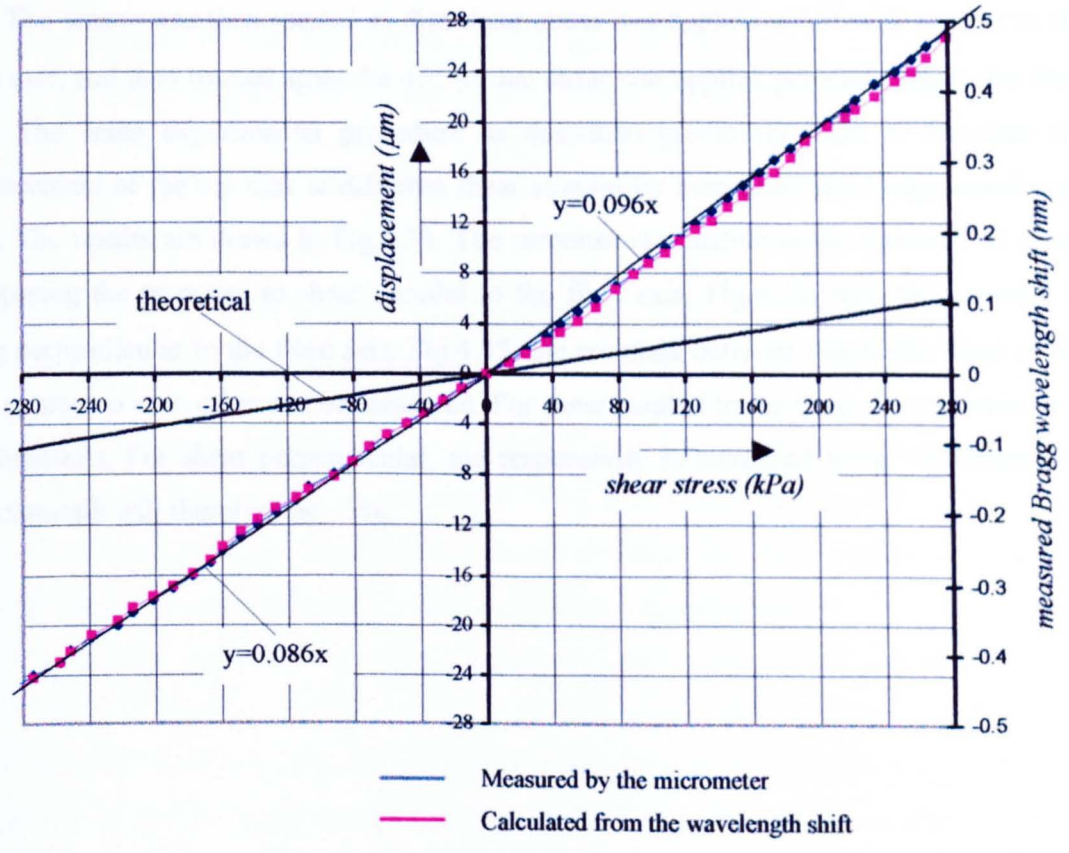

Fig.4.34: Variation of upper disk displacement with shear stress for the enlarged steel sensor, as measured by the micrometer and as calculated from the Bragg wavelength shift. The theoretically expected response is also plotted.

All the measurements were taken at 23°C, without any particular means of stabilising the temperature of the sensor. The whole experiment lasted approximately 1h. No temperature change was observed during the measuremetns.

The displacement, as measured by the micrometer, is in good agreement with the displacement calculated by the Bragg wavelength shift, especially for negative values of shear, which produce relaxation of the fibre. For positive shear stresses, the wavelength shift gives an underestimation of the displacement for a given shear stress. A possible reason is that the additional stress on the fibre produces elastic deformation of the glue, which must be added to the elongation of the fibre in order to calculate the actual displacement of the upper disk. The theoretical model presented in section 4.2.2.2 assumes that the fibre is firmly fixed on the disks, therefore no relative movement of the fibre with respect to the disks was considered when deriving eq.(4.36).

The average slopes of the linear approximation are 0.096μm/kPa and 0.086μm/kPa for positive and negative stress respectively. The small difference was expected, mainly due to the asymmetrical response of the metallic structure to shear direction (Fig.4.29). Furthermore, the sensor was manually rotated at 180°, which introduces uncertainty to the angle of rotation and hence to the direction of shear stress when measuring the negative values.

The sensor was then rotated so that shear stress was applied at 45° with respect to the fibre axis, and then rotated again for 45° so that shear was applied perpendicular to the fibre axis. The same experimental procedure as described previously used to calculate the displacement of the top disk at different shear stresses by measuring the Bragg wavelength shift. The results are drawn in Fig.4.35. The response is sensitive to the direction of shear. Comparing the response to shear parallel to the fibre axis, Fig.4.34, with the response to shear perpendicular to the fibre axis, Fig.4.35, the crosstalk between two FBGs fitted at 90° with respect to each other can be measured. For shear parallel to the fibre, the responsivity is 0.096nm/kPa. For shear perpendicular, the responsivity is measured to be ~0.005nm/kPa. The crosstalk will therefore be ~5%.

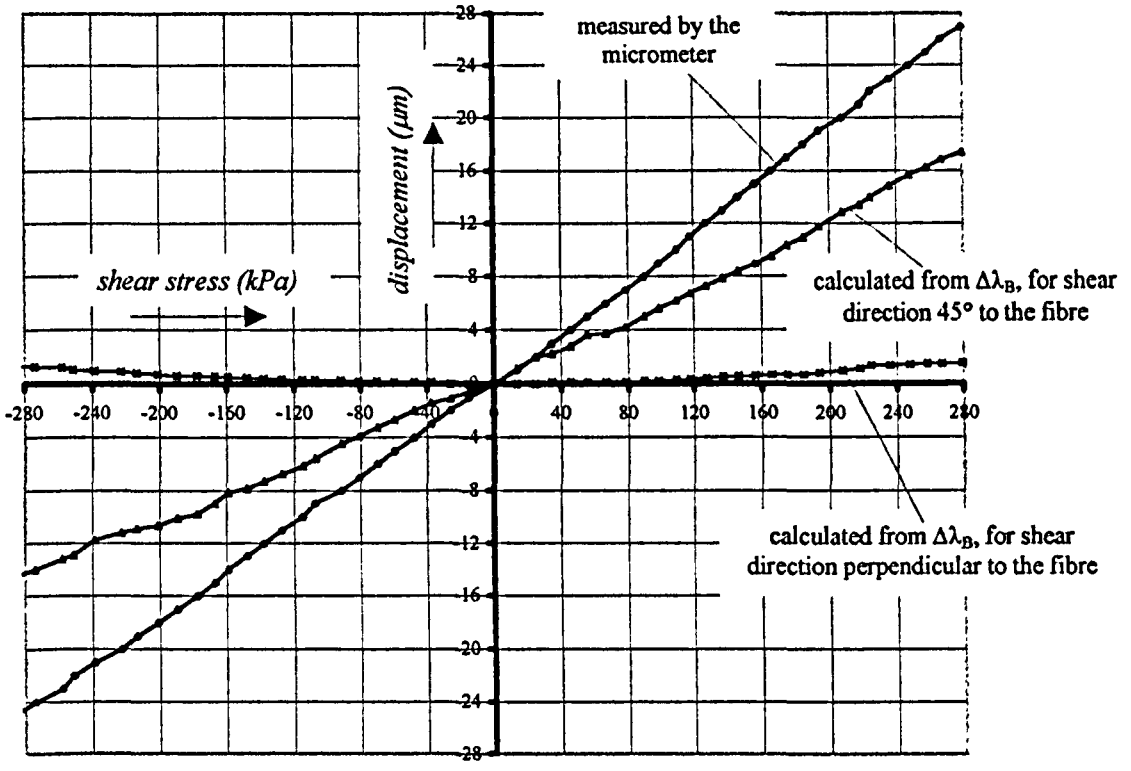

Fig.4.35: Variation of upper disk displacement with shear stress for the enlarged steel sensor, as measured by the micrometer and as calculated from the Bragg wavelength shift, for shear direction at 45° and 90° with respect to the fibre axis.

4.3.2.3. General comments on the results from the testing of the enlarged structures

In the previous sections, we have mentioned the differences between the experimental results obtained from the aluminium disk, and the steel disk sensor structures. It is clear that the use of a hard material, like steel, as well as the precise alignment of the pins, are key parameters for equal elastic response of the sensor at any direction of shear stress.

The elastic displacement under maximum shear stress was estimated to be approximately 8 times larger the theoretical predictions for the aluminium structure. The steel structure showed improvement, but still the response is larger by a factor of 4 compared with theory. Since the theoretical model of beam bending theory cannot produce a realistic result, it is necessary to use the experimental data in order to compensate the theoretical error. Assuming that we keep the same dimensions as the actual sensor, and using eq.(4.43) as a rule, we can say that the pin bending due to shear stress can be decreased by increasing i) the number of pins, ii) the pin diameter, iii) the Young's modulus of the pin material, or a combination of the above. Experimentation with the sensor parameters is therefore necessary before achieving the desired pin deflection.

The response to shear stress is significantly affected by the direction of shear in both structures. The fabrication of the steel structure was reconsidered in order to improve the sensor response. Although improvement was observed, the results were still unacceptable compared to the required shear sensor specifications. We can assume that this behaviour is caused by imperfections during the fabrication of the structure, which are limited by the accuracy and tolerances of the workshop equipment, and cannot be avoided. It is then reasonable to assume that, increasing the number of pins would possibly reduce the sensitivity of the structure to shear direction, as a result of the "averaging" of the individual response of every pin.

4.3.3 Laboratory testing of metallic structure. Experiment 3: Actual sensor with 8 pins

This section describes the last set of experiments conducted with the metallic sensor. The disks were made of stainless steel, and a similar procedure as shown in Fig.4.27 was followed for the pin installation. Each disk has 5mm diameter and 0.75mm thickness (0.5mm for the inner disk and 0.25mm for the outer), giving an overall sensor height 3.5mm. The overall dimensions are therefore close to those of the actual sensor, as given in Table 4.2.

Based on the comments presented in section 4.3.2.3, we decided to increase the number of pins, keeping the same material and pin diameter, which was already available. The sensor has now 8 pins, equally spaced around the periphery of the disks. 130μm inclined grooves were also etched on the inner sides of the disks to accommodate the fibre and improve the strength of the bond between the fibre and the disk. All the details of the design are given in the mechanical drawing given in appendix I. The sensor is also shown in pictures 9 and 10, appendix II.

The structure was tested using the setup described in section 3.1.1. New holding plates were made in a similar way to the ones used for testing the enlarged structures. The procedure followed for measuring the elastic displacement of the upper disk was identical to the one described in section 4.3.1.2.

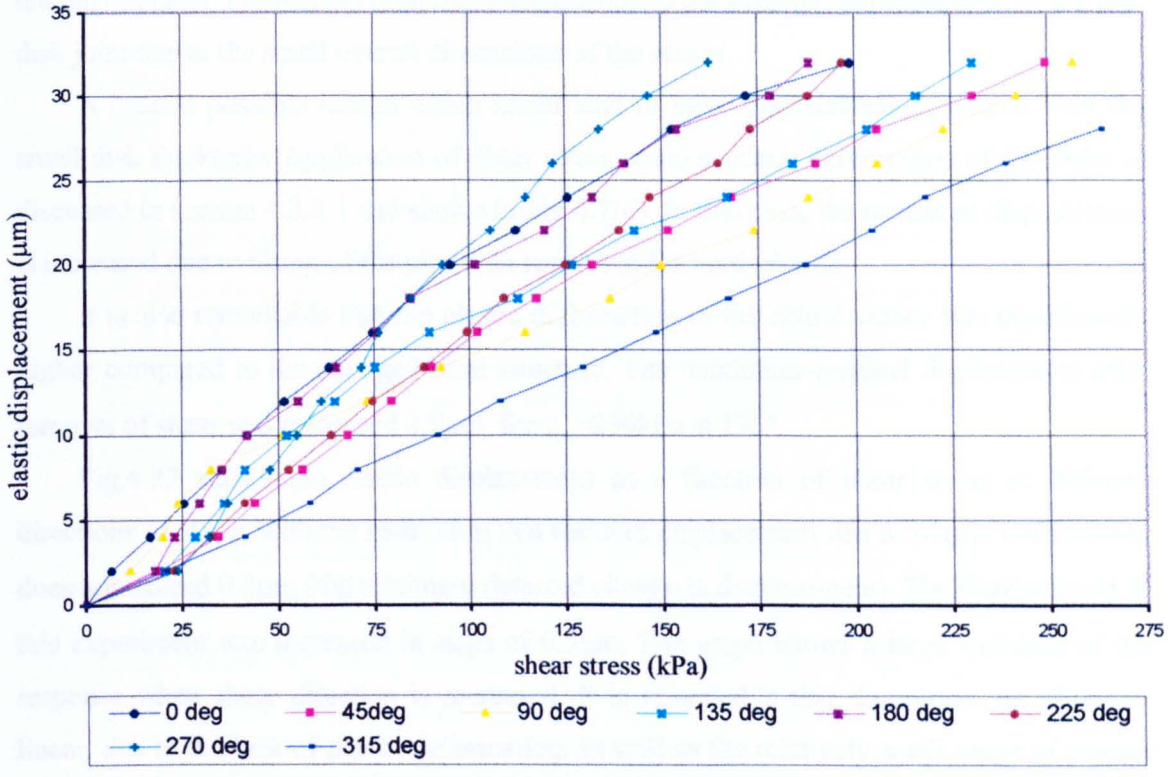

Fig.4.36: Elastic displacement of upper disk as a function of shear stress, for the actual sensor. Each curve corresponds to different direction of shear.

The experiments were focussed on measuring the sensitivity of the response to shear direction, which was the main problem observed on the enlarged steel structure. Fig.4.36 shows the elastic displacement of the upper disk as a function of shear stress, for different directions of shear. Examining the curves, and comparing them with those of the enlarged steel sensor, Fig.4.29, we notice that:

1. The response is strongly dependent on the direction of shear, even for low shear stresses.
2. Most of the curves, except the ones at 225° and 315°, are significantly non-linear.
3. Since the pins in the enlarged and the actual structures are identical, the measured maximum displacement (for shear stress equal to 250kPa) was expected to decrease. However, the smaller value of the maximum displacement was measured 27.5μm for the 315° curve, which is larger than the average maximum displacement measured on the enlarged structure (Fig.4.29).

It is clear that the miniaturisation of the structure produces results which are similar to the results obtained from the enlarged aluminium structure. The relatively large maximum displacement is related to the fact that the pins are not firmly fixed to the disks. In the case of the aluminium sensor, the problem was focussed on the deformation of the soft aluminium close to the interface region. In the case of the actual sensor on the other hand, even though the disk material is steel, the problem seems to occur due to the small penetration depth of the pins, which is just equal to the inner disk thickness (0.5mm), and, for this sensor, equal to

the pin diameter. Fabrication imperfections deteriorate the strength and robustness of the pin-disk joint due to the small overall dimensions of the sensor.

A second possible reason which could lead to large displacement is related with the small disk thickness. Application of shear stress could produce deformation of the disks as discussed in section 4.2.2.1 and shown in Fig.4.7(d). In that case, the measured displacement is increased due to tilting of the pins with respect to the vertical axis.

It is also remarkable that the plastic deformation of the actual sensor was significantly higher compared to the enlarged steel structure. The maximum residual displacement after removal of shear was measured 4.2μm, for τ_{yx}=250kPa at 135°.

Fig.4.37 shows the elastic displacement as a function of shear stress at different directions of shear, with the restriction that residual displacement due to plastic deformation does not exceed 0.1μm (the minimum detected change in displacement). The displacement in this experiment was increased in steps of 0.5μm. The graph shows a large variation of the response when shear direction is increased. It is remarkable that the curves are closer to linear, due to the lack of plastic deformation, as well as the relatively small range of change of the displacement.

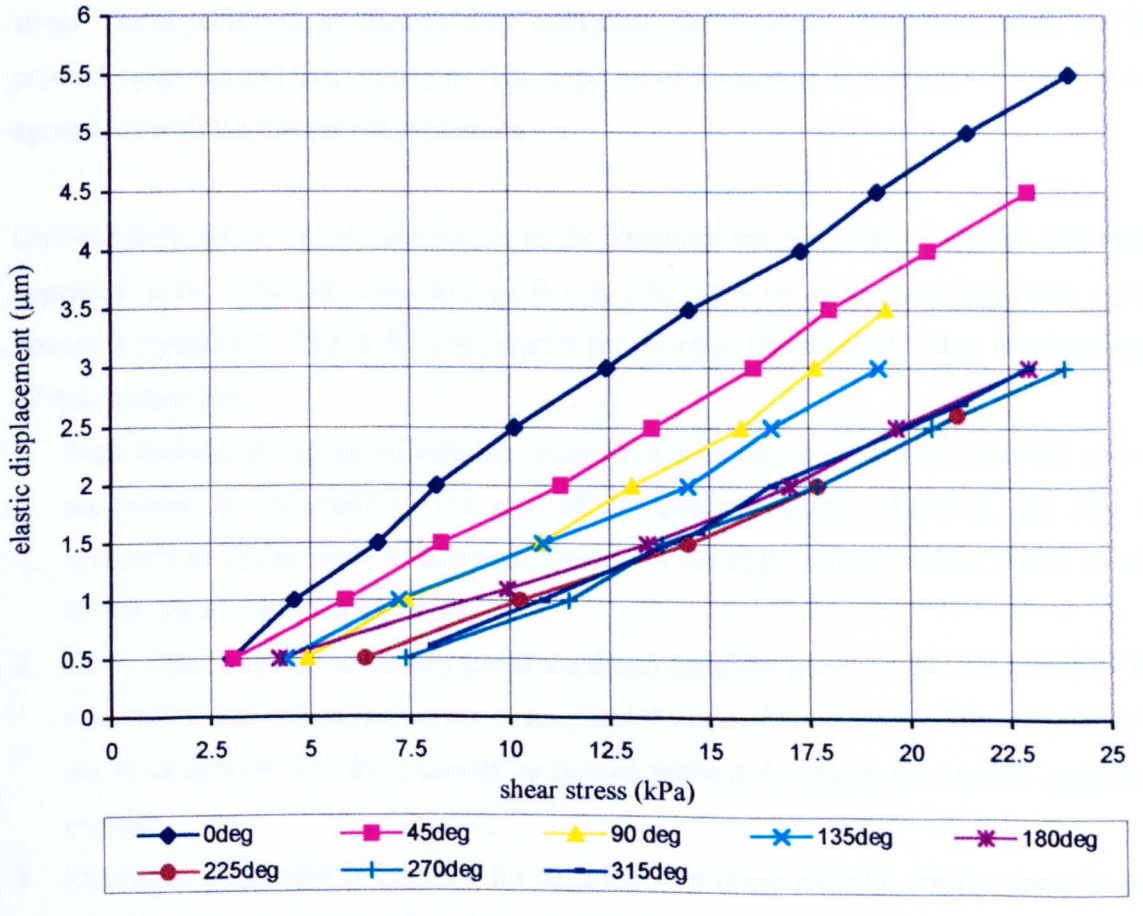

Fig.4.37: Elastic displacement of upper disk as a function of shear stress for the actual sensor. Each curve corresponds to different direction of shear.

4.4 Conclusions

In this chapter, a method for implementing a shear stress sensor using FBGs was described. The operation of the sensor is based on the transfer of stress to prestrained gratings which are attached on an elastically deforming structure.

The design was based on the beam bending theory of isotropic and elastic beams, firmly supported at both ends, which are free to deflect laterally under shear stress. This model, although it gives a rough estimation of the elastic response of the structure, was used as an easy and fast method for designing a prototype and to evaluate experimentally the feasibility of the method.

The aim of the experiments was to measure the essential properties of the sensor for its application to in-shoe measurements, which are i) the elastic deflection of the structure under shear stress where the shear direction is also variable, and ii) the fibre Bragg grating response. For that purpose, three structures were fabricated and tested.

The experimental results revealed the main problems of this method. The plastic deformation, which is present in the aluminium structure, as well as manufacturing imperfections, introduce significant non-linearity, and sensitivity to the direction of shear stress. Those problems are improved by fabricating the structure solely from steel, and by precisely aligning and fitting the pins. The response of the grating to shear stress was in good agreement with the theoretical prediction.

Unfortunately, after the miniaturisation of the structure the problems re-appear. Problems appeared in the structure, even though it was fabricated by specialised engineers, using precision equipment. That is the main reason for rejecting this method. Other disadvantages of this method are:

1. High manufacturing cost of metallic structure. It must be mentioned that the total cost of the sensor is governed by the cost of the Bragg gratings. However, the cost of commercial FBGs tends to decrease, especially for high volume orders, which finally comes close to the cost of the structure.
2. Every FBG must be accurately prestrained and carefully glued on the inner side of the sensor. This procedure is time consuming and the risk of breaking the fibre very close to the FGB is high. The fibre cannot be spliced without damaging the grating, making it useless.
3. Individual calibration is essential for each FBG on every metallic sensor, since the any misalignment of the fibre during the installation procedure (angle between the FBGs, lateral displacement with respect to the disk diameter), as well as the random variations

of the glued part of the fibre (length g, section 4.2.2.2) would affect the strain change on the grating, according to eq.(4.38).

Given these significant disadvantages, a different approach to the transducer design is required. This is detailed in the next chapter.

CHAPTER 5

Elastomer sensor – Fibre independent model

Introduction

This chapter describes the design and implementation of a sensor based on embedding FBGs in an elastomer material. The sensor is capable of measuring the vertical, and the two components of shear stress acting on its top surface. It consists of a solid block of elastomer material (10x10x3mm), in which three FBGs can be embedded at a specific orientation. The theoretical modelling of the sensor is based on the assumption that the elastic deformation of the sensor is independent of the embedded fibres, therefore the elastic properties of the material will determine the sensor response.

The chapter begins with a presentation of the theory of elasticity in solid polymers, and a brief description of the viscoelastic behaviour in real materials. The sensor design will then be described, where the required properties of the material, the number of FBGs, and their orientation inside the material for optimal sensor performance will be derived. The experimental work includes the measurement of E and G values in five materials, and the implementation and measurement of a simplified version of the sensor which contains only one FBG embedded horizontally into the material. Finally, the experimental results were used to evaluate the validity of the fibre independent model, and its applicability to accurately describe the sensor response.

5.1 Background theory

The following subsections describe the fundamental issues of the theory of elasticity, which is used for the elastomer sensor design. The theory presented in this section is based on the textbook by Timoshenko and Gere (1973). The same theory can also be applied for studying the elastic behaviour of solid polymers, which is described in similar way by Ward (1983). Contrary to metals, which can be assumed linearly elastic at low strains[1], polymers have properties which are intermediate between those of an elastic solid and a viscous liquid, depending on the temperature and the rate of change of stress applied on the material. This viscoelastic behaviour was observed in all the materials tested, as will be shown later in this

[1] The maximum allowable strain for linear elastic behaviour depends on the material, for structural steel (E=200Gpa) strain must be less than approximately 0.1% (Timoshenko and Gere, 1973, p.6).

chapter. The viscoelasticity will be briefly explained in this section. A more comprehensive discussion may be found in the textbooks by Aklonis *et al.* (1972), and Ward (1983).

The normal stresses and normal strains inside an elastic material, the Young's modulus of elasticity, and the Poisson's ratio, are defined in section 5.1.1. In section 5.1.2 the shear stresses and shear modulus of elasticity are defined. The internal strain at an inclined plane, as a function of the normal and shear stresses acting on one surface of the material will be discussed in section 5.1.3. Finally, brief description of the viscoelasticity observed in real materials will be given in section 5.1.4.

5.1.1 Normal stresses and strains

Let us consider a rectangular block of material which is subjected to stresses σ_x, σ_y, and σ_z acting normal to its sides, called normal stresses, parallel to the x, y, and z axis respectively, as shown in Fig.5.1. It is assumed that the stresses are small so that the resulting deformation of the material is linearly elastic[1], which is described by the constant modulus of elasticity E. The linear equation between stress σ and strain ε at the direction of stress in that case will be given by the Hook's law (Timoshenko and Gere, 1973, p.7):

$$\sigma = E\varepsilon \tag{5.1}$$

It is also assumed that the rectangular shape of the material is maintained while stress is applied.

[1] When a material behaves elastically and also exhibits a linear relationship between stress and strain, the material is said to be linearly elastic. This property can be found in many solid materials including most metals, plastics, wood, and ceramics. (Timoshenko and Gere, 1973, p.7)

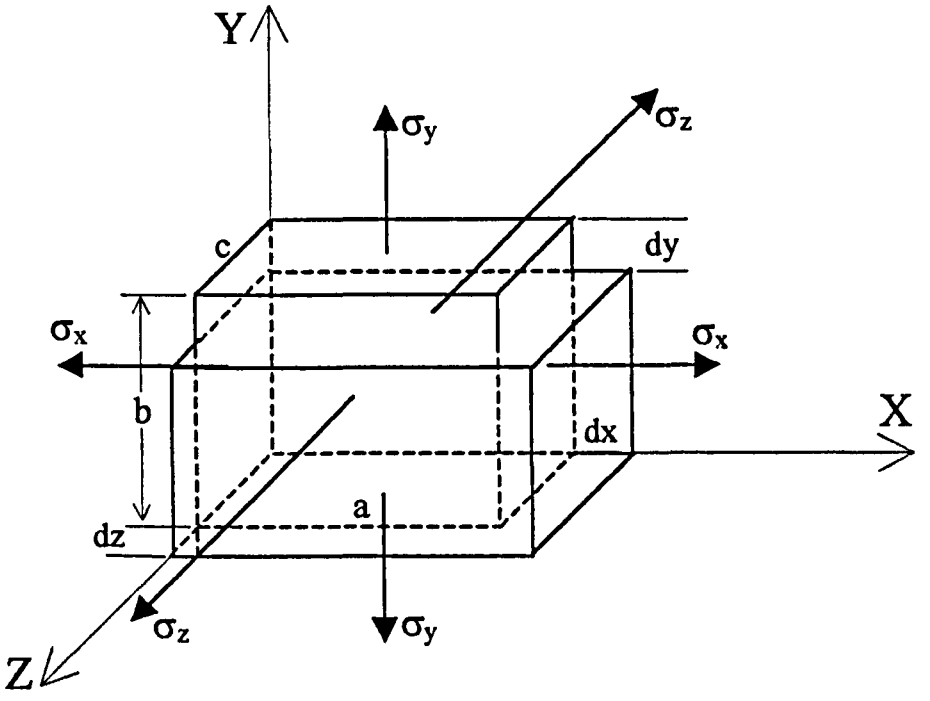

Fig.5.1: Element of material in triaxial stress.

In the particular case shown in Fig.5.1 the application of the three normal stresses produce compression of the material on the y-axis by dy, and extension on the x and z directions by dx and dz respectively. If a, b, and c are the initial dimensions of the block, then the normal strains ε_x, ε_y, and ε_z will be given by:

$$\varepsilon_x = \frac{dx}{a}, \quad \varepsilon_y = \frac{dy}{b}, \quad \varepsilon_z = \frac{dz}{c} \tag{5.2}$$

Timoshenko (1969, pp.39-40) describes the sign convention generally adopted for the stress analysis in solids. The normal stress is considered positive when it produces extension of the material, and negative when it produces compression. All normal stresses σ_x, σ_y, and σ_z shown in Fig.5.1 are positive since they tend to extent the material at the direction of stress. A normal strain at one direction is considered positive when elongation is observed at that particular direction, and negative for compression. In this particular example, strains ε_x, and ε_z are positive, while ε_y is negative. The length change dx, dy, and dz follow the same sign as normal strains, as shown by eq.(5.2).

The elongation or contraction of the material at a particular direction depends not only on the stress acting at that particular direction, but also on the other normal stresses acting on the material. For example, let σ_y be the only stress applied on the material, which produces elongation of the material at the y-direction (dy positive). Such an elongation is always accompanied by lateral contraction of the material at the other two dimensions (dx, dz negative). Within the elastic limit of the material, the ratio (Timoshenko, 1969, pp.53-54):

$$\frac{\text{unit lateral contraction}}{\text{unit axial elongation}}$$

is constant for a given material. This constant is called Poisson's ratio ν. For materials which have the same elastic properties in all directions, called isotropic materials, ν=0.25. Typical ν values are 0.3 for steel, 0.5 for rubber, and 0.4-0.5 for most solid polymers. The Poisson's ratio has the same value in case of lateral extension caused by longitudinal compression. In this example where the material is assumed isotropic and if σ_y is the only stress applied, ν will be given by:

$$\nu = \frac{\varepsilon_x}{\varepsilon_y} = \frac{\varepsilon_z}{\varepsilon_y} \tag{5.3}$$

In the general case where all three normal components of stress are applied, the strain in the x direction due to σ_x is σ_x/E, due to σ_y is $-\nu\sigma_y/E$, and due to σ_z $-\nu\sigma_z/E$. Thus, the total strain ε_x will be (Timoshenko and Gere, 1973, p.73):

$$\varepsilon_x = \frac{\sigma_x}{E} - \frac{\nu}{E}(\sigma_y + \sigma_z) \tag{5.4}$$

Similarly, for the strain in the y direction, we obtain:

$$\varepsilon_y = \frac{\sigma_y}{E} - \frac{\nu}{E}(\sigma_x + \sigma_z) \tag{5.5}$$

Also, the normal strain in z-direction is:

$$\varepsilon_z = \frac{\sigma_z}{E} - \frac{\nu}{E}(\sigma_x + \sigma_y) \tag{5.6}$$

In the special case where $\sigma_x=\sigma_z=0$, the above equations become:

$$\varepsilon_x = \varepsilon_z = -\frac{\nu}{E}\sigma_y \tag{5.7}$$

$$\varepsilon_y = \frac{\sigma_y}{E} \tag{5.8}$$

5.1.2 Shear stress and shear strain – Shear modulus

Let as now consider a square element of material, which is subjected to stress τ_{yx} acting tangential on its top surface parallel to the x-axis, as shown in Fig.5.2. Stress acting tangential to a surface is called shear stress (Timoshenko, 1969, p.38). The first subscript denotes the plane on which the stress acts (y surface in this case), while the second subscript denotes the direction of shear stress (x-axis in this case). Following the usual sign convention in the theory of elasticity, a shear stress is considered positive when acting towards the positive direction of the axis indicated by the second subscription (Timoshenko and Gere, 1973, p.64). It is assumed that shear stress is small so that the material deformation is linearly elastic. It is also assumed that the lower surface is firmly fixed.

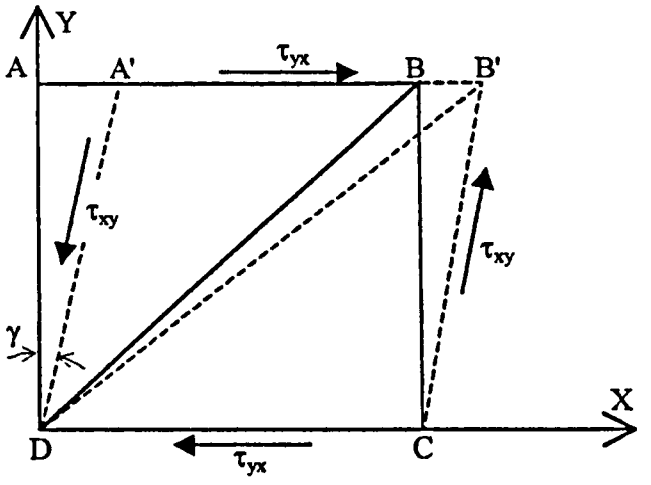

Fig.5.2: Shear stress and shear strain.

If there are no normal stresses acting on the element, then equal and oppositely directed shear stress must also act on the lower surface in order for the element to be in static equilibrium in the horizontal direction. Furthermore, the shear stresses on the top and the bottom of the element produce a moment which must be balanced by the moment of shear stresses acting on the vertical sides of the element. These vertical shear stresses must also be equal to the horizontal ones since the element is in static equilibrium (Timoshenko and Gere 1973, p.30). Therefore, $\tau_{yx}=\tau_{xy}$.

Since there are no normal stresses acting on the element, the lengths of the sides AB, BC, CD, and DA will not change under shear. Instead, the shear stresses will cause the square to distort into a rhombus as indicated in the figure with the dashed lines, causing the diagonal DB to increase and AC to decrease. The angle ADC which was $\pi/2$ before deformation, is now reduced to $A'DC=\pi/2-\gamma$, where γ is the small angle shown in Fig.5.2. At the same time, the angle DAB will increase to $DA'B'=\pi/2+\gamma$. The angle γ is a measure of the distortion of the element due to shear and is called shear strain. It is given by (Fig.5.2):

$$\gamma = \arctan\frac{\overline{AA'}}{\overline{AD}} \tag{5.9}$$

For small strains it can be taken equal to the ratio AA'/AD.

In the linearly elastic region of the material, the shear stress and shear strain are directly proportional and given by the Hook's law in shear (Timoshenko and Gere, 1973, p.31):

$$\tau = G\gamma \tag{5.10}$$

where G is the shear modulus of elasticity for the material. It can be proved[1] that, in the linearly elastic region of the material, E, G, and ν satisfy the following equation:

[1] The relationship is derived by considering the length change of the diagonal in an element under pure shear, and is presented in Timoshenko and Gere (1973) pp.60-61.

$$G = \frac{E}{2(1+\nu)} \tag{5.11}$$

5.1.3 Strain along an inclined axis

Fig.5.3 shows the front face of a rectangular element which is subjected to simultaneous normal stress σ_y and shear stress τ_{yx}, both acting on the top surface of the element. The vertical stress, which is negative since acting towards the surface, will produce the normal strain ε_y, as well as the normal strains ε_x and ε_z due to Poisson's effect, and can be calculated by eq.(5.7) and eq.(5.8) respectively. Shear strain γ_{yx} will also appear as the result of shear stress τ_{yx}.

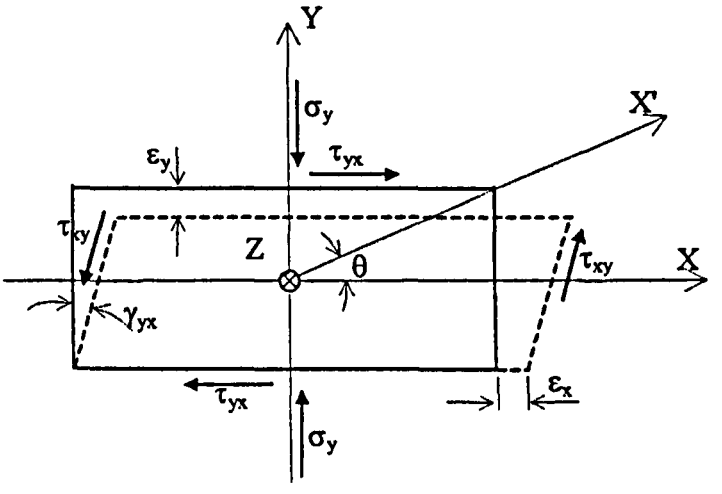

Fig.5.3: Simultaneous normal and shear stresses acting on top surface.

The objective of the following analysis is to determine the strain inside the element in the direction of the x'-axis, which lies on the xy plane at an angle θ with respect to the x-axis. In other words, the strain ε_θ will be expressed as a function of the angle θ and the strains ε_x, ε_y and γ_{yx}, which are assumed known. This analysis is presented in the textbook by Timoshenko and Gere (1973, pp.74-80) with the assumption that the element is subjected to plane strain, which is described by the conditions:

$$\varepsilon_x \neq 0 \quad \varepsilon_y \neq 0 \quad \gamma_{yx} \neq 0 \tag{5.12}$$

$$\varepsilon_z = \gamma_{xz} = \gamma_{yz} = 0 \tag{5.13}$$

Eq.(5.13) requires that ε_z=0 which is not satisfied in the stress situation shown in Fig.5.3, due to the Poisson's extension at z-direction caused by the vertical compression of the element. The actual problem therefore involves triaxial strain than plane strain. However, it is clearly stated (Timoshenko and Gere, 1973, p.75) that the equations derived for an element in plane strain are also valid for triaxial strains, provided that the new direction (x' axis) is taken by rotation around a coordinate axis (rotation of x axis around z axis by θ).

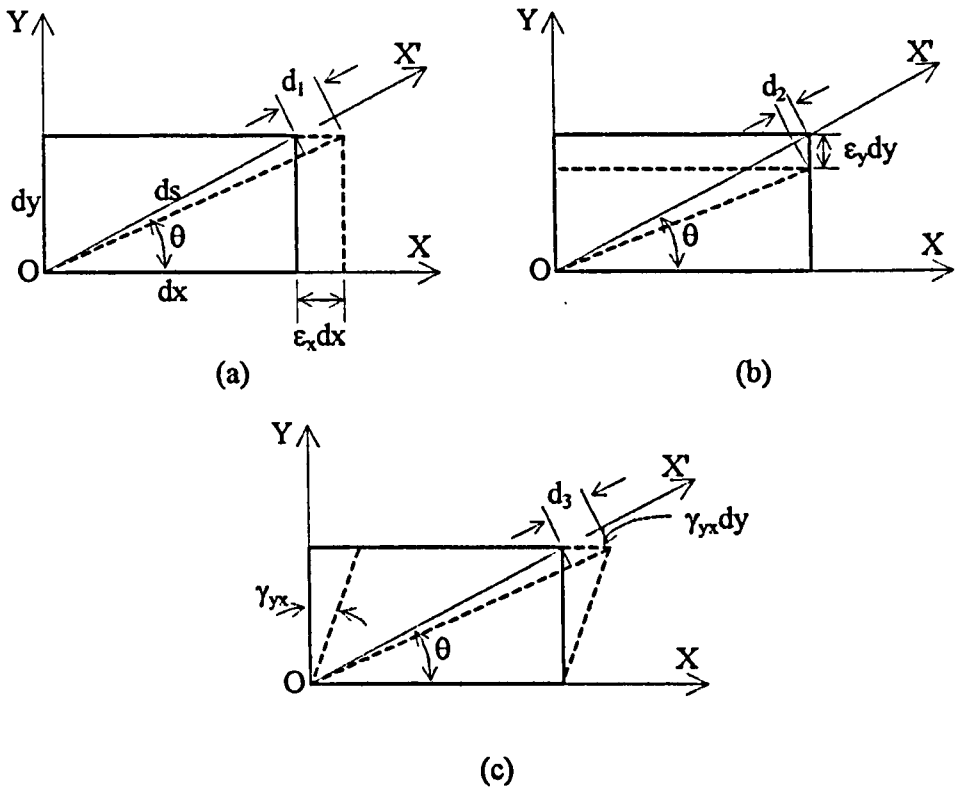

Fig.5.4: Deformation of an element due to strains (a) ε_x, (b) ε_y, and (c) γ_{yx}.

Let us consider an element of undeformed width dx and undeformed breadth dy, with the diagonal parallel to the x' axis, as shown in Fig.5.4. As a result of the strains ε_x, ε_y and γ_{yx} the element will elongate in the x direction by an amount $\varepsilon_x dx$ (Fig.5.1a), compress in the y direction by $\varepsilon_y dy$ (Fig.5.4b), and the right angle xOy will decrease by an amount γ_{xy} (Fig.5.4c). Each of these three deformations will cause the length of the diagonal to change. The corresponding changes in the diagonal length are:

$$d_1 = \varepsilon_x dx \cos\theta \tag{5.14}$$

$$d_2 = \varepsilon_y dy \sin\theta \tag{5.15}$$

$$d_3 = \gamma_{yx} dy \cos\theta \tag{5.16}$$

The total change in the length of the diagonal is the sum of these three quantities and the corresponding strain ε_θ in the x' direction is obtained by dividing this sum with the initial length of the diagonal ds:

$$\varepsilon_\theta = \varepsilon_x \frac{dx}{ds}\cos\theta + \varepsilon_y \frac{dy}{ds}\sin\theta + \gamma_{yx} \frac{dy}{ds}\cos\theta \tag{5.17}$$

Observing that dx/ds=cosθ and dy/ds=sinθ we obtain:

$$\varepsilon_\theta = \varepsilon_x \cos^2\theta + \varepsilon_y \sin^2\theta + \gamma_{yx} \sin\theta\cos\theta \tag{5.18}$$

By using the following trigonometric relations:

$$\cos^2\theta=\frac{1}{2}(1+\cos 2\theta),\quad \sin^2\theta=\frac{1}{2}(1-\cos 2\theta),\quad \sin\theta\cos\theta=\frac{1}{2}\sin 2\theta$$

eq.(5.18) can be written:

$$\varepsilon_\theta=\frac{1}{2}(\varepsilon_x+\varepsilon_y)+\frac{1}{2}(\varepsilon_x-\varepsilon_y)\cos 2\theta+\frac{1}{2}\gamma_{yx}\sin 2\theta \tag{5.19}$$

Eq.(5.19) can be used to calculate the strain ε_θ. The fact that, ε_θ is independent of the shear strain ε_z, can be realised by considering its effect on the diagonal Ox', Fig.5.4. The length of the diagonal remains unaffected by the presence of strain at the z direction, since Ox' lies on the xy plane.

Eq.(5.19) can also be expressed in terms of the normal and shear stresses acting on the top surface. ε_x and ε_y are given by eq.(5.7) and eq.(5.8) respectively. The shear strain can be obtained by eq.(5.10):

$$\gamma_{yx}=\frac{\tau_{yx}}{G} \tag{5.20}$$

Substitution of G by eq.(5.11) gives:

$$\gamma_{yx}=\frac{2(1+\nu)}{E}\tau_{yx} \tag{5.21}$$

Finally, eq.(5.19) gives:

$$\varepsilon_\theta=\frac{\sigma_y}{2E}(1-\nu)-\frac{\sigma_y}{2E}(1+\nu)\cos 2\theta+\frac{(1+\nu)}{E}\tau_{yx}\sin 2\theta \tag{5.22}$$

It is reminded that the stresses follow the sign convention mentioned in the previous sections. The normal stress σ_y will therefore be negative, and τ_{yx} positive.

5.1.4 Viscoelasticity in polymers

In the preceding sections we have assumed that the material is ideally an elastic solid. The elastic solid deforms when subjected to stress and returns exactly to its original shape on removal of stress. Another type of ideal material is the viscous liquid. A viscous liquid has no definite shape and flows irreversibly under the action of external stress. Real materials have properties which are intermediate between those two ideal materials. A polymer in particular can display all the intermediate range of properties depending on the temperature and the rate of change of the applied stress (Ward, 1983, pg.79).

Let us consider an elastic solid which is subjected to constant stress σ_o at t_o. The stress is removed at t_1, as shown in Fig.5.5. The strain follows the pattern of the applied stress exactly, Fig.5.5(a). If on the other hand the same stress pattern is applied on a viscoelastic solid, Fig.5.5(b), a different strain pattern will be recorded. In general, the total strain ε in a viscoelastic solid is the sum of the immediate elastic deformation ε_1, the delayed elastic deformation ε_2, and the Newtonian flow ε_3. In solid polymers, the term ε_3 can be neglected

(Ward, 1983, pg.82). The observed dimensional change with time of a viscoelastic solid under constant stress following the initial instantaneous elastic deformation is called creep (Modern Plastics, 1999, pg.A.7).

The counterpart of creep is stress relaxation, where the viscoelastic material is subjected to constant strain ε, and a decay of stress σ is observed, Fig.5.6. At sufficiently long times, the stress decays to a finite value (Ward, 1983, pg.84).

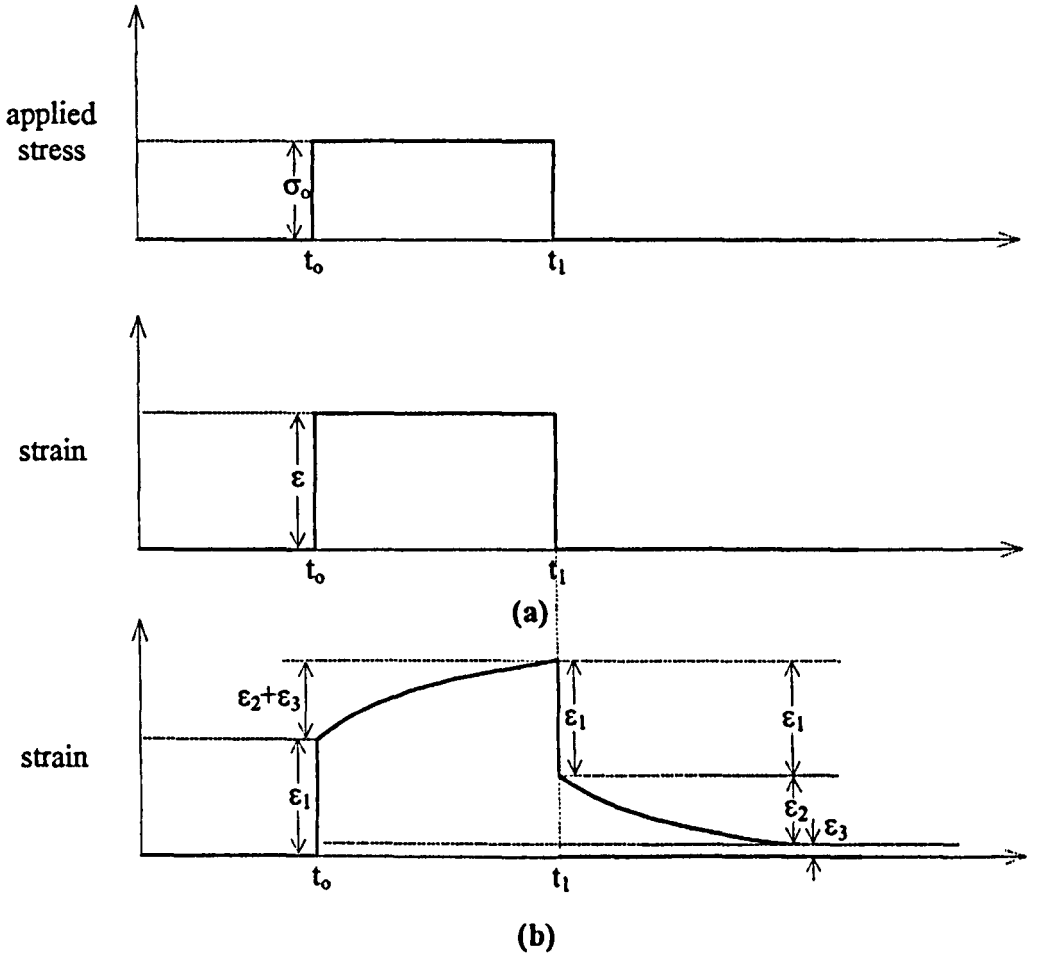

Fig.5.5: Deformation of a (a) ideally elastic solid, and (b) viscoelastic solid under a fixed load.

The presence of viscoelastic behaviour will introduce error in calculating the strain inside the material at a given angle, following the procedure explained in section 5.1.3. The reason is that the elastic properties of the material E and G, cannot be considered constant. The dependence of the stress - strain relation with time, as this is shown in Fig.5.5 and Fig.5.6 for the creep and stress relaxation respectively, shows that the elastic constants are also time dependent. Several mathematical models have been developed for the stress analysis of creep (Kelvin or Voigt Model) (Ward, 1983, pg.91) and stress relaxation (Maxwell model) (Ward, 1983, pg.89). For the dynamical stress analysis of viscoelasticity, complex expressions of the E and G modulus must be introduced (Ward, 1983, pp.95-107).

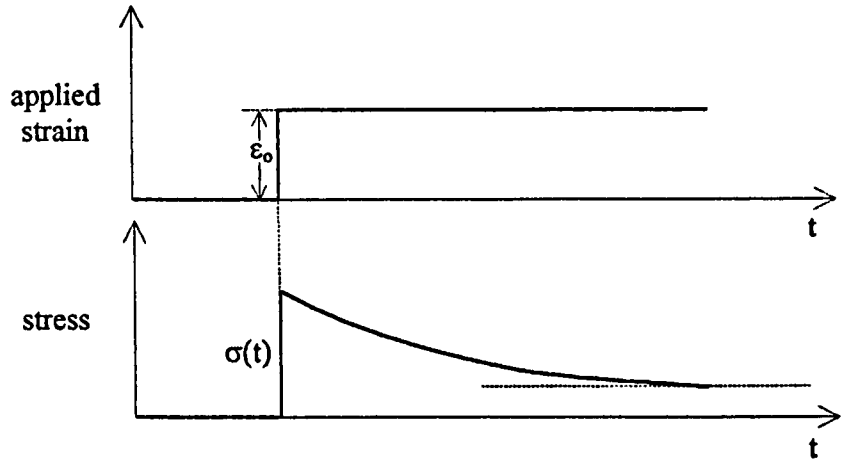

Fig.5.6: Stress relaxation in viscoelastic solid.

The theory of elasticity presented in sections 5.1.1 to 5.1.3 is therefore expected to give an approximation of the strain inside the material at a particular direction. However, because the model of elasticity is significantly simpler than the models which describe viscoelasticity, it was chosen for the design of the sensor. Even though it cannot be used to quantitatively describe the embedded FBG sensor, it can be used to obtain an estimation of the axial strain on the fibre for different orientations, as it will be presented in the next sections.

More information on the viscoelastic behaviour of polymers, which includes study of nonlinear viscoelasticity and commercial methods of measuring viscoelasticity, is given by Ward, 1983, chapters 5-9. A detailed mathematical modelling of viscoelasticity may be found in standard textbooks (Gross, 1953, McCrum *et al.*, 1967, Ferry, 1970, Aklonis *et al.*, 1972).

5.2 Sensor design

In the following sections, the method for measuring vertical and shear stress using fibre Bragg gratings embedded in elastomer, as well as the theoretical design of the sensor will be described. The objectives of the following analysis are:

1. To estimate the number of FBGs needed for the measurement of the vertical stress σ_y and the magnitude and direction of shear on the top surface of the sensor. The shear stress vector can be uniquely identified by measuring the two orthogonal components τ_{yx} and τ_{yz} which are shown in Fig.5.7.
2. To find the orientation of the FBGs inside the material for optimal performance of the sensor. Optimal performance in this case will be achieved by fitting the FBGs in such a way that i) the maximum strain range of the fibre is achieved without the risk of fibre breakage, and ii) the system of equations which can be derived by measuring the Bragg wavelength shift of the FBGs must give a unique solution for the stress components σ_y,

τ_{yx}, and τ_{yz} under any vertical and shear stress in the range defined by the initial specifications of the sensor (see section 2.3).

3. To estimate the required mechanical properties of the material for optimal performance. In the ideal case of a linearly elastic material, the elastic parameters E, G, and ν must be calculated. Since those three parameters are related by eq.(5.11), any two parameters are sufficient for the third to be calculated. In the following analysis we will estimate the required E modulus and Poisson's ratio ν of the elastomer.

As has already been mentioned in the introduction of this chapter, the design is based on the theory of elasticity in solids. The model of the sensor was kept simple by assuming the ideal case of a linearly elastic material, neglecting nonlinearity and viscoelasticity. For the same reason we have assumed that the deformation of the material is not affected by the presence of the fibres inside the material, in other words the fibres follow exactly the deformation of the material. This assumption results in significant variation of the theoretical sensor responsivity with respect to the measured one, as will be seen in section 5.3.2.

5.2.1 Principle of operation

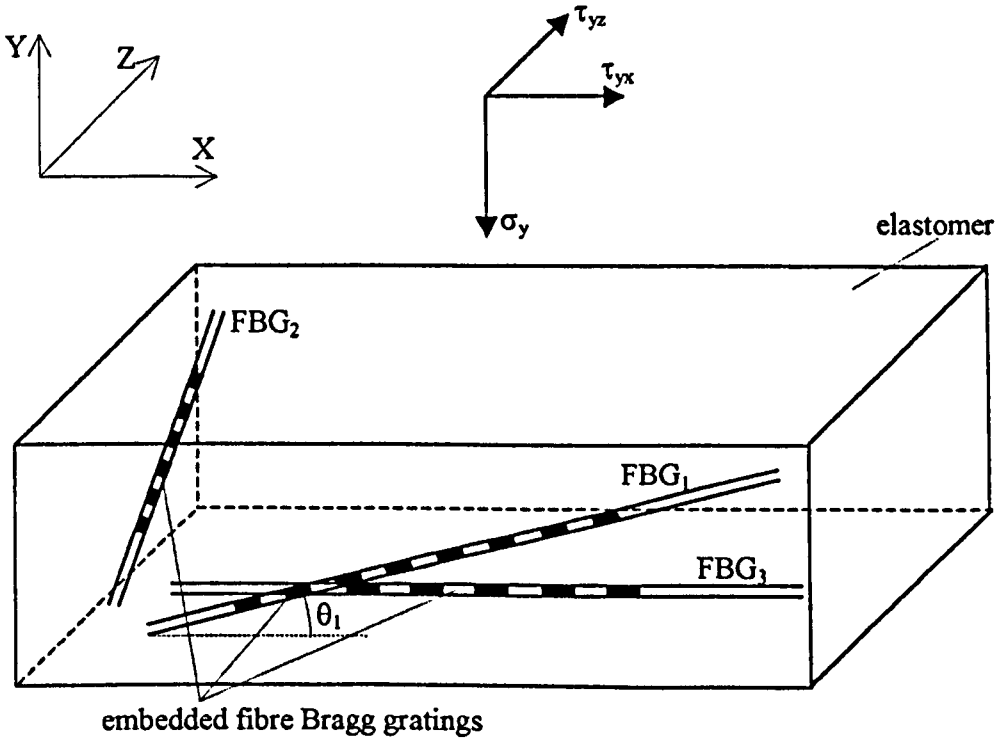

Fig.5.7: General diagram of the shear and vertical stress sensor using FBGs embedded in elastomer.

The sensor consists of a rectangular block of solid elastomer with FBGs embedded in it, as shown in Fig.5.7. Application of vertical pressure or shear stress will produce deformation of the material. If the bonding of the fibre to the material is sufficient to prevent slippage of the

fibre, then the strain in the fibre will be identical to the local strain in the material. The induced strain on each fibre can be calculated by measuring the Bragg wavelength shift of each FBG.

In order to comply with the specifications presented in section 2.3 for the particular application of this design for in-shoe measurements, the dimensions of the elastomer were restricted to 10x10x3mm (WxDxH), which are in fact the overall dimensions of the sensor.

5.2.2 Assumptions

Before proceeding to the theoretical analysis of the sensor it is important to mention the assumptions made in order to simplify the design. Some of them have already been mentioned and will be summarised here.

1. The material deformation is linearly elastic in the entire operating range of the sensor (0-500kPa for vertical and –250 to 250kPa for shear stress, section 2.3).
2. The stress is equally distributed over the upper (active) surface of the sensor. Uneven stress on the top surface will produce distortion like the one shown in Fig.5.8(a), which will result in unequal and unpredicted stress along the fibre.
3. The lower surface is considered permanently fixed, in a way that no horizontal or vertical movement is allowed. It is also assumed that the lateral expansion due to vertical stress, as the result of Poisson's ratio, is not prevented, contrary to the situation of the sensor been glued to a fixed surface, Fig.5.8(b).
4. No torsion with respect to the vertical axis occurs when stress is applied. That would result in unpredicted stresses inside the material and hence along the FBG, Fig.5.8(c).
5. The fibres are perfectly adhered with the elastomer. In the opposite situation where slippage occurs between the fibre and the material, the responsivity of the sensor is expected to be significantly reduced since the stress cannot be fully transferred from the material to the fibre.
6. The fibres follow exactly the deformation of the elastomer. This is the main assumption which differentiates the theoretical approach discussed in this chapter with the one presented in the next chapter.
7. The vertical surfaces of the sensor remain parallel after the lateral expansion of the material due to vertical stress and Poisson's ratio. Fig.5.8(d) shows the actual case of the barrel-shape deformation due to friction on the upper and lower surfaces.

8. The temperature of the material remains constant. Hence, any observed Bragg wavelength shift is due to axial strain only, and will be given by eq.(2.9) for $\Delta T=0$:

$$\frac{\Delta\lambda_B}{\lambda_B} = 0.8\varepsilon \tag{5.23}$$

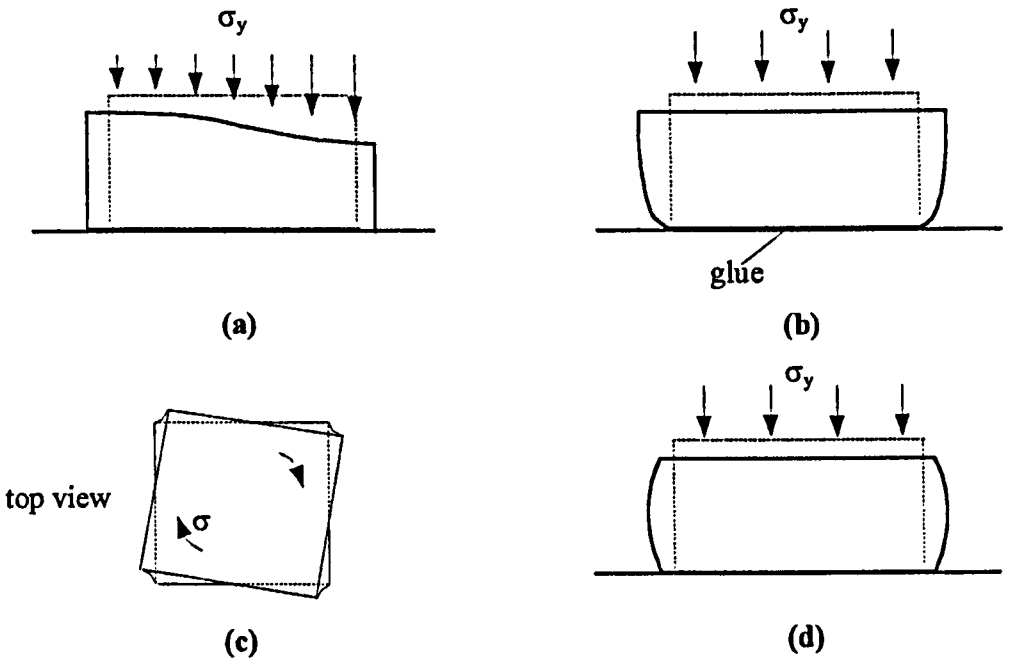

Fig.5.8: Possible deformations of the material that could affect the stress transferred on the embedded optical fibres. (a) unequal loading, (b) lower surface not able to expand laterally, (c) torsion, (d) barrel- shape Poisson's extension.

5.2.3 Theoretical evaluation of required number and orientation of the embedded FBGs

Let as assume that a FBG lies on the yx plane at an angle θ_1 with respect to the x-axis, FBG_1 shown in Fig.5.7. Following the analysis presented in section 5.1.3, the strain on the grating FBG_1 will be given by (eq.5.22):

$$\varepsilon_1 = \frac{\sigma_y}{2E}[1-\nu-(1+\nu)\cos 2\theta_1] + \frac{\tau_{yx}}{E}(1+\nu)\sin 2\theta_1 \tag{5.24}$$

which shows that ε_1 is independent of shear stress τ_{yz}. It is clear that, in order to measure σ_y, τ_{yx}, and τ_{yz}, providing that we know E, ν, and the angle θ for every grating, we need 3 equations similar to eq.(5.24). Therefore, we need at least 3 FBGs embedded in the elastic material. Due to symmetry, the strain on a second FBG which lies on a plane parallel to yz plane at an angle θ_2 to the horizontal one (FBG_2, Fig.5.7) will be given by:

$$\varepsilon_2 = \frac{\sigma_y}{2E}[1-\nu-(1+\nu)\cos 2\theta_2] + \frac{\tau_{yz}}{E}(1+\nu)\sin 2\theta_2 \tag{5.25}$$

which is independent of the shear component τ_{yx}.

A simpler expression can be derived for the strain on the third grating by placing it horizontally (FBG_3, Fig.5.7), as given by eq.(5.22) for $\theta=0$:

$$\varepsilon_3 = \frac{-\nu\sigma_y}{E} \tag{5.26}$$

Eq.(5.26) shows that the horizontal FBG is insensitive to the shear stress applied on the top surface. Eq.(5.24) to eq.(5.26) is a system of 3 equations where the unknowns are the three components of stress. The strains ε_1, ε_2, and ε_3 will be calculated from the Bragg wavelength using eq.(5.23).

We will now examine the solution of the above system of equations. The system can be written in a matrix form:

$$\begin{bmatrix}\varepsilon_1\\ \varepsilon_2\\ \varepsilon_3\end{bmatrix} = \begin{bmatrix}A_1 & B_1 & 0\\ A_2 & 0 & B_2\\ C & 0 & 0\end{bmatrix}\begin{bmatrix}\sigma_y\\ \tau_{yx}\\ \tau_{yz}\end{bmatrix} \tag{5.27}$$

where:

$$A_1 = \frac{1-\nu-(1+\nu)\cos 2\theta_1}{2E} \tag{5.28}$$

$$A_2 = \frac{1-\nu-(1+\nu)\cos 2\theta_2}{2E} \tag{5.29}$$

$$B_1 = \frac{(1+\nu)\sin 2\theta_1}{E} \tag{5.30}$$

$$B_2 = \frac{(1+\nu)\sin 2\theta_2}{E} \tag{5.31}$$

$$C = -\frac{\nu}{E} \tag{5.32}$$

The system shown in eq.(5.27) can be solved for σ_y, τ_{yz}, and τ_{yx}, if only the coefficient matrix is reversible, which requires that:

$$\begin{vmatrix}A_1 & B_1 & 0\\ A_2 & 0 & B_2\\ C & 0 & 0\end{vmatrix} = B_1B_2C \neq 0 \tag{5.33}$$

The above condition is satisfied because $C\neq0$ (eq.5.32), $B_1\neq0$ and $B_2\neq0$ for $\theta_1\neq0$ and $\theta_2\neq0$ (eq.5.30 and eq.5.31 respectively). Hence the system has the unique solution:

$$\begin{bmatrix} \sigma_y \\ \tau_{yx} \\ \tau_{yz} \end{bmatrix} = \begin{bmatrix} 0 & 0 & \frac{1}{C} \\ \frac{1}{B_1} & 0 & -\frac{A_1}{B_1 C} \\ 0 & \frac{1}{B_2} & -\frac{A_2}{B_2 C} \end{bmatrix} \begin{bmatrix} \varepsilon_1 \\ \varepsilon_2 \\ \varepsilon_3 \end{bmatrix} \tag{5.34}$$

The strains ε_1, ε_2, and ε_3, can be calculated by measuring the Bragg wavelength shift of the corresponding FBGs using eq.(5.23). We conclude therefore that three FBGs are only necessary to resolve the vertical and shear components of stress acting on the top surface of the sensor.

The two inclined gratings, FBG_1 and FBG_2, were placed at the same angle θ in order to achieve equal sensitivity of those two gratings to σ_y, τ_{yx} and σ_y, τ_{yz} respectively, as can be inferred by the symmetry of eq.(5.24) and eq.(5.25). However, if a particular application of the sensor requires different sensitivity at y and z directions, the fibres can be placed at different angles. The system of equations will still have a unique solution given by eq.(5.32) for different coefficients A, B, and C.

5.2.4 Estimation of E value and angle θ for optimal performance

Eq.(5.24) can be used to calculate the required Young's modulus E of the elastomer. We need to find the E value which will make maximum use of the available strain range of the fibre. This condition will provide maximum sensitivity without overstraining the fibre. As it has already been mentioned, the typical strain range for telecommunication fibres used in this application is ±2500με.

The axial strain which will be transferred on the fibre also depends on the value of the Poisson's ratio ν. Typical value for ν for solid polymers is in the range of 0.35 to 0.45 (Hull and Clyne, 1996, pg.11). In this theoretical analysis we assume the average value ν=0.4.

The angle θ also affects the axial strain on the fibre, eq.(5.24). The nature of the glass fibre as well as the dimensions of the sensor, set the limit for the maximum angle that the fibre can be embedded into the material. The sensor will eventually be mounted in a 3mm thick insole, which will accommodate the elastomer sensor and the optical fibres. The inclined fibre will therefore be necessary to be bent inwards after leaving the sensor. A large bending radius could result in increased bending loss of the optical power, or to fibre breakage. For the particular fibre used in the laboratory testing of the sensor we found experimentally that no significant bending loss (which would produce deterioration of the FBG readout system resolution, as discussed in section 3.6.2) occurs for bending up to approximately 30°. The theoretically predicted strain on the fibre will therefore be tested for θ in the range 0 to 30°.

The axial strain on the fibre, for different values of E and θ, can be calculated by eq.(5.24), where the vertical stress σ_y varies from 0 to –500kPa, and the shear stress τ_{yx} from –250 to 250kPa, which cover the required operating range of the sensor. Maximum axial strain occurs for σ_y= –500kPa and τ_{yx}=250kPa. The maximum values are plotted in Fig.5.9 for several θ and E values. The minimum axial strain (maximum axial compression of the fibre) occurs for σ_y=0 and τ_{yx}= –250kPa, and is given in Fig.5.10 for several θ and E values. Examining those plots we conclude that safe operation of the sensor under any value of angle θ can only be guaranteed if E≥136MPa where the maximum strain does not exceed the safety limit of 2500με. Further increase of E value (use of harder material) will suppress the operating range by reducing the induced strain on the fibre, and hence decrease the sensitivity of the sensor. For optimal operation, it is therefore necessary to choose E=136MPa.

The predicted strain range of the FBG embedded in a material having E=136MPa, as a function of angle θ, is given in Fig.5.11. Each data point is the relative difference between the maximum and minimum values, as plotted in Fig.5.9 and Fig.5.10 respectively for E=136MPa. The plot shows that maximum sensitivity will be achieved for θ=30°. In that case, the operating range of the FBG will be –2270 to +2368με.

The predicted induced strain on the inclined FBGs for the optimal values E=136MPa and θ=30° as a function of vertical and shear stress is given in the contour plot in Fig.5.12(left). The predicted induced strain on the horizontal grating (FBG_3), for E=136MPa, is also given in Fig.5.12(right). The operating range in this case is 0 to +1470με, which is inside the safe for the fibre region.

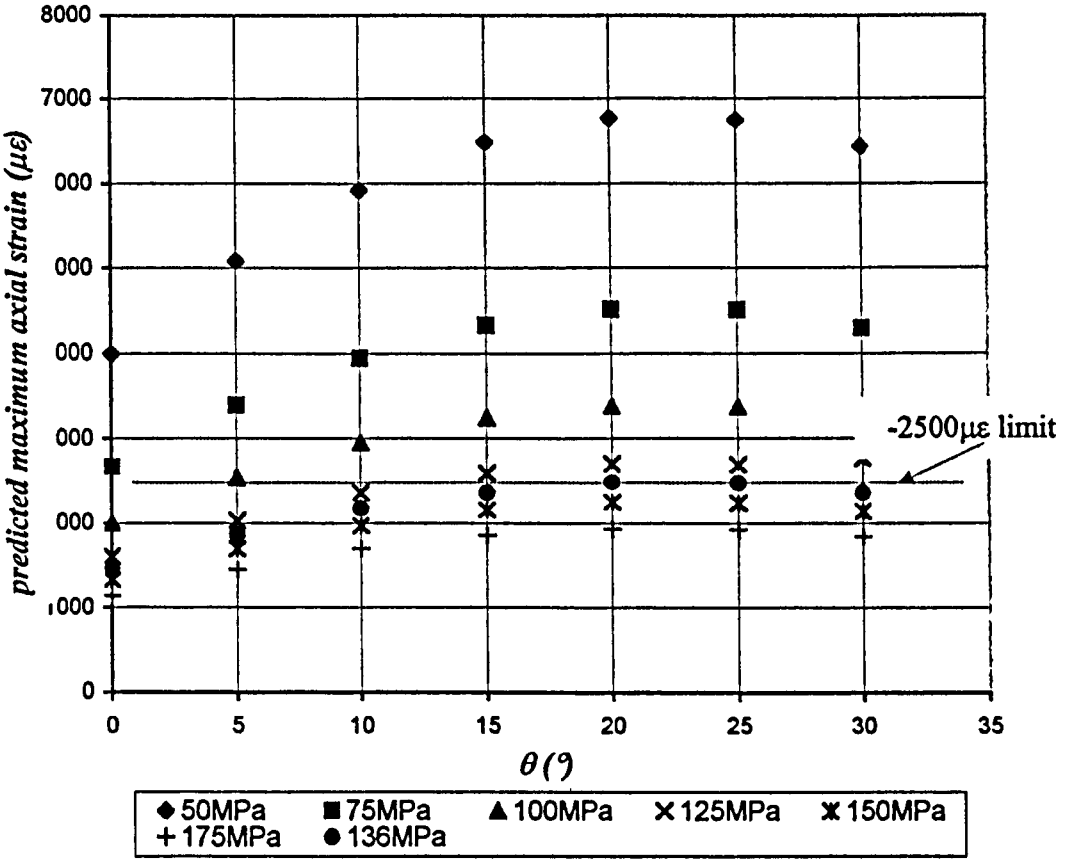

Fig.5.9: Modelled maximum axial strain on the fibre as a function of angle θ, for several E values.

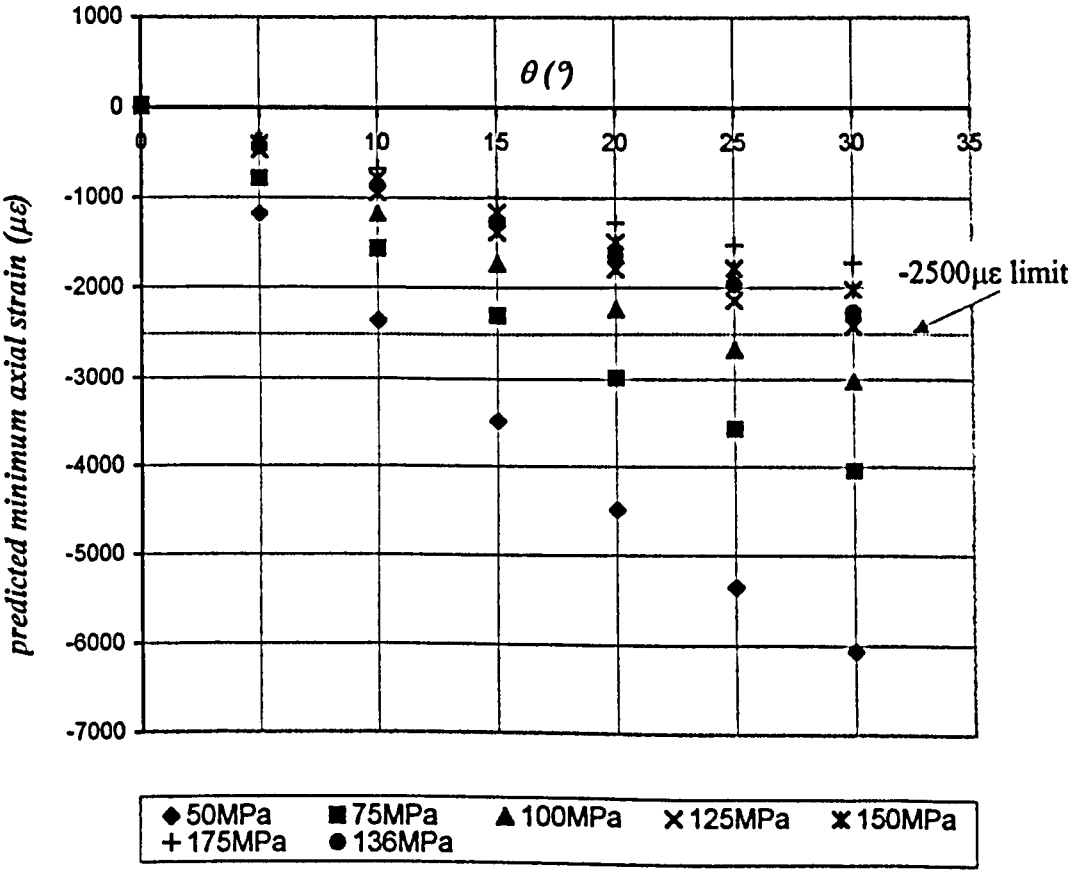

Fig.5.10: Modelled minimum axial strain on the fibre as a function of angle θ, for several E values.

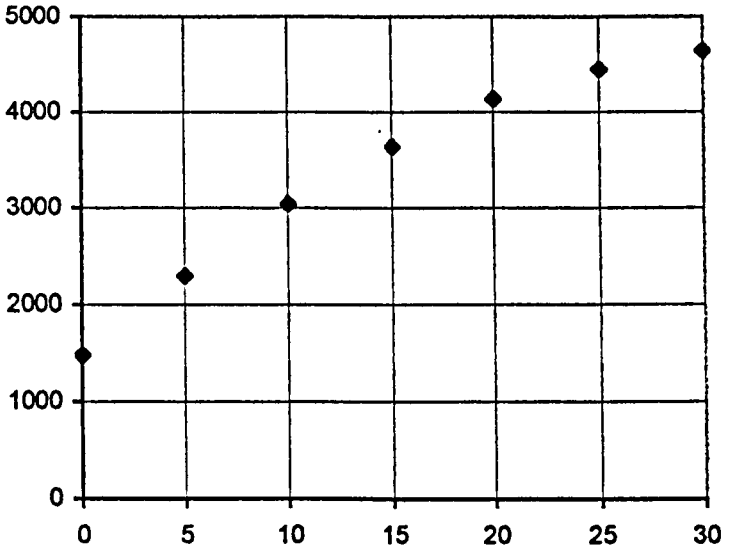

Fig.5.11: Operating strain range for a FBG embedded in a E=136MPa elastomer, as a function of angle θ.

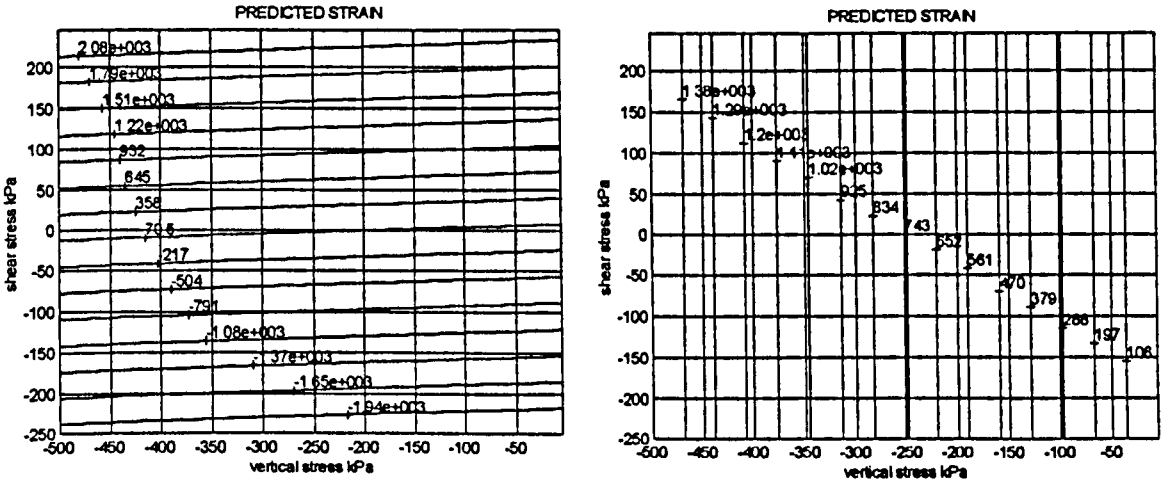

Fig.5.12: Predicted axial strain (in με) on the inclined FBGs for E=136MPa and θ=30° (left), and for the horizontal FBG for E=136MPa (right) as a function of shear and vertical stress.

Due to the relatively low ratio of height to width of the sensor, the optimal angle θ=30° cannot be achieved in this particular implementation of the sensor. That would require the fibre to leave the sensor from the horizontal surfaces (upper or lower surface) instead of the sides of the sensor. The condition which must be satisfied, in order to ensure that the fibre will enter and leave the material from the two opposite side surfaces of the sensor, is (Fig.5.13):

$$\theta \leq \arctan\frac{h}{w} = \arctan\frac{3mm}{10mm} \approx 17^{\circ} \tag{5.35}$$

where h and w is the height and width of the sensor. In applications where the height of the sensor is not restricted to 3mm the angle can be increased up to the optimal value of 30°. The same could be achieved by keeping h=3mm and reducing the width and depth of the sensor. For example, if w=5mm, eq.(5.35) gives θ≤31°. A reduction of the width and depth of the sensor is possible as long as the grating region of the fibre remains entirely inside the material, which is obvious for short gratings (length <2mm). However, in order to keep the construction of the sensor as simple as possible, we kept the dimensions of the sensor to the initial specifications (10x10x3mm) throughout this study.

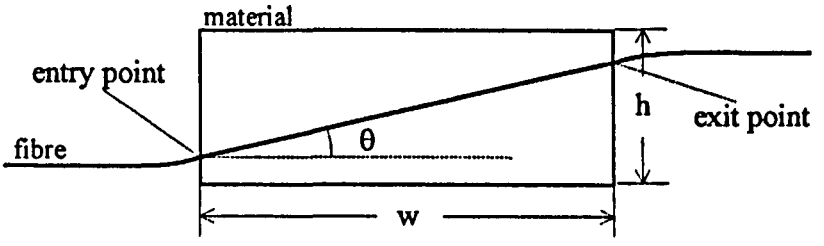

Fig.5.13: Dimensional restriction of maximum angle θ.

Assuming the maximum permitted angle θ=17° and using eq.(5.24) we obtain the optimal value for E modulus, which in this case is E=133MPa. The operating range in this case is -1461 to +2496με. The predicted induced strain on the inclined FBGs for E=133MPa and θ=17° as a function of vertical and shear stress is given in the contour plot in Fig.5.14(left). The predicted induced strain on the horizontal grating (FBG_3), for E=133MPa, is also given in Fig.5.14(right).

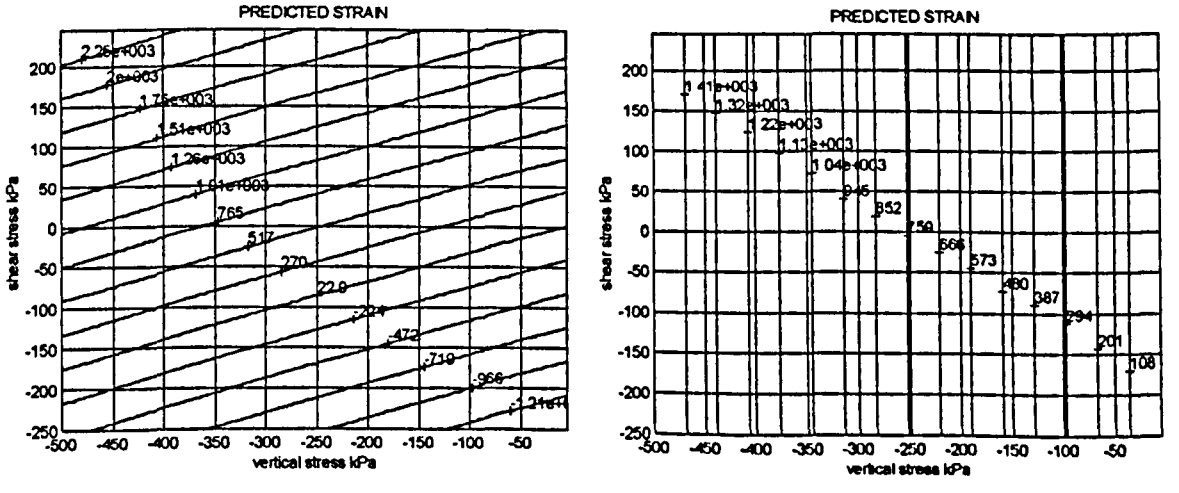

Fig.5.14: Predicted axial strain (in με) on the inclined FBGs for E=133MPa and θ=17° (left), and for the horizontal FBG for E=133MPa (right) as a function of shear and vertical stress.

We have assumed so far that the Poisson's ratio is constant and equal to ν=0.4. An estimation of the sensitivity of the axial strain in the fibre to ν can be obtained by examining how the maximum predicted axial strain varies with ν. The maximum strain was previously found to be +2496$\mu\varepsilon$. (for E=133MPa, θ=17°). If we assume the minimum value of ν, which is equal to 0.35, then eq.(5.24) gives ε_{max}=2300$\mu\varepsilon$. This corresponds to error in estimating the axial strain equal to −8%. If on the other hand, we assume the maximum value ν=0.45, then the maximum axial strain is ε_{max}=2749$\mu\varepsilon$, which corresponds to error equal to +10%.

5.2.5 Material requirements

Some important specifications of the material have already been presented in the previous section during the theoretical analysis of the sensor, and are directly related to the assumptions mentioned in section 5.2.2. The properties are summarised here:

- Linear elastic material under the expected stresses. Viscoelasticity should be as low as possible.
- Good adhesivity with the glass fibre to avoid debonding and slippage of the fibre.
- Material insensitive to temperature variations. The thermal expansion coefficient of the material must be low. In the opposite case, the dimensions of the sensor, and hence the stress distribution inside the material, will be altered. The elastic parameters of the material (E, G, ν) must also be ideally insensitive to temperature.
- E and ν values should be close to the theoretical optimum values discussed in section 5.2.4.

In order to simplify the fabrication, and to enable the laboratory testing of the sensor, the material is required to satisfy some additional requirements:

- The material must be in a proper form to enable the embedding of the fibres. Several materials are in liquid form prior to polymerisation. Those are ideal for this application, since the fibres can be aligned in a proper mould which can then be filled with the liquid elastomer and held until cured. All the materials examined in this study were of this type (see next section).
- The curing of the material should not require high pressure or temperature. Prolonged exposure of the Bragg gratings to elevated temperatures results in reduction of the grating reflectivity. Erdogan *et al.* (1994) have measured the Bragg grating thermal decay of FBGs written in Ge-doped fibre. Permanent reduction of the grating strength by 75% of it's initial strength at 25°C was observed after heating the grating to 350°C for 70min and then further heating to 550°C for 80min. Some polymers, like for example

PVCs, require temperatures in the range 300-600°C for polymerisation (Ashby, 1993, pg.187), therefore should be avoided for the sensor fabrication.

- Shrinkage of the material occurs during curing. This will result in permanent prestraining of the embedded grating or bending of the fibre inside the material. It can also lead to distortion of the shape of the sensor. Those situations can result in unpredicted behaviour of the sensor or sensor damage. Materials which exhibit low shrinkage are preferred.
- Due to the delicate nature of the optical fibre, the material should be easily removable from the mould in order to avoid bending moments on the fibre which could result in fibre breakage. The material should therefore not react with the mould or mould releasing agents.

The application of the sensor for in-shoe measurements, the material must also comply with the following requirements:

- Non-toxic and hypoallergenic.
- The elastic properties of the material should be insensitive to moisture for a time period at least equal to the duration of a typical measurement on the subject, which is expected to be less than 10mins.

5.3 Experimental results

The experimental evaluation of the elastomer sensor design begins with the measurement of the elastic properties of the material. The results from the measurement of the Young's modulus for the selected materials are given in section 5.3.1.1. The measurement of shear modulus is given in section 5.3.1.2.

The first implementation of the sensor, which utilises only one FBG embedded horizontally in the elastomer, is presented in section 5.3.2. The response of the sensor to vertical stress will also be discussed.

5.3.1 Material characterisation

The first task was to find the material with the required E and ν values. Categories of materials that cover the range 100-200MPa are soft PVC, soft epoxies, silicone elastomers, and plastics with several compositions. Information on the chemical composition, fabrication, physical properties, and main applications of solid polymers can be found on many handbooks for materials (Ashby, 1993; Shakelford *et al.*, 1994). Although the required specifications were well known, the choice of the appropriate material was difficult due to the lack of information regarding the elastic properties for every material. The precise value of E, G and ν are not usually given in the data sheet supplied by the manufacturers because

those values are highly dependent upon the composition of the material and the fabrication procedure. Samples of materials were therefore ordered and the elastic parameters measured.

Five samples were chosen:

1. SYLGARD-184, Dow Corning, 2-part silicone rubber.
2. EPOTEK-310, Epoxy Technology, 2-part epoxy resin.
3. TRACAST-3010 RESIN, TRA-CON Inc., 2-part epoxy resin.
4. ATLAS 60/40/19/24, Rutherford Appleton Laboratory, 2-part epoxy resin.
5. SCOTCHCAST 815, 3M, 2-part epoxy resin

The above materials were selected mainly because they are all in liquid state, having E values of the same order of magnitude as that required. Curing starts after mixing the two parts in a particular ratio. Materials 1, 2, 3, and 5 are low temperature cured. Material 4 requires heating at 90° for 24h in order to be cured. Even though material 4 should be avoided for the sensor fabrication (section 5.2.5), it was useful to measure its elastic properties, since it was the only material with Young's Modulus given by the manufacturer (E=142MPa), provided that the recommended mixing ratio and curing scheme is carefully followed. It provides the reference for testing the accuracy of the experimental setup.

5.3.1.1. Measurement of E modulus

The experimental setup for measuring E value was described in section 3.1.4. The samples were made equal to the actual dimensions of the sensor, 10x10x3mm. The vertical compression was varied by discretely increasing the weight of the top plate. The plate was manually moved on and off the top plate. The weights plate was slowly placed on the top plate to prevent high impact forces which could damage the force sensor. The plate was then lifted rapidly.

Fig.5.15 shows the time responses of the force and micrometer sensor when the only the weights plate is slowly placed over the top plate and then released, for the EPOTEK sample. The viscoelastic behaviour of the material is clearly observed. Comparing the micrometer output trace with the creep curve shown in Fig.5.5(b) (section 5.1.4), we observe the relatively fast reduction of the vertical strain (absolute value) immediately after removing the load, followed by a further slow reduction due to creep. The material returns to its initial dimensions approximately 15s after load removal.

It was observed experimentally in many measurements for all the samples tested, that the micrometer output changes rapidly for approximately 0.1s after removing the load, and then continues to decrease due to creep of the material. The voltage ΔV_e measured during that time can therefore be considered as the displacement corresponding to the purely elastic deformation of the material.

Fig.5.16 to Fig.5.19 show the time responses for the other 4 samples tested. Viscoelastic behaviour is observed in all the materials. TRACAST response is less

viscoelastic compared to the other materials, where the creep deformation is approximately 20% of the elastic deformation of the material. ATLAS epoxy shows the strongest viscoelastic behaviour, where the deformation due to creep is approximately 140% of the elastic deformation. In terms of viscoelasticity, TRACAST is the most appropriate material for the sensor implementation.

The stress – strain curve was measured for every sample by measuring the voltage ΔV_e and applying eq.(3.7) (strain due to elasticity), and the vertical stress by measuring ΔV_l and applying eq.(3.4), for different vertical loads. The results are given in Fig.5.20 to Fig.5.24 for all five materials.

Because of the manual lifting of the weights plate, the experiment suffers from low repeatability. The error in measuring voltage ΔV_e is the result of the uncertainty in identifying the precise location in time of the 0.1s interval of the transient. The faster the lifting of the weights, the easier it is to observe the discontinuity in the recorded micrometer trace. The non-repeatability increases as the weight since the effort to lift the weights is getting higher. In order to reduce this problem as much as possible, each data point was taken after recording the micrometer trace for 5 to 10 loading circles (total time approx. 1min) and measuring the sharpest of the obtained transients only. The time responses shown in Fig.5.15 to Fig.5.19 are the selected ones for each material and for the particular vertical stress of 78kPa. Careful observation of the traces in Fig.5.17 and Fig.5.18 for example, shows that both traces displayed in Fig.5.18 are sharper than the ones shown in Fig.5.17. In the later case it is relatively difficult to accurately set the reference lines and measure ΔV_e.

Due to the poor repeatability of the measurements, it is not possible to confidently conclude on the precise shape of the stress – strain curve. SYLGARD and TRACAST responses are close to linear, whereas EPOTEK seems to increase stiffness as the stress increases. The data points in case of ATLAS and SCOTCHCAST on the other hand show a slight sigmoid stress – strain curve.

Since the purpose of testing the material at this initial stage of the sensor design was to get an estimation of the E value, rather than to accurately characterise it, we will assume that the stress-strain response is linear. The Young's modulus will be given by the slope of the linear trendlines drawn in Fig.5.20 to Fig.5.24 based on the experimental data. Table 5.1 gives the measured E-modulus for the 5 materials. Only the ATLAS sample is close to the theoretically required value (133MPa) which was rejected for the sensor implementation due to the high curing temperature as well as the relatively strong viscoelastic behaviour. The E modulus for the rest of the samples is significantly lower than the required.

The measured E value for ATLAS is approximately 118MPa, instead of 142MPa as given by the manufacturer. Possible reasons for the error are:

1. Different mixing ratio, curing conditions (temperature and duration), or environmental conditions during testing.
2. Error due to the choice of the 0.1s time where elastic relaxation of the sample occurs, which was purely based on the experimental observations of the time response curves.

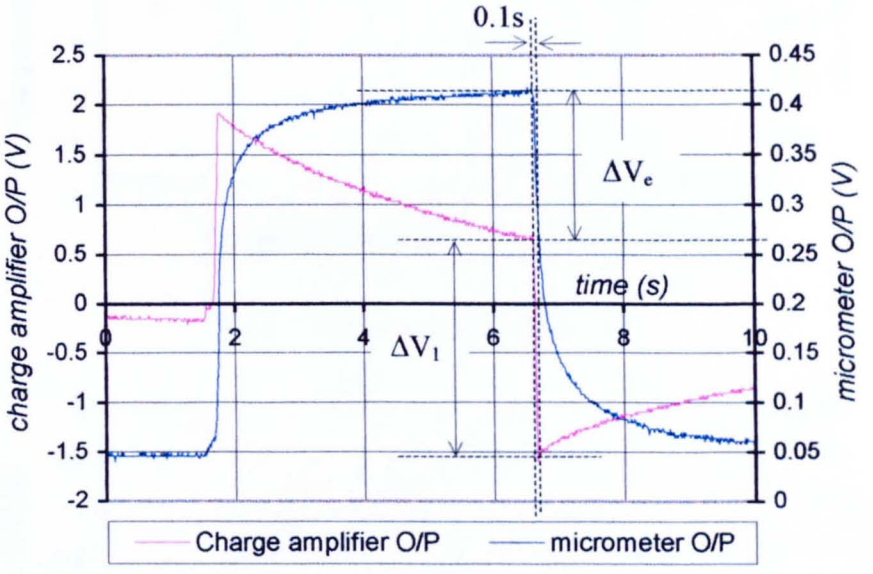

Fig.5.15: Time response of EPOTEK.

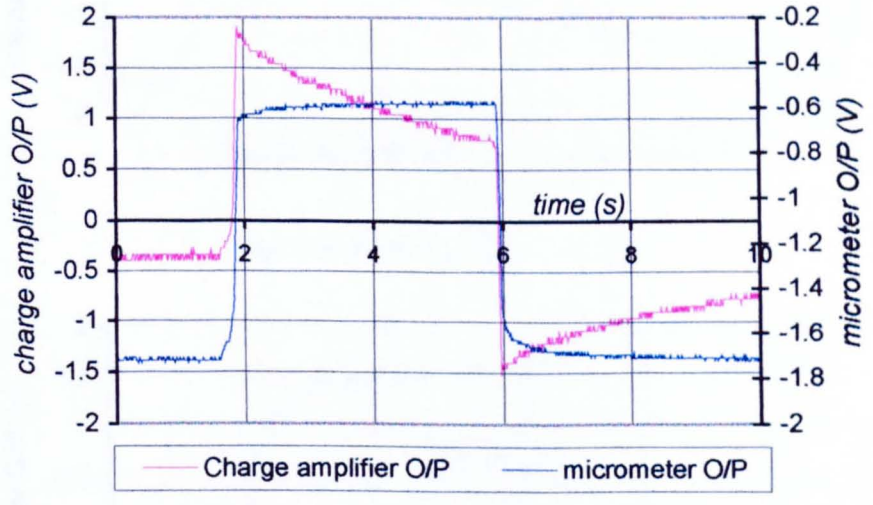

Fig.5.16: Time response of SYLGARD.

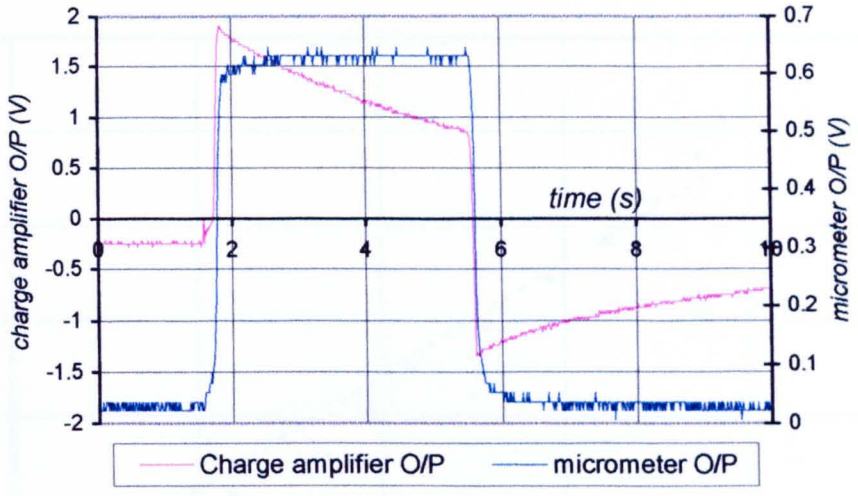

Fig.5.17: Time response of TRACAST.

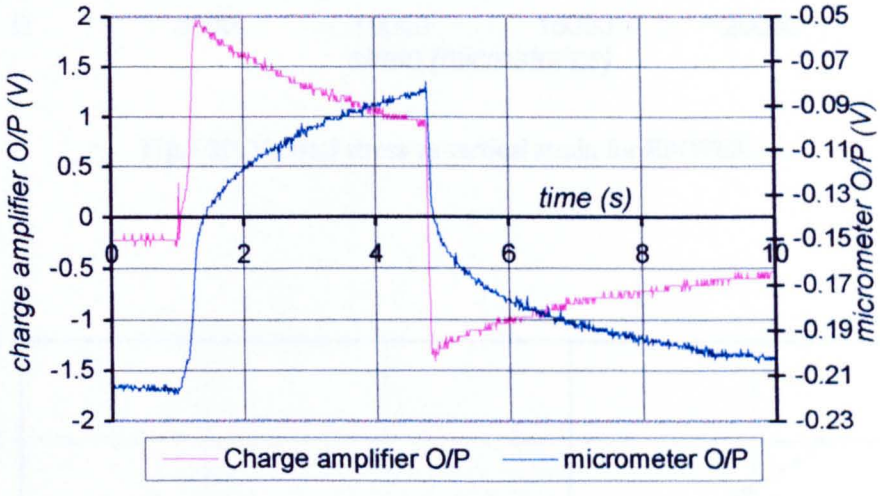

Fig.5.18: Time response of ATLAS.

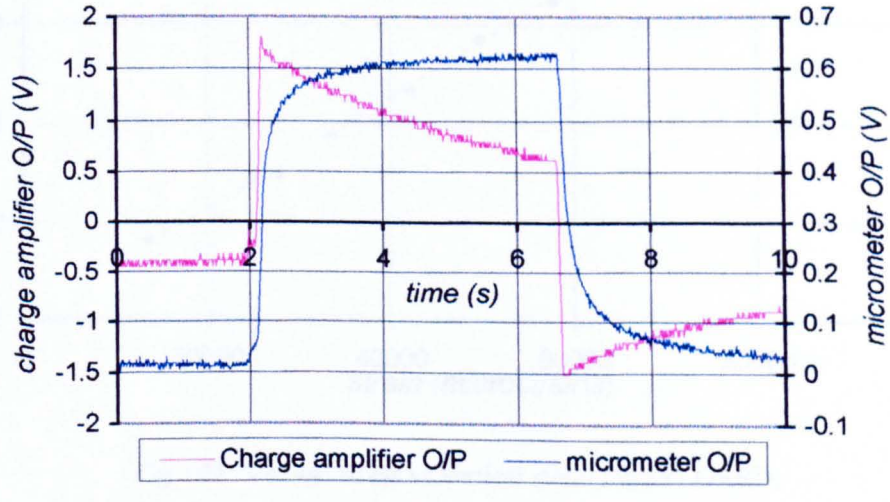

Fig.5.19: Time response of SCOTCHCAST.

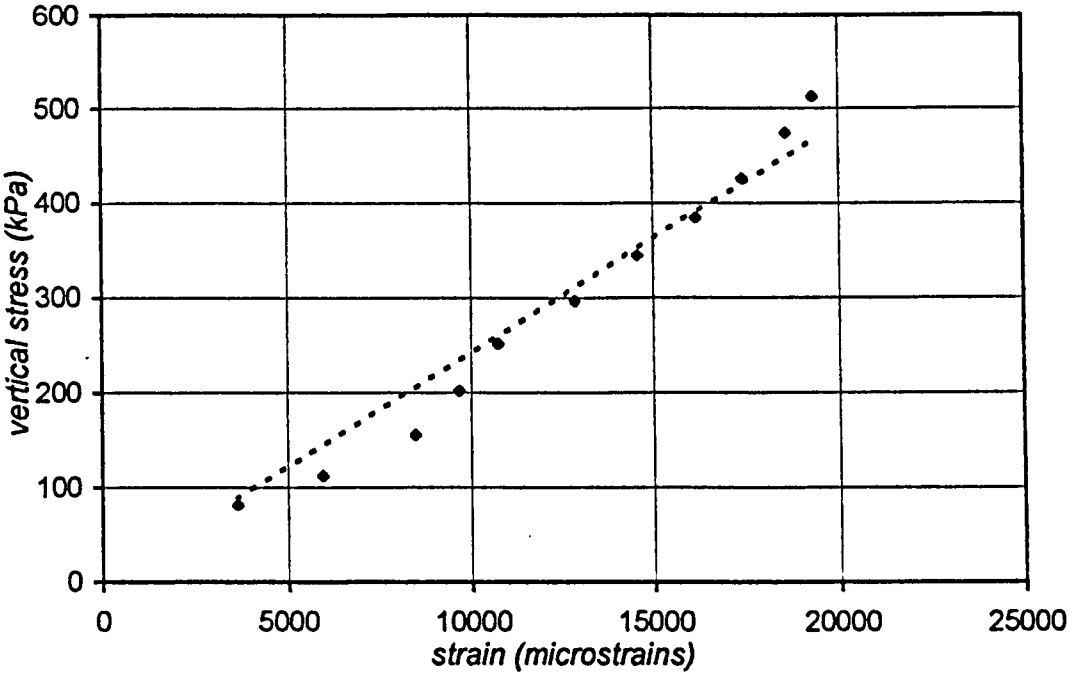

Fig.5.20: Vertical stress vs vertical strain for EPOTEK.

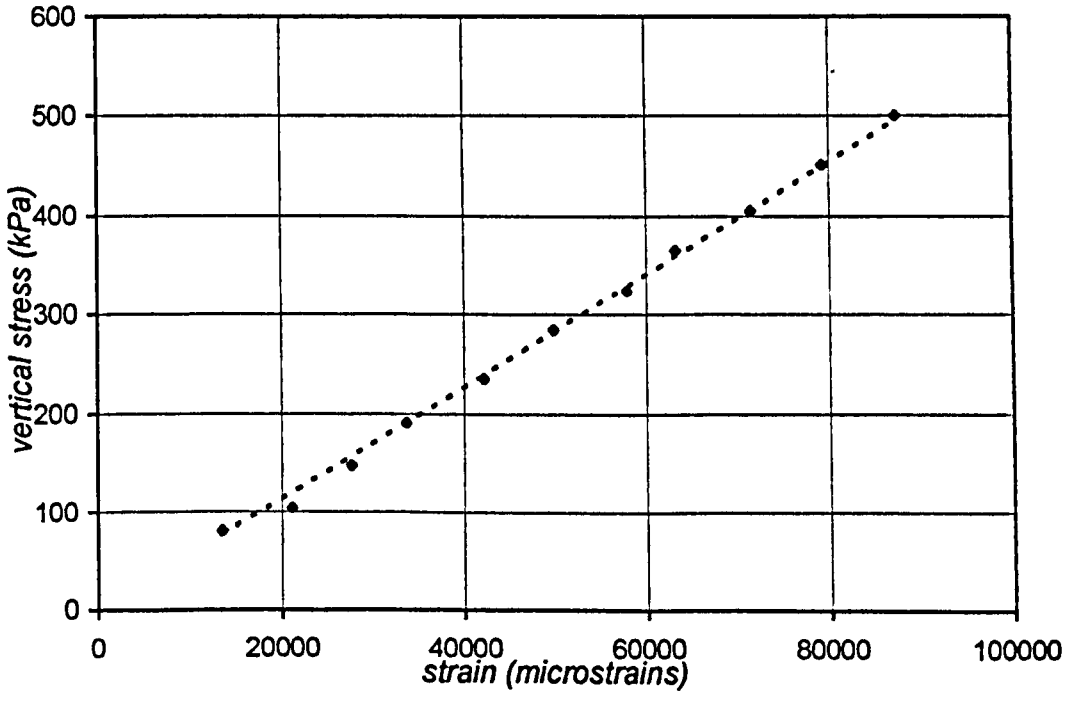

Fig.5.21: Vertical stress vs vertical strain for SYLGARD.

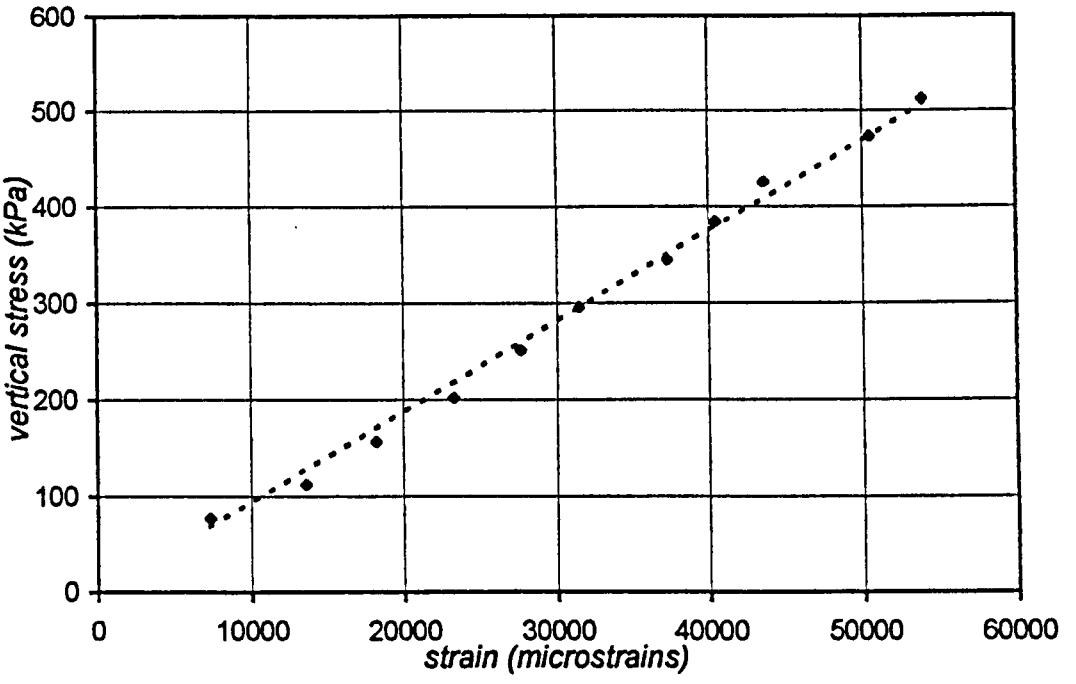

Fig.5.22: Vertical stress vs vertical strain for TRACAST.

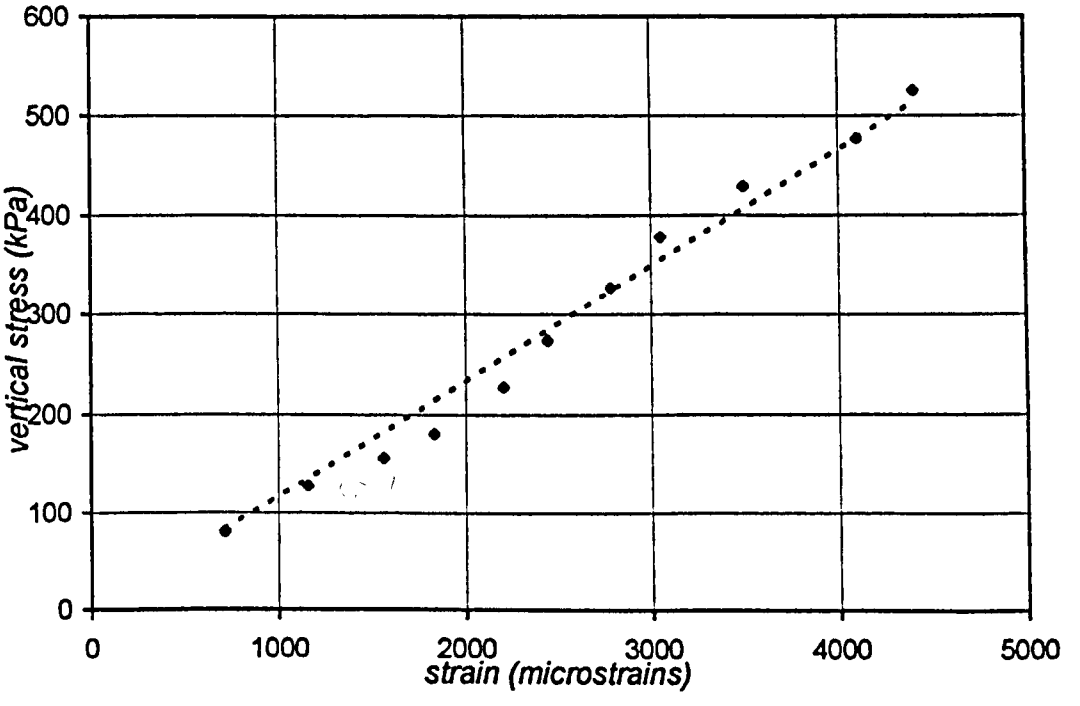

Fig.5.23: Vertical stress vs vertical strain for ATLAS.

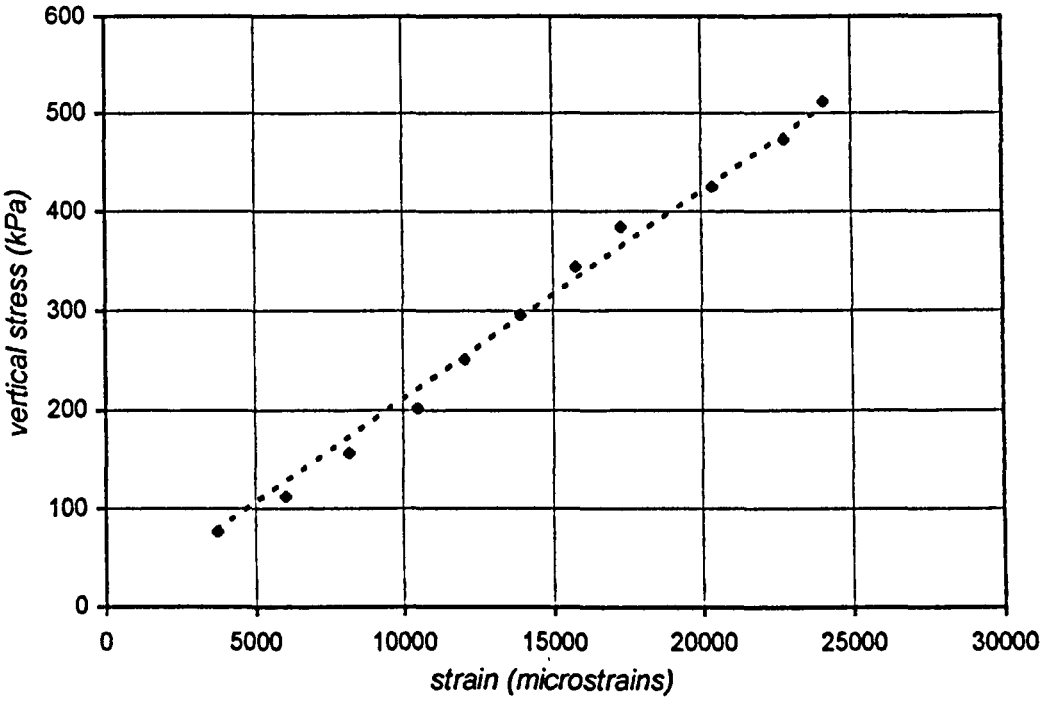

Fig.5.24: Vertical stress vs vertical strain for SCOTCHCAST.

Material	E modulus (MPa)
EPOTEK	25
SYLGARD	6
TRACAST	10
ATLAS	118
SCOTCHCAST	21

Table 5.1: Measured values of Young's modulus of elasticity.

5.3.1.2. Measurement of G modulus

The method for measuring G modulus was presented in sections 3.1.2 and 3.1.3. The vertical load, which provides the necessary friction between the material under test and the testing apparatus, was kept constant throughout this experiment, equal to 250kPa. The measurements were taken on the same samples used previously for the E-modulus measurement. The shear stress was applied using the E/M vibrator, which was driven by variable amplitude, 0.5Hz square pulses. The same procedure as the one described in the previous section was used to measure the elastic deformation of the material.

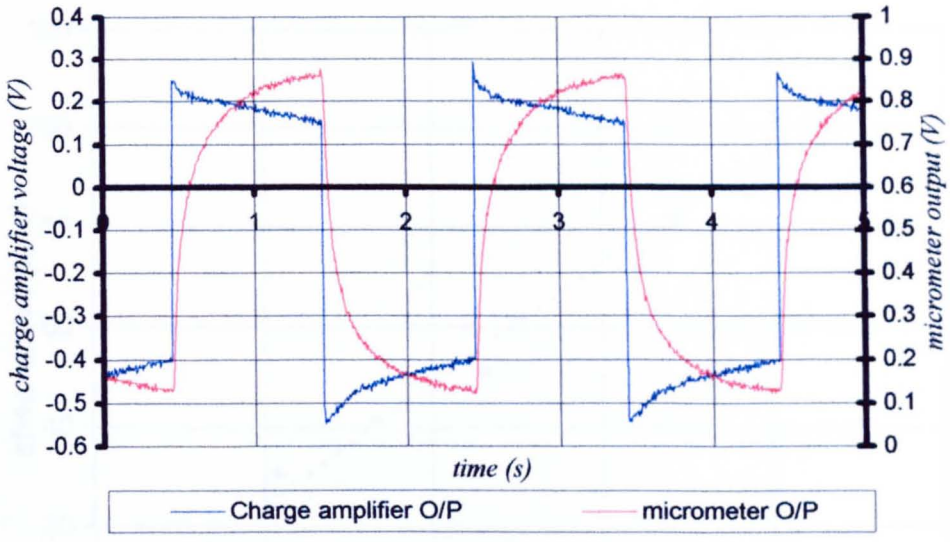

Fig.5.25: Time response of force and displacement transducers for SCOTCHCAST.

The measured shear stress – shear strain response for each material is given in Fig.5.26 to Fig.5.30. The measurements were restricted to a maximum shear of approximately 120kPa in order to avoid slippage between the top plate and the samples. The G value is calculated from the slope of the linear trendline, given in Table 5.2.

Application of eq.(5.11) gives the value of the Poisson's ratio ν:

$$\nu = \frac{E}{2G} - 1 \tag{5.36}$$

Using the measured values for E (Table 5.1) and G (Table 5.2) we obtain an overestimation of ν, which cannot be accepted since it exceeds the expected range of 0.35 to 0.45. In the case of ATLAS for example, the measured value are ν=1, which is the smallest value of the materials tested. The other extreme was SCOTCHCAST, which gives ν=2.7. A possible reason for this error is the uncertainty in separating the pure elastic response from the viscoelastic creep, which was done by measuring the response in the 0.1s interval. A second reason is the assumption of linear viscoelastic[1] behaviour of the materials where the linear approximation of the stress – strain curves is based on. Eq.(5.34) is valid if only the stress on the material does not exceed the linearly elastic region, which cannot be examined using this particular experimental setup.

[1] Linear viscoelastic behaviour occurs when the deformation of the material is described by combining Hook's Law of elasticity (eq.5.1), and the Newton's Law of viscosity (Ward, 1983, pg.80).

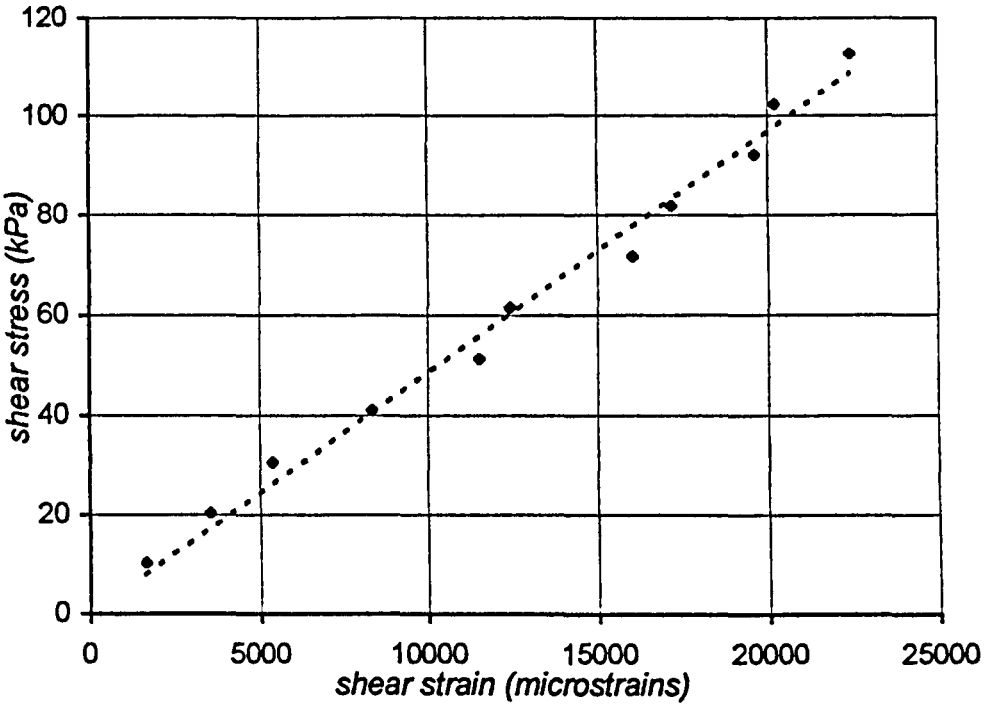

Fig.5.26: Shear stress vs shear strain for EPOTEK.

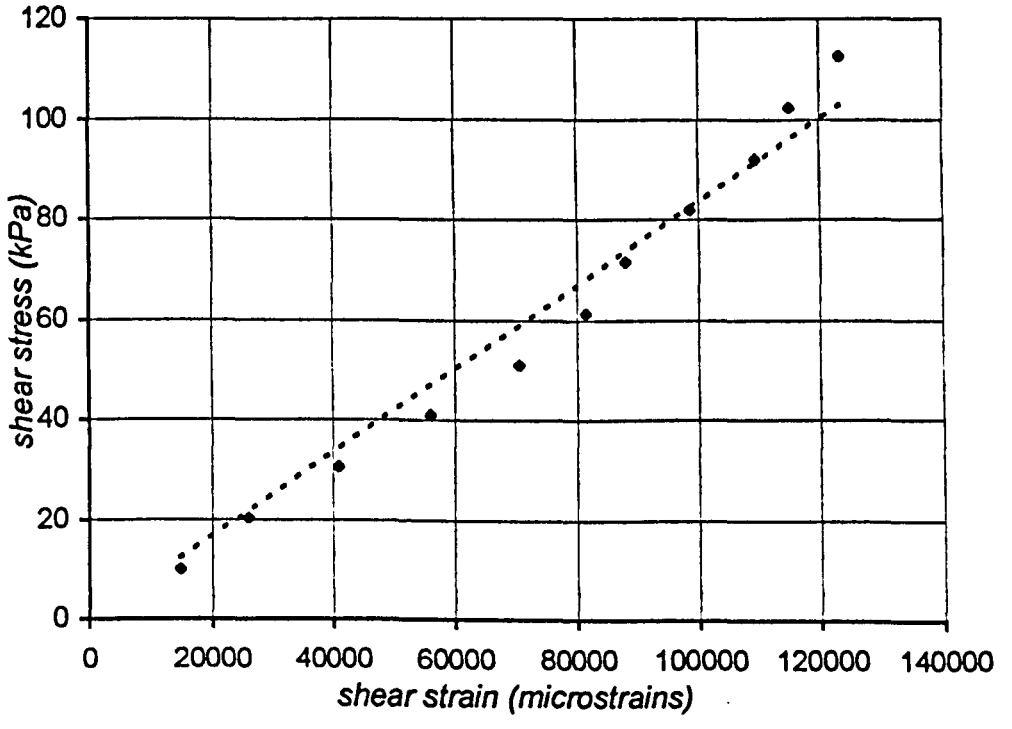

Fig.5.27: Shear stress vs shear strain for SYLGARD.

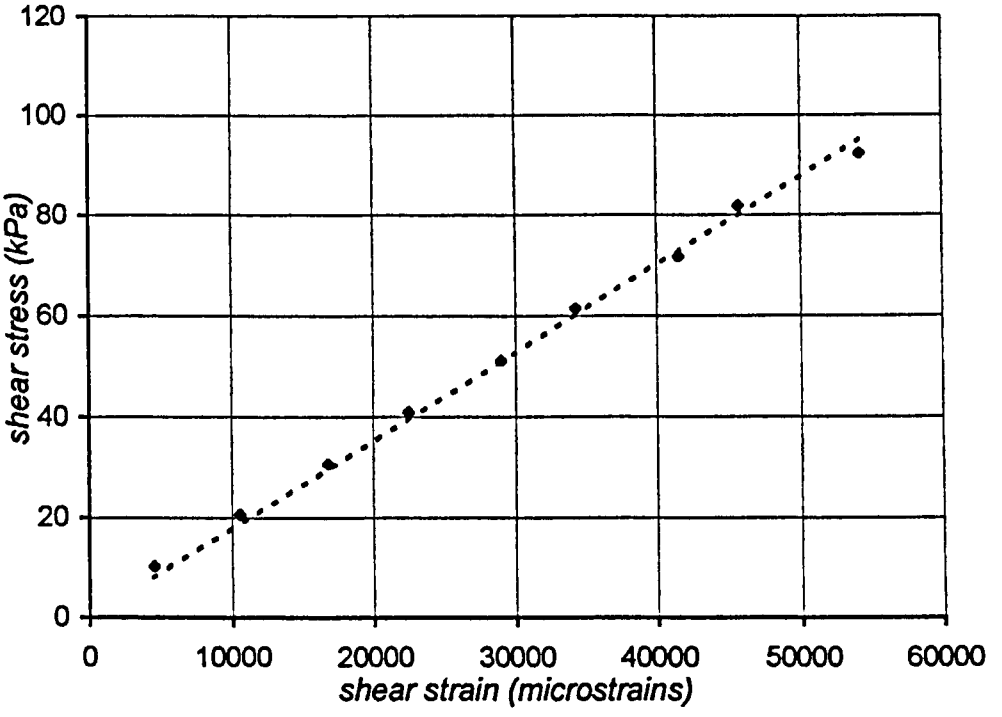

Fig.5.28: Shear stress vs shear strain for TRACAST.

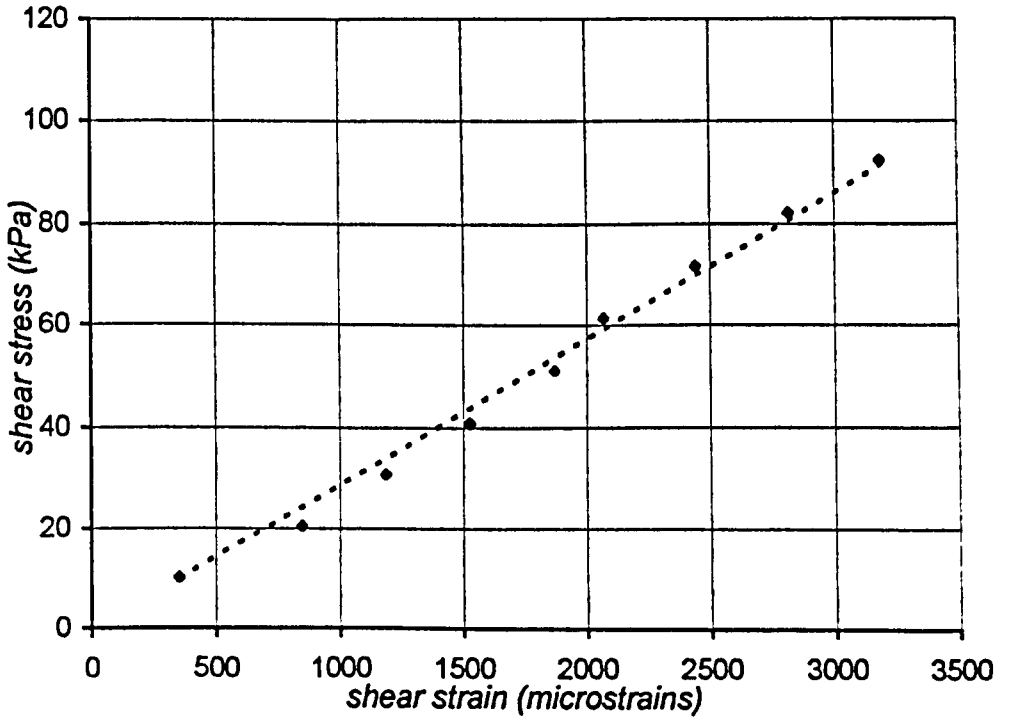

Fig.5.29: Shear stress vs shear strain for ATLAS.

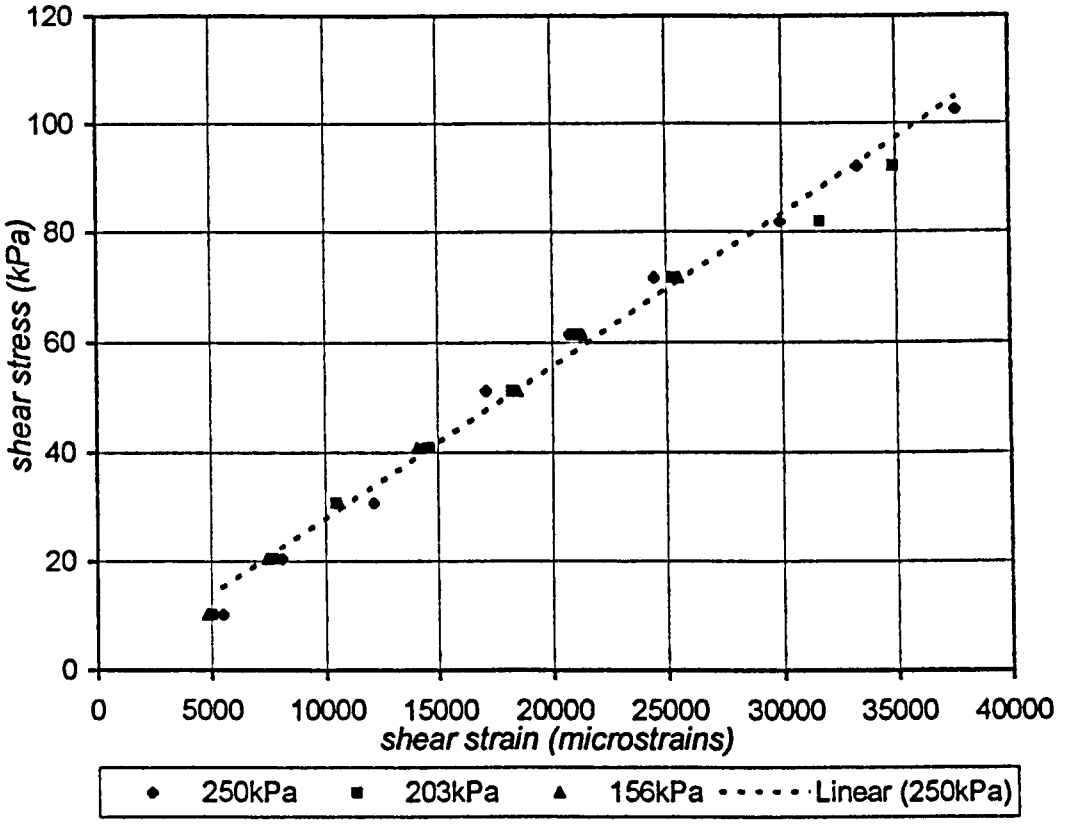

Fig.5.30: Shear stress vs shear strain for SCOTCHCAST.

The presence of the vertical stress has little effect on the stress – strain curve. Fig.5.30 shows the data points measured under 3 different vertical stresses, 250, 203, and 156kPa, where no significant change of the curve is observed. The maximum applied shear stress was 70kPa for a vertical stress of 156kPa, and 90kPa for a vertical stress of 203kPa, which are the limits before slippage.

Material	G modulus (MPa)
EPOTEK	5
SYLGARD	0.9
TRACAST	1.8
ATLAS	29
SCOTCHCAST	2.8

Table 5.2: Measured values of shear modulus of elasticity.

5.3.1.3. Comments on material testing

The experimental setup used for the for the measurement of the elastic properties of the material has the following disadvantages:

1. It can only be used to measure E and G values at low frequencies. For the complete design and characterisation of the sensor, dynamical measurement of the elastic parameters will be necessary (measurement of complex E and G modulus, Ward, 1983, pp.95-107). In particular, static measurement of the E modulus can only be done, since the vertical load is manually lifted. Regarding the shear modulus, dynamic measurements up to 10Hz can only be measured, as discussed in section 3.4.
2. Poor repeatability which introduces uncertainty in the stress – strain curve, as explained in section 5.3.1.1.

However, this experiment provided an estimation on the average value of the E and G modulus, which was not known by the manufacturers (except ATLAS epoxy), both key parameter in selecting the proper material for the sensor implementation (section 5.2.5). Even though the experimental setup cannot be used to accurately measure E and G, it provides information on the relative stiffness between samples. Comparing the stiffness of the materials in terms of E value (Table 5.1), or G value (Table 5.2), we obtain the same sequence in terms of stiffness (with ATLAS being the stiffest) regardless of the property we examine.

The experiments for measuring the material properties were important to observe the viscoelastic creep, to measure its magnitude compared to the elastic deformation, and to compare the samples in terms of viscoelasticity.

Several techniques have been developed for the dynamic measurement of viscoelasticity in solids. A popular industrial technique for polymer evaluation is the vibrating reed technique, first introduced by Horio and Onogi, 1951. A small sample is clamped on a vibrating apparatus which is driven by a variable frequency oscillator (typical range 200-1500Hz). The motion of the sample modulates the intensity of the light arriving on a photodetector. Measuring the amplitude of the light intensity modulation, the resonance frequency can be measured. E modulus is a function of the resonance frequency and the dimensions of the sample. The entire apparatus is placed in a cryostat and measurements can be carried out over a wide temperature range (-150 to +200°C). The disadvantage of this method is that it only provides the E value at a particular frequency depending on the sample dimensions.

Another technique used for dynamical measurement of extensional E modulus, for materials having E>10MPa, has been presented by Pinnock and Ward (1966). The system uses a servo-controlled motor which provides sinusoidal strain on the sample. The stress is measured using a strain gauge attached on the other end of the sample. The frequency can be

varied up to 1kHz, and the phase between the stress and strain is recorded. The system is capable of measuring extensional E modulus at any frequency up to 1kHz, for temperatures between –150 to +200°C.

Ward (1983, pp.126-131) describes a method of measuring E modulus in the frequency range 1 to 10kHz using acoustic wave propagation on the sample. The Young's modulus is related to the propagation constant and the attenuation coefficient of the material, which are measured experimentally.

Commercially available systems are:

1. Polymer Laboratories Dynamic Mechanical Thermal Analyser (Polymer Laboratories Ltd., Church Stretton, Salop, UK).
2. Du Pont 981 Mechanical Analyzer (Du Pont Company, Scientific and Process Instruments Division, Wilmington, Delaware, USA).
3. The Autovibron (Toyo Baldwin Co. Ltd, Tokyo Japan).

5.3.2 Single-grating elastomer sensor

In order to experimentally evaluate the elastomer sensor response, a simple version of the sensor was fabricated. The sensor contains only one FBG which was horizontally embedded into the material. SCOTCHCAST was chosen for this implementation because it is low-temperature cured (25°C) and also exhibits the lowest shrinkage during curing, compared to the other 3 low-temperature cured materials. The sensor fabrication, which is a simpler version of the 3-fibre sensor, will be explained in chapter 6. A picture of the sensor is given in appendix II, picture 5. The specifications of the FBG are given in Table 3.13, where the transmission loss for this particular one is 4dB.

The objectives of the experiments on the simplified version of the sensor are:

1. To measure the response of the sensor to vertical stress, and compare it with the theoretically predicted one. The Bragg wavelength shift was measured using the setup presented in section 3.6.
2. To examine the effect of the presence of the optical fibre inside the material. This can be done by comparing the elastic properties of the material with and without FBG embedded into it. In this particular test we will compare the Young's modulus of SCOTCHCAST sample measured in section 5.3.1.1, with the Young's modulus of the single-fibre version of the elastomer sensor. For that purpose, the fabrication procedure of the material (mixing ratio, curing temperature and duration), as well as the dimensions of the material sample and elastomer sensor, were identical. The E value of the sensor was measured using the same experimental setup and procedure used for measuring the material sample, as described in sections 3.1.4 and 5.3.1.1.

3. To experimentally investigate the applicability and accuracy of the fibre-independent model for the analysis of the more complex version of the 3-fibre sensor.

Fig.5.31 gives the measured stress – strain curve of the sensor. The response of the material sample (see also Fig.5.24) is also drawn for comparison. The average E value of the sensor is calculated by the slope of the linear trendline, which gives E=25MPa. Comparing this with the E value of the material sample (E=21MPa), we notice an increase of stiffness due to the presence of the fibre. This is the first indication that the behaviour of the material is not independent of the fibre.

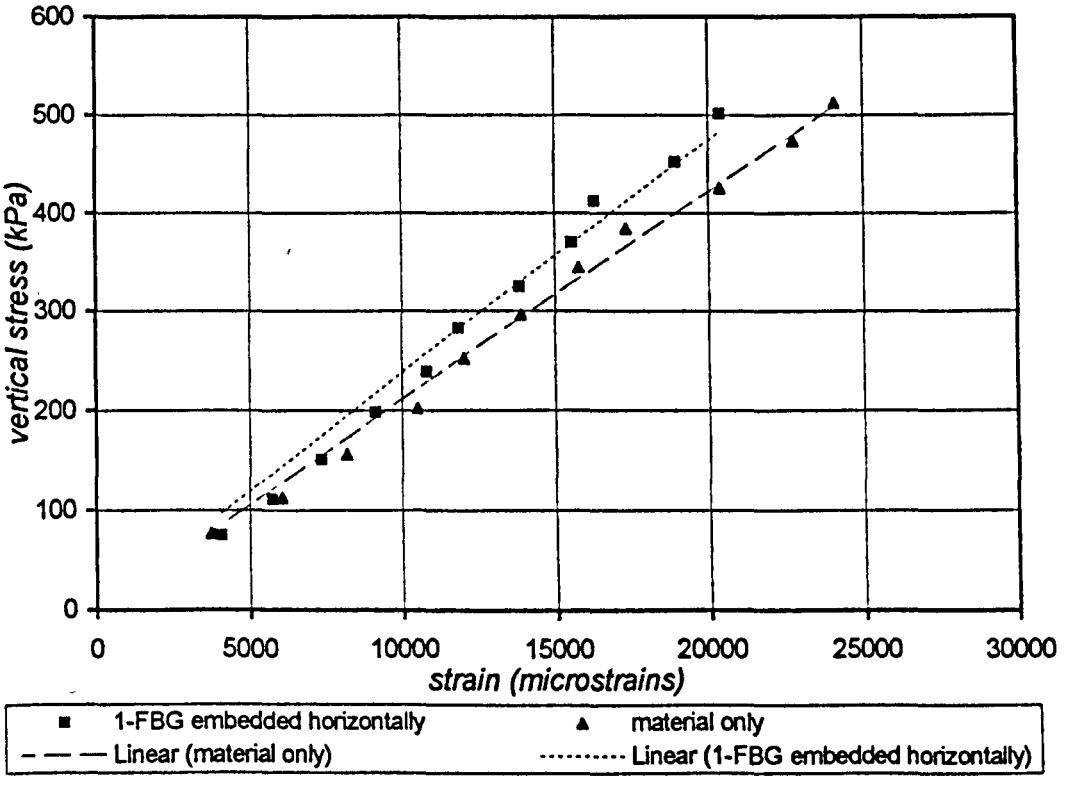

Fig.5.31: Comparison of stress – strain curve of SCOTCHCAST sample and of the single-fibre sensor.

The response of the sensor to vertical stress was measured by increasing the number of weight units and then manually moving the weights plate up and down the top plate. The measured Bragg wavelength is given in Fig.5.32 for 3 different vertical stresses. The FBG readout system was set to 6scans/s, SLD current 82mA, giving resolution 0.02nm, section 3.6.2. For vertical stress <110kPa, the Bragg wavelength remains constant (inside the ±10pm noise of the FBG readout system) while the vertical stress is constant. As the vertical stress increases, distortion of the pulses is observed. More specifically, the Bragg wavelength slowly reduces while the vertical load is applied. On removal of the load it returns to a value lower than the unstressed sensor Bragg wavelength (836.72nm), and then slowly increases towards that value. This behaviour seems to be related with the viscoelastic nature of the material, and is more pronounced at slow varying stresses. Fig.5.33 shows the time response

of the same grating when the load is applied for ~19s, followed by ~18s rest. The similarity with the stress relaxation curve shown in Fig.5.6 is clearly observed.

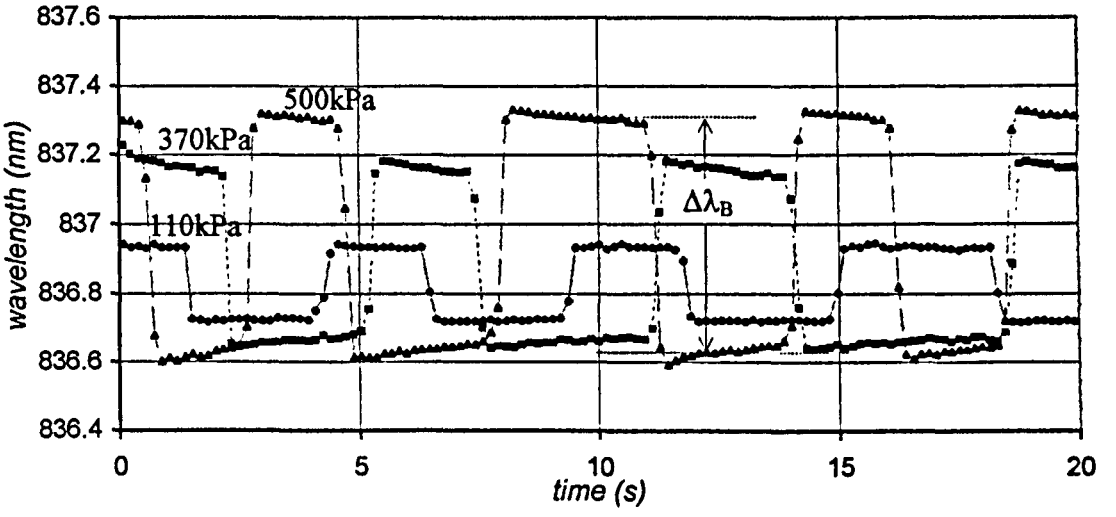

Fig.5.32: Time response of sensor-1Fh to vertical stress. Each curve corresponds to different vertical load.

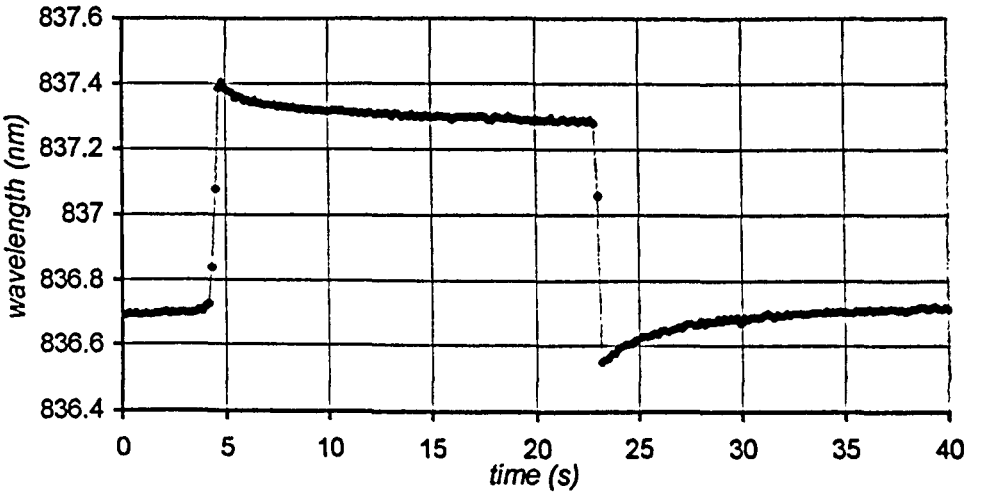

Fig.5.33: Time response of sensor-1Fh for 500kPa vertical stress, showing the effect of the viscoelastisity to the measured Bragg wavelength.

In order to reduce the error in measuring $\Delta\lambda_B$ due to the drift in wavelength, the vertical load was applied for a relatively short time (~0.5 to 1s), followed by equal unstressed period. The average values of the Bragg wavelength during, and after removal of stress, were then used to calculate $\Delta\lambda_B$, as shown schematically in Fig.5.32.

Fig.5.34 shows the measured Bragg wavelength shift of the embedded grating against vertical stress. The error bars correspond to the ±10pm noise of the FBG readout system. The

results from two different measurements are given on the same plot, the second one taken the next day. The average responsivity of the sensor is approximately 1.3pm/kPa. The overlapping of the error bars shows good repeatability of the sensor response. Non-linearity is also observed, which conflicts with the theoretical analysis presented in section 5.2.3. Based on the assumption that the response of the sensor is independent of the fibre, the strain inside the material in the horizontal direction will be given by eq.(5.26):

$$\varepsilon = \frac{-\nu\sigma_y}{E} \tag{5.37}$$

which is positive (produces extension of the fibre) since $\sigma_y<0$. The induced increase in the Bragg wavelength will be given by eq.(5.23). Combining eq.(5.23) with eq.(5.37) gives:

$$\Delta\lambda_B = -\frac{0.8\lambda_B\nu}{E}\sigma_y \tag{5.38}$$

Eq.(5.38) is plotted against $|\sigma_y|$ in Fig.5.35 for E=21MPa, ν=0.4, and λ_B=836.45nm . The experimental data from measurement 1 (Fig.5.34) are also plotted. The theoretically predicted sensor responsivity (12.7pm/kPa, eq.5.38) is approximately 10 times higher than the experimentally measured value. This result shows that the strain transferred on the fibre is significantly lower than the strain due to Poisson's ratio inside the material. The fibre does not follow the material as we have initially assumed. The fibre and the material expand differently due to the large difference of their E modulus (21MPa for the material, 72GPa for the silica fibre). This is the second indication that the material deformation does not dominate the sensor response. A model which includes the presence of the fibre must therefore be examined in order to predict the sensor performance accurately. This will be discussed in the next chapter where the sensor is considered as a composite material.

The observed non-linearity can be explained by the following reasons:

1. Fabrication imperfections. The fibre is not precisely parallel to the horizontal plane, and/or it is not centred inside the material. Both conditions would affect the axial strain on the fibre in a non-predictable way.
2. Distortion of the FBG reflection spectrum as the result of the non-uniform distribution of stress along the fibre length. This condition can be described by considering the theory of chirped Bragg gratings, which will be discussed in chapter 6.

Both conditions above could affect the reflection spectrum from the grating. The measured reflection spectra from the embedded grating for the data points measured are plotted on the same graph, as shown in Fig.5.36. Comparing this graph with the one shown in Fig.3.34, where the plots from an identical, non-embedded grating are plotted, we notice the following:

1. The peak intensity of the curves in Fig.5.36 initially varies according to the SLD source resonances (see Fig.3.22 top left), but as the vertical stress increases the peak intensity is reduced (right 3 plots).

2. The FWHM bandwidth of the grating increases with vertical stress. The bandwidth was measured from the plots drawn in Fig.5.36. The approximate values are shown in Fig.5.37 for the different vertical stresses. The bandwidth increases from 0.48nm of the unstressed sensor, to 0.59nm for vertical stress 510kPa.

The observed distortion of the reflected spectrum is another indication that the stress along the fibre length is not uniform, contrary to the prediction of the fibre-independent model.

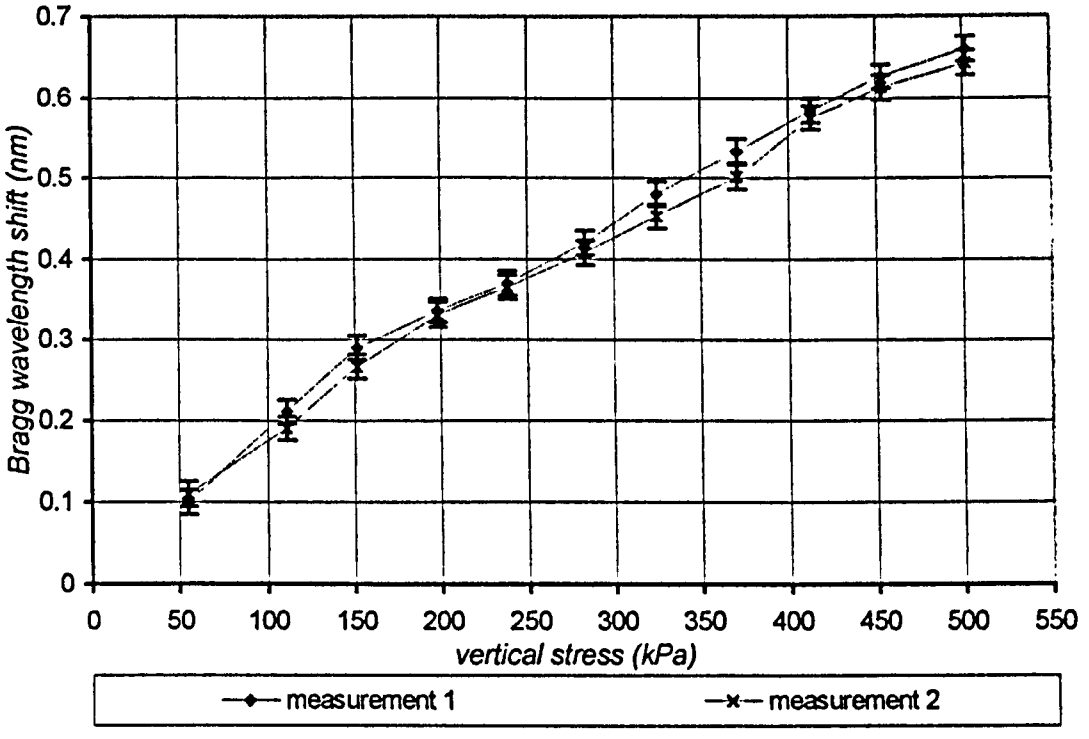

Fig.5.34: Measured Bragg wavelength shift against vertical stress of the FBG embedded horizontally into SCOTCHCAST.

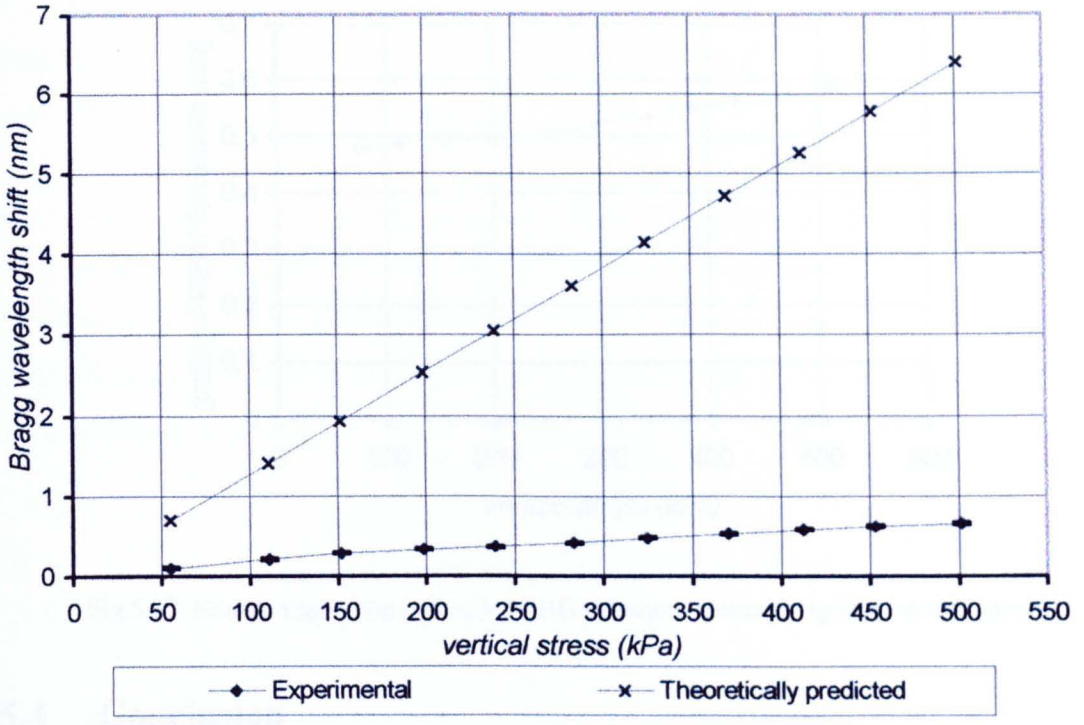

Fig.5.35: Comparison of experimental data and theoretical prediction.

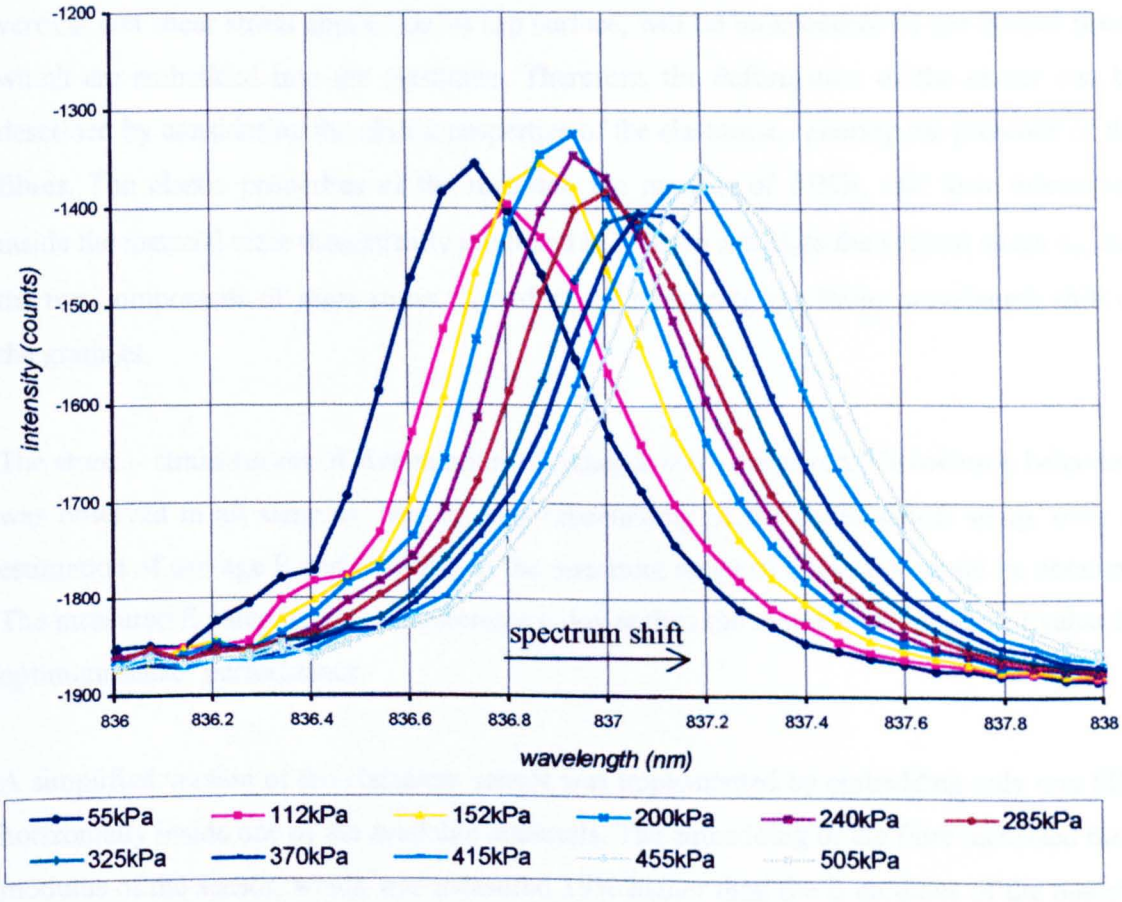

Fig.5.36: Reflection spectra of the embedded FBG under different vertical stresses.

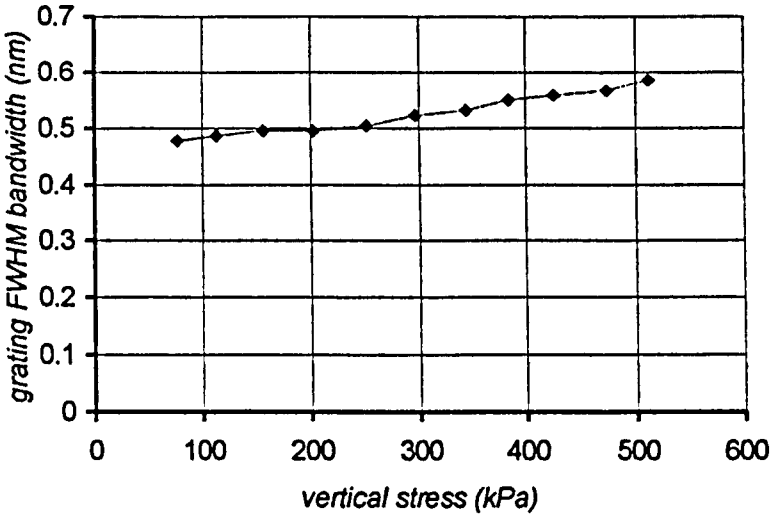

Fig.5.37: Broadening of the embedded FBG reflection spectrum against vertical stress.

5.4 Conclusion

The design of the sensor using FBG embedded in elastomer was discribed in this chapter. The operation of the sensor was explained using the theory of elasticity of solid polymers. The design was based on the assumption that the elastic deformation of the sensor, under the vertical and shear stress applied on its top surface, will be independent of the optical fibres which are embedded into the elastomer. Therefore, the deformation of the sensor can be described by considering the elastic properties of the elastomer, ignoring the presence of the fibres. The elastic properties of the material, the number of FBGs, and their orientation inside the material were theoretically predicted in order to calculate the vertical stress σ_y, and the two components of shear stress τ_{yx} and τ_{yz} by measuring the Bragg wavelength shift of the gratings.

The stress – strain curves of five samples of material were measured. Viscoelastic behaviour was observed in all samples. Due to poor repeatability of the experimental setup, only an estimation of average E and G values in the operating range of the sensor could be obtained. The measured E value in all five samples was lower than the theoretically predicted value for optimum sensor performance.

A simplified version of the elastomer sensor was implemented by embedding only one FBG horizontally inside one of the available materials. The embedding of the fibre increased the E modulus of the sensor, which was measured 19% higher than the E modulus of the material sample. The response of the sensor to vertical stress up to 500kPa was measured. Good repeatability of the Bragg wavelength shift with respect to vertical load was observed. The measured average responsivity of the sensor was 13pm/kPa, which is 10 times lower than the

theoretically predicted value. Non-linearity was also observed in the sensor response, possibly due to the distortion of the FBG reflected spectrum as the result of the non-uniform stress distribution along the fibre axis.

The experimental observations shows that the fibre independent model significantly deviates from the experimental observations. The model should be reconsidered in order to include the effect of the embedded optical fibres, and derive a more accurate calculation of the stress distribution along the fibre axis. This model, based on the theory of composites, will be described in the next chapter.

CHAPTER 6

Elastomer sensor – Fibre dependent model

Introduction

The design and principle of operation of the elastomer sensor was described in the previous chapter, based on the assumption that the embedded fibre follows the deformation of the material without disturbing the stress distribution inside the elastomer. The first experimental results, however, showed significant variation from the theoretical results. The embedded FBG was much less sensitive to vertical stress applied on the sensor than expected, showing the need for a more accurate theoretical model.

In this chapter the elastomer sensor design will be reconsidered using the theory of composites. The sensor will be considered as a single-fibre composite, where stress is applied on its top surface. The theory presented here is capable of predicting the FBG response for vertical stress only, and for the simple version of the sensor where only one FBG is embedded horizontally in the elastomer. According to this model, the interfacial shear stress acting on the fibre varies along the fibre length. This will produce variable strain along the grating length. The Bragg wavelength response in this case can be explained by considering the grating as a chirped FBG.

The chapter begins with a brief presentation of the stress distribution along the fibre length of a single-fibre composite, and with the description of a chirped Bragg grating. The theory will then be applied for the design of the single-fibre horizontal sensor. The design is concerned with the calculation of the E modulus of the elastomer for optimal sensitivity and fibre safety. A prediction of the Bragg wavelength shift and the reflection spectrum broadening will then be given in terms of the grating length and the offset from the centre of the embedded fibre length. The theoretical predictions of this model will be compared with those of the fibre-independent model and the experimental results from the single-fibre sensor.

The experimental results regarding the elastomer sensor will be presented in the rest of this chapter. The fabrication procedure of the elastomer sensor will be explained in detail. Three sensors were fabricated and tested. The shear stress response of the single-fibre sensor with the horizontal FBG will be presented. The second sensor tested was again single-fibre but with the FBG inclined. Finally, the prototype of the 3-fibre sensor was tested. The

experiments are concerned with the measurement of the Bragg wavelength shift and the reflection spectrum deformation for low frequency (0.5Hz) vertical and shear stress pulses. The time response of the sensor for shear stress up to 4Hz will also be presented.

6.1 Background theory

The calculation of the axial stress distribution of the embedded fibre in a single-fibre composite, will be presented in section 6.1.1. The definition of the chirped fibre Bragg grating, and principles that are directly related to the sensor design, will be given in section 6.1.2.

6.1.1 Stress and strain distribution in a single-fibre composite

The following analysis is based on the shear lag model, initially proposed by Cox (1952), which describes the effect of loading an aligned short-fibre composite. The axial stress in the fibre is transferred from the matrix[1] by means of shear stresses developed in the interface between the fibre and the matrix. The calculation of the stress distribution along the embedded fibre, which is briefly presented here, has been described in detail by Hull and Clyne (1996, chapter 6), for a single short fibre composite stressed along the fibre axis. In case of the elastomer sensor discussed in this chapter, the stress is applied perpendicular to the fibre axis, therefore the stresses developed along the fibre axis are due to Poisson's ratio of the matrix.

Assumptions

Generally, assuming cylindrical coordinates, the stress at any point in the matrix around the fibre is a function of the distance x from the centre of the fibre, the radius r, and the angle ϕ, Fig.6.1. For the single fibre composite model which is described by Hull and Clyne, however, it is assumed that stress is independent of ϕ. In this particular sensor design, compressive stress is only applied on the upper and lower surfaces of the sensor, therefore the stress distribution around the fibre is expected to be dependent of ϕ. At this preliminary stage of the sensor design we were mainly interested to obtain an estimation of the axial stress distribution along the fibre axis. We can therefore tolerate at this stage error due to inaccuracy of the model, and to assume that the stress around the fibre is independent of ϕ, so that the model can be directly applied to the sensor design.

---

[1] The term "matrix" will be used instead of elastomer material, in accordance to the usual terminology of the textbooks on composites.

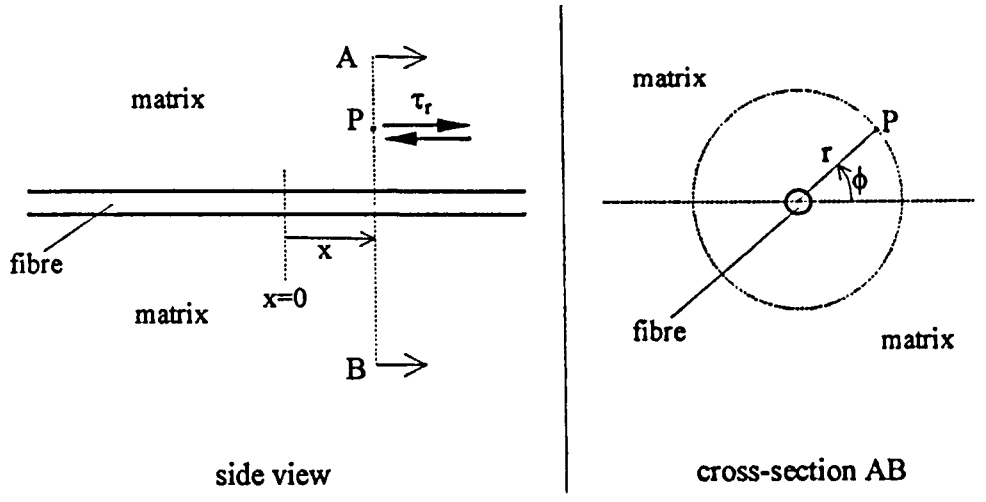

Fig.6.1: The stresses at any element P in the matrix depends on the coordinates x, r, and ϕ. The design is based on the assumption that the stress is equal anywhere on the circumference with radius r (independent of the angle ϕ).

The model also assumes that i) the length of the fibre is small compared to the length of the matrix, ii) The matrix radius R is much larger than the fibre radius r_f, iii) the fibre is entirely embedded into the matrix, as shown in Fig.6.2(a). In the actual sensor on the other hand, the embedded fibre is equal to the width of the sensor, since it enters and leaves the matrix material as shown in Fig.6.2(b). Ideally, the model should take into account the finite width and height of the sensor, and the stress distribution at the matrix-air interface near the fibre. For simplicity of the design, we will assume that the sensor is described by the short fibre composite theory.

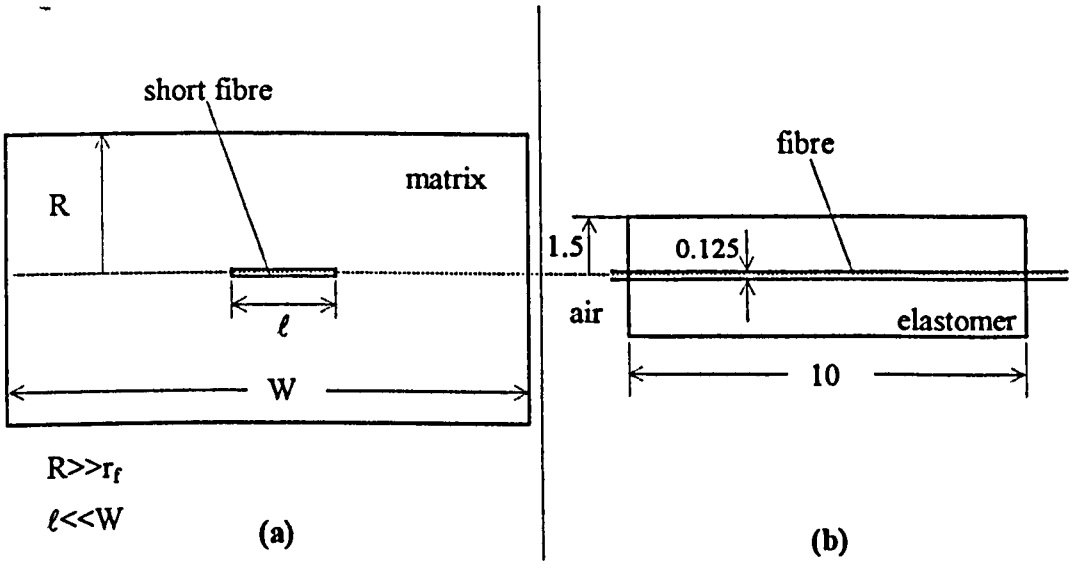

Fig.6.2: (a) single short fibre composite model. (b) actual sensor (dimensions in mm).

The model described by Hull and Clyne assumes that the axial stress inside the fibre is constant across the fibre cross-section, and that no shear stress is developed in the fibre, as shown in Fig.6.3(a). The axial stress is therefore independent of r and ϕ. The actual stress deformation is closer to the one shown in Fig.6.3(b). At any element inside the fibre, both axial and shear stresses are applied, which depend on x, r, and ϕ (in cylindrical coordinates). Hence, the reference lines representing the displacement of the material inside the fibre are not straight lines perpendicular to the fibre axis, but curved in a way shown in Fig.6.3(b).

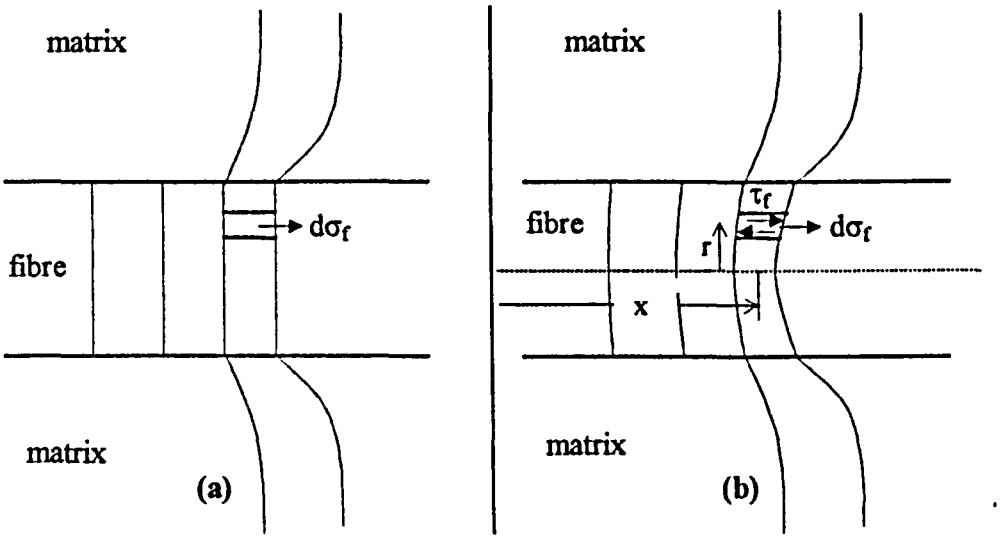

Fig.6.3: (a) The axial stress $d\sigma_f$, constant across the fibre cross-section, is assumed to be the only stress applied on every element inside the fibre. (b) Actual internal stresses depend on x, r, and ϕ.

The application of vertical compression on the sensor, hence perpendicular to the fibre axis, will produce deformation of the fibre due to Poisson's ratio. This is shown schematically in Fig.6.4. The circular cross-section of the fibre will be turn to elliptical under the application of vertical stress, due to the elastic compression at the y-direction, and the Poisson's extension at the z-direction.

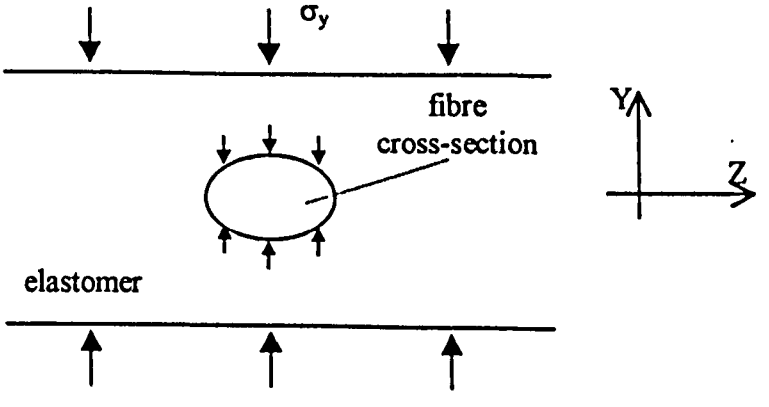

Fig.6.4: Deformation of the fibre due to compression perpendicular to the fibre axis. Dimensions out of scale.

Both conditions shown in Fig.6.2(b), and Fig.6.3(b) are possible to affect the reflection properties of the embedded FBG in terms of bandwidth and reflectivity. The effect of diametric point loading of FBGs was examined by Wagreich *et al.* (1996). A FBG was written in a low birefringent fibre. With no load applied, the reflection spectrum was a single peak centred around the Bragg wavelength (1558nm). As the load increased, broadening of the spectrum and reduction of the peak intensity was observed, until the applied load was increased above ~40N, where two distinctive peaks separated by ~0.2nm were observed. For load equal to ~90N, the wavelength separation was measured to be ~0.4nm. Wagreich and Sirkis (1997) reported that multiple peaks appear on the reflection spectrum of a FBG written in a single-mode fibre, as the result of both unequal transverse strain and gradient axial strain. Unequal transverse strain and gradient axial strain were unambiguously determined by using a polarising element. The precise type of the fibre was not reported.

It is clear from Fig.6.4 that unequal transverse strain of the fibre is expected due to vertical stress on the sensor. The situation, although similar, is not identical to the situation described by Wagreich *et al.* The vertical stress is distributed over the entire surface of the fibre, instead of transverse point loading. Furthermore, the transverse load which is applied on the embedded fibre is significantly lower than the test loads in Wagreich *et al.* (1996). A rough estimation of the maximum transverse compressive load on the fibre can be obtained by considering the maximum vertical stress (σ_{ymax}=500kPa), the embedded length of the fibre (L=10mm), and the fibre diameter ($2r_f$=125μm). The overall maximum transverse force will therefore be:

$$F_{tr,max} = \sigma_{y,max} A = \sigma_{y,max} L(2r_f) \cong 0.6N$$

where A is the area of the diametrical and horizontal cross section of the entire embedded length of the fibre. At such a low transverse load, no distinctive peaks, or reflection spectrum broadening, are expected to be observed.

In the following analysis, the effect of transverse fibre loading will be neglected. The ideal case shown in Fig.6.3(a) will be assumed.

Calculation of axial stress distribution along the fibre

The basis of the calculations is shown in Fig.6.5. In this diagram, reference lines representing the material displacement are drawn on the fibre and the surrounding matrix. Initially, the lines are straight and normal to the fibre axis, Fig.6.5(a). External loading is then applied perpendicular to the fibre axis, Fig.6.5(b). The reference lines distort as shown. The shear distortions of the matrix close to the fibre is represented schematically in Fig.6.5(c).

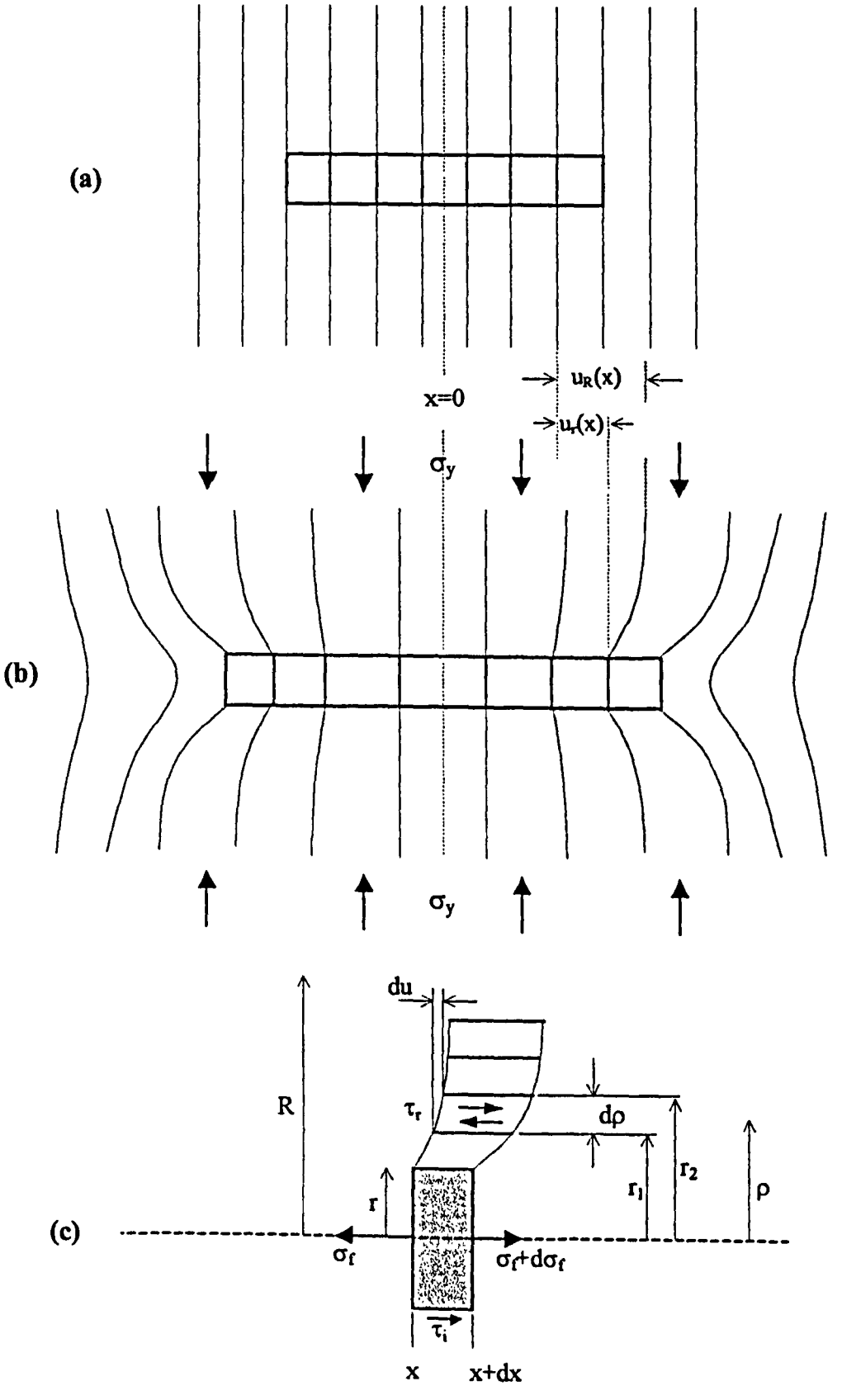

Fig.6.5: (a) Unstressed single-fibre composite, (b) axial displacements u introduced on applying vertical stress σ_y, and (c) variation with radial location of shear stress and strain in the material. (Hull and Clyne, 1996, pg.106).

The radial variation of shear stress in the matrix τ at a given axial distance x from the fibre mid-point, is obtained by equating the shear forces on the inner and outer surface of the annulus[1] with inner radius r_1, outer r_2, and length dx, Fig.6.5(c):

$$2\pi r_1 \tau_1 dx = 2\pi r_2 \tau_2 dx \tag{6.1}$$

which gives:

$$\frac{\tau_1}{\tau_2} = \frac{r_2}{r_1} \tag{6.2}$$

The shear stress τ in the matrix at any radius ρ is therefore related to that at the fibre/matrix interface τ_i by:

$$\tau = \tau_i \left(\frac{r}{\rho}\right) \tag{6.3}$$

where r is the fibre radius.

The strain field around the fibre can be defined in terms of the displacement u of the matrix in the x-direction, relative to the position for no applied stress (Fig.6.5). The increment of this displacement du, on moving out from the fibre axis by $d\rho$, is determined by the shear strain γ, and hence by the shear modulus of the matrix G_m:

$$\frac{du}{d\rho} = \gamma = \frac{\tau}{G_m} = \frac{\tau_i}{G_m}\left(\frac{r}{\rho}\right) \tag{6.4}$$

For any given value of x, the difference between the displacement of the matrix at a radius R and that of the interface is given by the integration:

$$\int_{u_r}^{u_R} du = \frac{\tau_i r}{G_m} \int_r^R \frac{d\rho}{\rho} \tag{6.5}$$

$$(u_R - u_r) = \frac{\tau_i r}{G_m} \ln\left(\frac{R}{r}\right) \tag{6.6}$$

Far away from the fibre it is assumed that the influence of the fibre has disappeared so that the deformation of the matrix is only determined by its elastic properties. The radius R represents a location where this condition becomes valid.

The tensile stress in the fibre σ_f is determined from the distribution of the interfacial shear stress. Referring to Fig.6.5(c), the balance of the external forces acting on an element of the fibre is:

[1] This is due to the static equilibrium of the annulus at the horizontal direction.

$$2\pi r dx\tau_i = -\pi r^2 d\sigma_f \tag{6.7}$$

$$\frac{d\sigma_f}{dx} = -\frac{2\tau_i}{r} \tag{6.8}$$

where $d\sigma_f$ is considered to be constant across the fibre cross-section. It is assumed that there is no shear strain inside the fibre and the interfacial adhesion is perfect, so that $u_r=u_f$, where u_f is the displacement of the fibre surface. The shear modulus of the matrix is given by the known equation (eq.5.11):

$$G_m = \frac{E_m}{2(1+\nu_m)} \tag{6.9}$$

where E_m, ν_m the Young's modulus and Poisson's ratio of the matrix. Substitution of G_m (from eq.6.9), and τ_i (from eq.6.8) to eq.(6.6) gives:

$$\frac{d\sigma_f}{dx} = -\frac{(u_R - u_r)E_m}{(1+\nu_m)r^2 \ln\frac{R}{r}} \tag{6.10}$$

Referring to the element in Fig.6.5(c):

$$\frac{du_f}{dx} = \varepsilon_f = \frac{\sigma_f}{E_f} \tag{6.11}$$

where ε_f is the axial strain of the fibre, and E_f the Young's modulus of the fibre. The differential of u_R will approximate to the far-field matrix strain ε_m:

$$\frac{du_R}{dx} \approx \varepsilon_m = -\frac{\nu_m \sigma_y}{E_m} \tag{6.12}$$

The overall strain of the composite ε_l will be equal to the matrix strain ε_m. This assumption represents a good approximation because the far-field matrix strain is approximately uniform along and beyond the length of the fibre. The matrix stress and strain builds up with distance from the ends of the fibre, as shown in Fig.6.5(b) (Hull and Clyne, 1996, pg.109). Hence:

$$\frac{du_R}{dx} \approx \varepsilon_m \sim \varepsilon_l \tag{6.13}$$

The stress distribution in the fibre can be determined by differentiating eq.(6.10) and substituting the differentials from eq.(6.11) and eq.(6.13):

$$\frac{d^2\sigma_f}{dx^2} = \frac{n^2}{r^2}(\sigma_f - E_f\varepsilon_m) \tag{6.14}$$

where n is a dimensionless constant given by:

$$n = \sqrt{\frac{E_m}{E_f(1+\nu_m)\ln\left(\frac{R}{r}\right)}} \tag{6.15}$$

Eq.(6.14) is a second order differential equation with the solution:

$$\sigma_f(x) = E_f\varepsilon_m + B\sinh\left(\frac{nx}{r}\right) + D\cosh\left(\frac{nx}{r}\right) \tag{6.16}$$

Coefficients B and D are calculated from the boundary conditions:

$$\sigma_f = 0 \quad \text{at} \quad x = \pm L \tag{6.17}$$

where L is the fibre half length. Eq.(6.16) gives:

$$\sigma_f(x) = E_f\varepsilon_m\left[1 - \cosh\left(\frac{nx}{r}\right)\operatorname{sech}\left(\frac{nL}{r}\right)\right] \tag{6.18}$$

The last equation clearly shows the variation of the axial stress inside the fibre along its length. The situation discussed in this section is similar with the single-fibre sensor described in section 5.3.2. In the later case, the fibre is embedded horizontally in the elastomer, where the vertical stress acts perpendicular to the fibre axis. The non-uniform stress along the length of the embedded Bragg grating will result in non-uniform elongation of the fibre. If we assume that the distance between successive reference lines drawn in Fig.6.5(a) is equal to the period of the unstrained Bragg grating, we notice that the non-uniform stress will result in larger grating period in the middle of the grating and smaller at the grating edges, Fig.6.5(a). The gradient of the axial stress will also affect the local refractive index of the fibre core due to the strain-optic effect. The reflection properties of the grating (Bragg wavelength, reflectivity, and bandwidth) in this case can be explained using the theory of chirped fibre Bragg gratings, which is presented in the next section.

6.1.2 Chirped fibre Bragg gratings

The uniform fibre Bragg grating was described in section 2.6.2. We saw that the reflection properties of those gratings depend on the period of the refractive index perturbation, which is constant along the grating length. Bragg gratings that have a non-uniform period along their length are known as chirped fibre Bragg gratings. Chirp in gratings is observed in many different forms. The period may vary symmetrically, either increasing or decreasing in period around a pitch in the middle of the grating, linearly with the length of the grating, or may even have jumps in the period (Kashyap, 1999, pg.312). Chirp grating can also be achieved by changing the refractive index along the length of a constant-period Bragg grating (Byron *et al.*, 1993).

Chirped gratings are mainly used in telecommunications as in-fibre band-pass filters (Zhang *et al.*, 1995), and for chromatic dispersion compensation (Ouellette, 1987). They can be fabricated using the holographic technique of two-beam interferometer (Kashyap *et al.*, 1990) described in section 2.6.3, in a tapered boron/germania doped fibre. This method has been proposed by Byron *et al.* (1993). Tapers were designed such that the fibre diameter

decreases smoothly from 125μm to 50μm over a distance of 10mm. Peak reflectivity of 20% and FWHM bandwidth of 2.9nm have been reported. Sugden *et al.* (1994) have presented another technique for chirp Bragg grating fabrication. The photosensitive fibre is curved in the two-beam interference field with uniform fringe spacing. Chirped Bragg gratings with parameters 99% reflectivity and 7.5nm bandwidth, to 5% reflectivity and 17nm bandwidth have been reported. Kashyap *et al.* (1994) have reported a method for fabricating step-chirped gratings using step-chirped phase mask. Reflectivity of 95% and bandwidths between 3 and 15nm were demonstrated.

Fig.6.6 shows a schematic of a chirped grating of length L_g. This grating can be approximated by a series of smaller length uniform Bragg grating elements increasing in period (Othonos and Kalli, 1999, pp.108-109). The Bragg wavelength reflected from the short-period grating λ_{short} is (eq.2.1):

$$\lambda_{short} = 2n_{eff}\Lambda_{short} \tag{6.19}$$

Similarly, the Bragg wavelength reflected from the long-period grating λ_{long} will be:

$$\lambda_{long} = 2n_{eff}\Lambda_{long} \tag{6.20}$$

The bandwidth of the chirped grating B_{chirp} will be given by (Kashyap, 1999,pg.313):

$$B_{chirp} \approx \lambda_{long} - \lambda_{short} = 2n_{eff}\left(\Lambda_{long} - \Lambda_{short}\right) \tag{6.21}$$

Eq.(6.21) shows that the broadening of the reflection spectrum bandwidth depends on the difference between the longest pitch and the shortest pitch of the grating.

Eq.(2.2) shows that the maximum reflectivity of a uniform Bragg grating, which occurs at the Bragg wavelength, increases as the length of the grating increases. Since the length of each element is much shorter than the total length of the grating, the reflectivity of the chirped grating at any wavelength between λ_{short} and λ_{long} will be lower than the reflectivity of a uniform Bragg grating with the same length L_g as the chirp grating. The broadening of the reflection bandwidth is therefore accompanied with reduction of the peak reflectivity. Sugden *et al.* (1994) have measured the reduction of reflectivity as the grating period difference increases, in 5mm long chirp gratings. Four gratings were fabricated by bending the fibre in the UV interference pattern. The uniform grating (fabricated without bending the fibre) was measured 88% reflectivity and 0.4nm bandwidth. The measured reflectivity and bandwidth for the other three chirped gratings were 40% and 2.9nm, 13% and 4.4nm, 4% and 17.3nm respectively.

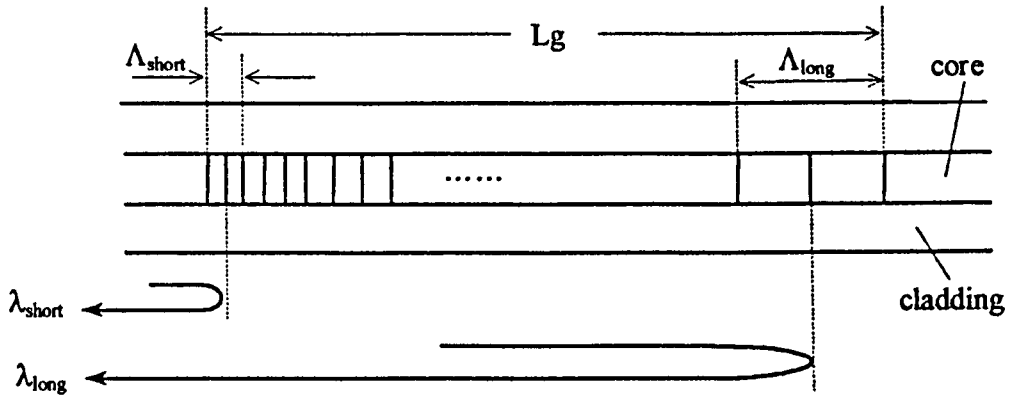

Fig.6.6: Schematic diagram of a chirp grating. Short wavelengths of the incident light are reflected from the short-pitch regions, whereas longer wavelengths travel further into the grating. (Othonos and Kalli, 1999, pg.108).

6.2 Sensor design

Let us now consider the single-fibre elastomer sensor which was fabricated and tested in the previous chapter. The sensor will now be modelled using the theory of single-fibre reinforcement composites, and the theory of chirped Bragg gratings, which were presented in the previous sections.

It is assumed that the fibre is horizontally aligned inside a rectangular block of ideally elastic material, with the grating centred with respect to the sensor surfaces, Fig.6.7(a). The sensor deforms under vertical stress σ_y as shown in Fig.6.7(b). All the assumptions mentioned in section 6.1.1 will also be accepted.

Objectives of the design are:

- To calculate the required E_m which provides the highest sensitivity of the sensor, and at the same time satisfies the safety condition $\varepsilon_{max} \leq 2500\mu\varepsilon$, where ε_{max} is the maximum strain inside the fibre.
- To predict the sensor response to vertical stress, i.e. the Bragg wavelength shift against vertical stress curve.
- To estimate the broadening of the FBG reflected spectrum due to chirp.

Those issues are discussed in the next subsections.

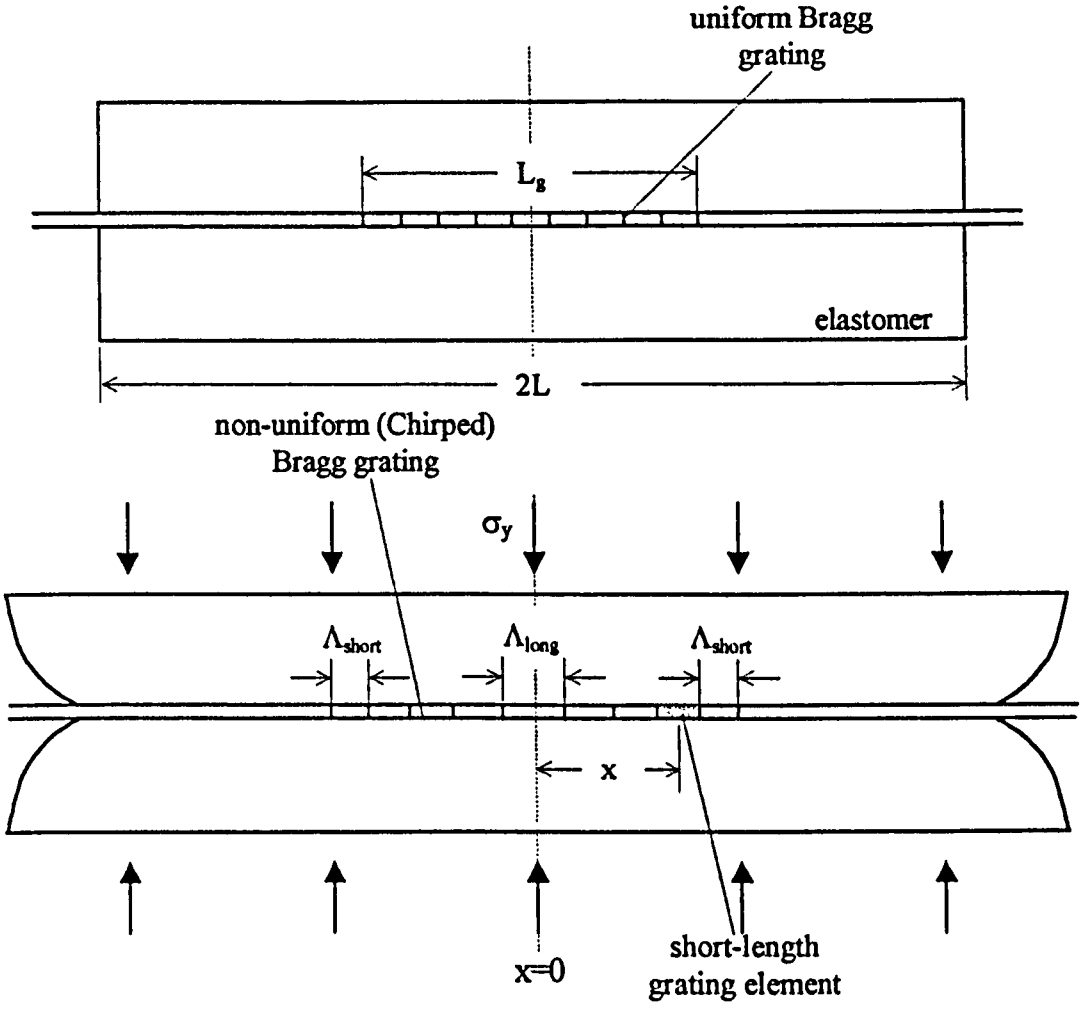

Fig.6.7: Model of the single-fibre elastomer sensor. (a) The uniform grating is embedded horizontally (Dimensions not in scale). (b) Deformation of the material and chirping of the grating due to vertical compression (Deformation exaggerated).

6.2.1 Estimation of E_m

The stress distribution inside the fibre along the fibre axis is given by eq.(6.18), which is plotted in Fig.6.8 as a function of the vertical stress and the distance from the mid point of the grating. The graph was obtained for the following parameters: embedded fibre half length L=5mm, FBG full length L_g=5mm, E_f=72GPa, E_m=100MPa, ν_m=0.4, r=62.5μm, R=1.5mm. The graph shows that, for a given value of vertical stress, the maximum axial stress is observed in the middle, and the minimum at the two edges of the grating. Therefore, the period of the resulted chirped grating will vary from a maximum value Λ_{long} in the middle, to a minimum Λ_{short} at the edges of the grating, as shown in Fig.6.7. The axial strain inside the fibre, and along the fibre axis, will be given by:

$$\varepsilon(x)=\frac{\sigma(x)}{E_f} \tag{6.22}$$

Substitution of σ(x) from eq.(6.18) gives:

$$\varepsilon(x)=\varepsilon_m\left[1-\cosh\left(\frac{nx}{r}\right)\operatorname{sech}\left(\frac{nL}{r}\right)\right] \tag{6.23}$$

Eq.(6.23) is plotted in Fig.6.9. The maximum axial strain is observed in the middle (x=0), where as the lower axial strain at the edges of the grating ($x=\pm L_g/2$). Eq.(6.23) for x=0 gives:

$$\varepsilon_{max}=\varepsilon(0)=\varepsilon_m\left[1-\operatorname{sech}\left(\frac{nL}{r}\right)\right] \tag{6.24}$$

where the far-field matrix strain ε_m is given by eq.(6.12). Eq.(6.24) is plotted in Fig.6.10 against the Young's modulus of the matrix E_m, for E_m=0.1 to 200Mpa, and for maximum vertical stress σ_y=–500kPa. The maximum strain is always lower than the safety limit of 2500με. Increasing the stiffness of the material reduces the sensitivity of the sensor, since less strain is transferred from the matrix to the fibre. For the given sensor dimensions it is therefore necessary to use a low-E_m material in which to embed the fibre. It is reminded that this conclusion is inferred from the effect of the vertical stress only and on the single horizontal FBG, therefore it cannot be generalised for the response of an inclined grating or the 3-fibre sensor, where the stress distribution on the fibres will differ.

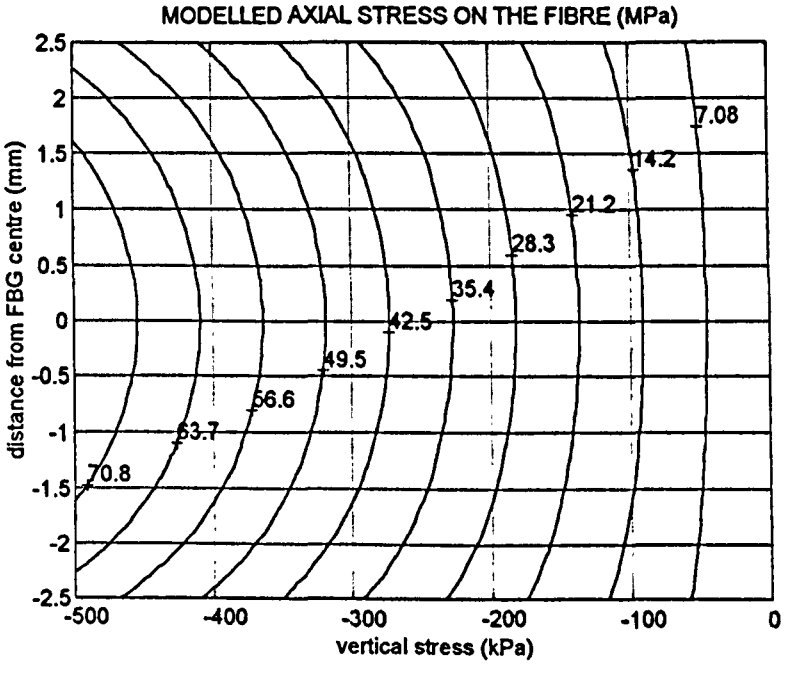

Fig.6.8: Modelled axial stress along the embedded FBG as a function of vertical stress.

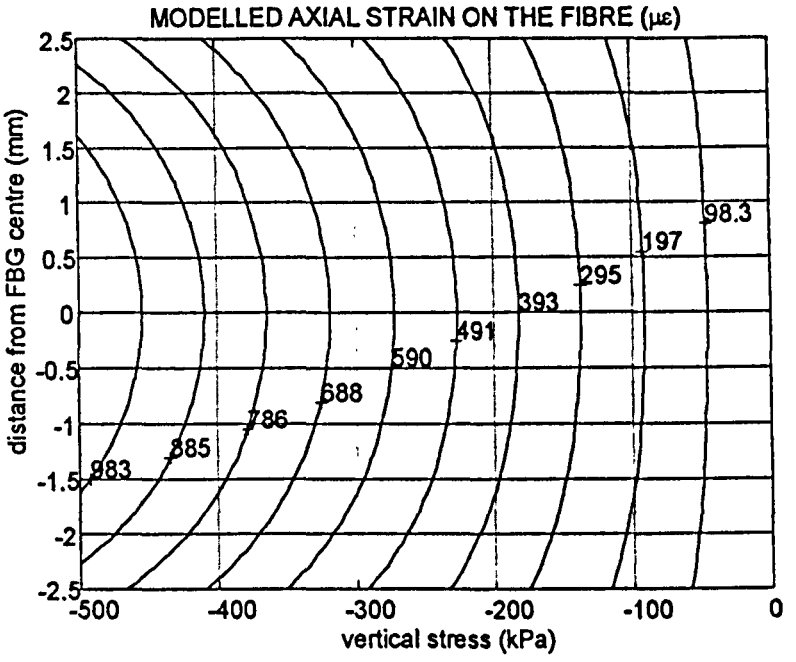

Fig.6.9: Modelled axial strain along the embedded FBG as a function of vertical stress.

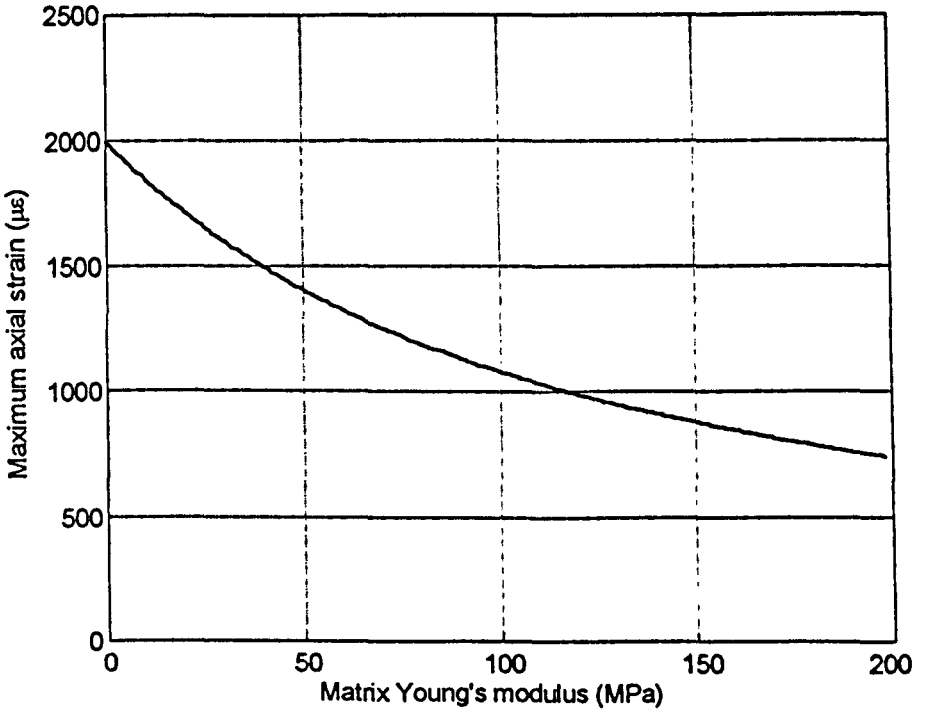

Fig.6.10: Predicted maximum strain inside the fibre against E_m, for the maximum vertical stress equal to 500kPa.

6.2.2 Reflection spectrum broadening

It was found in the previous section that the axial strain inside the fibre varies along the fibre length. This will result in change of the period along the grating, as well as change in the effective refractive index due to strain-optic effects. In this section, an estimation of the

reflection spectrum broadening as the result of chirping of the FBG, due to the axial strain variation, will be derived.

Let us consider a short-length Bragg grating element at a distance x from the middle of the embedded FBG, Fig.6.7. The Bragg wavelength shift corresponding to that element will be given by eq.(2.8) for $\Delta T=0$:

$$\frac{\Delta\lambda_B}{\lambda_B}=\left(\frac{1}{n_{eff}}\frac{\partial n_{eff}}{\partial\varepsilon}+\frac{1}{\Lambda_B}\frac{\partial\Lambda_B}{\partial\varepsilon}\right)\varepsilon(x) \tag{6.25}$$

where $\varepsilon(x)$ is the axial strain at the location of the element, and $\lambda_B=2n_{eff}\Lambda_B$ is the Bragg wavelength of the unstrained uniform grating. Substitution gives:

$$\Delta\lambda_B=2\left(\Lambda_B\frac{\partial n_{eff}}{\partial\varepsilon}+n_{eff}\frac{\partial\Lambda_B}{\partial\varepsilon}\right)\varepsilon(x) \tag{6.26}$$

The first term represents the strain-optic induced change of the effective refractive index, and the second term the change in the pitch period for that particular grating element. Eq.(6.26) may be expressed as (Othonos and Kalli, 1999, pg.98):

$$\Delta\lambda_B=\lambda_B(1-p_e)\varepsilon(x) \tag{6.27}$$

where p_e is a strain-optic constant defined as:

$$p_e=\frac{n_{eff}^2}{2}[p_{12}-\nu(p_{11}+p_{12})] \tag{6.28}$$

p_{11} and p_{12} are components of the strain-optic tensor, and ν is the Poisson's ratio. For a typical germanosilicate optical fibre $p_{11}=0.113$, $p_{12}=0.252$, $\nu=0.19$, and $n_{eff}=1.482$ (Othonos and Kalli, 1999, pg.99). Using these parameters, eq.(6.28) gives $p_e\cong0.2$. Substitution to eq.(6.27) gives:

$$\Delta\lambda_B=0.8\lambda_B\varepsilon(x) \tag{6.29}$$

Each element along the embedded FBG will exhibit different wavelength shift, which is proportional to the axial strain at the location of the element, and will be given by eq.(6.29). The maximum wavelength shift will therefore be observed by the element at x=0, where the axial strain is maximum:

$$\Delta\lambda_{B,max}=0.8\lambda_B\varepsilon(0) \tag{6.30}$$

Similarly, the minimum wavelength shift will be observed at $x=\pm L_g/2$:

$$\Delta\lambda_{B,min}=0.8\lambda_B\varepsilon(\pm\frac{L_g}{2}) \tag{6.31}$$

The maximum strain $\varepsilon(0)$ is given by eq.(6.24). The minimum strain $\varepsilon(\pm L_g/2)$ is given by eq.(6.23) for $x=\pm L_g/2$:

$$\varepsilon\left(\pm\frac{L_g}{2}\right)=\varepsilon_{min}=\varepsilon_m\left[1-\cosh\left(\frac{nL_g}{2r}\right)\operatorname{sech}\left(\frac{nL}{r}\right)\right] \tag{6.32}$$

Fig.6.11 shows schematically the wavelength shift and spectrum distortion of the embedded FBG when the sensor is subjected to vertical stress. Under no vertical stress, the embedded FBG is unstrained and uniform. The bandwidth B of the uniform FBG will be given by eq.(2.5). An approximate value of the bandwidth broadening of the chirped FBG can be obtained by eq.(6.21):

$$B_{chirp} \approx \lambda_{long} - \lambda_{short} \tag{6.33}$$

From Fig.6.11 we obtain:

$$B_{chirp} \approx \Delta\lambda_{B,max} - \Delta\lambda_{B,min} \tag{6.34}$$

Substitution of $\Delta\lambda_{B,max}$, $\Delta\lambda_{B,min}$ from eq.(6.30) and eq.(6.31) respectively, and ε_m from eq.(6.12), the spectrum broadening B_{chirp}, after the algebraic calculations, can be written as:

$$B_{chirp} = -\frac{0.8\lambda_B \nu_m \sigma_y}{E_m} \operatorname{sech}\left(\frac{nL}{r}\right)\left[\cosh\left(\frac{nL_g}{2r}\right) - 1\right] \tag{6.35}$$

Eq.(6.35) is shown graphically in Fig.6.12 as a function of vertical stress σ_y, for different grating lengths L_g, from 1mm to 5mm. The following parameters were used: E_f=72GPa, r=0.0625mm, R=1.5mm, L=10mm, λ_B=836.5nm. The elastic properties of the matrix are E_m=10MPa and ν_m=0.4, typical values for silicone elastomers (Ashby, 1993, pp.28-29). Silicone elastomers are the most appropriate materials for the sensor fabrication because their E modulus is generally lower than other engineering polymers. Low E_m is important for high sensitivity of the sensor, as shown in section 6.2.1. Furthermore, silicone elastomers comply with the additional specifications presented in section 5.2.5.

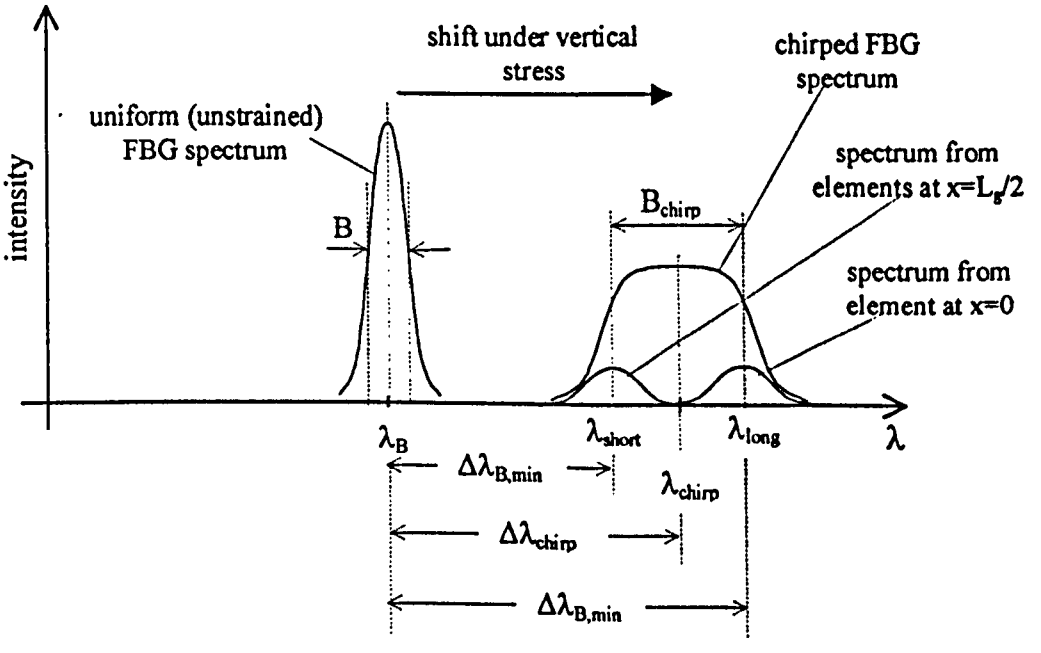

Fig.6.11: Schematic diagram of Bragg wavelength shift and reflection spectrum broadening as the result of FBG chirp due to vertical stress.

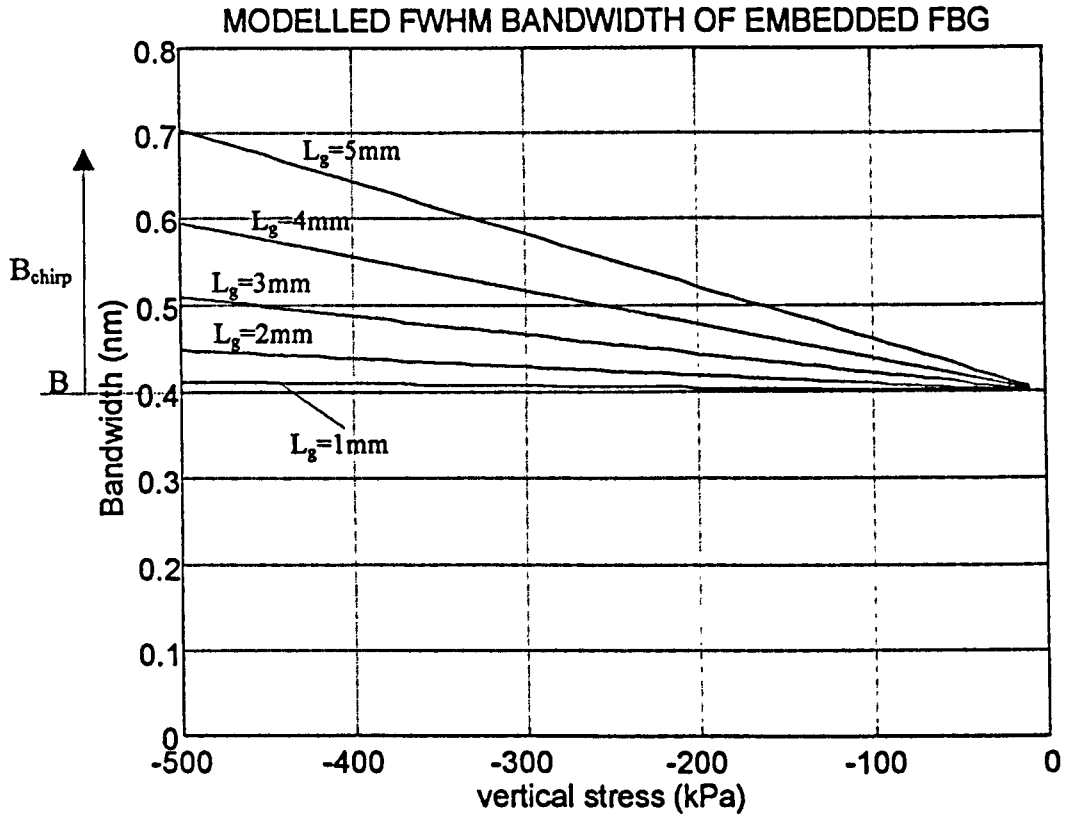

Fig.6.12: Modelled reflection spectrum broadening as a function of vertical stress, for E_m=10MPa and for different grating lengths.

Fig.6.12 shows the predicted increase of the grating bandwidth as the vertical compression increases from 0 to 500kPa with respect to the uniform bandwidth B. The value B=0.4nm is equal to the FWHM of the FBGs used in the experiments, as this was measured using the CCD spectrometer. The reflection spectrum was also measured using an optical spectrum analyser as shown in Fig.3.24(right), section 3.5.3, which gives B≈0.2nm. The value B≈0.4nm was used in the above graph in order to enable the comparison of the theoretical with the experimental results, which were all measured using the CCD spectrometer. The dependence of the spectrum broadening with the length of the grating is significant. For L_g=5mm (equal to the grating length of our FBGs), the bandwidth is ~75% higher at maximum vertical stress compared to the unstressed value. The broadening is smaller for shorter gratings. Particularly for L_g=1mm, the spectrum broadening is less than 5% at any vertical stress. The linear variation of the reflection spectrum with the vertical stress is also observed, which can be directly inferred from eq.(6.35).

The broadening of the reflection spectrum is possible to produce error in the calculation of the Bragg wavelength shift. The Bragg wavelength shift is measured by applying a quadratic polynomial fit in 5 sequential pixels around the reflection peak, as discussed in section 3.6.1. The accuracy of the measured Bragg wavelength therefore, depends on the accuracy of the fitting curve to approximate the actual reflection spectrum of the grating. Any distortion of

the reflected spectrum other than the shift in wavelength would affect the accuracy of the algorithm to detect the Bragg wavelength. In this particular application there are several factors which could affect the spectrum shape in a non-predictable way. For example, E_m is assumed constant in the 0 to 500kPa stress range, which depends on the material, and could not be verified during this study for the five materials which were examined, as explained in section 5.3.1.1. The presence of 3 non-parallel fibres in the material is also expected to alter the in-fibre stress distribution, therefore the actual shape of the reflection spectrum. Non-uniform stress on the top surface could also produce unpredicted reflection shape, as the result of non-symmetric chirp. Let us assume for example an off-centre point load F_L on the top surface of the sensor. The axial strain distribution along the fibre axis can be similar in shape with the sketched curve, Fig.6.13. The non-symmetric axial strain could lead to non-symmetric reflection spectrum shape. This can be understood by considering the contribution of the reflection spectra of the Bragg grating elements along the full length of the grating. Elements having Bragg wavelength between λ_1 and λ_{max} (located between $-L_g/2$ and x_1) appear twice, whereas elements with Bragg wavelengths between λ_1 and λ_{min} (located between x_1 and $L_g/2$) appear once. The overall intensity of the chirped FBG is therefore expected to be higher between λ_1 and λ_{max}, and lower between λ_{min} and λ_1, with respect to the shape of a symmetrically chirped FBG.

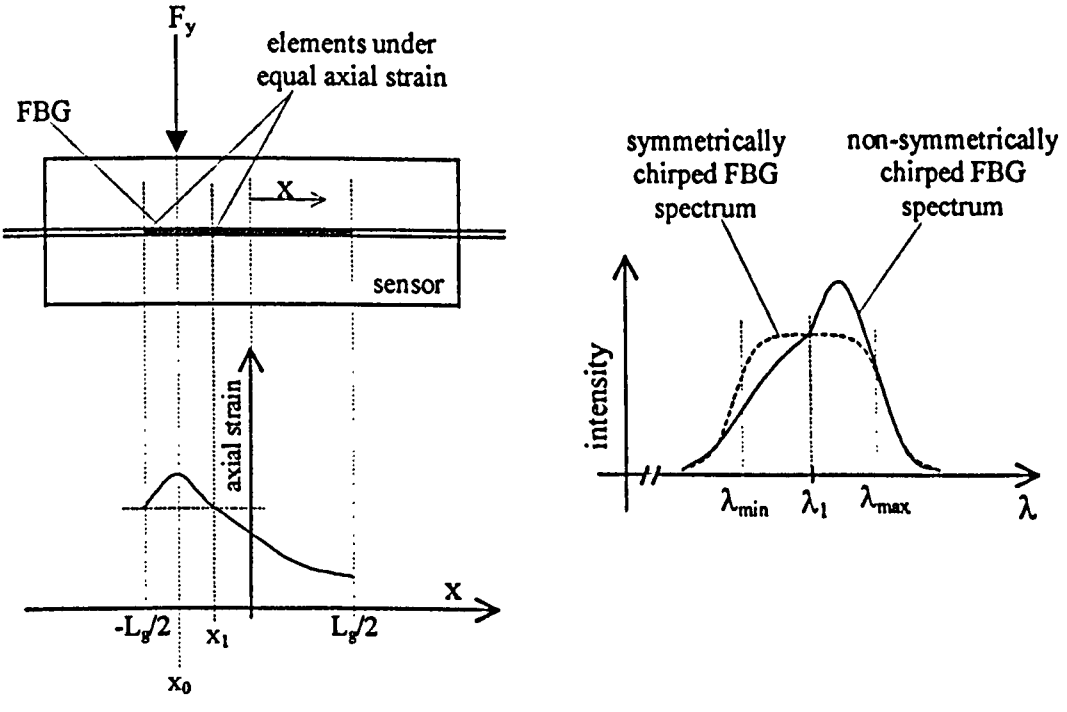

Fig.6.13: Effect of non-symmetric axial strain along the embedded grating on the reflection spectrum shape.

It is therefore important to minimise the sensitivity of the reflection spectrum shape to the in-fibre stress distribution by keeping the length of the grating as small as possible.

Reducing L_g on the other hand reduces the reflectivity of the grating (eq.2.2) which in turn reduces the SNR of the reflected light, eventually decreasing the readout system resolution. Accurate modelling for stress analysis of the sensor and experimentation will therefore be necessary in order to obtain the optimal value of the fibre length.

6.2.3 Mean wavelength shift

Let us now assume that the reflection spectrum of the chirped grating is symmetrical with respect to the mean wavelength λ_{chirp}, as shown previously in Fig.6.11, then we can define the mean Bragg wavelength shift of the chirped FBG as the average:

$$\Delta\lambda_{chirp} = \frac{\Delta\lambda_{B,max} + \Delta\lambda_{B,min}}{2} \tag{6.36}$$

Substitution of $\Delta\lambda_{B,max}$, $\Delta\lambda_{B,min}$ from eq.(6.30) and eq.(6.31) respectively, and ε_m from eq.(6.12), eq.(6.36) gives:

$$\Delta\lambda_{chirp} = -\frac{0.4\lambda_B \nu_m \sigma_y}{E_m}\left\{2 - \operatorname{sech}\left(\frac{nL}{r}\right)\left[1 + \cosh\left(\frac{nL_g}{2r}\right)\right]\right\} \tag{6.37}$$

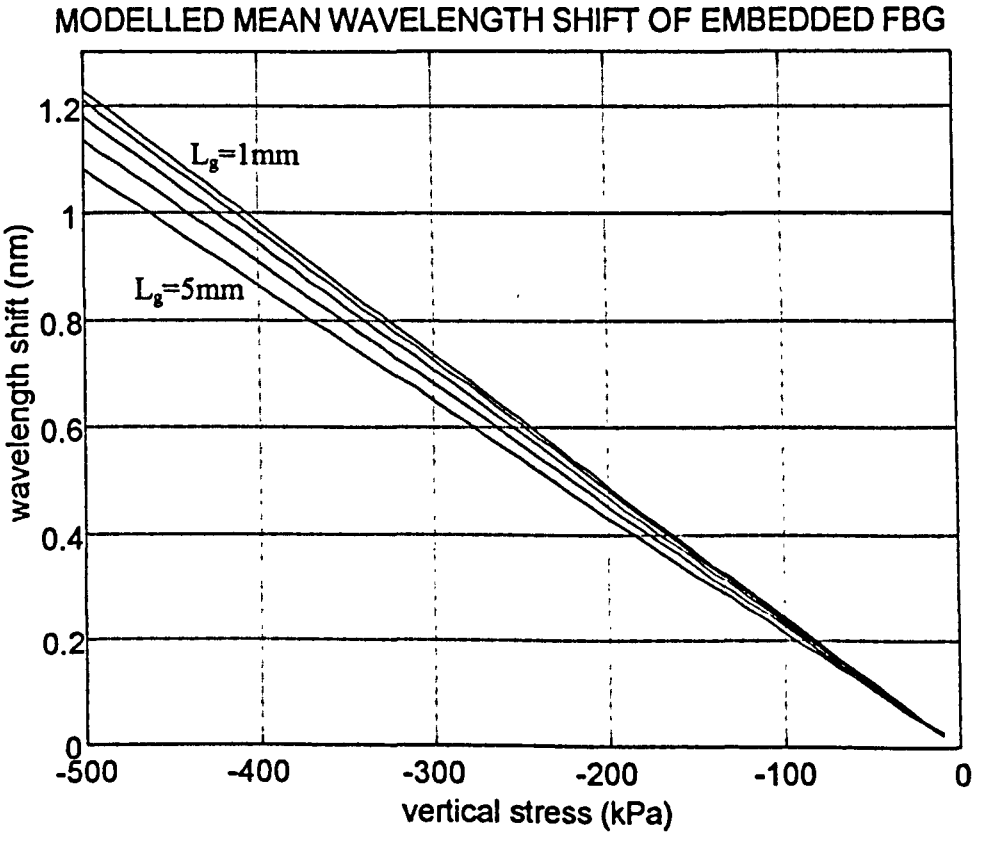

Fig.6.14: Modelled mean Bragg wavelength shift of the embedded grating for E_m=10MPa.

Eq.(6.37) shows the linear relationship between the mean Bragg shift of the chirped grating with σ_y. The above equation is plotted in Fig.6.14 as a function of vertical stress, for grating lengths L_g=1mm to 5mm. All other parameters are identical to those presented in section

6.2.2. The predicted responsivity is 2.2pm/kPa for L_g=5mm. The reduction in grating length from 5 to 1mm increases the responsivity by ~11%. The improvement of sensor responsivity, together with the reduction of spectrum broadening (Fig.6.12), are the two advantages of using short FBGs.

6.2.4 Sensitivity of the FBG response to off-centre placement

In the previous sections we have assumed that the grating is located in the centre of the embedded fibre. In practice, this is difficult to be achieved, due to the uncertainty in finding the precise location of the FBG on the fibre. During the fabrication procedure, the coating of the fibre was removed for a length of approximately 25mm, and then centred in the interference pattern region. The UV exposed region of the fibre was then marked before removing the fibre. The location of the grating is known by approximately ±2mm.

In this section we assume that the FBG is not in the centre of the embedded length of the fibre. Let d be the distance between the centre of the fibre and the centre of the FBG (d≥0), Fig.6.15.

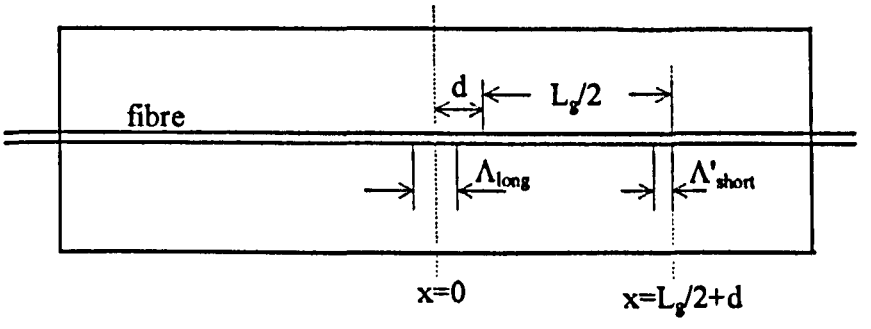

Fig.6.15: Displacement of FBG from the centre of the embedded fibre by distance d.

The maximum axial strain occurs in the middle of the embedded fibre (x=0), given by eq.(6.24). The maximum wavelength shift therefore occurs for a grating element located at x=0, which is given by (eq.6.30):

$$\Delta\lambda_{B,max} = 0.8\lambda_B\varepsilon(0) \tag{6.38}$$

Due to the displacement of the grating, the minimum strain on the fibre will now appear at $x=L_g/2+d$, which will be given by eq.(6.23) for $x=L_g/2+d$:

$$\varepsilon\left(\frac{L_g}{2}+d\right) = \varepsilon_{min} = \varepsilon_m\left[1-\cosh\left(\frac{n(L_g+2d)}{2r}\right)\operatorname{sech}\left(\frac{nL}{r}\right)\right] \tag{6.39}$$

Therefore, the minimum wavelength shift occurs for a grating element located at at $x=L_g/2+d$:

$$\Delta\lambda_{B,min} = 0.8\lambda_B\varepsilon(\frac{L_g}{2}+d) \tag{6.40}$$

The spectrum broadening due to chirp, as a function of the grating offset, will be given by eq.(6.34), which, after substitution finally gives:

$$B_{chirp} = -\frac{0.8\lambda_B\nu_m\sigma_y}{E_m}\operatorname{sech}\left(\frac{nL}{r}\right)\left[\cosh\left(\frac{n(L_g+2d)}{2r}\right)-1\right] \tag{6.41}$$

The mean Bragg wavelength shift, as a function of the grating offset, will be given by eq.(6.36), which finally gives:

$$\Delta\lambda_{chirp} = -\frac{0.4\lambda_B\nu_m\sigma_y}{E_m}\left\{2-\operatorname{sech}\left(\frac{nL}{r}\right)\left[1+\cosh\left(\frac{n(L_g+d)}{2r}\right)\right]\right\} \tag{6.42}$$

Eq.(6.41) and eq.(6.42) are plotted in Fig.6.16 and Fig.6.17 respectively. The displacement is increased up to 2.5mm, where the grating reaches the side of the sensor. The parameters are set equal to those mentioned in section 6.2.2, for grating length L_g=5mm. As the displacement increases, the bandwidth of the chirped grating increases. For d=2.5mm, the bandwidth broadening has been increased by a factor of 4 compared to the centred FBG. The mean Bragg wavelength shift is less sensitive to displacement and decreases as d increases. It is therefore important that the grating offset from the centre of the fibre is minimised in order to avoid loss of sensitivity and broadening of the reflection spectrum.

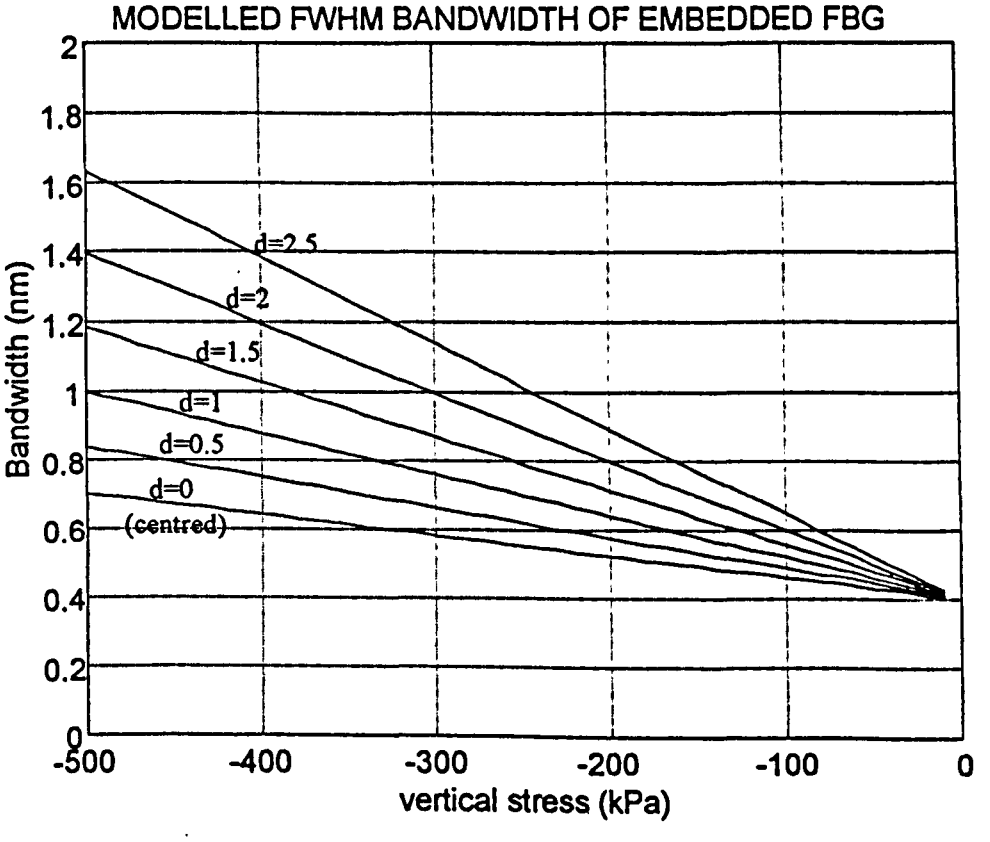

Fig.6.16: Modelled mean Bragg wavelength of the chirped FBG as a function of vertical stress, for different values of grating displacement d (in mm).

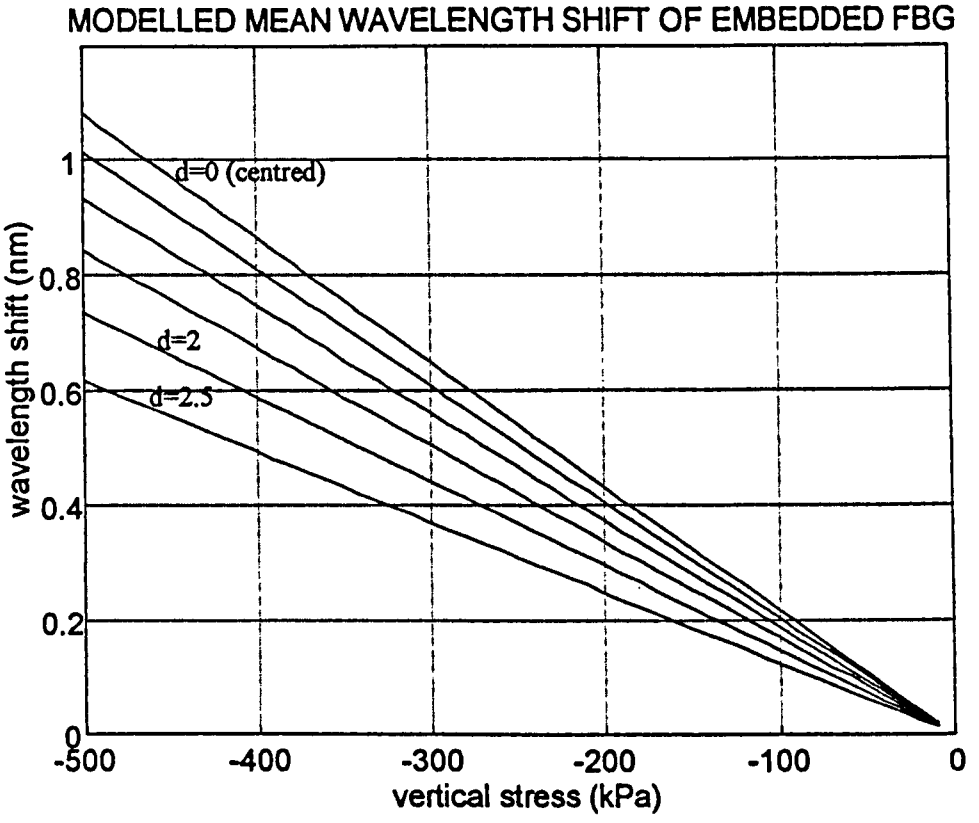

Fig.6.17: Modelled mean Bragg wavelength of the chirped FBG as a function of vertical stress, for different values of grating offset d (in mm).

The grating offset is also expected to affect the symmetry of the reflection spectrum shape around the mean Bragg wavelength, since the axial strain distribution inside the FBG, hence the chirp of the grating, is not symmetric. Referring to the offset condition shown in Fig.6.18, the reflection spectrum will contain spectra from grating elements at distances x where $L_g/2-d \leq x \leq L_g/2+d$. These spectra correspond to Bragg wavelengths which are lower compared to the rest of the grating elements in the embedded FBG, which explains the spectrum broadening. Due to the lack of symmetry, they only appear once in the overall spectrum, contrary to the elements located between $-L_g/2+d$ and $L_g/2-d$, which appear in couples. This explains the non-symmetrical shape of the overall reflection spectrum shown in Fig.6.18.

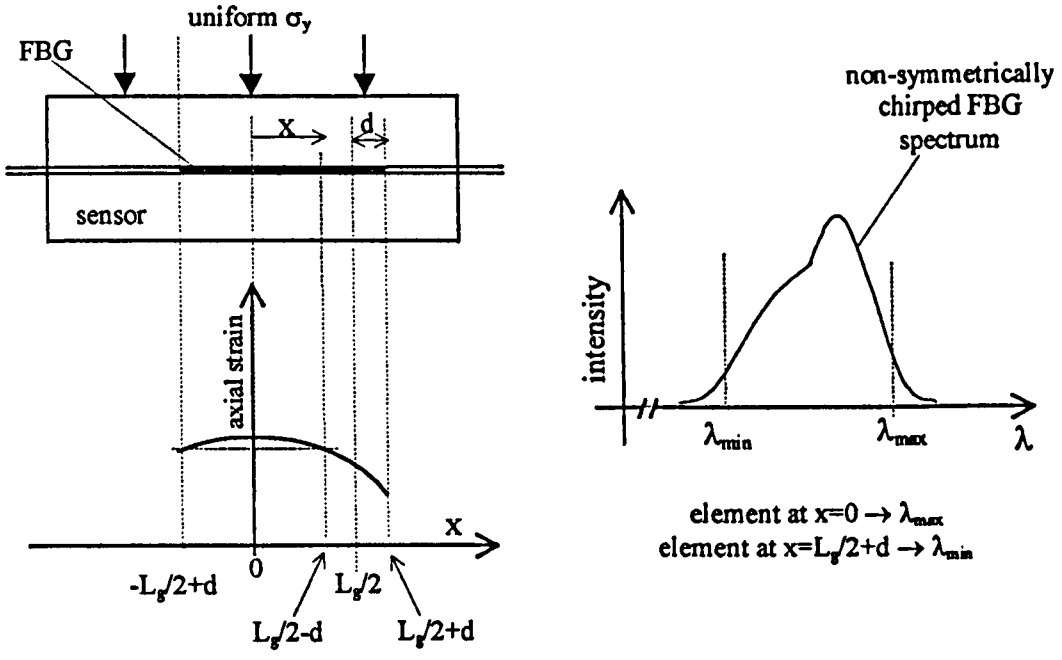

Fig.6.18: Effect of off-centre placement of the embedded FBG on the axial strain along the embedded grating, and on the reflection spectrum shape.

6.3 Comparison of theoretical predictions and experimental results using both models for the single-fibre sensor

The experimental results from measuring the single-fibre sensor have been presented in section 5.3.2. The comparison of the measured sensor response to vertical stress, with the theoretical predictions based on the fibre independent model, was given in Fig.5.35. The theoretical prediction and the experimental measurement of the sensor responsivity are significantly different. The theoretical prediction overestimates the stress transferred from the elastomer to the fibre by an order of magnitude, and hence the induced Bragg wavelength shift. The assumption that the embedded fibre follows the deformation of the surrounding material, which was the basis of the theoretical analysis presented in the previous chapter, was inaccurate.

In this section the prediction of the fibre dependent model described in this chapter will be compared with the experimental results, and with the prediction of the fibre independent model. For that purpose, the same mechanical parameters will be used for both models, which are summarised in Table 6.1. It is reminded that the elastic properties of the material could not be measured accurately. We will use the measured average value E=21MPa (see Table 5.1), and Poisson's ratio v=0.4.

The measured $\Delta\lambda_B$ - σ_y curve, and the theoretically predicted ones are plotted on Fig.6.19. The curve corresponding to the fibre independent model is obtained using eq.(5.38). The predicted curve of the fibre dependent model is given by eq.(6.37).

Parameter	Value	Parameter	Value
grating length L_g	5mm	sensor half height R	1.5mm
Bragg wavelength λ_B	836.5nm	matrix modulus E_m	21MPa
fibre half length L	5mm	fibre modulus E_f	72GPa
fibre radius r	62.5μm	matrix ν_m	0.4

Table 6.1: sensor parameters for modelled results.

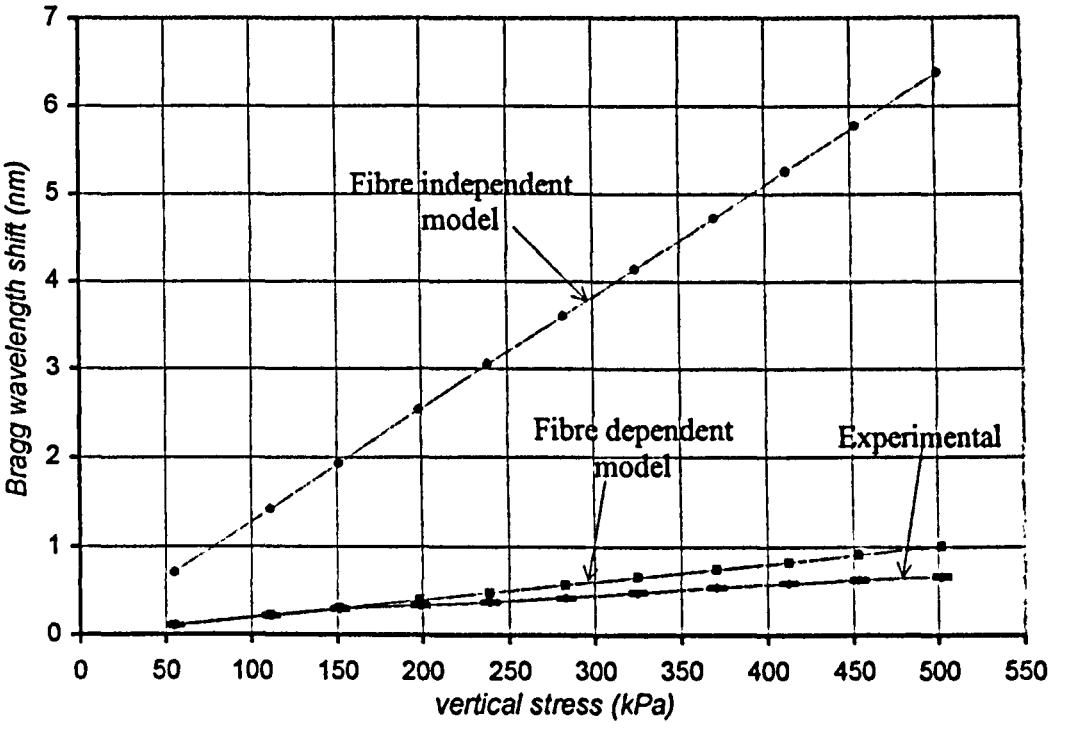

Fig.6.19: Bragg wavelength shift against vertical stress, as predicted by the two models, and as measured experimentally.

It is apparent that the fibre dependent model provides a significantly better approximation of the actual response of the sensor compared to the fibre independent model. However, the average measured sensor response is approximately 45% lower than the theoretical prediction. One reason for this error is the uncertainty of the actual elastic properties of the elastomer.

Fig.6.20 shows the effect of E_m and ν_m variation to the predicted sensor response. The experimental and theoretical (for E_m=21MPa, ν_m=0.4) curves are drawn for comparison. The other curves are obtained using eq.(6.37), by change one parameter only with respect to the theoretical curve, which parameter is shown as label next to the corresponding curve. The response is sensitive to ν_m by approximately 10% for $0.35 \leq \nu_m \leq 0.45$. Error in Poisson's ratio cannot therefore produce the observed deviation between the theoretical and experimental results. Variation of E_m in the range 1 to 200MPa, which covers the entire range of the engineering elastomers (Ashby, 1993,pg.28), produces significant variation of the predicted

sensor response. The prediction for E_m=130MPa is close to the experimental curve. However, this value significantly differs from the measured E_m=21MPa.

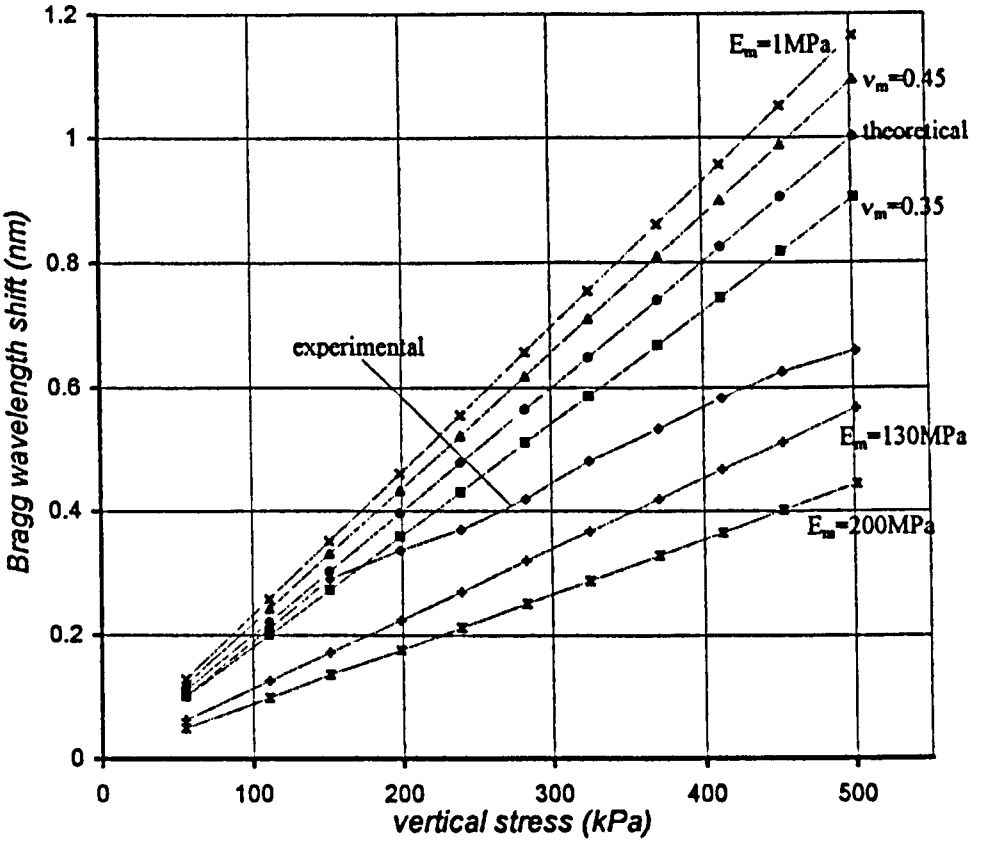

Fig.6.20: Modelled sensor sensitivity to E_m and ν_m variation. The experimental response is also drawn for comparison.

A second reason which could explain the error of the theoretical prediction, is the assumption of the theoretical model that the interfacial shear stress acting on the fibre at a distance x from the middle point, is uniform at the circumference of the fibre at that particular distance x. In other words, it was assumed that the interfacial stress around the fibre is independent of the angle ϕ in cylindrical coordinates[1]. This is true for the single-fibre model presented by Hull and Clyne (section 6.1.1), where a composite material is subjected to stress along the fibre axis. In this application however, stress is applied perpendicular to the fibre axis. Furthermore, the stress is applied in the y-direction only, which is normal to the top surface of the sensor, and not symmetrically around the fibre. This loading condition is possible to produce actual interfacial stresses around the fibre which depend on the angle ϕ. In that case, the overall interfacial shear stress, will not be given by the LHS part of eq.(6.7), eventually leading to error in estimating the in-fibre axial stress distribution by using eq.(6.18). The validity and the importance of this explanation can only be verified by accurately calculating the interfacial stress distribution using a theoretical model which will

consider both the shape and dimensions of the sensor, as well as the direction of the applied stress.

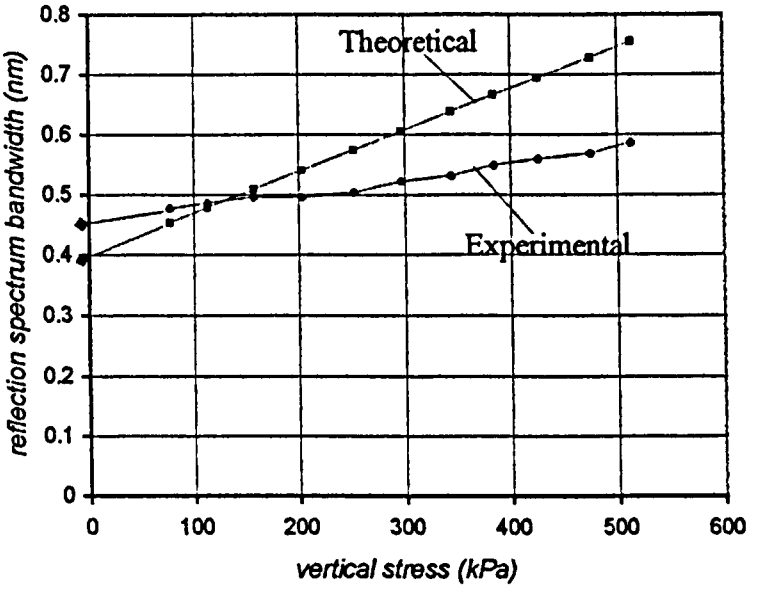

Fig.6.21: FBG reflection spectrum bandwidth. Comparison of theoretical prediction and experimental results.

The examination of the reflection spectra under different vertical stress, which were plotted in Fig.5.36, showed broadening of the reflection spectrum, which was also plotted in Fig.5.37. The experimental measurement of the spectrum broadening are plotted again in Fig.6.21 together with the theoretical prediction, given by eq.(6.35) increased by the bandwidth of the uniform grating B=0.4nm. The actual FBG bandwidth was measured[2] to be 0.46nm for the unstrained sensor, which explains the downwards shift of the theoretical curve. The measured average increase in bandwidth is 0.22pm/kPa. The fibre dependent model gives a significantly larger increase of 0.7pm/kPa. The overestimation of the bandwidth increase is related with the overestimation of the stress transferred to the embedded fibre for the reasons explained previously. The significant dependence of the spectrum broadening on the length of the grating L_g, which was shown previously in Fig.6.12, is another possible reason for the overestimation of the spectrum broadening. It is reminded that the length of the grating was not measured. We accepted that L_g is equal to the UV beam diameter. This requires that the intensity of the UV beam is uniform along the 5mm diameter, and the fibre is precisely aligned inside the interference pattern at the point where the two UV beams fully overlap, as can be inferred from the geometry of the FBG fabrication setup, explained in section 2.6.3. Neither the beam profile, nor the precise location of the fibre was known for the FBG. If the actual length of the grating is lower than

---

[1] The cylindrical coordinates are (x, r, ϕ), where x is the direction of fibre axis, r the radius, and ϕ the azimuth, as used previously in section 6.1.1.
[2] using the FBG readout system presented in section 3.5.

5mm, then the actual rate of broadening will be less than the predicted 0.7pm/kPa. The mean Bragg wavelength shift on the other hand is much less sensitive to L_g variation, as shown in Fig.6.14. This is a possible reason for the relatively larger error in estimating the spectrum broadening compared to the error in predicting the Bragg wavelength shift.

The fibre dependent model predicts a linear increase in Bragg wavelength with vertical stress. However, the measured sensor response is not linear, as shown in Fig.6.20. The observed non-linearity is repeatable within the error range of the experimental setup, as shown previously in section 5.3.2, Fig.5.34. The calibration results presented in chapter 3, particularly the force sensor response shown in Fig.3.13, as well as the FBG readout system response shown in Fig.3.34, which are both linear, are strong evidence that the non-linearity is not caused by the experimental setup. A possible reason, mentioned in section 5.3.2, is the non-uniform stress distribution which produces distortion of the reflection spectrum due to chirping of the grating. The spectrum broadening is an evidence of this distortion. However, the fact that the shapes of the wavelength shift and spectrum broadening curves, shown in Fig.5.34 and Fig.5.37 respectively, are not similar (the rate of wavelength shift tends to decrease as σ_y increases, contrary to the rate of spectrum broadening which slightly increases), is an indication that, not only the bandwidth, but also the spectrum envelope is distorted. The interaction of the distorted spectrum envelope with the peak detection algorithm (see section 3.6.1) could result in false calculation of the mean wavelength shift.

6.4 Experiments

The experimental results of the single-fibre sensor response have already been presented as a means of comparison between the prediction of the two theoretical models. However, the vertical stress response was only examined, in the simple form of the sensor where only one FBG is embedded horizontally in the elastomer. This is the only situation where the theory of single-fibre composite, as presented section 6.1.1, can be used to provide a reasonable prediction of the stress along the fibre.

In this section, all the laboratory work done regarding the elastomer sensor will be presented in detail. Objectives of the experiments are:

1. To measure the response of the horizontally embedded FBG to shear stress. The fibre-dependent model cannot be used to predict shear response. The fibre-independent model however, even though it cannot accurately model the actual response of the sensor, predicts that zero axial stress should be transferred on a horizontal grating, eq.(5.26). The shear response will therefore be measured and compared with the response to vertical stress.

2. To measure the response of an inclined FBG to vertical and shear stress. Based on the fibre-independent model, the vertical stress, and the parallel to the fibre axis component of shear stress, will result in axial strain on an inclined fibre, eq.(5.24). For that purpose, a second sensor had to be implemented, where the FBG is embedded at an angle. Conclusions on the effect of the fibre angle can then be derived by comparing the experimental results on those two single-fibre sensors.
3. To examine the feasibility of the 3-fibre sensor. The final version of the sensor will contain 3 optical fibres in a relatively small volume of material, which complicates the fabrication procedure. The fabrication of the sensor at a reasonable cost was an essential task.
4. To investigate the effect of the presence of 3 fibres on the response of each individual grating, by comparing the response of a 3-fibre sensor with that of the single-fibre sensors.
5. To re-examine conclusions which have already been derived from the single-fibre horizontal sensor, regarding the observed non-linearity, spectrum distortion, and bandwidth broadening, by collecting data from more than one sensors.
6. To examine the time response of the gratings to shear and vertical stress, which will provide an experimental evidence of any effects caused by the viscoelastic nature of the elastomer.
7. To measure the dynamic response of the sensor at low frequencies (0 to 4Hz). The upper frequency limit is set by the sampling rate of the FBG readout system, as explained in section 3.6.

Due to the lack of an accurate theoretical modelling of the 3-fibre sensor, it is not possible to predict the sensor behaviour and to quantitatively explain the results. Our comments and conclusions are based on the experimental data, collected on a limited number of sensors. The study of the two models presented so far can only help us to understand the principle of operation and to qualitatively explain the experimental results. The following experiments will provide essential information in order to accomplish the aim of this preliminary study, which was to examine the feasibility of the embedded FBG sensor.

Three sensors have been fabricated and tested. They are named as follows:

- **sensor-1Fh**: 1 FBG embedded horizontally. The response of this sensor to vertical stress has already been tested.
- **sensor-1Fi**: 1 FBG embedded at an angle.
- **sensor-3F**: This sensor contains 2 FBGs, one horizontal and one inclined. A third fibre (no grating) is also embedded inside the material.

The fabrication procedure of the elastomer sensor is described in section 6.4.1. The measurement of the shear stress response of sensor-1Fh will be described in section 6.4.2. The results from the measurement of the response of sensor-1Fi and sensor-3F to vertical and shear stress, is given in sections 6.4.3 and 6.4.4 respectively. The time response of the elastomer sensor, and particularly of the inclined FBG in sensor-3F, to variable frequency shear stress pulses (up to 4Hz), is given in section 6.4.5.

6.4.1 Fabrication of the elastomer sensor

The fabrication of the elastomer sensor will be presented in this section. The procedure will be explained for the 3-fibre sensor. The single-fibre sensors were fabricated using the same procedure, where the other two FBGs were omitted.

The fabrication procedure should satisfy the following requirements:

- All opposite surfaces of the sensor, or at least the upper and lower surfaces, must be precisely parallel to each other and smooth. Non-parallel (see also Fig.5.8a) and/or rough surfaces of the sensor will result in variation of the contact area between the sensor and the metallic surfaces of the testing apparatus. This condition will introduce error in calculating the vertical and shear stress applied on the sensor using eq.(3.1) and eq.(3.4) respectively.
- The elastomer is in liquid form prior to curing. It will therefore have to be poured into a mould, which must prevent leakage from gaps around the fibres, or other openings of the mould. Leakage will result in unsuccessful fabrication of the sensor and permanent damage of the FBGs due to contamination of the fibre surface from residual elastomer.
- The sensor should easily be removed from the mould, without over-bending or applying excessive axial stress on the fibres.

The first task of the sensor fabrication procedure was the construction of the mould. It was found that metal or plastic could not be used. A first attempt to make the sensor was achieved by pouring the material into a plastic box (BIM 109PB ABS potting box[1], 11x11x9mm). A bare fibre was horizontally installed by cutting two 0.25mm-width slits on the opposite vertical sides of the box, beginning from the open top, down to 1.5mm from the base of the box. The elastomer was then poured into the bow, filling it at a height of 3mm. Even in this simple case where only one fibre was installed, several problems were encountered. Leakage of the material was observed from the gap between the fibre and the mould wall. Even though we used mould releasing agent as recommended in the elastomer data sheet, it was impossible to remove the cured material without breaking the fibre due to

[1] Boss Industrial Mouldings Ltd, James Carter Road, Mildenhall, Suffolk IP28 7DE, England. Tel: +44 (0)1638 716101 Fax:+ 44 (0)1638 716554.

relatively strong bonding with the mould walls. Plastics, and for the same reasons metals, were rejected for use as the sensor mould.

A material which is easy to process, and also satisfies the requirements mentioned earlier, is engineering wax. Since the elastomer is low-temperature cured, a low-temperature melting wax is preferred, which is easier to process. The melting point of the particular wax was 85°C. The wax mould consists of two identical parts as drawn in Fig.6.22(a). When these two parts are held together, the rectangular cavity inside the wax has the required sensor dimensions, Fig.6.22(b). The liquid elastomer is poured inside the cavity using a syringe, via the 1.5mm diameter tube. A second tube is used to allow the air escape from the cavity while filling it with the material.

Each part of the wax mould can be individually fabricated in the workshop by cutting and milling. The sensor specifications and fabrication process require the two mould parts to be identical. An easy, time-effective method, for precise replication of the mould parts is to melt the wax and pour it in a metallic negative mould. Picture 4 in appendix II shows the metallic negative mould, and two identical wax parts made with it. The metallic mould was first preheated in an oven to ~100°C, and the liquid wax was then poured into it via the circular openings (see picture). The mould was preheated in order to avoid cracks on the wax mould due to rapid cooling of the wax. The wax mould can be easily removed after curing by opening the metallic mould and pushing it carefully with the fingers via the two circular openings.

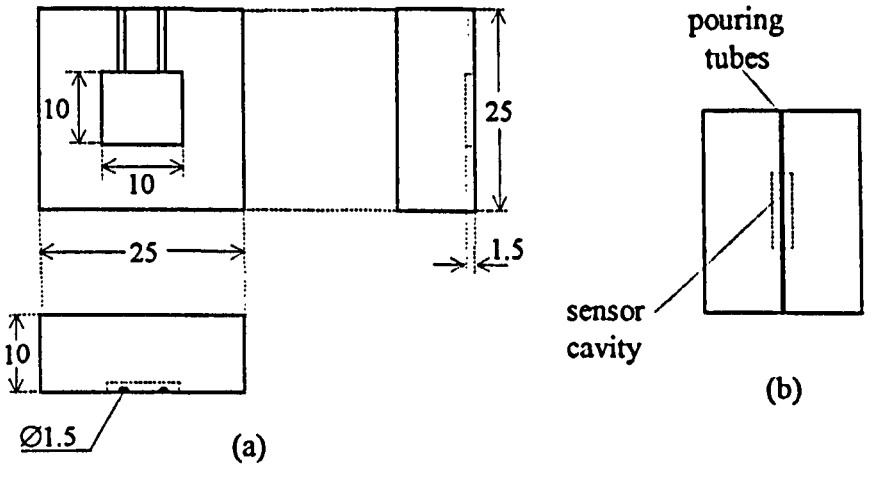

Fig.6.22: (a) Dimensions of each wax mould part (mm). (b) Two identical wax parts are used to form the sensor mould.

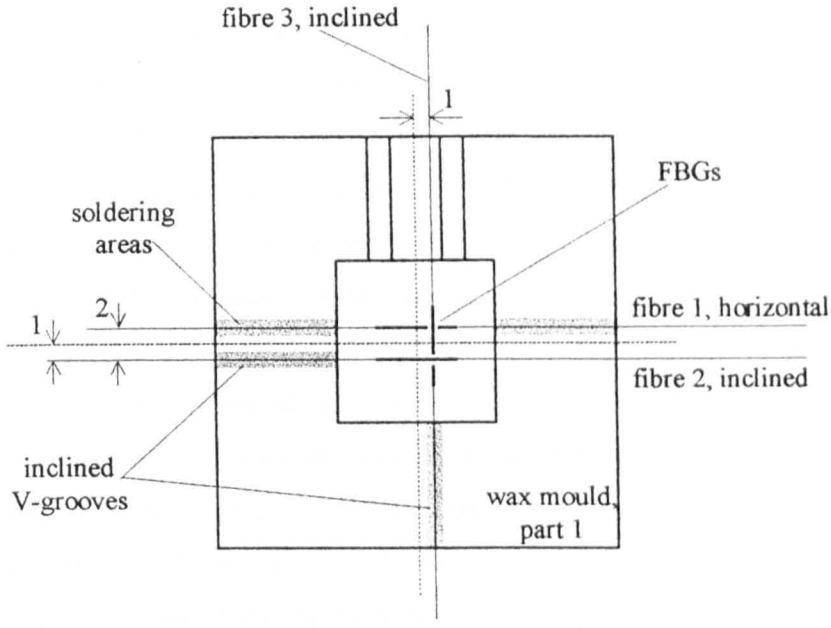

Fig.6.23: Fibre orientation and soldering areas on the wax mould (dimensions in mm, scale 2:1).

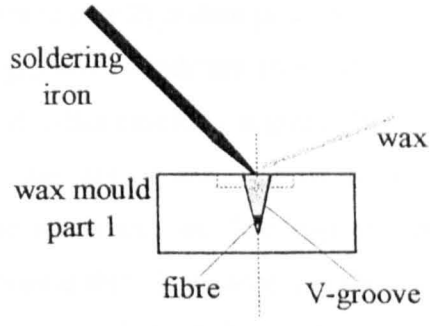

Fig.6.24: Soldering of the optical fibre on the wax mould.

Fig.6.23 shows the orientation of the 3 fibres inside the mould (top view). Fibre-1 is horizontal, fibre-2 lies on a vertical plane parallel to the vertical plane defined by fibre-1, and fibre-3 on a vertical plane perpendicular to the other two. The FBGs on each of the fibres are placed close to the centre of the rectangular cavity. In order to avoid contact of the fibres, which could affect the sensor response, or even lead to fibre breakage, the fibres are off-centred by 1mm. Any debris on the bare-fibre region around the FBG of each fibre is removed using methanol. The fibre is then temporarily mounted between two fixed, steel rods using blue tag, at the desired angle θ with respect to the horizontal plane. Fig.6.25 shows the alignment of one of the inclined fibres. The other two fibres are placed in the same way on 4 separate rods (not shown), so that the 3 FBGs intercept as shown in Fig.6.25. After this stage, a stereoscope is necessary to simplify the next steps. One of the wax mould parts is placed horizontally on a translation stage, and positioned underneath the gratings. Careful manipulation is required to avoid breakage of the fibres or misalignment. Two inclined V-

grooves have been previously etched on the wax using a small, flat screwdriver, to accommodate the inclined fibres 2 and 3. A picture of the fabrication setup at the point where the V-grooves are etched and the wax mould is properly aligned at the intersection of the 3 fibres is given in appendix II, picture 3. The fibres are then soldered to the wax mould using a soldering iron set at ~300°C. A droplet of wax fills the groove and permanently fixes the fibre, as shown in Fig.6.24. The soldering iron is then carefully placed inside the V-groove, just above the fibre in order to melt the wax around the fibre and provide a smooth top surface. It is important to keep the soldering temperature high in order to reduce the time required for this stage to be completed, and prevent degradation of the grating due to heating. The contact of the soldering iron with the fibre was avoided throughout this procedure.

The installation of the horizontal FBG does not require V-groove etching. The fibre is placed in contact with the mould and the soldering iron is moved along and parallel to the fibre at a distance ~1mm away from the fibre, with the hot tip just touching the wax surface. Experimentation with a bare fibre is required to perfect the technique. This is repeated for the other end of the fibre, until the entire fibre is embedded in the wax (grey regions, Fig.6.23), just underneath the top surface.

A second mould part (wax part 2) is then positioned on the top of part 1, as shown in Fig.6.25. Two inclined V-grooves, which are required to accommodate the two inclined FBGs, have also been etched. After carefully aligning the two parts by slightly moving and rotating the top part only, they are permanently fixed by soldering the contact interface around the corners with the soldering iron. The V-groves are then filled with wax which fixes the inclined fibres. Because there is no access in the interior of the mould (close to the sensor cavity), there will unavoidably be left a small air gap between the fibre and the V-groove close to the sensor cavity. This will eventually be filled with elastomer. However, the sensor performance will not be affected, due to the small height of the residual material around the inclined fibre, compared to the overall height of the sensor.

The fibres are now released from the rods. The gap along the contact interface of the two mould parts is then sealed by melting additional wax all around the mould. Care must be taken not to accidentally release the fibres, or block the input tubes. The mould is then filled with the elastomer, which was mixed and degassed according to the manufacturer instructions. The 1mm-diameter syringe needle is used to allow easy flow of the viscous material.

After the curing time is completed, (24h at 24°C for SCOTCHCAST), the sensor is removed by melting the surrounding wax using a hot-air gun[1]. The wax is removed in layers with a pause period of a few minutes between them, in order to avoid excessive heating of the sensor. The upper and lower surfaces of the sensor are finally cleaned by heating (with

[1] The output temperature from the air-gun was measured to be approximately 400°C.

the hot-air gun) and pulling a lens cleaning tissue over the surfaces, absorbing any residual wax of the surfaces.

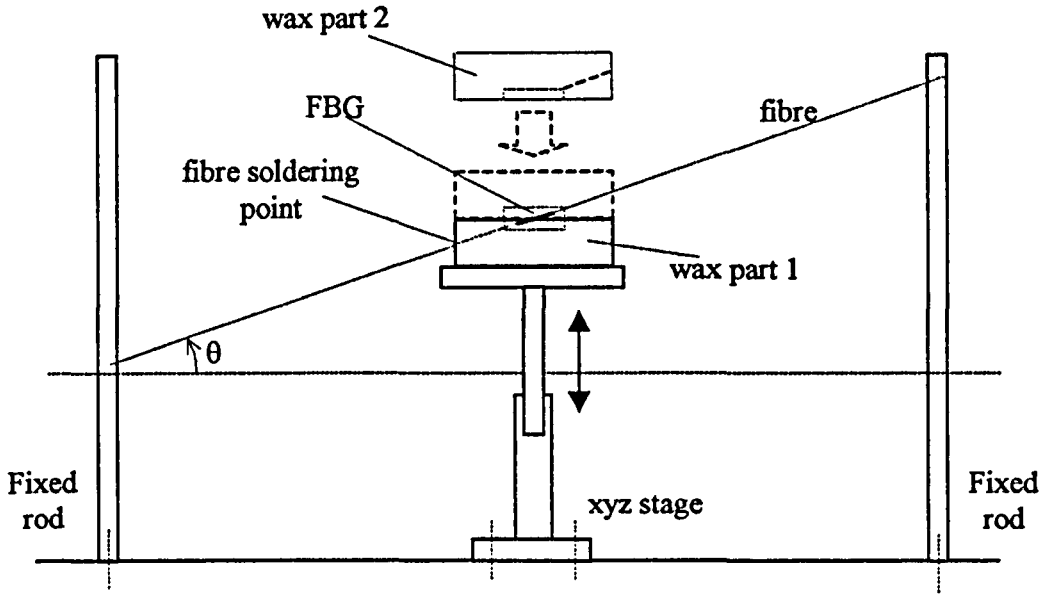

Fig.6.25: Alignment of the inclined FBG in the wax mould.

6.4.2 Measurement of sensor-1Fh to shear stress

The experimental setup for measuring the shear response of sensor-1Fh was described in section 3.1.2. The FBG readout system was set to 6scans/sec, and the SLD source to 82mA. Following the procedure described in section 3.6.2, the wavelength resolution of the system was measured to be 0.02nm. The sensor was measured under constant vertical stress of approximately 250kPa. In order to avoid slippage and prevent breakage of the fibre, shear stress was restricted to the range −110 to +110kPa.

Initially the sensor was subjected to 0.5Hz, variable amplitude, shear stress pulses. Even at relatively large shear stresses (up to 80kPa) it was difficult to observe shift in the Bragg wavelength due to the ±0.01nm system noise. Instead, the sensor was subjected to continuous shear which was manually triggered on and off by the signal generator. Shear was applied for approximately 10s and the average value of the Bragg wavelength shift was recorded. The magnitude of shear stress was measured during the off-transient, in exactly the same way as described in section 3.2.1 (Fig.3.7, voltage ΔV_2).

The Bragg wavelength shift against shear stress is plotted in Fig.6.26. Shear was applied in two directions, parallel and perpendicular to the FBG axis. In order to measure the sensor response to negative shear (opposite way), the sensor had to be manually rotated and aligned for each of the 4 curves plotted. Positive wavelength shift is observed in both

positive and negative shear. The average responsivity to shear stress is approximately +0.45pm/kPa, which is 3 times lower than the average responsivity of the same grating to vertical stress (1.3pm/kPa, section 5.3.2). This result is in contrast with the fibre-independent model, which predicts that the horizontal FBG is independent of shear stress, eq.(5.26). However, the response of the grating to vertical and shear stress is significantly different.

Because of the relatively large noise on the FBG readout system, it is not possible to examine the sensor response accurately in terms of linearity. Neither the actual shape, nor the relative difference of the response curves under different shear directions can be obtained, due to the overlapping of the curves, as they are defined by the error bars.

The reflection spectra for several values of shear stress, in the range −110kPa to +110kPa, parallel and perpendicular to the FBG, are given in Fig.6.27 to Fig.6.30. Each spectrum on any of those graphs corresponds to a random acquisition during the period where the sensor is under constant shear stress, and are therefore not directly related to the data points shown in Fig.6.26, which are average values of the Bragg wavelength shift. The relatively small wavelength shift, as well as the random noise on the intensity of each pixel, which, for this particular grating and readout system settings, was measured as ±6counts (see also section 3.6.2), does not allow the measurement of change in the spectrum bandwidth. The rotation of the sensor, which determines the direction of shear, alters the power of the reflected light. The peak intensity varies between the maximum value of −1570counts, Fig.6.28, to the minimum value of −1670counts, Fig.6.29. The placement of the sensor inside the testing apparatus (Fig.3.1) results in bending of the optical fibre. The change in the intensity is caused by the bending losses of the fibre, which are different each time the sensor is relocated, since the fibre is disturbed. The sensitivity of the fibre to bending was observed experimentally by carefully tweaking the fibre while the sensor was placed in the experimental apparatus. Keeping the readout system settings unaltered, the variation of the maximum intensity of the reflected light was measured to be approximately 200 counts. The bending radius, however, could not be accurately measured due to the limited access[1] to the sensor.

[1] The sensor and the lead-in fibre could only be viewed by the 3mm gap (equal to the sensor height) between the base and the top plate of the setup.

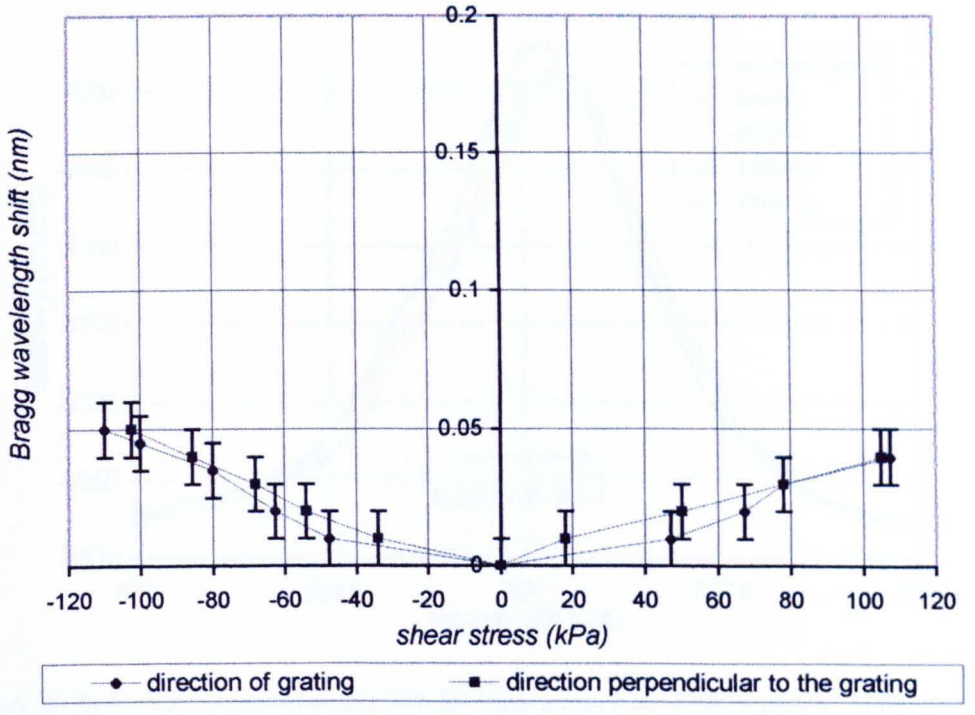

Fig.6.26: Bragg wavelength shift of sensor-1Fh against shear stress. Shear was applied on two directions, parallel and perpendicular to the FBG.

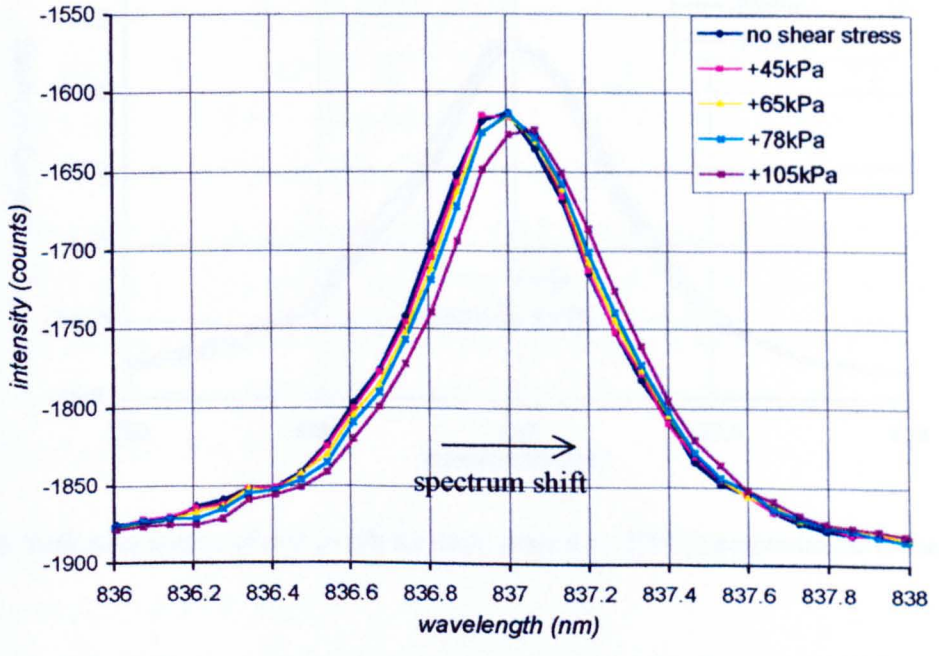

Fig.6.27: Reflection spectra of sensor-1Fh for shear stress 0 to +120kPa parallel to the grating.

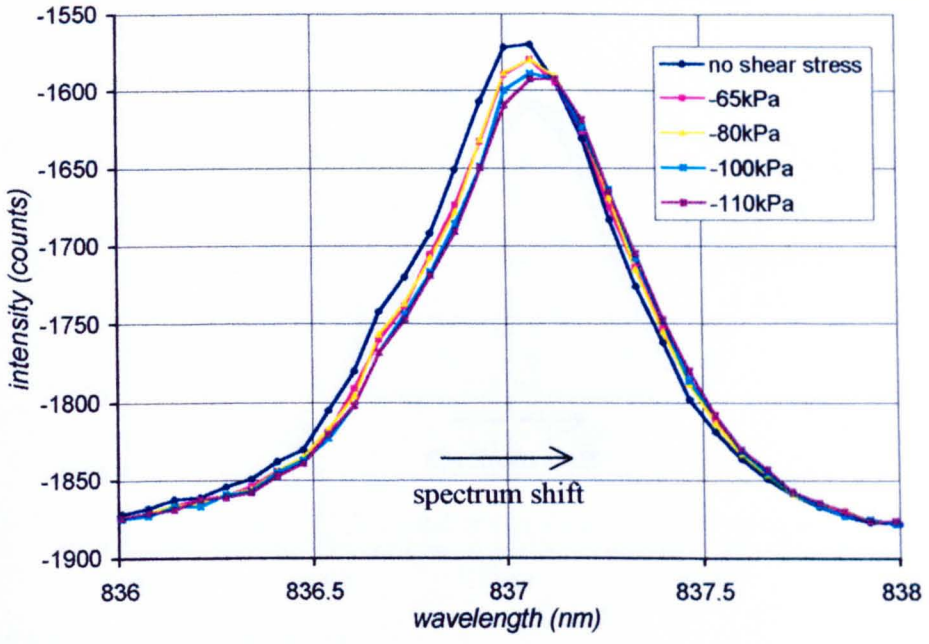

Fig.6.28: Reflection spectra of sensor-1Fh for shear stress 0 to -120kPa parallel to the grating.

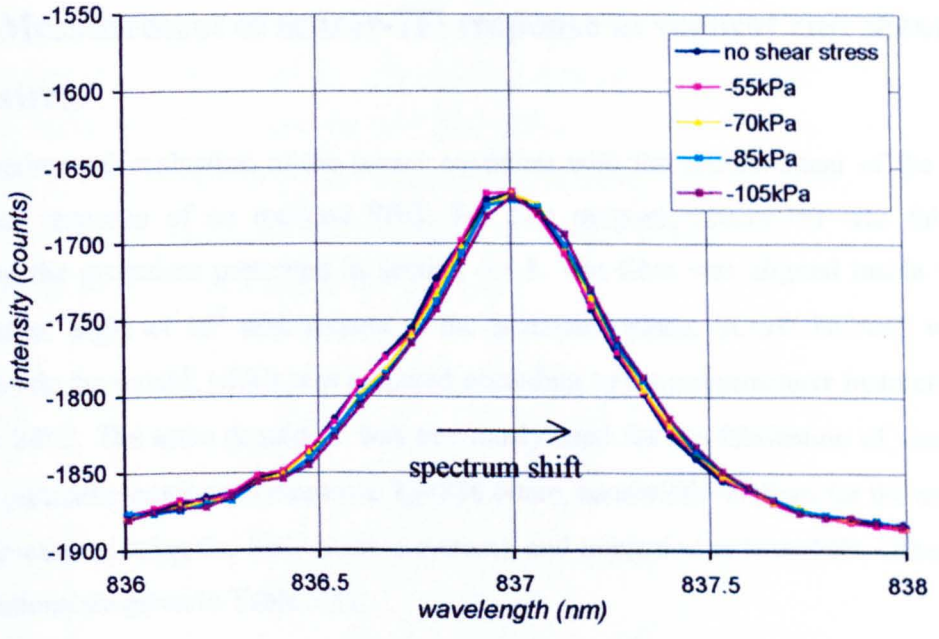

Fig.6.29: Reflection spectra of sensor-1Fh for shear stress 0 to -120kPa perpendicular to the grating.

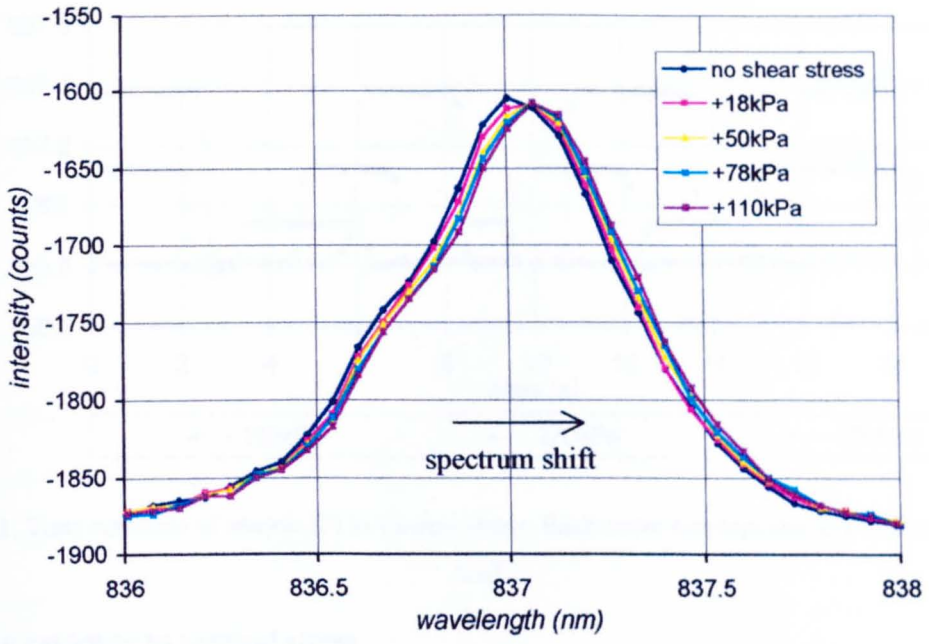

Fig.6.30: Reflection spectra of sensor-1Fh for shear stress 0 to +120kPa perpendicular to the grating.

6.4.3 Measurement of sensor-1Fi response to vertical and shear stress

The experimental evaluation of the sensor continues with the measurement of the vertical and shear response of an inclined FBG. For that purpose, sensor-1Fi was fabricated, following the procedure presented in section 6.4.1. The fibre was aligned inside the wax mould at an angle of 16° with respect to the horizontal plane. SCOTCHCAST was then potted inside the mould, which was prepared according to the manufacturer instructions and cured at 24°C. The same procedure was previously used for the fabrication of sensor-1Fh. For this particular grating we measured λ_B=836.60nm, bandwidth=0.49nm for the unstressed sensor (measured using the FBG readout system), and transmission loss=6dB. Other grating specifications are given in Table 3.11.

6.4.3.1. Measurement of sensor response to vertical stress

Time response to vertical stress

The sensor response to vertical stress was measured using the setup presented in section 3.1.4. Fig.6.31 shows the variation of the Bragg wavelength in time. The weights plate is manually moved on and off the top plate, as described previously for sensor-1Fh (section 5.3.2). A significant difference compared to the horizontal grating response, Fig.5.32, is that the effect of viscoelasticity is less noticeable, but still exists.

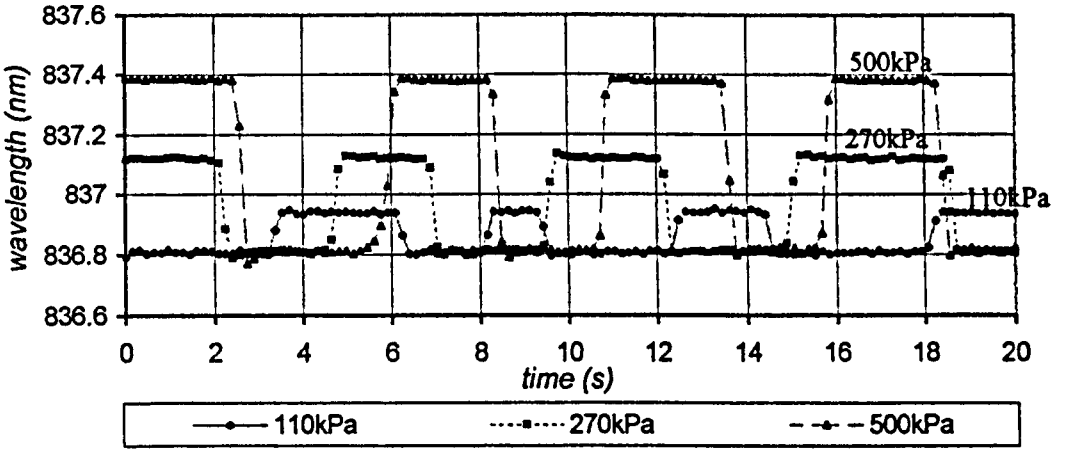

Fig.6.31: Time response of sensor-1Fi to vertical stress. Each curve corresponds to a different vertical load.

Grating response to vertical stress

Fig.6.32 shows the measured Bragg wavelength shift against vertical stress. $\Delta\lambda_B$ was calculated by measuring the average value of Bragg wavelength, as explained in section 5.3.2. The SLD source was set to 82mA and the acquisition speed to 6scans/sec, giving 0.016nm resolution (section 3.6.2). Two measurements are plotted on the graph, the second taken approximately 30min after the first one, without removing the sensor from the testing apparatus. The response is very close to linear. The responsivity is measured 1.2pm/kPa.

The reflection spectra are given in Fig.6.33. Spectrum broadening is clearly observed, which is plotted in Fig.6.34 against vertical stress.

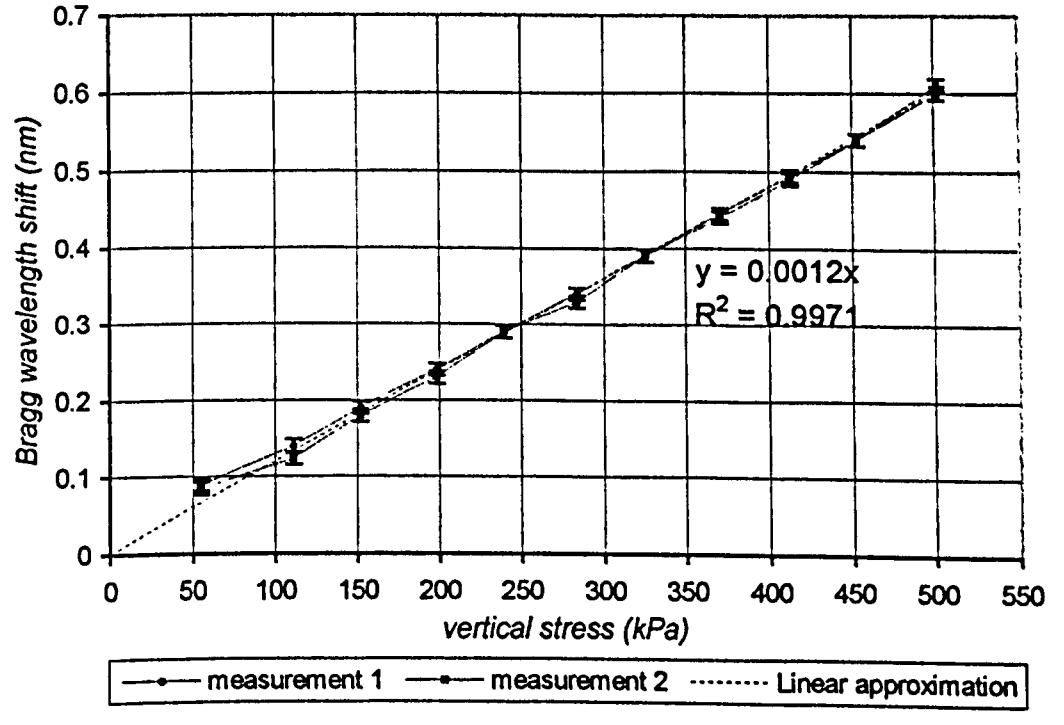

Fig.6.32: Measured Bragg wavelength shift against vertical stress for sensor-1Fi.

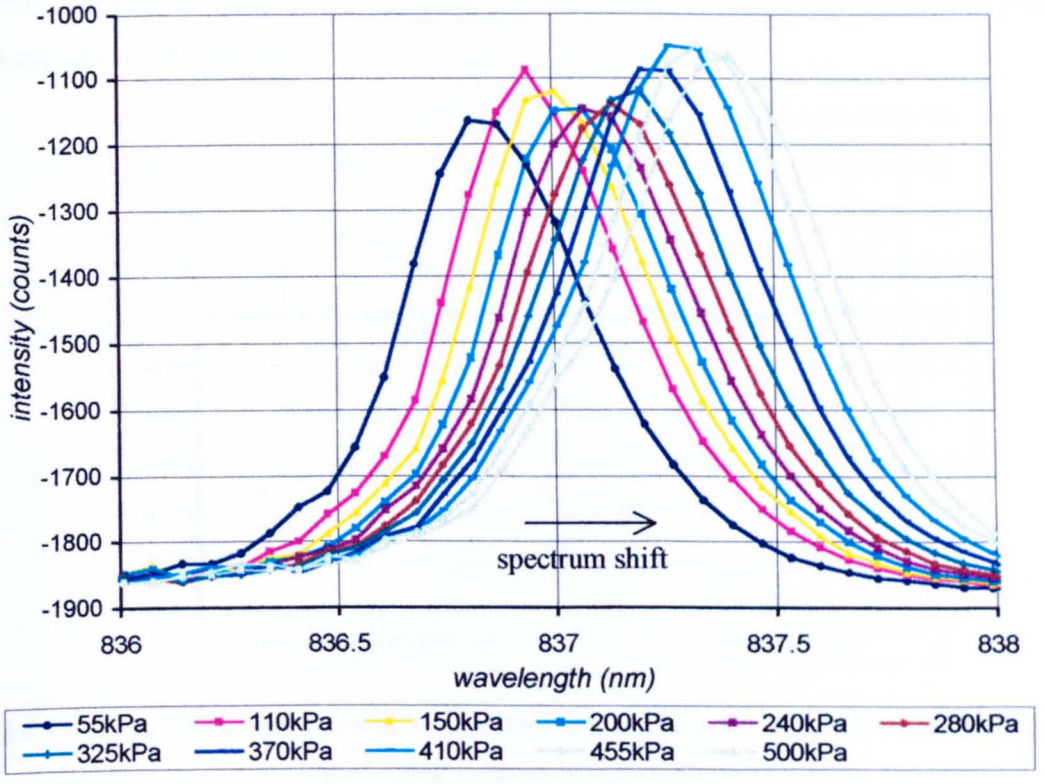

Fig.6.33: Reflection spectra of sensor-1Fi under different vertical stress.

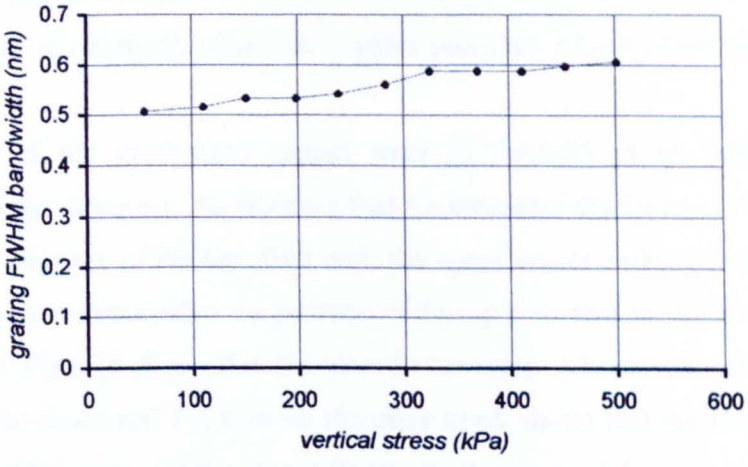

Fig.6.34: Spectrum broadening of the grating in sensor-1Fi under vertical stress.

6.4.3.2. Measurement of the sensor response to shear stress

Time response to shear stress

The response of sensor-1Fi to shear stress was measured using the setup presented in section 3.1.2. The FBG readout system was set to 6scans/sec, and the SLD source to 82mA, the same settings as used during the measurement of the response to vertical stress. The vertical stress, which provides the friction between the sensor and the testing apparatus, was kept

constant and approximately equal to 250kPa. 0.5Hz, variable amplitude, shear stress pulses were applied on the top plate.

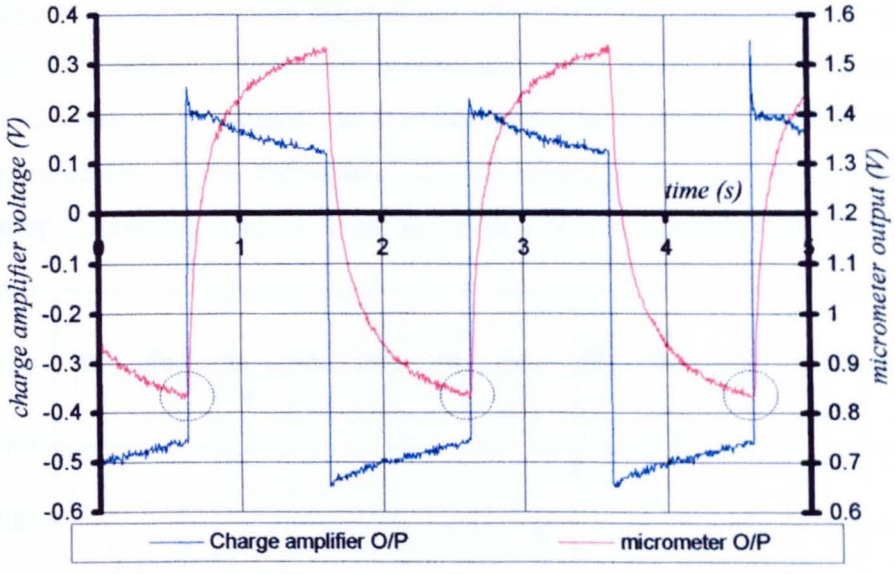

Fig.6.35: 0.5Hz, 32kPa shear stress pulses used for the measurement of sensor-1Fi shear response. The measured shear strain is also shown.

A typical time response of the force and displacement readout system is shown in Fig.6.35. The Bragg wavelength was measured simultaneously, which is shown in Fig.6.36. Good repeatability is observed, where each pulse produces $\Delta\lambda_B$=0.17nm ±0.01nm due to noise.

The shape of the micrometer output trace in Fig.6.35 is an indication of the viscoelasticity of the elastomer. An evidence that the measured displacement of the top plate is not caused by slippage of the top plate with the upper sensor surface, is the observation that, before each shear stress pulse, the position of the top plate remains unchanged (points in circles, Fig.6.35). Fig.6.35 shows that the viscoelastic creep is larger than the initial elastic deformation of the elastomer. Fig.6.36 on the other hand, shows that the Bragg wavelength shift of the embedded grating is almost unaffected by the creep of the surrounding elastomer matrix. Even though the elastomer creeps, it seems that the axial stress which is transferred on the fibre is nearly constant. This effect was also observed previously when the response of the same sensor to vertical stress was examined, Fig.6.31. Only a small drift in the wavelength is observed, which is comparable to the noise of the readout system. This explains the random appearance of this drift in successive pulses shown in Fig.6.36, and in the expanded view in Fig.6.37. Without altering the input stress, the acquisition speed increased to 12scans/sec (maximum speed). The measured trace of the Bragg wavelength shift is shown in Fig.6.38. The first 5s are expanded in Fig.6.39, which shows clearly the viscoelastic drift in Bragg wavelength (in circles). The noise significantly degrades the wavelength resolution down to 0.04nm. Observing the transitions between the 0 and 32kPa states, immediate response of the grating is observed. The rise time from 0 to 32kPa is

measured 83ms (=1s/12scans). The actual response can probably be faster than the measured, but could only be examined using a faster FBG readout system than that available.

The experimentally observed insignificant effect of viscoelasticity on the embedded FBG response is beneficial to the sensor performance, since it reduces the measuring errors and enables the use of the sensor for low frequency measurements. The reason for the observed insensitivity of the embedded FBG to viscoelasticity has to be theoretically investigated by considering a model which will incorporate the viscoelasticity of the matrix.

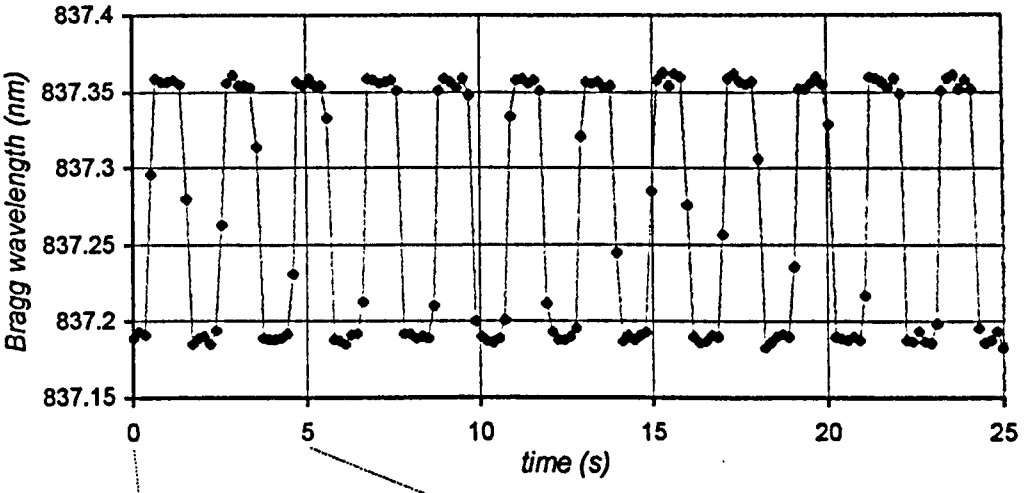

Fig.6.36: Bragg wavelength shift of sensor-1Fi due to 0.5Hz, 32kPa shear stress pulses, measured for 25sec at 6scans/sec.

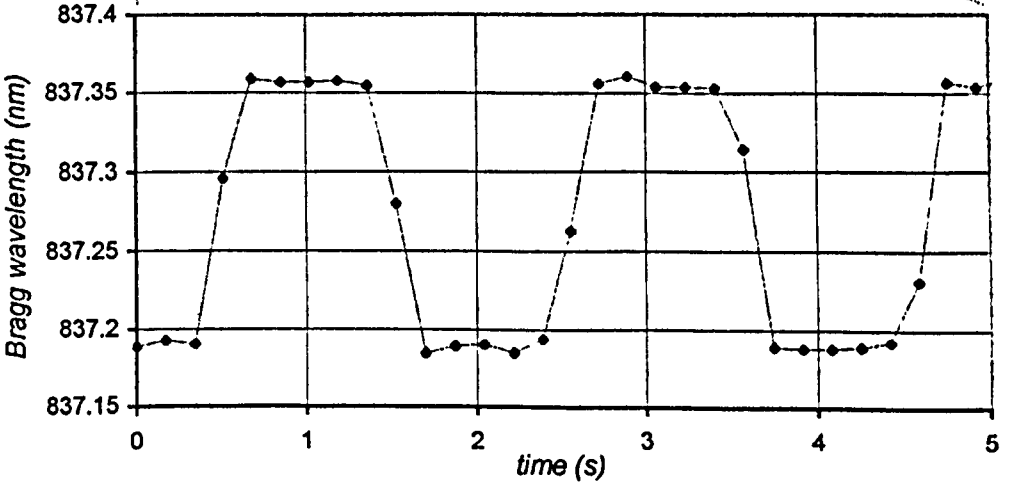

Fig.6.37:Detail of Fig.6.36.

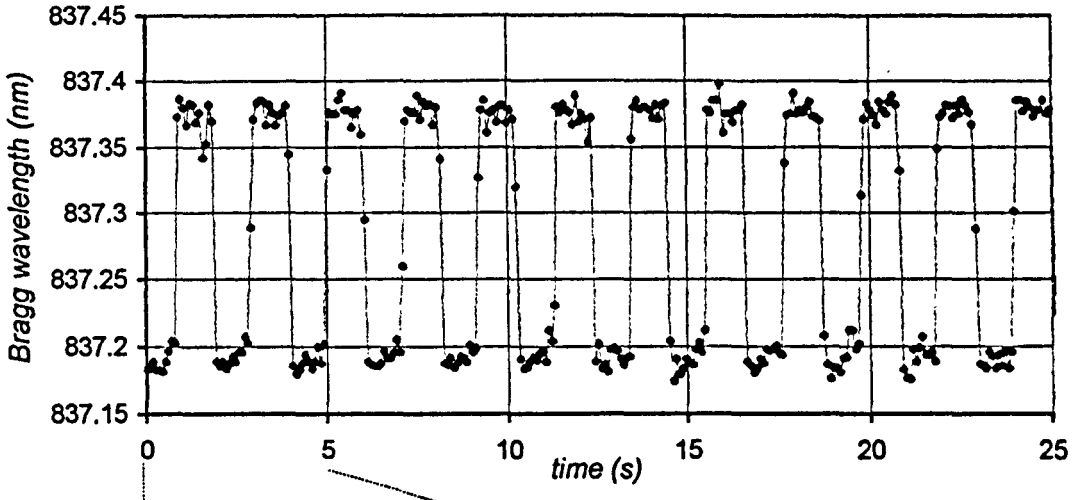

Fig.6.38: Bragg wavelength shift of sensor-1Fi due to 0.5Hz, 32kPa shear stress pulses, measured for 25sec at 12scans/sec.

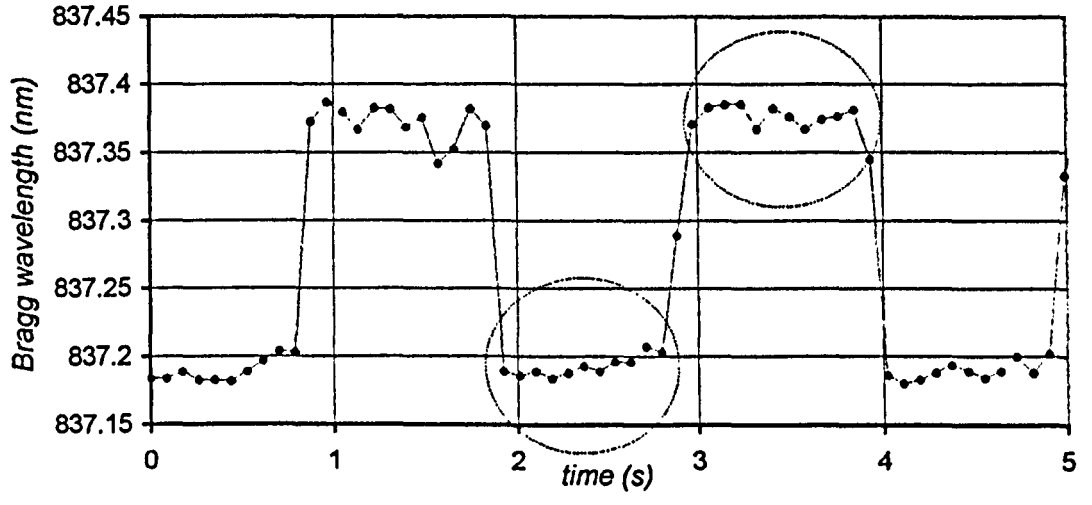

Fig.6.39: Detail of Fig.6.38. The drift in Bragg wavelength due to viscoelasticity is shown in circles.

Bragg wavelength response to shear stress

The Bragg wavelength shift of the inclined FBG, as a function of shear stress applied parallel, and perpendicular to the fibre axis, is given in Fig.6.40. The duration of the experiment, for all three sets of data, is approximately 3hours. The air temperature close to the setup (closer than 10cm from the sensor) was 22±0.5°C throughout the experiment. This temperature fluctuation corresponds to fluctuation of the Bragg wavelength by ~±0.003nm. Since this is much less than the wavelength resolution of the readout system, which was measured to be ~0.02nm, the effect of the wavelength shift due to temperature variation can be neglected.

The second measurement was taken after completing the first set of measurements in both ways (-110kPa to 0kPa, and 0kPa to 110kPa), which requires rotation of the sensor. The

position of the sensor, and the fibre orientation in the two measurements are therefore not identical, which is a possible reason for the 5% average difference between the two measurements. Non-linear response is also observed for both positive and negative shear. Average responsivity of the inclined FBG to shear parallel to the fibre is 4.8pm/kPa and –3.5pm/kPa for positive and negative shear respectively. The responsivity of the grating when shear is applied perpendicular to the fibre, decreases by an order of magnitude.

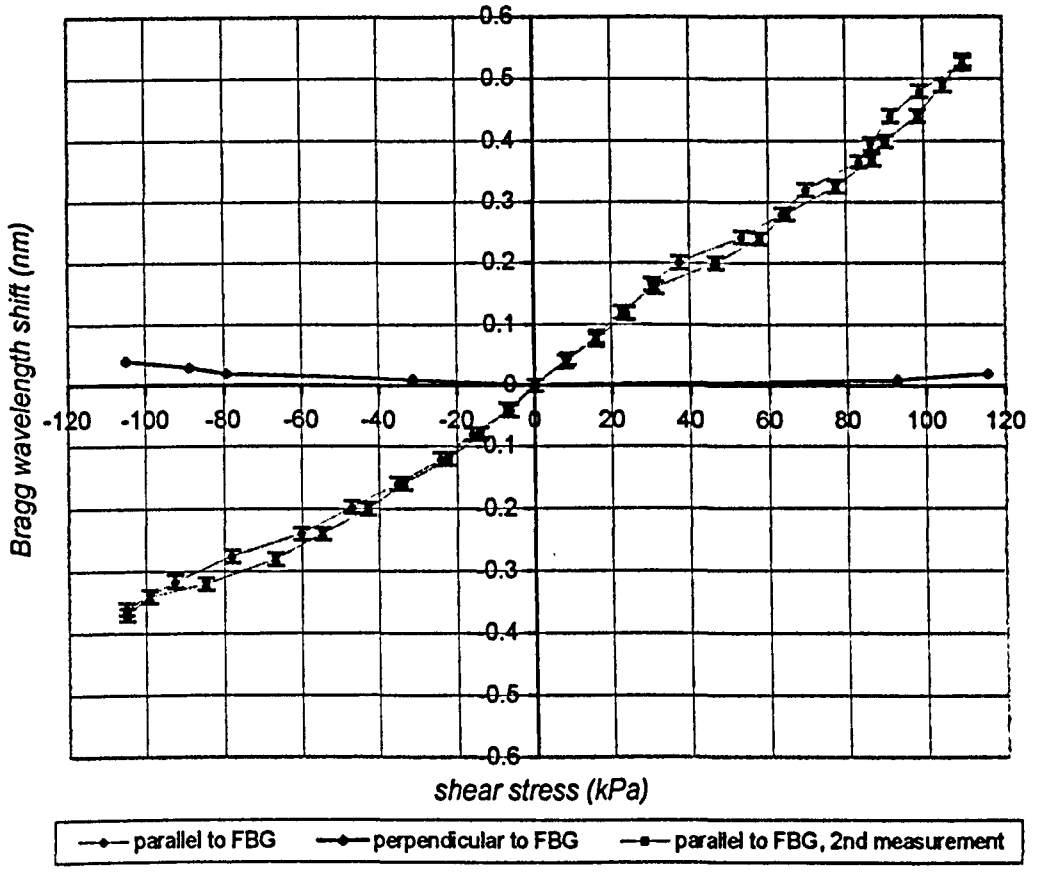

Fig.6.40: Bragg wavelength shift of sensor-1Fi against shear stress applied parallel, and perpendicular to the FBG.

This result is the first experimental evidence that the inclined FBG responds to shear applied parallel to the fibre axis, which gives $\Delta\lambda_B>0$ for $\tau>0$, and $\Delta\lambda_B<0$ for $\tau<0$, which can be obtained by the fibre-independent model. Combining eq.(5.23) and eq.(5.24), for $\sigma_y=0$[1], we obtain:

$$\Delta\lambda_B = \frac{0.8\lambda_B\tau_{yx}}{E}(1+\nu)\sin 2\theta \qquad (6.43)$$

where E=21MPa (Table 5.1), ν=0.4, λ_B=836.60nm and θ=16°. Eq.(6.43) is plotted in Fig.6.41, together with the experimental results. The prediction for shear perpendicular to the grating is $\Delta\lambda_B=0$. Similar to the prediction for the sensor response to vertical stress, Fig.5.35,

[1] In the experimental results we examine the shear response by assuming $\Delta\lambda_B=0$ for $\sigma_y\approx$250kPa. The actual Bragg wavelength shift with respect to the unstrained sensor is the summing of the measured, plus ~0.3nm due to vertical compression, Fig.6.32.

the predicted responsivity is an order of magnitude larger than the measured. As it has been mentioned in section 5.3.2, the reason for this error is the overestimation of the strain transferred by the elastomer to the matrix, based on the assumption that the fibre follows precisely the deformation of the material.

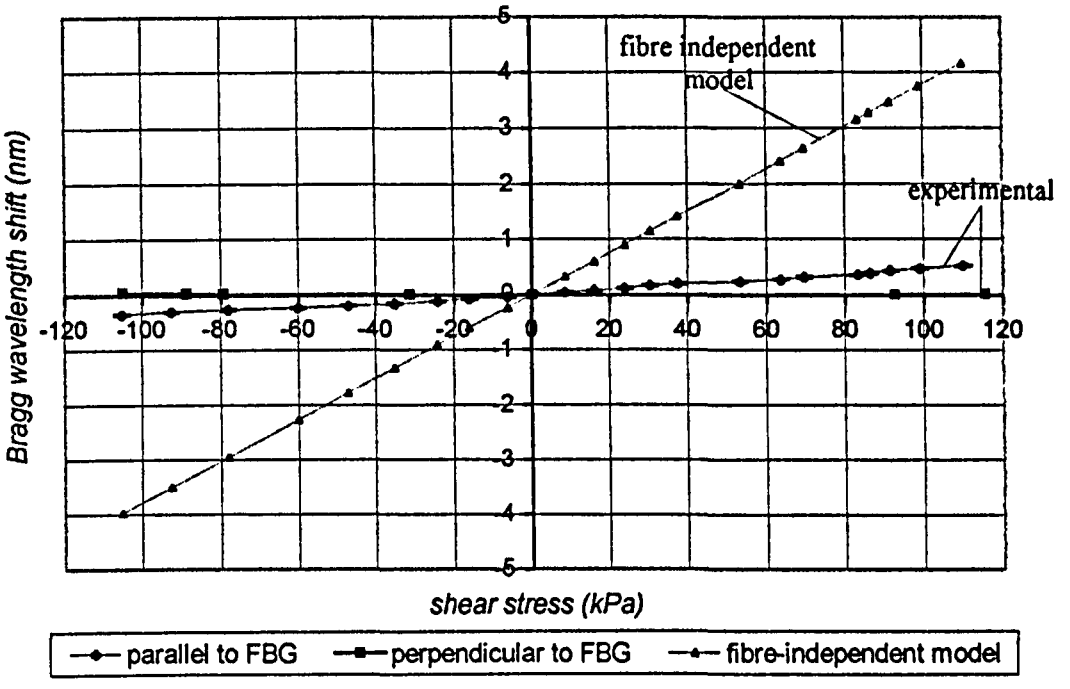

Fig.6.41: Comparison of the theoretical prediction based on the fibre-independent model, with the experimental results, for the inclined grating under shear stress.

Spectrum distortion due to shear stress

The reflection spectra for sensor-1Fi, for positive and negative shear stress parallel to the fibre axis are given in Fig.6.42 and Fig.6.43 respectively. Positive shear causes spectrum broadening and distortion of the left side of the spectrum envelope (around 837nm), which is particularly observed for shear stress >80kPa (last 5 spectra). A possible reason for this non-symmetric spectrum broadening is the accidental offset of the grating from the centre of the sensor during the fabrication procedure. This condition produces non-symmetric axial strain along the grating length, which results in non-symmetric chirp, and eventually non-symmetric reflection spectrum, as discussed in section 6.2.4 and shown in Fig.6.18 for the case of a horizontally embedded FBG.

Negative shear stress on the other hand, decreases the spectrum bandwidth. The bandwidth as a function of shear stress applied parallel to the FBG, is plotted in Fig.6.44. The reduction of the spectrum bandwidth cannot be theoretically predicted using the fibre dependent model because the fibre in this situation is inclined, which prevents the calculation of the axial strain along the grating. Under no shear stress the inclined fibre is strained due to the presence of the vertical stress. The measured bandwidth (0.55nm) is larger than it's

unstrained value (0.49nm), due to chirp. If negative shear stress is simultaneously applied parallel to the fibre axis, then the reduction in the axial strain will result in reduction of both the mean Bragg wavelength shift, and the FWHM bandwidth of the reflection spectrum. In this particular experiment, the bandwidth was always measured above 0.49nm. Therefore, axial compression of the FBG never occurred. This could happen if a sufficiently large negative shear stress was applied to produce axial compression of the fibre. This condition could not be satisfied during these experiments, because shear stresses greater than approximately 110kPa lead to slippage between the sensor and the metallic surfaces of the apparatus.

The bandwidth decreases between 0kPa and –110kPa with an average rate –0.54pm/kPa. The rate which the bandwidth increases from shear stress 0kPa to +110kPa, is +0.91pm/kPa. The difference in the rate of bandwidth change, as well as the different responsivity between positive and negative values of shear (Fig.6.40), shows that the sensor response is not symmetrical, but depends on the sign of shear stress. This is contrary to the prediction of the fibre-independent model, where $\Delta\lambda_B$ is a linear function of τ, eq.(6.43), therefore the responsivity should be equal for both signs of shear stress.

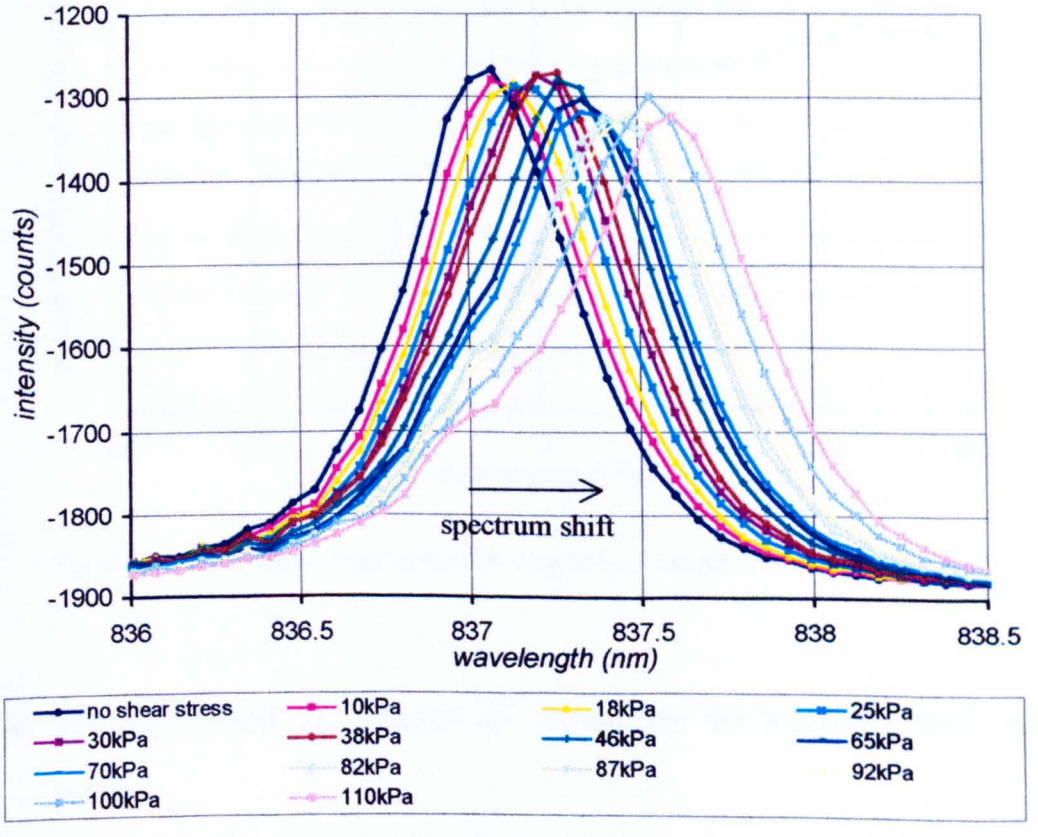

Fig.6.42: Reflection spectra of sensor-1Fi for shear stress 0 to +120kPa parallel to the grating.

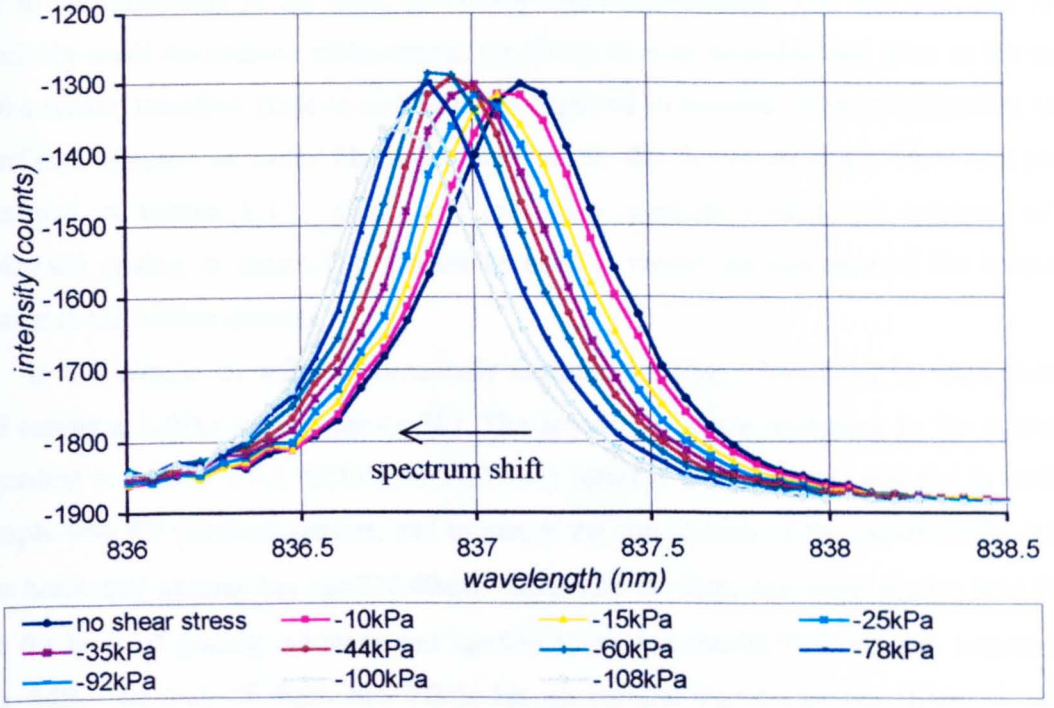

Fig.6.43: Reflection spectra of sensor-1Fi for shear stress 0 to -120kPa parallel to the grating.

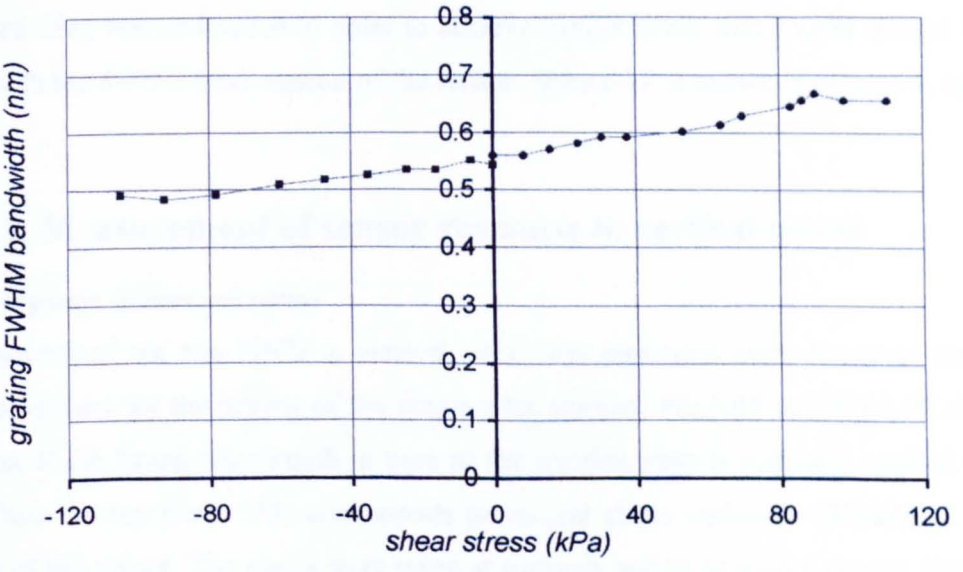

Fig.6.44: Reflection spectrum bandwidth of grating in sensor-1Fi under shear stress.

6.4.4 Measurement of sensor-3F response to vertical and shear stress

In the previous experiments, the response of a horizontal and an inclined grating was measured in two individual, single-fibre sensors. The final version of the sensor will include 3 FBGs embedded in the elastomer. The presence of 3 fibres will produce variation of the stress distribution inside the matrix compared to the single-fibre sensor. The stress field around each of the fibres cannot be considered symmetrical with respect to the fibre axis,

due to the interaction of the other two fibres with the elastomer. The fact that, due to the relatively small dimensions of the sensor, the fibres have to be embedded close to the centre of the sensor, therefore close to each other, is expected to increase the non-uniformity of the interfacial stresses on every fibre. For that reason, the theory of single-fibre composites presented in section 6.1.1, which was previously used to predict the response of the horizontal grating in sensor-1Fh, cannot be used to model the response of the horizontal grating in the 3-fibre sensor.

In this section we will experimentally examine the sensor behaviour by implementing and testing a 3-fibre sensor (sensor-3F). The sensor was made according to the procedure described in section 6.4.1. SCOTCHCAST was selected as the matrix material in order to comply with the previous sensors, and to permit the comparison of the experimental results. The horizontal grating has λ_B=836.40nm, bandwidth 0.54nm, and transmission loss 10dB. For the inclined grating we measured λ_B=836.52nm, bandwidth=0.47nm, and transmission loss 6dB. The axis of those two FBGs lay on parallel vertical planes (fibres 1 and 2, Fig.6.23). A third fibre with its axis perpendicular to the two others is also embedded. In order to save FBGs for future experiments, a bare fibre was used instead of a third grating. The third fibre was embedded in order to achieve similar stress distribution around the two FBGs with the 3-FBG final version of the sensor. Sensor-3F is shown in picture 6, appendix II.

6.4.4.1. Measurement of sensor response to vertical stress

Time response to vertical stress

The response of the two FBGs to vertical stress was measured using the same setup and settings as used for the testing of the single-fibre sensors. Fig.6.45 and Fig.6.46 show the variation of the Bragg wavelength in time as the weights plate is manually applied on, and lifted from the top plate. This corresponds to vertical stress variation ~370kPa on the top surface of the sensor. The traces were taken at 6scans/s and SLD source current 82mA, and the wavelength resolution was measured as 0.02nm for both gratings. Good repeatability of the measured Bragg wavelength shift is observed for both gratings. Drift due to viscoelasticity is observed in both gratings, which is more pronounced for the inclined grating. The time response of both gratings is similar to the response of sensor-1Fh, Fig.5.33.

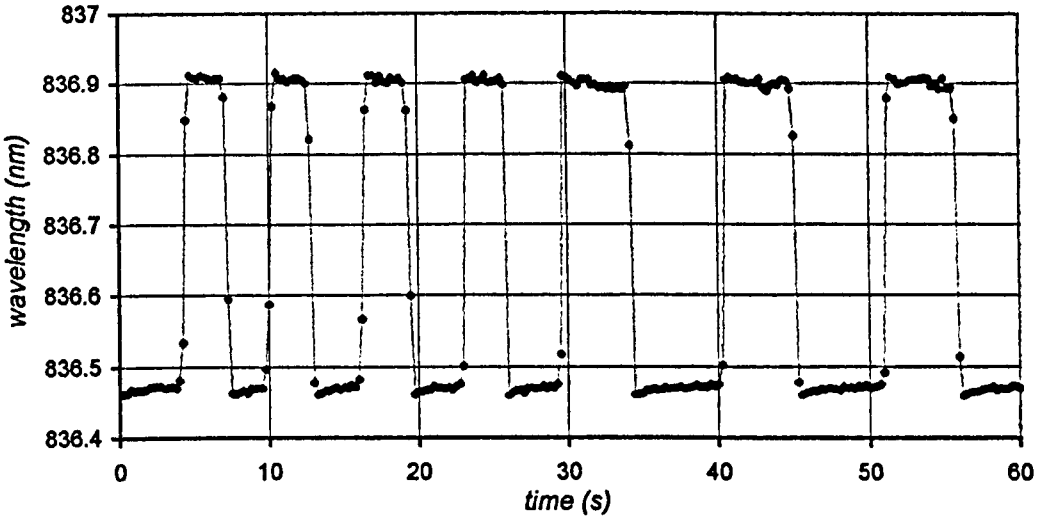

Fig.6.45: Measured Bragg wavelength shift of the horizontal FBG in sensor-3F under manual variation of vertical stress from 0 to ~370kPa.

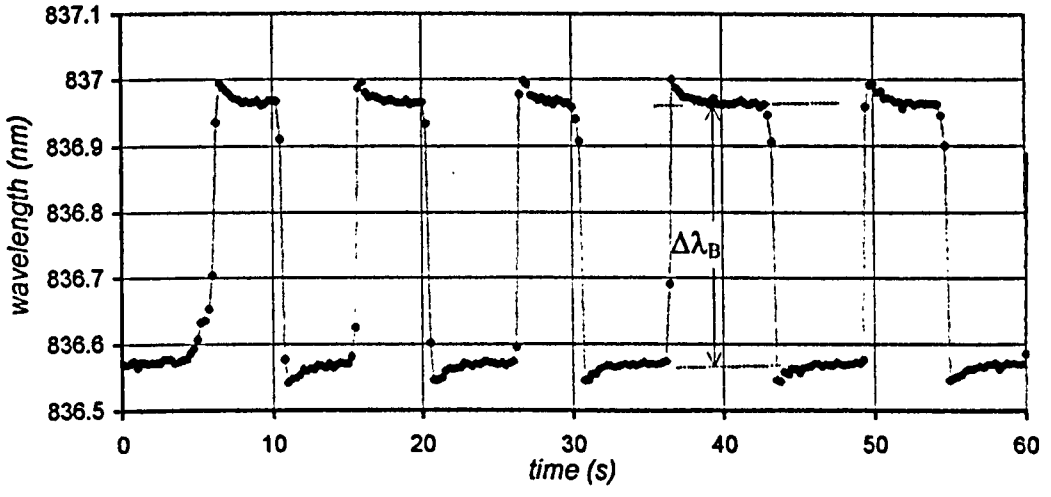

Fig.6.46: Measured Bragg wavelength shift of the inclined FBG in sensor-3F under manual variation of vertical stress from 0 to ~370kPa.

Grating response to vertical stress

Fig.6.47 shows the Bragg wavelength shift – vertical stress curve for the horizontal grating, where the second measurement was taken immediately one after the first one. Every data point was obtained by measuring the average wavelength difference, as described previously (section 5.3.2) and shown in Fig.6.46. The vertical load was manually varied at approximately 0.5Hz. The time responses previously shown in Fig.6.45 and Fig.6.46, were taken at a lower frequency in order to emphasise the effect of viscoelasticity. The accuracy of the measurements therefore, depends not only on the FBG readout system resolution, but also on the duration of the applied vertical stress. The uncertainty of the actual $\Delta\lambda_B$ is greater in the measurement of the inclined grating due to the relatively large drift due to viscoelasticity. This explains the poor repeatability between the two measurements taken for

the inclined grating, compared to the measurements for the horizontal grating. It is noted that the error bars in Fig.6.47 and Fig.6.48 are only related to the FBG readout system resolution.

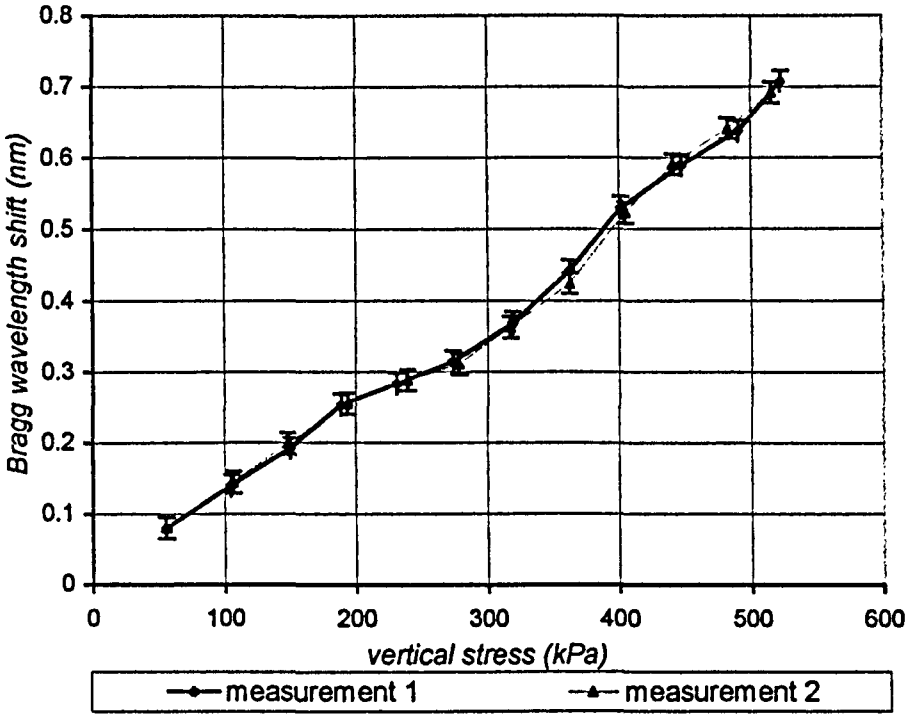

Fig.6.47: Measured Bragg wavelength shift against vertical stress for the horizontal FBG of sensor-3F.

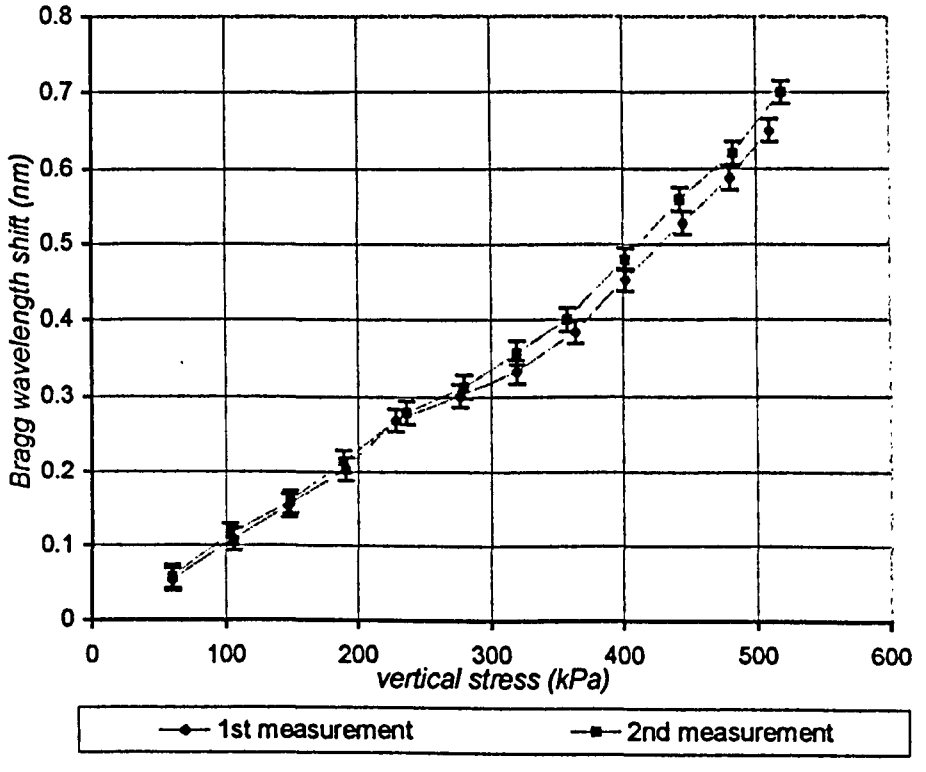

Fig.6.48: Measured Bragg wavelength shift against vertical stress for the inclined FBG of sensor-3F.

Non-linear response is observed for both FBGs. The average responsivity of the horizontal FBG is 1.35pm/kPa. The same average responsivity is measured for the inclined grating, Fig.6.48. The reflection spectra for the horizontal and the inclined gratings are given

in Fig.6.49 and Fig.6.50 respectively. The bandwidth of the two gratings is also given in Fig.6.51. We notice that, even though both gratings have very close responsivities, their spectrum envelope and bandwidth vary in a different way. In case of the horizontal FBG, a second peak appears around 836.7nm, for vertical stress ≥360kPa, Fig.6.49. This seems to be the reason for the difference in the measured bandwidths of the two gratings as the vertical stress increases, which is shown in Fig.6.51.

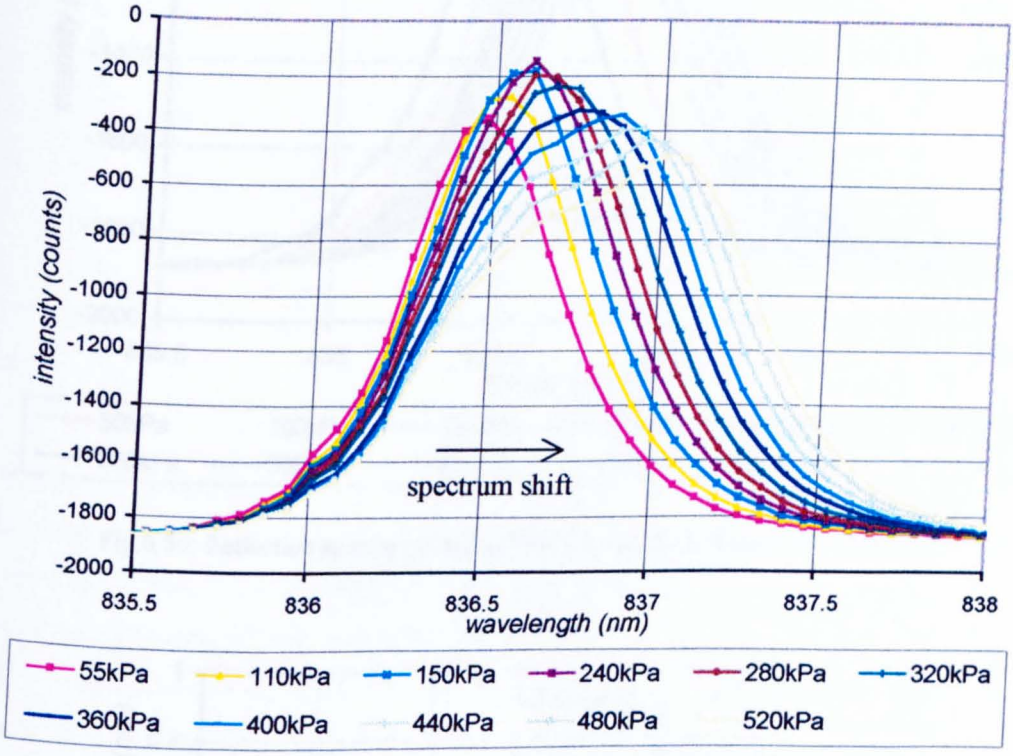

Fig.6.49: Reflection spectra of horizontal FBG in sensor-3F under vertical stress.

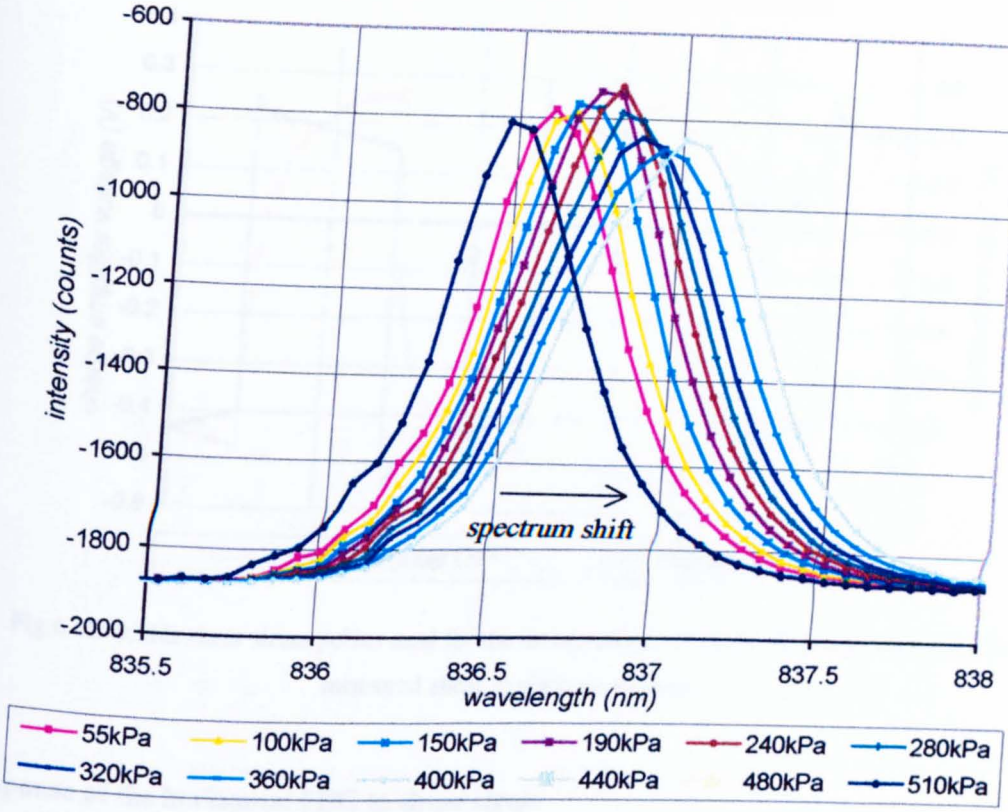

Fig.6.50: Reflection spectra of inclined FBG in sensor-3F under vertical stress.

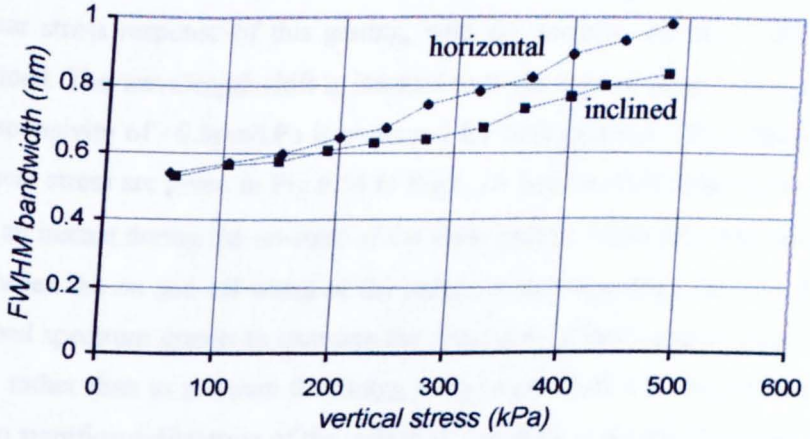

Fig.6.51: Spectrum broadening of the horizontal and inclined FBGs in sensor-3F as a function of vertical stress.

6.4.4.2. Measurement of sensor response to shear stress

The response of sensor-3F to shear stress was measured using an identical setup and settings, as used previously for measuring the single-fibre sensors (section 6.4.3). A typical time response for the shear force and displacement readout systems is shown in Fig.6.52.

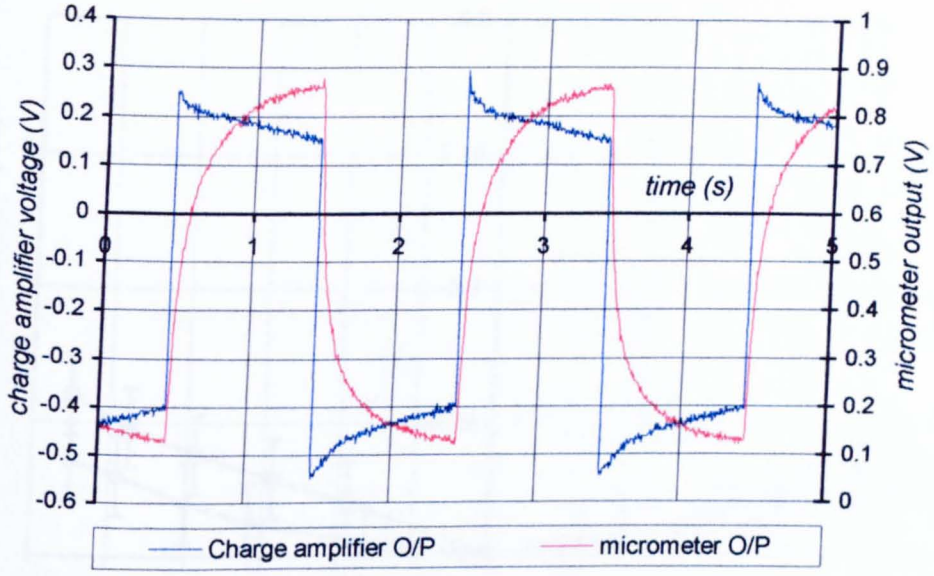

Fig.6.52: 0.5Hz shear stress pulses used for the measurement of sensor-3F shear response. The measured shear strain is also shown.

Response of the horizontal FBG to shear stress

The Bragg wavelength shift of the horizontal FBG to shear stress parallel and perpendicular to the fibre axis is given in Fig.6.53. Each curve is obtained by rotating the sensor, in a similar way as presented for the single-fibre sensors. The similarity between the wavelength shift – shear stress response of this grating, with the response of sensor-1Fh, Fig.6.26, is clearly noticed. The wavelength shift is insensitive to the sign of shear stress, and a positive average responsivity of ~0.5pm/kPa is measured for both gratings. The reflection spectra at different shear stress are given in Fig.6.54 to Fig.6.57. It is reminded that those spectra were captured at an instant during the on-state of the shear pulses, while $\Delta\lambda_B$ was measured as the average between the on and off states of the pulse, as shown in Fig.6.46. We therefore use the overlapped spectrum graphs to examine the distortion of the spectrum due to vertical or shear stress, rather than to measure the Bragg wavelength shift. For the horizontal FBG in sensor-3F, no significant distortion of the reflection spectrum is observed, except of variation of the peak intensity after each rotation due to the bending losses of the fibre, as explained in section 6.4.2.

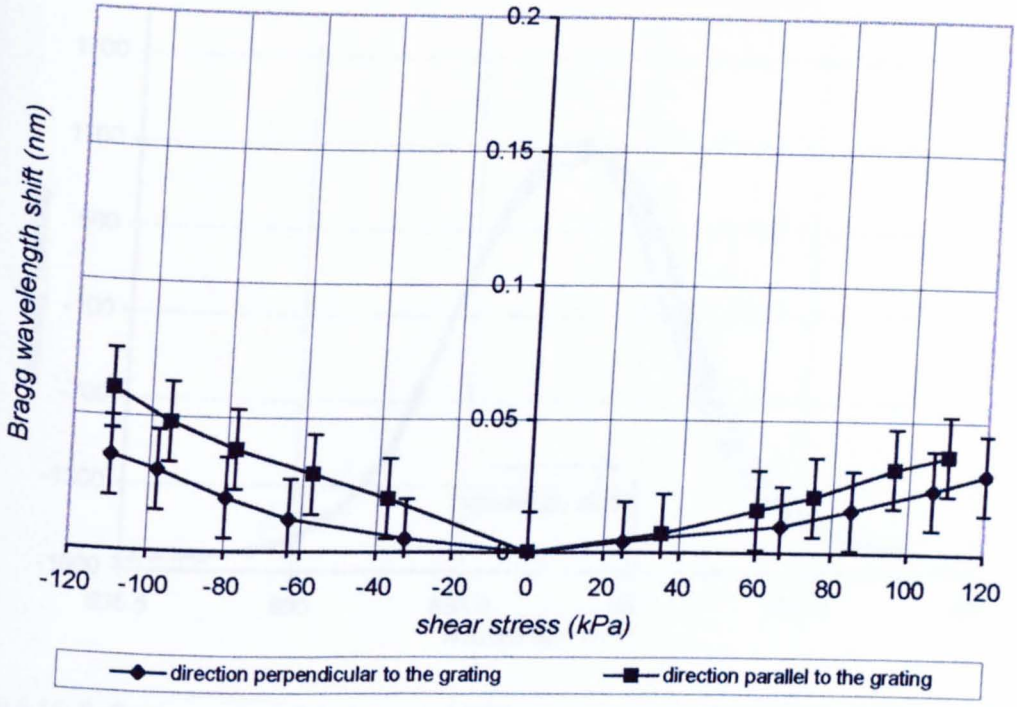

Fig.6.53: Bragg wavelength shift of the horizontal FBG of sensor-3F against shear stress, applied parallel and perpendicular to the FBG.

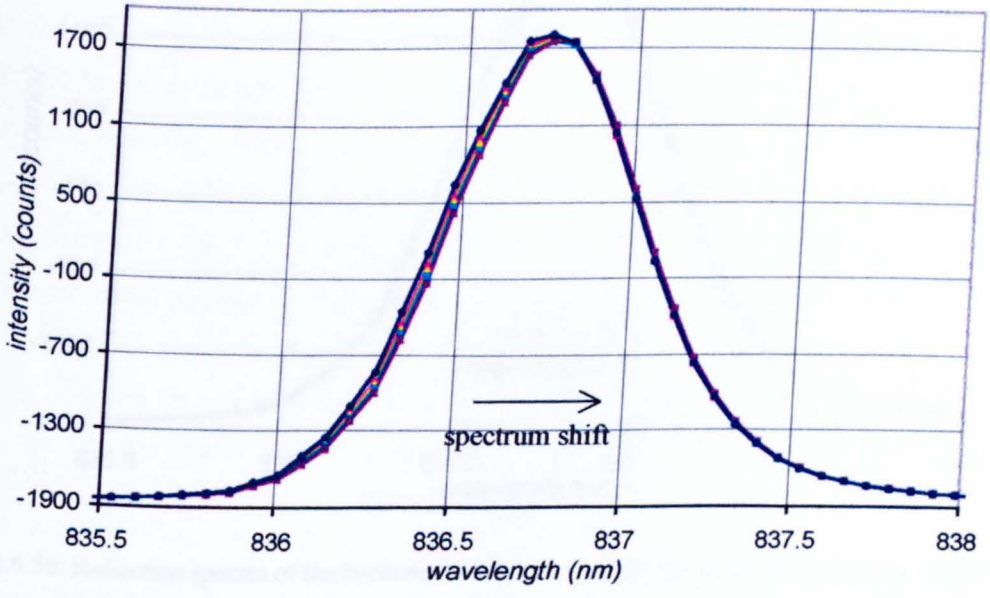

Fig.6.54: Reflection spectra of the horizontal FBG in sensor-3F, for shear stress 0 to +120kPa parallel to the grating.

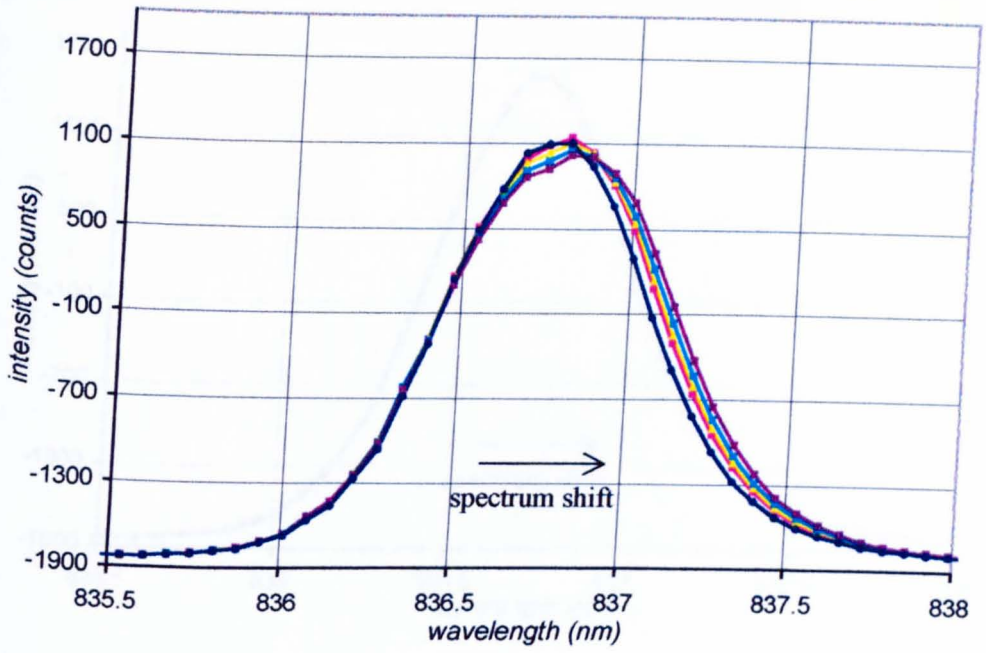

Fig.6.55: Reflection spectra of the horizontal FBG in sensor-3F, for shear stress –120kPa to 0kPa parallel to the grating.

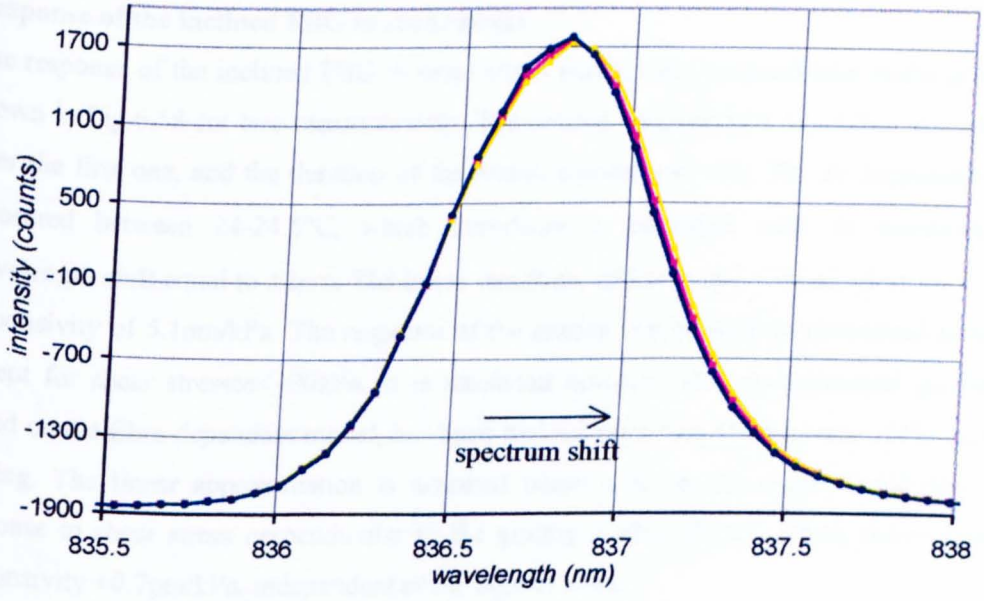

Fig.6.56: Reflection spectra of the horizontal FBG in sensor-3F, for shear stress 0kPa to +120kPa perpendicular to the grating.

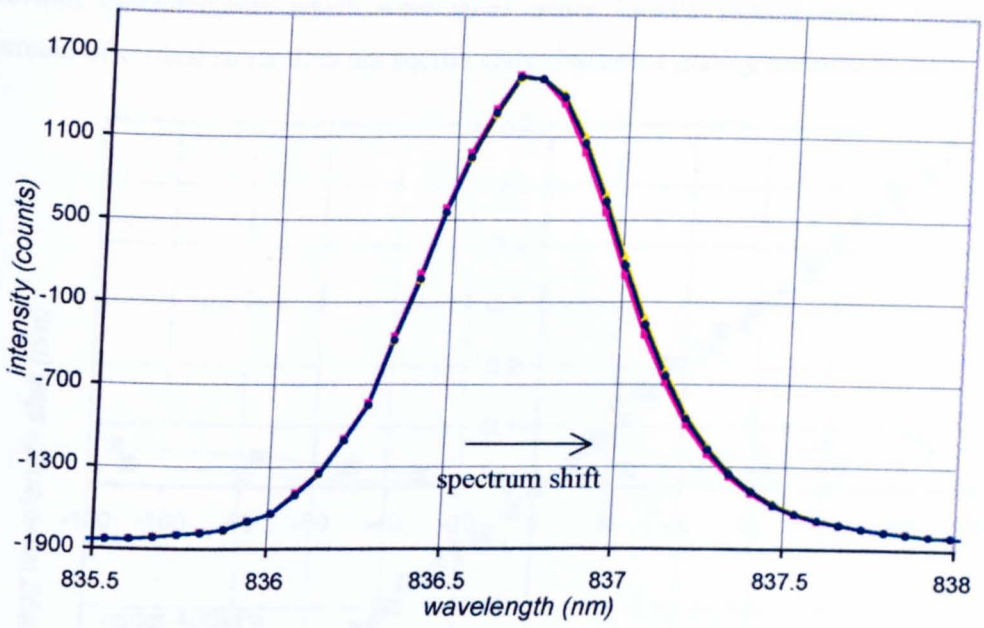

Fig.6.57: Reflection spectra of the horizontal FBG in sensor-3F, for shear stress -120kPa to 0kPa perpendicular to the grating.

Response of the inclined FBG to shear stress

The response of the inclined FBG to shear stress parallel and perpendicular to the grating is shown in Fig.6.58 for two measurements. The second measurement was taken immediately after the first one, and the duration of the measurements was ~1h. The air temperature was measured between 24-24.5°C, which introduces a maximum error in measuring the wavelength shift equal to ±2pm. The linear trendline, which is also plotted, gives an average responsivity of 5.1pm/kPa. The response of the grating can be well approximated as linear, except for shear stresses<–90kPa. It is reminded however, that no theoretical prediction, based on the fibre-dependent model, has been derived regarding the response of the inclined grating. The linear approximation is assumed based only on the experimental data. The response to shear stress perpendicular to the grating is also plotted, which shows average responsivity +0.7pm/kPa, independent of the sign of stress.

In order to examine a possible relationship between the vertical stress and the observed non-linearity for shear stress <–90kPa, a third measurement was taken. The sensor was measured using the same setup, but now the vertical stress increased to 400kPa. The experiment was done one week after the previous measurements. The fibre had to be fusion spliced again, since the sensor had been removed from the FBG readout system. The resolution reduced to 0.03nm compared to the 0.02nm of the previous two measurements. The Bragg wavelength shift is shown on the same graph, Fig.6.58, for shear stress –110kPa to 0kPa. The obtained curve is in good agreement (taking into account the error of the readout system) with the

previous measurements which were taken under 250kPa vertical stress. Therefore the increase of vertical stress does not significantly change the grating response to shear.

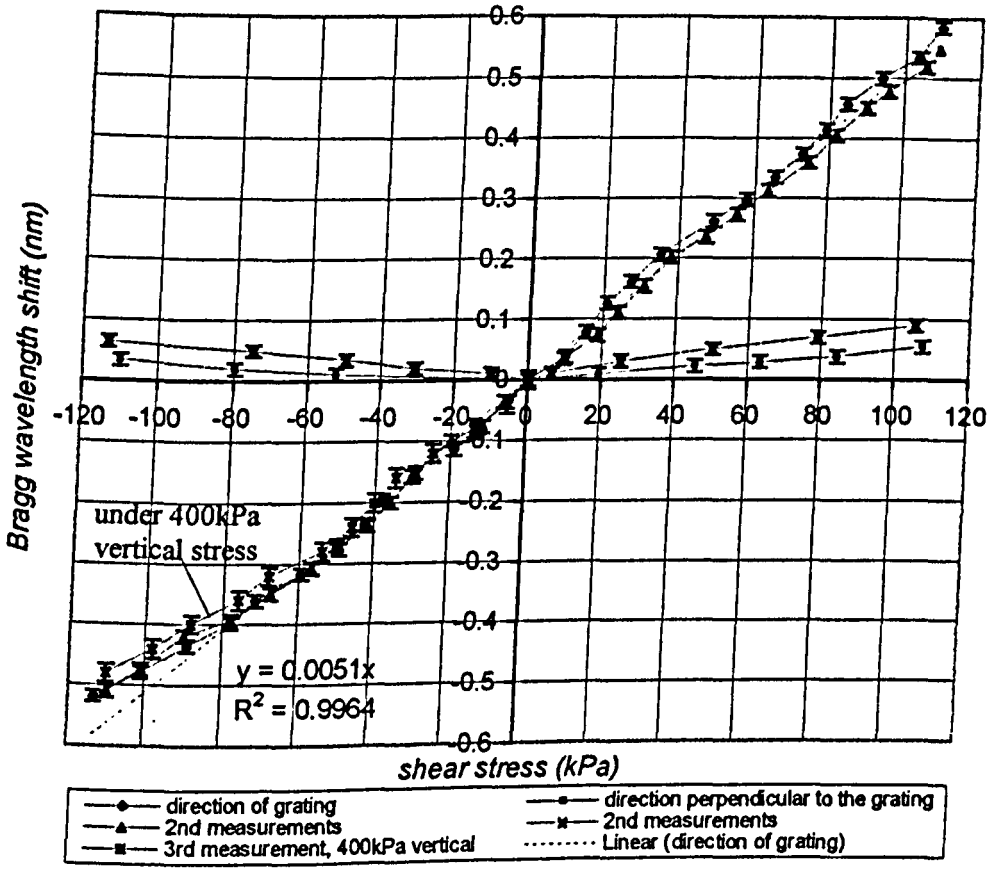

Fig.6.58: Bragg wavelength shift of the inclined FBG of sensor-3F against shear stress applied parallel, and perpendicular to the FBG.

The reflection spectra for the first measurement, for shear parallel to the fibre axis, are given in Fig.6.59 and Fig.6.60. The reflection spectrum is highly distorted as the vertical stress increases. The bandwidth increases, and a second peak appears at ~837nm. Negative shear on the other hand results in reduction of the spectrum bandwidth. The shape initially (under no shear) shows an increase in intensity around ~837nm, which disappears as shear increases to –120kPa. Comparing the first[1] spectrum in Fig.6.59 with the first spectrum in Fig.6.60, significant differences regarding the spectrum shape, bandwidth, and central wavelength are observed, even though the sensor is subjected to the same vertical stress, ~250kPa, and no shear is applied. Possible reasons for this difference will be examined in section 6.5. The reflection spectra for the 3rd measurement are given in Fig.6.61. The intensity difference compared to Fig.6.60 is due to the splice losses, which were larger during the 3rd measurement. This is the reason for the deterioration of the wavelength resolution mentioned previously. It can be observed that, even though the reflection spectra

[1] The spectrum shifts towards the direction shown by the arrow, Fig.6.60. The beginning of the arrow shows the first measured spectrum, which corresponds to zero shear stress.

are different under different vertical stress, the measured $\Delta\lambda_B$ due to shear is not significantly changed.

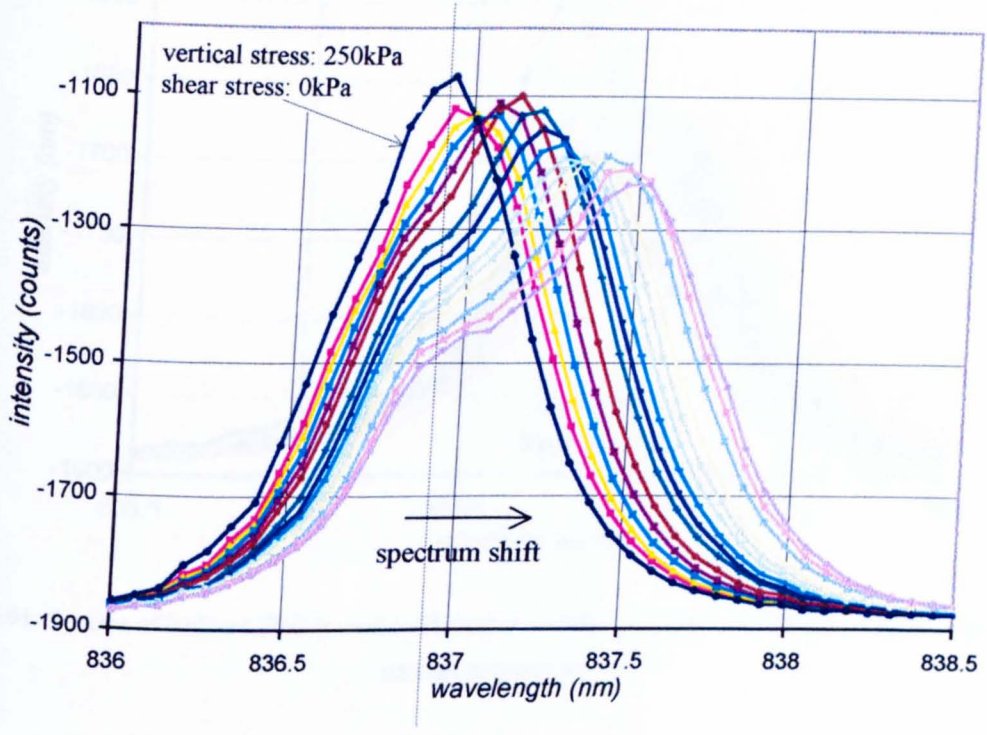

Fig.6.59: Reflection spectra of inclined FBG in sensor-3F under 0 to +110kPa shear stress, applied parallel to the FBG.

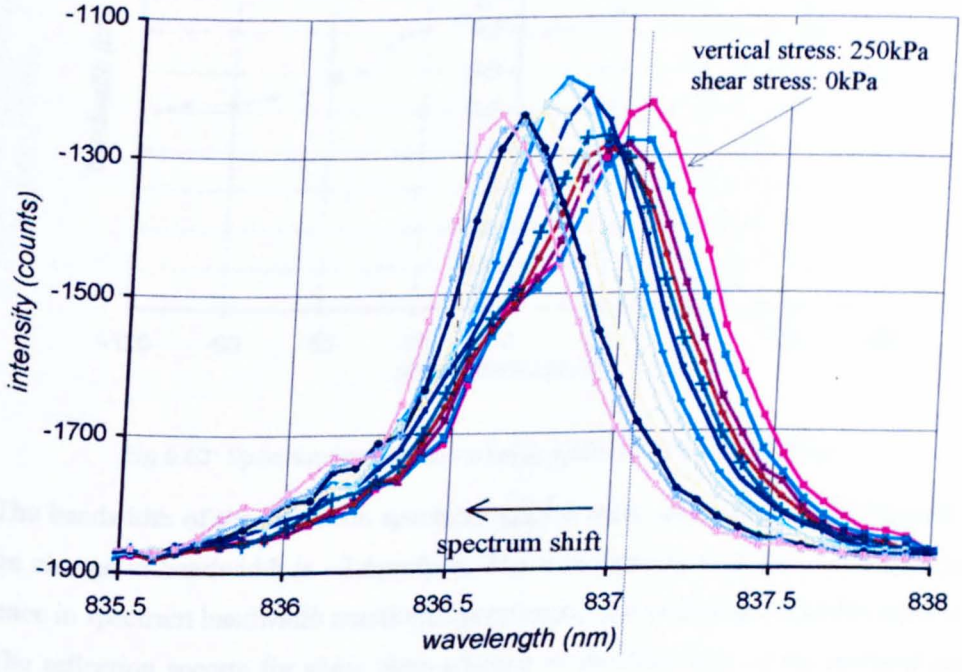

Fig.6.60: Reflection spectra of inclined FBG in sensor-3F under 0 to -110kPa shear stress, applied parallel to the FBG.

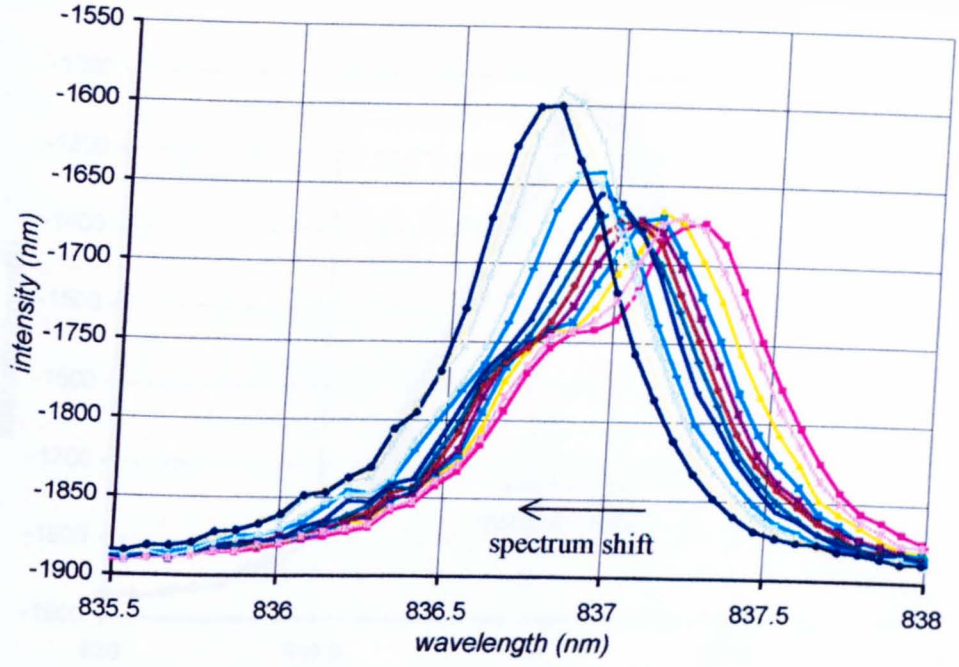

Fig.6.61: Spectra of inclined FBG in sensor-3F, under ~400kPa, for 0 to –110kPa shear stress, applied parallel to the FBG.

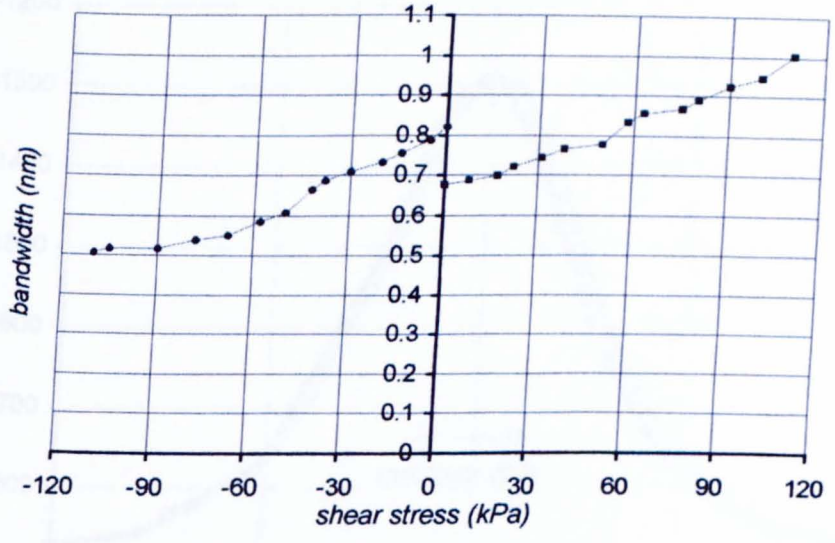

Fig.6.62: Spectrum bandwidth variation under different shear stress.

The bandwidth of the reflection spectrum against shear stress is given in Fig.6.62. The average change in bandwidth is ~2.6pm/kPa. The discontinuity at 0kPa is related with the difference in spectrum bandwidth mentioned previously, and will be discussed in section 6.5.

The reflection spectra for shear perpendicular to the fibre axis of the inclined grating are given in Fig.6.63 and Fig.6.64. Relative shift between the central wavelength of the first spectrum of each graph (corresponding to 250kPa vertical, 0kPa shear stress) is also observed, as seen previously in Fig.6.59 and Fig.6.60.

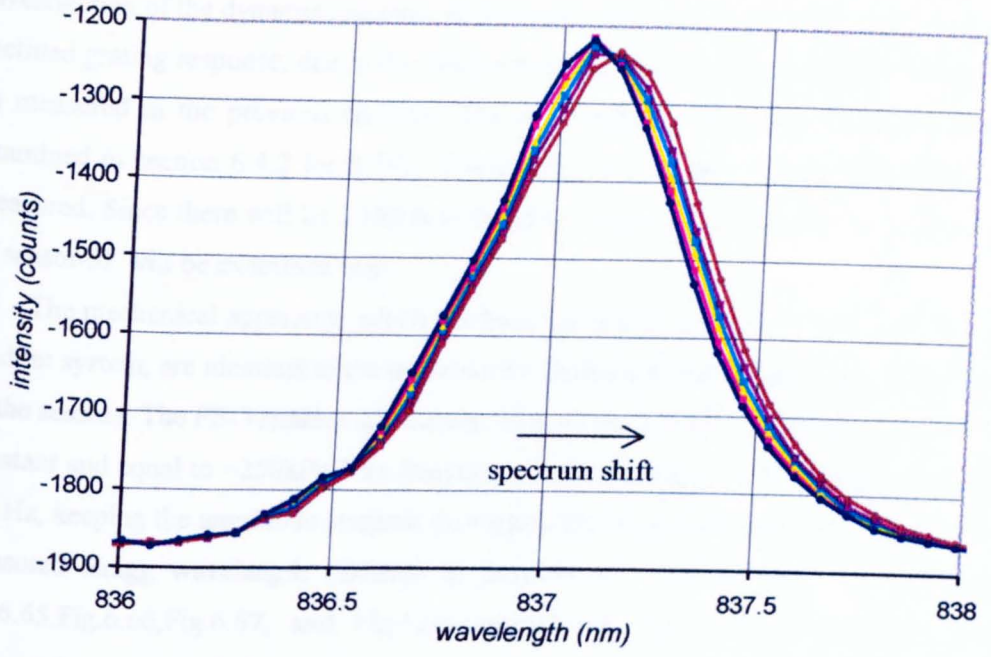

Fig.6.63: Reflection spectra of inclined FBG in sensor-3F under 0 to +110kPa shear stress, applied perpendicular to the FBG.

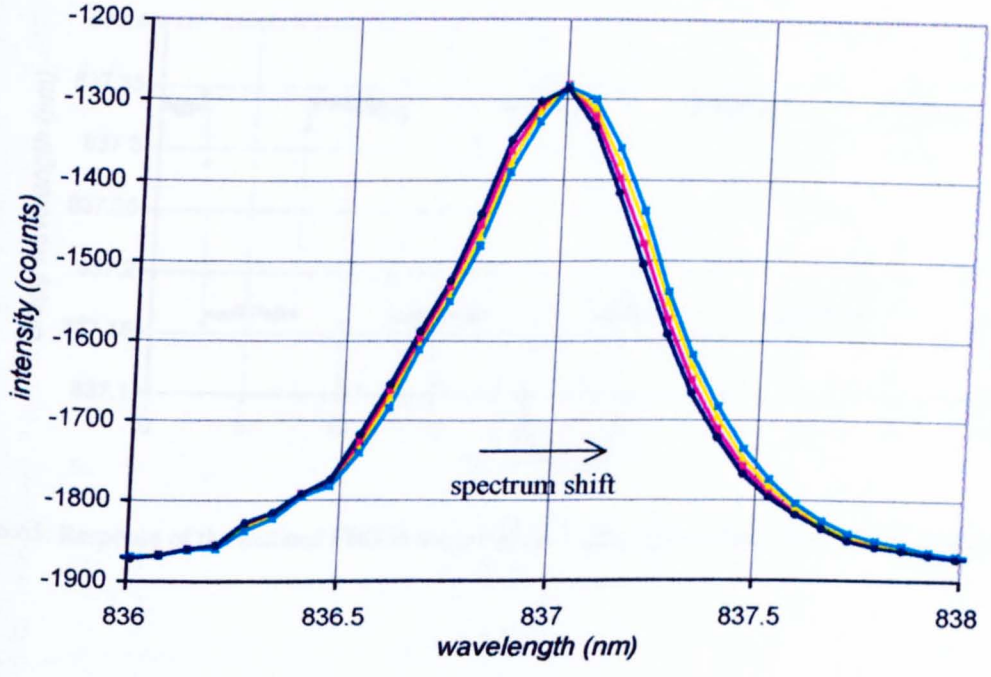

Fig.6.64: Reflection spectra of inclined FBG in sensor-3F under 0 to -110kPa shear stress, applied perpendicular to the FBG.

6.4.5 Dynamic response

The time response of the elastomer sensor to variable frequency shear stress pulses will be examined in this section. Only shear stress will be considered, since the time response to

vertical stress can only be measured by manually applying a vertical load. The experimental investigation of the dynamic response of the sensor will be limited to the measurement of the inclined grating response, due to the relatively low response of the horizontal FBGs to shear, as measured in the previous sections. The time response of sensor-1Fi has already been examined in section 6.4.2 for 0.5Hz, 32kPa shear stress pulses, where 83ms rise time was measured. Since there will be 3 FBGs in the final version of the sensor, the inclined grating of sensor-3F will be examined next.

The mechanical apparatus, which has been presented in section 3.1, as well as the FBG readout system, are identical to the those used previously for the quasi-static characterisation of the sensors. The FBG readout system was initially set to 6scans/s. The vertical load is kept constant and equal to ~250kPa. The frequency of shear stress pulses was increased from 0.1 to 1Hz, keeping the amplitude constant throughout the experiment and equal to +25kPa. The measured Bragg wavelength variation in time for 0.1, 0.2, 0.5, and 1Hz are given in Fig.6.65,Fig.6.66,Fig.6.67, and Fig.6.68 respectively. The Bragg wavelength shift is measured $\Delta\lambda_B$=0.17±0.01nm, independent of the input stress frequency. The shape of the wavelength trace is distorted for frequencies ≥1Hz, Fig.6.68, due to the low sampling speed of the readout system.

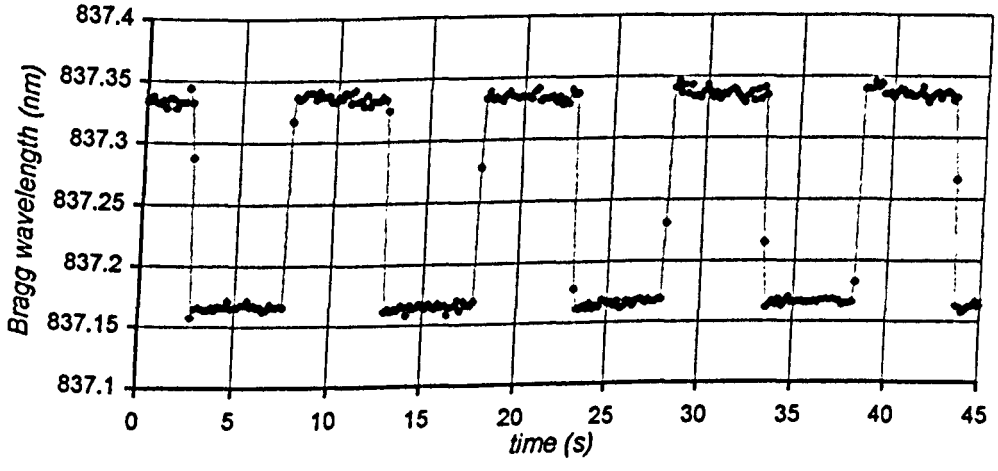

Fig.6.65: Response of the inclined FBG in sensor-3F, to 0.1Hz, 25kPa shear stress pulses, at 6scans/s.

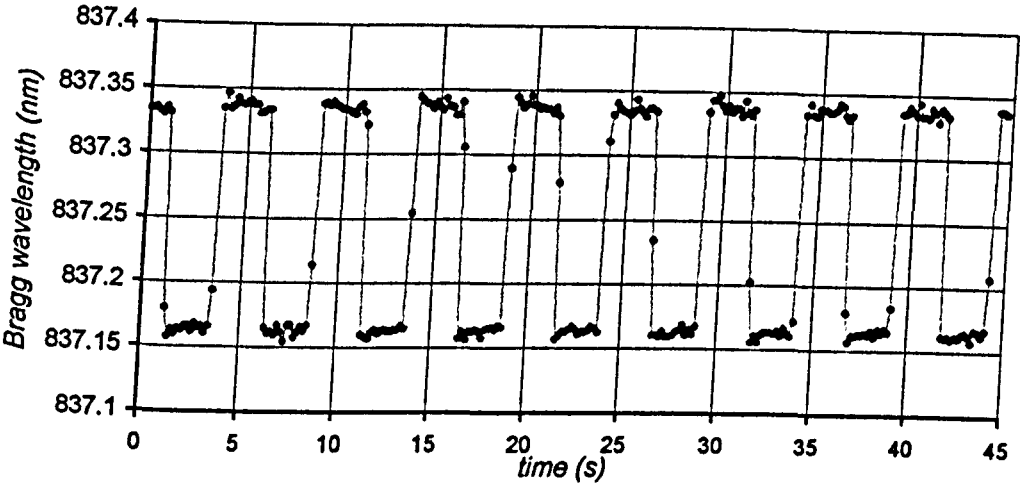

Fig.6.66: Response of the inclined FBG in sensor-3F, to 0.2Hz, 25kPa shear stress pulses, at 6scans/s.

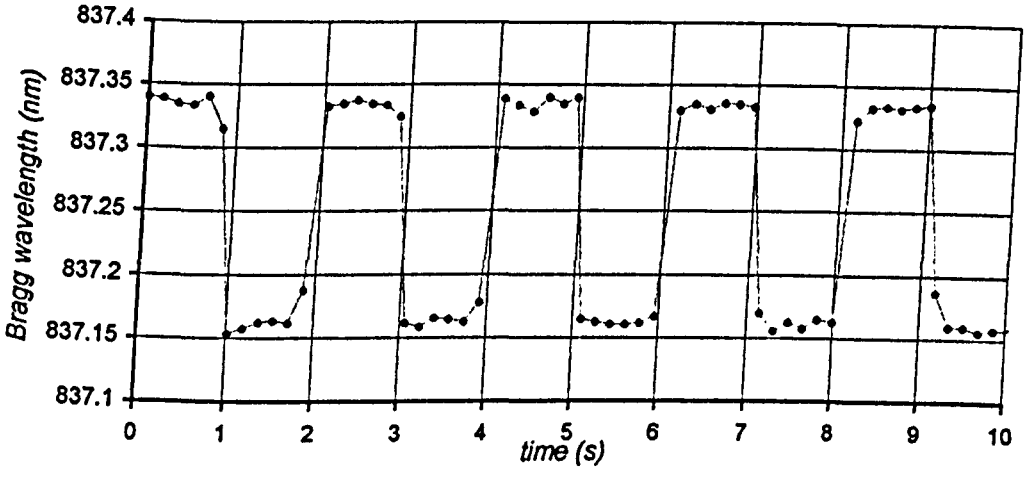

Fig.6.67: Response of the inclined FBG in sensor-3F, to 0.5Hz, 25kPa shear stress pulses, at 6scans/s.

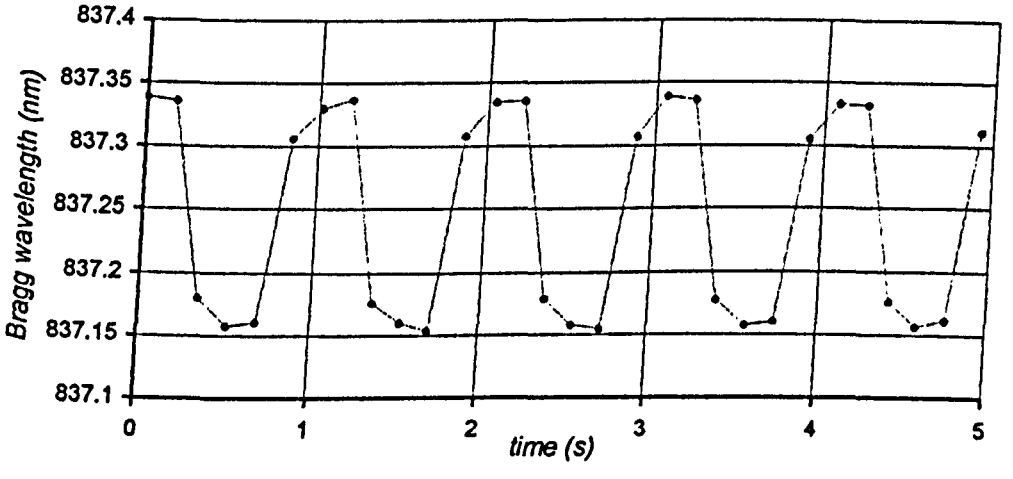

Fig.6.68: Response of the inclined FBG in sensor-3F, to 1Hz, 25kPa shear stress pulses, at 6scans/s.

The acquisition speed was then increased to the maximum value of 12scans/sec. The pulse shape at 1Hz is not distorted, as shown in Fig.6.69. The rise time between 0 and 25kPa is

measured to be 83ms, which is the time resolution of the system. The frequency was further increased up to 4Hz, Fig.6.70, Fig.6.71, and Fig.6.72. It appears that the measured average $\Delta\lambda_B$ is still equal to 0.17nm for shear stress frequency 4Hz. However, no information on the actual shape of the grating response can be derived for frequencies >2Hz using the existing readout system.

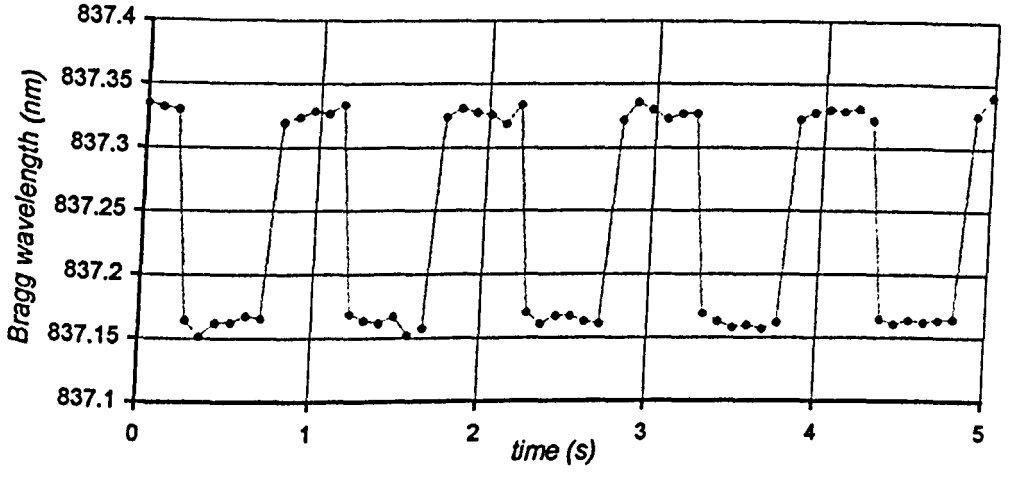

Fig.6.69: Response of the inclined FBG in sensor-3F, to 1Hz, 25kPa shear stress pulses, at 12scans/s.

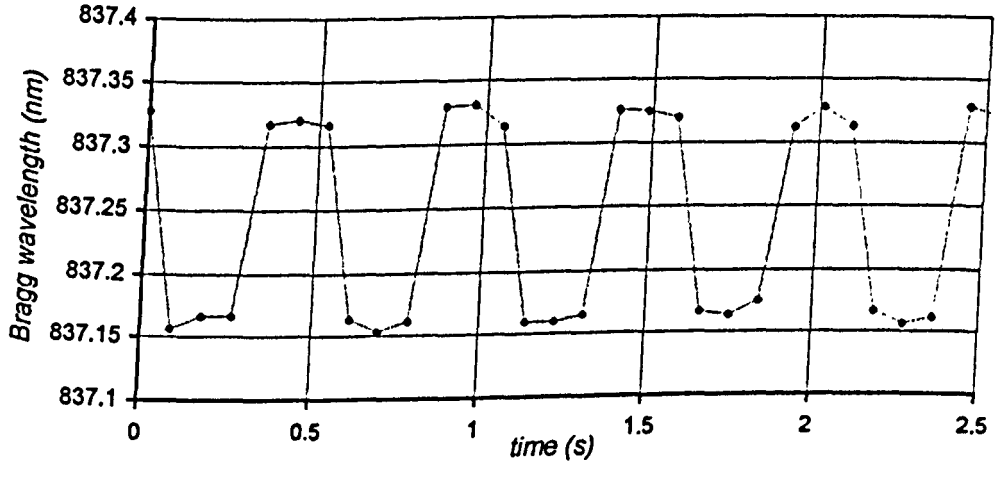

Fig.6.70: Response of the inclined FBG in sensor-3F, to 2Hz, 25kPa shear stress pulses, at 12scans/s.

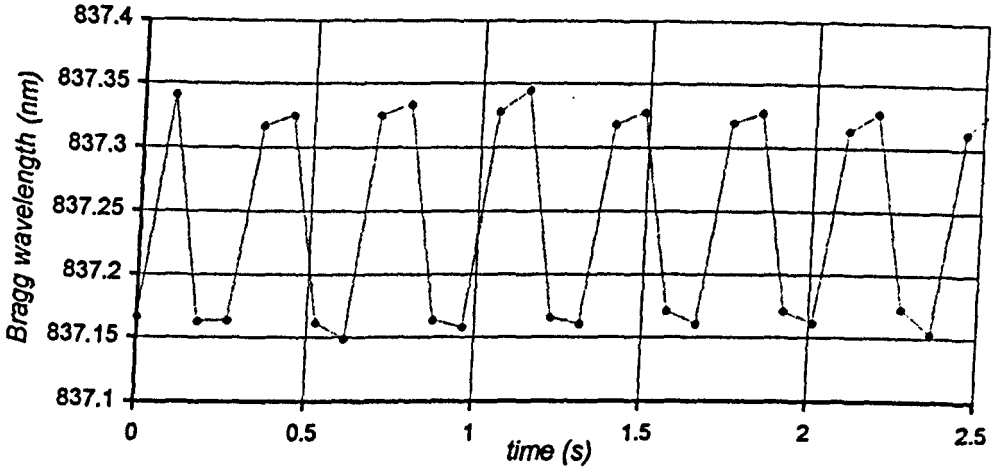

Fig.6.71: Response of the inclined FBG in sensor-3F, to 3Hz, 25kPa shear stress pulses, at 12scans/s.

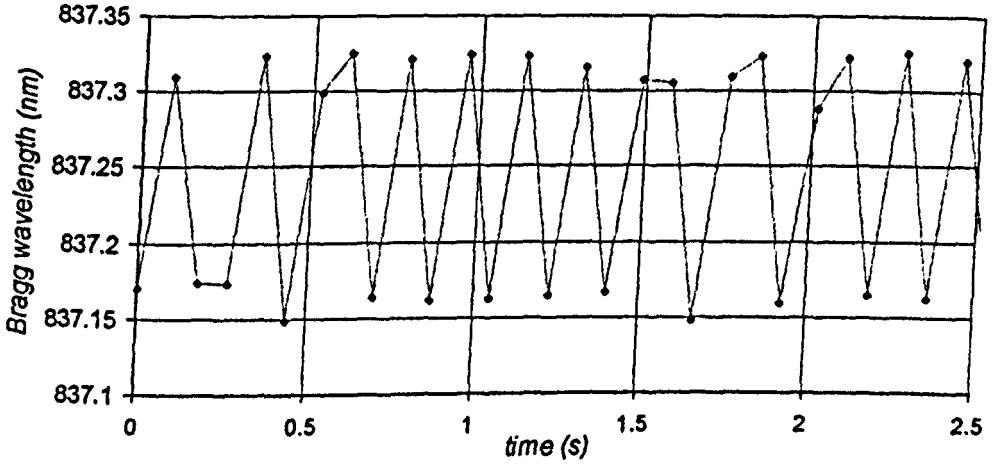

Fig.6.72: Response of the inclined FBG in sensor-3F, to 4Hz, 25kPa shear stress pulses, at 12scans/s.

6.5 Comments on the experimental results

The first observation while measuring the Bragg wavelength shift, under vertical or shear stress pulses, was a drift in wavelength. Taking into account the relatively strong viscoelastic behaviour of the elastomer, which was observed as creep, simultaneously measured by the micrometer, it is reasonable to believe that the wavelength drift is due to stress relaxation of the material surrounding the fibre. This can only be theoretically verified by examining the stress distribution around the fibre using a more accurate model, which will incorporate the viscoelasticity of the material. The drift in wavelength was observed in all four embedded FBGs, for both vertical and shear stress. However, it is not observed to the same extent for all gratings. For example, the horizontal grating in sensor-1Fh, Fig.5.32, shows significantly larger drift compared to the inclined FBG in sensor-1Fi, Fig.6.31. Based on the experimental data, the angle of the fibre axis with respect to the horizontal plane is not the reason for the

presence of drift. The inclined grating in sensor-3F is embedded at the same[1] angle as the FBG in sensor-1Fi. However, comparing Fig.6.31 with Fig.6.46 (first 20s), it is apparent that the drift is significantly larger for the inclined FBG in sensor-3F. Furthermore, the two FBGs in sensor-3F, which are embedded in the same sample of material[2], show different drift under the same stress, as it can be seen in Fig.6.45 and Fig.6.46. The drift is therefore more likely to be caused by the interaction of the particular fibre with the material, rather than to be caused by the properties of the material itself. The type of fibre is also not related to the drift, since all gratings are written on the same type of fibre. Further experimentation will be required by fabricating and testing more sensors, in order to ensure that the variation in drift is not caused by manufacturing imperfections, like contamination of the fibre surface during the alignment of the fibre in the mould, or the presence of a thin layer of paint used to identify the precise location of the grating. Marking of the fibre in the 10mm-region around the grating should be avoided. Debris on the uncoated length of the fibre can be removed using a combination of apropriate chemical and physical methods prior to fitting into the wax mould. The fibre installation procedure into the wax mould is possible to contaminate the fibre surface with wax. This could result in weakness of the fibre bonding with the elastomer material and slippage of the embedded fibre. The wax moulds should carefully be aligned so that the fibre only touches the wax beyond the 10mm-region which is going to be embedded. Melted wax during fibre fixing with the soldering iron could also result in contamination of the fibre near the edges of the sensor. Observing the melting of the wax with the stereoscope during fibre installation could reduce this risk.

The FBG responses to vertical stress, for all three sensors tested, are plotted on the same graph in Fig.6.73. It can be observed that the responses differ in terms of linearity and responsivity. Calibration of each individual FBG in every sensor is therefore necessary in order to derive the actual response curve. Comparing the responses of the horizontal FBGs with those of the inclined ones, it seems that the angle θ (~14°-17°) does not significantly affect the FBG response. In terms of linearity, no conclusion can be derived, since the

---

[1] The sensors are made with a non-automatic way. The accuracy in achieving the desired angle θ depends on the precision of the inclined V-grooves, which are manually etched on the wax mould. However, it is relatively easy to achieve fitting of the fibre close to the upper and lower surfaces of the sensor with a maximum error of ~0.25mm, which gives maximum error in angle $\theta \approx 3°$ (see also Fig.5.13, and eq.5.35, for $h=3-2*0.25=2.5mm$).

[2] The 3 sensors were fabricated at a different time in an 8-month period. It is mentioned in the data sheet of this particular epoxy (SCOTCHCAST), that the mechanical properties of the elastomer depend on the time period for which the two parts (prior to mixing) are stored. Water absorption of the uncured resin, particularly of the hardener material, can also affect the mechanical properties of the epoxy. It is mentioned that the properties of the material may significantly vary after 12months from the date of production of those two parts. It is therefore possible that the mechanical properties of the material in each of the sensors to be different. In this case, however, both FBGs are embedded in the same sample, therefore the matrix around those two gratings has identical mechanical properties.

measured response varies from fairly good linearity in sensor-1Fi (see also Fig.6.32), to significantly non-linear in sensor-1Fh.

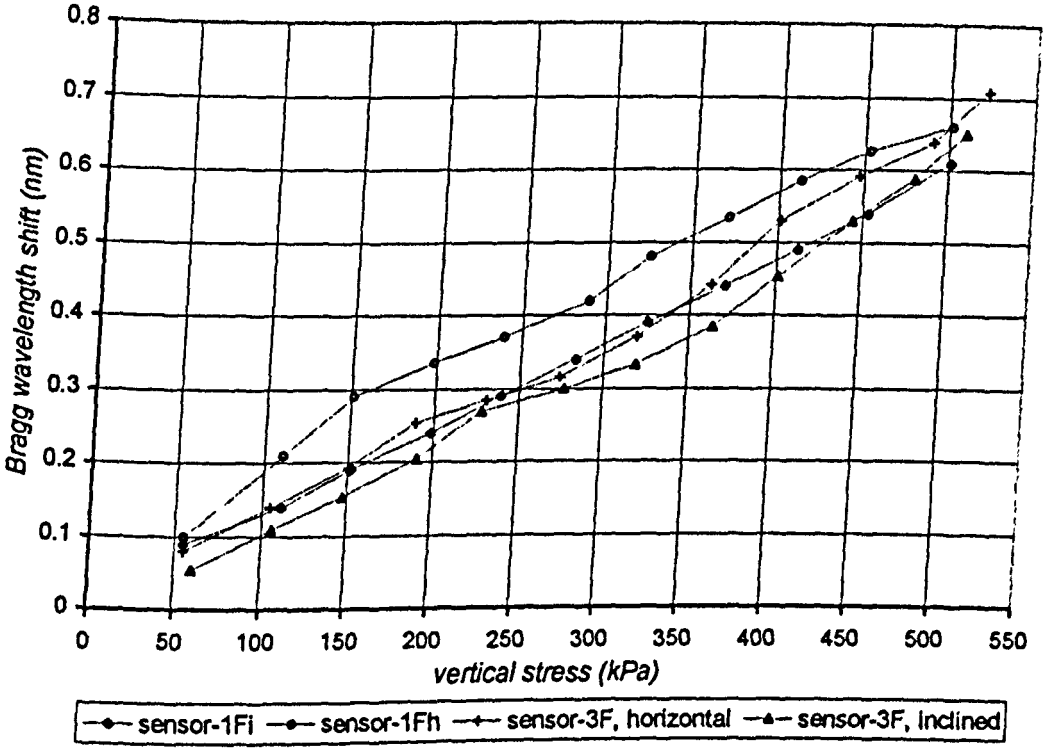

Fig.6.73: FBG response to vertical stress for the 3 sensors. Only the first set of measurements for each FBG are shown.

The repeatability in measuring the FBG response is better for sensor-1Fi and for the horizontal grating in sensor-3F than the other two FBGs, as can be inferred by examining the difference between the 2 measurements taken for each grating, Fig.5.34, Fig.6.32, Fig.6.47, and Fig.6.48. The repeatability is related to the drift in wavelength due to viscoelasticity, which reduces the accuracy in calculating the average wavelength shift, as explained in section 6.4.4. The drift in wavelength was less for sensor-1Fi and for the horizontal FBG of sensor-3F, as mentioned previously. Comparing the reflection spectra measured for all gratings, Fig.5.36, Fig.6.33, Fig.6.49, and Fig.6.50, we observe that the repeatability is not sensitive to the spectrum deformation. For example, a secondary peak appears on the reflection spectra of the horizontal FBG in sensor-3F as the vertical stress increases, however the repeatability is better than that of the inclined FBG of the same sensor, even though the reflection spectra of the latter are less distorted.

The horizontal FBGs in sensor-1Fh and sensor-3F show similar response to shear stress, in both parallel and perpendicular directions, Fig.6.26 and Fig.6.53. Positive $\Delta\lambda_B$ is measured, regardless the sign and direction of shear. The theoretical prediction based on the fibre independent model, eq.(5.26), shows that the horizontal FBG should be insensitive to shear stress. The fibre dependent model only predicts the response of the FBG to vertical stress. A

theoretical model which will predict the interfacial stresses as a function of both vertical and shear stress is necessary in order to explain this experimental observation. The actual response curve of the horizontal FBGs (as well as the inclined FBGs for shear direction perpendicular to the fibre axis), can only be measured if a higher resolution readout system is used, or this particular one is improved. This can be done by replacing the SLD source with the more powerful one, which will increase the signal-to-noise ratio of the reflected signal (section 3.6). Careful fusion splicing of the FBG to the fibre coupler will minimise splice losses. Substitution of the fibre coupler with an optical circulator will increase the power arriving at the input port of the spectrometer, but will also increase the cost of the system.

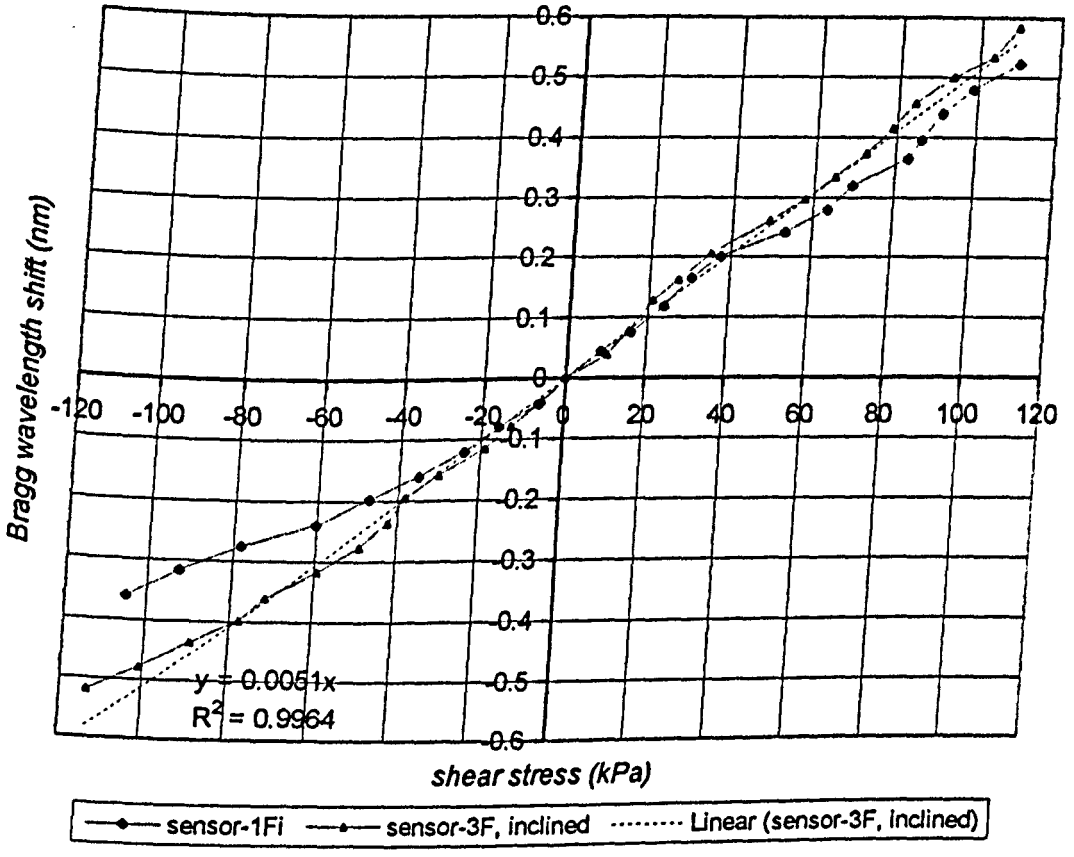

Fig.6.74: Response of the inclined FBGs to shear stress parallel to the fibre axis. Only the first set of measurements are shown.

The response of the inclined FBGs in sensor-1Fi and sensor-3F to shear stress applied parallel to the fibre axis is different for the two FBGs, as shown on the same graph in Fig.6.74. Sensor-3F shows a nearly linear response in the entire stress range –110kPa to +110kPa, while for sensor-1Fi the responsivity in the –110kPa to 0kPa range is smaller than in the 0kPa to +110kPa. Calibration of each individual FBG to both vertical and shear stress is therefore required.

The response of the inclined FBGs to shear stress applied perpendicular to the fibre axis shows no significant variation for the two FBGs (Fig.6.40 and Fig.6.58), although, as

mentioned previously, a higher resolution system is required to measure the response accurately. In fact, all four FBGs tested show approximately the same response to shear stress applied perpendicular to the fibre axis, as can be inferred comparing the relevant figures.

Factors which could possibly contribute to the difference in the vertical and shear stress response of the FBGs, are: i) different number of fibres in the sensors, ii) the 1mm-offcentering of the inclined FBG in sensor-3F (fibre 2 in Fig.6.25), iii) non-identical mechanical properties of the elastomer of the three sensors (see footnote 2, pg.54), iv) the grating is not in the centre of the embedded length of the fibre, vi) fabrication imperfections, mentioned previously in this section, including difference in the angle θ. These issues should be examined by modelling and experimentation on a larger sample of sensors.

Significant difference is also observed in the reflection spectrum shape of the FBGs when subjected to shear stress, as has already been mentioned in section 6.4. This can be clearly seen for example by observing Fig.6.42 and Fig.6.43 for sensor-1Fi under shear stress parallel to the fibre axis, and the relevant spectra in Fig.6.59 and Fig.6.60 for the inclined FBG in sensor-3F. The distortion of the spectra in sensor-3F is noticeable, with secondary peaks appearing for both positive and negative shear stresses. The spectra in sensor-1Fi are less distorted, and the secondary peak only appears for 250kPa vertical and +110kPa shear stress (last spectrum in Fig.6.42). The difference in spectrum distortion can also be seen by observing the large difference of the corresponding bandwidth change with shear, which is shown in Fig.6.44 for sensor-1Fi, and Fig.6.62 for sensor-3F.

It is possible for the spectrum deformation to produce an error in measuring the Bragg wavelength shift. The peak detection algorithm calculates the Bragg wavelength by utilising the intensity of five pixels around the main peak of the spectrum (section 3.6.1). If the distortion of the spectrum occurs close to the main peak, then the intensity of the pixels around the main peak will change which in turn will result in a different polynomial fit, and therefore an error in the calculated Bragg wavelength.

Examining the spectra in Fig.6.59 and Fig.6.60, which correspond to 250kPa vertical and 0kPa shear, we notice that, even though both spectra refer to the same FBG under the same stress, their shape and central wavelength differ. These spectra were taken at approximately 40min time difference, without altering the setup and readout system settings. No temperature variation was observed during this time. In order to minimise the effect of viscoelasticity, the spectra were take after ~2min from the application of vertical stress, after which no drift in the Bragg wavelength was observed. A second indication of the different spectrum shape between those two spectra is the discontinuity of the spectrum bandwidth at 0kPa shown in Fig.6.62. Similar differences in spectrum shape and bandwidth are also

observed to some extent in all four FBGs, Fig.6.27 to Fig.6.30 for sensor-1Fh, Fig.6.42 and Fig.6.43 for sensor-1Fi, and Fig.6.54 to Fig.6.57 for the horizontal FBG in sensor-3F.

The observations mentioned above show that the displacement and/or rotation of the sensor in order to change the shear direction must be related to these spectral differences. Fabrication imperfections of the sensor itself are not expected to produce these differences. If, for example, we consider abnormalities like non-uniform elastomer around the fibres due to air bubbles or debris, uneven and non-parallel upper and lower surfaces of the sensor, then we would expect the FBG response to be different from an ideally perfect sensor. However, those factors should not affect the FBG response if the sensor is rotated or displaced in the testing apparatus, provided that the vertical and shear stress are applied on the sensor in exactly the same way after each rotation or displacement. Imperfections of the experimental setup, as well as interaction of the elastomer surfaces with the metallic plates, are likely to affect the stress distribution along the fibre axis, which results in a different response of the grating.

In order to examine those issues, some experiments were carried out using one of the sensors. Sensor-1Fi was placed inside the experimental setup shown in Fig.3.1. Vertical load equal to ~320kPa was applied on the sensor. The reflection spectra are given in Fig.6.75.

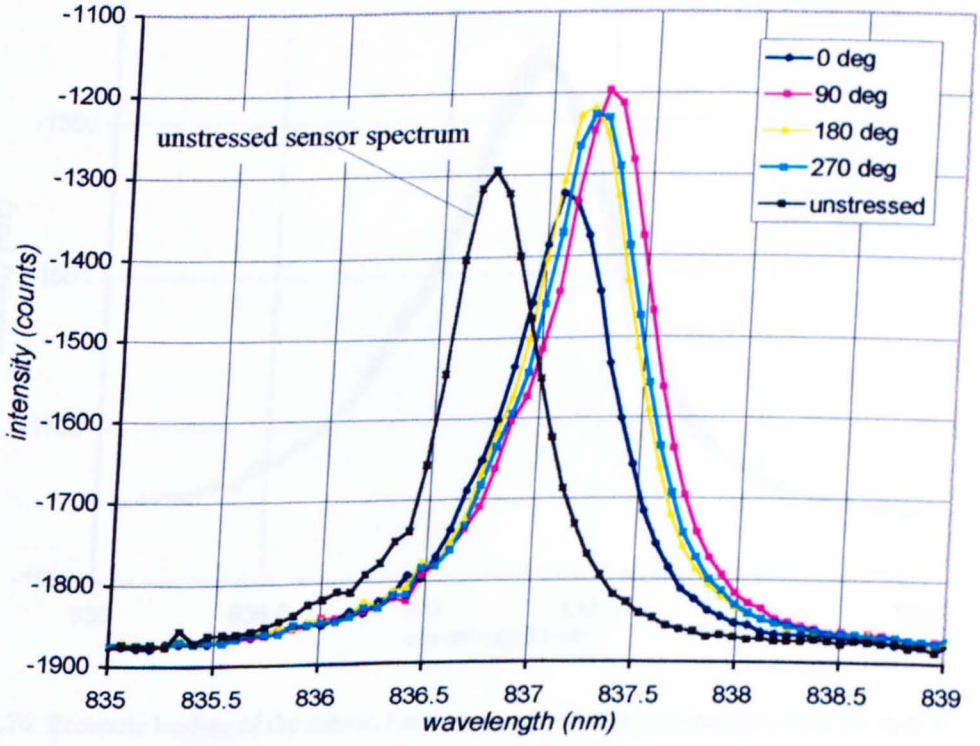

Fig.6.75: Reflection spectra of sensor-3Fi after random rotation of the sensor, under ~320kPa vertical stress.

Each spectrum is obtained after removing the weights plate, lifting the top plate, and rotating the sensor by 90° with respect to the vertical axis. The top plate, and the weights

plate are then placed on the sensor. A time period of ~2min was allowed before recording each spectrum. The difference of the four spectra in wavelength and shape is clearly observed. It is reminded that the amplitude variation is also affected by the bending of the fibre and the intensity fluctuations of the SLD source.

One reason which could affect the stress distribution on the top surface of the sensor is the tilting of the top plate with respect to the horizontal plane as the weights plate is applied to the top plate. The sensor is placed between the two metallic plates without accurate control of the precise location of the sensor. The weights plate is placed on the top plate approximately above the centre of the sensor, again without precision. With careful alignment, however, it is possible to achieve an accuracy equal to ±3mm from the normal to the centre of the sensor. In order to examine the effect of the eccentric loading, the weights plate was deliberately applied off-centre. The sensor was not removed during this experiment, the weights plate was moved instead. Fig.6.76 shows the reflection spectrum for vertical stress ~320kPa applied above the centre of the sensor (±3mm). The other spectra were obtained after moving the weights plate parallel to the fibre axis, with step ~2mm up to 6mm.

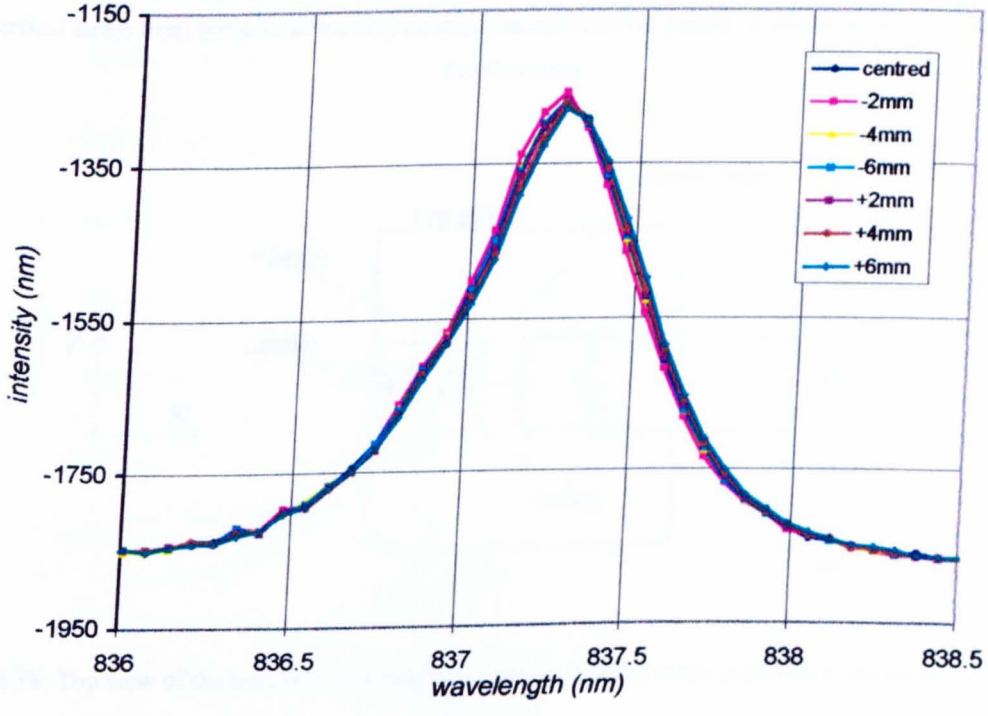

Fig.6.76: Eccentric loading of the sensor. Each curve corresponds to a specific offset (in mm) of vertical stress from the normal passing through the centre of the sensor, at direction parallel to the fibre axis.

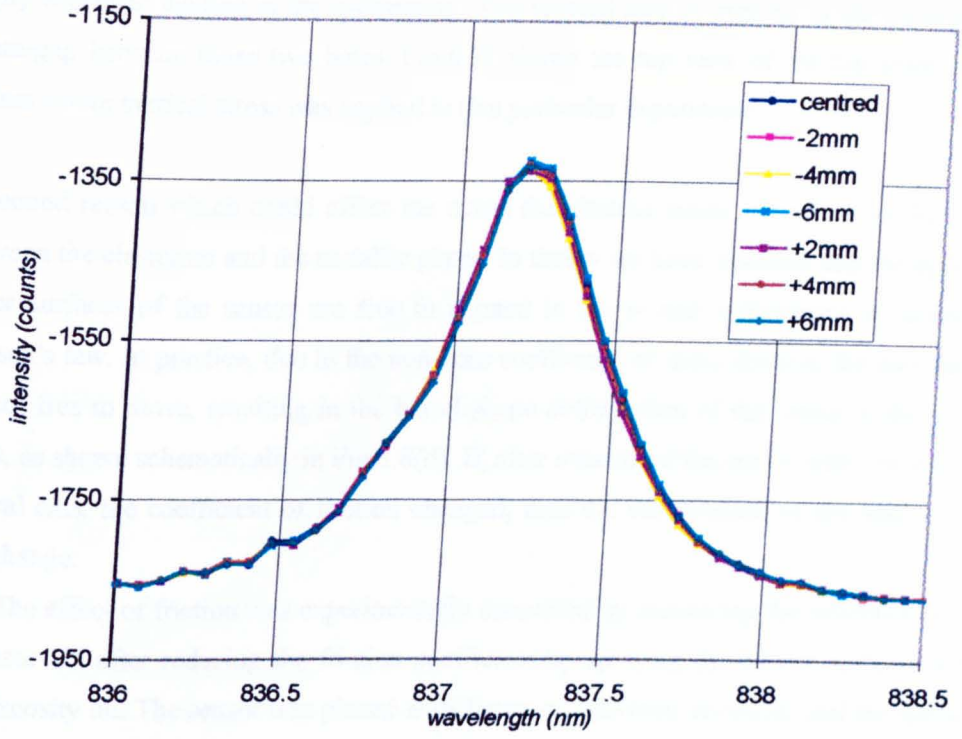

Fig.6.77: Eccentric loading of the sensor. Each curve corresponds to a specific offset (in mm) of vertical stress from the normal passing through the centre of the sensor, at direction perpendicular to the fibre axis.

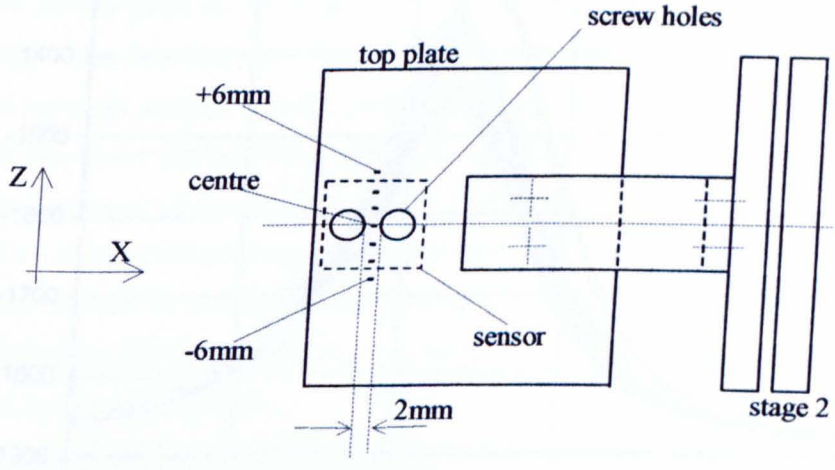

Fig.6.78: Top view of the top plate, showing the eccentric loading in the z-direction (dimensions out of scale).

The sensor was then rotated by 90° and the previous experiment repeated. The same vertical load was applied in the same way as previously, causing eccentric loading of the top plate perpendicular to the fibre axis. The measured spectra are given in Fig.6.77. No significant variation of the reflected spectrum is observed for eccentric loading on the z-direction (Fig.3.1), in both cases where eccentric loading is applied parallel or perpendicular to the fibre axis. Due to the presence of two screw holes on the top plate, it is not possible to

apply eccentric loading at the x-direction. The vertical load is applied in the middle of the 2mm-gap between those two holes. Fig.6.78 shows the top view of the top plate, and the points where vertical stress was applied in this particular experiment.

A second reason which could affect the stress distribution inside the sensor is the friction between the elastomer and the metallic plates. In theory we have assumed that the upper and lower surfaces of the sensor are free to expand in the z- and x-directions as defined by Poisson's law. In practice, due to the non-zero coefficient of static friction, the two surfaces are not free to move, resulting in the barrel-shape deformation of the sensor under vertical stress, as shown schematically in Fig.5.8(d). If, after rotation of the sensor with respect to the vertical axis, the coefficient of friction changed, then the deformation of the sensor would also change.

The effect of friction was experimentally examined by measuring the reflection spectra of sensor-1Fi after reducing the friction coefficient by spraying the sensor surfaces with a low viscosity oil. The sensor was placed at different orientations, reversed, and the spectrum was recorded after ~2min from the application of 320kPa vertical stress. The spectra are given in Fig.6.79. No improvement in terms of spectrum repeatability is observed.

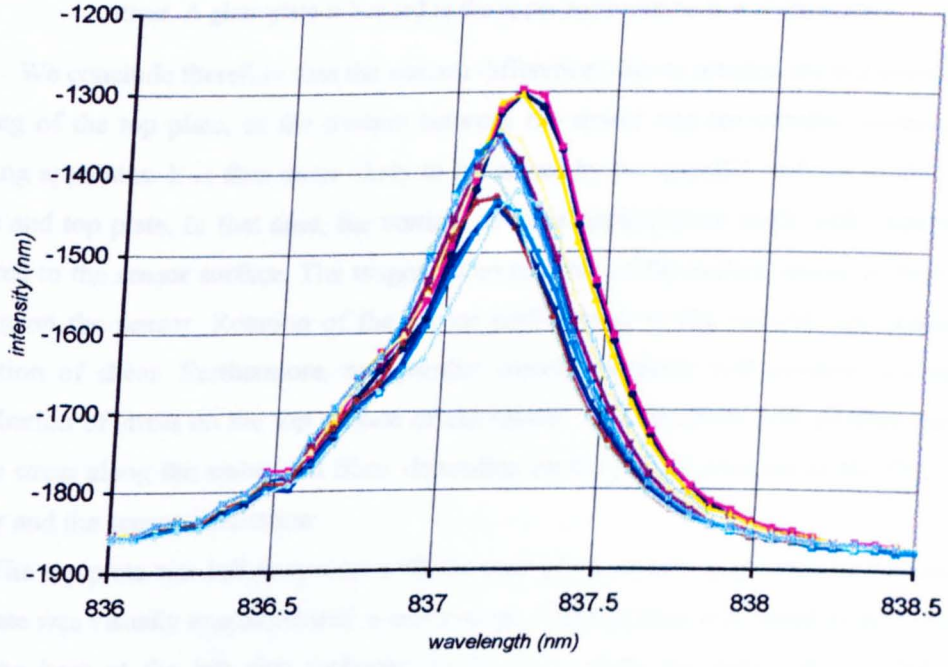

Fig.6.79: Reflection spectra of sensor-3Fi after random rotation of the sensor, under ~320kPa vertical stress. The sensor surfaces were lubricated prior to the measurements.

The extreme situation where the friction is so high that the two sensor surfaces cannot deform, was simulated by fixing a glass plate (microscope slide) on each surface using a cyano-acrylate glue. The sensor was measured as previously, and the spectra are given in Fig.6.80. The spectra still remain sensitive to sensor orientation. Reduction of the average

responsivity of the grating to vertical stress is also observed, as the result of bonding the two surfaces of the sensor.

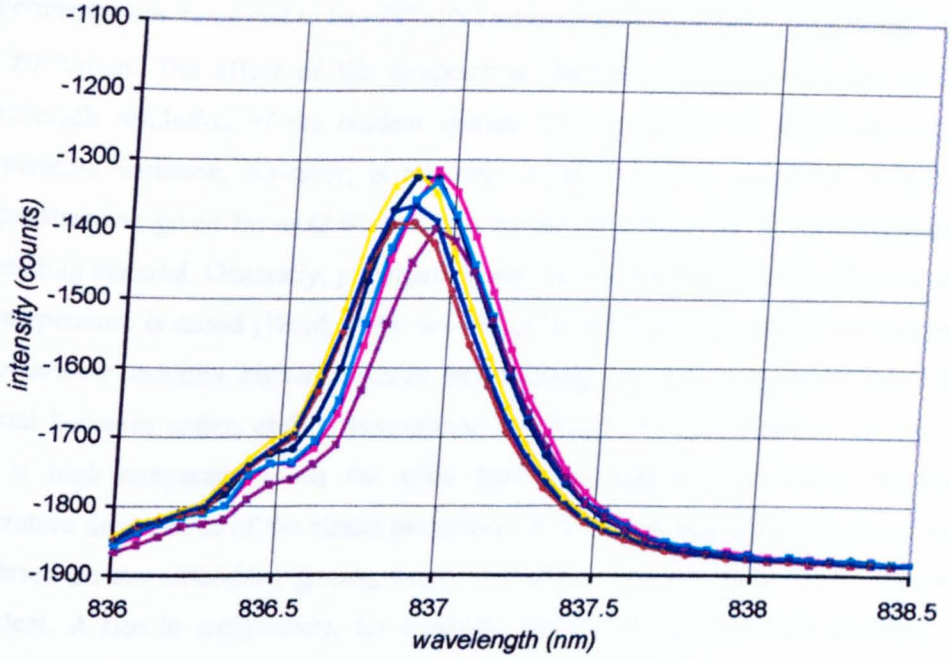

Fig.6.80: Reflection spectra of sensor-3Fi after random rotation of the sensor, under ~320kPa vertical stress. A glass plate is bonded to the upper and lower surface of the sensor.

We conclude therefore that the spectra differences due to rotation are not caused by the tilting of the top plate, or the friction between the sensor and the metallic surfaces of the testing apparatus. It is thus more likely to be caused by non-parallel surfaces of the metallic base and top plate. In that case, the vertical stress is applied at an angle with respect to the normal to the sensor surface. The tangential component of the vertical stress, is shear stress acting on the sensor. Rotation of the sensor with respect to the vertical axis changes the direction of shear. Furthermore, non-parallel metallic surfaces will produce non-uniform distribution of stress on the top surface of the sensor. This condition will produce variation of the stress along the embedded fibre, depending on the precise location of the FBG in the sensor and the sensor orientation.

The top plate was left in contact with the base plate, and the gap between the base and top plate was visually examined with a stereoscope. The top plate was found to be in contact with the base at the left side (referring to Fig.3.1), while the right side was lifted by approximately 200μm. The width of the base plate is 60mm, hence the tilt angle is approximately 0.2°. The tangential component of stress τ can be calculated by:

$$\tau = \sigma_y \sin(0.2°) \cong 1.5\text{kPa}$$

for σ_y=320kPa.

The experimental results presented in this thesis were carried out by measuring the elastomer sensors under approximately constant temperature. The room temperature during the experiments was measured to be ~24°±1°C, which results in change of the Bragg wavelength by ±0.006nm. The effect of this temperature variation was neglected due to the lower wavelength resolution of the readout system. The sensitivity of the sensor response to temperature variation, however, is not only affected by the sensitivity of the FBG to temperature, as given by eq.(2.9), but also by the change in the elastic properties of the embedding material. Generally, polymers change from glass-like to rubber-like behaviour as the temperature is raised (Ward, 1983, pp.136-137). In the glassy state at low temperatures, the elastomer exhibits higher modulus of elasticity. As the temperature increases, the material becomes softer, and its viscoelastic behaviour more pronounced. In the rubbery state at high temperatures, on the other hand, the material gets more flexible. The temperature dependence of the elastic properties of the matrix will affect the stress which is transferred on the embedded grating, hence the sensor response will also be temperature dependent. A rise in temperature, for example, will reduce the Young's modulus of the matrix, which in turn will increase the measured Bragg wavelength shift for a given vertical stress, as shown by eq.(6.37).

Stress measuring errors due to temperature change can be reduced by measuring the material properties and calibrating the sensor at a temperature close to the temperatures expected to be measured inside the shoe (30-40°C, Hossein, 1996). An appropriate time period should also be allowed before measuring in-shoe stresses in order to ensure thermal equilibrium of the insole. The required time period will depend on the thermal conductivity and the thickness of the insole material and the elastomer matrix. Since this waiting period could be inconveniently long, due to the poor thermal conductivity of the materials, possibly the insole could be preheated to an appropriate temperature.

6.6 Conclusions

In this chapter, the operation of the elastomer sensor was theoretically predicted by considering the sensor as a single-fibre composite material. The objective of this approach was to explain the large difference between the theoretical prediction of the fibre-independent model, which was presented in the previous chapter, and the experimental results from the measurement of the Bragg wavelength shift of sensor-1Fh, and hence to obtain a more accurate model. The stress distribution along the FBG was calculated for a sensor containing only one FBG which is embedded horizontally. The reflection spectrum properties are then explained using the theory of chirped Bragg gratings. The measured Bragg wavelength shift is approximately 45% less than the predicted one. This difference can be explained by the uncertainty in knowing the precise elastic properties of the material, and the assumption of uniform distribution of the interfacial stress around the fibre at a

particular distance from the centre of the grating. The prediction of this model, however, is significantly closer to the experimental data than the fibre independent model which overestimates the grating response by an order of magnitude.

Three sensors were fabricated by aligning the FBGs in a wax mould, two single-fibre, and one 3-fibre sensor. Viscoelastic drift in Bragg wavelength was observed for all FBGs. The Bragg wavelength against vertical stress curve for all 4 FBGs tested was measured to be approximately ±15% from the average linear approximation (Fig.6.73) with responsivity 1.3pm/kPa. The response of all 4 FBGs to shear perpendicular to the fibre axis, as well as the response of the horizontal FBGs to shear parallel to the fibre axis, is similar in all gratings. Positive Bragg wavelength shift was measured for both positive and negative shear stress, with an average responsivity approximately equal to 0.5pm/kPa. The Bragg wavelength shift of the inclined FBGs has the same sign as the applied shear stress, and the responsivity is of the order of 5pm/kPa. The variation of the FBG response curves shows that individual grating calibration is required.

Due to the relatively slow readout system, the dynamical measurements were restricted to low frequencies (up to 4Hz). The frequency response of the sensor was measured equal to 4Hz, limited by the acquisition speed of the readout system. The rise time from 0kPa to 32kPa was measured 83ms, also limited by the sampling period of the readout system.

Significant distortion of the reflection spectrum, and bandwidth broadening was observed in all FBGs, as the result of the non-uniform distribution of stress along the grating. The spectra shape differ between the embedded FBGs, which is a possible reason for the observed non-linearity in the Bragg wavelength response, due to possible error in calculating the precise Bragg wavelength using the curve-fitting and peak detect algorithm.

6.7 Future work

The experimental results from the measurement of the three elastomer sensors, clearly shows that further investigation is required for a complete characterisation of the sensor. More specifically, the next steps on the sensor development might be:

- Implementation and testing of a large number of sensors. This will provide information regarding the different sensitivity of the gratings to the viscoelastic behaviour, which is believed to be caused by fabrication imperfections. It is important that the sensors are fabricated from the same elastomer mixture, with identical curing procedure for all sensors. This will certify that the elastic properties are the same for all sensors. It is also important that the fibre surfaces are cleaned prior to fitting into the fibre, and extra care should be taken not to contaminate the fibre with wax.

- The uncertainty regarding the precise location of the FBG in the sensor should be minimised. This requires careful marking of the grating location during its fabrication.
- Accurate measurement of the elastic properties of the elastomer, and the verification that linear viscoelastic behaviour is observed in the entire operating range of the sensor. Commercial methods and systems for material testing were suggested in section 5.3.1.3.
- As shown in Fig.6.10, the matrix material can be made of a softer material than SCOTCHCAST. Silicone elastomers (like SYLGARD) and rubbers have generally lower E modulus, exhibit lower viscoelastic creep than other engineering polymers, and can withstand larger elastic deformations (Ashby, 1993, pg.15).
- Short FBGs are required for the reduction of spectrum deflection, and its implications on the sensor performance, as shown in sections 6.2.2 and 6.2.3.
- Further miniaturisation of the sensor is possible using shorter FBGs, provided that the fibre angle does not exceed 30° (section 5.2.4). The shape of the top surface area could also be other than square. For instance, cylindrical shape of the sensor of 10mm diameter (equal to the width and depth of the implemented sensors) will provide the same embedded length of fibre, reducing at the same time the sensor volume.

CHAPTER 7

Discussion

7.1 Introduction

It has been well established during the last 30 years that mechanical stresses acting on soft tissue are an important factor in the development of pressure sores. Both pressure and shear stress have been found to be responsible for the occlusion of blood supply in the skin and the underlying soft tissue. Prolonged application of sufficiently high magnitude of normal and shear stresses could lead to tissue breakdown and ulceration. Subjects who are at high risk of developing pressure sores are persons with paralysis, peripheral vascular disease, diabetes, and patients with lower-limb prostheses. Many researchers have tried to measure the magnitude and distribution of those stresses, and several transducers have been developed. Recent discrete-sensor transducers provide accurate measurement of the magnitude of normal stress, and offer high spatial resolution which allows quasi-distributed sensing of pressure in the interface region between the skin and the external surface (prosthetic limb, shoe, wheelchair). The systems for measuring shear stresses, on the other hand, are less developed. Several electromechanical techniques have been utilised, however the developed transducers suffer from large size, electromagnetic interference, low signal-to-noise ratio, inability in multiplexing a large number of sensors, and some are only able to measure uni-directional stress.

The aim of the study described in this thesis was the design and implementation of a transducer with main target application the measurement of in-shoe shear stresses. The use of optical fibres, particularly the use of the newly developed fibre Bragg gratings as the strain sensing elements, offer significant advantages compared to the existing methods in terms of multiplexing and size. The design was based on the specifications required for in-shoe measurements, however the sensor could be applied for stress measurements in other soft tissue biomechanics.

7.2 Conclusions

In this thesis, a method for the simultaneous measurement of pressure and shear stress using FBGs embedded at a particular orientation into a block of elastomer material, was described

for the first time. The sensor is capable of measuring the normal stress, and the two components of shear stress acting on the top surface of the elastomer.

The classic theory of elasticity in solids was used to derive the required number of embedded FBGs, their orientation, and the elastic properties of the material, in order to calculate the three components of stress. More accurate prediction of the Bragg grating response was obtained using the theory of single-fibre composites, which was applied to describe the specific case where only one FBG is embedded horizontally in the material.

A novel method for measuring biaxial shear stress using FBGs fitted in an elastically deforming structure was also developed. Two FBGs are fixed between two metallic disks which are separated by a number of steel pins. Application of shear stress on the top disk produces relative displacement of the disks as the result of the elastic deflection of the pins, which in turn induces strain on the attached FBGs. The aim of the theoretical design was to estimate the E modulus and the diameter of the pins for maximum sensitivity in the desired dynamic range. The sensor was designed and developed in parallel with the elastomer sensor. It was initially considered as an alternative solution to the elastomer sensor while searching for the elastomer with the required properties.

An experimental setup was implemented for the accomplishment of the experiments regarding the material testing, and the testing of the sensor response to vertical and shear stress. The setup, which was made by high precision, commercially available positioning stages, enables the simultaneous application of vertical and uni-directional shear stresses on the sensor under test. The mean stress and displacement resolution of the system were measured to be 0.5kPa and 0.1μm respectively. The Bragg wavelength shift was measured using a spectrometer equipped with a 1024 pixel CCD detector. Software written in LabVIEW was used to display and store the FBG reflection spectra, and a peak detect algorithm was used to measure the absolute Bragg wavelength of the gratings. This FBG readout system was capable of acquiring up to 12spectra/s with a wavelength resolution in the order of 10pm.

The main objective of the experiments was to evaluate the feasibility of the sensors and to check the accuracy of the theoretical modelling for the two sensor approaches. Regarding the metallic sensor, an enlarged version of the sensor was made from steel (height=10mm, diameter=40mm), and the displacement of the disk to shear stress was measured. Linear elastic displacement was observed across the entire measuring range (0 to 250kPa), within approximately ±10% from the average linear approximation. The average error in measuring shear stress due to vertical stress variation was measured to be less than 5% for any value of disk displacement. Sensitivity of the structure to shear direction was observed, which was

measured to be approximately ±15% with respect to the average linear approximation. The principle of operation of the sensor was evaluated by installing one FBG and calculating the upper disk displacement by measuring the Bragg wavelength shift. Linear response was observed. The displacement as this was calculated from the Bragg wavelength shift, was in good agreement with the displacement measured by the micrometer.

Miniaturisation of the metallic sensor to acceptable dimensions for installation in an insole revealed several problems. The deformation of the structure was found to be non-linear, and highly dependent on the direction of shear. Plastic deformation was also observed. For those reasons, the metallic sensor approach was rejected for use as the in-shoe stress sensor. The enlarged version of the sensor, however, can be used in any application where biaxial shear stress has to be measured, and the sensor dimensions can be accepted.

The feasibility of the elastomer sensor was experimentally evaluated by fabricating and testing three sensors. The response of the horizontal gratings to vertical stress was closer to the prediction based on the theory of composites, than that of the classic theory of elasticity. However, the measured Bragg wavelength shift was approximately 45% lower than the theoretical prediction. This is thought to be mainly due to the uncertainty of the actual elastic properties of the elastomer, and the theoretical assumption of uniform stress distribution around the fibre axis.

The average responsivity of all the embedded FBGs to vertical stress was measured to be ~1.3pm/kPa, but the measured wavelength shift – stress curve differs significantly between the embedded gratings.

The comparison of the inclined and horizontal FBG response to shear stress parallel to the fibre axis clearly shows the significant effect of the embedding angle to the grating response. The sign of the wavelength shift of the inclined FBGs follows the sign of the applied shear stress, and the average responsivity was measured to be approximately 5pm/kPa. On the contrary, the responsivity of the horizontal FBGs is an order of magnitude lower (~0.5pm/kPa), although it was expected to be zero, based on the prediction of the fibre independent model. Due to the relatively low wavelength resolution of the FBG readout system, the response of the horizontally embedded gratings to shear stress, as well as the response of the inclined FBGs to shear perpendicular to the fibre axis, could not be accurately measured. It seems, however, that positive wavelength shift always occurs regardless of the sign of shear stress.

The above results are the experimental evidence that, embedding the FBGs at different angle and orientation inside the material, different responses with respect to the three components of stress can be achieved. Provided that each FBG is individually calibrated, then three

uncoupled equations can be obtained and solved for the vertical and shear components of stress.

7.3 Future work

The theoretical and experimental work presented in this Thesis was mainly focused on the evaluation of the principle of operation of the triaxial stress sensor. Several problems have been encountered which must be investigated before proceeding to clinical applications of the transducer. The experimental results from the measurement of the three elastomer sensors, clearly show that further investigation is required for a complete characterisation of the sensor. Issues which must be carefully examined are:

- the effect of the viscoelastic behaviour on the grating response and methods to avoid or compensate it. The experimental results showed that the embedded FBGs exhibit different sensitivity to viscoelasticity. The reasons for this should be further investigated by implementing and testing a large number of sensors made of the same material and fibre. Further research is also required in order to find a material with the required E modulus and low viscoelasticity.
- The sensor must be designed using a more accurate theoretical model of the 3-fibre sensor. Finite element analysis is thought to be the best approach. Accurate modelling will allow the modification of the sensor parameters (sensor dimensions, material properties and fibre dimensions) when different specifications of the sensor are required (increasing for example the dynamic range of the sensor). It is essential that the model will carefully examine all the assumptions accepted in this thesis (section 6.2.1). The model should provide a precise prediction of the non-uniform axial and shear stress distribution inside the fibre. These factors should be examined with respect to their effect on the properties of the embedded FBG.
- The sensitivity of the sensor response to environmental parameters, like temperature and humidity, which will affect the material properties, must be examined before the sensor is used for in-shoe measurements.
- The testing apparatus, shown in Fig.3.1, must be improved in order to enable dynamical measurements of the sensor for frequencies above 10Hz (section 3.4). The mass of the top plate must be reduced in order to reduce its inertia. Substitution with a hard polymer or composite material will significantly reduce the weight. A faster readout system will be required for the measurement of the Bragg wavelength shift. A FBG readout system capable of acquiring 300scans/s is proposed in the next section.

7.4 FBG interrogation system for the in-shoe transducer

A readout system for the interrogation of the in-shoe FBG sensor array will be proposed in this section. The system is based on multichannel WDM of the reflected light from the FGB array using an imaging spectrograph and a CCD camera, Fig.7.1. The basic system was demonstrated by Hu *et al.* (1997), which was briefly presented in section 2.8.5. The proposed system uses a faster CCD detector, satisfies both scanning speed and resolution requirements (section 2.3), and maintains a reasonably simple FBG arrangement, which requires only 2 fibres per shoe insole.

Typical wavelength resolution of commercially available spectrographs employing CCD detection is ~0.1nm, which can be improved by utilising peak detection algorithms, as discussed in section 3.6.1. Because the wavelength resolution strongly depends on the signal-to-noise ratio of the obtained spectra, it is important to verify that the optical power arriving on the active area of the CCD camera is sufficiently high. Ezbiri *et al.* (1998) used a commercially available CCD spectrometer having a resolution equal to 0.1nm, in order to measure the wavelength resolution obtained after using peak detection algorithms. They concluded that resolution in the order of 1pm can be achieved if the optical energy during each integration time is >10% of the energy which leads to saturation of the CCD.

In this section the optical energy arriving at the detector will be estimated, considering that commercial devices and components are used for the implementation of the system. Parameters like source power, insertion loss of fibre couplers, bulk grating efficiency and spectrometer dispersion, which determine the spectral power density arriving on the CCD active area, are taken from the manufacturer data sheets[1].

The 800nm wavelength band was selected as the operating band of the system. Reasons for choosing this band are i) the wide variety of commercial spectographs and CCD cameras in that band at relatively low cost, ii) the relatively high efficiency of CCDs compared to longer or shorter wavelengths, iii) the availability of broadband and high power, fibre-pigtailed sources.

[1] The survey for components and devices was done between December 1998 and March 1999. It is therefore possible that the particular components are not yet available, or the specifications and prices have been changed.

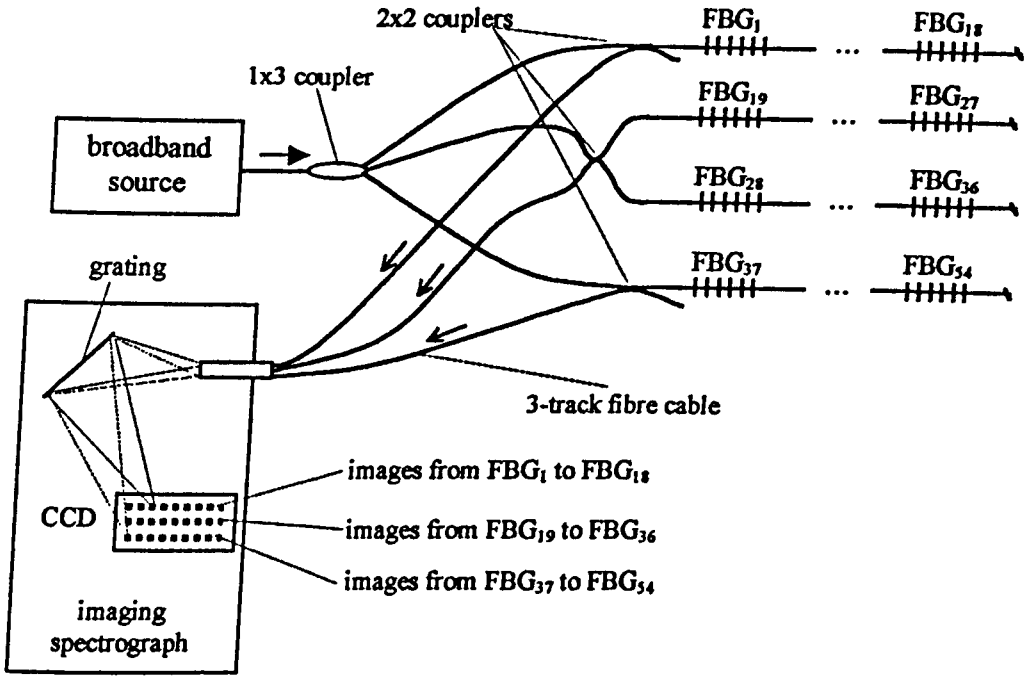

Fig.7.1: Proposed interrogation system for the in-shoe stress transducer.

The 800nm band broadband light source to be considered is the SLD-371 (SUPERLUM[1]), which has FWHM bandwidth=80nm, operating range =775-855nm, optical power =1.7mW. Assuming uniform distribution of the source power over the 80nm spectrum, the spectral power density of the source output is 21.3μW/nm. After passing the 1x3 coupler[2] the power in each output will be equal to 5.6μW/nm (-1dB losses, 33% coupling ratio). The power which arrives at the FBGs, after passing through the 2x2 coupler[3] is equal to 2.2μW/nm (-1dB losses, 50% coupling ratio). Assuming reflectivity 20% and grating bandwidth=0.3nm for all FBGs, the reflected power will be equal to 133nW over a band of 0.3nm (x0.2 due to reflectivity, x0.3 due to bandwidth). The light passes once again through the coupler, and the power becomes equal to 53nW. Assuming 6db attenuation due to splicing and bending losses[4], the power becomes equal to 13nW. This is the spectral power density which arrives at the spectrograph via the 3-fibre cable[5]. Using MultiSpec imaging spectrograph[6] with a 1200lines/mm grating[7], then the spectral power density which arrives at the CCD will be 20% of the input power, hence equal to 2.6nW.

---

[1] SUPERLUM Ltd., P.O. Box 73, E-538, 111538 Moscow, Russia.
[2] Product ID: L2K23-10685-13-08131, coupling ratio 33/33/33 %, excess loss =1dB. Available by LASER 2000 (UK), Britannia House, Denford Road, Ringstead, NN14 4DF.
[3] Product ID: L2K22-10685-50-22231, coupling ratio 50/50 %, excess loss =1dB. Available by LASER 2000 (UK), Britannia House, Denford Road, Ringstead, NN14 4DF.
[4] assuming 0.1db per splice, 18 splices per fibre, plus 3db bending losses
[5] Product ID: 77679 3 Track Fibre, available by L.O.T.-Oriel Ltd., 1 Mole Business Park, Leatherhead, Surrey KT22 7AU, UK, Tel: 01372-378822.
[6] Product ID: 77400 MultiSpec spectrograph, available by L.O.T.-Oriel Ltd.
[7] Product ID: 77752 Single grating, 1200l/mm, 750nm blaze, available by L.O.T.-Oriel Ltd.

The light from each fibre is focused on the CCD active area as shown in Fig.7.2. The active area of the 1024 x 256 pixel EEV CCD camera[1], is equal to 25x5mm. The image of the spectrum from each of the three fibres is a narrow line, clearly separated from the images of the two others. For this particular spectrograph, the thickness of each line is approximately 0.4mm. The overall bandwidth which is dispersed on each of the 25mm lines can be calculated by the dispersion parameter of the spectrograph, which is equal to 3.1nm/mm. Hence, the overall spectrum captured by the CCD camera will be equal to 25mm x 3.1nm/mm =77.5nm, which is only 2.5nm less than the available source bandwidth. The 2.5nm bandwidth loss can be tolerated, since the overall bandwidth required for the WDM of the FBGs is 72nm (4nm per FBG, 18 FBGs per fibre).

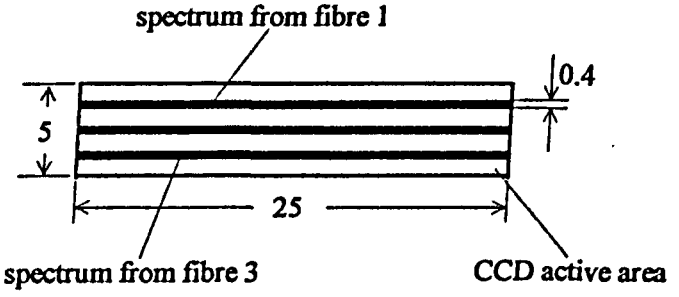

Fig.7.2: Images from the three fibres on the CCD active area. Dimensions in mm.

Knowing the dispersion parameter of the spectrograph and the thickness of each line, the power density over the area of the CCD can be calculated. It will be assumed that the spectral power density which arrives on the CCD (2.6nW over a band of 0.3nm, as found previously) is uniformly distributed over the rectangular area shown in Fig.7.3. The dispersion parameter is 3.1nm/mm, therefore the width of the rectangular area, which corresponds to 0.3nm, will be 0.3/3.1≅0.1mm. The optical power density on the CCD area will therefore be $P=6.5\mu W/cm^2$ (2.6nW over $0.1x0.4mm^2$).

This particular CCD camera gives the ability to acquire data from user-defined regions of pixels. If, for example, only one row of 1024 pixels which lies inside the spectral line is selected for each line as the sensor array, only 3 of the 256 available pixel rows are used for sensing. The remaining 253 rows can be used for a temporary storage area. This means that 253/3=84 rows can be used for storage on the CCD chip, for each line. The frame grabber which is supplied with the camera acquires 4frames/s (1024x256pixel frames). Multiplying the acquisition speed, with the number of spectra stored on the CCD, the maximum number

[1] Product ID: 78435 1024x256 EEV UV CCD System, including TEC to -60°C, software, and 1MHz controller card. Available by L.O.T.-Oriel Ltd.

of spectra which can be achieved is equal to 336spectra/s per line, which is above the required speed of 300Hz[1].

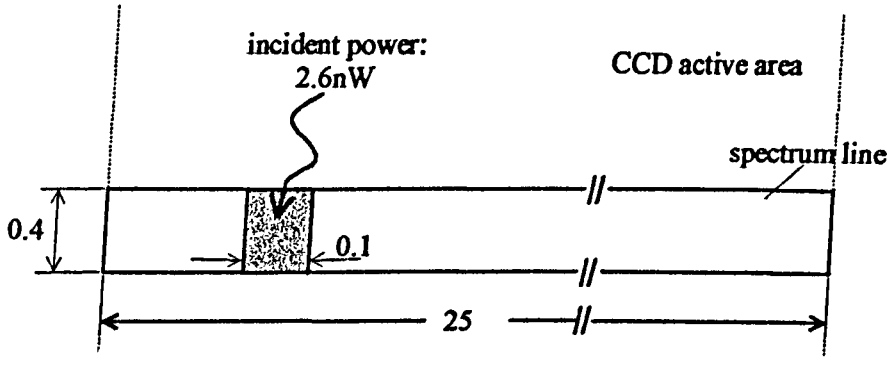

Fig.7.3: Calculation of power density on the CCD active area. Dimensions in mm.

Adjusting the camera settings for 300spectra/s, the maximum integration time is t_{int}=3.3ms. The optical energy arriving on the CCD active area in 3.3ms will be: $E=Pxt_{int}=21.5nJ/cm^2$. The saturation exposure limit for this camera is $250pJ/cm^2$, which is well below the estimated power density on the CCD, therefore promising high signal-to-noise ratio of the acquired spectra.

[1] This information is found in "ORIEL Instruments, InstaSpec IV CCD detection system" brochure, and with personal communication with the company. The terms "fast kinetics" and "multi-track spectroscopy" are used to classify this particular application.

APPENDIX I

Mechanical drawing of the metallic sensor (actual size)

APPENDIX II

Pictures

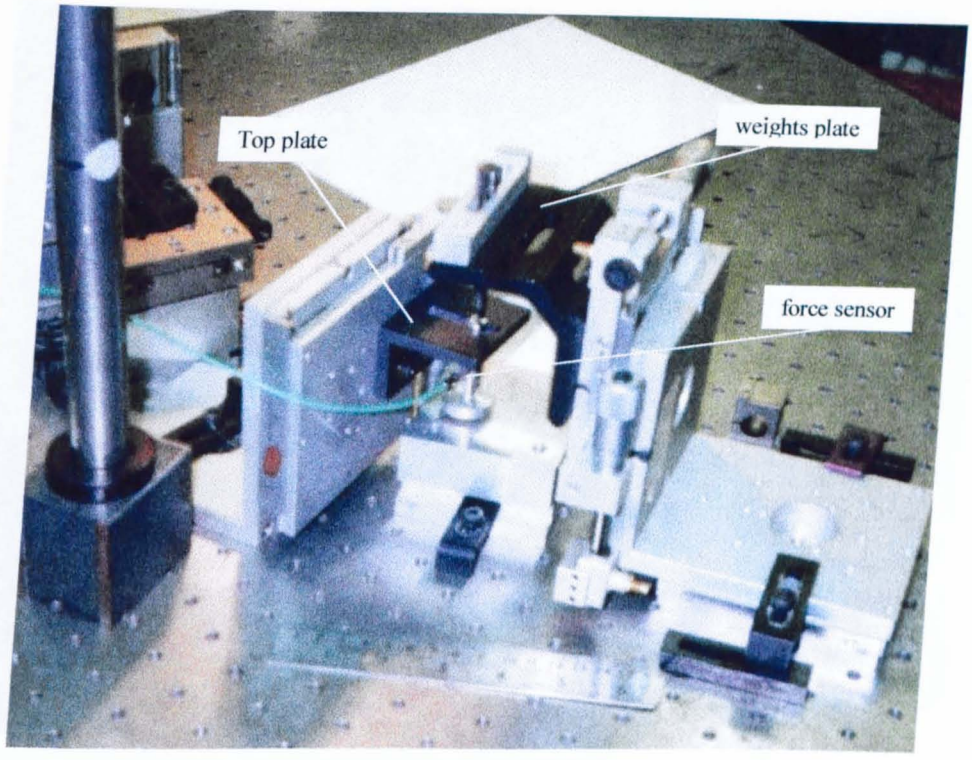

Picture 1: Experimental apparatus for the measurement of E-modulus, and the sensor response to vertical stress.

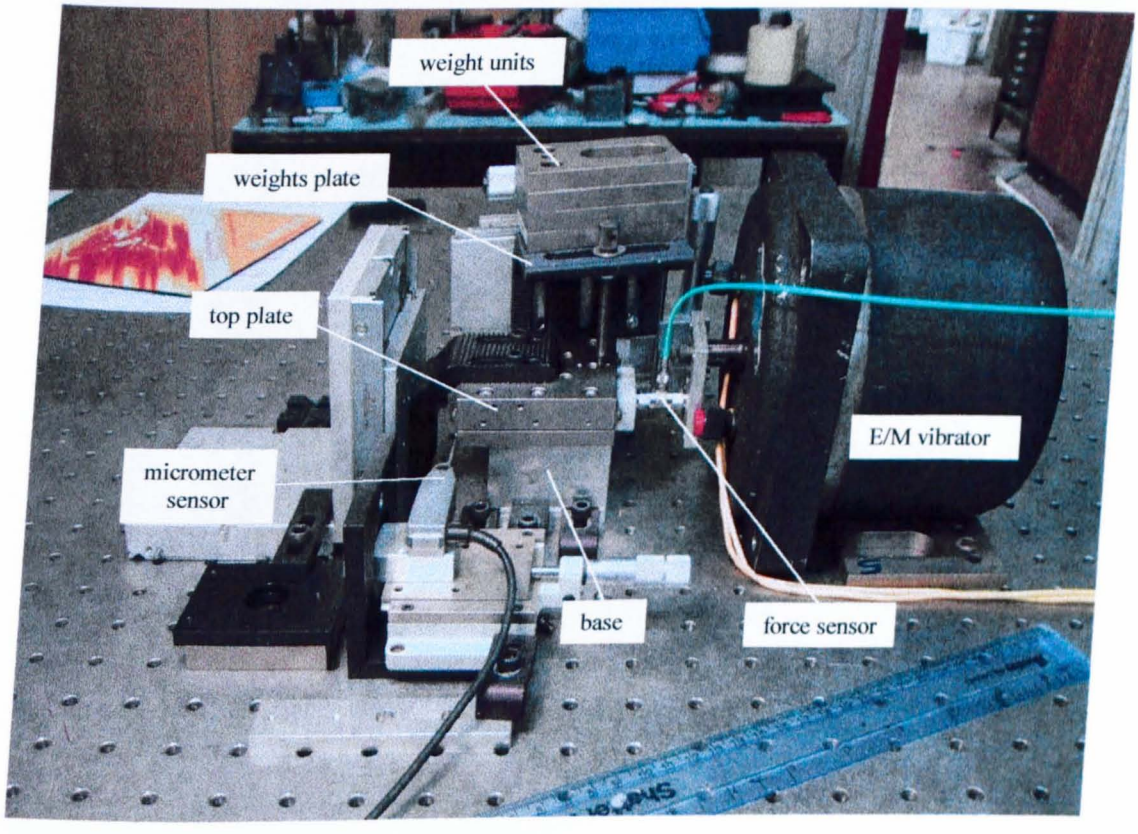

Picture 2: Apparatus for measuring the G modulus, as well as for the measurement of the sensor response to shear stress.

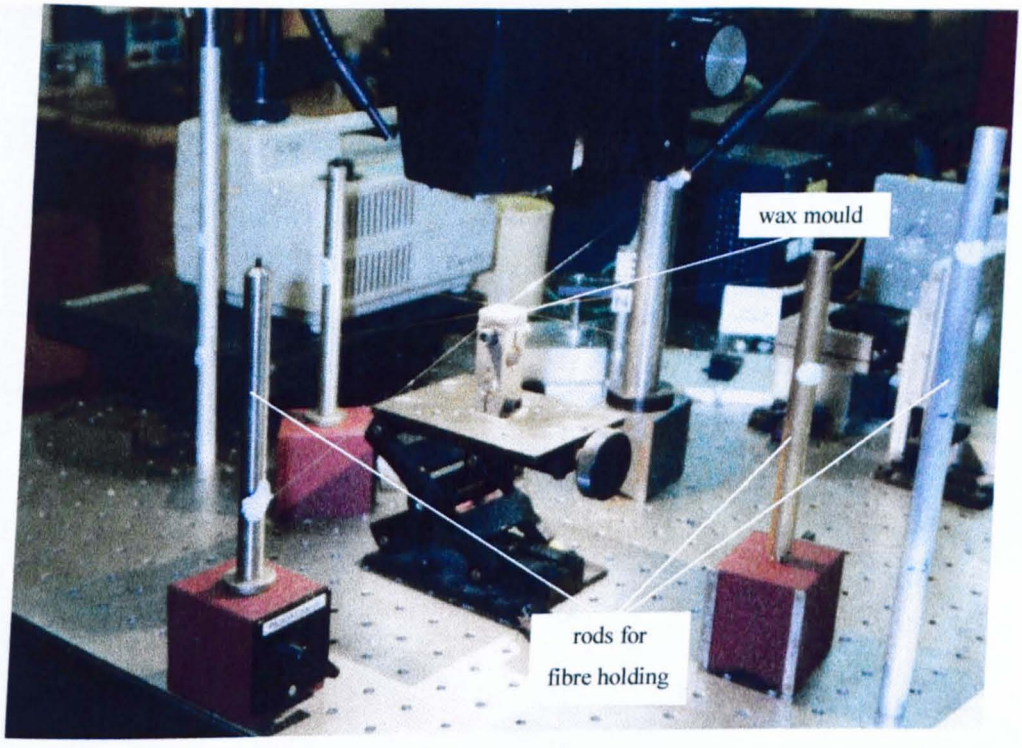

Picture 3: Apparatus for fibre alignment in the wax mould for the construction of sensor-3F.

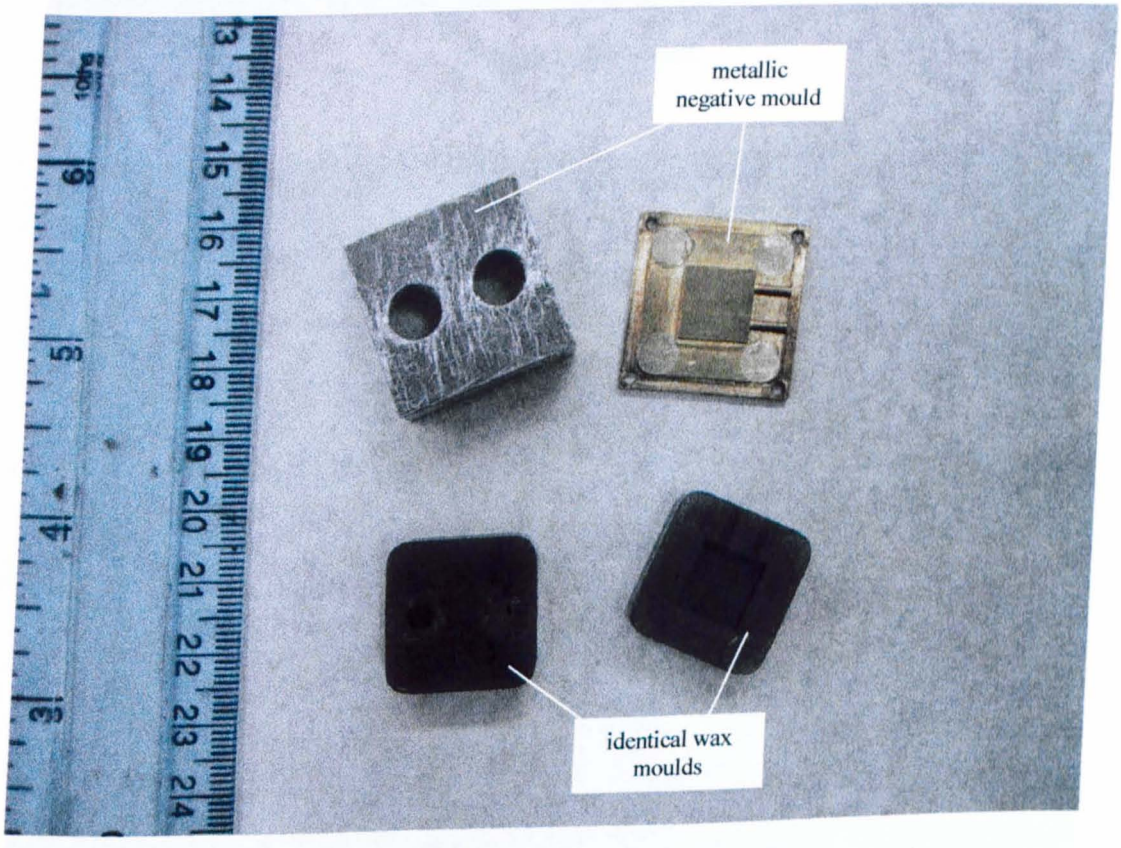

Picture 4: Metallic negative mould and wax moulds (actual dimensions)

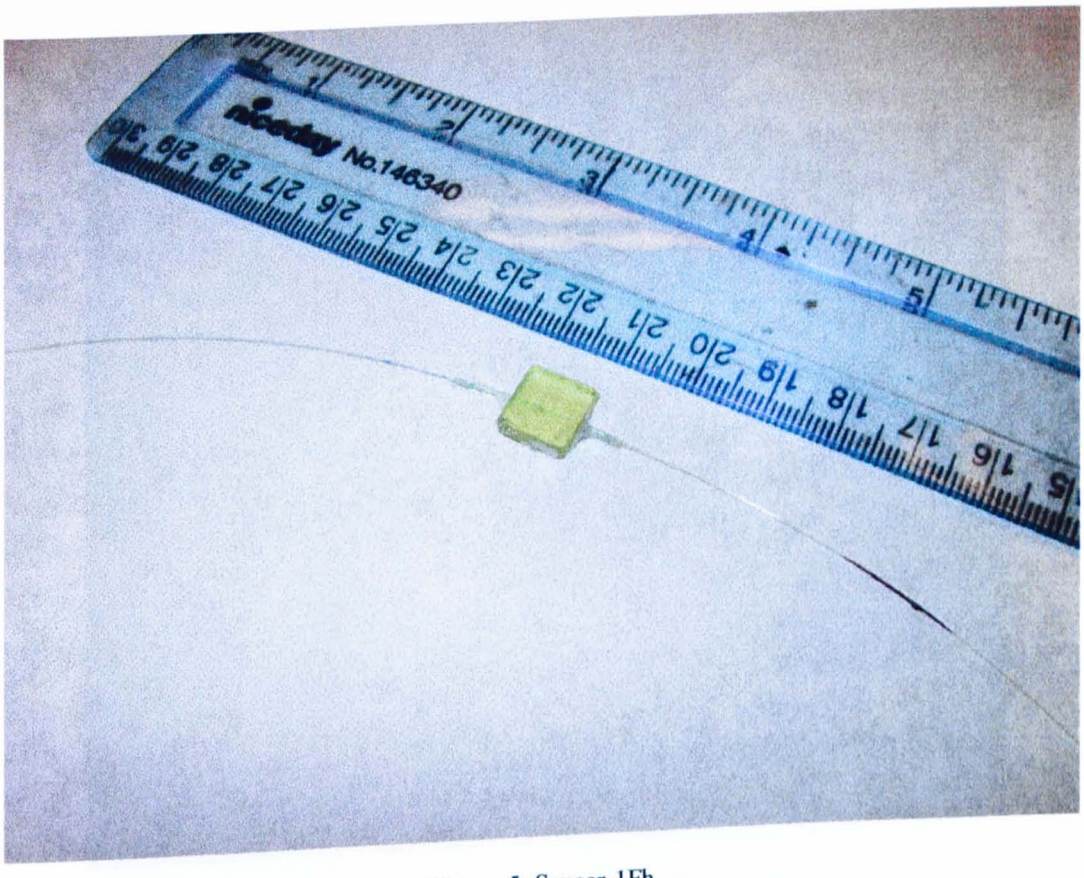

Picture 5: Sensor-1Fh.

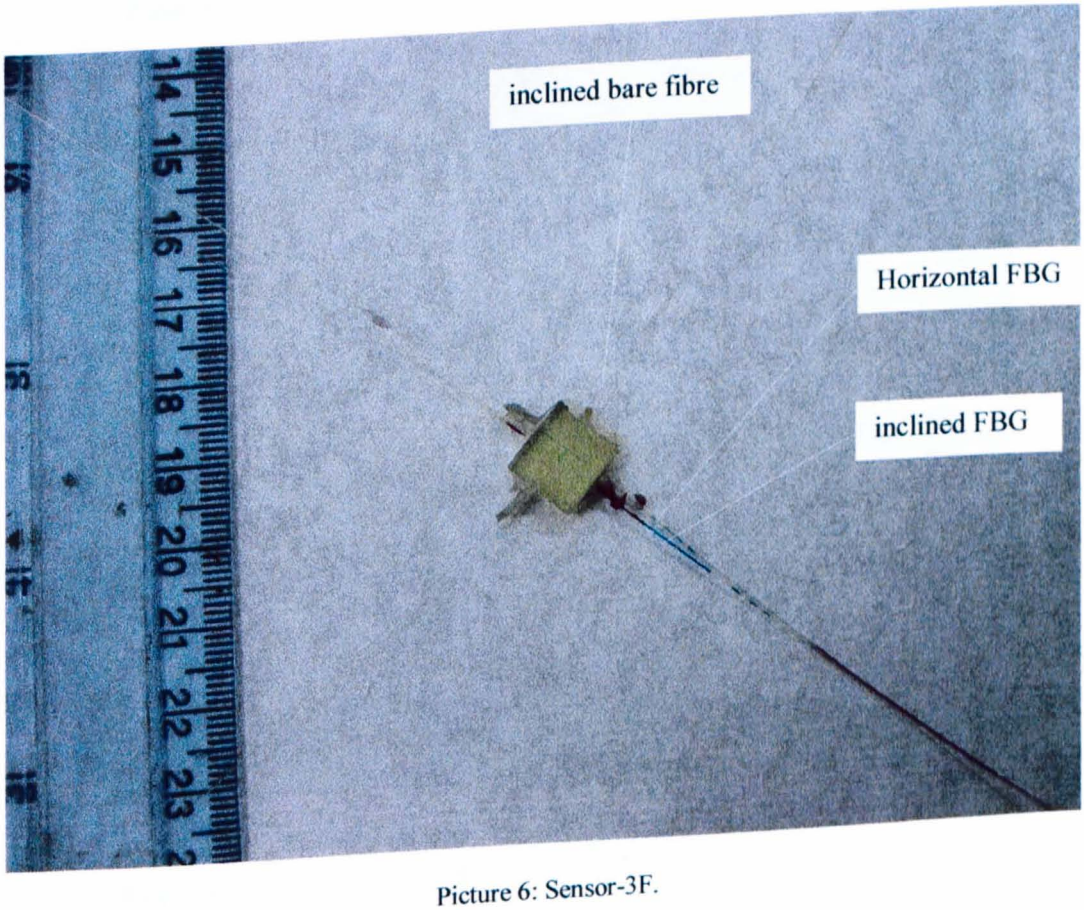

Picture 6: Sensor-3F.

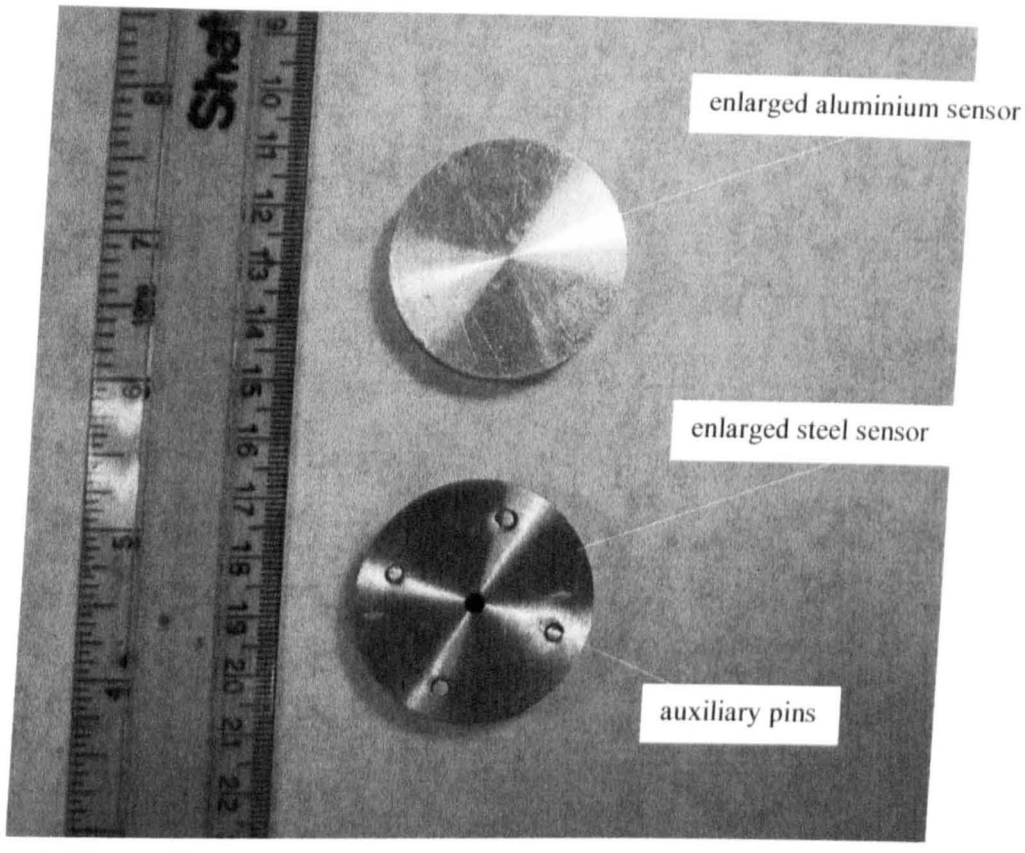

Picture 7: Enlarged metallic structures (top view).

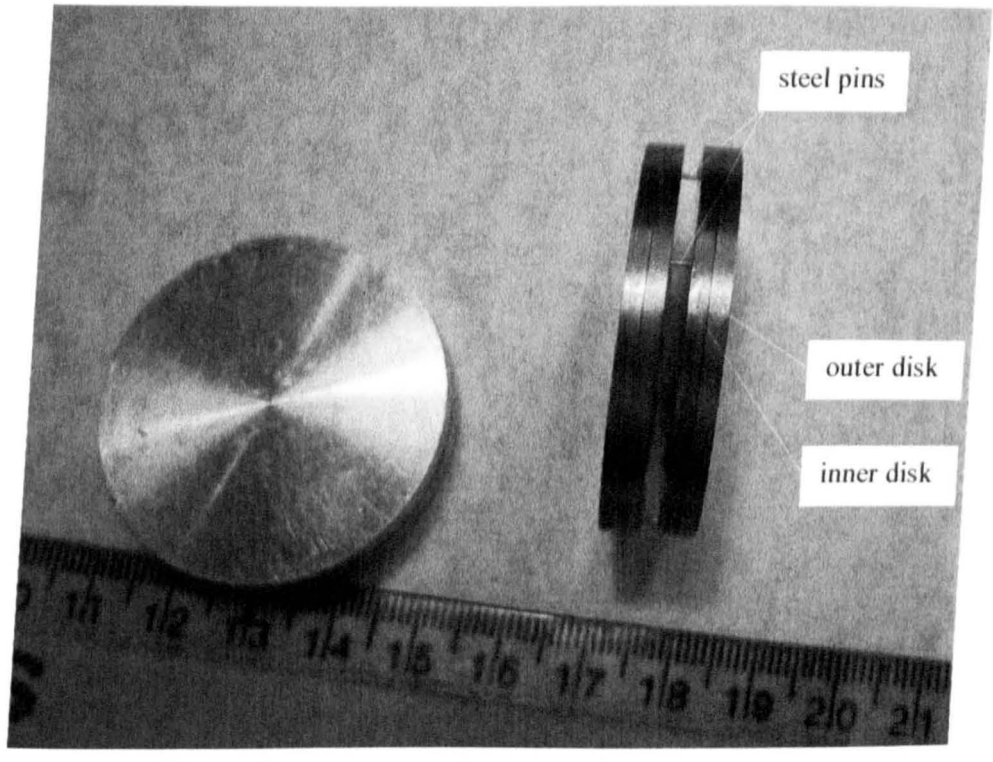

Picture 8: Enlarged metallic structures (side view).

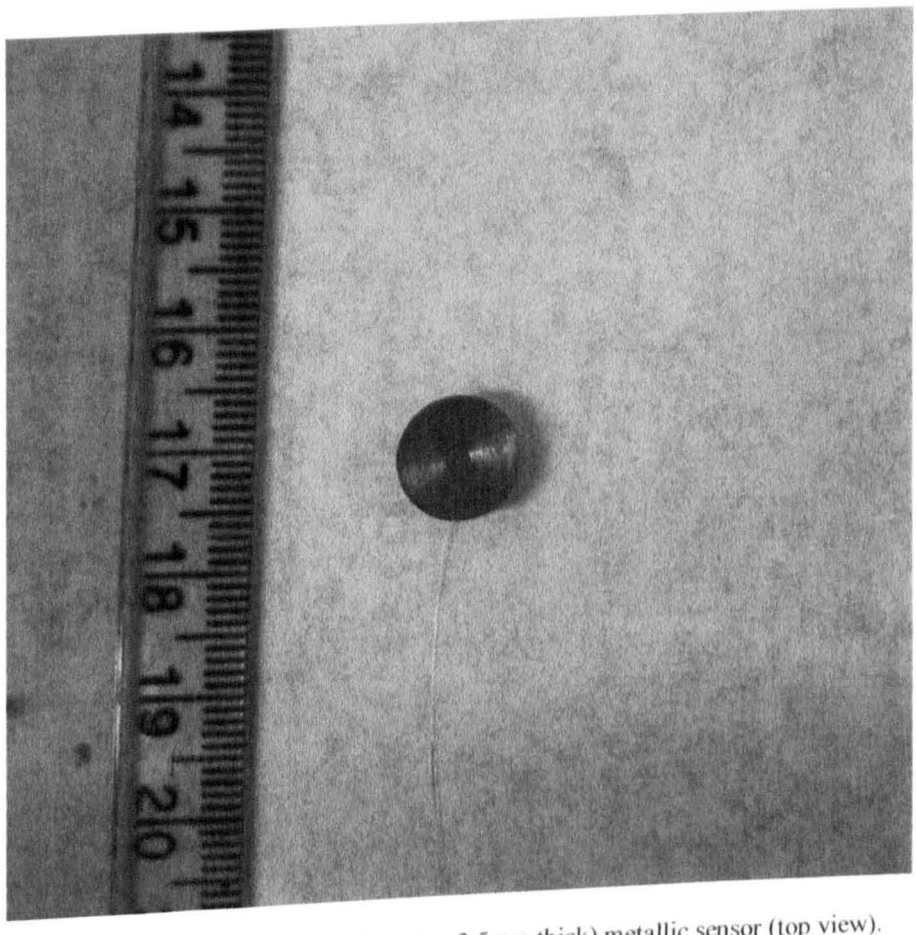

Picture 9: Actual size (10mm diameter, 3.5mm thick) metallic sensor (top view).

Picture 10: Actual size (10mm diameter, 3.5mm thick) metallic sensor (side view).

APPENDIX III

Readout system screenshots

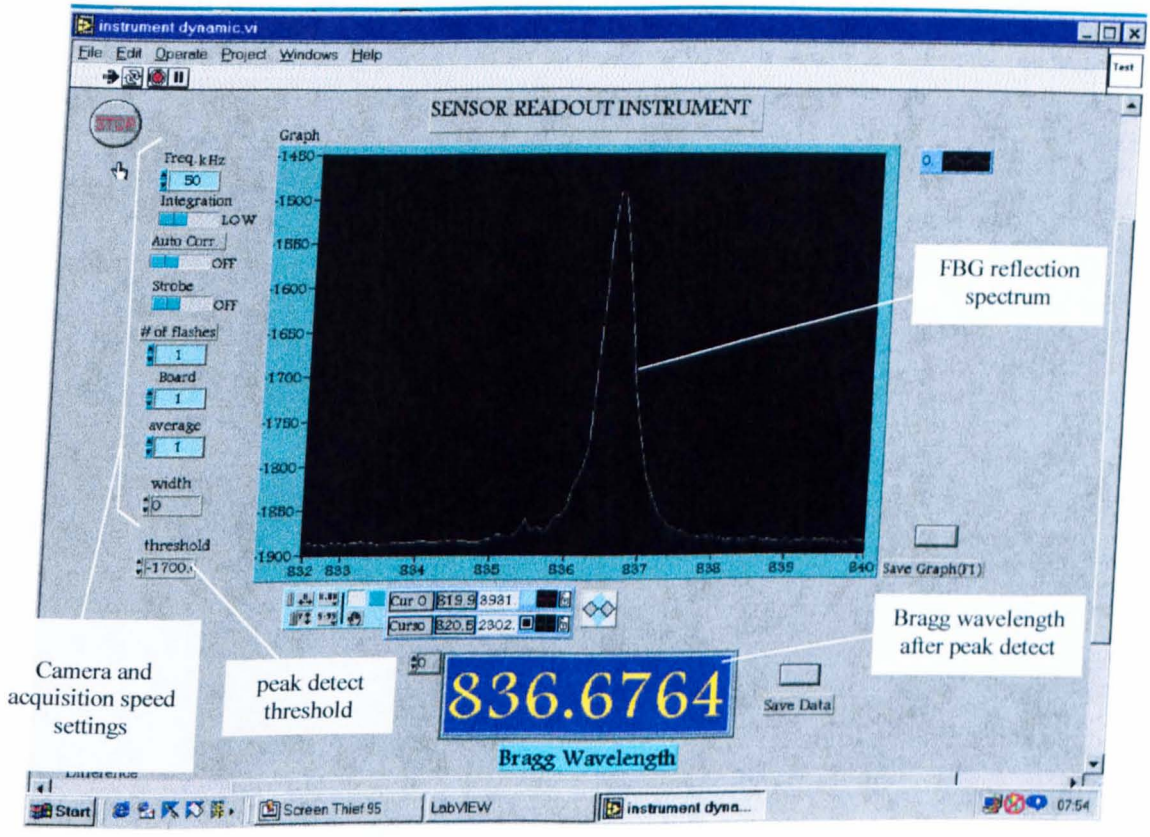

Picture 1: Screenshot from the FBG spectrum acquisition software, written in LabVIEW®. The unstrained reflection spectrum of the inclined FBG in sensor-3F is shown.

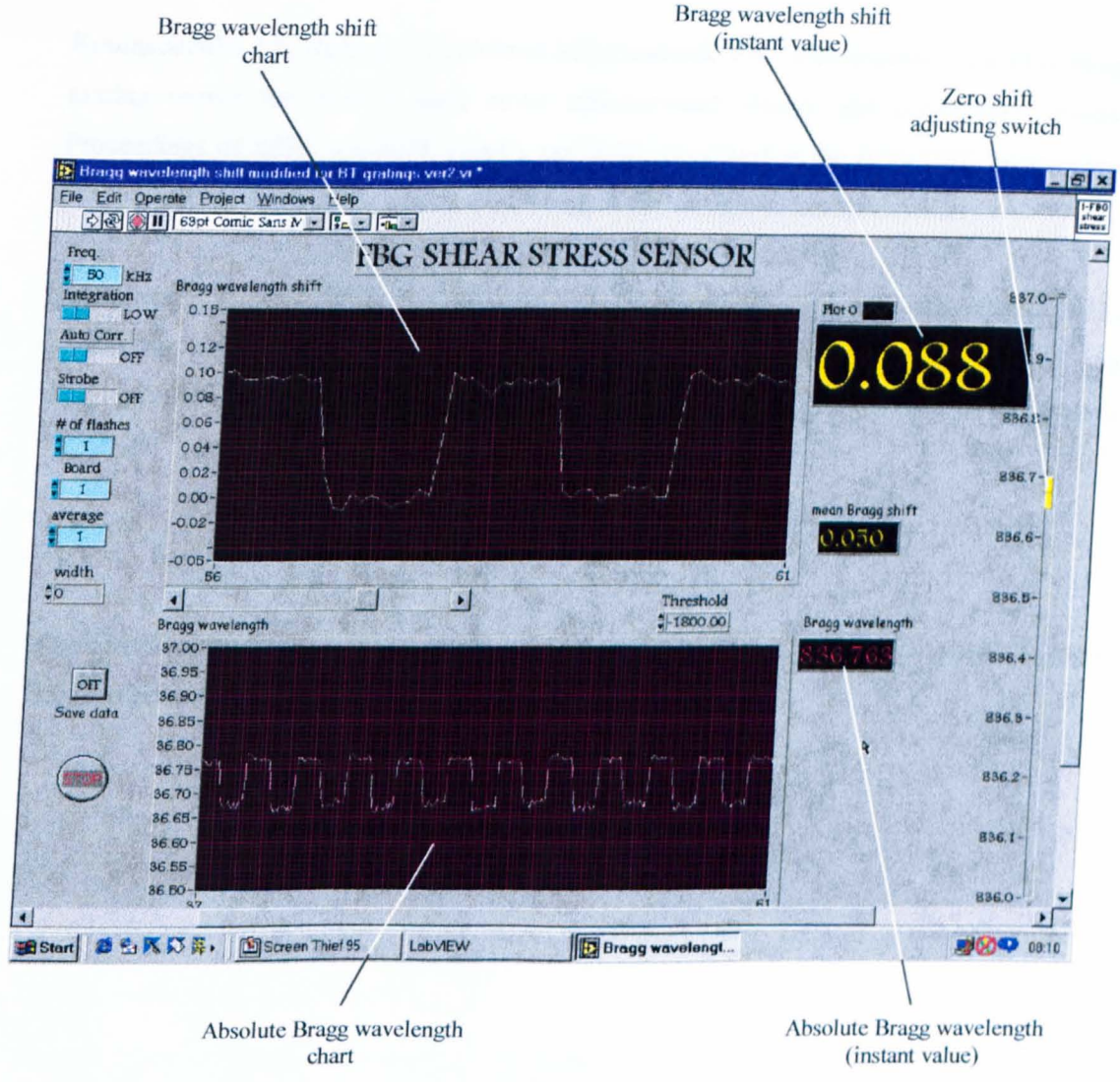

Picture 2: Screenshot from the Bragg wavelength shift acquisition software, written in LabVIEW®. The graphs show the response of the inclined FBG in sensor-3F to ~0.5Hz, ~20kPa shear stress pulses.

LIST OF PUBLICATIONS

The research described in this Thesis has lead to the publication and presentation of the following papers:

Koulaxouzidis AV, Roberts VC, Holmes MJ, Handerek VA, "Development of a fibre Bragg grating sensor for in-shoe shear stress measurement: design and preliminary results", Proceedings of SPIE, vol.4074, (2000), pp.79-88, presented at the EOS/SPIE International Symposium on Applied Photonics, 22-24 May 2000, Glasgow, Scotland, UK.

Koulaxouzidis AV, Holmes MJ, Roberts VC, Handerek VA, "A shear and vertical stress sensor for physiological measurements using fibre Bragg gratings", Proceedings of the World Congress on Medical Physics and Biomedical Engineering, 23-28 July 2000, Chicago IL, USA.

Application for patent protection for both sensor designs (metallic and elastomer sensors) has also been submitted. (UK Patent Application: 0011130.2)

REFERENCES

Aklonis JJ, MacKnight WJ, Shen M, (1972), "Introduction to Polymer Viscoelastisity", Wiley-Interscience, New York.

Akhlaghi F, Pepper MG, (1996), "In-shoe shear force measurement: the Kent shear system", Medical & Biological Engineering & Computing, vol.34, pp.315-317.

Alexander IJ, Chao EYS, Johnson KA, (1990), "The assessment of dynamic foot-to-ground contact forces and plantar pressure distribution: a review of the evolution of current techniques and clinical applications", Foot & Ankle, vol.11, no.3, pp.152-167

Archambault JL, Reekie L, Russell PSJ, (1993), "High reflectivity and narrow bandwidth fibre gratings written by a single excimer pulse", Electronics Letters, vol.29, no.1, p.28-29.

Ashby MF, (1993), "Materials Selection in Mechanical Design", 2nd ed., Pergamon Press, Oxford UK.

Askins CG, Tsai TE, Williams GM, Putnam MA, Friebele EJ, (1992), "Fiber Bragg reflectors prepared by a single excimer pulse", Optics Letters, vol. 17, no. 11, p.833-835.

Bader DL, (1990), "Pressure Sores, Clinical Practice and Scientific approach", Macmillan Press, London.

Ball GA, Morey WW, Cheo PK, (1994), "Fiber laser source/analyser for Bragg grating sensor array interrogation", Journal of Lightwave Technology, vol.12, no.4, pp.700-703.

Begg RK, Rahman SM, (2000), "A method for the reconstruction of ground reaction force-time characteristics during gait from force platform recordings of simultaneous foot falls", IEEE Transactions on Biomedical Engineering, vol.47, no.4, pp.547-551

Bennett D., Kavner D., Lee BK, Trainor FA, (1979), "Shear vs pressure as causative factors in skin blood flow occlusion", Arch. Phys. Med. Rehabil., vol.60, pp.309-314.

Berkoff TA, Kersey AD, (1996), "Fiber Bragg grating array sensor system using a bandpass wavelength division multiplexer and interferometric detection", IEEE Photonics Technology Letters, vol.8, no.11, pp.1522-1524.

Booth J, Birch I, Barnett S, (1998), "Foot pressure measurement and diabetes: where are we now?", The Diabetic Foot, vol.1, no.1, pp.28-32.

Brand PW, (1976), Pressure sores – the problem. In Kennedi RM, Cowden JM, Scales JT, "Bedsore Biomechanics", Macmillan Press, London and Basingstoke, pp.19-23.

Boulton AJM, "The Pathway to Ulceration: Aetiopathogenesis". In Boulton AJM, Connor H, Cavanagh PR, (2000), "The foot in Diabetes", 3rd edn., John Wiley & Sons Ltd., Sussex.

Budinsky KG, Budinsky MK, (1999), "Engineering Materials, Properties and Selection", 6th ed., Prentice Hall, pp.690-703.

Bures J, Lacroix S, Lapiere J, (1982), "Bragg reflector induced by photosensitivity in an optical fibre: Model of growth and frequency response", Applied Optics, vol. 21, no. 19, p.3052.

Byron KC, Sugden K, Bricheno T, Bennion I, (1993), "Fabrication of chirped Bragg gratings in photosensitive fibre", Electronics Letters, vol.29, no.18, pp.1659-1660.

Charles JA, Crane FA, Furness JA, (1997), "Selection and Use of Engineering Materials", 3rd ed., Butterworth Heinemann, pp.63.

Cobb J, Claremont DJ, (1995), "Transducers for foot pressure measurement: survey of recent developments", Medical and Biological Engineering and Computing, vol.33, pp.525-532.

Cox HL, (1952) "The elasticity and strength of paper and other fibrous materials, British Journal of Applied Physics, vol.3, pp.72-79.

Culshaw B, Dakin J, (1989), "Optical Fiber Sensors: Systems and Applications", Artech House, Norwood MA, USA.

Dalsa Inc., (1995), "1996-1997 Databook, Advancing Image Capture Technology", Dalsa CCD Image Capture Technology, pp.19-30.

Davis MA, Bellemore DG, Kersey AD, (1995), "Design and performance of a fibre Bragg grating distributed strain sensor system", Proceedings SPIE North American Conference on Smart Structures and Materials, San Diego, CA, Feb. 1995, vol.2446, p.227.

Davis MA, Bellemore DG, Putnam MA, Kersey AD, (1996), "Interrogation of 60 fibre Bragg grating sensors with microstrain resolution capability", Electronics Letters, vol.32, no.15, pp.1393-1394.

Davis MA, Kersey AD, (1995), "Matched-filter interrogation for fibre Bragg grating array", Electronics Letters, vol.31, no.10, pp.822-823.

Erdogan T, Mizrahi V, Lemaire PJ, and Monroe D, (1994) "Decay of ultraviolet-induced fiber Bragg gratings", Journal of Applied Physics, vol.76, no.1.

Ezbiri A., Kanellopoulos S. E., Handerek V. A. (1998), "High resolution instrumentation system for fibre-Bragg grating aerospace sensors", Optics Communications, 150, pp.43-48.

Feced R, Roe-Edwards MP, Kanellopoulos SE, Taylor NH, and Handerek VA, (1997) "Mechanical strength degradation of UV exposed optical fibres", Electronics Letters, vol.33, no.2, pp.157-159.

Ferreira LA, Diatzikis EV, Santos JL, Farahi F, (1998), "Frequency-modulated multimode laser diode for fiber Bragg grating sensors", IEEE Journal of Lightwave Technology, vol.16, no.9, pp.1620-1630.

Ferry JD, (1970), "Viscoelastic Properties of Polymers", 2nd Ed., Wiley, New York.

Flavin DA, McBride R, Jones JDC, (1997), "Absolute measurement of wavelengths from a multiplexed in-fibre Bragg grating array by short-scan interferometry", Proceedings of the 12th International Conference on Optical Fiber Sensors (OFS-12), Washington, DC, OSA Technical Digest Series, vol.16, pp.24-27.

Franks CI, Betts RP, Duckworth T, (1986), "An image processing system for dynamic foot pressure studies", Journal of Medical Engineering and Technology, pp.42-46

Franks CI, (1997), "Calibration of optical foot pressure systems", Medical & Biological Engineering & Computing, vol.35, pp.69-72

Geiger H, Xu MG, Eaton NC, Dakin JP, (1995), "Electronic tracking system for multiplexed fibre grating sensors", Electronics Letters, vol.31, no.12, pp.1006-1007.

Grattan KTV, Meggitt BT, (1995), "Optical Fiber Sensor Technology", Chapman & Hall, London.

Grattan KTV, Meggitt BT, (1998), "Optical Fiber Sensor Technology, volume 2: Devices and Technology", Chapman & Hall, London.

Grattan KTV, Ning YN, (1998), "Classification of optical fiber sensors". In Grattan KTV, Meggitt BT, (1998), "Optical Fiber Sensor Technology, volume 2: Devices and Technology", Chapman & Hall, London.

Grattan KTV, Sun DT, (2000), "Fiber optic sensor technology: an overview", Sensors and Actuators, vol.82, pp.40-61

Gross B, (1953), "Mathematical Structure of the Theories of Viscoelasticity", Hermann, Paris.

Hand DP, Russell PSJ, (1990), "Photoinduced refractive index changes in germanosilicate fibers", Optics Letters, vol.15, no.2, p.102-104.

Handerek VA, (1998), "Fiber Gratings: principles, fabrication and properties". In Grattan KTV, Meggitt BT, (1998), "Optical Fiber Sensor Technology, Volume 2, Devices and Technology", Chapman & Hall, London.

Hill KO, Fujii Y, Johnson DC, Kawasaki BS, (1978),"Photosensitivity in optical fiber waveguides: Application to reflection filter fabrication", Applied Physics Letters, vol. 32, p.647-649.

Hill KO, Malo B, Bilodeau F, Johnson DC, Albert J, (1993), "Bragg gratings fabricated in monomode photosensitive optical fiber by UV exposure through a phase mask", Applied Physics Letters, vol.62, no.10, pp.1035-1037.

Hill KO, Meltz G, (1997), "Fiber Bragg Grating Technology Fundamentals and Overview", Journal of Lightwave Technology, vol.15, no.8, pp.1263-1276.

Horio M, Onogi S, (1951), Journal of Applied Physics, vol.22, pg.977.

Hosein R, (1996), " An investigation of in-shoe plantar pressures and shear stresses with particular reference to diabetic foot neuropathy". A thesis submitted for the degree of Doctor of Philosophy at the University of London.

Hosein R, Lord M, (2000), "A study of in-shoe plantar shear in normals", Clinical Biomechanics, vol.15, pp.46-53.

Hu Y, Chen S, Zhang L, Bennion I, (1997), "Multiplexing Bragg gratings using combined wavelength and spatial division techniques with digital resolution enhancement", Electronics Letters, vol.33, no.23, pp.1973-1975.

Hughes R, Rowlands H, McMeekin S, (2000), "A laser plantar pressure sensor for the diabetic foot", Medical Engineering & Physics, vol.22, pp.149-154.

Hull D, Clyne TW, (1996), "An Introduction to Composite Materials", 2nd Ed., Cambridge University Press.

Jones JDC, McBride R, (1998), "Multiplexing optical fiber sensors". In Grattan KTV, Meggitt BT, (1998), "Optical Fiber Sensor Technology, volume 2: Devices and Technology", Chapman & Hall, London.

Kanellopoulos S, Handerek VA, Rogers AJ, (1995), "Simultaneous strain and temperature sensing with photogenerated in-fibre gratings", Optics Letters, vol.20, no.3, pp.333-335.

Kashima Y, Kobayashi M, Takano H, (1988), "High output power GaInAsP/InP superluminescent diode at 1.3μm", Electronics Letters, vol.24, no.24, pp.1507-1508.

Kashyap R, (1994), "Photosensitive optical fibers: Design and applications", Optical Fiber Technology, vol.1, pp.17-34.

Kashyap R, (1998), "Assessment of tuning the wavelength of chirped and unchirped fibre Bragg grating with single phase-masks", Electronics Letters, vol.34, no.21, pp.2025-2027.

Kashyap R, (1999), "Fiber Bragg Gratings", Academic Press, London.

Kashyap R, Armitage JR, Campbell RJ, Williams DL, Maxwell GD, Ainslie BJ, Millar CA, (1993), "Light-sensitive optical fibres and planar waveguides", BT Technology Journal, vol.11, no.2, pp.150-160.

Kashyap R, Armitage JR, Wyatt R, Davey ST, Williams DL, (1990), "All-fibre narrowband reflection gratings at 1500nm", Electronics Letters, vol.26, no.11, p.730-732.

Kashyap R, McKee PF, Campbell RJ, Williams DL, (1994), "Novel method of producing all fibre photoinduced chirped gratings", Electronics Letters, vol.30, no.12, pp.996-997.

Kersey AD, Berkoff TA, Morey WW, (1992), "Fiber-grating based strain sensor with phase sensitive detection", Proceedings of the 1st European Conference on Smart Structures and Materials, Glasgow 1992, pp.61-67.

Kersey AD, Davis MA, Patrick HJ, LeBlanc M, Koo KP, Askins CG, Putnam MA, Friebele EJ, (1997), "Fiber Grating Sensors", IEEE Journal of Lightwave Technology, vol. 15, no. 8, p. 1442-1463.

Koo KP, Tveten AB, Vohra ST, (1999), "Dense wavelength division multiplexing of fibre Bragg grating sensors using CDMA", Electronics Letters, vol.35, no.2, pp.165-167.

Laing P, Deogan H, Cogley D, Crerand S, Hammond P, Klenerman L, (1992), "The development of the low-profile Liverpool shear transducer", Clinical Physics & Physiological Measurements, vol.13, no.2, pp.115-124.

Lebar AM, Harris GF, Wertsch JJ, Zhu H, (1996), "An optoelectric plantar 'shear' sensing transducer: Design, validation, and preliminary subject tests", IEEE transactions on Rehabilitation Engineering, vol.4, no.4, pp.310-318.

Lee CE, Taylor HF, (1988), "Interferometric optical fibre sensors using internal mirrors", Electronic Letters, vol.24, pp.193-194.

Lemaire P, Atkins RM, Mizrahi V, Reed WA, (1993), "High pressure H_2 loading as a technique for achieving ultrahigh UV photosensitivity and thermal sensitivity in GeO_2 doped optical fibres", Electronics Letters, vol. 29, no.13, pp.1191-1193.

LINOS Photonics, (1999), "The Catalog, GE5", LINOS Photonics GmbH, pp.T2.

Lord M, (1993), "The application of advanced technology to orthopaedic footwear design". A thesis submitted for the degree of Doctor of Philosophy at the University of London.

Lord M, Hosein R, (2000), "A study of in-shoe plantar shear in patients with diabetic neuropathy", Clinical Biomechanics, vol.15, pp.278-283.

Lord M, Reynolds DP, Hughes JR, (1986), "Foot pressure measurement: a review of clinical findings", Journal of Biomedical Engineering, vol.8, pp.283-294

Meltz G, Morey WW, Glenn WH, (1989), "Formation of Bragg gratings in optical fibers by a transverse holographic method", Optics Letters, vol.14, no.15, p.823-825.

McCrum NG, Read BE, Williams G., (1967), "Anelastic and Dielectric Effects in Polymeric Solids", Wiley, New York.

Modern Plastics, Charles H, (1999), " Modern Plastics Handbook", McGraw Hill.

Nevill AJ, Pepper MG, Whiting M, (1995), "In-shoe foot pressure measurement system utilising piezoelectric film transducers", Medical & Biological Engineering & Computing, vol.33, pp.76-81.

Olshansky R, Maurer DR, (1976), "Tensile strength and fatique of optical fibers", Journal of Applied Physics, vol.47, pp.4497-4499.

Othonos A, Kalli K, (1999), "Fibre Bragg Gratings: Fundamentals and applications in telecommunications and sensing", Artech House, Boston.

Othonos A, Lee X, (1995), "Novel and Improved Methods of Writing Bragg Gratings with Phase Masks", IEEE Photonics Technology Letters, vol.7, no.10, pp.1183-1185.

Ouellette F, (1987), "Dispersion cancellation using linearly chirped Bragg grating filters in optical waveguides", Optics Letters, vol.12, pp.847-850

Paek EG, Choe JY, Oh TK, (1998), "Transverse grating-assisted narrow-bandwidth acousto-optic tunable filter", Optics Letters, vol.23, no.16, pp.1322-1324.

Pataky Z, Faravel L, DaSilva J, Assal JP, (2000), "A new ambulatory foot pressure device for patients with sensory impairment. A system for continuous measurement of plantar pressure and a feed-back alarm", Journal of Biomechanics, vol.33, pp.1135-1138

Patterson RP, Fisher SV, (1979), "The accuracy of electrical transducers for the measurement of pressure applied to the skin", IEEE Trans. on Biomedical Engineering, vol.26, pp.450-456

Pinnock PR, Ward IM, (1966), Polymer, vol.7, pg.255

Pitei DL, (1998), "Foot ulceration in diabetes mellitus: methods of foot pressure measurement and neuro-vascular responses". A thesis submitted for the degree of Doctor of Philosophy at the University of London

Pollard JP, Le Quesne LP, Tappin JW, (1983), "Forces under the foot", Journal of Biomedical Engineering, vol.5, pp.37-40.

Prohaska JD, Snitzer E, Rishton S, Boegli V, (1993), "Magnification of mask fabricated fibre Bragg gratings", Electronics Letters, vol.29, no.18, pp.1614-1615.

Rangan CS, Sarma GR, Mani VS, (1994), "Instrumentation Devices and Systems", 13th reprint, McGraw-Hill New Delhi.

Reynolds DP, Lord M, (1992), "Interface load analysis for computer-aided design of below-knee prosthetic sockets", Medical & Biological Engineering & Computing, vol.30, pp.419-426

Rochford KB, Dyer SD, (1999), "Demultiplexing of interferometrically interrogated fiber Bragg grating sensors using Hilbert transform processing", Journal of Lightwave Technology, vol.17, no.5, pp.831-836.

Rose NE, Feiwell, LA, (1992), "A method for measuring foot pressures using a high resolution, computerised insole sensor: the effect of heel wedges on plantar pressure distribution and centre of force", Foot & Ankle, 13, pp.263-270

Sakai I, (1986), "Frequency-division multiplexing of optical-fibre sensors using a frequency-modulated source", Optical and Quantum Electronics, vol.18, pp.279-289.

Sanders JE, Daly CH, Burgess EM, (1992), "Interface shear stresses during ambulation with a prosthetic limb", Journal of Rehabilitation Research & Development, vol. 29, no.4, pp.1-8

Sanders JE, Daly CH, (1993), "Measurement of stresses in the three orthogonal directions at the residual limb-prosthetic socket interface", IEEE Trans on Rehabilitation engineering, vol.1, no.2, pp.79-85

Sanders JE, (1995), "Review: Interface mechanics in external prosthetics: review of interface stress measurement techniques", Medical & Biological Engineerng & Computing, vol.33, pp.509-516

Sanders JE, Silver-Thorn MB, Brienza DM, (1996), "Introduction to Soft Tissue Interfaces in Rehabilitation", IEEE Trans. on Rehabilitation Engineering, vol.4, no.4, pp.285-287.

Scales JT, (1990), "Pathogenesis of pressure sores". In Bader DL, (1990), "Pressure sores. Clinical practice and scientific approach", Macmillan Press, London.

Semenov AT, Shidlovski VR, Safin SA, (1993), "Wide-spectrum single-quantum well superluminescent diodes at 0.8μm with bent optical wave guide", Electronics Letters, vol.29, no.10, pp.854-856.

Senior JM, (1992),"Optical Fibre Communications", 2nd edition, Prentice Hall, London.

Shakelford J, Alexander W, Park J, (1994) "CRC Materials Science & Engineering Handbook", CRC Press.

Silfvast WT, (1996), "Laser Fundamentals", Cambridge University Press, New York.

Simon SR, Paul IL, Mansour J, Munro M, Abernethy PJ, Radin EL, (1981), "Peak dynamic force in human gait", Journal of Biomechanics, vol.14, no.12, pp.817-822.

Sirkis J, Berkoff TA, Jones RT, Singh H, Kersey AD, Friebele EJ, Putnam MA, "In-line fiber etalon (ILFE) fiber-optic strain sensors", IEEE Journal of Lightwave Tachnology, vol.13, no.7, pp.1256-1263.

Sugden K, Bennion I, Molony A, Copner NJ, (1994), "Chirped gratings produced in photosensitive optical fibres by fibre deformation during exposure", Electronics Letters, vol.30, no.5, pp.440-441.

Tappin JW, Pollard J, Beckett EA, (1980), "Method of measuring 'shearing' forces on the sole of the foot", Clinical Physics & Physiological Measurements, vol. 1, no. 1, pp.83-85

Timoshenko S, (1969), "Strength of Materials, Part I, Elementary Theory and Problems", Van Nostrand Reinhold Company.

Timoshenko SP, Gere JM, (1973), "Mechanics of Materials", Redwood Press.

Turner RD, Valis T, Hogg WD, Measures RM, (1990), "Fibre-optic strain sensors for Smart Structures", Journal of Intelligent Materials Systems and Structures, vol.1, pp.26-49.

Udd E, (1991), "Fiber Optic Sensors", Wiley Interscience, New York.

Varasi M, Signorazzi M, Vannucci A, Dunphy J, (1996), "A high-resolution integrated optical spectrometer with applications to fibre sensor signal processing", Meas. Sci. Technol., pp.173-178.

Varelas D, Limberger HG, and Salathe RP, (1997), "Enhanced mechanical performance of single-mode optical fibres irradiated by a CW UV laser", Electronics Letters, vol.33, pp.704-705.

Wagreich RB, Atia WA, Singh H, Sirkis JS, (1996), "Effects of diametric load on fibre Bragg gratings fabricated in low birefringent fibre", Electronics Letters, vol.32, no.13, pp.1223-1224.

Wagreich RB, Sirkis JS, (1997), "Distinguishing fibre Bragg grating strain effects", Proceedings of the 12th International Conference on Optical Fiber Sensors, Washington DC, 1997, Optical Society of America, OSA Technical Digest Series, vol.16, pp.20-24.

Ward IM., (1983), "Mechanical Properties of Solid Polymers", 2nd Ed., John Wiley &Sons Ltd., England.

Williams RB, Porter D, Roberts VC, (1992), "Triaxial force transducer for investigating stresses at the stump-socket interface", Medical & Biological Engineerng & Computing, vol.30, pp.89-96

Wilson A, James SW, Tatam RP, (1997), "Time-division-multiplexing of in-fibre Bragg gratings using a pulsed laser diode source", Proceedings from the 12th International Conference on Optical Fiber Sensors, 1997 OSA Technical Digest Series, vol.16, pp.475-478, Optical Society of America, Washington, DC, USA.

Wojtek JB, Eftimov TA, (1993), "Polarimetric and intermodal interference sensitivity to hydrostatic pressure, temperature, and strain of highly birefringent optical fibers", Optics Letters, vol.18, no.11, pp.1977-1979.

Wosinski L, Betend-Bon JP, Breidne M, Sahlgren B, Stubbe R, (1992), "Quasi-distributed fiber-optic sensor for simultaneous absolute measurement of strain and temperature", Proceedings of the 1st International Conference on Smart Structures and Materials, Glasgow, UK.

Xu MG, Geiger H, Archambault JL, Reekie L, Dakin JP, (1993), "Novel interrogating system for fibre Bragg grating sensors using an Acousto-Optic Tunable Filter", Electronics Letters, vol.29, no.17, pp.1510-1511.

PLATE 2 & 3

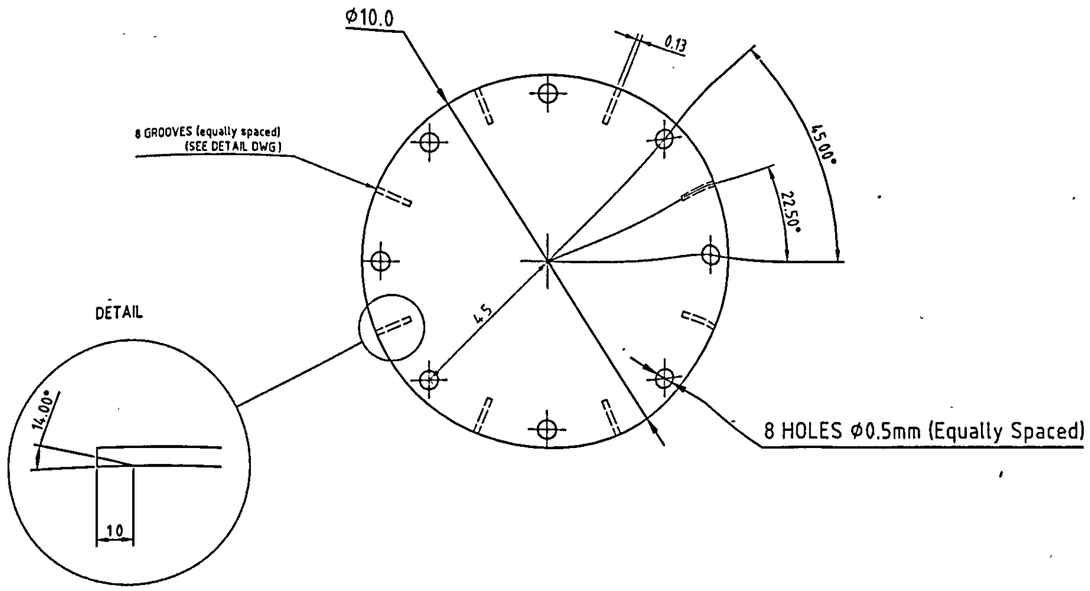

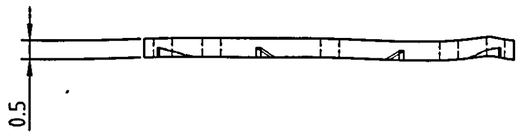

PLATE 1 & 4

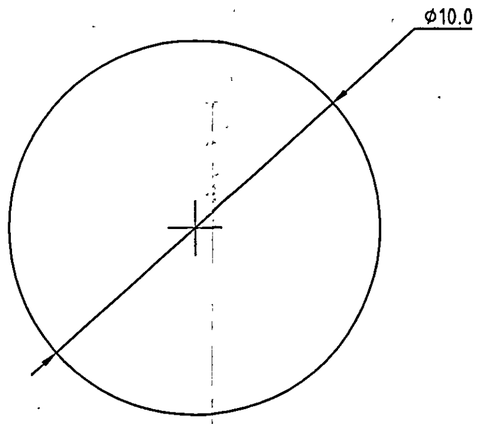

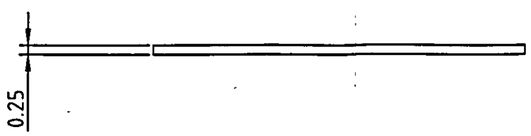

PIN

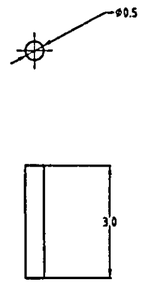

ASSEMBLY

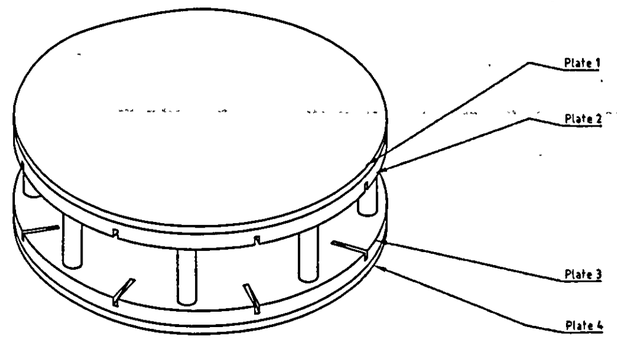

ASSEMBLY (actual size)

ISSUE	REMARKS	JOB NO.	CHANGE NOTE NO.

MATERIALS

ALL DIMENSIONS IN MILLIMETRES

TOLERANCES:

MM	TWO DECIMAL PLACES	+/- .05
	ONE DECIMAL PLACE	+/- .1
	NO DECIMAL PLACE	+/- .5
INS	THREE DECIMAL PLACES	+/- .005
	FRACTIONAL	+/- 1/64
ALL ANGULAR DIMENSIONS		+/- 1/2 DEGREE

ALL MACHINED SURFACES TO BE LESS THAN N8

SCALE 1:8

DRAWN S Hails

DATE 28.09.99

CHECKED

DATE

DEPT OF MEDICAL ENGINEERING & PHYSICS

DWG Part Drawing - Transducer 3

PROJECT Transducer

DWG NO. 350_003

KING'S HEALTHCARE